THE APPLICATION OF BRUSH SEALS TO STEAM TURBINE GENERATORS.

Jason S.Waite.

A thesis submitted in part fulfilment of the requirements for the degree of Doctor of Philosophy.

Department of Mechanical Engineering and Manufacturing Systems.
University of Northumbria at Newcastle

May 1999

ACKNOWLEDGEMENTS

I wish to express my thanks and appreciation to Dr. K. Leung of the Department of Mechanical Engineering and Manufacturing Systems, the University of Northumbria, for his supervision throughout the course of my study. Thanks also go to Professor P.K.Datta of the Surface Engineering Research Group, the University of Northumbria for the discussion and help given during the preparation of the thesis.

Thanks also go to Mr C.B.Jolly and Mr.C.Cordiner of Siemens Power Generation Limited, C.A. Parsons Works, for their continual assistance with background information and experimental leakage testing.

I am also appreciative of the assistance given to me by the technical staff and others, both at the University of Northumbria and at Siemens.

I hereby declare that: -

during the periods I have been registered for the degree of Ph.D., for which the thesis is submitted, I have not been a registered candidate for any other award of a university.

and

that I have attended: selected lectures from the Integrated Graduate Diploma Scheme in Corrosion and Materials engineering; internal seminars within the Surface Engineering Research Group of the University of Northumbria; annual symposia of the Institute of Corrosion; and followed the course of guided reading laid down by my supervisors.

ABSTRACT

THE APPLICATION OF BRUSH SEALS TO STEAM TURBINE GENERATORS.

By
Jason S. Waite.

This thesis addresses three aspects of the development of brush seals for blade tip sealing purposes in steam turbine generators associated with tribological aspects, experimental leakage testing and computational fluid dynamic modelling of brush seals.

An elaborate materials selection/screening process was carried out to identify the candidate brush seal bristle materials for the application of brush seals for steam turbines. 25 candidate bristle materials from 4 superalloy groups were tested against an uncoated steam turbine rotor steel in a purpose built (pin on wheel) high temperature wear rig at 540 °C. Pre and post test hardness, coefficient of friction, and weight change were recorded. The wear scars produced were examined using a scanning electron microscope **(SEM)** and energy dispersive x-ray spectroscopy **(EDAX)**.

The results demonstrated that iron oxides from the rotor steel were responsible for forming a wear resistant surface glaze on the contacting surfaces of the tribopair which, once formed, prevented further damage or extensive material removal from the tribopair. The tribopair surface wear scars appeared to be very similar under examination by **SEM** and **EDAX** for each test. No clear relationship between specific material properties and wear resistance was found for the materials tested. Haynes 25 the current gas turbine brush seal bristle material, was one of the materials recommended for further testing.

Back to back experimental leakage testing of conventional single labyrinth fins, single thickness and double thickness brush seals was carried out on a purpose built test rig. The rig and tests were designed to test large diameter (330 mm) brush seals under selected flow conditions encountered in steam turbines. A range of interferences and clearances were tested (-0.5, -0.2, 0, +0.5 and +0.9 mm). Shaft rotation (0-3000 rpm), shaft offset (0-0.9 mm), shaft eccentricity (0.5 mm peak to peak), shaft starting torque, and vibrational characteristics were variables that were explored.

The extensive range of test parameters was specifically aimed at generating a more comprehensive and realistic profile of brush seal operation for steam turbine application. The primary concern was to understand the changes in leakage characteristics of brush seals under changing operating conditions and due to changes in seal geometry. Examination of the extensive results provided evidence that can be compared to results from other studies. The leakage rates for single thickness and double thickness 330 mm brush seals in these tests were approximately 5% and 3 % respectively compared to the leakage rate through a single fin at the same clearance.

Computational Fluid Dynamics techniques were used to model brush seals in 2-dimensional form in radial and axial cross-section. Idealised bristle packing patterns were modelled and the results produced were used to calculate porosity coefficients. A further model was used to study bristle pack and backing plate clearance variations using different sets of porosity coefficients.

Plots from both model types allowed detailed examination of flow characteristics. The results and conclusions drawn can be used to improve the design and performance of future brush seals. It was found that non-Darcian porosity coefficients applied to an area of porous media/distributed resistance could be successfully used to model the leakage through the bristle pack. Calculated coefficients from the Bristle Packing Pattern Models were found to provide poor results when used in axial cross sectional/porous media modelling. Empirically determined porosity coefficients provided the best **CFD** results but the models were not sufficiently robust to predict seal performance for significant changes in geometry or conditions.

CONTENTS

1.0 INTRODUCTION.....1

2.0 LITERATURE REVIEW: - HIGH TEMPERATURE WEAR TESTING AND TRIBOLOGICAL ASPECTS OF BRUSH SEALS.. 17

2.1. INTRODUCTION. 17

2.2 BACKGROUND. 18

2.3 INTRODUCTION TO WEAR; CLASSIFICATION AND MECHANISM 22

2.4 MATERIALS SELECTION CRITERIA. 26

2.5 CLASSIFICATION OF SUPERALLOYS. 26

2.6 PREVIOUSLY USED BRISTLE MATERIALS. 29

2.7 LITERATURE REVIEW ON TRIBOTESTING OF BRUSH SEAL MATERIALS FOR GAS TURBINES..... 31

2.8 LITERATURE REVIEW ON THE GENERAL WEAR OF SUPERALLOY MATERIALS..... 38

2.9 FINAL CANDIDATE BRUSH SEAL BRISTLE MATERIAL SELECTION. 46

3.0 RATIONALE AND EXPERIMENTAL ASPECTS:- HIGH TEMPERATURE WEAR TESTING. 71

3.1 INTRODUCTION 71

3.2 DESIGN OF THE HIGH TEMPERATURE WEAR RIG 73

3.3 DESCRIPTION OF THE HIGH TEMPERATURE WEAR RIG. 78

3.4 150 MM ROTOR STEEL TEST WHEEL INITIAL SCREENING TESTS. 79

3.5 50 MM ROTOR SLEEVE TESTS. 80

3.6 OXIDATION TESTS. 80

3.7 PARAMETERS RECORDED. 80

3.8 SUMMARY OF THE MAIN AIMS. 83

4.0 RESULTS, DISCUSSION AND CONCLUSIONS ANDFURTHER WORK:- HIGH TEMPERATURE WEAR TESTING. 86

4.1 150 MM TEST WHEEL TESTS. 86

4.2 OXIDATION TESTS. 103

4.3 50 MM ROTOR STEEL SLEEVE TESTS. 105

4.4 GENERAL DISCUSSION. 114

4.5 FINAL CONCLUSIONS 116

4.6 RECOMMENDATIONS FOR FURTHER WORK. 117

5.0 LITERATURE REVIEW - EXPERIMENTAL LEAKAGE TESTING AND FLOW THROUGH BRUSH SEALS. 147

5.1 INTRODUCTION. 147

5.2 Introduction to Experimental Work. 149

5.3 Introduction to Theoretical Modelling of Leakage Flow through Brush Seals. 163

6.0 RATIONALE AND EXPERIMENTAL ASPECTS: - EXPERIMENTAL LEAKAGE TESTING..... 181

6.1 Introduction 181

6.2 Main Aims of the Tests. 182

6.3 Description of the Test Rig..... 182

6.4 Experimental Procedure 183

7.0 RESULTS, DISCUSSION, CONCLUSIONS AND FURTHER WORK: - EXPERIMENTAL LEAKAGE TESTING 192

7.1 Introduction. 192

7.2 Description, Comparison and Discussion of Experimental Leakage Test Results. 193

7.3 General Discussion. 208

7.4 Conclusions..... 208

7.5 Recommendations for Further Work..... 210

8.0 LITERATURE REVIEW: - COMPUTATIONAL FLUID DYNAMICS MODELLING OF BRUSH SEALS…….....230

8.1 Introduction 230

8.2 Background to flow through porous media. 231

8.3 Literature Review on the CFD Approach to Brush Seals. 233

9.0 RATIONALE AND EXPERIMENTAL ASPECTS: - COMPUTATIONAL FLUID DYNAMICS MODELLING OF BRUSH SEALS. 253

9.1 Introduction 253

9.2 CFD Modelling of Brush Seals 254

9.3 Effects to be Studied 258

10.0 RESULTS, DISCUSSION, CONCLUSIONS, AND FURTHER WORK: - COMPUTATIONAL FLUID DYNAMICS MODELLING OF BRUSH SEALS 262

10.1 Introduction 262

10.2 Comparison to results from the Brush Seal Leakage Test Rig..... 263

10.3 Brush Seal Bristle Packing Pattern Models. 264

10.4 Backing Plate (Labyrinth Fin) Model..... 269

10.5 Porous Media/Distributed Resistance Models. 273

10.6 General Discussion 277

10.7 Conclusions..... 279

10.8 Recommendations for Further Work..... 280

11.0 FINAL CONCLUSIONS AND FURTHER WORK.....305
11.1 FINAL CONCLUSIONS.....305
11.2 RECOMMENDATIONS FOR FURTHER WORK.....309
REFERENCES

LIST OF TABLES

Table 1.1 High pressure turbine rotor to cylinder clearance details..... 9
Table 1.2 Intermediate pressure turbine rotor to cylinder clearance details. 9
Table 1.3 Low pressure turbine rotor to cylinder clearance details. 9
Table 1.4 330 mm (13 inch) brush seal dimensions 10
Table 2.1 General operating conditions of a gas turbine and a steam turbine..... 48
Table 2.2 The Properties of Haynes 25..... 48
Table 2.3 Table 2.3 2% Chromium molybdenum nickel tungsten vanadium steel rotor forging..... 48
Table 2.4 Parameters often seen in wear equations. 49
Table 2.5 Classifications of wear processes..... 49
Table 2.6 Test conditions **(Hawthorne (1994)).** 49
Table 2.7 Details of flexible element materials **(Hawthorne (1994)).**..... 50
Table 2.8 Details of counterface materials **(Hawthorne (1994)).**..... 50
Table 2.9 Test conditions **(Atkinson and Bristol (1991)).**..... 50
Table 2.10 Test seal dimensions **(Atkinson and Bristol (1991)).**..... 51
Table 2.11 Hard coating compositions **(Atkinson and Bristol (1991)).**..... 51
Table 2.12 Bristle properties at 480 °C **(Atkinson and Bristol (1991)).**..... 51
Table 2.13 Room temperature combinations ranked by brush weight loss (gms) **(Atkinson and Bristol (1991)).**..... 52
Table 2.14 Room temperature combinations ranked by rotor scar depth (μm) **(Atkinson and Bristol (1991)).**..... 52
Table 2.15 480 °C rotor and brush wear at 100 hrs **(Atkinson and Bristol (1991)).**..... 52
Table 2.16 Wear/fatigue tests **(Derby and England (1992)).**..... 52
Table 2.17 Screening tests (ring-on-ring) **(Derby and England (1992)).**..... 53
Table 2.18. Primary tests **(Derby and England (1992)).**..... 53
Table 2.19 Brush specimen and current brush seal design geometries **(Fellenstein and Dellacorte (1994)).**.53
Table 2.20 Test Conditions **(Fellenstein and Dellacorte (1994)).**..... 53
Table 2.21 Wear factor interpretation to achieve goal of 10000 hours **(Fellenstein and Dellacorte (1994)).**.54
Table 2.22 I718 journal wear.* **(Fellenstein and Dellacorte (1994))**..... 54
Table 2.23 Haynes 25 brush wear **(Fellenstein and Dellacorte (1994)).** 54
Table 2.24 Haynes 25 brush vs I718 journal friction coefficient **(Fellenstein and Dellacorte (1994)).** 55
Table 2.25 Brush seal, and gas turbine engine specification and operating conditions **(Hendricks, Griffin, Bobula, Bill and Howe (1993)).**..... 55
Table 2.26 Test conditions **(Stott (1978)).** 56
Table 2.27 Test materials **(Stott (1978)).**..... 56
Table 2.28 A selection of the materials **(Stott (1978)).**..... 57
Table 2.29 Composition of Alloys **(Bhansali (1979)).**..... 57
Table 2.30.Test conditions **(Bhansali (1979)).**..... 57
Table 2.31 Wear volume (mm^3) as function of surface finish **(Bhansali (1979)).**..... 58
Table 2.32 Wear of base alloys **(Johnson, Moorhaouse and Nichols (1990))** 59
Table 2.33 Comparison of coefficients and compatibility ratings of metal pairs. 60
Table 2.34 Materials for high temperature wear tests..... 60
Table 3.1 Service and rig conditions..... 84
Table 3.2 Test preparation and analysis methods 84
Table 4.1. Pre-test and post-test hardness and weight change for the 7 hour, 10N, 5 m/s 150 mm rotor steel wheel tests. 118
Table 4.2 General description of glaze using SEM micrographs..... 119
Table 4.3 Oxide type previously found on High temperature wear scars. 119
Table 4.4 Weight change due to 7 hour oxidation tests.. 120
Table 5.1 Brush seal specification **(Carlile, Hendricks, and Yoder(1993)).**..... 168
Table 5.2 Test conditions **(Carlile, Hendricks, and Yoder(1993)).**..... 168
Table 5.3 Initial seal test matrix **(Carlile, Hendricks, and Yoder(1993)).**..... 169
Table 5.4 Parameter values for brush seals evaluated **(Chupp and Holle (1991)).** 170
Table 6.1 Brush seal leakage test rig rotor and seal fit details 189
Table 6.2 Brush seal leakage test rig seal specifications..... 190
Table 6.3 Details of high temperature wear rig instrumentation..... 191
Table 6.4 Test programme 192
Table 7.1 Comparison of pedestal vibration data with and without 60 psi pressure differential applied across the single thickness brush seals at 3000 r.p.m..... 211
Table 8.1 Comparison of flow rate (in^3/sec) results from FIDAP compared to Cross Manufacturing experimental results **(Mullen, Braun and Hendricks (1990)).**..... 248
Table 8.2 Physical characteristics and parameters used in the numerical computations **(Kudriavtsev and Braun (1995)).**..... 248
Table 8.3 Resistance coefficients for "blown down" clearance seals **(Turner, Chew and Long (1997)).**.... 248

Table 8.4 Brush Seal dimensions and brief comparison of some test details **(Chew and Hogg (1997)).**..... 249
Table 8.5 Resultant pressure differentials due to variations of the $PTDR_L$ **(Braun and Kudriavtsev (1993))**249
Table 9.1 Packing pattern model dimensions 260
Table 9.2 Porous media/distributed resistance model dimensions..... 260
Table 10.1 Comparison of Chew et al and CFD calculated C and k coefficients. 282

LIST OF FIGURES

Figure 1.1 A single cylinder 67 MW steam turbine. 11
Figure 1.2 A high pressure steam turbine showing the location of blade tip seals. 12
Figure 1.3 Turbine rotor shaft showing rows of rotating blades. 13
Figure 1.4 Turbine rotor shaft showing rows of rotating blades and labyrinth fins on the shaft and blade tips. 13
Figure 1.5 A comparison of labyrinth seal geometries. 14
Figure 1.6 A schematic of a typical brush seal configuration. 14
Figure 1.7 Frontal view (high pressure side) of a brush seal showing the front plate and bristle lay angle. ... 15
Figure 1.8 Back view (low pressure side) of a brush seal showing the backing ring/plate and bristle overhang. 15
Figure 1.9 End view of the brush seal bristle pack showing bristle packing density/pattern and the bristle ends. 16
Figure 1.10 Full view of the brush seal. 16
Figure 2.1 Illustration of variation in case to rotor clearance during engine operation. 62
Figure 2.2 Typical results from extended sliding of brush specimens, under moderate normal loads **(Hawthorne (1994))**. 62
Figure 2.3 Extended sliding test results from different brush / counterface specimens, under conditions indicated **(Hawthorne (1994)).** 63
Figure 2.4 Extended sliding test results from different brush, under conditions indicated **(Hawthorne (1994))**. 63
Figure 2.5 Relative wear ranking of different material combinations from short sliding tests (after running in) under moderate loads **(Hawthorne (1994))** 64
Figure 2.6 Summary of room temperature wear data 100 hour endurance **(Atkinson (1991)).** 64
Figure 2.7 Summary of room temperature leakage **(Atkinson (1991)).** 65
Figure 2.8 Hot rotor wear as a function of time **(Atkinson (1991)).** 65
Figure 2.9 Hot brush seal wear as a function of time **(Atkinson (1991)).** 66
Figure 2.10 Idealised thermogravimetric analysis (TGA) response for candidate alloys in wire form. 66
Figure 2.11 Brush wear factor, in mm^3/Nm for Haynes 25 cobalt based superalloy bristles sliding against I718 nickel based superalloy shaft. Wear factor goal for adequate wear life is 10^{-8} mm^3/Nm **(Fellenstein (1994))**. 67
Figure 2.12 Average friction coefficient of Haynes 25 tufts vs. I750 journal under various test conditions. Error bars represent standard deviation of averages of 9 test runs **(Fellenstein (1994)).** 67
Figure 2.13 Examples of irregular non-linear response of wear rate to operating parameters. 68
Figure 2.14 Plot of wear vs. sliding velocity **(Bhansali (1979)).** 68
Figure 2.15 Plot of applied load vs. wear volume : Sliding distance, 320 ft (2.19.5 m); applied load 90 lbf (40.9 kgf) **(Bhansali (1979)).** 69
Figure 2.16 Plot of sliding distance vs. wear volume **(Bhansali (1979)).** 69
Figure 2.17 The three common types of crystal structure. 70
Figure 2.18 Hot hardness values of some alloys. 70
Figure 3.1 High Temperature Wear Rig. 85
Figure 3.2 High Temperature Wear Rig. 85
Figure 4.1 Pre-test and post-test hardness of candidate brush seal bristle materials. 121
Figure 4.2 Weight change of 25 candidate bristle materials after 7 hours 10N and 5m/s in sliding contact with the 150 mm rotor steel test wheel. Results arranged in superalloy categories and in ascending pre-test hardness. 121
Figure 4.3 Weight change of 25 candidate bristle materials plotted against pre-test and post-test hardness after 7 hours 10N and 5m/s in sliding contact with the 150 mm rotor steel test wheel. 122
Figure 4.4 Pre-test hardness plotted against weight change of 25 candidate bristle materials after 7 hours 10N and 5m/s in sliding contact with the 150 mm rotor steel test wheel. 122
Figure 4.5 **SEM** micrographs and **EDAX** digimaps of Haynes 25 surface after 7 hours at 540 °C in sliding contact with the 150 mm rotor steel test wheel. 123
Figure 4.6 **SEM** micrographs and **EDAX** digimaps of X-750 surface after 7 hours at 540 °C in sliding contact with the 150 mm rotor steel test wheel. 124
Figure 4.7 **SEM** micrographs and **EDAX** digimaps of Waspalloy surface after 7 hours at 540 °C in sliding contact with the 150 mm rotor steel test wheel. 125
Figure 4.8 **SEM** micrographs and **EDAX** digimaps of Ultimet surface after 7 hours at 540 °C in sliding contact with the 150 mm rotor steel test wheel. 126
Figure 4.9 **SEM** micrographs and **EDAX** digimaps of Rotor Spec 297 surface after 7 hours at 540 °C in sliding contact with the 150 mm rotor steel test wheel. 127
Figure 4.10 Coefficient of Friction against Time for Cobalt Base Candidate Bristle Materials. 128
Figure 4.11 Coefficient of Friction against Time for Nickel Base Solution Hardened Candidate Bristle Materials. 128
Figure 4.12 Coefficient of Friction against Time for Nickel Base Age Hardening Candidate Bristle Materials.
Figure 4.13 Coefficient of Friction against Time for Iron Base Candidate Bristle Materials. 129

Figure 4.14 Weight change due to exposure to air at 540 °C for 7 hours. 130
Figure 4.15 **EDAX** cross-sectional digimaps of Haynes 25 sample wear track showing possible trace elements. After 3 hours at 540 °C in sliding contact with the 50 mm rotor steel test wheel. 131
Figure 4.16 **EDAX** cross-sectional digimaps of Haynes X-750 sample wear track showing possible trace elements. After 3 hours at 540 °C in sliding contact with the 50 mm rotor steel test wheel. 132
Figure 4.17 **EDAX** cross-sectional digimaps of Waspaloy sample wear track showing possible trace elements. After 3 hours at 540 °C in sliding contact with the 50 mm rotor steel test wheel. 133
Figure 4.18 **EDAX** cross-sectional digimaps of Haynes 718 sample wear track showing possible trace elements. After 3 hours at 540 °C in sliding contact with the 50 mm rotor steel test wheel. 134
Figure 4.19 **EDAX** cross-sectional digimaps of rotor steel Spec. 297 sample wear track showing possible trace elements. After 3 hours at 540 °C in sliding contact with the 50 mm rotor steel test wheel. 135
Figure 4.20 **EDAX** cross-sectional digimaps of possible trace elements from test wheel on a sample of rotor steel Spec. 297 exposed to 540 °C for 3 hours (no wear). 136
Figure 4.21 **EDAX** surface digimaps of rotor steel Spec. 297 showing possible trace elements from test wheel and Haynes 25 sample. After 3 hours at 540 °C in sliding contact with the 50 mm rotor steel test wheel. 137
Figure 4.22 **EDAX** surface digimaps of rotor steel Spec. 297 showing possible trace elements from test wheel and Ultimet sample. After 3 hours at 540 °C in sliding contact with the 50 mm rotor steel test wheel. 138
Figure 4.23 **EDAX** surface digimaps of rotor steel Spec. 297 showing possible trace elements from test wheel and Haynes X-750 sample. After 3 hours at 540 °C in sliding contact with the 50 mm rotor steel test wheel. 139
Figure 4.24 **EDAX** surface digimaps of rotor steel Spec. 297 showing possible trace elements from test wheel and Waspalloy sample. After 3 hours at 540 °C in sliding contact with the 50 mm rotor steel test wheel. 140
Figure 4.25 **EDAX** surface digimaps of rotor steel Spec. 297 showing possible trace elements from test wheel and Haynes 718 sample. After 3 hours at 540 °C in sliding contact with the 50 mm rotor steel test wheel. 141
Figure 4.26 **EDAX** cross-sectional digimaps of rotor steel Spec. 297 test sleeve showing possible trace elements from test wheel and Haynes 25 sample. After 3 hours at 540 °C in sliding contact with the 50 mm rotor steel test wheel. 142
Figure 4.27 **EDAX** cross-sectional digimaps of rotor steel Spec. 297 test sleeve showing possible trace elements from test wheel and Ultimet sample. After 3 hours at 540 °C in sliding contact with the 50 mm rotor steel test wheel. 143
Figure 4.28 **EDAX** cross-sectional digimaps of rotor steel Spec. 297 test sleeve showing possible trace elements from test wheel and Haynes X-750 sample. After 3 hours at 540 °C in sliding contact with the 50 mm rotor steel test wheel. 144
Figure 4.29 **EDAX** cross-sectional digimaps of rotor steel test Spec. 297 sleeve showing possible trace elements from test wheel and Waspalloy sample. After 3 hours at 540 °C in sliding contact with the 50 mm rotor steel test wheel. 145
Figure 4.30 **EDAX** cross-sectional digimaps of rotor steel test Spec. 297 sleeve showing possible trace elements from test wheel and Haynes 718 sample. After 3 hours at 540 °C in sliding contact with the 50 mm rotor steel test wheel. 146
Figure 5.1 Sketches of typical flow formations in brush seals 171
Figure 5.2 Effect of surface finish on bristle wear **(Ferguson (1988))**. 171
Figure 5.3 Sealing performance of brush seals compared with various five-finned labyrinth seals at a pressure ratio of 2.0 **(Ferguson (1988))**. 172
Figure 5.4 Graph showing effective bristle closure with pressure **(Ferguson (1988))**. 172
Figure 5.5 Effect of rotational speed on leakage flow test results **(Ferguson (1988))**. 173
Figure 5.6 Typical pressure/leakage curve for a 5.1" diameter brush seal **(Flower (1990))**. 173
Figure 5.7 Typical pressure/leakage curve after offset test for a 5.1" diameter brush seal **(Flower (1990))**. 174
Figure 5.8. Typical hysteresis loop **(Flower (1990))**. 174
Figure 5.9 Analytical predictions of flow and pressure drop as functions of clearance for the experimental results from Cross Mfg. 130 mm (5.1 in.) brush seal **(Hendricks et al (1991))**. 175
Figure 5.10 Analytical predictions of flow and pressure drop as functions of clearance for a 38 mm (1.5 in.) brush seal **(Hendricks et al (1991))**. 175
Figure 5.11 Generalised brush seal static and dynamic performance. Seal leakage parameter, f - lbm °R/lbf-sec (10^3) **(Holle and Krishnan (1991))**. 176
Figure 5.12 Typical brush seal leakage characteristics during accelerated wear rate endurance tests in the high temperature seal test rig. Seal leakage parameter, f - lbm °R/lbf-sec (10^3) **(Holle and Krishnan (1991))**. 176
Figure 5.13 Variation of measured and predicted mass flows, m, with pressure ratio, Rp **(Bayley and Long 1992))**. 177

Figure 5.14 Comparison of measured and calculated flow performance for the labyrinth seal **(Chupp and Nelson (1992)).** 177
Figure 5.15 Engine simulation cycle results for brush seal configurations #1 and #5 **(Chupp and Nelson (1992)).**. 178
Figure 5.17 Measured flow performance for a brush seal configuration #4 with a smaller backplate gap. **(Chupp and Dowler (1992)).** 178
Figure 5.18 Measured flow performance for brush seal configuration #8 with two seals in series **(Chupp and Dowler (1992)).**. 179
Figure 5.19 Measured flow performance for brush seal configuration #A1 manufactured by a second vendor **(Chupp and Dowler (1992)).** 179
Figure 5.20 Cross plot of flow performance data from Cross Manufacturing showing effect of increasing backplate gap **(Chupp and Dowler (1992)).** 180
Figure 5.21 Uniformly staggered cylinder arrangement modelling an average random bristle bed. 180
Figure 6.1 Schematic of the Brush Seal Leakage Test Rig 190
Figure 6.2 Photograph of the Brush Seal Leakage Test Rig. 190
Figure 6.3 Photograph of the stepped rotor lands after testing showing wear tracks on all five lands. 191
Figure 7.1 A Comparison of measured and calculated leakage flows for a single fin labyrinth seal. 212
Figure 7.2 Measured flows for a single fin labyrinth seal with a rotating shaft. 213
Figure 7.3 Leakage rate through one single thickness seal with two identically handed seals installed. 214
Figure 7.4 The starting torque required to turn the shaft from rest with two single thickness, oppositely handed seals installed. 215
Figure 7.5 The effect of an offset rotor on the leakage rate of one single thickness brush seal with two identically handed seals installed (where the offset is approximately equal to the installed interference.)216
Figure 7.6 The effect of an offset rotor on the leakage rate of one single thickness brush seal with two identically handed seals installed. 217
Figure 7.7 The effect of an offset rotor on the leakage rate of one single thickness seal with two identically handed seals installed (where offset is approximately equal to the installed clearance.) 218
Figure 7.8 Measured leakage flows for one single thickness brush seal with ... two single thickness oppositely handed seals installed. 219
Figure 7.9 Measured leakage flows for one single thickness brush seal with two single thickness oppositely handed seals installed. 220
Figure 7.10 Measured leakage flows for one single thickness brush seal with two single thickness, oppositely handed seals installed. 221
Figure 7.11 Figure 8.11 Waterfall plot of the vibrational characteristics of the **BSLTR** bearing pedestals during run-down with no seals installed and no pressure differential. 222
Figure 7.12 Waterfall plot of the vibrational characteristics of the **BSLTR** bearing pedestals during run-down with two single thickness brush seals installed and a 4 bar pressure differential. 223
Figure 7.13 Leakage rate through one double thickness seal with two identically handed seals installed. ... 224
Figure 7.14 Comparison of leakage for a single fin labyrinth seal to single and double thickness brush seals with comparable fin and backing ring clearances. 225
Figure 7.15 The effect of a 0.50 mm (peak -peak) rotor eccentricity on the leakage for a 0.2 mm bristle interference fit for a single thickness brush seal. 226
Figure 7.16 The effect of a 0.50 mm (peak-peak) rotor eccentricity on the leakage for a size for size bristle fit for a single thickness brush seal. 227
Figure 7.17 The effect of a 0.50 mm (peak-peak) rotor eccentricity on the seal. 228
Figure 7.18 Photograph of the stepped rotor showing the wear tracks on all five lands.. 229
Figure 8.1 Schematic of the two model geometries generated for use with **FIDAP (Mullen, Braun and Hendricks (1990)).** 250
Figure 8.2 Seven of the basic brush seal models tested **(Braun and Kudriavstev (1993))** 250
Figure 8.3 Schematic of the brush seal and cavity arrangement tested **(Kudriavtsev and Braun (1995).** .. 251
Figure 8.4 Schematic depiction of the domain enclosing a streamwise repeating module of bristles **(Sharatchandra and Rhode (1996)).** 251
Figure 8.5 Schematic of brush seal **(Chew, Lapworth and Millener (1995)).** 252
Figure 8.6 Schematic of the experimental brush seal **(Turner, Chew and Long (1997).** 252
Figure 9.1 Schematic of the Bristle Packing Pattern Model. 261
Figure 9.2 Schematic of the Porous Media/Distributed Resistance Model. 261
Figure 10.1 A graph of experimental results from the Brush Seal Leakage Test Rig for comparison to **CFD** results. 283
Figure 10.2 Finite element grid plot of the "Square" packing pattern. 284
Figure 10.3 Pressure plot of the "Square" packing pattern. 285
Figure 10.4 Velocity vector plot of the "Square" packing pattern. 286
Figure 10.5 Finite element grid plot of the "Hexagonal" packing pattern. 287
Figure 10.6 Pressure plot of the "Hexagonal" packing pattern. 288
Figure 10.7 Velocity vector plot of the "Hexagonal" packing pattern 289
Figure 10.8 Inlet velocity against pressure differential for "Square" and "Hexagonal" bristle packing patterns. 290

Figure 10.9 Theoretical inlet velocity against pressure differential comparing **Chew et al** and CFD calculated C and k coefficients. 290
Figure 10.10 Line plot of the Backing Plate Model. 291
Figure 10.11 Finite element mesh of the Backing Plate Model. **BPC**=1 mm. 292
Figure 10.12 Pressure plot of the Backing Plate Model. **BPC**=1 mm. 293
Figure 10.13 Velocity vector plot of the Backing Plate Model. **BPC**=1 mm. 294
Figure 10.14 Finite element mesh of the Backing Plate Model. **BPC**=1.8 mm. 295
Figure 10.15 Pressure distribution plot of the Backing Plate Model. **BPC**=1.8 mm. 296
Figure 10.16 Velocity vector plot of the Backing Plate Model. **BPC**=1.8 mm. 297
Figure 10.17 Comparison of **CFD** and experimental leakage results for fins with different **BPC** with and without swirl. 298
Figure 10.18 Pressure plot of the Porous Media Model. **BPC**=1 mm, **BSC**=0 mm. 399
Figure 10.19 Velocity vector plot of the Porous Media Model. **BPC**=1 mm, **BSC**=0 mm. 300
Figure 10.20 Pressure plot of the Porous Media Model. **BPC**=1.8 mm, **BSC**=1 mm. 301
Figure 10.21 Velocity vector plot of the Porous Media Model. **BPC**=1.8 mm, **BSC**=1 mm. 302
Figure 10.22 A comparison of **CFD** and experimental leakage results for a brush seal with and without swirl **BPC**=1 mm, **BSC**=0 mm. 303
Figure 10.23 A comparison of **CFD** leakage results for a brush seal with and without swirl **BPC**=1.8 mm, **BSC**=1 mm. 303
Figure 10.24 A comparison of **CFD** and experimental leakage results for different porosity coefficients **BPC**=1 mm, **BSC**=0 mm. 304
Figure 10.25 Comparison of calculated leakage results directly from **Chew et al** and recalculated results from **CFD** using **Chew et al** coefficients. 304

1.0 Introduction.

Large land based steam turbine generators are used throughout the power generation industry to generate electricity. Increasing concern over the depletion and cost of the raw materials required to power this plant have given continuing impetus to improve the efficiency of the equipment (i.e. to generate more electricity per unit of fuel). This project is concerned with improving the efficiency of a key component area within the steam turbine, known as "blade tip sealing".

Steam turbine generator operation can be described very simply as follows. Fuel (oil, gas, coal, or nuclear) is used to boil water and generate high pressure, high temperature steam. This steam is allowed into the high pressure **(HP)** inlet **(Figure 1.1-1.2)** of the steam turbine, where it encounters large numbers of circular rows of blades **(Figure 1.3-1.4).**

The rows alternate between stationary blades connected to the turbine casing and rotating blades connected to the turbine rotor. The stationary blades are designed to guide the flow of steam onto the rotating blades. The guiding action maximises the potential for work when the flow impinges on the rotating blades. The latter are aerodynamically designed to generate rotation of the turbine rotor they are attached to. Shaft rotation is eventually converted to electricity by the generator.

The rotating blade tips pass close to the turbine casing. The stationary blade tips are in close proximity to the rotor **(Figure 1.2)**. A working clearance (e.g. 0.9 mm) must be maintained, as contact between the rotating and stationary surfaces would cause damage and possibly failure of the components (blades/seals/casings). The clearance is calculated from the maximum expected thermal and mechanical expansion of both surfaces throughout the operating cycle, vibration and flexure characteristics of the system, movement of the rotor within the bearings under changing loads and a safety factor to

allow for transient unpredictable rotor excursions. Examples of the resulting changes in clearance were summarised in **Table 1.1-1.3.**

Steam that flows through the blade tip clearance is known as parasitic leakage or secondary loss. Parasitic blade tip leakage makes no contribution to useful work and is thought to detrimentally interfere with the steam flow that is travelling towards the next blade row.

Attempts to reduce blade tip leakage have been made since the invention of the steam turbine. Labyrinth seals are the most popular **(Figure 1.4-1.5)**. They consist of a series of knife-edged rings (fins) machined or located onto the exposed periphery of the blade rows. The fins are sometimes made from a softer material (e.g. phosphor bronze) than the journal they are adjacent to and their thin section would preferentially and quickly wear without dramatically damaging the journal in the event of a transient shaft excursion. Steam passing through the series of fins, encounters tight constrictions followed by expansion and recirculation cavities. The process of throttling followed by expansion causes turbulence and dissipates kinetic energy. The multi-finned sealing arrangement therefore offers a far superior seal to that of a seal with the same minimum clearance and axial width, without the expansion cavities.

Gas turbines and steam turbines are typically designed to be assembled and stripped in completely different ways. Steam turbines are designed with a horizontal split in the main outer casing. The split casing allows the assembled rotor shaft and rotating blades to be lowered vertically onto its bearing housings. The rotating blades are interspersed with static blades found in the lower half of the casing. Very little axial movement of the rotating blades relative to the stationary blades is allowable to ensure safe and efficient operation. The top half of the casing (which contains the top section of static blades) can then be lowered and the joint sealed. Gas turbine engines are assembled into a full casing. The rotor assemblies are designed to be assembled horizontally into the casing. This has a great effect on the type and nature of blade tip seals that can be used. Gas turbine labyrinth

seals consisted of "non-interleaved" or "straight through" designs **(Figure 1.5)**. Steam turbines tend to use the more efficient "interleaved" type. Other designs include chevron, vernier, stepped, and castellated arrangements. Further developments were spring-backed seals and abradable inserts of honeycomb or feltmetal (for the fins to rub on if the clearance was reduced). These designs attempted to preserve the fin whilst reducing the forces on the rotor if contact occurred. After a hard rub situation, sealing would be marginally impaired but would still be relatively efficient.

More recently, improvements in materials manufacture and technology have allowed the development of a new type of blade tip seal. These seals were generally known as compliant contacting seals. One compliant seal is the brush seal **(Figure 1.6-1.10)**. Typical seal dimensions are given in **Table 1.4**. The seal consists of a ring of bristles sandwiched between two supporting plates. The front (upstream) plate is usually small in radial height starting at the seal outside diameter. The downstream plate or backing plate/ring is again attached at the seal outside diameter and is usually larger, providing axial support to the bristle pack over nearly all of its radial height.

Brush seals are manufactured by feeding individual lengths of wire (for the bristles) from a large number of spools through a machine that gathers them together in a tight bunch (a tuft) and places a tight plastic sleeve around one end. The tuft is then cropped to the required length. Using a large number of spools ensures that individual tufts have a similar average material specification. The tufts are then inserted into **CNC** drilled holes in a regular pattern in the periphery of the seal. The wire bristles (usually made from 0.071 mm diameter, Haynes 25) protrude radially inwards at an angle of approximately 45 degrees and are eventually ground to a specific internal diameter that also leaves a smooth bore of bristle tips. When the brush seal is installed in its appropriate housing the bristle tips provide the design interference or clearance with the rotor.

The backing plate clearance (e.g. 1.5 mm) must be maintained to allow for radial shaft movements whilst the bristle pack provides the compliant, flexible part of the seal.

The backing plate clearance **(BPC)** is usually greater than that of a labyrinth seal as the backing plate is made from a wear resistant superalloy material and in the event of a hard rub the backing plate would not preferentially wear as a labyrinth fin would. The designed bristle pack interference is usually in the order of 0.2 mm. A welding process is used to fuse together the outside diameters of the side plate, backing ring and the bristle ends sandwiched between them. At this point the plastic sleeve melts. Machining the weld forms the outside diameter of the seal, which can then be fitted into a suitable housing. The backing plate prevents the bristle tips from "blowing under" by offering axial support. The angle of the bristles allows them to comply with radial movements of the rotor. The bristles should flex (rather than buckle) and can be modelled under ideal conditions using simple cantilever theory. The surface adjacent to the bristle tips (the rotor surface) is usually coated with a hard wear resistant coating (alumina, chromium oxide, chromium carbide, and tungsten carbide) in gas turbine engines, to avoid damage caused by the rubbing.

Careful quality and manufacturing control are essential for the optimum operation of the brush seal. Damage is easily incurred and usually results in localised irregularities in the sealing. The bristle pack is encapsulated in wax after manufacture to reduce the risk of damage during the installation process. The wax melts when the brush is installed and exposed to high temperatures.

The brush seal was primarily developed for use in limited life (10000 hours between strip down) military aircraft powered by gas turbine engines. Their success has aroused interest and subsequently studies have been carried out to apply brush seals to commercial aircraft aero engines and large land based gas turbine generators **(Mahler and Boyes (1995)), Chupp, Johnson and Loewenthal (1995)).** The natural progression would be to apply brush seals to steam turbine generators.

The foremost advantage of the brush seal over (5 finned) straight through labyrinth seals is the reported parasitic leakage reduction of up to 90% **(Ferguson (1990)).** Other sources report smaller but still impressive improvements of between a third and a quarter

(Flower (1990), Gorlov et al (1988)). The improvements in parasitic leakage flow are closely associated with the specific conditions in the operating environment. The experimental results were, in many cases, for seals that were significantly different in geometry and subjected to inappropriate operating conditions compared to those encountered in steam turbine applications.

Attempts have been made by other researchers to experimentally quantify the effects of some of the brush seal design and operational variables and parameters **(Chapter 5)**. These included changes in backing plate clearance **(BPC)**, changes in brush seal bristle pack clearance **(BSC)** and interference **(BSI)**, changes in pressure differential, the effect of shaft rotation, the effect of eccentric and offset shaft rotation, changes in operating fluid, changes in bristle material, changes in bristle diameter, changes in bristle lay angle, changes in bristle packing density, and changes in bristle pack thickness. However the relationship between the design geometry and operating characteristics were still not fully understood and experimental results were limited. There were no experimental results for operating conditions applicable to brush seals in steam turbines.

The major drawback to contacting compliant seals is the wear of one or both of the tribopair. If the brush seal bristles or the rotor land they are adjacent to wear, the resulting clearance would allow increased leakage to occur. Increased clearances can have a tremendous effect on overall turbine efficiency. As little as less than 1 % blade tip leakage can equate to millions of pounds throughout the plant lifetime. The degree and nature of wear in brush seal bristles and the adjacent land was largely undetermined (or proprietary) for brush seals for gas turbines. Several studies (that are discussed in **Chapter 2**) attempted to select improved tribopairs for brush seal bristle packs and rotor land coating for gas turbines. The materials selection process was based on the operating requirements of a gas turbine but the experimental testing in many cases had little in common with the difficult to simulate conditions in a gas turbine.

The rotor shafts adjacent to brush seals in gas turbines are treated with a wear resistant surface coating. It was desirable to run brush seals against an uncoated rotor due to the difficulty and cost of applying a surface coating. It was also apparent that the operating conditions and requirements in gas turbine engines are substantially different to those in steam turbine generators. The tribological variables include working fluid, operating temperature, rubbing speed, pressure differential, contact pressure, rotor surface coating and rotor surface finish. No materials selection process or experimental work had previously been carried out to apply brush seals to steam turbine.

The specific wear rates of brush seals and the adjacent land required quantifying to enable the continuing calculation of leakage rates throughout their service life. Unpredictable leakage rates could have serious effects on the sensitive flow paths within turbine generators.

There was an ever increasing demand to reliably predict the leakage rate through brush seals of different geometries and under different operating conditions through numerical and theoretical methods. Theoretical methods could offer a quicker and cheaper alternative to prototype seal manufacture and experimental leakage testing. Several attempts have been made to produce numerical models. These are described in **Chapter 5**. The models produced so far have shown promising results when compared to specific experimental results but have lacked universal applicability when faced with new applications with different seal geometries and operating conditions. This is especially the case when the brush seal installed geometry changes from a **BSI** to a **BSC.**

More recently emphasis had been directed towards the calculation of leakage flow using Computational Fluid Dynamics **(CFD)** to produce bristle packing pattern models and porous media models **(Chapter 9)**. **CFD** analysis has enabled the theoretical calculation and examination of flow patterns surrounding brush seals and bulk flow predictions for changes in brush seal geometries. The flow patterns were compared to experimental flow visualisation results and the bulk flow predictions were compared to experimental leakage

results. To date the **CFD** models have been promising but were again not universally applicable to changes in brush seal geometry without a greater range of resistance coefficients. The resistance coefficients are most reliably calculated empirically from experimental leakage results.

This thesis explores the three main inter-related areas of brush seal design and operation for their application to steam turbines. An increased understanding of the fluid dynamics and tribological aspects of the brush seal would enable confidence in the predicted efficiency improvements. This increased confidence is an essential step towards the eventual implementation of the sealing technology and a realisation of the savings (fuel/money) associated with improved overall turbine efficiency. The financial saving is predicted to be well in excess of the installation costs of the new seals.

Tribological aspects were addressed by carrying out a literature review on high temperature (unlubricated) wear and materials testing of brush seals for gas turbines. The specific operating conditions and requirements were identified and a materials selection process was carried out for the brush seal bristle material for steam turbines. A single cylinder rotor steel was taken to be the rotating component of the tribopair. The selected materials were then tested in a purpose built high temperature wear rig. The results of the wear tests from the bristle samples and the rotor materials are compared and contrasted in **Chapter 4**. The results help to identify the method and mode of wear from both the bristle and the rotor material and to identify the most suitable bristle material for operation in a steam turbine with an uncoated shaft. General materials properties and test results that were previously associated with wear resistance are also examined and relationships are drawn. The most promising materials are identified and suggested for further development testing under more representative conditions or in service.

The lack of representative experimental leakage testing results applicable to steam turbine prompted a further literature review on experimental leakage testing **(Chapter 5)**. Further to the findings of the literature review an experimental leakage test rig was

designed and built to specifically examine leakage flow effects through real brush seals under more realistic steam turbine operating conditions **(Chapter 6)**. Large (330 mm) diameter, single and double thickness brush seals were tested at a range of **BPC, BSI/C**, pressure differentials, shaft rotating speeds, shaft offsets and eccentricities. A labyrinth fin was also tested for comparison **(Chapter 7)**. The results are plotted and comparisons to the current blade tip sealing methods are made. The leakage results are also used as a comparison for the theoretical work.

CFD work was carried out using **FLOTRAN**, part of the **ANSYS** finite element package. This work modelled the brush seal in radial cross-section as a series of cylinders in regular packing arrangements. Velocity and pressure distribution patterns can be seen in **Chapter 10** and the bulk flow predictions were used to calculate porosity coefficients. The **CFD** work continued to model the brush seal in axial cross-section with the bristle pack being modelled as an area of distributed resistance or porous media. Non-linear resistance coefficients were set in three orthogonal directions. The coefficients were either from published work, from the experimental leakage tests or from the bristle packing pattern models. Several **BPC** and **BSC** were modelled for a range of pressure differentials. The flow patterns were plotted and bulk flow values calculated. These are shown in **Chapter 10** and are compared to experimental findings.

The thesis is composed of eleven chapters. After the introduction **(Chapter 1)**, the thesis is split into the three main research areas, Tribological Aspects **(Chapters 2, 3, and 4)**, Flow Through Brush Seals **(Chapters 5, 6, and 7)**, and **CFD** Analysis of Brush Seals **(Chapters 8, 9 and 10)**. Within the three research areas, the chapters included a literature review, experimental aspects and rationale, results and discussion, conclusions and further work. **Chapter 11** is the final chapter and includes final conclusions and further work.

Table 1. 1 High pressure turbine rotor to cylinder clearance details.

Component	**Value**	**Method of determining values**
Bearings-Lift.	0.1 mm	Calculated using classical hydrodynamic bearing theory- with allowances for jacking oil
Bearings Relative Vibration.	<0.26 mm	As recommended by ISO7919-2
Bearings Relative Vibration Aim.	0.025-0.040	Usually achieved.
Expansion-Pressure, Thermal, Centrifugal.	<0.28 mm	Calculated using finite element of blades and casing.
Casing Ovality (unbolted, prior to heat treatment).	<1.5 mm	Measured.
Hard Seal Clearance.	1.0 mm	No rubbing.
Spring Back Seal Clearance.	0.4-0.6 mm	Some rubbing.

Table 1.2 Intermediate pressure turbine rotor to cylinder clearance details.

Component	**Value**	**Method of determining values**
Bearings-Lift.	0.15 mm	Calculated using classical hydrodynamic bearing theory- with allowances for jacking oil
Bearings Relative Vibration.	<0.26 mm	As recommended by ISO7919-2.
Bearings Relative Vibration Aim.	0.025-0.040	Usually achieved.
Expansion-Pressure, Thermal, Centrifugal First Stage.	<0.42 mm	Increase.
Last Stage.	<0.44 mm	Decrease.
Casing Ovality (unbolted, prior to heat treatment).	<2.0 mm	Measured.

Table 1.3 Low pressure turbine rotor to cylinder clearance details.

Component	**Value**	**Method of determining values**
Bearings-Lift.	0.2-0.25 mm	Calculated using classical hydrodynamic bearing theory- with allowances for jacking oil and measured.
Bearings Relative Vibration.	<0.26 mm	As recommended by ISO7919-2.
Bearings Relative Vibration Aim.	0.025-0.040	Usually achieved.
Expansion-Pressure, Thermal, Centrifugal.	N/A	N/A
Casing Ovality (unbolted, prior to heat treatment).	<2.0 mm	Measured.
Hard Seal Clearance.	1.5-2.2 mm	No rubbing.
Spring Back Seal Clearance.	1.0-1.7 mm	Some rubbing.

Table 1.4 330 mm (13 inch) brush seal dimensions.

Brush seal details	**Dimension**
Bristle Bore (mm)	327 mm
Backing Ring Bore (mm)	328.832 mm
Backing Ring Height (mm)	14.4 mm
Backing Ring Outside Diameter (mm)	357.632 mm
Bristle Overhang (mm)	0.918 mm
Bristle Pack Thickness (mm)	≈ 1 mm
Bristle Free Length (mm)	16 mm
Backing Arrangement Thickness (mm)	3.9 mm
Number of Bristles Wide	11 bristles wide
Number of Bristles per inch of circumference	2250 (89)-2650 (104) bristles per inch (mm) of circumference
Bristle Thickness	$1.1e^{-4}$ mm
Bristle Angle	45 degrees

No	Name	Proposed application of brush seal.
1	Bearing pedestal oil seal	Possible
2	Bearing seal	Not applicable
3	Bearing seal	Not applicable
4	Turbine gland (HP end)	Possible
5	Dummy piston	Possible
6	Cylinder blade tip/shaft seal first row (HP)	Possible
7	Rotating blade tip/cylinder seal first row (HP)	Possible
8	Cylinder blade tip/shaft seal last row (HP)	Possible
9	Rotating blade tip/cylinder seal last row (HP)	Possible
10	Cylinder blade tip/shaft seal last row (LP)	Possible
11	Turbine gland (LP end)	Possible
12	Bearing seal	Not applicable

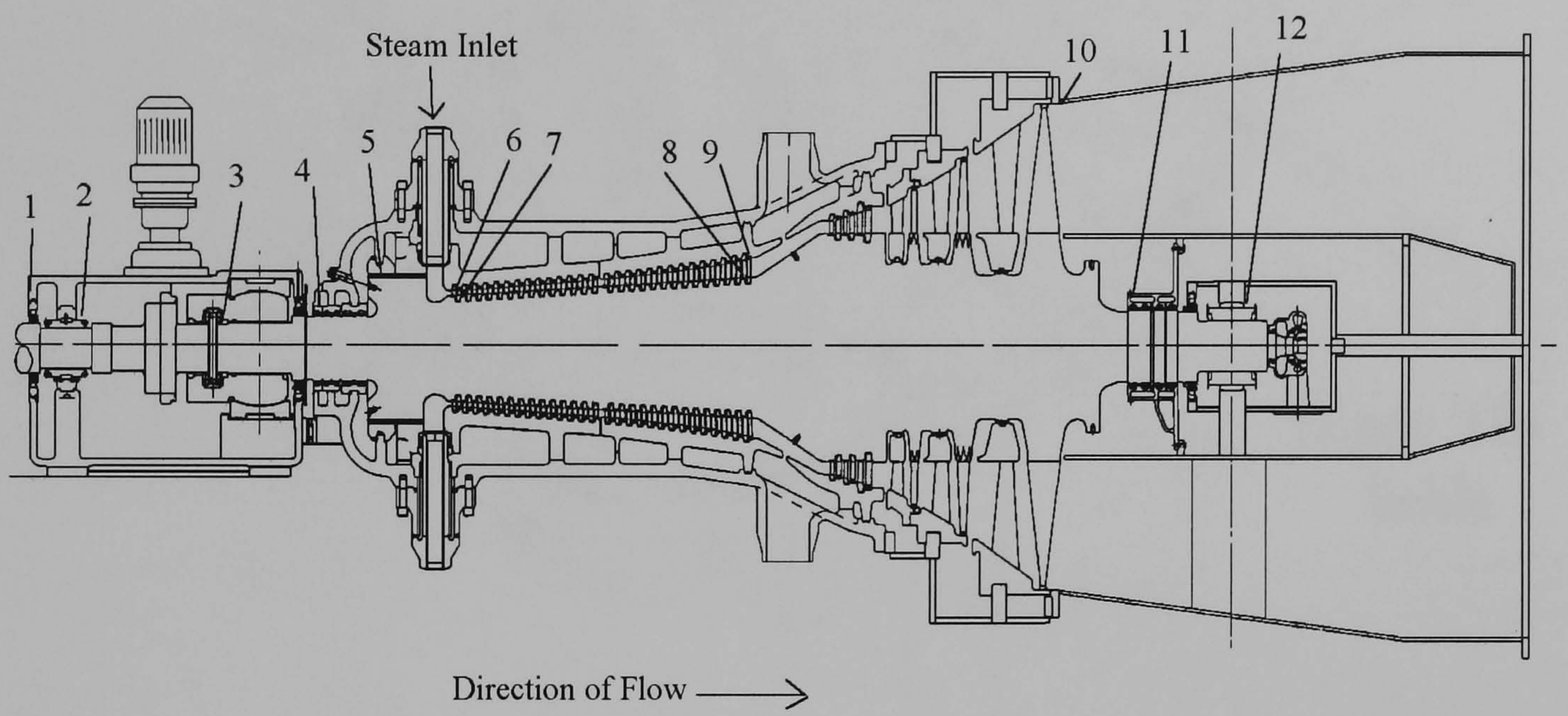

(Steam Flow Rate 62 kg/s, 30 Stages in HP)

Operating Conditions at Specific Points of Application

No	4	5	6	7	8	9	10	11
Inlet temp (°C)	460.6	498.6	498.6	494.8	186.9	179.2	51.4	177.0
Outlet temp (°C)	458	460.6	494.8	491.0	179.2	171.2	44.0	180.0
Inlet press. (bar)	5.66	76.8	76.8	74.9	6.64	6.14	0.132	0.091
Outlet press. (bar)	1.207	5.66	74.9	73.1	6.14	5.66	0.091	1.207
dP per contact (bar)	0.165	0.66	0.475	0.45	0.125	0.12	0.01	0.279
Rub dia (m)	0.490	0.100	0.7276	0.8331	0.9735	1.1948	3.048	0.515
Rub speed (m/s)	77.0	157.0	114.3	130.9	152.9	187.7	478.8	80.9
No of contacts	27	108	4	4	4	4	1	24
Leakage rate (kg/s)	0.126	2.253	3.34	2.51	1.20	0.68	0.32	0.09
Estimated financial saving by implementing brush seal (millions £) *	0.0428	0.7660	1.1356	0.8534	0.408	0.2312	0.1088	0.0306

* This financial estimation is based on brush seals offering a pessimistic sealing improvement of 66% over the existing labyrinth seals. £1000/kW is used as an estimate of the cost of electricity provided by the power plant over its financial life. At the HP steam inlet, 1kg/s = 1 kW.

Figure 1.1 A single cylinder 67 MW steam turbine.

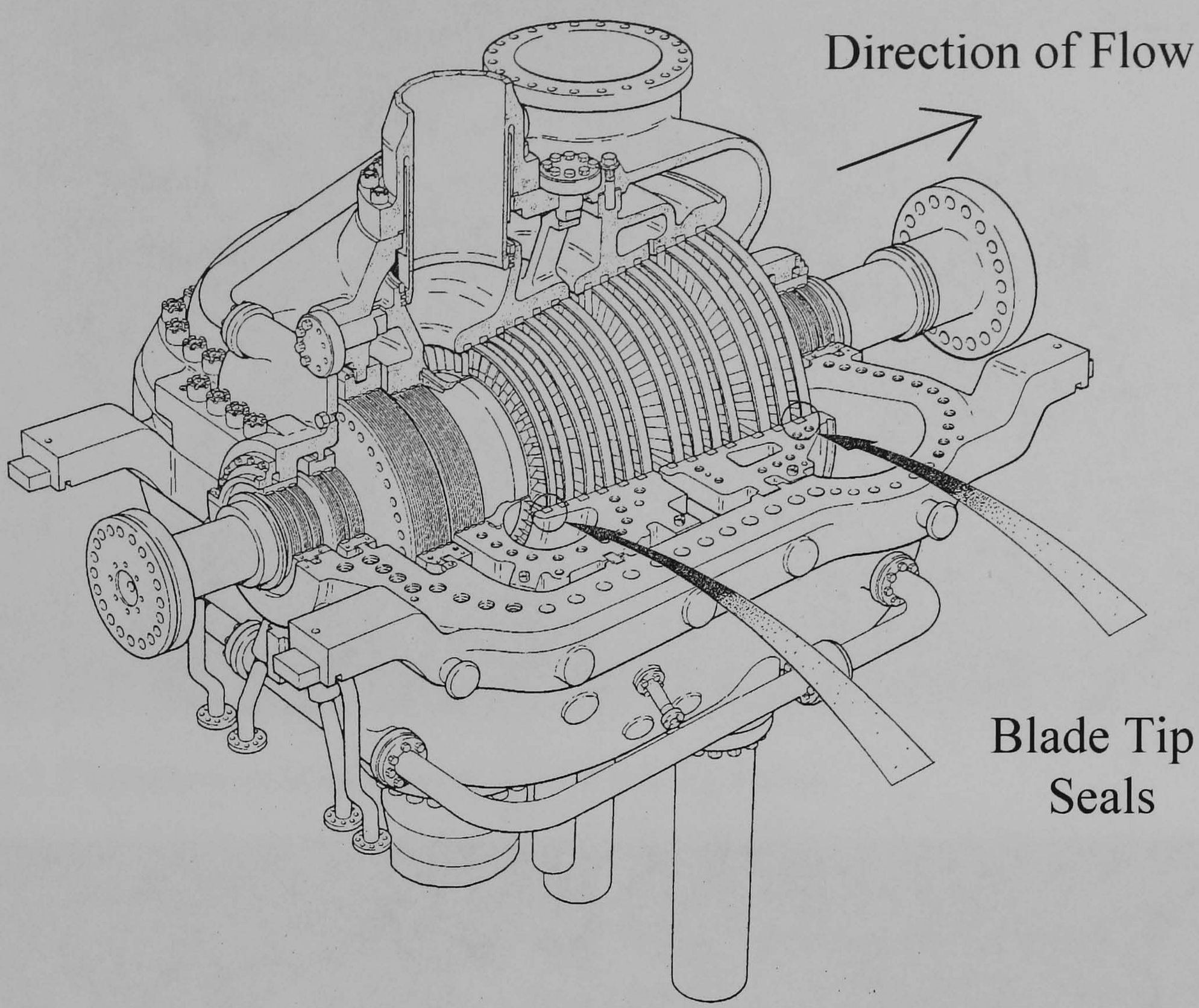

Figure 1.2 A high pressure steam turbine showing the location of blade tip seals.

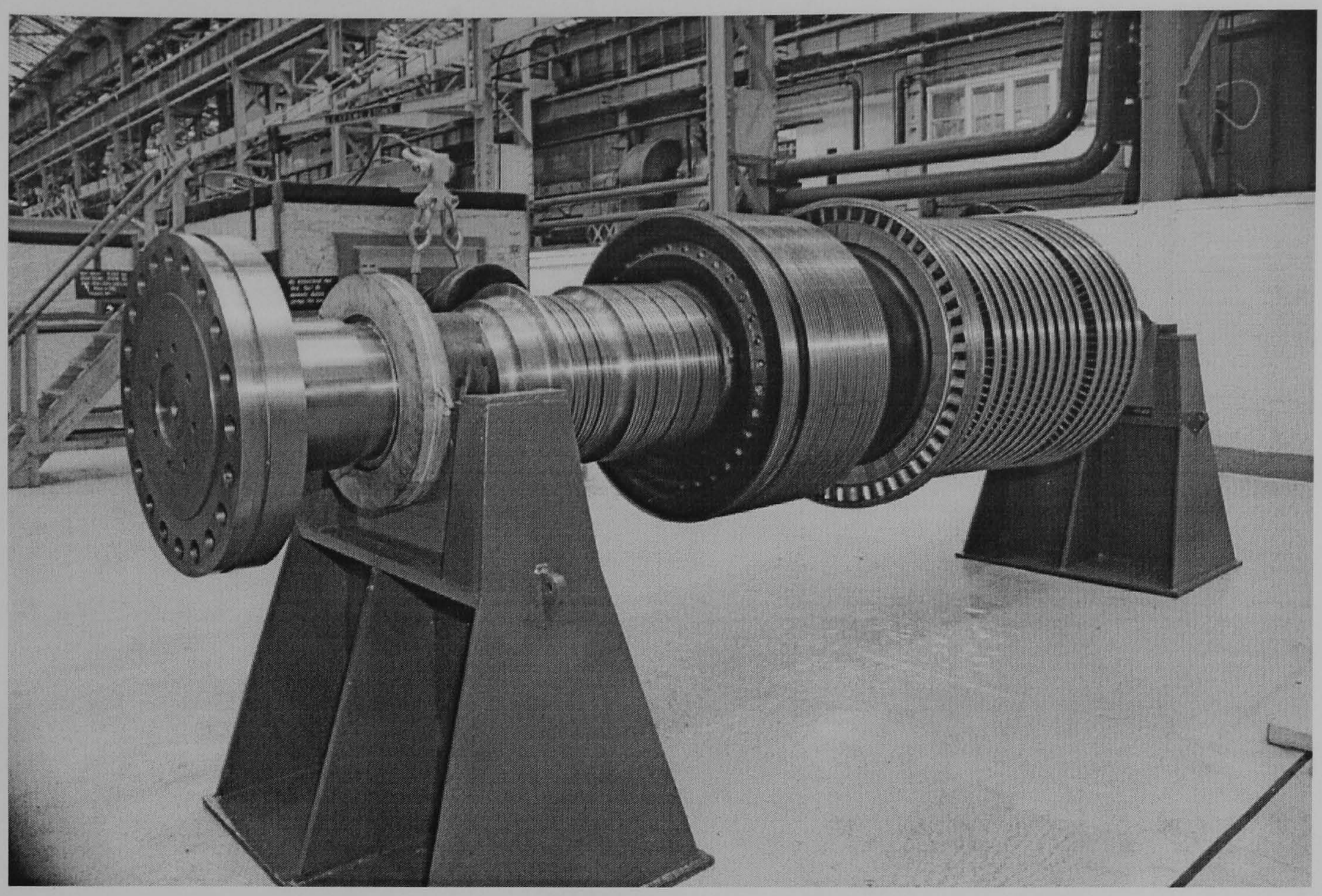

Figure 1.3 Turbine rotor shaft showing rows of rotating blades.

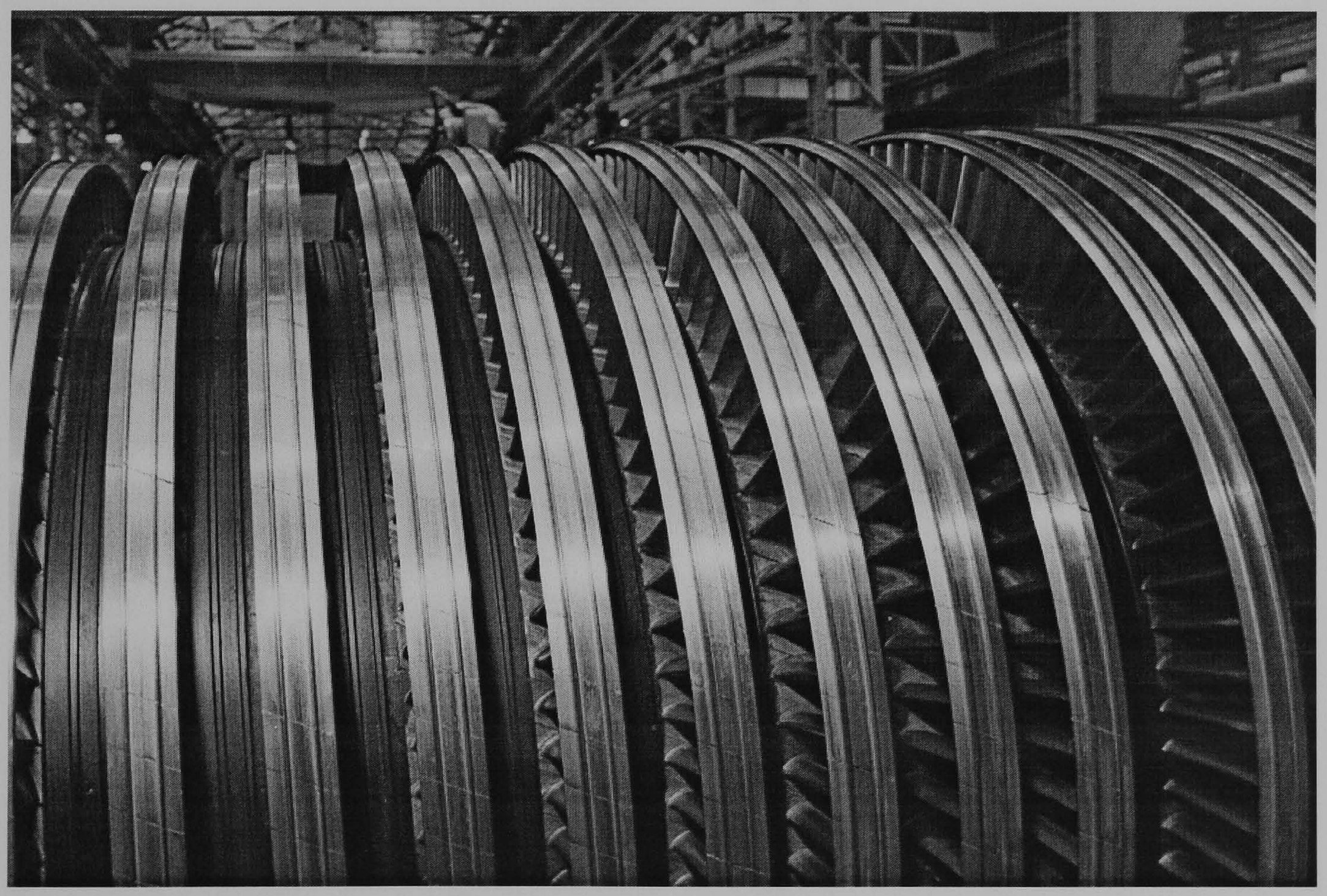

Figure 1.4 Turbine rotor shaft showing rows of rotating blades and labyrinth fins on the shaft and blade tips.

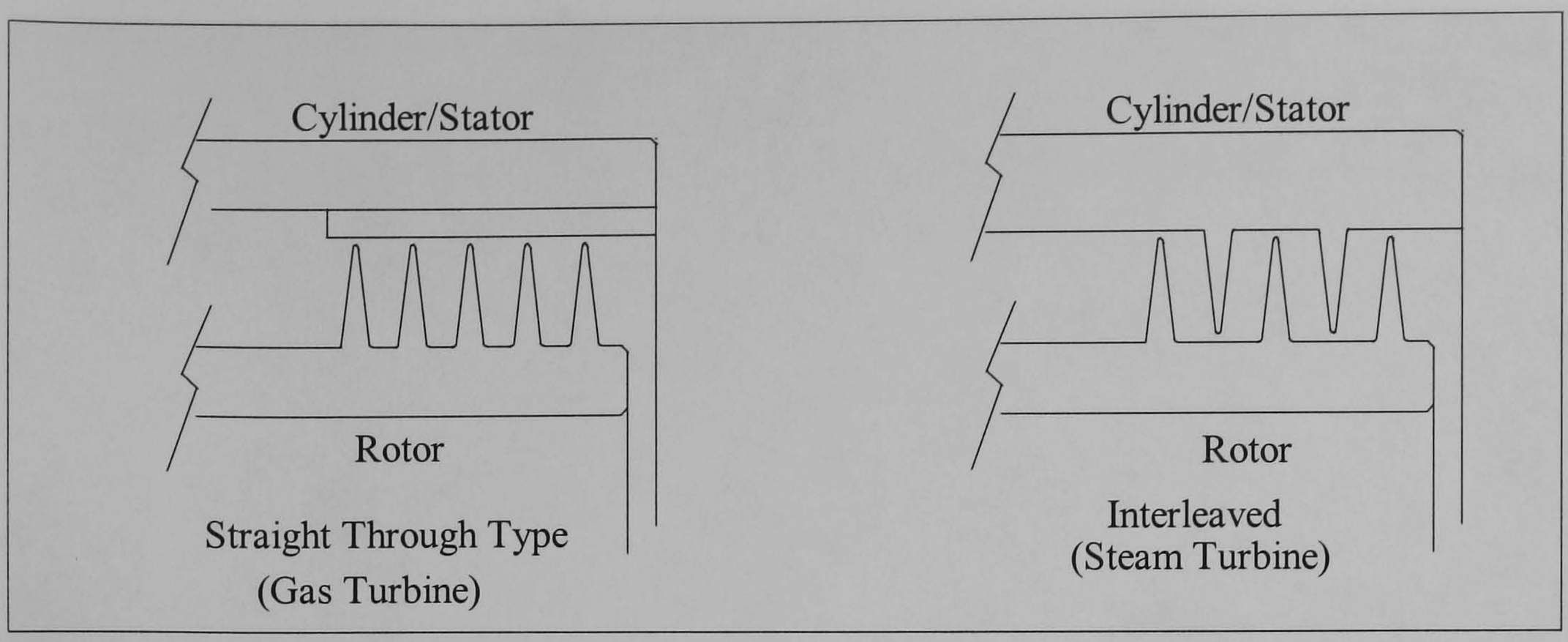

Figure 1.5 A comparison of labyrinth seal geometries.

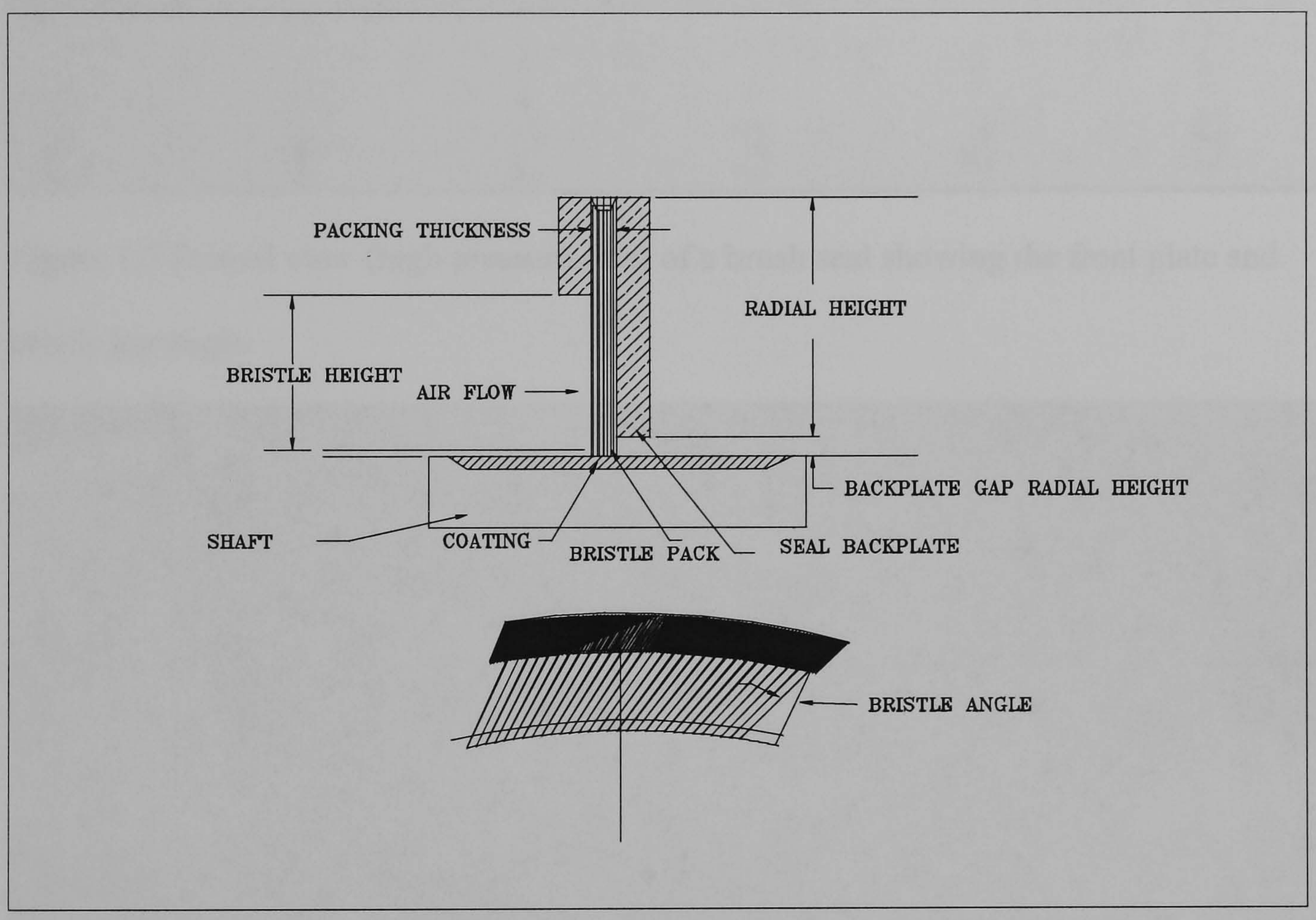

Figure 1.6 Schematic of a typical brush seal configuration **(Chupp and Holle (1994))**.

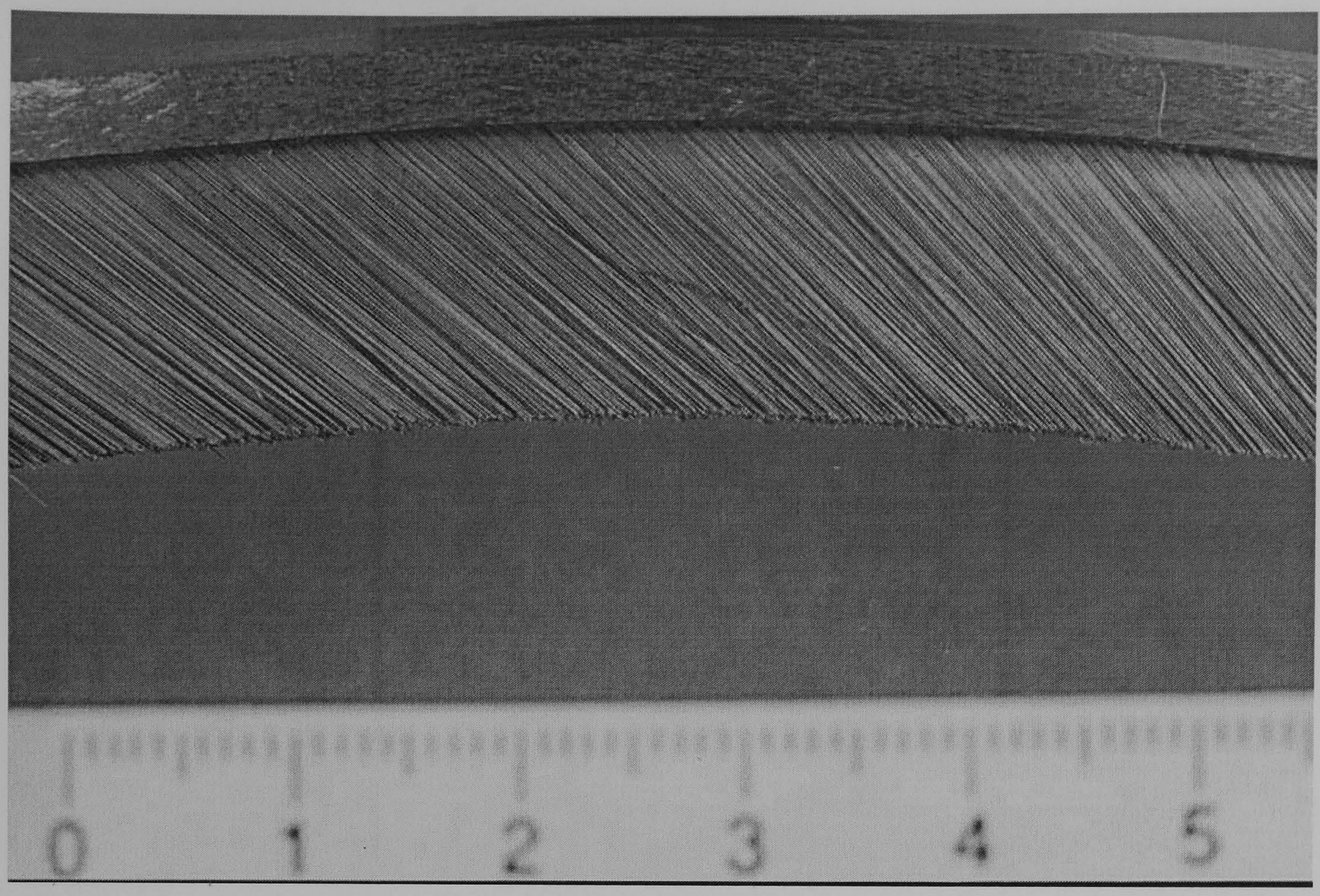

Figure 1.7 Frontal view (high pressure side) of a brush seal showing the front plate and bristle lay angle.

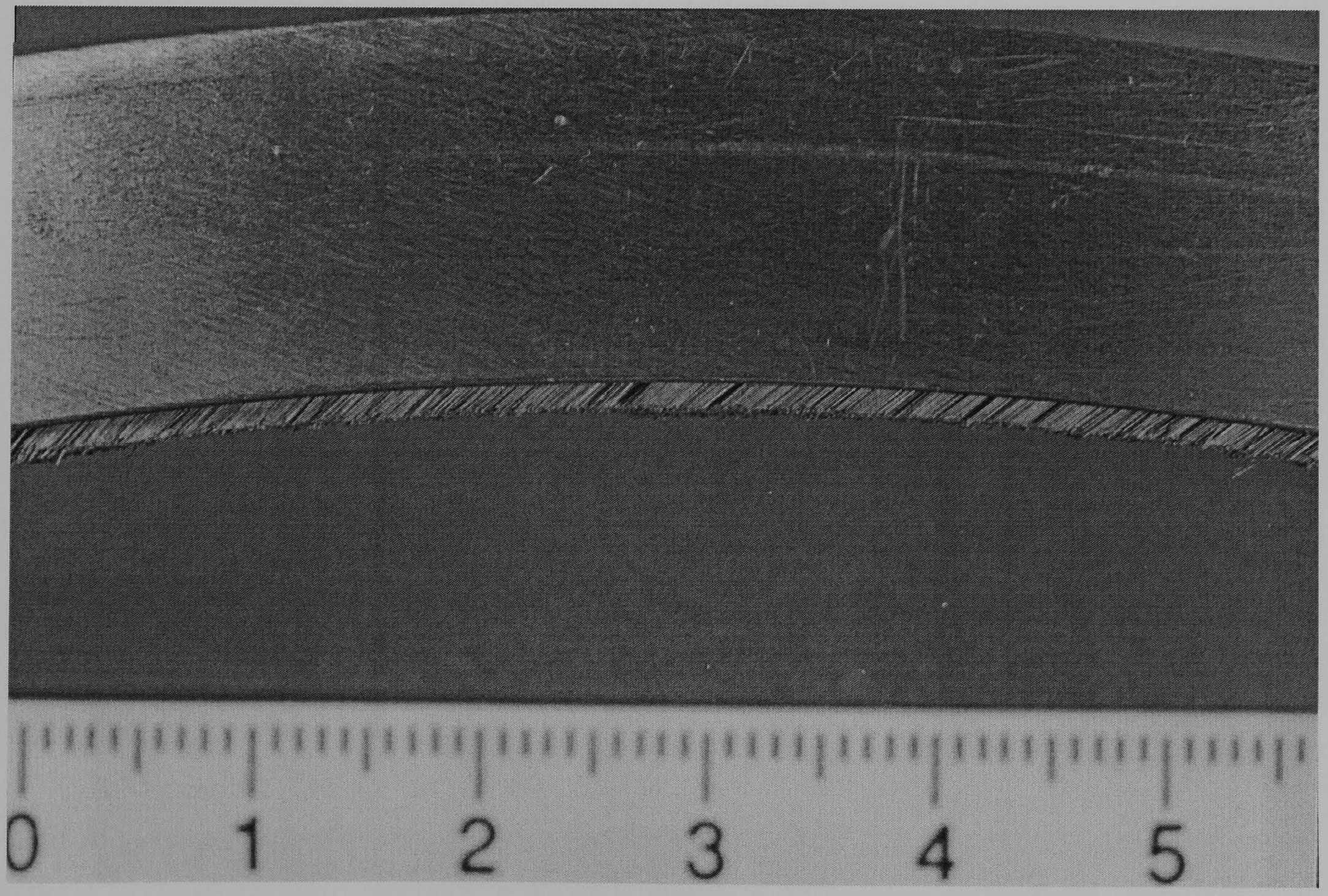

Figure 1.8 Back view (low pressure side) of a brush seal showing the backing ring/plate and bristle overhang.

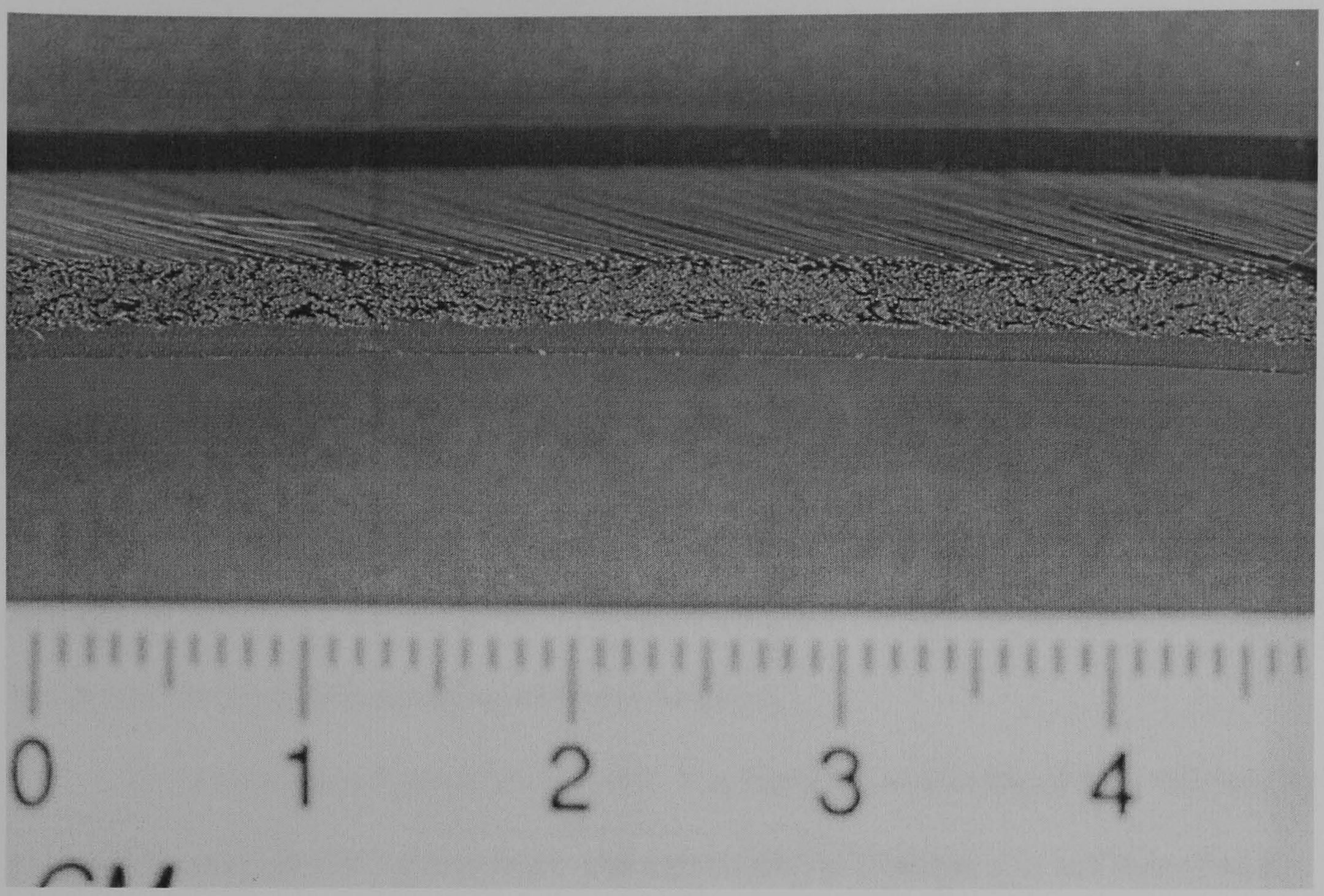

Figure 1.9 End view of the brush seal bristle pack showing bristle packing density/pattern and the bristle ends.

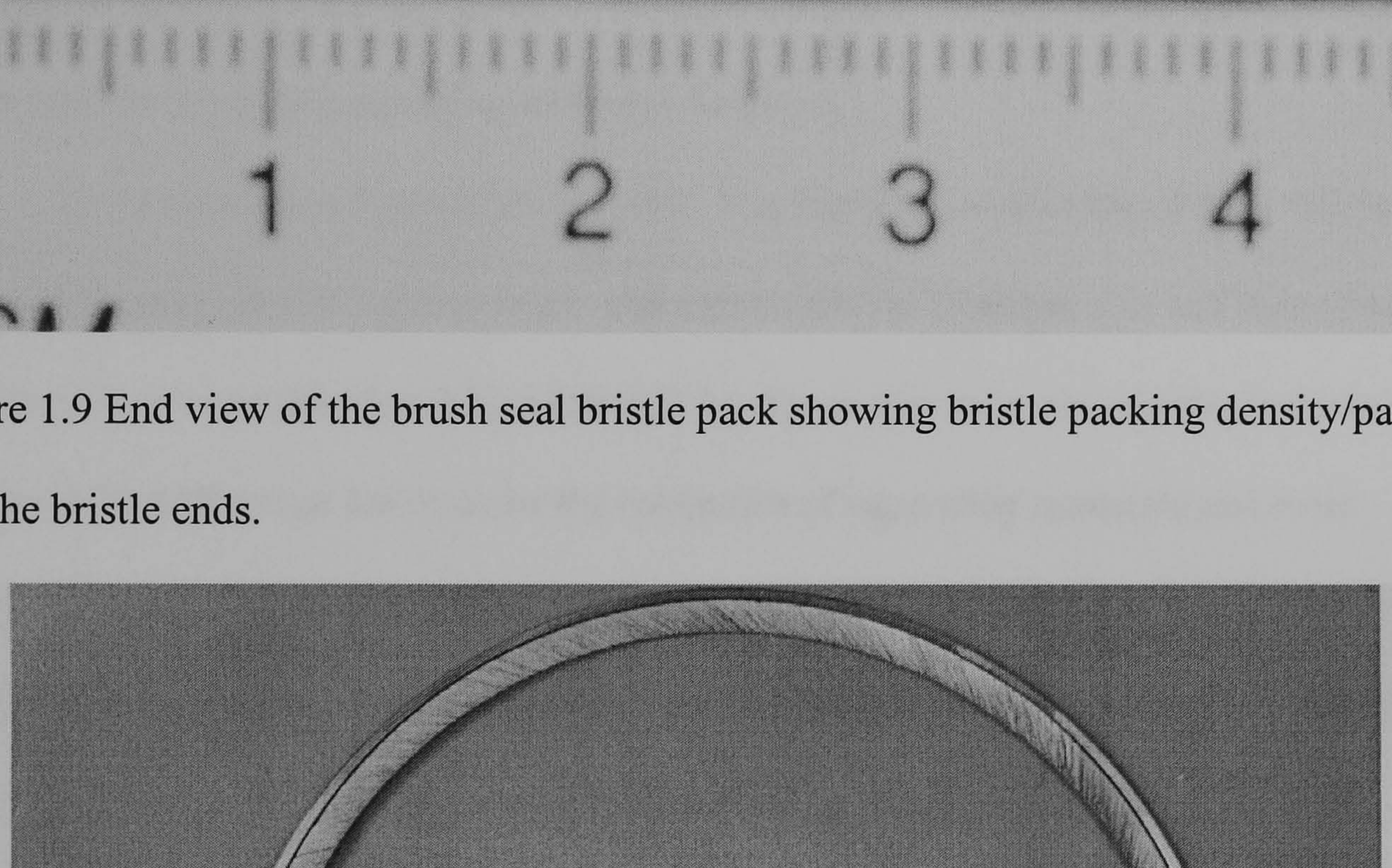

Figure 1.10 Full view of the brush seal

2.0 Literature Review: - High Temperature Wear Testing and Tribological Aspects of Brush Seals.

This chapter provides a critical review of available literature pertaining to high temperature (dry sliding) wear and the various factors that influence it. The aim was to provide a context for the tribological portion of the present project and a framework to facilitate interpretation of the results of the study. A materials survey and selection process was also carried out to identify possible candidate bristle materials for the application of brush seals in steam turbines using available literature.

There are nine sections in this chapter. The introduction **(Section 2.1)** is followed by the background materials aspects in gas and steam turbines **(Section 2.2)** and then a brief introduction to wear **(Section 2.3)**. **Section 2.4** outlines the materials selection criteria and **Section 2.5** and **Section 2.6** describe the categories of superalloy materials and more specifically materials that have been previously used for brush seal bristles respectively. **Section 2.7** is a comprehensive literature review of published work on brush seal tribological testing and section **Section 2.8** is a literature review on more general superalloy high temperature wear testing. Finally, **Section 2.9** lists the candidate brush seal materials selected using the available information.

2.1. Introduction.

Improved seals are being developed and tested to reduce parasitic steam leakage in many of the steam leakage paths in steam turbines. Brush seals are contact seals that have been used in gas turbine engines with some success in terms of efficiency improvements throughout service life and are being considered for steam turbines.

A materials selection process was carried out when brush seals were first applied to gas turbines. The materials that were used to manufacture brush seals for gas turbines were carefully selected to provide desirable properties for that specific application. The conditions

in a gas turbine differ significantly to those in a steam turbine. Brush seals have yet to be applied to steam turbines and there was no information available on the most appropriate materials to use. It was therefore necessary to carry out a materials selection process for brush seals for steam turbines.

This chapter examines existing information on the conditions within a gas turbine and the materials selected and tested for use as brush seal bristle materials for gas turbine applications. Steam turbine operating conditions are examined and compared to the conditions that apply to current gas turbine brush seals. General high temperature unlubricated sliding wear and wear testing is examined. Specific emphasis is applied to current gas turbines bristle materials, previously suggested alternative gas turbine brush seal materials and superalloy materials in general. The information provided by the literature was used to develop a general brush seal bristle material profile. The materials profile was used in conjunction with the steam turbine operating conditions to select promising brush seal bristle candidate materials for use in steam turbine applications. The candidate materials were then tested in a purpose built high temperature wear rig to determine the wear mechanism, the wear resistance, and possible effect on an uncoated single cylinder rotor. The latter is covered in **Chapter 4.**

2.2 Background.

Brush seals were designed to be a compliant contact seal. They are installed with an initial interference between the bristles and the rotor to minimise the available fluid leakage path and they are also able to deflect and return without damage if a change in the rotor orbit should occur.

A wear "system" is in operation in a contact seal, the two materials in contact being known as a tribopair. Orange sparks produced on initial gas turbine start up indicted that severe wear can occur to brush seals installed with an interference fit **(Hendricks et al (1993)).** The bristle length is worn to a working clearance or small interference. After this,

mild wear occurs. Wear on both the brush seal and the rotor must be minimised to maintain a low parasitic leakage rate. Of the two, the rotor is more difficult to refurbish and therefore the consensus within industry and academia is that if any wear should occur it should be on the bristle tips and not on the rotor.

Material selection and wear characteristics (models and processes) are thought by tribologists to be very significant to future development of brush seals for turbines. Wear is extremely complicated, therefore some general background information is required prior to material selection. In addition an understanding of the possible applications of brush seals within steam turbines was required. The author carried out a study assessing the operating requirements at several points in a typical steam turbine and the feasibility of installing brush seals at those positions **(Waite (1994))**. **Figure 1.1** summarises the results of the study. Possible seal applications included the HP, IP and LP turbine, oil seals, and both rotating blade tip to static casing steam path seals, and static blade tip to rotor steam path seals. The most promising application with the greatest potential saving was thought to be rotating blade tip to static casing steam path seals in the HP steam turbine.

2.2.1 Brush seals for Gas Turbines.

The operating conditions should always determine the selection of a tribopair in any wear system. Some typical conditions in a gas turbine (and a steam turbine) are given in **Table 2.1**. **Table 2.2** shows the properties of Haynes 25, a cobalt bas superalloy that is a typical gas turbine brush seal material. Haynes 25 is currently established as the aerospace industry standard brush seal bristle material. No information is available as to the specific selection process prior to Haynes 25 becoming the industry standard (but it was presumably based on either specific brush seal testing or non-specific geometry, high temperature materials testing). However, Haynes 25 is a well tried and tested material for use in hot sections of gas turbine engines and is known to have an excellent high temperature wear resistance and that can have a good wear resistance for the relatively

short periods between engine refurbishments (approximately 10000 hours). The mechanical properties of Haynes 25 are typical for a high temperature superalloy and form a datum for the mechanical properties required for brush seal bristles for HP steam turbine applications.

The improvement in sealing efficiency by using brush seals is accomplished at a relatively high hardware cost as military aero engine gas turbines only operate for 8000-10000 hours between strip downs and seal replacement. The operating conditions are continually changing as the engine accelerates and decelerates. This means the brush seal/rotor interference is continually changing due to the changing thermal and mechanical expansions between concentric cylindrical rotating and non-rotating components. An example of an aeroengine thermal expansion cycle is given in **Figure 2.1**. It is generally thought throughout the turbo-machinery industry that these expansions may be detrimental to brush seal life.

Historically tribologists have generally accepted, as a rough guide, that hardness was of major importance when selecting wear resistant tribopairs. The softer of the two materials would be expected to wear more than the harder. Most systems are prone to abrasion from foreign particles (such as silica) and to combat this the tribopair would normally be harder than silica (800 Hv). Extremely hard materials are difficult and costly to use in manufacturing therefore one approach is to use a surface treatment or coating to increase the surface hardness.

Aeroengine gas turbine rotors combine the desirable properties of an alloy steel with a hard surface coating to combat wear. A surface coating can be relatively easily applied in a special booth (by the gas turbine engine manufacturer or coating supplier) as the rotor is reasonably small and the coating does not have to be applied in situ. The use of an extremely hard wear resistant coating allows the use of hard, wear resistant bristles that would normally be expected to remove excessive material if used against an uncoated shaft.

Research by the author on wear in brush seal applications has revealed that information is scarce, and is usually proprietary. Data that is collated involved the rubbing of bristles on a hard surface coating. Generally brush seal debris generation rates were high during incubation (rub in) followed by a period of steady state operation and low wear which increased as the rotor surface fractured and pits occurred. Finally a period of wear generated only by dynamic excitation existed. Effective sealing was gradually diminished because of the loss of bristle pre-load and spreading. The results of several papers are discussed in depth in **Chapter 3.**

Brush seals can accommodate significant short duration rotor excursions due to changing loads or thermal transients, but wear rapidly under sustained excursions (due to loss of rotor to stator concentricity).

Ideal wear in brush seals would be characterised by minimal material removal from both the bristles and the rotor surface. However, reality dictates that one must usually trade a higher degree of bristle wear for minimal rotor wear. The choice of the tribopair is complicated by changing relative rates of wear with temperature, contact load and surface speed. One initial study showed that the majority of wear occurred during the first 30 hours of rubbing contact **(Atkinson (1992))**. It was expected that wear would reduce asymptotically as a result of decreasing contact pressure (with system wear). Another set of factors contributing to the decreasing rate of wear was inter-bristle friction and bristle-to-backplate friction. Under the influence of differential pressure across the seal, friction assists in inhibiting all of the bristles in the seal bore from maintaining contact with the rotor subsequent to transient rotor/bristle interference. Unexpected radial clearance has also been detected by a rise in leakage rate. The leakage rate recovered when the differential pressure was allowed to drop to zero for a short period before applying further pressure loads. In most reported tests, as the brush seal bore and rotor surface wore, the seal leakage increased, but the leakage was still better than that through a comparable 5 finned labyrinth seal.

2.2.2 Brush seals for Steam Turbines.

The basic operating conditions for brush seals in steam turbines are given in **Table 2.1**. They are clearly different to those in a gas turbine. The overriding manufacturing constraint here is that the size of the rotor makes surface coating both difficult and costly. Simple theory would suggest that an uncoated rotor (e.g. Spec.297 single cylinder steam turbine rotor **Table 2.3**) would wear preferentially when in contact with Haynes 25 bristles. This would be extremely undesirable as it would increase the leakage path, would be difficult to refurbish in situ, and may cause rotor failure by crack initiation. The operating conditions and requirements may allow the use of other brush seal bristle materials, in conjunction with an uncoated rotor that may have better wear characteristics.

Typical steam turbine manufacturers currently state a required operating life between major overhauls of 50000 hours (which may increase to 70000 hours due to customer requirements for extended refurbishment intervals) and a shaft life of 250000 hours (based on fatigue calculations from thermal and mechanical cycles). However the nature of operation is less detrimental to brush seal life than in gas turbine engines. The mode of operation is typically long periods of steady state running interspersed with 10000 to 12000 start and stop cycles. This means that thermal/mechanical expansions are kept to a minimum. The only wear that should occur after the initial starting period where the brush seal is worn to a zero interference/clearance fit would be caused by rotor excursions due to eccentric movement in the journal bearings.

2.3 Introduction to Wear; Classification and Mechanism

Wear could be very simply defined as the removal of material from two surfaces interacting with one another. Wear is a complex phenomenon consisting of many different mechanisms. There are many variables, physical, chemical and mechanical that will affect the type, degree and mode of wear. Some of the most important variables that are often included in wear equations are given in **Table 2.4.**

Four principal wear types are described in **Table 2.5.** Adhesive wear is prevalent between two metals when the relative motion leads to material transfer that may produce a wear particle. Abrasive wear results from the ploughing, cutting or chipping action when a hard body slides or interacts with the surface. Fatigue wear occurs where surface loads are applied repeatedly and fatigue cracks are formed which propagate to release wear fragments.

Before selecting materials or treatments to resist wear, it is necessary to identify which wear processes may be present. This is usually possible by an examination of worn surfaces, and of wear particles generated, together with knowledge of the mode of surface interaction, the surface properties and whether or not abrasive material is present.

Archard (1961) originally classified the sliding wear of metals and alloys into two main categories, mild and severe wear. The theory was however primarily derived from adhesive and abrasive wear modes. Severe wear was characterised by large metallic debris particles (10μm to 1 mm) and usually occurred in the early stages of sliding contact. Mild wear was characterised by small debris particles size (0.01-1.0μm), smooth wear surfaces and high contact resistance occurring in the later stages of sliding contact. Mild wear was sometimes associated with the development of oxides on the wearing metallic surfaces and was sometimes known as oxidational wear.

It was necessary to identify the mechanisms of wear occurring during the contact of brush seal materials with an uncoated rotor. A reasonable life can only be expected if the mild wear regime can be ensured for the majority of the operating life.

2.3.1 The Archard Equation.

The most commonly stated wear equation was suggested by **Archard (1961)** and **Rabinowicz (1966)**.

$$V = \frac{k.L.S}{3H} \qquad \textbf{Equation 2.1}$$

V = Wear volume (m^3)

k = Wear Coefficient

L = Load (N)

S = Sliding Distance (m)

H = Hardness of the wearing surface (N/m^2)

Equation 2.1 can be applied to predict mild sliding wear (adhesive/abrasive) and is not readily applicable to high temperature oxidative wear. H represents the room temperature hardness of the harder material in contact. The wear coefficient k must be determined experimentally. For specific tribopairs it has been shown by numerous researchers that the equation is an over simplification and should only be used as a very rough guide. The complexity of wear processes has hindered the development of a more sophisticated equation.

2.3.2 Theories of High Temperature Wear.

It has been observed that for many alloys at a critical load or critical speed the friction and wear rate changes (increase or decrease depending on specific material tribopair and conditions). **Stott et al (1971-1985)** found that for nickel-base alloys a clearly defined temperature occurs in the plots of friction and wear against increasing temperature, above which a noticeable reduction in friction and wear values takes place. These observations were thought to be related to the presence of oxide films that form on the surface.

During sliding at low temperature (room temperature), interactions between asperities result in the development of junctions (the actual areas of contact between the two surfaces). If the asperities are metallic, these junctions can grow significantly, resulting in relatively high coefficients of friction and subsequent wear can be substantial. However, with oxide asperities, the junctions grow relatively little before failure occurs resulting in lower coefficients of friction and wear rates. The termination of junction growth occurs

when the contact area has increased to such an extent that the reduced pressure over the points of contact result in the oxide reverting to its brittle nature. However, as junction growth proceeds, and the contact pressure is reduced, such cracks can enlarge and act more effectively as stress-raisers, leading to a reduction in the shear strength of the oxide and ultimately brittle failure of the junctions.

It has been observed that the wear rate is related to the growth of oxide films that are strongly influenced by temperature **(Stott et al 1971-1985)**. However, it is not known whether the controlling temperature is the brief "flash temperature" which exists during the short period of asperity contact or the bulk temperatures which occurs for much longer periods between contacts.

Stott et al (1971-1985) suggested that at the start of wear the oxide films found on unworn surfaces are progressively destroyed and a period of severe wear ensues. During this time metallic and oxide wear debris accumulate to form thick layers in the appearance of a 'glaze' which eventually reduces the wear rate to mild wear. Analysis reveals that these films consist of a thin physically homogenous surface layer. This film occurs on top of either highly compacted crystalline oxide particles above a steady-state oxide layer or on metal substrate deformed to varying degrees. The layers formed are dependent on the time of sliding, ambient temperature and strength of the alloy. The glaze and the underlying oxide contain all the alloying elements, approximately in the same proportions as in the alloy with the concentrations of the metal elements remaining fairly constant across the glaze.

The development of a 'glaze' as defined by **Stott (1971)**, probably involves three simultaneous stages: formation, agglomeration, and compaction of wear debris. Following the formation of oxide debris, a relatively weak bond develops between the debris particles, causing them to adhere. Compaction of the particles under the pressures between the sliding surfaces increases this bonding by increasing the number of contact points between the particles and enlarging the existing areas of contact. The external pressure promotes

closer packing of the particles by a process of redistribution and deformation. The tribological properties of the glazes have been said to be associated with their low shear strength and the high strength of the underlying alloy substrate.

2.4 Materials Selection Criteria.

The operating conditions immediately disqualify several groups of materials. The atmosphere of super-heated steam at 540 °C prevents the use of most plastics, bronzes and many low alloy steels as flexible elements in a sliding contact seal. Wear resistance (and oxidation resistance) at high temperature (well above 540 °C) is a known advantage of superalloy materials (nickel, iron or cobalt base alloys, which usually have substantial amounts of chromium) which maintain their properties throughout a wider temperature range.

An extensive list of possible candidate materials for bristles for brush seals in steam turbines was generated. The list was then narrowed to concentrate initially on those materials which were the most desirable based on the following factors; known performance in high temperature environments, availability in the form required (wire for bristles), previous experience, melting point, tensile strength, oxidation resistance, creep resistance, and wear resistance (**Table 2.1** gave the operating conditions and **Table 2.2** gave some typical material property values for brush seal bristles for gas turbine applications). Superalloys were thought to possess materials properties that were thought to be desirable for high temperature brush seal (from this investigation and many previous studies). The term is generally applied to several groups of alloys that are described in Section **2.5**.

2.5 Classification of superalloys.

Four main superalloy types were available. A review of academic papers and materials reference books including "The Handbook of Tribology Materials, Coatings and Surface Treatments **(Gupta (1976))** provided the basis for the following classifications

2.5.1 Iron base.

Iron-based superalloys are defined as those which have iron as the major constituent and which are hardened by a carbide or intermetallic precipitate. The iron-based grades (with high nickel and chromium content) are less expensive than cobalt or nickel-based superalloys making them commercially more attractive for applications where these materials are suitable and material cost is important. Iron-based superalloys are grouped into three types, **(i)** those that are strengthened by a martensitic type of transformation, **(ii)** those that are austenitic and are strengthened by a sequence of hot and cold working, and **(iii)** those that are austenitic and are strengthened by precipitation-hardening. In general, the materials of type **(i)** are used at temperatures below 550 °C.

The significant properties of iron-based superalloys, are high temperature as well as room temperature strength and resistance to creep, oxidation, corrosion, and wear. Wear resistance increases with carbon content. The compositions of several iron base superalloys are given in **Table 2.34.**

2.5.2 Cobalt base.

Cobalt-based alloys are used extensively in high temperature applications because of their inherent high strength, corrosion resistance and ability to retain hardness at elevated temperatures. Binary alloys of cobalt and chromium with more than 10 percent chromium exhibit excellent resistance to oxidation and corrosion plus outstanding hardness at temperatures up to 1000 °C (as indicated by manufacturers specification sheets), e.g., Haynes alloys 25 and 188. Tungsten and molybdenum are often added to increase strength and to improve frictional and wear properties e.g., Haynes Stellite 6B and 6KC.

Two general types of cobalt-based alloys are available commercially: carbide containing alloys and alloys containing Laves phase. The high carbon content of Co-Cr-W-C alloys (e.g. 6B and 6KC) promote the formation of chromium, cobalt and tungsten carbides during solidification that are dispersed in a cobalt-rich face centred cubic matrix.

The amount of carbide phase varies from 12 to 16 wt % for various Stellites. The best protection from abrasion is provided by alloys having large particle sizes and large volumes of the hard constituents (carbides) **(Gupta 1976)**. Since hardness usually decreases by increasing the particle size of the harder phase at constant volume, hardness is not a good indicator of abrasive wear resistance. In metal to metal wear, the role of the hard phase (carbide MC, M_6C, M_7C_3 and $M_{23}C_6$) is found to be less critical, and the wear rate is less sensitive to structural features. Superalloy manufacturers maintain that properties that distinguish Co-Cr-W-C alloys from other materials used in bulk or as hard facing materials are their outstanding resistance to liquid impingement and cavitation, erosion and galling **(Gupta (1976))**.

There are also cobalt and nickel-based alloys that during solidification formed hard metallic compounds (Laves phase e.g. CoMoSi and Co_3Mo_2Si) rather than hard carbides. Tribaloys are free of carbide phase. Carbon is kept low so that carbide will not form in preference to the Laves phase. The wear resistance of Tribaloys is attributed to the Laves phase.

Chromium partitions itself about one third in the Laves phase and two-thirds in the solid solution, contributing significantly to the corrosion resistance of both phases. At higher chromium concentrations, the corrosion resistance is excellent in most aggressive environments. The compositions of several cobalt base superalloys are given in **Table 2.34.**

2.5.3 Nickel Base.

Nickel and its alloys are used widely in a variety of structural applications usually requiring moderate resistance to wear under corrosive environments or strength at high temperatures. Several nickel-based superalloys are specified for temperatures up to 1100 °C. The nickel-based alloys have ultra high strength and high moduli compared to steel.

However, nickel-based alloys in metal-to-metal sliding usually exhibit poor galling resistance. Mo and/or Co are normally added to obtain superior sliding characteristics. This is thought to be because of the formation of beneficial oxide films.

Most commercially available nickel-based alloys can be divided into four groups: nickel alloys, carbide-containing alloys, and boride containing alloys and Laves containing alloys. Nickel and Duranickel alloys have a nickel content over 94 percent. The compositions of several nickel base superalloys were given in **Table 2.34.**

2.6 Previously used bristle materials.

Potential bristle materials suggested for use in gas turbines were Inconel 718, Inconel X-750, Hasteloy X, Haynes 25, Waspaloy, stainless steels, fibreglass and ceramics. **Table 2.34** gives a selection of material compositions for the final candidate brush seal bristle materials. Papers reporting brush seal wear testing (described in detail in section **2.7**) all use brush seal bristles in conjunction with wear resistant rotor surface coatings. These rotor coatings include chromium carbide/oxide, tungsten carbide and aluminium oxide. Descriptions of some of the most frequently suggested bristle materials are given in **Sections 2.6.1-2.6.5** and help to build up a profile of the mechanical and physical properties necessary for use as a bristle material in a steam turbine.

2.6.1 Haynes 25.

Haynes 25 is a cobalt, chromium, nickel, tungsten-based superalloy that derives its strength from solid solution strengthening. **Table 2.2** gives the composition and some material properties. Alloys that are solid-solution strengthened have lower strengths than the precipitation-hardenable alloys at intermediate temperatures, but they possess good strength properties at high temperatures up to 980 °C for prolonged exposures. The oxidation resistance of Haynes 25 is due to the formation of a Cr_2O_3 film and it has excellent resistance to metallic galling.

2.6.2 Inconel 718.

Inconel 718 is a precipitation hardenable nickel-chromium superalloy that has a good combination of properties up to 700 °C. The alloy is strengthened by precipitation of a modified γ', YNi_3 (AL, Ti) precipitate. This strengthening phase goes into solution above 700 °C, leading to drastic reductions in the mechanical properties (e.g. at 538 °C yield stress = $148*10^3$ MN/m^2, at 816 °C yield stress = $80*10^3$ MN/m^2). It is therefore only a candidate for applications below this temperature.

2.6.3 Inconel X-750.

Inconel X-750 is a nickel-chromium alloy with good oxidation resistance at high temperatures and resistance to chloride-ion stress-corrosion cracking, corrosion by high-purity water and caustic corrosion. It is made precipitation hardenable by additions of aluminium and titanium. It has high tensile and creep-rupture properties at temperatures up to about 700 °C and has an excellent relaxation resistance.

2.6.4 Hastelloy X.

Hastelloy X is a nickel-chromium-iron-molybdenum alloy with outstanding strength and oxidation resistance at temperatures up to 1200 °C. Matrix stiffening provided by the molybdenum content results in high strength in a solid solution alloy having good fabrication characteristics. Hastalloy X is used in gas turbines, industrial furnaces, heat treating equipment and nuclear engineering.

2.6.5 Waspaloy.

Waspaloy alloy is an age hardenable, nickel base superalloy with very good strength at temperatures up to about 980 °C. Its strength is generally superior to that of alloy 718 at temperatures above 650-705 °C. The alloy exhibits good resistance to gas turbine combustion environments at temperatures of use up to 870 °C.

2.7 Literature Review on Tribotesting of Brush Seal Materials for Gas Turbines

Hawthorne (1994) carried out high speed, high temperature "pin-on-disk"(and bristle tuft) sliding experiments on materials simulating conditions in gas turbine flexible element gas path seals. The experimental test conditions were given in **Table 2.6.** Superalloys and ceramics were thought to be the most likely to resist wear at the high temperatures (up to 500 °C) and sliding speed (up to 100 m/s). Details of the bristle materials and counterface disks are given in **Tables 2.7** and **2.8.**

The bristle ends were brazed to bond them into a single tuft. The tuft was than clamped and mounted vertically against the counterface. The free length was adjusted to achieve acceptable brush compliance.

Initial tests were carried out with a fixed brush specimen, to visually assess the change in interference. The load was constantly diminishing therefore a wear rate could not be determined. Further to these tests a constant load, test rig was used with temperatures up to 500 °C and speeds up to 100 m/s. The load, 2-10*10^{-4} N was calculated from the actual seal bristles at 45°. Normal and tangential forces and disk surface temperature were monitored continuously. Bristle height was measured by weight loss and counterface wear measured by profilometric traces. Scanning Electron Microscope **(SEM)** micrographs were used to examine the worn surfaces. They clearly showed the wear tracks and a compacted surface layer on both the rotor and the bristle tips.

Figures 2.2 - 2.7 graphically display the results of the wear testing. Nickel and cobalt base superalloys appeared to have the greatest wear resistance of the materials tested. **Hawthorne** found that prolonged sliding on the same track could lead to either smaller or larger wear rates depending on the load level applied and that there seemed to be a strong correlation between decreasing wear rate and increasing surface smoothness.

Profilometer readings revealed little evidence of wear of the actual surface coating and only served to show that there was material transfer to that surface. In conclusion

Hawthorne stated that fixed load rather than fixed interference (i.e. the sample pivot arm was loaded and allowed to move with wear, rather than being rigid) testing was more useful for obtaining tribological information on flexible element seal component materials. The author felt that a valid simulation of the element seal tribosystem could be achieved using a brush on disk laboratory tribotester. From the materials tested the nickel based wires sliding against the nichrome bonded chromium carbide coating offered the most promising combination of materials for high temperature, flexible element seals, based on their running in behaviour and low wear rates.

Atkinson (1991) approached the problem of brush seal wear along two parallel paths. The first tests were at room temperature, simulating conditions towards the front of a gas turbine aero engine. The second experiment involved tests at higher temperatures spanning from 425 to 650 °C. Experimental test details of **Atkinson's** test rigs and operating conditions are given in **Table 2.9.**

The purpose built room temperature rig was able to move the static brush seal both radially and axially while the rig was running at full speed, and whilst the seal was subjected to pressure differentials. Flight cycles could be simulated by programming a specific pattern of speed, pressure and seal location changes.

The second rig was a high speed, high temperature brush seal rig with similar features to the first rig but it also had the facility to enable eccentric rotor set ups and out of plane misalignment of the rotor to stator. Back to back seals of up to 457 mm could be tested at speeds up to 335m/sec and temperatures up to 590 °C. the seal dimensions are given in **Table 2.10.** The surface coatings and bristle materials are given in **Table 2.11 and 2.12**.

Brush wear in the room temperature tests was difficult to measure due to the flexibility of the bristles so the wear was reported as reduction in exposed radial height and weight loss. Rotor wear was reported as rotor scar depth.

The tests clearly showed that cobalt alloy produced the least rotor and bristle wear at room temperature even though this was below its oxidational temperature. The tungsten carbide coating developed a circumferential crack that suggested that it might not be suitable for a coating for rub surfaces.

Tables 2.13, 2.14, and 2.15 summarises the rotor and brush wear at 480 °C. Vibration over long duration testing caused a radial offset of 510 μm. This caused difficulty in direct comparison of the results however it appeared that although tungsten carbide produced less wear on either bristle material than chromium carbide, its wear scar was many times deeper than that of the chromium carbide coating. It was evident that the relative standings of the chromium carbide and tungsten carbide were very temperature dependent.

Figures 2.8-2.9 showed that the majority of wear occurs during the first 30 hours of rubbing contact. This was expected due to the decreasing bristle interference and therefore contact pressure. Bristle pack internal and backplate friction also inhibited full contact after radial excursions and pressure differential changes. This was detected by an increase in leakage rate.

Derby and England (1992) addressed the tribological aspects of candidate brush seal materials for both the bristles and the rotor coating. The purpose of this was to extend the performance life of brush seals. The areas of investigation were oxidation testing of bristle alloys using thermal analysis techniques, wear tests (fatigue) of bristles using high radial displacements, dry sliding friction and wear tests for screening purposes, and miniature brush seal tests approximating high radial excursion conditions.

Seven bristle materials were selected based on critical physical and mechanical properties (melting point, tensile strength, hardness, oxidation resistance, creep resistance, fatigue resistance, and availability). The materials tested included Haynes 25, Inconel 718 and five other alloys that were described briefly but their identities (commercial names) were not given.

Seven rotor coatings were also selected including chromium carbide, Triboglide, tungsten carbide, chromium oxide, aluminium oxide, Tribaloy and Tribomet T-104C.

Thermogravimetric analysis **(TGA)** was used to define the oxidation resistance of the candidate alloys by very accurately measuring the weight change under carefully controlled conditions. Only three out of the seven results were discussed and **Figure 2.10** shows the generalised response curve. The oxidation of metals is attributed to the following events i) adsorption of oxygen, ii) formation of oxide nuclei, iii) lateral growth of a continuous oxide film and iv) thickening of the oxide film.

Wear/fatigue tests using high radial displacements were carried out using a 1 mm (0.040 inch) radial shaft run out, at 300 r.p.m. and 650 °C (1200 °F). The fatigue specimens were taken from actual miniature brush seals and the rotor was uncoated Inconel 718. The test specimens accumulated in excess of 15 million fatigue cycles. **Derby and England's (1992)** experimental test details are given in **Table 2.16.**

SEM was used to examine the specimens and showed no evidence of classical metal fatigue, macroscopic deformation or significant change in overall geometry. From a microscopic point of view, the leading edge of the Haynes 25 showed material loss due to alloy fracturing and the fibres were noticeably oxidised. Wear debris pile up was observed at the fibre trailing edge. Similar trends were observed for the Inconel 718.

Screening tests for friction and wear were also carried out using ring on ring type specimens. The contact pressure was 0.14 N/m^2 (2 p.s.i.), at temperatures up to 650 °C (1200 °F) and rotational speeds of 10 000, 20 000 and 30 000 r.p.m. for 1.5 hours. Experimental test details are summarised in **Table 2.17.**

SEM micrographs and surface profilometry measurements from each tribopair surface were studied. Generally most of the coatings showed some evidence of microcracking but the two oxide coatings were found to have extensive microcracks and some evidence of spalling.

Two bristle alloys consistently produced lower friction than the other alloys. For the first material this was accompanied by a high wear rate. It is thought that the yield strength of the material at high temperature was low and therefore little force was required to remove the material. The second alloy low wear rate was due to an adherent oxide film. It was also noticed that the friction coefficient was highly dependent on the bristle material it runs against. These ranged from $\mu = 0.3$ to 0.8.

The primary tests were miniature brush seal tests. Experimental test details are given in **Table 2.18.** The brush seal inside diameter was 50.65 mm (1.994 inches) and the rotor outside diameter was 51.16 mm (2.014 inches) producing a nominal radial interference of 0.254 (0.010 inches). Tests were carried out at speeds of 2 000, 20 000, 40 000 and 60 000 r.p.m. at 427 °C (800 °F). Torque and temperature readings were continuously recorded.

The findings were highly specific to individual tribopairs and generally included changes in surface finish, Energy Dispersive Analysis by X-Ray (**EDAX)** identification of material transfer, micrographs of microcracking, surface wear, bristle tip wear, changes in coefficient of friction with speed, changes in torque and changes in the temperature of the backing plate due to running speed and bristle interference.

The results of the analysis showed that it was best to avoid materials that exhibit microcracking and spalling or excessive material transfer. Materials that showed superior oxidation resistance due to the formation of a tenacious oxide layer tended to show superior wear and friction performance. The cobalt alloys, including Haynes 25 performed poorly in the oxidation and tribology tests and it was suggested that they should be limited to lower temperatures (<400 °C) where the cobalt was stable in its hexagonal close packed structure.

Fellenstein and Dellacorte (1994) developed a brush seal bristle tuft tribological testing machine, which was similar in design to a standard "block-on-ring" wear testing

machine. Friction and wear of candidate wire and counterface materials were monitored under controlled loading conditions of 0.5 to 10 N at speeds up to 27 m/s and temperatures of up to 700 °C.

The journals evaluated were made of Inconel 718. They were 38.1 mm in diameter and 53.3 mm long. They could accommodate six wear tracks, each 3 mm wide. The brush tuft specimens were made of Haynes 25. The test brush seal and current brush seal designs were compared in **Table 2.19.**

Each test consisted of nine, 2 hour test runs for a total of 18 hours of testing under simulated gas turbine engine start and full speed running cycles. After the tests, journal wear was measured with a profilometer. Photomicrographs (magnification x 40) were taken before the initial test run and after every third run. Further test details are given in **Table 2.20.**

The journal wear tracks showed either mild polishing or more severe abrasive type wear after 18 hours. The wear factor used to quantify wear was the ratio of the material volume worn (V_w) to the normal load (N) and the sliding distance (D). A physical interpretation of the wear factor was presented in **Table 2.21.** To achieve the goal of 10000 hours the brush wear factor would have to be in the order of 1.31 $*10^{-8}$ mm^3/Nm. The journal wear factors for each configuration were shown in **Table 2.22**. The effect of increasing the test temperature from 20 °C to 650 °C was to reduce the overall journal wear. The Haynes 25 brush specimens showed abrasive wear on the brush interface surface. The bristle ends were worn and appeared polished with wear debris between the bristles and on the collar. In one case the wear rate was so high that a second tuft was required to complete the last three test runs.

The brush wear factors for the tests were thought to be moderate to low and ranged from $6.0*10^{-7}$ to $8.1*10^{-5}$ mm^3/Nm. Increases in either the temperature or surface speed resulted in lower brush wear factors. These were shown in **Table 2.23 and Figure 2.11.**

The coefficient of friction was in general, constant during each test (from $\mu = 0.25$ to 0.47) the average results are given in **Table 2.24** and **Figure 2.12**. Again the effect of temperature was to reduce the value of the coefficient of friction.

Surface analysis using (Energy Dispersive Spectroscopy **(EDS)**) was used on selected brush specimens to determine if any material transfer occurred between the brush and the journal. This confirmed qualitatively that there was material transfer. The journals were too large to fit in the **SEM-EDS** analytical chamber.

Fellenstein and Dellacorte felt that the rig successfully duplicated wear and friction characteristics encountered in full-scale brush seal testing both in mechanism and in magnitude. The wear factors were similar of slightly higher than those in full scale brush testing, which was probably caused by the constant loading.

Hendricks, Griffin, Bobula, Bill and Howe (1993) conducted tribological tests using a brush seal installed in a T-700 gas turbine engine. A split-ring brush seal was fabricated and installed between two labyrinth-honeycomb shroud seals. The annealed Haynes 25 bristles rubbed against a non-conditioned, irregular Rene 80 turbine blade shroud surface.

The objectives of the study were to demonstrate that a well designed and manufactured brush seal could survive the "pounding" of an irregular rotor surface without catastrophic failure, to demonstrate the concept of running a combined brush seal and labyrinth seal system and to acquire metalographic data on bristles subjected to such an environment.

The seal did not disintegrate and a summary of the test results is given in **Table 2.25.** The program proved that a segmented seal could be successfully installed in-between two labyrinth seals. The brush seal could operate at surface speeds up to 335 m/s, temperatures up to 620 °C and with a non-centred orbit of 0 to 0.8 mm, during steady and cyclic loading. The seal could operate against an irregular surface without disintegrating

but quickly wore to a line to line fit with an initial generation of fines and some larger elements. The seal was still functional after the tests.

2.8 Literature Review on the General Wear of Superalloy Materials.

It has been pointed out by many investigators who have studied the wear of superalloys, that the formation of an oxide film on at least one of the sliding surfaces is a necessary requirement for smooth sliding of unlubricated metals in order to reduce metallic adhesion. Oxide formation is likely to be temperature dependent, therefore, in selecting appropriate materials for brush seals in steam turbines, the temperature stability of the candidate materials (<600 °C) needed consideration.

Little tribological experimental data at elevated temperatures was available until the late 1950's and 1960's. This early work was restricted to the measurement of friction. It was shown by **Peterson, Florek and Lee (1960)**, that excessive surface damage resulted from sliding until a transition temperature was reached and above this temperature a considerable improvement in the sliding characteristics occurred as the wear mechanism changed from severe to mild wear or visa versa. **Figure 2.13** shows several, extreme examples of the varied response of wear rate to changes in operating conditions. These changes in wear rate are totally dependent on the operating conditions that control the dominant wear mode/type at those conditions. As a result of the sometimes irregular wear rate behaviour of materials under changing operating conditions, prediction of changes in wear rate is difficult without testing at representative conditions. The transition temperatures for materials of interest in the present work were found to be 40-90 °C for iron, 430 °C for chromium, 650-760 °C for nickel, and 320-550 °C for cobalt. **Peterson** suggested that transition was associated with the formation of oxides in the sliding path. This hypothesis was confirmed by simulated tests. When tested as lubricants a number of these oxides, particularly the softer ones were found to be effective in reducing friction and preventing surface damage.

The friction and wear behaviour of several nickel base alloys was investigated by **Stott et al (1973-1985)** during the 1970's and 1980's. The general test conditions and compositions of these and other materials investigated were given in **Tables 2.26, 2.27**, and **2.28.** At room temperature they found that the changes in the coefficient of friction and the wear rate during sliding could be correlated with work hardening, and possibly some degree of age hardening of the load bearing areas due to the severe mechanical and thermal stresses developed. Any oxide films that were formed had no significant effect on the tribological behaviour as they were removed from the surface as wear debris.

Bhansali (1979) carried out metal to metal wear tests on commercial nickel and cobalt base alloys under unlubricated conditions at room temperature. In general the wear volumes increased linearly with speed, load and sliding distance. **(Figures 2.14, 2.15,** and **2.16)**. In cobalt base alloys wear volumes were found to increase rapidly at high rubbing speeds whereas in nickel base alloys, wear volumes decreased at high rubbing speeds. In the course of his work it became evident that wear volumes under dry sliding conditions were affected by the oxidation characteristics of the alloy. Furthermore, nickel-base alloys appeared to be superior to cobalt-base alloys. Nickel base alloys displayed oxidative wear behaviour over a wide range of applied loads compared with cobalt-base alloys **(Figure 2.14)**.

Silence (1978) attempted to predict the performance of wear resistant alloys using several of their mechanical and physical properties. Most success was encountered using hardness. However, hardness is not a simple term since most wear resistant alloys consisted of several phases of differing micro hardness and the bulk hardness is related to the size and distribution of these second phases.

Within a given class of material, similar in composition, wear resistance can often be related to hardness. Equations have been developed to represent this relationship. For dissimilar classes of alloys such as iron base and cobalt base, no correlation between hardness and wear resistance was found. However, since hardness is usually decreased by

increasing the particle size of the harder phase, (at constant volume) hardness correlations are not a good indication of abrasive wear resistance. Evidently the **Archard** equation **(Equation 2.1)** could be qualitatively useful but did not allow accuracy better than about one order of magnitude.

Johnson, Moorhouse and Nicholls (1990) also identified a transition temperature, above which a noticeable change in wear and coefficient of friction existed after an incubation period. Such changes were closely related to the formation of a stable, adherent, thermally softened oxide layer or glaze on the load bearing areas during sliding. Once the glaze was established very little further wear took place. These favourable tribological properties of the glaze seemed to be associated with its low shear strength and the high strength of the underlying alloy substrate.

Johnson et al also showed that low chromium nickel alloys were damaged even at temperatures above the transition temperature. Comparisons of the performance factors between these binary Ni-Cr alloys and Nimonic alloys indicated that minor elements in the latter played only a relatively minor role in determining the tribological behaviour. High strength, relatively rapid transient oxidation rates and appropriate physical properties of the oxide films were important properties in alloys employed under sliding conditions in air at elevated temperatures.

It was very likely that the transition temperature defined the onset of oxide glaze formation capable of reducing wear and friction. The glazes (as defined by **Stott (1978)**) consisted of very fine, compacted crystalline particles of almost any oxide or oxides.

2.8.1 Effect of Mechanical Parameters/Operating Conditions.

The operating conditions and both physical and chemical compositions had a dramatic effect on the wear of a tribopair. Unfortunately wear mechanisms were complex and only generalisations could be made. However tests that have been carried out on tribopairs with comparable compositions or from the same materials classifications group can help to

identify wear mechanisms and trends that can be used as a guide for other tribopairs of interest.

Bhansali (1979) explored the effect of changing mechanical parameters under dry sliding conditions for high temperature alloys, the compositions of which were given in **Table 2.29** and the test conditions given in **Table 2.30**. Some of his results and general aspects are summarised in **Sections 2.82-2.8.9**.

2.8.2 Crystal Structure.

The crystal structure of nearly all metals may be one of three configurations: body-centred cubic **(bcc)**, face-centred cubic **(fcc)** or hexagonal close packed **(hcp)**. These arrangements are shown in **Figure 2.17.** Of these three, the hexagonal close packed has the most limited deformation characteristics, because it can only deform by slip along the basal plane. Wear is associated with plastic deformation. Therefore metals such as cobalt which has a hexagonal close packed structure gave good wear resistance. Unfortunately, such crystal structures were not always stable under all operating conditions. For example, cobalt had a good wear resistance at low temperatures but its wear increased one hundred-fold when the contact temperature rose above 417 °C. This sudden change was directly related to the change in the crystal structure of cobalt, which was hexagonal close packed below 417 °C and face-centred cubic above that temperature. In normal environments the oxide films on metal surfaces offered considerable protection against wear by restricting the extent of the metal-to-metal contact.

2.8.3 Effect of Speed.

Idealised sliding contact speed is generally expected to have a linear relationship with wear volume or have a wear rate that is directly proportional to rubbing velocity. However, under certain circumstances the sliding contact speed can induce dramatic changes to the wear rate as the schematic in **Figure 2.13** shows. This may be due to several

reasons related to contact temperature, oxidation rate or wear debris entrapment or removal.

Wear volumes from published work are plotted as a function of speed in **Figure 2.14**. Among the cobalt base alloys the Haynes Stellite alloys numbers 6 and 12 show an increase in wear volume at speeds greater than 0.2195 m/s (13.17m/min). Correspondingly, wear debris analysed for alloy no 12 at 0.329 m/s (19.75 m/min) show the presence of a **fcc** matrix and no oxides. It is possible that the apparent effect due to the speed increase arose from the frictional heating. Higher speeds would tend to produce higher interfacial temperatures leading to thermal softening of the cobalt-base alloys numbers 6 and 12. Haynes Stellite alloy no 1 displayed virtually no effect of speed on wear volumes. However, the wear debris analysis indicated the presence of oxides of metallic wear. Thus, it appeared that higher speeds tended to shift the transition from mild to severe wear at low applied loads.

Ward (1970) showed there was similar behaviour at high speeds for pure cobalt. In contrast, all the nickel base alloys showed a slight or virtually no decrease in volume losses at high speeds. Here again, the wear debris showed the presence of oxides throughout the speed range tested. Similar findings in the case of pure iron and nickel were observed by **Soda (1977)** where the wear volumes were independent of sliding speed over a wide range owing to oxidative wear.

2.8.4 Effect of Load.

The idealised relationship between load and wear volume was also thought to be linear but this could again change dramatically **(Figure 2.13)** when certain loads are reached. This may be due to the shear or compressive strength of the substrate or glaze layer or the contact temperature achieved under different loads.

In general, when the wear volume was plotted against applied load for unlubricated sliding conditions for **Bhansali's** tests the relationship was linear. In the case of Haynes

Stellite numbers 6 and 12 two distinct regions are observed **(Figure 2.15)**. At applied loads greater than 669 -802 N (68.18-81.81 kgf) an abrupt change in slope was seen. This was accompanied with course metallic wear debris **(Figure 2.15)**.

Load was however a contributing factor in glaze formation due to frictional heating. In commercial nickel base alloys wear volumes have been observed to decrease significantly at temperatures above bulk temperatures of 150 °C accompanied by the formation of glaze layers. In contrast, studies done on commercial cobalt-base alloys have indicated an increase in wear volumes with bulk temperatures up to 300 °C above which spinel oxide (which are beneficial to a glaze layer) formation has been observed, i.e., Fe_2O_3 , Cr_2O_3, and $NiO\text{-}Cr_2O_3$. It could be concluded that in general nickel base alloys containing chromium, form spinel type oxides at much lower temperatures than cobalt-base alloys. Once the oxide was formed further heat transfer to the bulk material from the interface could be slowed down, which in turn reduces the amount of thermal softening near the subsurface region therefore producing a strong substrate at the interface. However, in the case of Haynes Stellite alloys numbers 6 and 12, at high loads the oxide layer may not have been sufficiently thick to retard heat transfer to the subsurface and cause thermal softening, which in turn could not support any newly formed oxide layer. This was further substantiated by the behaviour of Haynes Stellite alloy no. 1 at high loads. Haynes Stellite no. 1 contains approximately 29 %wt carbides as opposed to 12 and 16 %wt in alloys numbers 6 and 12 respectively. The high volume fraction of carbides in turn minimised thermal softening as well as providing a hard phase on which the mating ring (on the ring on ring wear test machine) could ride. This was further substantiated by the fact that wear debris obtained at high loads from alloy no. 1 contains a **bcc** phase from the steel ring in addition to a **fcc** phase from the matrix. At loads greater than 401 N (40.91 kgf) volume losses for alloy no. 1 were virtually independent of applied loads. It was possible that carbides were in contact with the steel ring.

2.8.5 Effect Of Sliding Distance/Test Duration.

Sliding distance or test duration again had a linear idealised relationship with wear volume. However, again the wear rate could unpredictably change. If sufficient wear debris had been generated to produce a self sustaining glaze layer when the wear debris generation rate or retention rate was low the wear mode may change from severe to mild. In most cases glaze formation occurs in the early stages of high temperature sliding tests and after this the wear rate would be fairly constant.

The effect of sliding distance on wear volumes for the **Bhansali** tests was plotted in **Figure 2.16**. Since the applied load was 401 N (40.91 kgf) all the alloys were essentially in the mild wear regime. Almost all the alloys displayed running in periods of varying length. It was interesting to note that the relative ranking of the alloys was similar to the one obtained in **Figure 2.15** for varying loads. The three nickel base alloys displayed very low volume losses owing to what was believed to be glaze type formation of spinel oxides. Among the cobalt base alloys, Haynes Stellite alloys numbers 6 and 12 and Tribology alloy T-400 showed running in for a distance of 54.8 m or less, whereas nickel base alloys displayed a change in the rate of wear, albeit a small change at 109.6-164.6 m. Haynes Stellite alloy no. 6 showed another change in slope at 164.5 m which was believed to be due to a change in the type of oxide formed at the interface. Wear volumes for Haynes Stellite alloy no. 1 were virtually independent of sliding distance after 219.5 m. It was believed that the matrix was worn down to expose carbides and as a result no further loss in wear volume was observed.

2.8.6 Effect of Lubrication.

The presence of a lubricant, whether a continuous one or a discontinuous one as with some compacted iron materials, reduced the wear rates by a factor of up to one hundred in some cases, depending on the load and the speed. The wear coefficients were also changed by a similar factor. Within a HP turbine the steam is super-heated (dry

steam). However, the pressure drop across a seal and pressure variation within a bristle pack, may cause some condensation in cooler stages, which may act as a lubricant (mainly during start up conditions). The oxides formed in dry high temperature sliding contact with certain tribopairs may also act as a solid lubricant. Operational constraints would not allow a liquid lubricant to be introduced so the operation of the brush seal will be almost entirely under dry unlubricated sliding conditions.

2.8.7 Effect of Surface Finish

Archard's equation suggests that wear is independent of surface finish. It was found that types of finish between samples polished with 120-600 grit (50μm to 67μm. CLA) and 0.05 μm alumina polishing had virtually no effect on wear or coefficient of friction. However, cobalt base alloys did tend to show higher volume losses for a fine surface finish than those for a coarse finish as shown in **Table 2.31**. This would be expected (within limits). A coarse surface finish would tend to provide sites to trap wear debris which was oxidative under the conditions tested and therefore decreased the asperity contact. However, nickel base alloys were virtually unaffected by surface finish. This may be due to their tendency to form oxides at lower temperatures. Rolls-Royce have specified that they aim for a surface finish of 0.1 μm CLA and always achieve a surface finish of 0.48 μm CLA on their gas turbine rotors. The steam turbine specification was to machine rotors to 0.32 μin or 0.8 μm CLA (single point turned).

2.8.8 Effect of Hardness.

Historically tribologists generally thought, as a rough guide, that increasing hardness tended to reduce wear. Furthermore as the load increased it was common for wear to increase rapidly as the nominal contact pressure approaches H/3, where H was the indentation hardness of the material at the operating contact temperature (which equals the ambient temperature plus the temperature rise due to frictional heating).

Such a transition from mild to severe wear was associated with a plastic yielding of the material immediately below the asperities. It was also noted that the hardness of a material depended on the temperature, although some materials (most superalloys) have "hot hardness" characteristics, which enables them to retain their hardness to high temperatures **(Figure 2.18)**. The hot hardness characteristics are particularly significant due to the relatively high, localised contact temperature generated by sliding contact. In general, high hardness (in particular at the operational contact temperature) is associated with reduced wear. It has been suggested that attempts should be made to keep the applied normal load below that value which gives rise to nominal contact pressures approaching H/3.

The hardness of the alloys was expected to be a significant factor, along with glaze forming characteristics, in determining the wear rate. In tests carried out by **Johnson, Moorhouse and Nicholls (1990)**, the hardness at room temperature of a selection of wear resistant alloys and hardfacings were compared to wear resistance **(Table 2.32)**. There was found to be no significant correlation. However, relative hardness within relatively similar composition materials was found to give an indication of wear resistance.

2.8.9 Mutual Solubility.

It has been found that there is a correlation between mutual solubility, or compatibility of materials in contact and their relative the wear rate. In general, wear was less where the mutual solubility was low and was greatest where this was high. Generally the greatest wear occurred between identical metals in contact where the mutual solubility was 100% **(Table 2.33)**.

2.9 Final Candidate Brush Seal Bristle Material Selection.

Given the operating conditions within steam turbines, previously used gas turbine brush seal bristle materials, previously tested high temperature wear resistant alloys and a lack of general information on the high temperature wear of high temperature alloys in

sliding contact with a modern rotor material, a list of 25 candidate materials was compiled **(Table 2.34)**. The 25 materials are all superalloys (with the exception of the rotor Spec.297 material) and are separated into four main groups, Nickel Base Age Hardening, Solution Hardened Nickel Base, Cobalt Base and Iron Base. The test program was designed to identify the most appropriate materials group within the list and trends within the groups.

Table 2.1 General operating conditions of a gas turbine and a steam turbine.

Condition	Gas Turbine	Steam Turbine
Max. Temp. °C	667	560
Max. Rubbing Speed (m/s)	356	478
Max. dP per Seal (bar)	10.69	71.14

Table 2.2 The properties of Haynes 25.

Haynes 25 material Properties
Excellent high temperature strength
Good resistance to oxidising environments up to 980 C (1800 F) for prolonged exposures.
It can be fabricated and formed by conventional techniques
Available in many convenient forms (in this case wire).
The alloy has good ductility
Excellent resistance to metal galling.
It does however work harden.
Young's Modulus of 188 GN/m^2 at 538 C
Thermal conductivity of 19.5 w/m-K at 540 C.
Hardness at 540 C (1000 F) is 160 Hv (Rb 83) for solution treated Haynes 25.
For 25% work hardened is 300 Hv (30 Rc).

The chemical composition by percentage mass is:-

Co 51% Ni 10% Cr 20% W 20% Fe 3% Mn 1.5% Si 0.4% C 0.1%

Table 2.3 2% Chromium Molybdenum Nickel Tungsten Vanadium Steel Rotor Forging

	Percent	
Element	**Min**	**Max.**
Carbon	0.20	0.26
Silicon	-	0.25
Manganese	0.60	0.80
Sulphur	-	0.015
Phosphorus	-	0.015
Nickel	0.65	0.85
Chromium	2.00	2.20
Molybdenum	0.75	0.95
Vanadium	0.28	0.37
Tungsten	0.55	0.75
Aluminium (Total)	-	0.015
Tin	-	0.020
Copper	-	0.20
Antimony	-	0.020
Arsenic	-	0.025

Forging for high and intermediate pressure or single cylinder HP-LP turbine rotors.

Table 2.4 Parameters often seen in wear equations.

Operational parameters	**Material parameters**	**Environmental parameters**
Surface topography	Hardness, cold and hot	Type and amount of lubricant
Contact geometry	Ductility	Type and amount of dirt and debris
Applied load	Fracture toughness	Rigidity of supporting structure
Slide/role speed	Strength	Ambient temperature
Coefficient of friction	Work hardenability	Multiple pass of continuous contact
	Elastic moduli	Continuous, stop start reciprocation
	Material morphology	Clearance, alignment, and fit
	Type and thickness of surface film	Matched or dissimilar material pair
	Thermal Properties	

Table 2.5 Classifications of wear processes.

Adhesive wear	**Abrasive wear**	**Fatigue wear**	**Combined wear types**
(a) Mild wear	(a) Machining wear	(a) Contact fatigue wear	(a) Fretting
(b) Severe wear and scuffing	(b) Low-stress sliding abrasion	(b) Percussive wear	(b) Corrosive wear
	(c) Particle impact erosion	(c) Cavitation erosion	
	(d) Three-body abrasion	(d) Delamination wear	
	(e) Gouging abrasion		

Table 2.6 Test conditions **(Hawthorne (1994)).**

	Screening Tests (Pin on disk test rig)	**Primary Tests**
Temperature	Moderate	500 °C
Rubbing speed	Moderate	100 m/s
Load	Moderate	N/A
Disk diameter	N/A	280 mm, 12.5 mm thick
Material geometry	Pin	Bristle tufts mounted perpendicular.

Table 2.7 Details of flexible element materials **(Hawthorne (1994))**.

Type	**Nominal Composition**	**Diameter (μm, approx.)**
Nomex	100% Nylon	5*10
Kevlar 49	100% Aromatic polyamide	12
Nextel	$62Al_2O_3$, $24SiO_2$, $14B_2O_3$	8*13
Carbon	>99% C	8
Nicalon	63SiC, $24SiO_2$, 7C	15
Boron	>99% (on W core)	95
304 Stainless steel.	19Cr, 10Ni, <0.15C, Fe bal	38
Nichrome	80Ni, 20Cr	15
Haynes 25	50Co, 20Cr, 15W, 10Ni, <3Fe, 1.5Mn, 1Si	75
Inconel X750	72Ni,15.5Cr, 7Fe, 2.5Ti, 1Cb,<1Co,<1Mn, 0.7Al	80

Table 2.8 Details of counterface materials **(Hawthorne (1994))**.

Type	**Nominal Composition**	**Hardness (kg/mm^2)**
410 Stainless steel.	12.5Cr, 1Si, <1Mn, 0.5Ni, <0.15C, Fe bal.	340
A286 stainless steel.	26Ni, 15Cr, 2Ti, 1.35Mn, 1.25Mo, 0.5Si, 0.3V, 0.25Al <0.08C, Fe bal.	450
Cr_2O_3 coating[a]	>99% Cr_2O_3	1150
Cr_2C_2 coating[b]	80Cr_2C_2, 16 Ni, 4Cr	770
Solid Lubricated Cr_2C_2[c]	As above, plus CaF_2/BaF_2/Ag	-

[a] UCAR LC-4, on Greek Ascoloy disc.

[b] UCAR LC1C, on A286 steel disc.

[c] NASA coating

Table 2.9 Test conditions (Atkinson and Bristol (1991)).

Parameter	**Value**
Temperature	0-650 °C
Rubbing speed	0-335 m/s
Test Duration	100 hours
Pressure differential (Back to back)	345 kPa
Material geometry	Full brush seal
Seal diameter	457 mm (max.)

Table 2.10 Test seal dimensions **(Atkinson and Bristol (1991))**.

	a) Ambient tests	**b) Hot tests**
Wire diameter	0.071	0.071
Seal I.D.	129.339	280.111
Rotor O.D.	129.562	280.416
Seal O.D.	158.712	311.137
Backplate I.D.	131.509	282.829
Bristle Overhang	1.085	1.359
Bristle Interference	0.112	.0153
Front Plate I.D.	148.209	296.037
Bristle Lay Angle	45	45
Bristle Density (Bristles /(mm circumference))	96.5	96.5

Table 2.11 Hard coating compositions **(Atkinson and Bristol (1991))**.

Coating	**Application Process**	**Nominal Composition % Weight**
Chromium Carbide	Detonation gun	65(92 Cr-8C)+35(80Ni-20 Cr)
Tungsten Carbide	Detonation gun	83W-14Co-3C
Aluminium Oxide	Detonation gun	Al_2O_3

Table 2.12 Bristle properties at 480 °C **(Atkinson and Bristol (1991))**.

Composition (% weight)	**Nickel Alloy Cr-15, Fe-7, Ti-2.5, Al-0.7, Cb-.95, Mn-1 max., Si-0.5, S-0.010 max., Cu-0.5 max., C-0.08 max., Co-1.0 max., Ni-balance.**	**Cobalt Alloy C-0.010, Cr-2-.0, Mn-1.5, Ni10.0, Si-1.0, Fe-3.0, W-15.0, Co-Balance**
Coef. Of Therm. Exp (10^{-6}/C)	14.31	13.12
Thermal Conductivity (W/M-K)	18.10	18.32
Specific Heat (W/Kg-K)	531.7	527.51
Modulus of Elasticity (GPa)	187.67	195.81
Density (g/cc)	8.25	9.14
Tensile Strength (kPa)	692.9	461.9
0.2% Yield (kPa)	241.3	137.9
% Elongation	16.0	3.2

Table 2.13 Room temperature combinations ranked by brush weight loss (gms) **(Atkinson and Bristol (1991))**.

Tribopair	**Weight Loss**
Cobalt Alloy vs. Chromium Carbide	(.1)
Cobalt Alloy vs. Aluminium Oxide	(.19)
Cobalt Alloy vs. Tungsten Carbide	(.29)
Nickel Alloy vs. Tungsten Carbide	(.36)
Nickel Alloy vs. Aluminium Oxide	(.41)
Nickel Alloy vs. Chromium Carbide	(.57)

Table 2.14 Room temperature combinations ranked by rotor scar depth (μm) **(Atkinson and Bristol (1991))**.

Tribopair	**Weight Loss**
Cobalt Alloy vs. Tungsten Carbide	(12.70)
Nickel Alloy vs. Aluminium Oxide	(20.32)
Nickel Alloy vs. Tungsten Carbide	(45.72)
	Circumferential Crack
Cobalt Alloy vs. Chromium Carbide	(53.34)
Nickel Alloy vs. Chromium Carbide	(127.0)
Cobalt Alloy vs. Aluminium Oxide	(203.2)

Table 2.15 480 °C rotor and brush wear at 100 hrs **(Atkinson and Bristol (1991))**.

Test	**Bristle**	**Hardcoat**	**Rotor (μm)**	**Brush (gms)**
1a	Cobalt Alloy	Chromium Carbide	7.62	1.87*
1b	Cobalt Alloy	Tungsten Carbide	58.42	1.25*
2a	Nickel Alloy	Chromium Carbide	7.37	1.19
2b	Nickel Alloy	Tungsten Carbide	73.15	1.005

* Results of brush wear are inconclusive because of unintentionally large rotor to stator offset.

Table 2.16 Wear/fatigue tests **(Derby and England (1992))**.

Parameter	**Value**
Temperature	650 °C
Rubbing speed	50 m/s
Load/contact	Just touching
Test duration	In excess of 15 million fatigue cycles
Wheel diameter	49.7 mm with 4 lobes at 51.8 mm
Material Geometry	Miniature brush seal.

Table 2.17 Screening tests (ring-on-ring) **(Derby and England (1992))**.

Parameter	**Value**
Temperature	650 °C
Rubbing speed	30.5 m/sec
Load/contact pressure	2 psi
Test duration	1.5 hours
Specimen Geometry	Ring

Table 2.18 Primary tests **(Derby and England (1992))**.

Parameter	**Value**
Temperature	705 °C
Rubbing speed	100 m/s
Load/Contact	Light
Test duration	35 mins (accumulated at different speeds)
Wheel diameter	50 mm
Material Geometry	Miniature brush seal.
Atmosphere	Hot air/inert gas

Table 2.19 Brush specimen and current brush seal design geometries **(Fellenstein and Dellacorte (1994))**.

	Brush Specimen	**Current designs**
Bristle Materials	H25	H25 I718
Bristle Density	175 Bristles/mm Bore Circumference (4450 Bristles/mm Bore Circumference)	90-178 Bristles/mm Bore Circumference (2300-4500 Bristles/in Bore Circumference)
Bristle Area Ratio	0.82	0.42-0.83
Fence Height	1.27 mm (0.050 in.)	1.27 mm (0.050 in.)
Bristle Angle	45^0	40^0-50^0

Table 2.20 Test conditions **(Fellenstein and Dellacorte (1994)).**

Variable	**Value**
Temperature	20,650 °C 68 1200 °F
Surface Speed (Motor Speed)	1.99, 23.94 m/s 6.54, 78.54 ft/s (1000,12000 r.p.m.)
Contact Force (Test Load)	0.49, 0.98 N 2.18, 4.36 lbf (50 g,100 g)

Table 2.21 Wear factor interpretation to achieve goal of 10,000 hours **(Fellenstein and Dellacorte (1994))**.

Wear Factor (mm^3/Nm)	**Interpretation**
$>10^{-4}$	High Wear
10^{-5} to 10^{-6}	Moderate to Low Wear
$<10^{-7}$	Low Wear

Table 2.22 I718 journal wear* **(Fellenstein and Dellacorte (1994)).**

Test Conditions					
Temp.	**Surface Speed**	**Contact Force**	**Scar Depth (mm)**	**Wear Factor (mm^3/Nm)**	**Normalised Scar Depth (mm/Mrev)**
20 °C	1.99 m/s	0.49 N	4.55	1.4×10^{-8}	211
20 °C	1.99 m/s	0.98 N	0.23	4.2×10^{-10}	10.7
20 °C	23.94 m/s	0.49 N	0.71	2.2×10^{-10}	2.75
20 °C	23.94 m/s	0.98 N	0.92	2.2×10^{-10}	3.56
650 °C	1.99 m/s	0.49 N	0.17	1.6×10^{-11}	0.80
650 °C	1.99 m/s	0.98 N	0.02	2.9×10^{-11}	0.90
650 °C	23.94 m/s	0.49 N	0.14	3.5×10^{-11}	0.55
650 °C	23.94 m/s	0.98 N	0.26	1.4×10^{-11}	1.00

*Data error = +/- 6.5 % based upon external estimate.

Table 2.23 Haynes 25 brush wear **(Fellenstein and Dellacorte (1994)).**

Test Conditions					
Temp.	**Surface Speed**	**Contact Force**	**Bristle Wear (mm)**	**Wear Factor (mm^3/Nm)**	**Bristle Wear (mm/Mm)**
20 °C	1.99 m/s	0.49 N	0.34	$2.6 \pm 2.3 \times 10^{-5}$	2.630
20 °C	1.99 m/s	0.98 N	0.795	$8.1 \pm 4.0 \times 10^{-5}$	6.150
20 °C	23.94 m/s	0.49 N	0.119	$2.1 \pm 1.6 \times 10^{-6}$	0.077
20 °C	23.94 m/s	0.98 N	0.135	$1.2 \pm 0.5 \times 10^{-6}$	0.087
650 °C	1.99 m/s	0.49 N	0.030	$6.1 \pm 4.2 \times 10^{-6}$	0.232
650 °C	1.99 m/s	0.98 N	0.031	$3.2 \pm 1.9 \times 10^{-6}$	0.240
650 °C	23.94 m/s	0.49 N	0.061	$6.0 \pm 0.4 \times 10^{-6}$	0.039
650 °C	23.94 m/s	0.98 N	0.110	$9.7 \pm 1.1 \times 10^{-7}$	0.071

Table 2.24 Haynes 25 brush vs. I718 journal friction coefficient **(Fellenstein and Dellacorte (1994))**.

Test Conditions			
Temp.	**Surface Speed**	**Contact Force**	**Average Friction Coefficient**
20 °C	1.99 m/s	0.49 N	0.34 ± 0.05
20 °C	1.99 m/s	0.98 N	0.42 ± 0.03
20 °C	23.94 m/s	0.49 N	0.41 ± 0.06
20 °C	23.94 m/s	0.98 N	0.47 ± 0.03
650 °C	1.99 m/s	0.49 N	0.25 ± 0.06
650 °C	1.99 m/s	0.98 N	0.27 ± 0.02
650 °C	23.94 m/s	0.49 N	0.33 ± 0.04
650 °C	23.94 m/s	0.98 N	0.40 ± 0.03

Table 2.25 Brush seal and gas turbine engine specification and operating conditions **(Hendricks, Griffin, Bobula, Bill and Howe (1993))**.

Measured Diametrical Parameters.	**mm (in.) unless otherwise given**
Pre-test brush diameter (no taper)	321.79 (12.669)
Post-test brush diameter (tapered)	324.15 (12.762)
Differential	2.36 (0.093)
Pre-test rub interface diameter	322.30 to 322.81 (12.689 to 12.709)
Brush pre-test interface	0.51 to 1.27 (0.02 to 0.04)
Labyrinth cold clearance	2.29 to 2.46 (0.09 to 0.097)
Wear track diameter	323.42 (12.733)
Differential	0.74 (0.029) to 0.86 (0.034)
Stubble height	0.71 (0.028)
Possible material transfer	0.25 to 0.5 (0.01 to 0.02)
Possible engine eccentricity	0 to 0.8 (0 to 0.03)
Blade shroud height variation	0 to 0.23 (0 to 0.000)

Average Diametrical Clearance Estimates.	
Pre-test brush clearance	-0.51 to -1.3 (-0.02 to -0.04)
Post-test brush clearance	0 to 0.8 (o to 0.03)
Post-test labyrinth clearance	2.3 to 2.5 (0.09 to 0.10)

Engine Parameters.	
Turbine speeds to 20 000 r.p.m.	335 m/s (1100 ft/s)
Maximum turbine shroud temperatures	620 C (1150 F)
Average turbine shroud temperatures	455 to 566 C (850 to 1050 F)
Turbine inlet temperature	760 C (1400)
Seal pressure differential	0.007 MPa (1 psia)

Brush Seal Specification	
Bristle material	Annealed Haynes 25
Bristle diameter	0.071 (0.0028)
Bristle angle	43 to 50^0
Bristle packing density	98.4 per mm circumference (2500/in.circ.)
Backing plate angle	19^0
Seal outside diameter	333.9 (13.146)
Seal inside diameter	322.3 (12.690)
Bristle clearance	-0.51 to -1.27 (-0.02 to -0.05)

Shrouded Blades	
Material	Rene 80 (untreated)
Number of shrouded blades with irregularities	50
Irregularity radial distance	to 0.229 (0.009)
Irregularity circumferential distance	to 0.076 (0.003)
Irregularity axial distance	to 0.051 (0.002)
Number of impacts	4000 per second
Surface speed	168 m/s 550 (ft/s)

Table 2.26 Test conditions **(Stott 1978)).**

Test Conditions
Surface finish 25μm C.L.A.
Temperature room temp - 800 °C
Load 1.5 kg
Speed 500 cycles per min.
Reciprocation 2.5 mm
Duration 60 mins

Table 2.27 Test materials **(Stott (1978)).**

Alloy	C	Si	Cu	Fe	Mn	Cr	Ti	Al	Co	Mo	B	Zr	Pb	S	NI
N75	0.08 0.15	1.0 max.	0.5 max.	5.0 max.	1.0 max.	18.0 21.0	0.2 0.6	-	-	-	-	-	-	-	bal.
C263	0.03	0.25	0.20 max.	0.75 max.	0.40	20.0	2.15	0.45	20.0	5.9	0.001 max.	0.02 max.	-	0.007	bal.
N108	0.20 max.	1.0 max.	0.5 max.	2.0 max.	1.0 max.	13.5 15.75	0.9 1.5	4.5 4.9	18.0 22.0	4.5 5.5	-	-	0.005 max.	-	bal.
Incoloy 901	0.10 max.	0.60 max.	0.50 max.	bal.	2.00 max.	11.0 14.0	2.35 3.00	0.35 max.	-	5.00 7.00	0.010 0.020	-	-	-	40.0 45.0

Table 2.28 Selection of test materials **(Stott (1978))**.

wt % Element										
Alloy	Ni	Fe	Co	Cr	Al	Ti	Mn	Si	C	Other
Fecralloy 49	0.1	Bal.	-	14.3	4.18	-	-	0.1	-	-
Fecralloy BF1	0.1	Bal.	-	15.9	4.9	-	0.1	0.1	0.01	0.36Y
YT254	37.0	Bal.	20.0	5.0	-	-	-	-	-	0.1Y 0.04Zr
Dytal	-	Bal.	-	13.0	3.5	-	-	-	-	$0.5Y_2O_3$
Nimonic 80A	Bal.	2.0	-	19.5	1.4	2.4	0.3	0.3	0.06	0.06Zr
Nimonic 105	Bal.	-	20.0	15.0	4.7	1.2	0.3	0.3	0.01	5.0Mo 0.1Zr
Inconel 617	Bal.	1.5	12.5	22.0	1.2	0.3	0.5	0.5	0.07	9.0Mo
Inconel 671	52.0	-	-	48.0	-	-	-	-	-	-
MA754	Bal.	1.0	-	20.0	0.3	0.5	-	-	0.05	$0.6\ Y_2O_3$
MA956	-	-	-	20.0	4.5	0.5	-	-	-	$0.5\ Y_2O_3$
Inconel 738	Bal.	0.6	8.5	16.0	3.4	3.4	0.6	0.3	0.17	1.7Ta 2.6W 0.9Nb 1.7Mo

Table 2.29 Composition of alloys **(Bhansali (1979))**.

Alloy	Chemical Composition (wt. %)									
	Fe	Si	Cr	Ni	Co	Mo	W	C	B	Others
Stellite 1	-	-	30	-	55	-	12	2.5	-	-
Stellite 6	-	-	28	-	66	-	4	1.0	-	-
Stellite 12	-	-	29	-	62	-	8	1.3	-	-
Haynes-40	4.0	-	15	72	-	-	-	0.75	-	3.5
Haynes-41	-	2.6	8	-	62	28	-	0.06	-	-
Tribaloy 400	-	2.5	8.5	-	bal.	28.5	-	-	-	-
Tribaloy 700	-	3.4	15	bal.	-	32.5	-	-	-	-

Table 2.30 Test conditions **(Bhansali (1979))**.

Parameter	**Value**	**Increment/variation**
Load	0-204.5 kgf	14 kgf increments
Duration	2000 rev	
Sliding velocity	2.19-19.75 m/s	2.19 m/s increments
Sliding distance	54.8-548 m	54.8m increments
Surface finish	6-12 μin rms	120,240,400,600,0.05 μm

Table 2.31 Wear volume (mm ^{3}) as function of surface finish **(Bhansali (1979))**.

Surface condition	**Haynes Stellite alloys**			**Haynes Alloys**		**Triboloy Alloys**	
	No. 6	.No.12	No.1	No.40	No.41	T-400	T-700
120 grit	0.85	0.59	0.22	0.07	0.11	0.74	0.06
240 grit	0.94	0.69	0.38	0.13	0.15	0.72	0.10
400 grit	1.11	0.73	0.41	0.06	0.13	0.64	0.15
600 grit	0.92	0.83	0.29	0.12	0.12	0.63	0.07
0.05 μm alumina polish	1.06	0.72	0.55	0.11	0.2	0.57	0.08
0.05 μm alumina polish + electrolytic etch	1.22	0.80	0.29	0.15	0.15	0.83	0.06

Speed, 80 rev/min; sliding velocity, 28.8 ft/min (8.78m/min; load, 90 lbf (40.91 kgf)

Table 2.32 Wear of base alloys **(Johnson, Moorhouse and Nichols (1990)).**

Material	**Nominal Composition**	**Hardness Hv10 (at R/T before test)**	**Weight loss (mg)**	**Glaze Formation**
En 52	Fe-9Cr .5C 3.5Si .5Mn	323 316	208	poor
Nimonic 80A	Ni-20Cr 0.03Co 0.01Mo 2.4Ti 1.4 Al 0.12C 0.01Si	359 364	2813	poor
Nimonic 70	Ni-19Cr 1.2Ti 1.0Al 0.06C 1.5Nb 25Fe	345 370	350	good
Nimonic 91	Ni-29Cr 20Co 2.3Ti 1.2Al .5C .7Nb	276 287	6	good
Nimonic 81	Ni-30Cr 1.7Ti .9Al .05C	348 325	190	partial
UMT 520	Ni-19Cr 12Co 6Mo .3Ti 2Al .05C 1.0W 0.005B	312 317	10	good
Exp 1A	Wiggins exp. alloys	401 396	629	partial
Exp 2A	Wiggins exp. alloys	292 299	52	partial
Exp 3A	Wiggins exp. alloys	381 387	76	partial
Exp 4A	Wiggins exp. alloys	306 309	22	good
IN 718A	Ni-19Cr 3Mo .9Ti .5Al .03C 5.3Nb 18Fe	413 401	19	good
MA 757	Ni-16Cr 4.5Al .6Y	446 455	559	poor
MA 758/35	Ni-35Cr .5Ti .3Al .05C .6Y	405 409	33	good
MA 758/30	Ni-30Cr .5Ti .3Al .05C .6Y	315 308	296	good
IN 738 LC	Ni-16Cr 8.5Co 1.7Mo 3.4 Ti3.4Al .17C .9Nb 2.6W 1.7Ta	342 392	7	good
IN 671	Ni-46Cr .3Ti .05C	262-264	55	good
VA70	Fe-23Cr 1.0Mo .6C .2Si 2.5Mn 1.2Nb 8Ni 1V .5N	306 306	16	good
IMI 829	Ti-5.5Al 3.5Sn 3Zr1Nb .3Si .25Mo	348 345	218	good
IMI 834	Ti-5.8Al 4.5Sn 4Zr .7Nb .4Si .5Mo	363 363	228	good
UDM 720	Ni-18Cr 15Co 3Mo 5Ti 2.5Al 0.03C 1.2W	442-446	2	very good
MA 754	Ni-16Cr some Ti, Al, 6Y	309 305	3189	poor

Table 2.33 Comparison of coefficients and compatibility ratings of metal pairs.

Metal Pair	Compatibility(solubility)	Wear Coefficient, K
Nickel-Lead	Incompatible	0.21
Iron-Lead	Incompatible	0.69
Aluminium-Copper	Compatible	4.8
Aluminium-Iron	Compatible	6.0
Zinc-Zinc	Compatible	12
Iron-Copper	Limited Compatibility	19
Lead-Lead	Compatible	24
Aluminium-Aluminium	Compatible	30
Iron-Manganese	Limited Compatibility	38
Iron-Nickel	Compatible	59
Iron-Iron	Compatible	77
Nickel-Nickel	Compatible	290

Table 2.34 Materials for high temperature wear tests.

Nickel Base Age Hardening

Alloy	Ni	Cr	Co	Mo	Fe	C	NB/Ta Y B Zr	Ti	Al
263	52	20	20	6				2.4	.6
718	52	18		3	19	.05	5.0 NB + Ta.009 B	0.9	0.5
X750	70	16			8	.08	1.0 NB + Ta	2.5	.8
Wasp	58	19	13.5	4.3		.08	.006B.050Zr	3	1.5
R41	52	19	11	10		.09	.006B		
242	65	8		25		.03	.006B		
214	75	16				.05	0.1Zr.01Y		4.5

Solution Hardened Nickel Base

Alloy	Ni	Cr	Co	Mo	Fe	C	NB/Ta Y B Zr	Ti	Al
75	76	20				0.11		0.4	
625	62	21		9		0.1	3.5 NB + Ta		
230	57	22		2		0.1	.02 La 14 W.015 B		
X	47	22		9	18	0.1	.008 B .02 La		.25
G30	43	30		5.5	15	.03	2 Cu 1.5 NB		
C22	56	22		13		.01	3 W		
D205	64.5	20		2.5	6	.03	5 Si 2Cu		
B2	69			28		.01			
Hr160	37	28	29		2	.05	2.75 Si		

Cobalt Base

Alloy	Ni	Cr	Co	Mo	Fe	C	NB, Ta, Y B Zr	W
6B	2.5	30	58	1.5		1.0		
25	10	20	51			0.1		15
150		28	50		21	.05		
188	22	22	39			0.1	0.03 La	14
Ultimet	9	26	54		3	.06	0.08 N_2	2

Iron Base

Alloy	Ni	Cr	Co	Mo	Fe	C	NB, Ta, Y B Zr	W
HR-120	37	25		2.5	33	0.05	0.2 N_2 0.7 NB	2.5 0.004B
556	20	22	18	3	31	0.1	0.2 Zr 0.02 La	2.5 0.6 Ta 0.2 Zr 0
Ferralium	5.5	25		3.5	62	.04	1.7 Cu 0.17 N_2	

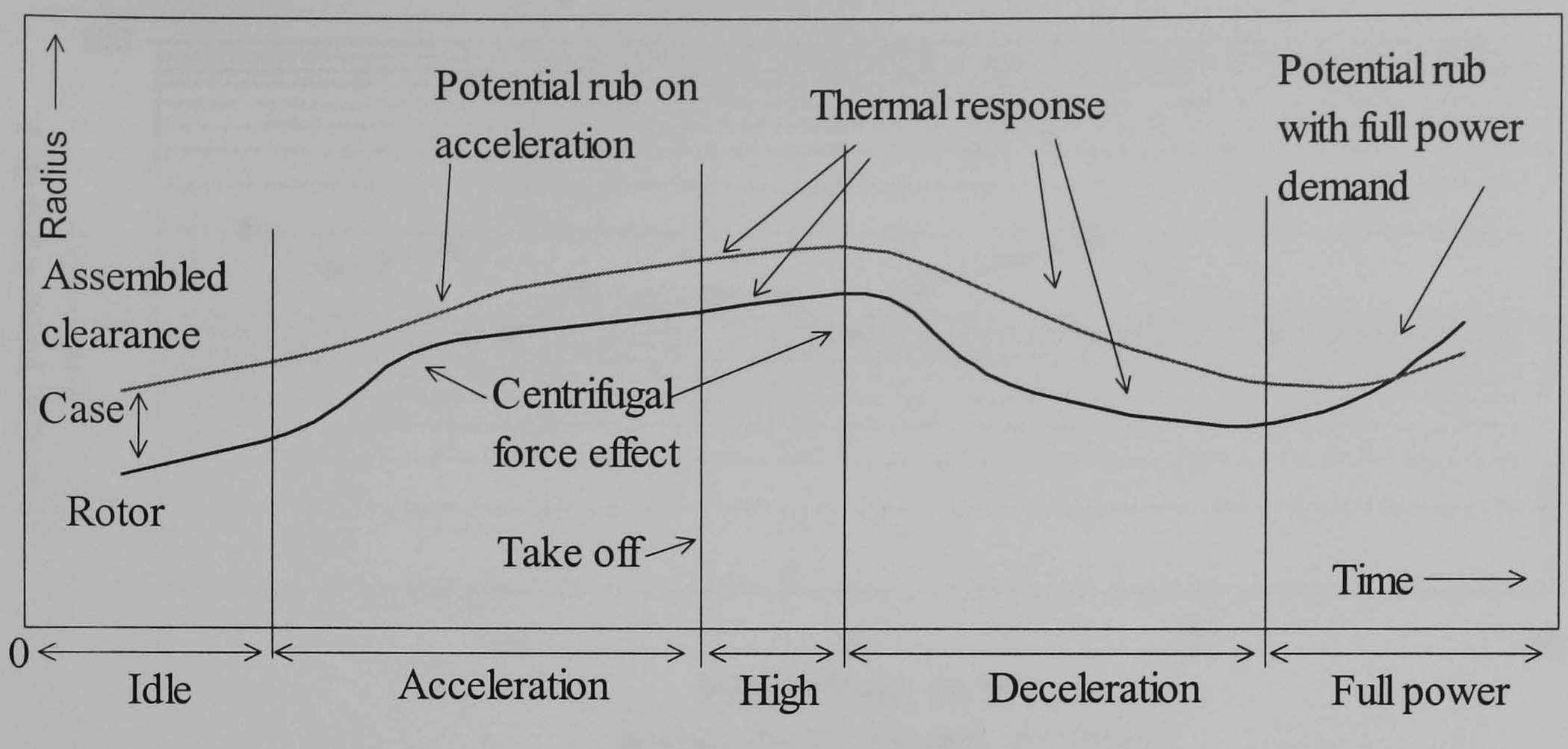

Figure 2.1 Illustration of variation in case to rotor clearance during engine operation.

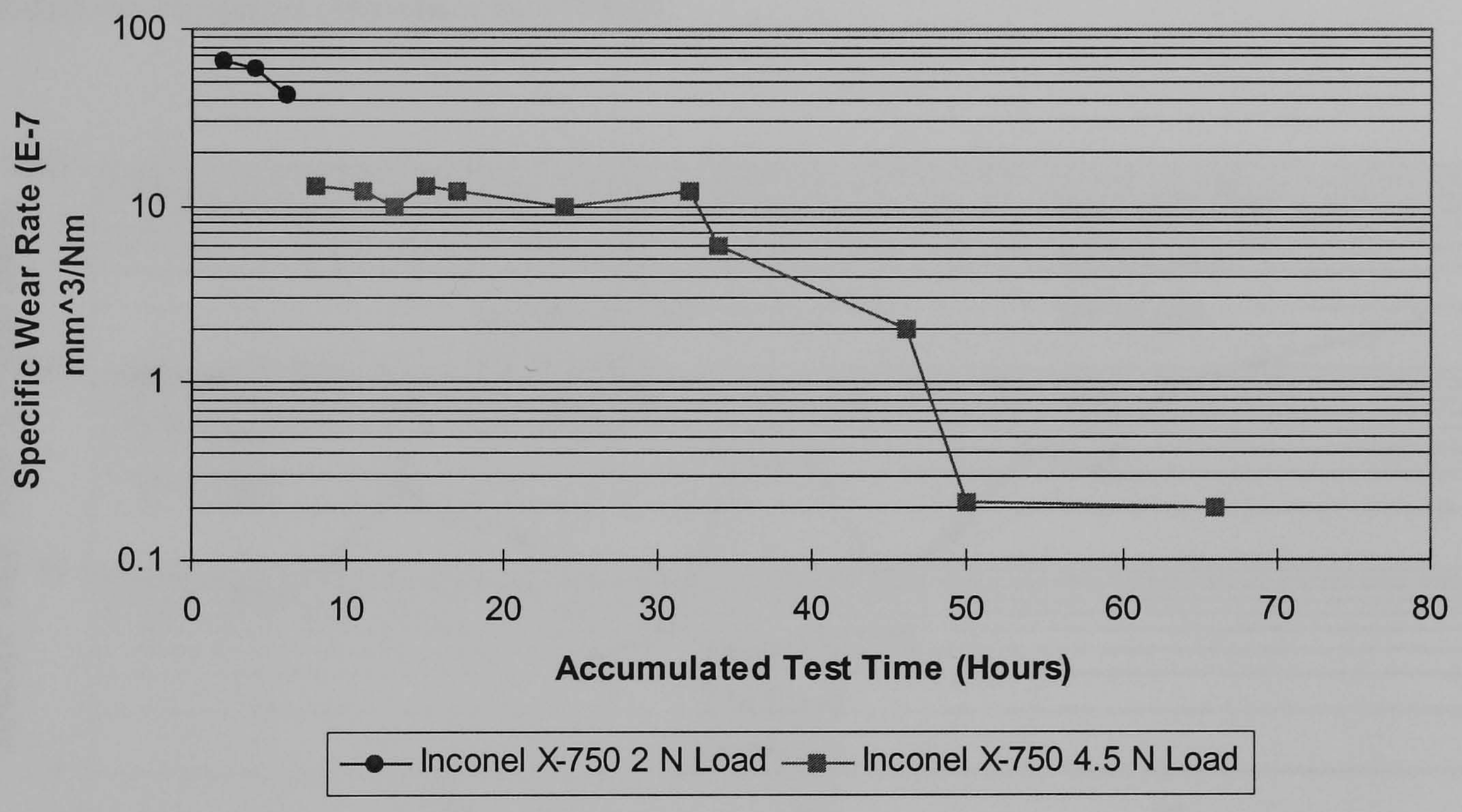

Figure 2.2 Typical results from extended sliding of brush specimens, under moderate normal loads **(Hawthorne (1994))**.

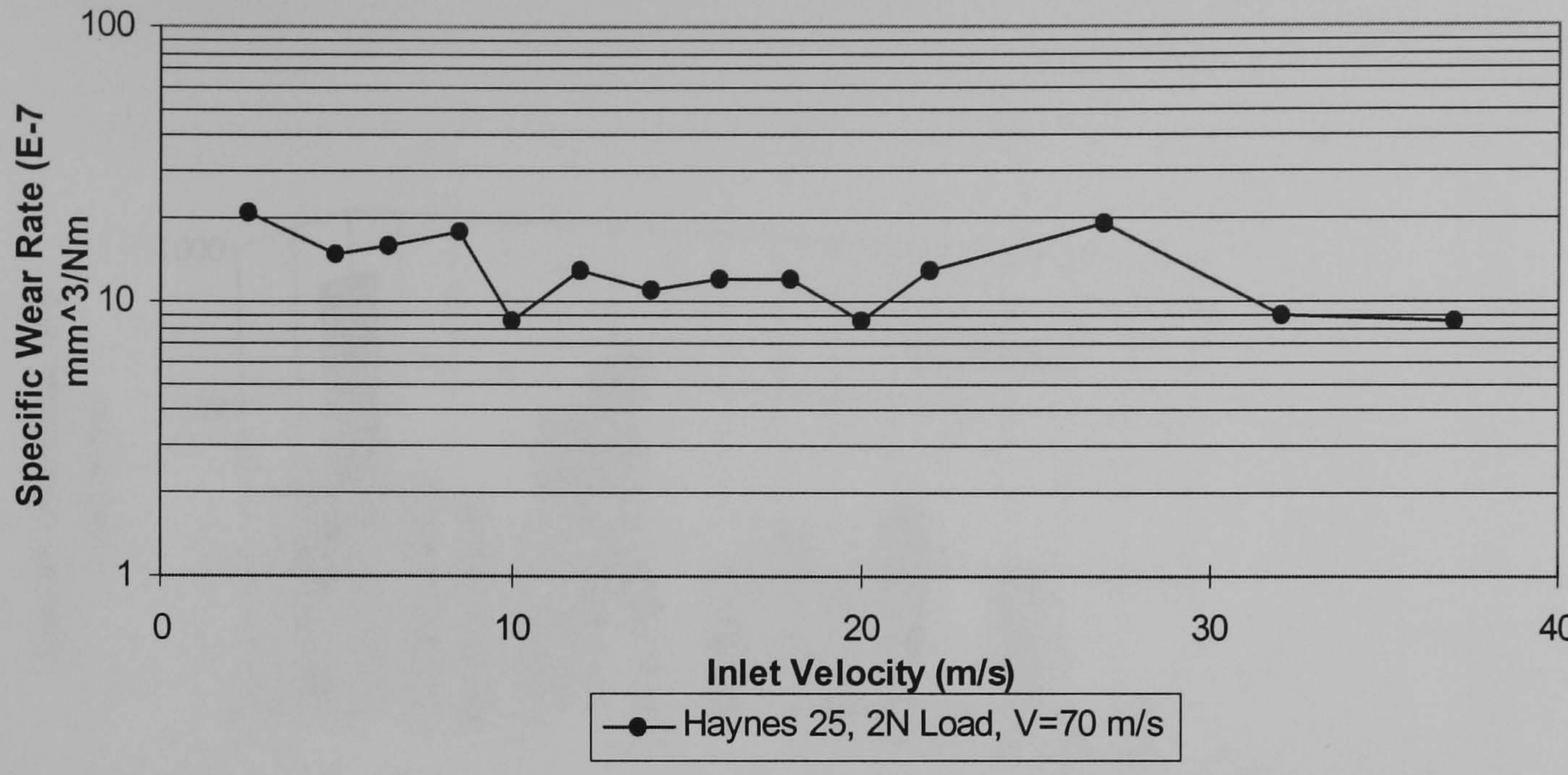

Figure 2.3 Extended sliding test results from different brush / counterface specimens, under conditions indicated **(Hawthorne (1994))**.

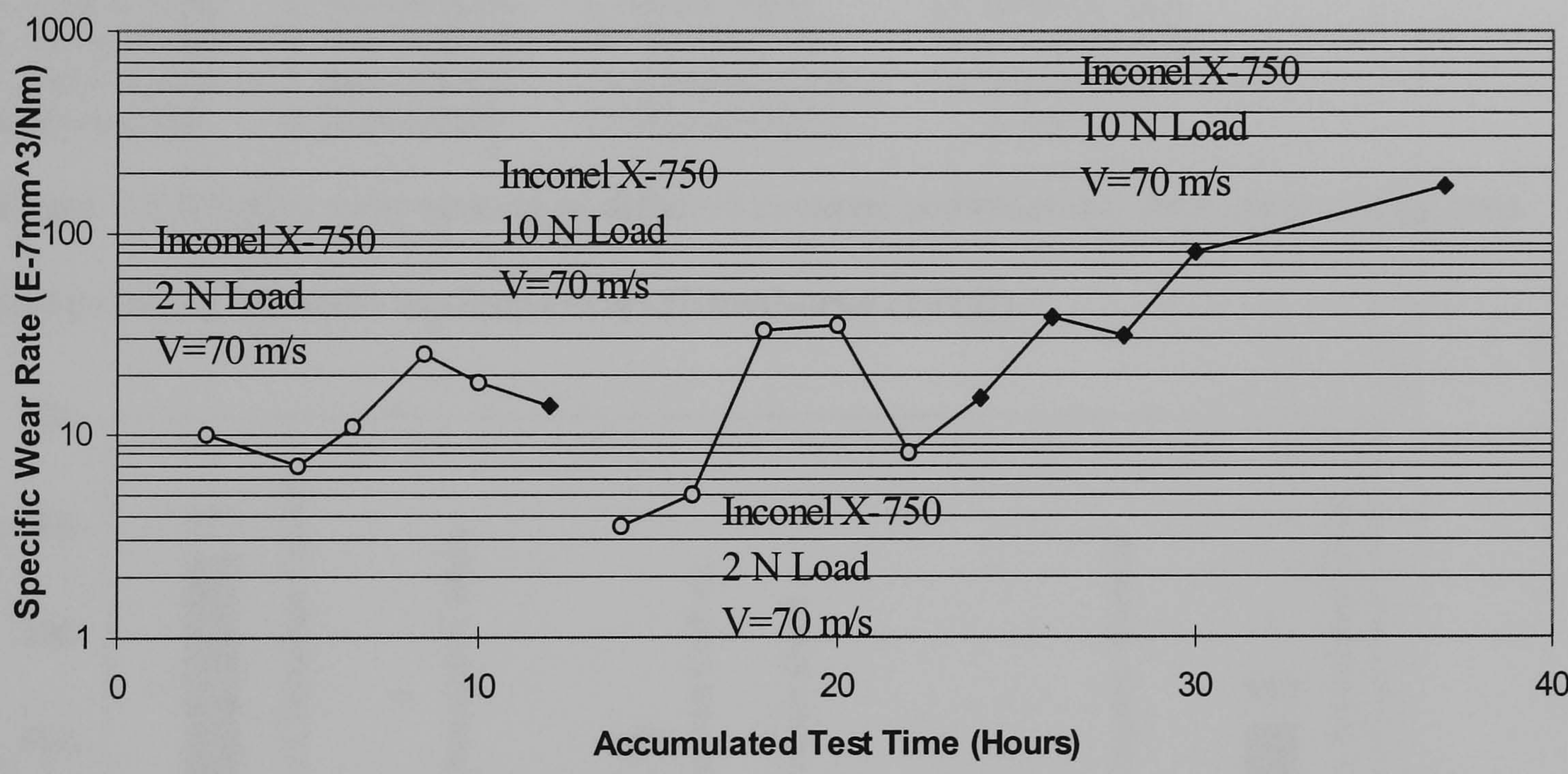

Figure 2.4 Extended sliding test results from different brush, under conditions indicated **(Hawthorne (1994))**.

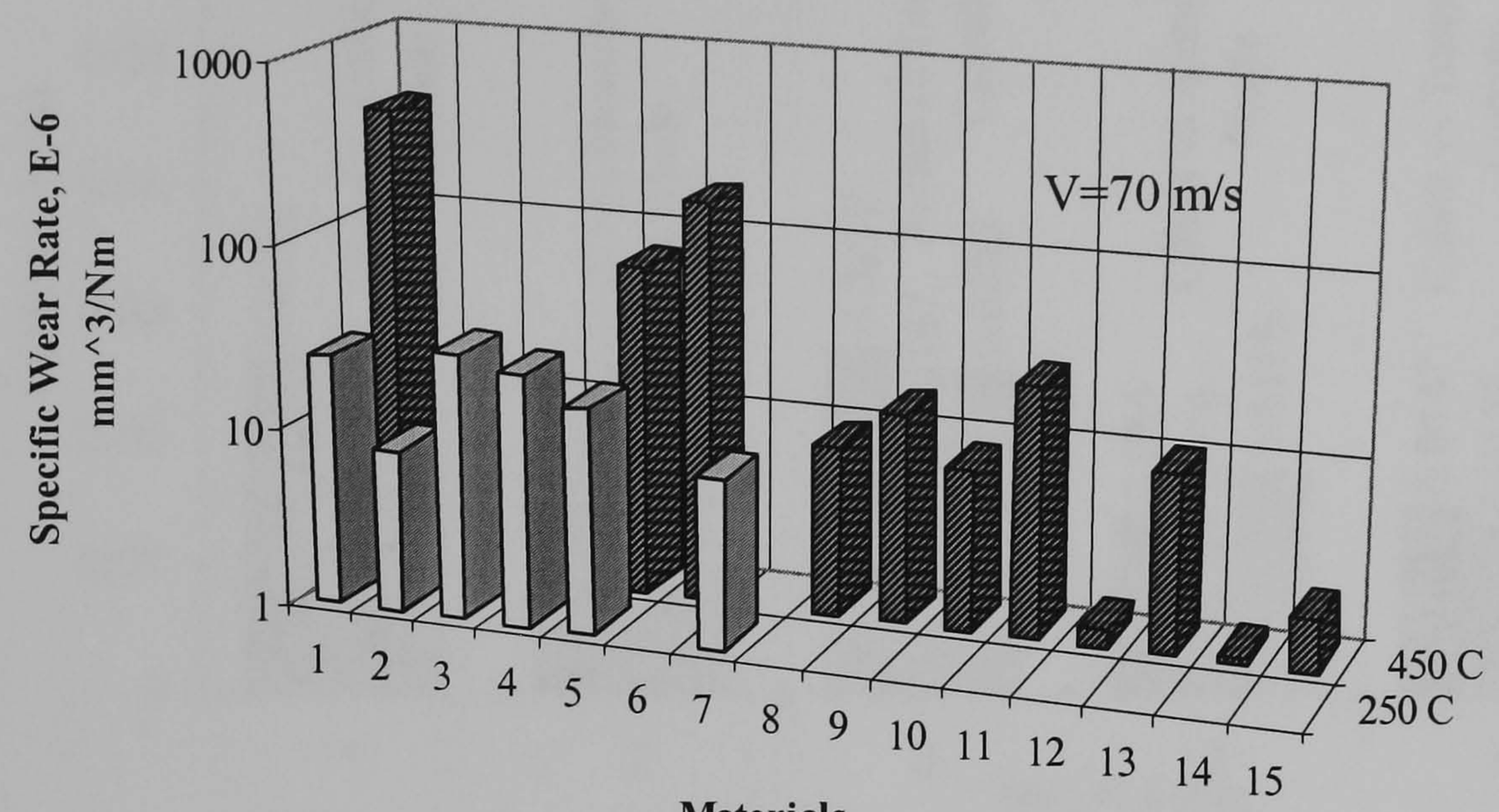

1. Carbon/A286
2. Carbon/Cr3C2
3. Nextel/Cr2O3
4. Nicalon/410
5. Nicalon/A286
6. Nicalon/Cr2O3
7. Boron/Cr3C2
8. 304SS/A286
9. 304SS/Cr2O3
10. 30433/Cr3C2
11. Nichrome/Cr3C2
12. Haynes/Cr3C2
13. Inconel/Cr2C2
14. Inconel/Cr3C2
15. Inconel/solid-lubed/Cr3C2

Figure 2.5 Relative wear ranking of different material combinations from short sliding tests (after running in) under moderate loads **(Hawthorne (1994))**.

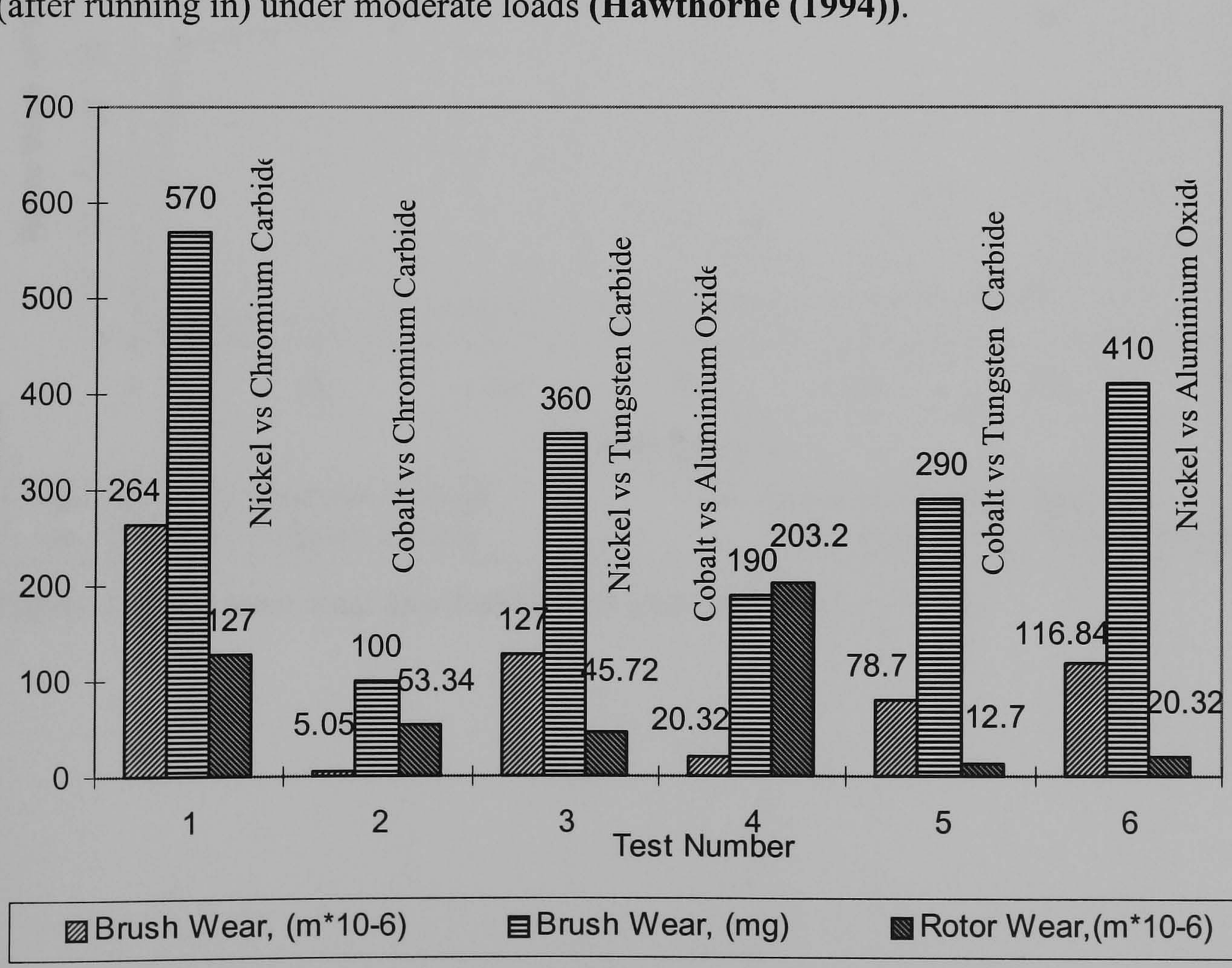

Figure 2.6 Summary of room temperature wear data 100 hour endurance **(Atkinson (1991))**.

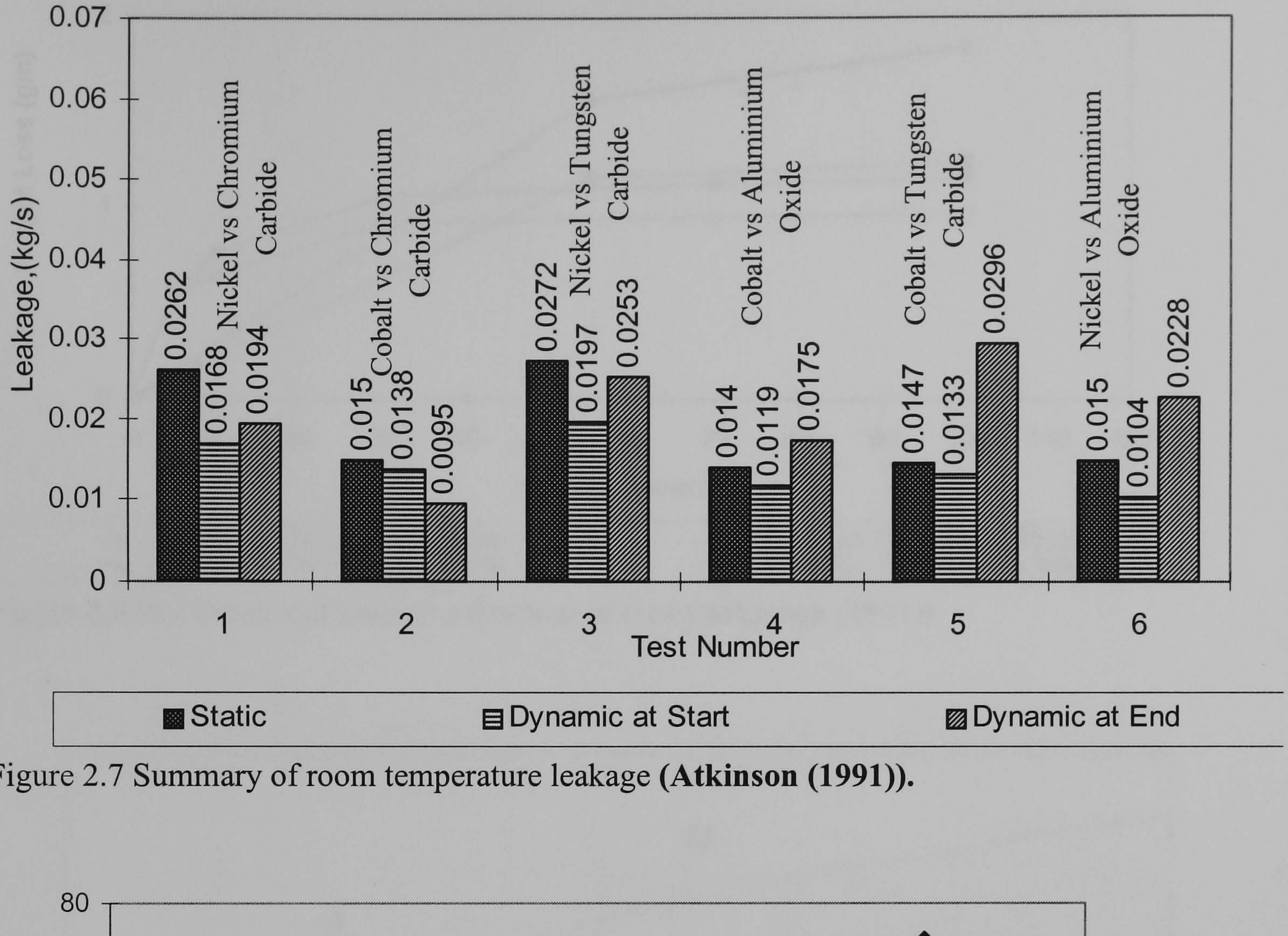

Figure 2.7 Summary of room temperature leakage **(Atkinson (1991)).**

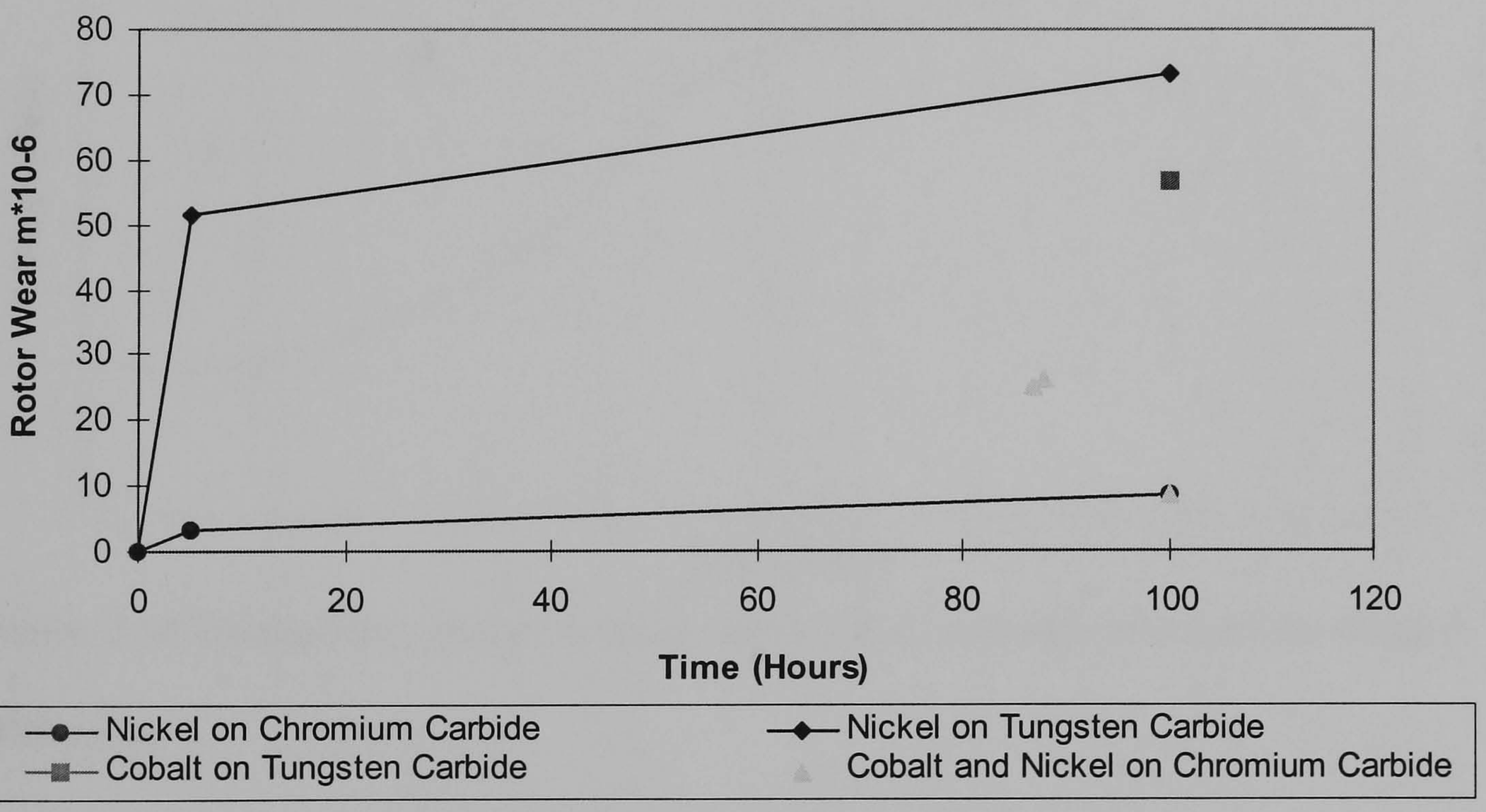

Figure 2.8 Hot rotor wear as a function of time **(Atkinson (1991)).**

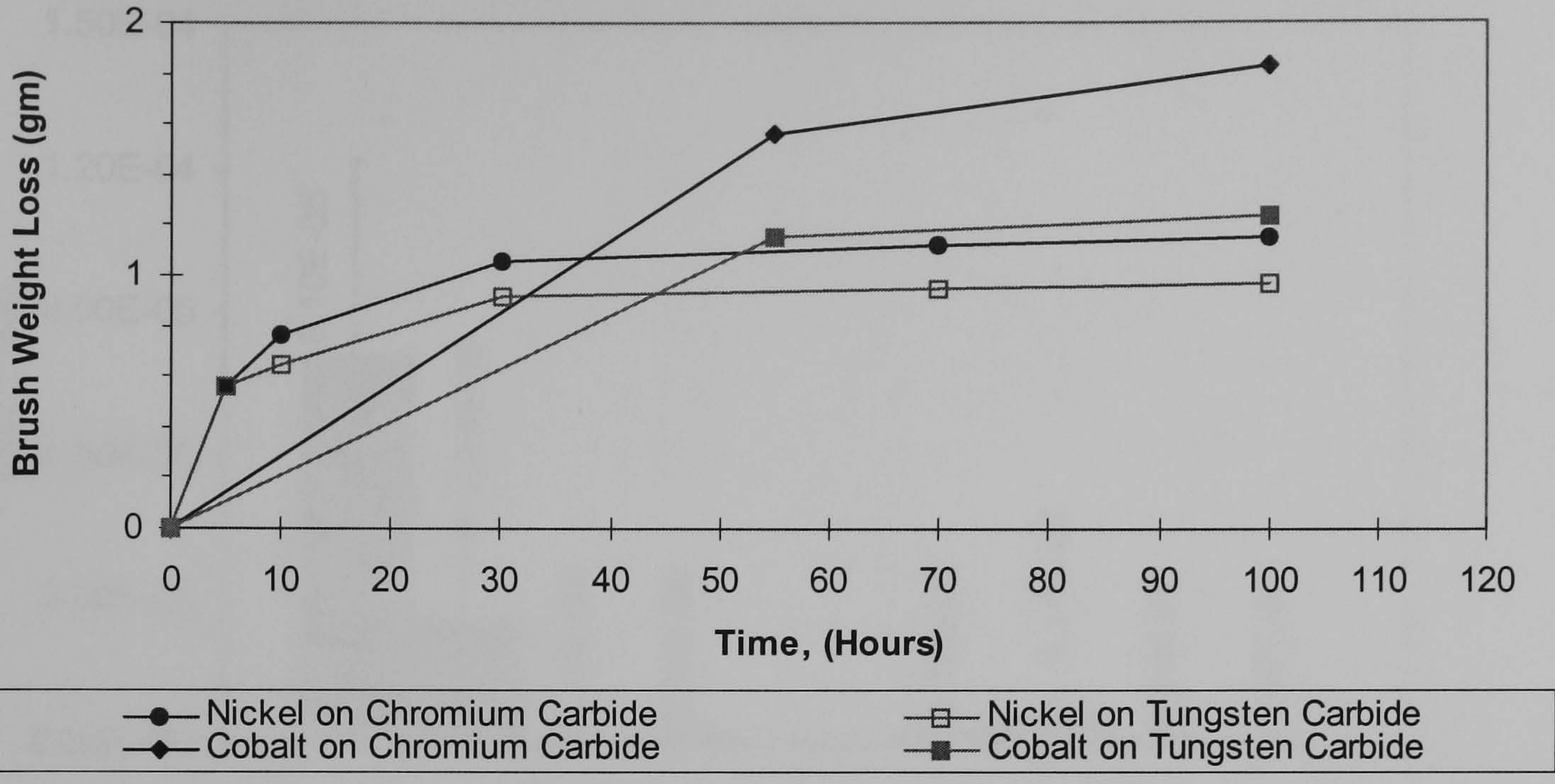

Figure 2.9 Hot brush seal wear as a function of time **(Atkinson (1991))**.

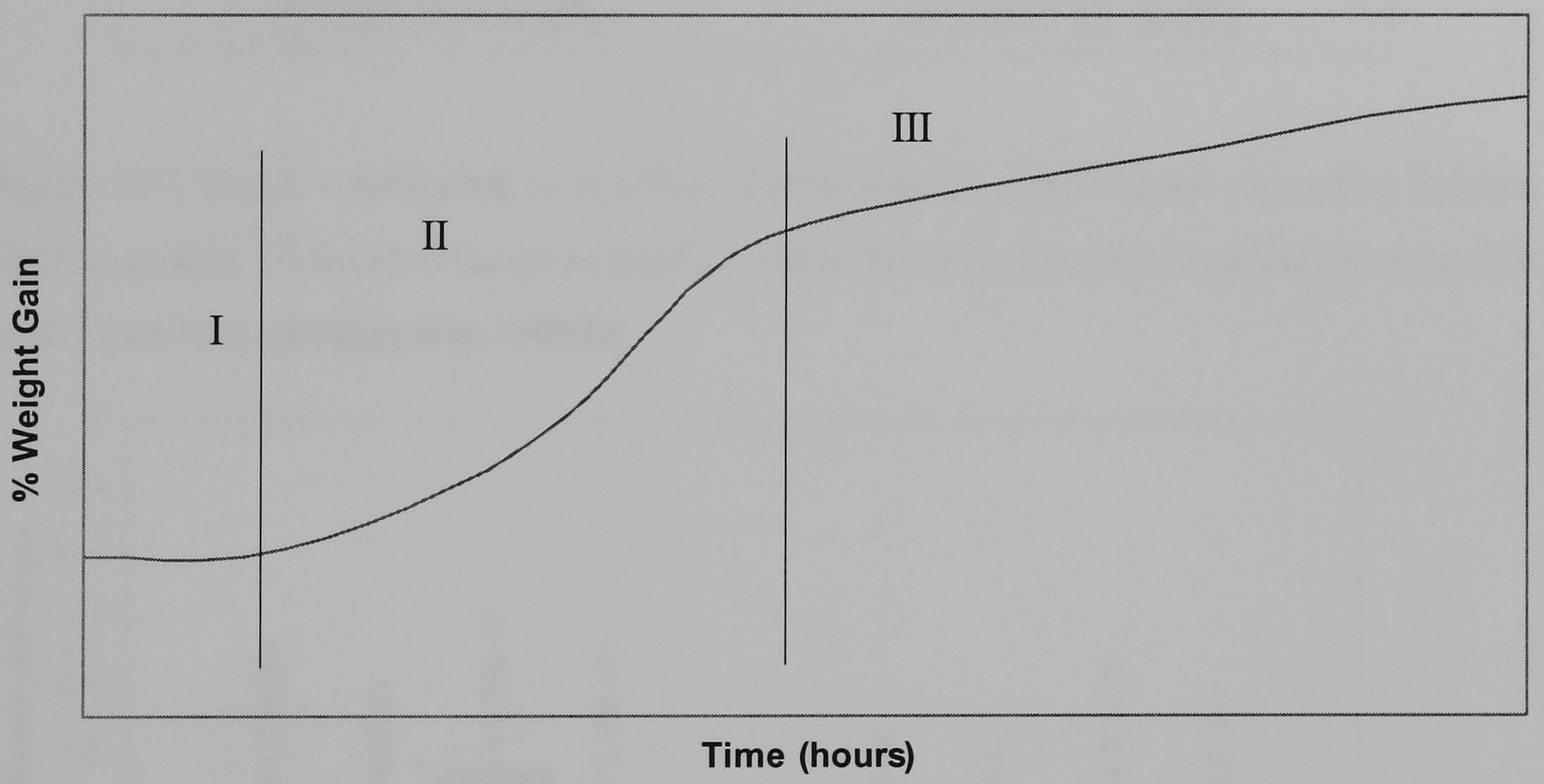

Figure 2.10 Idealised thermogravimetric analysis (TGA) response for candidate alloys in wire form.

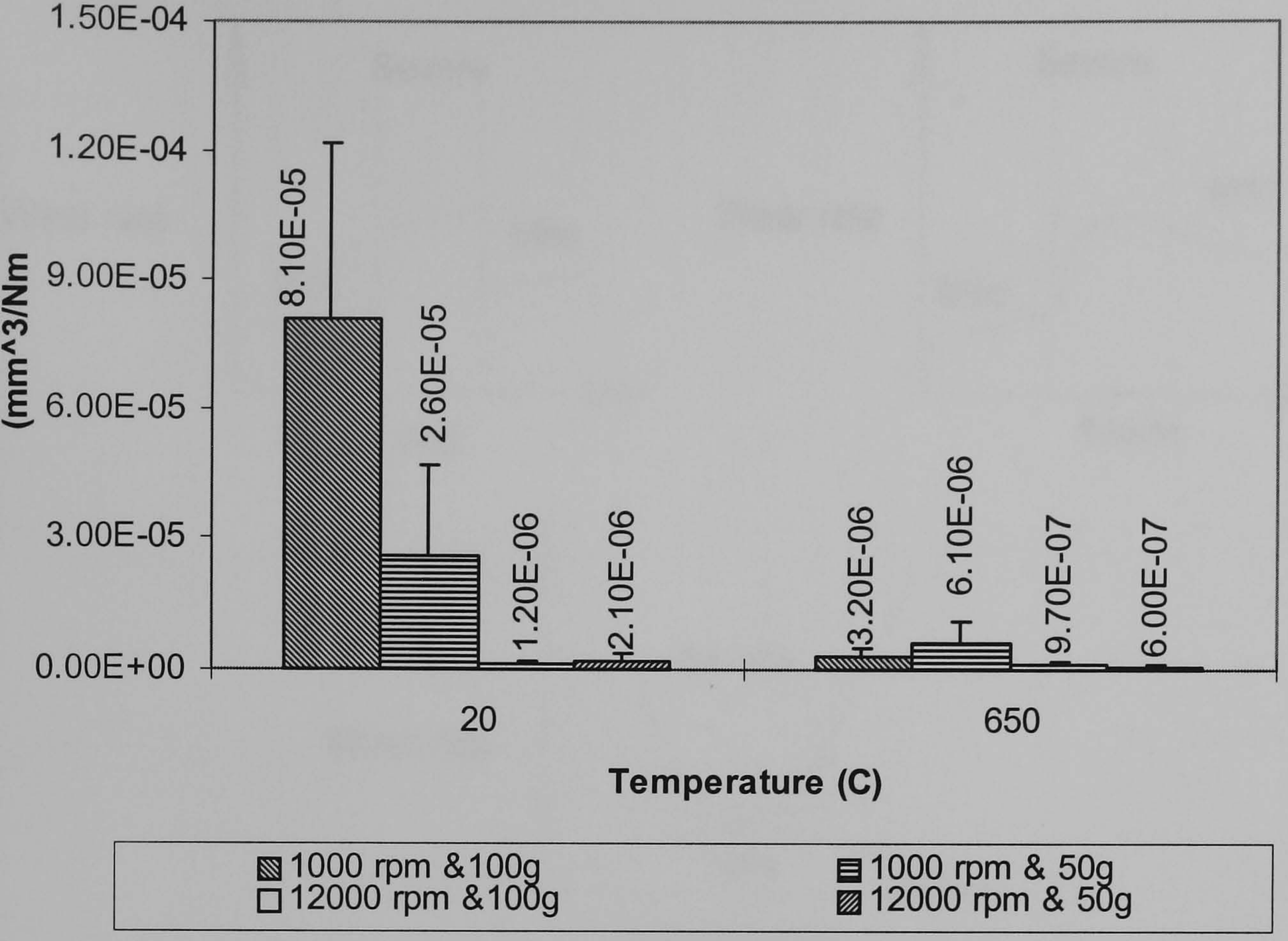

Figure 2.11 Brush wear factor, in mm^3/Nm for Haynes 25 cobalt based superalloy bristles sliding against I718 nickel based superalloy shaft. Wear factor goal for adequate wear life is 10^{-8} mm^3/Nm **(Fellenstein (1994))**.

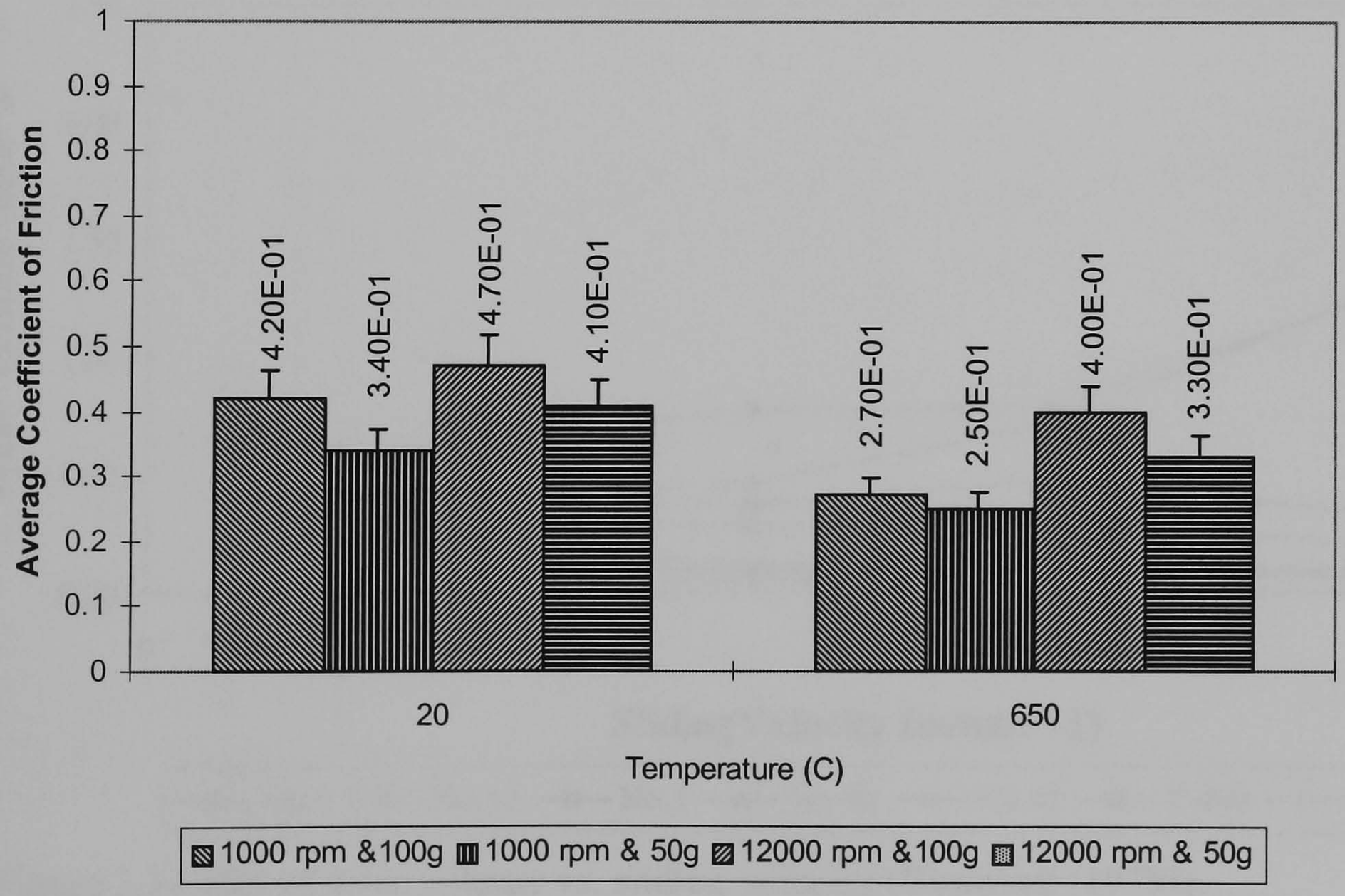

Figure 2.12 Average friction coefficient of Haynes 25 tufts vs. I750 journal under various test conditions. Error bars represent standard deviation of averages of 9 test runs **(Fellenstein (1994))**.

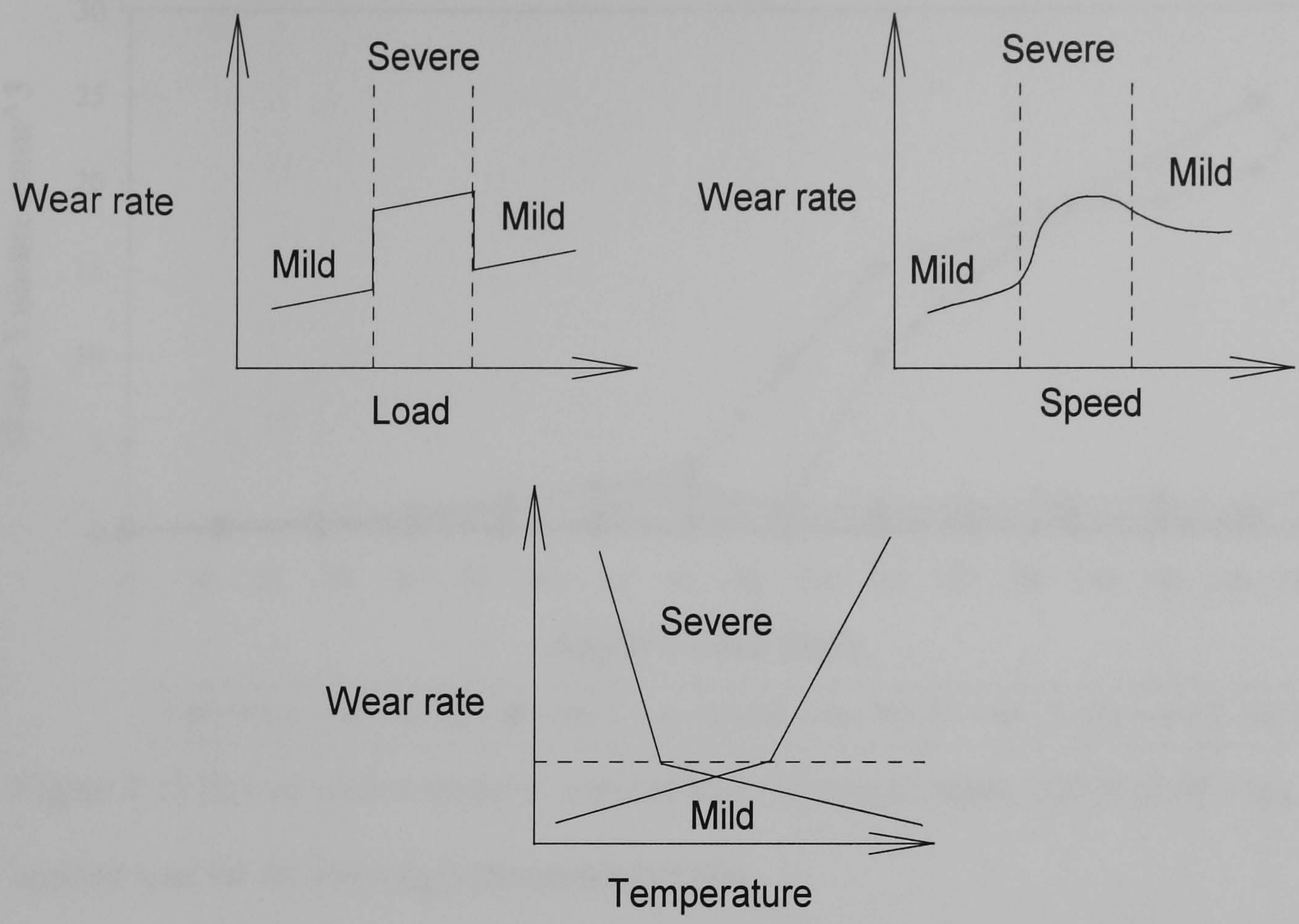

Figure 2.13 Examples of irregular/extreme non-linear response of wear rate due to operating parameters.

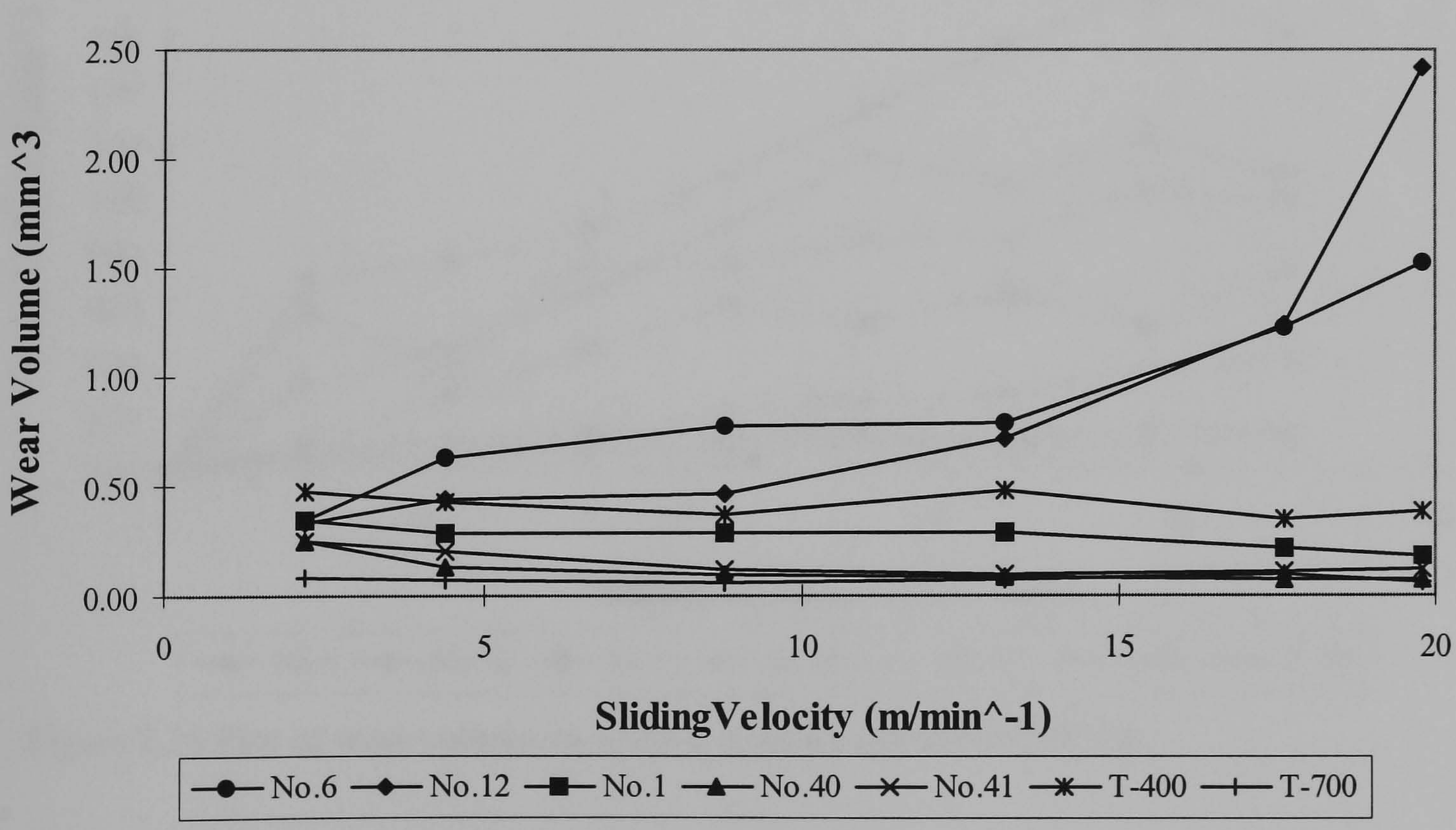

Figure 2.14 Plot of wear volume vs. sliding velocity **(Bhansali (1979))**.

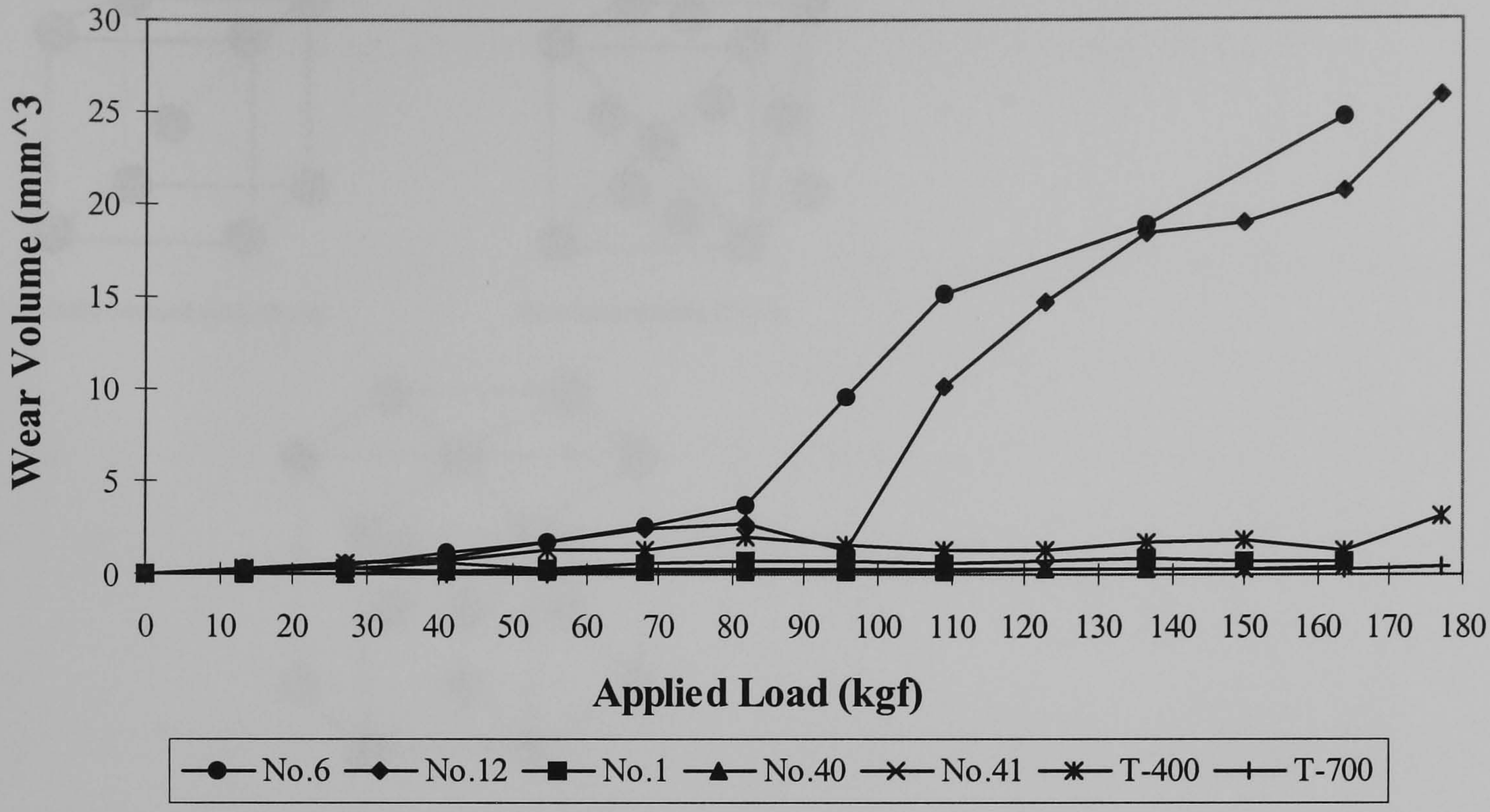

Figure 2.15 Plot of wear volume vs. applied load: Sliding distance, 320 ft (2.19.5 m); applied load 90 lbf (40.9 kgf) **(Bhansali (1979))**.

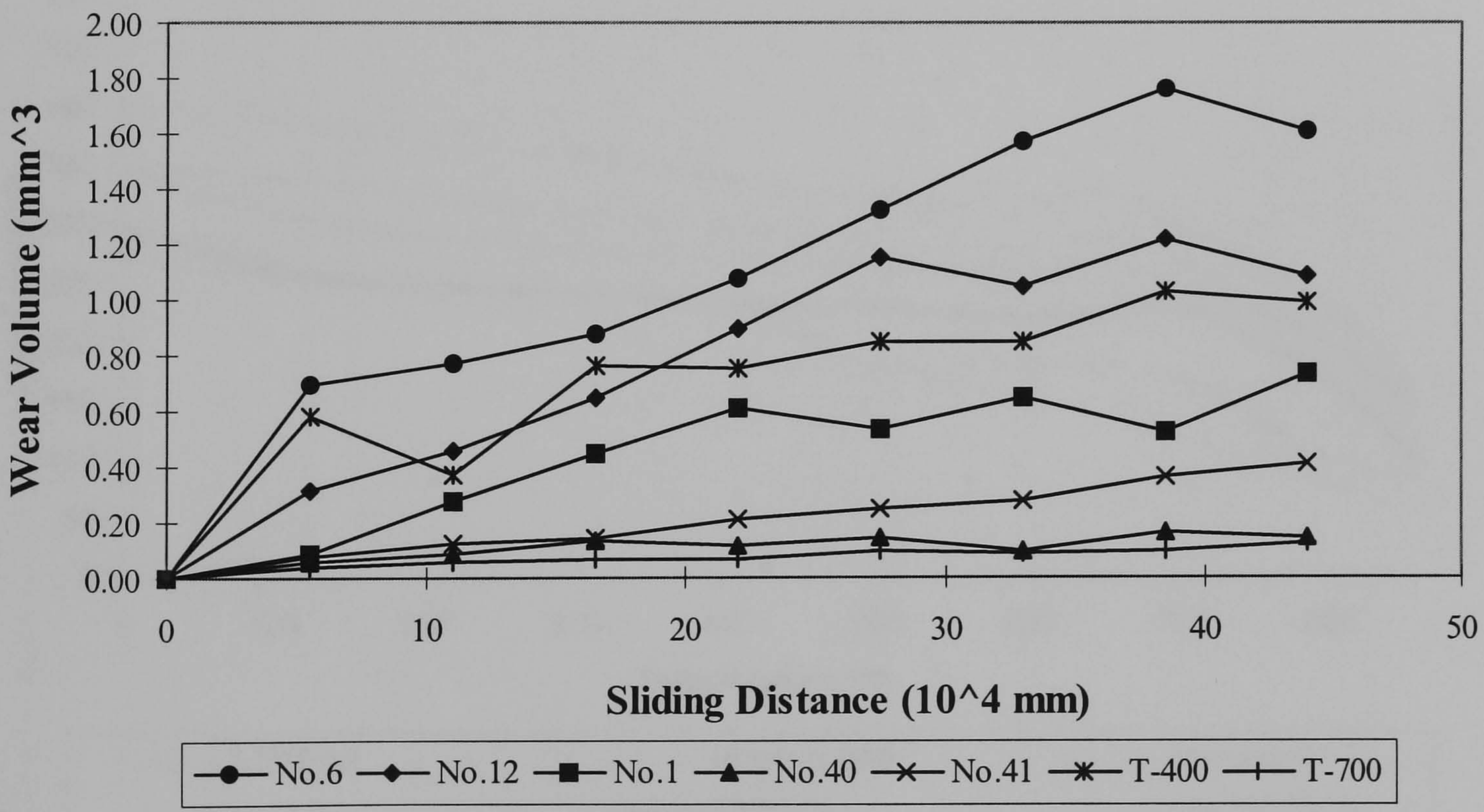

Figure 2.16 Plot of wear volume vs. sliding distance **(Bhansali (1979))**.

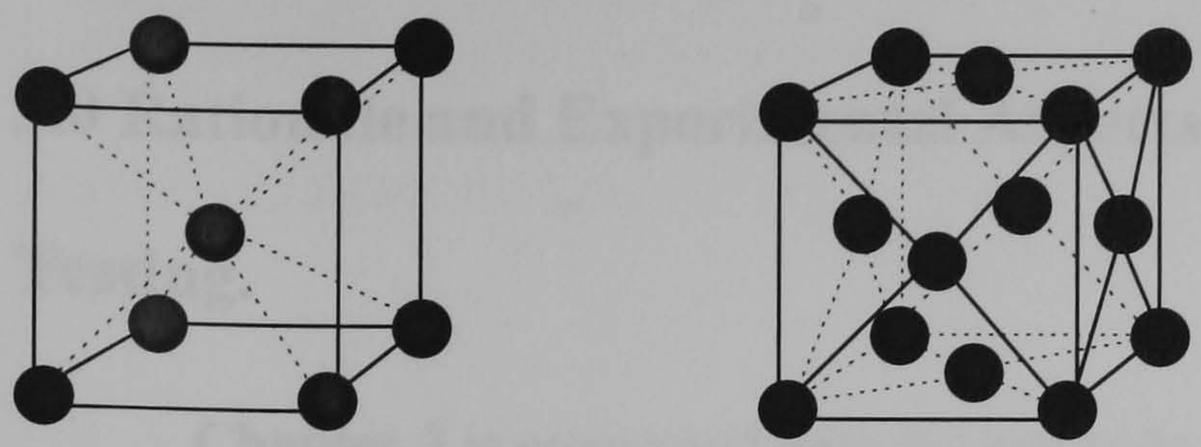

Body centered cubic (b.c.c)

Face centred cubic (f.c.c.)

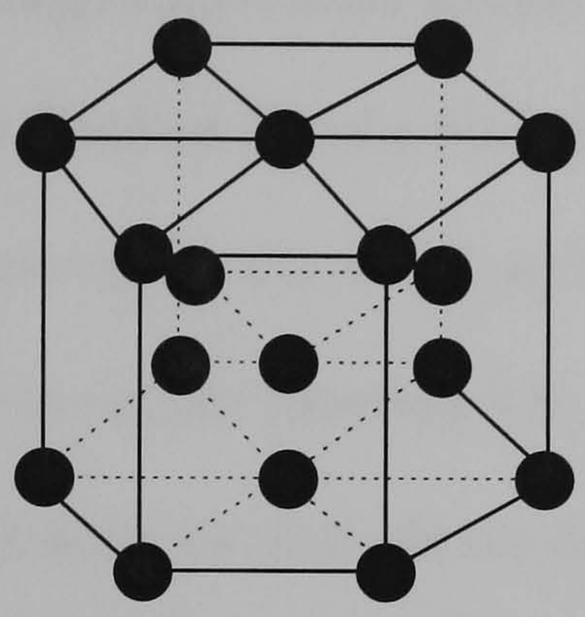

Hexagonal close packed (h.c.p.

Figure 2.17 The three common types of crystal structure.

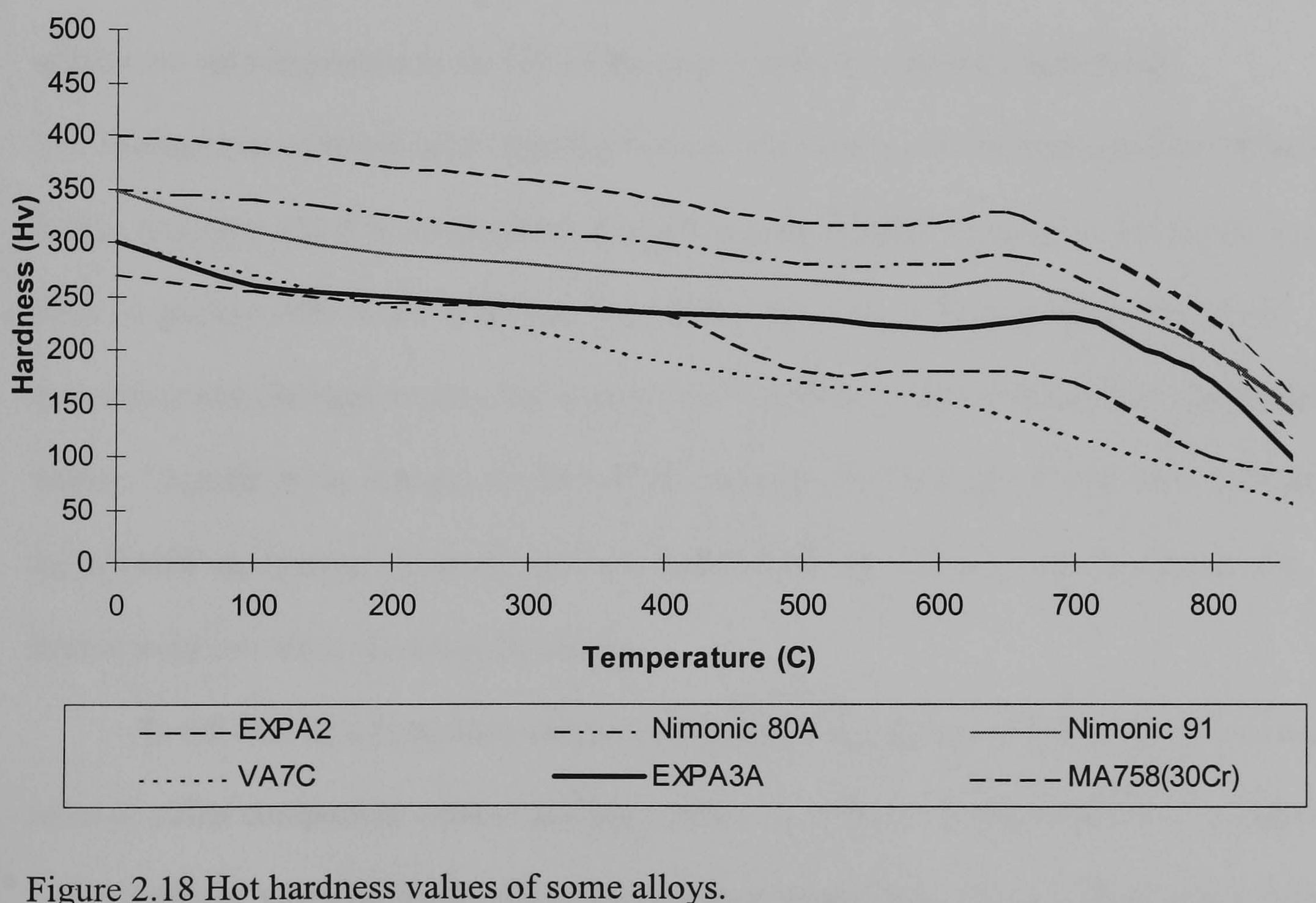

Figure 2.18 Hot hardness values of some alloys.

3.0 Rationale and Experimental Aspects: - High Temperature Wear Testing.

Chapter 3 is concerned with the rationale and experimental aspects of the materials tribotesting of high temperature alloys. The chapter is split into eight sections. After the introduction in **(Section 3.1)** the background considerations behind the design of the high temperature wear rig are discussed in **(Section 3.2).** The test rig design and operation is fully described in section **(Section 3.3). Section 3.4 - 3.6** describe the three groups of tests carried out. The analysis methods are described in section **(Section 3.7)** and in section **(Section 3.8)** a summary of the main aims of the testing is given.

3.1 Introduction

Brush seals have been generally described as compliant contact seals. Tribological effects are very important to the life of the seal and the contacting components.

The leakage rate of brush seals installed with an interference fit has been reported to be 90 % less than that of a five fin labyrinth seal **(Ferguson (1988)).** If however the brush seal were to quickly wear to a size for size fit and then a clearance fit (due to transient rotor excursions and thermal/mechanical expansions) the leakage rate may become substantially higher. Unpredictable changes in the specific leakage rate of blade tip seals are extremely undesirable as changes upstream can have dramatic effects downstream. The brush seal bristle wear rate must therefore be known.

In the case of a compliant contact seal in operation against a steam turbine rotor, wear of either component reduces sealing efficiency. If the wear is caused by a transient off centre rotation, when the rotor returns to its normal operating position a portion of bristle bore wear offers a smaller increase in leakage rate as opposed to a full ring of rotor wear. Ideally neither component should wear but realistically if wear does occur, it should be on the bristle bore. The brush seal is easily replaced during refurbishment whilst the rotor

journal is substantially harder to repair. A further consideration was the effect on the rotor surface of a contacting material with regards to producing or initiating surface defects (e.g. cracks).

In the past all brush seal industrial development has concentrated on applications in gas turbines. Brush seals have therefore been developed to withstand gas turbine operating conditions. The material combinations for gas turbines are usually Haynes 25 (for the brush seal bristles) and a hard, wear resistant coating of aluminium oxide, chromium oxide, or chromium carbide for the rotor land adjacent.

The operating conditions a brush seal would encounter inside a steam turbine are significantly different to those encountered inside a gas turbine. Some of the conditions can be compared in **Table 2.1**. The desire for an uncoated rotor for steam turbine brush seal applications imposed a further materials constraint. The cost and difficulty of applying surface coatings during the manufacture and refurbishment of large steam turbine rotors could be avoided if a wear resistant bristle material could be identified that would successfully operate in conjunction with the uncoated rotor (made of material Spec. 297 rotor steel see **Table 2.3**). In this application the general requirements were for the bristle material to withstand the operating conditions, be wear resistant but wear in preference to the rotor material (if at all). Crack initiation and embrittlement on the rotor surface due to materials contact or transfer were also to be avoided.

It was therefore proposed to design and manufacture a wear test rig (using existing components where possible) and conduct screening tests on a range of candidate bristle materials in sliding contact with Spec. 297 rotor material. The wear characteristics of the candidate materials and the Spec. 297 rotor material were to be examined. The candidate bristle material selection process is described in **Chapter 2** and the list of candidate bristle materials is given in **Table 2.34.** Superalloys were thought to offer the most desirable properties so a relatively large group of 25 materials from four superalloy groups, nickel base age hardening, nickel base solution hardening, cobalt base and iron base were

proposed for testing. A Spec. 297 rotor steel sample was also included as an example of like on like wear testing.

The limited amount of information on the high temperature wear of superalloys and the lack of information on the high temperature wear of Spec. 297 rotor steel meant that the wear testing proposed would be invaluable to steam turbine manufacturers. However, because of the large candidate group size initial screening tests were proposed to attempt to determine materials trends and characteristics, specific wear modes and to identify materials that were either promising or unsuitable.

The first stage of the screening tests aimed at identifying the wear resistance of the candidate bristle materials (rather than the rotor material) and to reduce the candidate list to a handful of more promising materials. The reduced list of candidate materials were then to be further tested to more specifically look at the effect of sliding contact on the rotor material. Oxidation tests were also carried out on the bristle materials to gauge weight change purely by exposure to air at the operating temperature 540 °C.

3.2 Design of the High Temperature Wear Rig.

3.2.1 Rig and Service Conditions.

Ideally experimental wear testing should be carried out under conditions and with component geometries that are identical to those encountered in service. However all the conditions inside a steam turbine could not easily be replicated and brush seals prototypes were extremely expensive to manufacture and purchase. Given these constraints and the need to design a general purpose high temperature wear test rig to carry out accelerated wear tests, a high load, low rubbing speed, high temperature wear rig was designed. The rig was a "pin on disc" type, designed to test flat plate samples under constant loads at high temperatures.

The High Temperature Wear Rig **(HTWR)** operating conditions and service conditions are given in **Table 3.1** and are discussed in turn in **Section 3.2.2-3.2.7**.

3.2.2 Operating Temperature.

The rig was designed to allow testing at temperatures up to 750 °C, covering the high pressure steam turbine service temperature of 540 °C. The correct operating temperature was thought to be essential for wear testing candidate bristle materials against an uncoated rotor, as the oxidation and corrosion resistance and mechanical properties of materials could change suddenly and dramatically with changes in temperature **(Figure 2.13)**. This could give rise to corresponding changes in wear resistance.

3.2.3 Test Atmosphere.

The atmosphere in steam turbine brush seal applications may be high temperature (540 °C), high pressure superheated steam. It was not feasible to reproduce this atmosphere in the **HTWR.**

The mechanism for reducing wear was thought to be glaze formation which might be brought about by the oxidation and compaction of wear debris. **Gordon (1964)** compared the oxidation behaviour of 30 selected materials during 18000 hours in steam at atmospheric pressure at 550 - 600 °C and the behaviour of eight alloys in oxygen at 500 - 750 °C for 8500 hours. The materials included ferritic steels, molybdenum-bearing stainless steels, austenitic stainless steels, nickel based alloys and stellites. The oxidation rates were stated to be twenty times higher in steam than in oxygen at 550 °C. This was due to the different type and nature of the oxide that was able to form under those conditions. It was less continuous and allowed further oxidation of the substrate.

Oxidation is an integral part of glaze formation. The above experimental results would indicate that the oxidation rate in service may be higher than those encountered in the laboratory air atmosphere in the **HTWR**. That would suggest that the reduced oxidation rate may slow down the onset of glaze formation and the mild wear regime. The tests carried out would therefore be under conditions that may increase the wear rate (compared

to in service conditions). An increase in wear rate was thought to be helpful to differentiate between wear resistant bristle candidate materials.

3.2.4 Operating Load.

The loading needed to be considerably higher in the **HTWR** than the bristle tip loading encountered in service, to perform accelerated wear tests. The loading on brush seal bristles in service is very small and if it were replicated in the wear tests the amount of wear during a short test would have been negligible. Bristle loading is further complicated in service, by the load imposed by the installed interference due to bristle bending (which reduces as the bristle tips wear), by the pressure differential across the seal causing blow down, rotor eccentricity and thermal/mechanical expansions. This variable loading could not be replicated easily without using bristle tufts or full brush seal. Full seals were prohibitively expensive and if a full seals were used the tests would not have been sufficiently accelerated enough (given the proposed operating speeds and times) to enable ranking of candidate bristle materials.

Idealised material wear would be expected to increase in a linear fashion with load. However, unusual stepped changes can sometimes occur with load **(Figure 2.14)**. The loading in this experiment was reasonably low (10 N) but high enough to enable the wear to be visually detected and measured in most cases, after short duration tests.

The flat plate specimens offered a greatly increased contact area compared to the bristle tips and the pivoted loading method exerted a constant load rather than one that decreased with wear, as a brush seals installed with a interference would.

Mild wear was thought to be prominent in brush seals in service for the majority of their operating life and mild wear was expected with a 10 N load on the flat plate sample.

3.2.5 Rubbing Speed.

The rubbing speed of the rig was fixed at a maximum of 4.7 m/s, by the existing variable speed electric motor and the 150 mm outside diameter test wheel (the maximum

diameter allowable in the furnace). The high rubbing speed encountered in service (100 m/s) could not be replicated using the test rig without extensive modifications and a substantial redesign.

The effect of rubbing speed on idealised wear rate was expected to be generally linear. However, rubbing speed could affect the wear rate by two non-linear mechanisms. At high speeds the increased frictional heating could increase the oxidation rate and produce protective films that may hasten the onset of mild wear. Alternatively at high speeds the oxidation rate may be less than the rate of oxide film removal. This may cause the wear mechanism to move from mild to severe.

It was proposed that the main effect of the reduced rubbing speed in these tests was to alter the period of time before possible changes in wear mechanism (e.g. from adhesive to oxidative). Except for the initial period of pre-glaze formation wear when the test began, mild wear was expected during the majority of running. The slower rubbing speed of the test rig would tend to maintain the wear mode in the mild regime and therefore increase the pre-glaze wear rate.

3.2.6 Test Duration/Sliding Distance.

The tests carried out in this study were materials compatibility screening tests and were not designed to accurately predict the wear rate of a bristle pack made of a specific material under service conditions. Gas turbine engine brush seals are replaced every 8000-10000 hours and steam turbine brush seals could only be replaced after every 50000 hours. It was thought that the majority of bristle pack wear would occur in the early stages of operation, after which further wear would only occur during transient rotor excursions or thermal/mechanical cycles.

Again, wear volume would generally be expected to increase linearly with test duration. In high temperature wear conditions, where glaze formation was expected, the linear relationship would only be expected after full glazes had been achieved. Glaze

formation was expected within the early stages of these tests, so wear volume was expected to increase linearly, in the mild regime for the majority of the test duration.

The test duration was therefore determined by two factors. The first factor was to produce a detectable amount of wear on the samples to rank them and examine the wear mechanism. The rig conditions were such that a low wear volume was expected in a short term test. Practical operation and safety requirements were also a consideration. Given these factors the continuos test duration was set at 7 hours.

3.2.7 Specimen Geometry.

Brush seals for gas turbine applications are generally made of 0.071 mm diameter Haynes 25 wire. The packing density is generally 89-104 bristles per mm of seal circumference. The cost of manufacturing brush seals was prohibitively expensive for the materials screening tests. Whilst the majority of the superalloy materials were available in wire form, many were not available without a production run. As such, they were subject to a high minimum order requirement.

The test specimens were therefore chosen as flat plate samples machined to 40*5*3 mm. Flat plate was more readily available for testing small samples of a large number of materials. The plate specimens were machined to size and polished to 1 μm on the contact side. The other sides were polished to 1200 grit. The flat plate geometry could be carefully controlled to within +/- 0.01 mm and the samples were easily prepared. The sample geometry also allowed them to be easily and accurately mounted in the sample holder and the scanning electron microscope chamber.

Specimen geometry may effect the wear rate in several ways. The large flat, constant top loaded samples may have tended to trap wear debris and to compact a greater percentage into the glaze layer. A multitude of constantly flexing bristle tips may either trap wear debris within the bristle pack or may push away and lose wear debris and material loosely adhered to the rotor surface. Bristle tip temperature due to contact pressure

was also thought to be significant. This temperature may be significantly higher (e.g. 10-20 %) than the operating temperature, and may cause severe bristle tip deformation, oxidation and increased wear rate. The specimen geometry affects the heat dissipation rate and whilst flash contact temperatures would still be expected under the flat plate sample, they were thought to be insignificant compared to the bulk operating temperature and would have a negligible effect.

3.3 Description of the High Temperature Wear Rig.

A schematic of the High Temperature Wear Rig **(HTWR)** can be seen in **Figure 3.1** and **3.2.** The test rig consisted of a main shaft supported between two self aligning rolling element bearings. The main-shaft had a flexible coupling at one end and was connected via an in line torque transducer to a variable speed electric motor. The motor was capable of running at 128 to 600 rpm. The main-shaft had a maximum outside diameter of 25.4 mm, and was threaded on the central portion. The rotor steel test wheel used for first screening tests had an outside diameter of 150 mm with 25.4 mm (clearance) diameter hole though the centre. The test wheel was 50 mm in axial length and was polished to 1200 grit on its periphery. The second set of tests were carried out with a 50 mm outside diameter thin walled rotor sleeve held in position by a sleeve carrier. The sleeve carrier had a central hole of 25.4 mm. The test sleeve was 50 mm in axial length and was again polished to 1200 grit on its periphery. The rotor test wheels and sleeves were located by two locking nuts at either side on the threaded portion of the main shaft. The maximum rotor surface speed was 4.7 m/s for the 150 mm rotor and 1.6 m/s for the 50 mm rotor.

A two part split furnace was designed to allow the central portion of the main-shaft and the test rotor to be enclosed. The temperature was carefully controlled and maintained at 540 °C, by a calibrated thermocouple located inside the furnace and a feedback controller.

The furnace incorporated two small holes at 90 degrees to the shaft inlet and outlet holes directly in line with the tops of the two test wheels. The holes allowed the sample holder to enter, horizontally perpendicular to the shaft, and the sample to be loaded on the top of either test wheel. The sample holder consisted of an arm (approximately 300 mm long) with a clamping mechanism on the end that enters the furnace. The clamping mechanism was able to accurately hold the 40*5*3 mm flat plate sample and maintain contact with the test wheel perifery. The sample holder and was attached to a pivoted reciprocation mechanism. The reciprocator allowed a much larger 12 mm wear scar to be produced.

Load could be applied to the sample holder or it could be counter-loaded to reduce the weight on the sample due to the sample holder. Masses were suspended from the sample holder arm at specific distances from the pivot point. The in line torque transducer was connected to a data logger and readings were taken at regular intervals. These readings allowed the calculation of the coefficient of friction.

3.4 150 mm Rotor Steel Test Wheel Initial Screening Tests.

The 150 mm rotor tests were primarily designed to be initial screening tests for the 25 candidate bristle materials given in **Table 2.34**. All the initial screening tests were carried out using a 150 mm, Spec. 297 rotor steel test wheel at a temperature of 540 °C, a load of 10N and for a test duration of 7 hours. The best material combinations based on the initial test results were to be examined more closely and less suitable material combinations were to be eliminated from the list. The effect of the contact of the sample materials on the rotor steel test wheel was more comprehensively addressed in the 50 mm rotor sleeve tests.

The 150 mm wheel initial screening tests were primarily designed to identify promising wear resistant candidate bristle materials and materials that performed badly in sliding contact with a rotor steel test wheel. The samples of superalloy materials could

easily be examined by **SEM** and **EDAX** whilst the rotor surface could not (without destroying it by sectioning).

Table 3.2 describes the pre-test preparations and post test procedures carried out for both sample and test wheel.

3.5 50 mm Rotor Sleeve Tests.

The 50 mm rotor sleeve tests were proposed to more closely examine the effect on the rotor of sliding contact with several of the more promising candidate bristle materials. The samples were prepared in exactly the same manner as in the previous tests. The rotor sleeve allowed a limited number of tests (6) to be carried out prior to sleeve sectioning. The load was again 10 N for these tests but the rubbing speed was reduced to 1.6 m/s due to the smaller rotor diameter.

The materials tested, from the results of the 150 mm tests were Haynes 25, Ultimet, Haynes X-750, Waspaloy, Haynes 718 and Spec. 297.

3.6 Oxidation Tests.

To determine the effect of oxidation on weight change of candidate bristle materials oxidation tests were carried out. The preparation was similar to the preparation for the wear tests, as given in **Table 3.2**.

The furnace was allowed to stabilise at 540 °X and the samples introduced, suspended on a ceramic crucible and oxidised for 7 hours. The samples were then re-weighed to determine weight increase or decrease due to oxidation in laboratory air.

3.7 Parameters Recorded/Analysis Methods.

3.7.1 Room Temperature Hardness.

The pre-test samples were to be polished to 1 μm prior to being micro hardness tested using a **Buehler Micromet II Indentor**. Several indentations were to be made in

each sample and average values were recorded. This information would allow the relationship of pre-test hardness to wear resistance to be examined when the results were compared to the weight change.

The average post-test hardness values were also to be recorded. In each case several areas of the wear scar were tested. The change in hardness due to the high temperature wear tests could also be assessed when these results were compared to the post test hardness results.

3.7.2 Weight Change.

In most cases weight change data due to material removal from one or both materials gives a good indication of wear resistance. For high temperature wear, weight change still gives an insight to wear resistance but may be complicated by the material transfer in the form of glaze formation.

Weight changes could be brought about by oxidation of both substrate and wear debris, material removal and loss, and material removal and adhesion to one or both of the tribopair. The latter has an important role in the formation of surface glazes.

The sample material weight was to be recorded before and after the tests using a **Mettler HL52** chemical balance that had an accuracy of +/- 0.00005 g. The samples were to be weighed several times in each case and an average taken. It was hoped that material removal would be sufficient to differentiate between the candidate test materials.

To obtain a complete picture, an analysis of the worn surfaces by **SEM** and **EDAX** examination were also necessary.

3.7.3 Scanning Electron Microscope.

SEM micrographs of each sample using an **Hitachi SN2400** were to be taken at different magnifications to show both the surface wear scar and cross-sectional analysis. Different aspects of the glaze formations and surface features were to be identified and recorded.

3.7.4 Energy Dispersive Analysis by X-Ray.

EDAX was to be used to generate elemental distribution digimaps of the wear scars and glaze formations. Surface and cross-sectional digimaps were to be produced and included areas of the wear scar having hollows and plateaux. Digimaps were to be produced showing the elements from both the sample and the test wheel.

EDAX would allow the qualitative identification of the elements and the elemental distribution in the wear scars. In each case an area of plateau and hollow was to be analysed and an elemental surface digimap for the expected elements was to be produced. After post processing the digimaps could be examined and the presence of specific elements in specific areas of the wear scar could be observed. It was thought that any material transfer would be determined and specific elements that were important to the wear process would be identified.

3.7.5 Talysurf.

Talysurf measurements were to be taken on the unworn test rotor as a datum and then across each wear track on the test wheel. The trace was to be started on untouched wheel surface and finished on untouched wheel surface. If sufficient wear had takes place, the depth of the wear scar and the volume of material removed can be gauged. A trace was also taken in the middle of the track to gauge the resultant surface finish of the wear scar.

3.7.6 Torque Transducer.

Torque transducer readings were taken continuously throughout each test. The readings were to be used to calculate the coefficient of friction between the sample and the test wheel during the tests and relate the results to wear resistance.

3.8 Summary of the Main Aims.

The high temperature wear tests were designed to be initial screening tests for candidate brush seal bristle materials to be used in conjunction with an uncoated Spec. 297 rotor in a **HP** steam turbine.

The ideal bristle material would be wear resistant but would wear preferentially to the Spec. 297 rotor. No detrimental surface effects were to be induced in the rotor material due to sliding contact with the bristle material. More specifically the tests would enable the wear mechanisms for the 25 candidate bristle materials and the Spec. 297 rotor material to be identified. The materials could then be ranked in order of preference given the selection constraints.

The tests would also allow several relationships between materials properties and wear to be examined.. These included:-

i.) The relationship between pre-test and post -test hardness to weight change.

ii.) The relationship between the coefficient of friction during the various stages of the test and weight change or wear mode.

iii.) The relationship between candidate bristle materials superalloy groups or elemental composition to weight change.

Table 3.1 Service and rig test conditions.

	Service conditions	**Test conditions in HTWR**
Temperature.	0-540 °C	0-540 °C
Rubbing speed	100 m/s	5 m/s
Rotor diameter	<1 m	150 and 50 mm
Load	$4.4x10^{-4}$ N/bristle	10 N
Rotor/test wheel material	Spec 297	Spec 297
Operation time	50000 hours	7 hours
Bristle/sample geometry	$7x10^{-3}$ mm dia	$45x5x3$ mm^3
Atmosphere	Superheated steam	Air
Pressure differential	5 bar max.	0

Table 3.2 Test preparation and analysis methods.

	Pre-test procedure
1.	Machine brush seal candidate material samples to 40*5*3 mm.
2.	Polish to 1μm.
3.	Microhardness test samples and test wheel.
4.	Wash in acetone and water.
5.	Weigh samples.
6.	Prepare test wheel surface using 1200 grit.
7.	Wash in acetone and water.
	Post-test procedure
1.	Re-weigh specimen to determine weight change due to the wear mechanism.
2.	Examine glaze formation on the sample material (and test wheel if applicable) - Scanning Electron Microscope **(SEM)**, Energy Dispersion Analysis by X-rays **(EDAX)**.
3.	Talysurf reading taken to determine the surface finish at the tested wheel.
4.	Retrieve, record and plot torque/friction readings at temperatures/times.

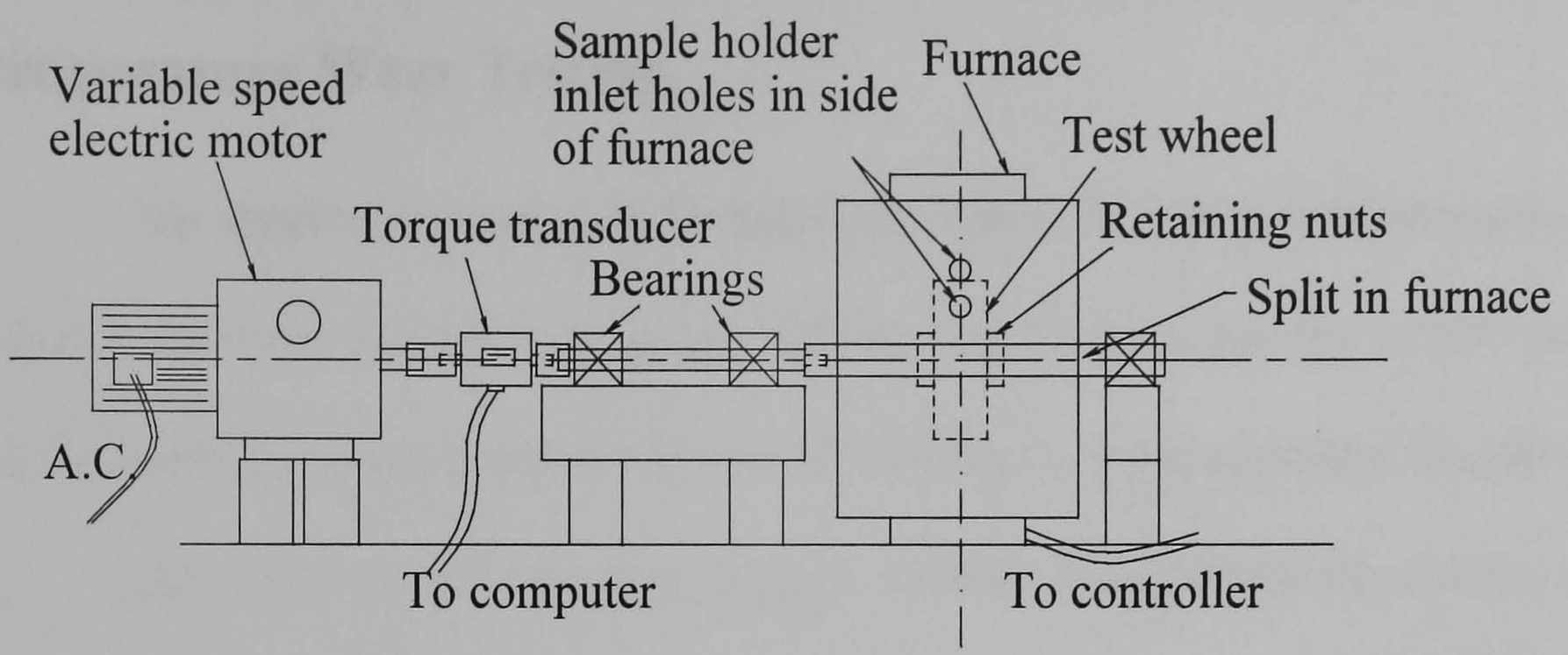

Figure 3.1 High temperature wear rig (side view).

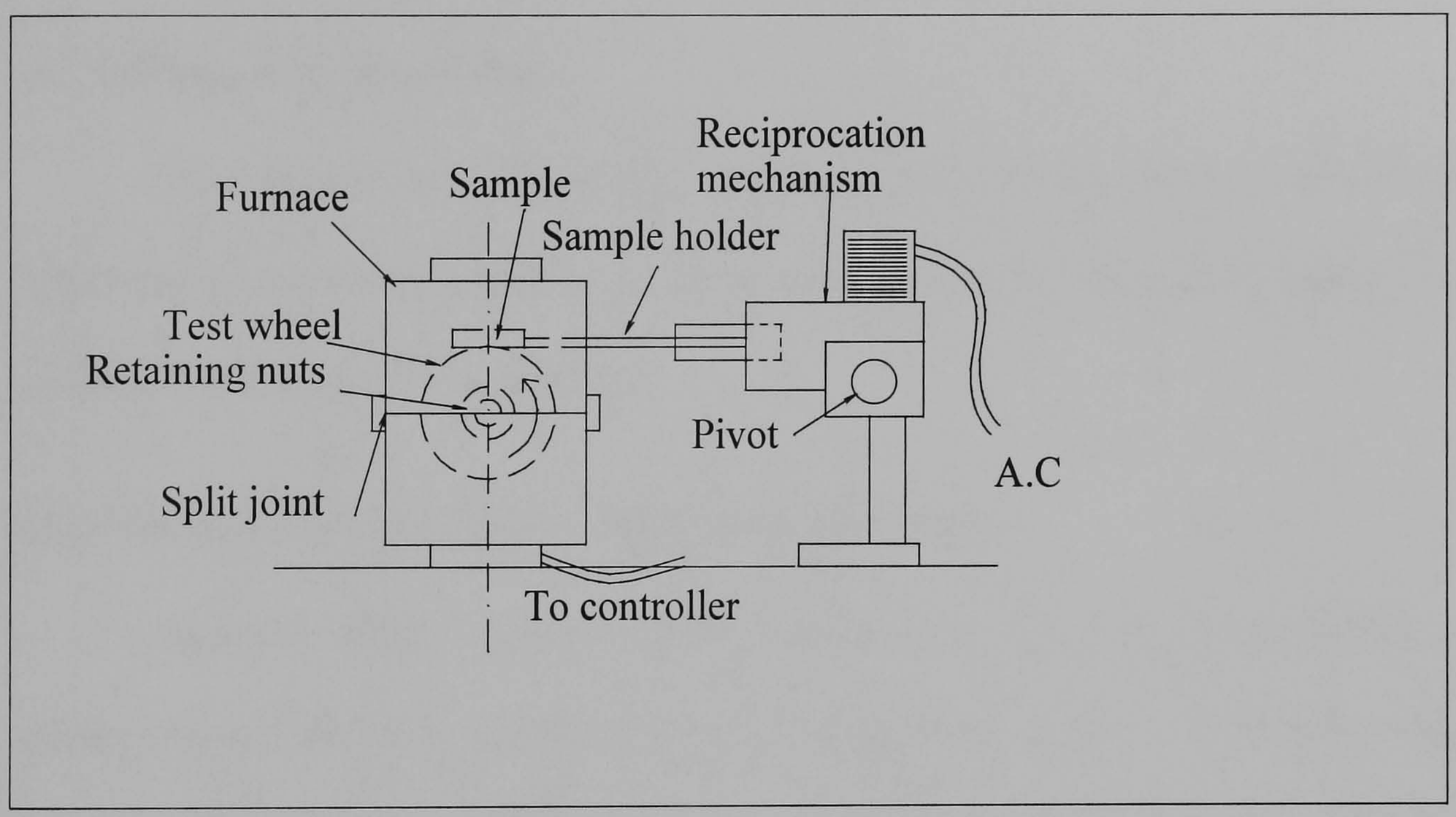

Figure 3.2 High temperature wear rig (end view).

4.0 Results, Discussion, Conclusions and Further Work: - High Temperature Wear Testing.

This chapter presents and discusses the results of the high temperature wear tests. Specific conclusions relating to individual tests are given at the end of each section and overall conclusions are given at the end of this chapter after a general discussion.

The chapter is split into six sections. **Section 4.1** presents results from the 150 mm test wheel tests. **Section 4.2** gives the results from the oxidation tests and **Section 4.3** describes the results from the 50 mm rotor steel sleeve tests. **Section 4.4** is a general discussion, **Section 4.5** gives the final conclusions and **Section 4.6** suggests further work.

4.1 150 mm Test Wheel Tests.

The 150 mm Test Wheel Tests were designed to explore several general aspects of high temperature wear, as well as addressing the specific problem of the wear testing of candidate brush seal bristle materials.

4.1.1 Pre and Post Test Room Temperature Hardness.

Archard (1953) suggested that for sliding conditions the softer of the tribopair would wear and the wear volume would be related to the hardness value of the softer material. The pre-test hardness and weight change results recorded in this study allowed **Archard's** theory to be assessed for the high temperature wear of a range of superalloy materials in sliding contact with a Spec. 297 test wheel. A wide range of pre-test hardness values were recorded for the 25 candidate brush seal bristle materials within each superalloy group **(Table 4.1, Figure 4.1)**. The hardness values had a minimum of 182 Hv and a maximum of 481 Hv. No individual group contained materials that were significantly harder or softer than any of the other groups of materials. However the mean hardness value of the **NBAH** materials was slightly higher than the other groups.

Figure 4.1 graphically displays the pre and post test hardness for the 25 test material samples. The Spec. 297 rotor material pre-test hardness was approximately mid range with a hardness of 253 Hv. The samples were arranged in their base material group and in ascending pre-test hardness. Within each superalloy group there was a range of hardness values above and below that of Spec. 297.

The post test hardness values were also recorded and are given in **Table 4.1** and **Figure 4.1.** The results described as post test hardness reflect glaze hardness (as opposed to substrate post test hardness). Micro-hardness testing was carried out on glazed areas on the wear scar. **Figure 4.1** and **Table 4.1** show that the glaze hardness values recorded were between 337 Hv and 654 Hv. The rotor Spec. 297 had the lowest hardness, whilst the 6B sample had the highest. The Haynes 25 sample was unusual in that it had a lower glaze hardness value (478 Hv) than the substrate hardness (481 Hv). The glaze layer in most cases was harder than both of the tribopair substrate materials. This was because the glaze consisted of mixed oxides and metallic debris (mainly from the Spec. 297 rotor) that were compacted (and work hardened and sintered) into a homogeneous surface layer. The oxide particles were typically harder than the substrate. For example chromium oxide can have a hardness value of 1300 Hv. Metallic particles, oxides and spinels of any of the individual elemental constituents may have been present. The higher oxides of Fe, Fe_3O_4 and Fe_2O_3 that were sometimes present in the glaze layer, are much harder than FeO which is only just harder than chilled cast iron **(Ohnuki (1985)).**

The post test glaze hardness test results were however subject to a high degree of variation for several reasons. The glaze was extremely brittle and porous and was therefore difficult to micro-hardness test without collapsing it. Many micro-hardness indentations were carried out in each case and this gave a wide spread of results over the plateaux tested. The glaze thickness had an average thickness of 10 μm for most of the superalloys but there were several differences in the porosity and the ability of the substrate to maintain

a good bond with the adhered glaze. The quality of the compaction and work hardening prior to glaze removal may have influenced the spread of recorded hardness values.

The superalloy samples all had the ability to maintain reasonable mechanical properties, including hardness, and oxidation resistance, up to high temperatures (up to and above the 540 °C test temperature plus the frictional heating temperature) however the rotor steel hardness may have suffered to a greater degree at 540 °C. Ideally it would have been more appropriate to compare hot hardness values for tribopairs at 540 °C.

The results allowed several observations and conclusions to be summarised.

i.) There was little direct relationship between pre test superalloy hardness and post test glaze hardness.

ii.) The post test glaze hardness was harder than both of the tribopair (except for the Haynes 25 sample, where the substrate was harder than the glaze).

iii.) The mean hardness of the post test glaze was 440 Hv. The range of post test hardness values above and below the mean glaze hardness was greatly reduced compared to the distribution of pre-test hardness values.

4.1.2 Weight Change

The results of the sample weight change are also given in **Table 4.1, Figure 4.2,** and **Figure 4.3.** Wear sample weight changes that occurred during the 7 hour tests carried out in the **HTWR** were all relatively small.

Figure 4.2 shows the weight changes resulting from 7 hour wear tests for the 25 candidate bristle materials. It was clear from the graph that under these test conditions there was no significant relationship between weight change and pre-test hardness (for the 25 sample materials). It was also apparent that several test samples gained weight (X750 +0.00026 g, Waspaloy +0.00000997 g, R41 +0.000607 g, HR160 +0.000383 g). The samples that gained weight were all Ni based (mainly **NBAH**). The Co alloys generally

lost a relatively small amount of weight (150 -0.0018299 g to 25 -0.0002633 g). The **NBSH** and Fe based superalloys generally lost more weight than the other two groups. The Spec. 297 rotor steel sample lost the most weight (-0.026 g). **Figure 4.3** allows the relationship between pre and post test sample hardness and weight change to be compared. There was a very slight trend within the individual **NBAH**, **NBSH**, and **CB** groups towards an improvement in wear resistance with increase in pre-test hardness. The results from the **IB** group showed the opposite trend.

The surface layer thickness and quality was not uniform in the individual samples. Different substrates supported a different quality and thickness of glaze layer. However, no clear relationship between material/substrate and glaze quality or thickness was observable from the results of these test materials. The surface layers formed on the samples were of reasonably equal thickness (10μm) but had variations in the ratio of plateau to hollow coverage.

The slight trend towards weight change in specific superalloy groups was thought to be linked to the relative wear resistance of the superalloy prior to glaze formation. The weight change of the substrate due to wear prior to glaze formation was very small. After the glaze formed the material removal/increase rate was thought to be negligible.

Generally, in most cases of sliding contact, weight change data due to material removal from one or both materials gives a good indication of wear resistance. For these high temperature wear tests, weight change still gave an insight to wear resistance but may have been complicated by severe oxidation and limited material removal/transfer. To obtain a complete picture, an analysis of the worn surfaces by **SEM** examination and **EDAX** analysis was necessary.

The disadvantage of using weight change as a measure of wear resistance could clearly be seen in the results for the samples that gained weight. Some substrate was removed in the early stages of the sliding contact. In all cases there was a change in the

surface finish/appearance and material transfer appeared to take place. The effect on weight loss by the small amount of material removal was masked by the subsequent adhesion of wear debris that was compressed and compacted into a surface glaze. The effect on weight change by non-wear related oxidation alone was also determined. It was however found to be negligible for the superalloy materials. This aspect is covered in more detail in **Section 4.2**.

The surface layer formed on the superalloy samples was primarily Fe transferred from the test wheel (from **EDAX** analysis in **Section 4.1.5**). The weight gain by some members of the **NBAH** group was due to this material transfer. It was suggested that little or no material was removed from the X-750, Waspaloy, 214 and R41 samples prior to the attachment of wear debris. In the other groups, more substrate material was removed from the superalloy prior to the adhesion of wear debris (assuming that the glaze layers have approximately the same density, thickness and mass).

General conclusions that were drawn are as follows.

i.) There was little direct relationship between pre-test hardness and weight change for the materials and conditions tested.

ii.) Weight change was a reasonable indication of the degree of wear on the sample material prior to glaze formation, assuming an average glaze thickness and covering.

iii.) The weight change results showed that under specific test conditions the superalloy samples were very wear resistant compared to the Spec. 297 rotor material sample.

iv.) Weight change in the candidate brush seal bristle material could only be loosely linked to general material composition and wear resistance.

v.). Weight change analyses can be misleading under low load/speed short term tests and require supplemental analysis and examination using **SEM** and **EDAX** to fully explain the results.

4.1.3 Scanning Electron Microscope Analysis of the Candidate Material Sample Wear Scar.

Several **SEM** micrographs were taken of all 25 samples. Each set consisted of a low magnification (≈ x 80) view showing the overall proportion of smooth glaze surface to rough substrate, an intermediate magnification (≈ x 500) view showing areas of interest and a higher magnification (≈ x 1500) view showing a more detailed view of the area of interest. In many cases the **SEM** results were very similar. A few selected examples of **SEM** results are given in **Figure 4.5-4.9. Table 4.2** summarises some of the features of the **SEM** micrographs for all 25 superalloy materials. These include the amount of cracking, the amount and size of wear debris, the size and ratio of plateaux/hollows and weight loss.

Stott (1972-1985) described the areas of glaze that are compacted, relatively smooth, flat and above the substrate as plateaux (or a plateau if there is a single area rather than discrete areas). He described the areas interspersed between the plateaux as hollows. The hollows are typically lower than the glaze plateaux and are relatively rough with wear debris scattered throughout. This terminology has been used throughout this chapter to describe the wear scars.

Figure 4.5a shows the Co based Haynes 25 sample wear scar. The scar consisted of an equal distribution of areas of dark glaze plateaux and light hollows (between the plateaux). On closer examination **(Figure 4.5b)**, areas of glaze cracking and lifting on the wear scar could be seen. The glaze appeared to be a relatively smooth, homogeneous layer attached to a relatively course substrate. Very fine powdery wear debris could be seen in the hollows **(Figure 4.5b). Figure 4.5c** is a higher magnification view (x 1.5k) showing the cracked glaze surface and small fragments of wear debris. The lifted glaze layer appeared to be homogeneous and revealed a subsurface area beneath. The area was free from loose wear debris. **Figure 4.5 d, 4.6d, 4.7d, 4.8d** and **4.9d** are Energy Dispersive Analyses by X-Ray **(EDAX)** surface digimaps. The discussion of the **EDAX** digimaps

associated with **Figures 4.5-4.9** is given in **Section 4.1.5**. **Figure 4.6a** is a micrograph of the wear scar surface on the **NBAH** X-750 sample. In this example there was a greater percentage distribution of areas of hollow than plateau as indicated by the light and dark areas respectively. The plateaux were relatively small with large areas of hollows between. **Figure 4.6b** shows that the glaze layer was relatively smooth and adhered to the rough surface below it. Large pieces of dislodged glaze layer were visible in the hollows but there was little evidence of cracking or lifting.

Figure 4.6c is a micrograph of the edge of the glaze layer. Wear debris and broken pieces of glaze layer could be seen resting on the surface of the hollow.

The Waspaloy wear scar is given in **Figure 4.7a**. The surface consisted mainly of large dark plateaux with smaller areas of hollow interspersed. Several areas of glaze lifting could clearly be seen. **Figure 4.7b** is a x 500 magnification of an area of glaze lifting. The glaze layer was relatively smooth and the hollows were relatively shallow and scattered with wear debris. **Figure 4.7c** displays the small particles of wear debris on the cracked edge of the glaze layer. The edge was undercut, overhanging the substrate.

The Co based Ultimet sample wear scar is shown in **Figure 4.8a**. The wear scar had a high percentage of light hollows compared to dark plateaux. The surface also had several examples of glaze cracking and lifting. **Figure 4.8b** is a view of an area of comparatively smooth glaze with surface cracks and portions of partially attached or lifted glaze. The hollow areas had little wear debris or broken glaze layer present. A small amount of particulate matter was present in the hollow **(Figure 4.8c)**. The substrate was rough and again the glaze layer appeared to overhang at its edges.

A micrograph of the wear scar created on the surface of the Spec. 297 rotor steel is given in **Figure 4.9a**. The wear scar consisted mainly of a surface glaze layer. Small areas of hollows could be seen mainly towards the edge of the wear scar. The glaze layer shown in **Figure 4.9b** was mainly smooth and dark but was interspersed with small areas of

contrasting light areas. The surface was covered in surface cracks. There were few examples of glaze lifting. A hollow is visible in **Figure 4.9c,** with a portion of glaze layer missing and an area of debris conglomeration that had yet to be compacted.

It was thought that the lifting areas of glaze were caused by a combination of several mechanisms. The glaze layer was formed at high temperature and was seen to be primarily composed of Fe and Fe oxides (from **EDAX** analysis). The superalloy substrate and the glaze layer had different degrees and rates of thermal contraction during cooling. The lifted apex type cracks were probably caused by the differences in thermal contraction rates. These formations (that were visible at the end of the test) certainly occurred after the test had ended, otherwise the contact between the sample and rotor would have removed them. Further cracks were thought to be formed by lateral contact forces pushing the plateaux as sliding contact took place. If the lateral forces were sufficient to shear relatively large portions of the glaze plateaux at, or near the substrate to glaze interface, the whole portion of glaze may have been moved without becoming completely disconnected. If however that portion of glaze collided with another rigidly attached portion, then the colliding edges may have lifted. The lifted portions would then have been removed by contact with the rotor.

Cracks and loosely adherent portions of glaze present at the edges of glaze plateaux were probably caused by direct surface loading by the contact of the sample on the test wheel. The edges of the plateaux could be seen to be porous and overhanged the hollow areas below in many cases. Surface loading at these points collapsed the glaze. The detached particles were removed and lost, or reattached, compressed and compacted.

Areas that were conspicuously free from wear debris, (usually next to plateau) were identified as areas that had recently been covered by a portion of glaze layer that had been removed. The surface below the glaze was rough in all cases. It clearly did not resemble the polished surface of the pre-test sample.

There seemed to be no direct relationship between plateaux to hollow size or ratio and the superalloy material group or material weight change results. However, the samples all showed very subtle differences. There was however a noticeable difference in the surface of the Spec. 297 sample. It had a greatly increased ratio of plateaux to hollow. The substrate was 100 % compatible with the glaze formation that allowed good bonding/adhesion to occur. Generally it was thought that larger plateaux would give rise to a reduced contact pressure and reduce the probability of material removal. However, effectively no actual contact of the substrate surfaces was possible, even after the formation of glaze layers that had a relatively low ratio of plateaux to hollow. Material was constantly being removed and lost from the glaze layer but was being replaced by further material removed from the Spec. 297 rotor.

Conclusions drawn and summarised observations are as follows.

i.) Many of the lifting apex type cracks appeared to have been formed at the end of the test, during cooling from the test temperature.

ii.) No surface cracks were visible in the hollows i.e. no substrate crack propagation.

iii.) The porous glaze sat on top of a rough surface. At glaze edges it could be seen to overhang the surface directly below it.

iv.) Differences were apparent in the ratio and size of the plateaux and hollows but no direct correlation to materials composition was clear.

4.1.5 Energy Dispersive Analysis by X-Ray of the Candidate Material Sample Surface Wear Scar.

Several examples of **EDAX** digimaps are included in **Figure 4.5-4.9**. **EDAX** analysis was carried out on the surface of each of the 25 sample wear scars. In each case an area containing plateaux and hollows was examined and elemental digimaps produced. In most cases the results were very similar. Digimaps are given to compliment the selected

materials examined by **SEM** in **Section 4.1.4**. Elemental digimaps of all of the elements found in the sample material and the rotor were produced in each case.

Figure 4.5d shows the Haynes 25 sample wear scar surface digimaps. The **SEM** micrograph shown in the top left hand corner is of a portion of glaze surrounded by hollow. The glaze portion had relatively sharp edges. The Fe digimap indicated that most of the area in the digimap was relatively rich in Fe. The plateau Fe elemental distribution was very dense, however the hollows indicated a reduced distribution density by comparison. The oxygen digimap provided evidence of a small distribution of oxygen at the edges of the plateau and in the hollows. The Co digimap showed that cobalt was present in the areas where oxygen was distributed. Cr and Ni had faint traces over the hollow and plateau but both had a very high concentration in several small areas of hollow next to the plateau.

The X-750 sample digimaps are given in **Figure 4.6d**. Again, an area of plateau surrounded by hollow could be seen in the **SEM** micrograph accompanying the digimaps. The Fe plot indicated an abundance of Fe in all areas. O presence was restricted to the edges of the glazed areas. Similarly these areas also showed the presence of S, Si and Al. Cr and Ni had an almost negligible distribution in the plateau but again had a single, small, very dense presence in the area of hollow, adjacent to the plateau.

Digimaps of the Waspaloy wear scar appear in **Figure 4.7d**. The **SEM** micrograph and digimaps showed that the portion of the wear scar examined had two medium sized areas of plateau surrounded by an area of hollow. The usual Fe trend was apparent, with a dense coverage on the plateau. Cr and Co had a relatively moderate distribution on both the plateau and the hollows but several areas of hollow were dominant. In this case they were not adjacent to the plateau. Ni had a very low distribution over the majority of both hollow and plateau but appeared strongly in areas where Cr and Co were at their highest concentration.

The wear scar digimaps of the Ultimet sample are given in **Figure 4.8d.** Two areas of hollow could be seen between two areas of plateau. The Fe map was less dense than most of the other candidate bristle materials but still had a very high presence in the hollows. O was present at the edge of the plateau and as discrete points in the hollows. Ni, Cr and Co clearly had a dense distribution in a single area (that was not on the main area of plateau). This area was adjacent to the plateau but had a different appearance compared to the bulk of the hollow area.

The final set of digimaps in this series **(Figure 4.9d)** was of the Spec. 297 sample tested against the Spec. 297 test wheel. The area examined, as seen in the **SEM** micrograph, was of an area of hollow dissecting a smooth dark area of glaze. Fe was very dominant in all areas. O was hardly visible with only a very small increase in distribution density at the edges of the hollow. Cr and Ni had a very slight, even distribution. The Al digimaps showed that Al distribution density increased slightly at the plateau/hollow interface.

The plateaux in all the superalloy material wear scars primarily consisted of Fe. In many cases the superalloy composition did not include Fe **(Figure 4.5 and 4.7)**. The Fe therefore must have been removed from the Spec. 297 rotor test wheel, either in the form of an oxide scale or as particles of substrate. The Spec. 297 test wheel was found to produce a loosely adherent, thick black scaly oxide that was easily removed.

The **EDAX** analysis clearly showed that areas of hollow that initially appeared to be the superalloy substrate were not substrate in the majority of cases. The hollows had an overwhelming distribution of Fe. This distribution was sufficiently uniform and thick to hide the superalloy substrate elements. Several digimaps showed small areas that were thought to be the substrate. These areas were adjacent to glaze plateau and showed the substrate elemental components. It was thought that the substrate was exposed due to the removal of portions of glaze that had sheared at the substrate surface. The freshly exposed

substrate areas quickly became oxidised and would have gradually been covered with wear debris.

The oxygen digimap in all cases appeared to be surprisingly sparse. O did not appear on the surface of the plateau and only appeared at the edges of freshly exposed glaze layers and as discrete particles in the hollows. This was unusual as the cross-sectional analysis showed that the whole glaze layer was rich in oxygen **(Section 4.3)**.

Trace elements found in Spec. 297 rotor material were evenly dispersed in the glaze layer, as would be expected if the glaze was primarily composed of rotor material. Al was the only other elemental digimap that was unusual. The Al digimaps indicated that Al was more prominent in the areas that also showed O was present. This was probably due to the Al present in the Spec. 297 wear debris migrating to the surfaces and becoming oxidised.

Some of the digimaps indicated areas that appeared to have no elemental composition. The "blank" areas were portions of the wear scar that were very rough, or were in the shadow of lifted portions of glaze. The results of the **EDAX** analyses were deficient in these areas due to the x-rays being deflected away from the detector.

The following is a summary of the main observations and conclusions drawn from the surface analyses.

i.) The composition of both the plateaux and the surface of the hollows was primarily Fe and Fe oxides. Slight traces of the other Spec. 297 elemental components were also visible.

ii.) Very small amounts of the superalloy elemental composition were, in some cases visible in the wear debris or glaze.

iii.) Several small areas of substrate material were visible in the hollows. These areas corresponded to portions of the sample wear scar glaze layer that were removed by shear occurring at the substrate to glaze interfacial junction.

4.1.6 Talysurf.

Wear tracks on the test wheel appeared as highly reflective, silver coloured, smooth surfaced lines (5 mm wide, the sample width) running around the periphery of the test wheel. Approximately 5 wear tracks could be produced adjacent to each other, separated by a 2-5 mm gap. The unworn areas of the test wheel were covered in a thick, black, scaly oxide. Tracks from previous tests were still clearly visible but lost their metallic silver lustre after several tests. They subsequently appeared to be covered in a less thick and more tenacious black oxide layer.

It was found that the scars generated by 7 hour tests under a load of 10N were not sufficiently deep or uniform to successfully differentiate between sample materials using the Talysurf. A brittle surface layer or glaze was formed in all cases. The wear tracks formed resembled those formed on the sample surface. They consisted of areas of plateaux and hollows. The results of Talysurf traces taken were therefore dependent on the portion of track tested. The results ranged from, a slight improvement to a slight reduction in surface finish. The stylus of the Talysurf tended to break the glaze. If the adhesion was poor the glaze would be completely removed, giving rise to poor Talysurf results.

A trough shape was expected as the stylus traversed axially across the wear track, starting and finishing on untouched material. A trough was not apparent and no clear indication of the amount of material addition or removal on the test wheel was achieved. The amount of material transfer was therefore very small. Examples of the traces are not included, as they we7re insufficiently clear to draw conclusions from.

Several general conclusions could be made however.

i.) The wear scars surface height above/below the datum untouched test wheel surface were insufficiently different to the datum to determine an accurate material transfer volume and differentiate between samples using the Talysurf results.

ii.) The surfaces of the wear tracks appeared to be highly polished, with a metallic silver lustre in all cases (by eye).

iii.) Wear tracks maintained their metallic lustre after being reintroduced into the furnace The lustre gradually dulled after several tests. The surface glaze may have been able to slow down the migration of Fe to the surface.

iv.) The Talysurf profilometer used to attempt to gauge the glaze surface finish and material removal or adhesion was unsuitable due to the loading required on the stylus, the brittle nature of the surface glaze, and the extremely low volume of material transfer encountered.

4.1.7 Torque Transducer/Coefficient of Friction Monitoring during Wear Tests

The friction plots of all of the test materials are given in **Figure 4.10-4.13**. The coefficient of friction was continually monitored during every test. The coefficient of friction traces are described and then discussed. The possible relationships between coefficient of friction and weight loss, base material group, pre-test and post test room temperature hardness are noted.

The coefficient of friction has often had a close relationship with the wear rate as wear rate usually falls when the coefficient of friction decreases **(Stott (1973, 1977, 1984, 1994))**. More specifically, general trends relating to the coefficient of friction can be found within the materials groups. The **NBAH** group **(Figure 4.10)** all had similar traces showing a small initial peak of $\mu = 0.7$ followed by a period of steady state operation at about $\mu =$ 0.6. Haynes 263 was the only exception to this general trend and had an initial peak of $\mu =$ 0.95 followed by a more gradual reduction, until 150 minutes, where it stabilised to a value of $\mu = 0.7$.

The **NBSH (Figure 4.11)** materials showed a clear difference in performance within the group. B2, C22, G3, and G30 showed a very similar trend to each other. The

results demonstrated that they initially peaked at $\mu = 0.5$-0.55 and then reduced to $\mu = 0.3$-0.4 by 75 minutes. The remaining materials in this group, 625, D205 and HR160 appeared to perform slightly differently. The D205 trace had an initial peak of $\mu = 0.75$ followed by a reduction after 75 minutes to a steady state value of $\mu = 0.6$. HR160 started at $\mu = 0.7$ and then showed a rapid reduction to $\mu = 0.45$ within 50 minutes. This was followed by a slight increase to $\mu = 0.5$ after 75 minutes. Haynes 625 had a similar trend. After the initial peak at $\mu = 0.7$ there was a reduction to $\mu = 0.55$ at 75 minutes, followed by a gradual, slight, increase to the steady state value of $\mu = 0.65$.

The **CB** group results **(Figure 4.12)** also had initial peaks that were maintained for a longer period than the **NBAH, NBSH** or **IB** materials and then returned to steady state operation at $\mu = 0.55$. Haynes 150 showed a different trend from the rest of the Co base group. Initially the coefficient of friction was $\mu = 0.7$. This dropped to the group mean value of $\mu = 0.55$ at approximately 80 minutes and then continued to drop steadily until it reached $\mu = 3.5$ towards the end of the test.

The **IB** materials **(Figure 4.13)** had short lived initial peaks followed by steady state operation at approximately $\mu = 0.4$-0.6. Haynes 556 had the lowest steady state value of $\mu = 0.4$. The rotor steel did not show an initial peak and maintained a value of $\mu = 0.55$. All of the materials seemed to reach steady state operation after approximately 75 minutes.

Some of the changes in the coefficient of friction traces could be explained as follows. The main wear mechanism in the high temperature wear tests carried out with the Spec. 297 rotor was the removal and compaction of Fe and Fe oxides formed on the surface of the rotor. The trapped wear particles adhered to the surfaces on both the test wheel and sample and were gradually compressed and compacted. As more particles became attached areas of high particle concentration were formed. When sufficient particles were trapped and compacted, raised surface areas (plateaux) were formed. The plateaux were generally

smooth surfaced and were harder than the substrate materials due to the composition of mixed oxides. Troughs or valleys were left between the raised plateaux that in turn collected wear particles that eventually became compacted. Ultimately the plateaux covered a large portion of the wear area and metal to metal contact no longer existed. The actual contact area between the surfaces due to the plateaux coverage was reduced as the plateaux size increased whilst the surface hardness of the test material also increased. The layer formed was of low shear strength, and was easily and preferentially removed compared to portions of substrate. The wear rate and the coefficient of friction between the tribopair went down due to the glaze formation.

The adhesive and shear strength of the glaze layer and glaze to substrate interface was dependent on the composition of both the substrate material and test wheel. Operating conditions such as temperature, load, speed, test duration and atmospheric conditions may also have had a large bearing on the formation and retention of glaze layers.

Almost all of the traces in all of the superalloy groups showed an initially high value of the coefficient of friction, followed by a reduction in the early stages and finally a period of steady state operation. These changes were thought to be linked to glaze formation and oxidation rate. At the start of the test there was no glaze present and metal to metal contact was taking place. This involved adhesive or abrasive wear, material transfer and removal and a high coefficient of friction. Gradually as metallic particles were removed they were oxidised and reattached and compacted in the form of a surface layer. Providing the oxidation rate and operating conditions were favourable the layer built up and reduced metal to metal contact. Friction and wear rate was reduced. The metal and metal oxide wear particles were compacted into discrete plateaux. The plateaux were further compressed, polished and then sintered due to the contact temperatures. It was at this point that a highly wear resistant glaze was formed. This resulted in a drop in the coefficient of friction value. In the early stages the glaze layer may not have been stable

due to surface loads and wear debris generation rates. Eventually the formation of a stable glaze layer was complete and this corresponded to the coefficient of friction and wear rate remain fairly low and constant (steady state operation).

Initially (in the early stages of the high temperature wear tests) a less adhesive surface layer may have been formed. The glaze or oxide layers may have had a low shear strength and could be easily removed. If insufficient oxidation or material removal took place a full glaze layer could not be produced. The removal and reforming of a low shear strength layer gave rise to a low coefficient of friction. Particles that were being generated but not reattached may also have acted as a solid lubricant. Eventually adhesion and compaction of wear debris occurred when sufficient particles were generated. The plateaux started to form and the coefficient of friction stabilised to a steady state optimum value.

In the case where there was a period of low coefficient of friction followed by an increase before steady state operation (Hr160 and 625), a different mechanism existed. This may have been one where initially a less adhesive layer was formed. The oxidation rate of the material may not have been fast enough to generate enough oxide particles to successfully maintain a glaze.

The Spec. 297 rotor material sample tested against the Spec. 297 test wheel coefficient of friction plot is given in **Figure 4.13.** This result showed a different characteristic compared to the superalloy samples. There was no initially high period of coefficient of friction (above the mean steady state value) followed by a reduction. The coefficient of friction increased as the test started but did not reach the maximum value for several minutes. At this point steady state operation was reached. The two materials, being identical, were 100 % mutually soluble and both rapidly oxidised. Initially the surface oxide layers were removed resulting in a period of metal to metal contact and an increase in coefficient of friction. High wear debris generation and rapid oxidation then allowed sufficient material to be reattached and compacted in a glaze layer. Material continued to

be removed from both surfaces of the tribopair and reattached on both surfaces. Steady state operation was reached relatively quickly, as both surfaces were equally compatible and relatively adhesive to Fe and Fe oxide particles.

The observations summarised and conclusions drawn are as follows.

i.) The traces from most test materials showed an initial rise in the coefficient of friction value (to a peak) followed by a reduction to steady state operation. The Spec. 297 rotor steel did not follow this trend as it reached a steady value almost immediately and remained at it.

ii.) Final weight change appeared to have little correlation with the steady state coefficient of friction for the tests carried out.

iii.) Pre and post test room temperature hardness appeared to have little or no relationship to the coefficient of friction plots.

iv.) It was proposed that the period where materials composition and properties have any effect on the coefficient of friction in these tests was the time between the start and approximately 175 minutes into the test where steady state operation was achieved for many of the samples. During this period the coefficient of friction was higher and the majority of wear probably took place.

4.2 Oxidation Tests.

A summary of the results of 7 hour, 540 °C, laboratory air oxidation tests is given in **Table 4.4** and **Figure 4.14**. The result of oxidation in air for 7 hours was the production of a very thin oxide layer on all the superalloy materials and a thick, black, scaley oxide on the Spec. 297 sample.

The results of the oxidation tests **(Table 4.4** and **Graph 4.14)** demonstrated that the weight changes due to oxidation alone were very small for the superalloys. The weight change values ($-9.97*10^{-6}$ to +0.00635 g) were well within the accuracy of the chemical

balance, but were almost negligible compared to the weight changes recorded after the wear tests due to material transfer.

The weight change recorded for the rotor steel (+0.025716 g) was significantly larger than the changes in the superalloy materials due to the thick, black, loosely adherent scaly oxide that was formed on its surface. Below this oxide layer was a further black oxide that was powdery and less easily removed. Several explanations for these oxides have been suggested previously by other researchers and are summarised in this section.

Several of the superalloy materials indicated a weight loss. These included Ultimet, G30 and 214. The remainder either had no weight change or a small increase.

Gordon (1964) carried out oxidation tests on a low alloy rotor steel (0.5Cr0.5Mo0.25V) at temperatures including 550 °C. In oxygen, the oxidising potential was great enough to oxidise all the metal at the metal/oxygen interface giving a spinel type oxide containing Fe and Cr. This spinel covered the metal surface completely and slowed down the diffusion of oxygen to the metal surface and the diffusion of cations to the oxide/gas interface. The diffusion rate of Fe in a Ni/Cr spinel is a few orders of magnitude lower than that of the inverse spinel Fe_3O_4. Inverse spinels have a higher electrical conductivity than normal spinel structures and hence greater diffusion rates occur. $NiCr_2O_4$ and $FeCr_2O_4$ are normal spinels and hence should lower the oxidation rate if they are formed on the metal surface. **Gordon (1964)** found that in cross-section samples tested in the less oxidising environment of steam showed two distinct regions. The outer layer contained large pores and consisted mainly of Fe_3O_4 with a small amount of Fe_2O_3. The inner oxide layer was not so porous and consisted of Fe_3O_4 with some FeO.

According to **Quinn et al (1962,1973)** (based on his oxidation studies), the presence of rhombohedral oxide (α-Fe_2O_3) as the main debris constituent would indicate sliding temperatures up to about 300 °C while significant amounts of spinel oxide (Fe_3O_4) should not be detected below about 300 °C. Other work **(Fursey 1962)** suggested that the

spinel oxide develops on Fe and Fe-Cr alloys during oxidation at room temperature, with α-M_2O_3, forming at higher temperatures. However it has also been reported by **Roberts (1961)** that α-Fe_2O_3 forms on Fe at room temperature, while **Ali (1969)** stated that Fe_3O_4 develops on Fe in air at room temperatures with α-Fe_2O_3 and some γ-Fe_2O_3 being observed after long periods. **Caplan and Cohen (1966)** found that on tests on Fe in air above 600 °C, FeO was formed below the other two possible oxides Fe_3O_4 and Fe_2O_3.

The uppermost layer on the Spec. 297 oxidation samples was therefore thought to be Fe_2O_3. Beneath that layer Fe_3O_4 was formed. Finally Fe0 was formed next to the metal substrate itself. These Fe oxide layers together with metallic wear debris from the rotor were thought to be the main constituents of the glazes formed on both the test wheel and the samples.

4.2.1 Conclusions: - Oxidation Tests.

i.) All of the superalloy materials were oxidation/scale resistant and formed very thin oxide layers.

ii.) The weight change was very small for all of the superalloys and could be ignored in wear test weight change results.

iii.) The Spec. 297 steel formed a thick, black, scaly oxide that was easily removed revealing a more powdery, adherent black oxide layer. The Spec. 297 oxide layer was significantly heavier than the superalloy oxide layers.

4.3 50 mm Rotor Steel Sleeve Tests.

4.3.1 Cross-Sectional Digimaps of Candidate Bristle Materials.

Figure 4.15-4.20 show cross-sectional digimaps of the candidate bristle materials tested on the 50 mm rotor sleeve tests.

The cross-sectional **EDAX** analysis of the Haynes 25 sample wear scar is shown in **Figure 4.15**. The **SEM** micrograph clearly indicated a surface layer, above the sample substrate. The layer appeared to be uniform and was approximately 2 μm thick. The digimaps of the Haynes 25 major elemental components, Co, Cr, Ni and W showed quite clearly that the surface layer contained negligible amounts of those elements. Haynes 25 does not contain Fe, but the Fe plot indicated that the surface layer was Fe rich. The O digimap showed a thin line of elemental concentration on the surface of the substrate. Above that there was a slight reduction in O content. The remainder of the surface layer was rich in O.

Figure 4.16 showed that the surface layer formed on the X-750 sample was significantly thicker (100 μm) than the mean superalloy sample surface layer thickness (10 μm). The layer appeared to be well adhered to the substrate. The Fe plot showed the layer was primarily composed of Fe. The O plot was almost identical, but the O content reduced slightly towards the surface layer/substrate interface. Cr and Ni, the major elemental components in X-750 appeared in the substrate and not in the surface layer. The X-750 sample had a small (0.8 %) Al content, as did the Spec. 297 (0.015 %) but there appeared to be an increase in the Al distribution in the surface layer compared to the substrate.

The Waspaloy sample **(Figure 4.17)** had a relatively thin surface layer of approximately 4 μm. It appeared to be well adhered to the substrate and was primarily composed of Fe and O. The oxygen again showed the densest elemental distribution towards the top of the layer and was less dense towards the substrate to surface layer interface. Ni, Cr and Co, key elemental components of Waspaloy were only present in the substrate and not in the surface layer.

Figure 4.18 shows a very thin surface layer (1 μm) on the 718 sample. The layer again indicated the overwhelming presence of Fe and O. Ni and Cr, the major elemental components (with the exception of Fe) of 718, were only present in the substrate.

The cross-sectional digimaps of the Spec. 297 sample tested against the Spec. 297 test wheel **(Figure 4.19)** and the Spec. 297 sample left in the furnace for 7 hours without contacting the test wheel **(Figure 4.20)** were almost identical. The following descriptions and discussions are equally applicable to either sample results. The **SEM** micrographs allowed the thickness (11 μm) and porosity of the surface layer to be seen. Fe was, as expected, the major component of the surface layer, however, the bottom third had a clear reduction in Fe content compared to the areas above (**Figure 4.19 and 4.20)**. This reduction corresponded to a band of Cr. However, above this band no further Cr was present. The Ni plot also indicated the presence of a thin band of Ni. Again, above the thin band, little further Ni was present. The Ni band was at the substrate/surface layer interface, and below the Cr layer. Al was present at the substrate to surface layer interface and in the area approaching the top of the surface layer. O was evenly dispersed throughout the surface layer. V, Mn and S were all slightly less densely distributed in the band occupied by the Cr layer compared to the area below it. However, their elemental concentrations were all greatly reduced in areas above the Cr layer.

The cross-sectional analysis of the superalloy materials all showed a reasonably thick layer that was rich in Fe and O. The other elemental digimaps indicate small traces of the other constituents of the test wheel in the glaze layer. There was very little evidence of Co or W in the glaze layer shown in **Figure 4.15** (Haynes 25) or Ni in the glaze layer shown in **Figure 4.16** (X-750). This indicated that the layer was almost entirely made up of material from the test wheel and very little material had been removed from the superalloy material and retained in the glaze.

The rotor steel test samples (worn and unworn, **Figure 4.19** and **Figure 4.20**) both indicated the presence of a thin Ni layer above the substrate surface and a thicker Cr layer above the Ni layer. The Fe layer was situated above the previous two layers and O was evenly dispersed in all three layers. The Fe content in the area occupied by the Cr was

reduced compared to the layers above and below. The Ni and Cr layers were accounted for by diffusion (and oxidation) of the Cr and Ni ions through the Spec. 297 substrate and surface oxide. The diffusion rates differed, as did the final position of the layers. The layers did however provide a strong, stable, tenacious and adherent layer for the development and maintenance of the Fe oxide layers above.

Examination of the other elemental digimaps in **Figure 4.19** and **Figure 4.20** showed a faint layer of Al at the substrate/glaze interface and towards the top of the layer. The W, S, Mn and V digimaps all showed that the area of glaze that was Cr rich had an even but slightly reduced distribution of these elements.

4.3.2 Surface Analysis of Rotor Steel Test Sleeve by Energy Dispersive Analysis by X-Ray.

The surface digimaps showing the post-test rotor steel surface are shown in **Figure 4.21-4.25.** Surface **EDAX** analysis was carried out to reveal the elemental components of the Spec. 297 rotor sleeve wear scar for each test. **Figure 4.21** presents a set of digimaps for the test carried out with the Haynes 25 sample. The areas of surface glaze plateaux were rich in Fe, as were most of the hollows, but to a slightly lesser extent. A high O concentration was indicated, mainly at the edges of the glaze or as discrete points in the hollows. Ni, present in Spec. 297 (0.65 %) and in Haynes 25 (10%) was negligible in all areas shown in the O digimap. Cr was prominent and was visible in portions of both hollow and glaze. Co was more evenly distributed with a slight covering in most areas.

Co was not present in the rotor steel and therefore must have been removed from the superalloy sample. Cr was prominent on the surface of the wear scar. Spec. 297 rotor steel contains 2 % Cr, and the cross sectional analysis showed a subsurface Cr rich layer. However the surface Cr was probably removed from the surface of the superalloy sample, as metallic particles, oxides or spinels.

The digimaps from the test using Ultimet are given in **Figure 4.22**. An area of wear scar was examined that included a portion of glaze adjacent to a hollow that was reasonably free from wear debris. The SEM micrograph shows this area. The Fe plot indicated there was little difference in composition between the areas of plateau and hollow with respect to Fe content. O was scarcely visible and only appeared at the edges of the plateau. Ni, present in both tribopairs was not present, whilst Co, the superalloy base material had an even scattering over the entire surface. However Cr was only visible in the clearly defined glaze areas.

Figure 4.23 presents the digimaps from the Haynes X-750 test. Again an area of glaze adjacent to an area of hollow was examined as can be seen in the SEM micrograph. Fe covered all the glaze area with a high elemental distribution density. O was visible at glaze edges and in the areas where Fe was present. Al showed a small but significant trace at the edge of one portion of glaze. Again the Cr distribution was almost entirely in the glazed areas and was quite evenly dispersed.

The Waspaloy wear scar **(Figure 4.24)** digimaps indicated a slightly different result. Fe as expected was dominant and covered all of the digimap, both the plateau and hollow. There were small traces of O at the edges of the glaze layer. Ni and Cr however had a small elemental distribution density that was just visible in the glaze areas but was quite conspicuous in the least built up areas of hollows.

The final group of surface wear scar digimaps in the series **(Figure 4.25)** were of the 718 tested against the Spec. 297 rotor. The **SEM** micrograph shows a portion of wear scar with a large, loose portion of glaze in the hollow. A high distribution density of Fe covered all the areas in the plot. O appeared at glaze boundaries, in areas with a large concentration of wear particles, and quite clearly in the glaze layer. An unusual concentration of Cr was present on the loose portion of glaze, together with a faint distribution in the glaze areas.

4.3.3 Cross-Sectional EDAX Analysis of Rotor Steel Test Wheel.

The digimaps presented, described and discussed in this section show cross-sectional analysis of portions of rotor steel sleeve, sectioned through the wear tracks for each of the materials tested against the 50 mm test wheel.

Figure 4.26 presents the cross-sectional analysis of the Spec. 297 rotor steel tested with a Haynes 25 sample. The surface layer was approximately 10 μm thick and was porous. This can be seen in the **SEM** micrograph in the top left hand corner of **Figure 4.26**. The surface of the substrate was uneven and showed signs of material removal. The Fe digimap displayed the full extent of the Fe coverage. The entire surface layer was primarily composed of Fe although there was a slight reduction in the distribution density of Fe at the surface layer to substrate interface. The O digimap indicated the heavy presence of O towards the top half of the surface layer. Cr appeared to be uniformly distributed in the substrate with several equally dense areas within the surface layer. A Ni layer was visible at the top of the substrate to surface layer interface. The Ni elemental distribution was significantly denser than in the rest of the substrate or the surface layer. V, W and Mn appeared uniformly in the substrate and had a sparse distribution in the surface layer. The Al digimap showed that Al was present in the top half of the surface layer, and in a thin layer at the top of the substrate. These areas corresponded to areas that had a high O presence.

The digimaps produced on examination of the wear scar from the test carried out with Ultimet are given in **Figure 4.27**. Again the **SEM** micrograph shows the glaze layer was porous and approximately 10 μm thick. The substrate surface was uneven. The Fe plot provided evidence of an overwhelming presence of Fe in the surface layer and again there was a slight reduction in the distribution density of Fe at the substrate to surface layer interface. The O digimap showed a heavy and uniform presence throughout the surface layer. Cr appeared as a thin band at the top of the substrate with negligible distribution in

the glaze layer. There was a slight increase in Ni distribution density at the top of the substrate (under the Cr layer) with negligible amounts in the surface layer. V, W and Mo had a lower distribution density in the surface layer than the substrate. Co, the base material of the test sample had a negligible distribution density in the surface layer. Al however had a slight increase in distribution throughout the surface layer compared to the substrate.

The **EDAX** digimaps of the Spec. 297 sectioned sleeve that was tested with X-750 are given in **Figure 4.28**. The surface layer was slightly thicker than average (for these tests) at 10 μm - 14 μm thick and was reasonably homogeneous. The substrate was again uneven. The Fe digimap showed the usual heavy presence of Fe. However, the bottom 2-3 μm of the glaze layer clearly had a lower Fe distribution density. This reduced Fe layer corresponded to an increased distribution density of Cr. The Cr distribution was almost negligible in the glaze layer but was uniform in the substrate up to the 2-3 μm increased distribution density band. The Ni digimap showed that there was relatively little Ni found in the substrate (0.65 % in Spec. 297). A greater distribution density of Ni, the X-750 base material, was found in the top half of the glaze layer. At the surface layer to substrate interface a thin dense line of Ni elemental distribution was apparent, under the Cr layer. The Ni digimap showed that the 5 μm band occupied by the Cr layer had no Ni distribution. V, W and Mn were present in the substrate but sparsely distributed in the glaze layer. O appeared to be distributed throughout the surface layer but was more prominent in the top half.

The **SEM** and **EDAX** analyses of the test carried out using a Waspaloy sample **(Figure 4.29)** showed a uniform, homogeneous surface layer, approximately 10 μm thick above a worn substrate surface. The Fe plot again indicated a relatively dense and even Fe distribution throughout the surface layer, apart from just above the substrate to glaze interface where there was a slight reduction in distribution density. Again the reduction in

Fe corresponded to an increase in the Cr distribution density. Little further Cr was present in the glaze layer. As with the other examples a thin Ni layer was found to exist under the Cr layer. There was a negligible amount of Ni or Co in the glaze layer. V, W and Mn were present in the substrate but were only visible as faint traces in the glaze layer. Again the O distribution was relatively uniform throughout the surface layer but had a slight reduction just above the surface layer to substrate interface.

The last set of digimaps **(Figure 4.30)**, for the rotor steel tested with the 718 sample were perhaps the clearest results of all. The glaze layer was slightly porous and had a thickness of approximately 10 μm. The substrate surface showed signs of material removal. The Fe digimap had a very dense Fe distribution in the glaze layer and had a 5 μm band of less dense distribution towards the bottom of the surface layer. Again the band of reduced Fe corresponded to an increase in the distribution density of Cr. A small amount of Cr was present, evenly dispersed, below the 5 μm band, but the Cr content was negligible above it. The Ni digimap also showed a thin (<1 μm) but clearly defined layer under the Cr layer. Ni, the base element of the 718 test sample, did not appear in the surface glaze. The V, W and Mo traces had a uniform but faint distribution in the substrate with a minimal, reduced distribution in surface layer. O was present in abundance throughout the surface layer but again had a slight reduction in the area occupied by the Cr and Ni bands.

The surface layer was easily identifiable in all cases, both on the **SEM** micrograph and on the **EDAX** digimaps. It was approximately 10 μm on all the wear scars. The **SEM** micrograph and **EDAX** digimaps showed that the surface layer was porous. This was expected as the layer was composed of discrete wear particles and mixed oxides that were attached and compacted on to the surface of the rotor. The surface layer was rich in Fe and O in all cases and showed negligible amounts of the superalloy. It was clear from the analysis of weight loss, **SEM** and **EDAX** that very little of the superalloy sample material

was removed in all cases. A small amount of material was probably removed in the early stages of the test, prior to surface films being sustained. The superalloy material appears to have had very little effect on the composition of the glaze layer on either the rotor steel test wheel or the superalloy sample.

The Spec. 297 rotor cross-sectional samples showed the presence of a subsurface band of Ni (1 μm thick). This band corresponded to the surface of the substrate. A band of Cr (5 μm thick) was apparent above the Ni rich area. The Fe distribution in the areas of high Ni and Cr concentration were reduced compared to the remaining area of surface layer. The digimaps indicated that diffusion was probably occurring through the rotor surface.

The surface layer was again clearly visible in all cases, both on the micrographs and on the elemental digimaps. The surface layer consisted, primarily of Fe and O with traces of other elements from the substrate and the superalloy tested. All of the examples indicated a thin Ni layer above the Spec. 297 substrate and a thicker Cr layer above the Ni.

4.3.4 Conclusions: - 50 mm Rotor Steel Sleeve Tests.

i.) No subsurface cracks were discovered in any of the tests in either the rotor steel sleeve or the superalloy samples.

ii.) The glaze layer found on the bristle sample material consisted mainly of Fe and Fe oxides from the test wheel (and a small amount of mixed trace element oxides).

iii.) Little material from the superalloy samples could be seen in the cross-sectional analysis of the rotor steel.

iv.) Ni, Cr and Fe layers could be found in the rotor steel cross-sections (both in worn and unworn condition). These layers showed that diffusion was occurring with Ni and Cr migrating through the rotor substrate to the interfacial junction and O was diffusing through the rotor surface layers.

4.4 General Discussion.

The results of the **SEM** and **EDAX** analysis showed that a compacted layer of mainly Fe and mixed oxides was present on both the surfaces of the candidate bristle sample and the surface of the rotor. The Fe layer originated on the surface of the rotor and above it as a thick black loosely adherent scaly oxide.

In the initial stages of the test, a small amount of wear occurred on the surface of the test wheel and the test sample. Both of the materials in all cases readily oxidised due to the test temperature and the contact temperature due to frictional heating. During this period the wear was classified as severe and the coefficient of friction was high. Metallic adhesion and abrasion probably occurred and wear particles were generated. Some of the wear particles became trapped between the rotor and the test sample. The particles were compacted into the surfaces of both the sample and test wheel and started to form areas of plateau. More wear particles were generated by the removal of the thick black loosely adherent oxide scale formed on the test wheel, which were in turn compacted, and increased the size of the plateaux. The operating temperature, frictional heating and contact pressure enabled a degree of sintering to occur.

As the plateaux size increased the amount of contact of the two substrates was reduced and the contacting surfaces were composed of low shear strength portions of compacted surface layer. At this point the wear regime was considered to be mild and there was a reduction in the coefficient of friction to a steady state value. The plateaux were continually compressed, compacted and added to by wear debris and removed portions of glaze. Areas of glaze were removed by surface loading, cracking, lifting or when the layer reached a maximum thickness criteria due to thermal/mechanical stresses. Little further wear took place on the superalloy samples after the glaze layer had been formed. In these tests the amount of wear on the rotor was small.

The geometry of the test sample was more conducive to glaze formation than the wire element brush seal on a rotor arrangement. The single point top loading allowed a greater opportunity for wear debris to be compacted without being lost and more opportunity for the rotor to oxidise during the remaining rotational cycle after contact had occurred. The brush seal bristle pack geometry alone may be more prone to material removal compared to flat plate samples. The relatively stiff bristles would be in continuous contact with the surface of the rotor. Wear debris retention may be hindered (or aided) by the small point loading and the constant flexure of the bristles. If plateaux were formed they may not prevent contact between the tribopair substrates as the bristle tips may drop into the hollows and would be continually rubbing against the plateaux edges. This may remove plateaux by wear at their edges or conversely may help to compact existing wear debris. The bristles in a brush seal may not allow the adhesion of a layer of glaze onto the bristle tips due to the tip size relative to the wear debris size (and perhaps their thermal conductivity and expansion). As the glaze prevents surface contact, the bristles and the rotor substrates may wear to a greater extent.

Slight material removal on the rotor surface may however be advantageous, as it would help to remove possible surface defects/effects such as embrittlement and crack propagation. The wear tests carried out showed little sign of rotor wear. However, in service the rotor would be expected to wear to a size for size condition with some bristle wear (unless it was installed with a size for size or a clearance fit). This would still provide an improvement on the leakage rate over standard labyrinth seal arrangements where a clearance fit is necessary.

All of the superalloy materials had low wear rates and performed well in wear tests with the Spec. 297 rotor material. However the wear resistance of the sample substrate was in reality only being tested in the very early stages of the wear tests prior to glaze plateaux formation. Given that the weight loss results were a reasonable indication of the pre-glaze

weight loss it appeared that the nickel base age hardening materials were generally the most wear resistant (e.g. R41, Waspaloy, X-750). The Co base alloys were on average slightly less wear resistant. The **NBSH** materials were the next best group, whilst the **IB** superalloys performed the least well. Of the **NBAH** materials R41 performed the best and Haynes 25 was the most wear resistant of the **CB** materials.

Material removal from the rotor was very low for the high temperature wear tests carried out but rotor wear was not quantified.

4.5 Final Conclusions

i.) No clear correlation existed between pre-test or post test hardness and wear resistance for the high temperature wear of the superalloy materials tested against a Spec. 297 rotor steel.

ii.) Protective surface layers consisting mainly of Fe and oxides from the test wheels were formed on all of the superalloy materials when wear tested at 540 °C in air. Very little material was removed from the superalloy material substrate during the high temperature wear tests.

iii.) The rotor material developed a surface layer. It was composed of three sub-layers. These were Ni and oxides attached to the substrate, Cr and oxides above the Ni layer and a thicker Fe and oxide layer occupying the remaining portion. Very little superalloy bristle candidate material was found in any of the surface layers.

iv.) NBAH and **CB** materials had on average a high wear resistance and desirable wear characteristics. Materials from the **NBSH**, and **IB** groups appeared to be less consistent throughout their group and produced larger weight losses.

v.) None of the tribopairs tested were found to initiate substrate cracks or exhibited severe wear on either component.

vi.) Combining the wear test results with gas turbine service experience it appeared that none of the superalloy materials performed sufficiently better in terms of their overall

tribological properties compared to Haynes 25. It was therefore recommended that Haynes 25 would be a reasonable starting point as a bristle material for an initial application in a high pressure steam turbine. However, rotor wear must be monitored carefully.

vii.) Rotor wear was very small in the high temperature wear tests and was not quantified. It was thought that the rotor would have a greater wear rate than the superalloy samples.

4.6 Further Work.

i.) Further tests with bristle tufts or full brush seals at increased sliding velocity, and for longer durations should ideally be carried out with new rotor sleeves that could be sectioned. This would help to determine the effect on the wear rate of sample surface geometry (bristle instead of flat plate) and sliding velocity.

ii.) Long term wear assessment should be carried out with actual brush seals in steam turbine conditions. This would be most feasible by installing a brush seal in tandem with a labyrinth seal and including instrumentation to monitor the clearance or leakage rate across the seal. A quantitative seal and rotor wear rate must be determined to enable performance data to be accurately calculated for the service life of the equipment.

Table 4.1 Pre-test and post-test hardness and weight change for the 7 hour, 10N, 5 m/s 150 mm rotor steel wheel tests.

Group	Material	Pre-test Hardness (HV)	Post-test Hardness (HV)	Weight loss g 7 Hours
Nickel	263	219	478	0.003786
Base	X750	233	517	-0.00026
Age	Wasp	253	519	-9.97E-06
Hardening	718	253	399	0.0006167
	242	265	378	0.0040867
	214	304	430	-0.00033
	R41	317	536	-0.000607
Nickel	G3	182	400	0.0142566
Base	G30	188	449	0.00507
Solution	C22	215	493	0.0047866
Hardening	D205	216	495	0.0018967
	X	226	436	0.0016969
	S	231	453	0.0028167
	HR160	243	406	-0.000383
	B2	243	367	0.0043367
	625	328	529	0.00205
Cobalt	6B	209	654	0.0007697
Base	188	255	466	0.0005467
	Ultimet	288	380	0.0007933
	150	324	498	0.0018299
	25	481	476	0.0002633
Iron	HR120	214	434	0.0026133
Base	556	267	450	0.0034667
	Ferrilium	309	482	0.00635
Rotor Steel	297	253	337	0.025716

Table 4.2 General description of glaze using **SEM** micrographs.

Group	Material	Amount of Cracking	Amount of Debris	Plateaux Size	Ratio Plateaux: Hollow	Weight Loss
Nickel	263	Small	Small	Large	60:40	Medium
Base	X750	Medium	Small	Medium	40:60	Gain
Age	Wasp	Large	Large	Large	70:30	Gain
Hardened	718	Medium	Small	Medium	50:50	Low
	242	Small	Small	Small	40:60	Medium
	214	Large	Large	Medium	50:50	Gain
	R41	Small	Small	Large	60:40	Gain
Nickel	G3	Small	Small	Large	80:20	High
Base	G30	Small	Small	Large	80:20	Medium
Solution	C22	Small	Medium	Large	80:20	Medium
Hardened	D205	Small	Large	Large	60:40	Low
	X	Small	Medium	Large	90:10	Low
	S	Small	Small	Large	70:30	Medium
	HR160	Medium	Small	Large	60:40	Gain
	B2	?	?	?	?	Medium
	625	Small	Medium	Large	90:10	Low
Cobalt	6B	Small	Small	Small	30:70	Low
Base	188	Small	Small	Medium	50:50	Low
	Ultimet	Medium	Small	Large	50:50	Low
	150	Small	Small	Medium	50:50	Low
	25	Small	Medium	Large	50:50	Low
Iron	HR120	Large	Small	Large	60:40	Medium
Base	556	Medium	Medium	Large	50:50	Medium
	Ferrilium	Large	Medium	Large	60:40	Medium
Rotor	297	Medium	Small	Large	70:30	High

Table 4.3 Oxide types previously found on high temperature wear scars using superalloy test materials.

Chromium	**Aluminium**	**Cobalt**	**Iron**	**Nickel**
Cr_2O_3	Al_2O_3	Co	Fe_2O_3	$NiO\text{-}Cr_2O_3$ spinel
CrO_3		$CoO.Cr_2O_3$	FeO	NiO
			Fe_3O_4	$NiCr_2O_4$
			$(Fe.Fe(2\text{-}x)Cr_xO_4)$	

Table 4.4 Weight change due to 7 hour oxidation tests.

Group	Materials	Weight Increase (g)	Total weight loss after 7 hr wear test (g)	Total weight loss - Oxidation weight increase (g)
Nickel	263	0.00011	0.003786	0.003676
Base	X750	0	-0.00026	-0.00026
Age	Wasp	6.33E-05	-9.97E-06	-7.3E-05
Hardened	718	5.33E-05	0.0006167	0.000563
	242	6.67E-05	0.0040867	0.00402
	214	-4E-05	-0.00033	-0.00029
	R41	0	-0.000607	-0.00061
Nickel	G3	5E-05	0.0142566	0.014207
Base	G30	-3.33E-05	0.00507	0.005103
Solution	C22	0	0.0047866	0.004737
Hardened	D205	0	0.0018967	0.001897
	X	0.0001166	0.0016969	0.00158
	S	0	0.0028167	0.002817
	HR160	3.3E-06	-0.000383	-0.00039
	B2	0	0.0043367	0.004337
	625	4.33E-05	0.00205	0.002007
Cobalt	6B	3.34E-05	0.0007697	0.000736
Base	188	0	0.0005467	0.000547
	Ultimet	-8E-05	0.0007933	0.000873
	150	9E-05	0.0018299	0.00174
	25	0	0.0002633	0.000263
Iron	HR120	1.333E-05	0.0026133	0.0026
Base	556	0	0.0034667	0.003467
	Ferrilium	0	0.00635	0.00635
Rotor	297	0.005463	0.025716	0.020253

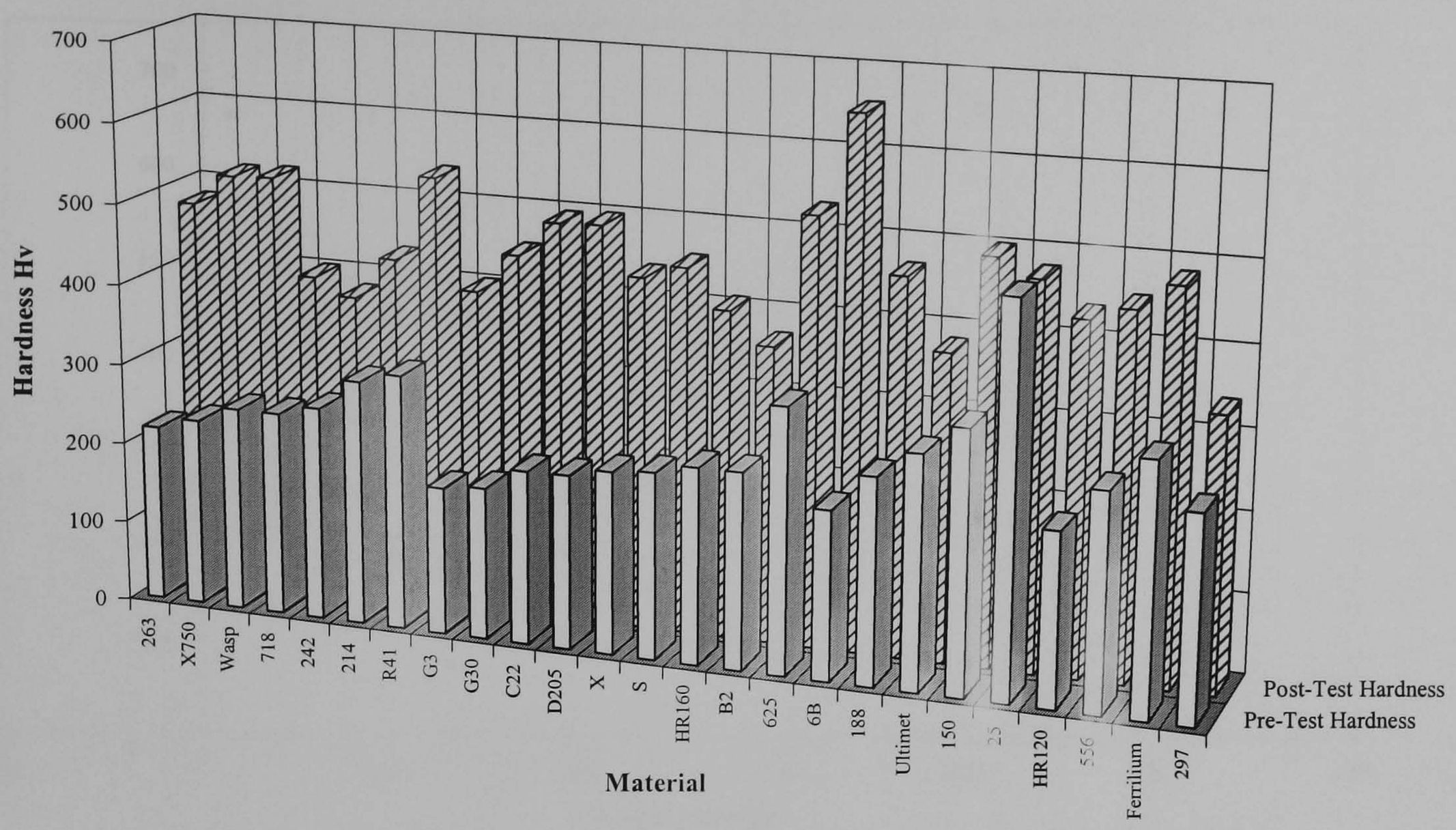

Figure 4.1 Pre-test and post-test hardness of candidate brush seal bristle materials.

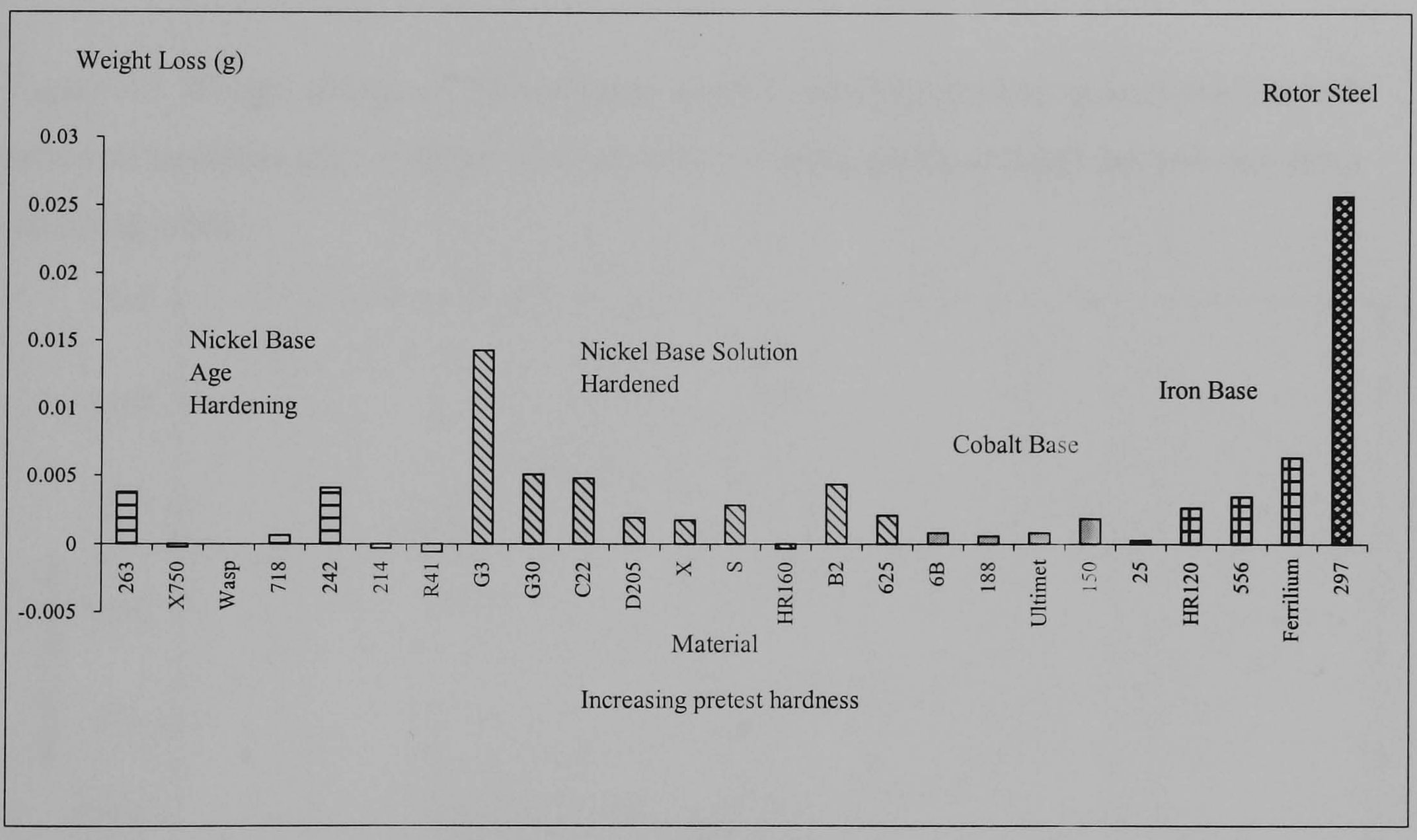

Figure 4.2 Weight change of 25 candidate bristle materials after 7 hours 10N and 5m/s in sliding contact with the 150 mm rotor steel test wheel. Results arranged in superalloy categories and in ascending pre-test hardness.

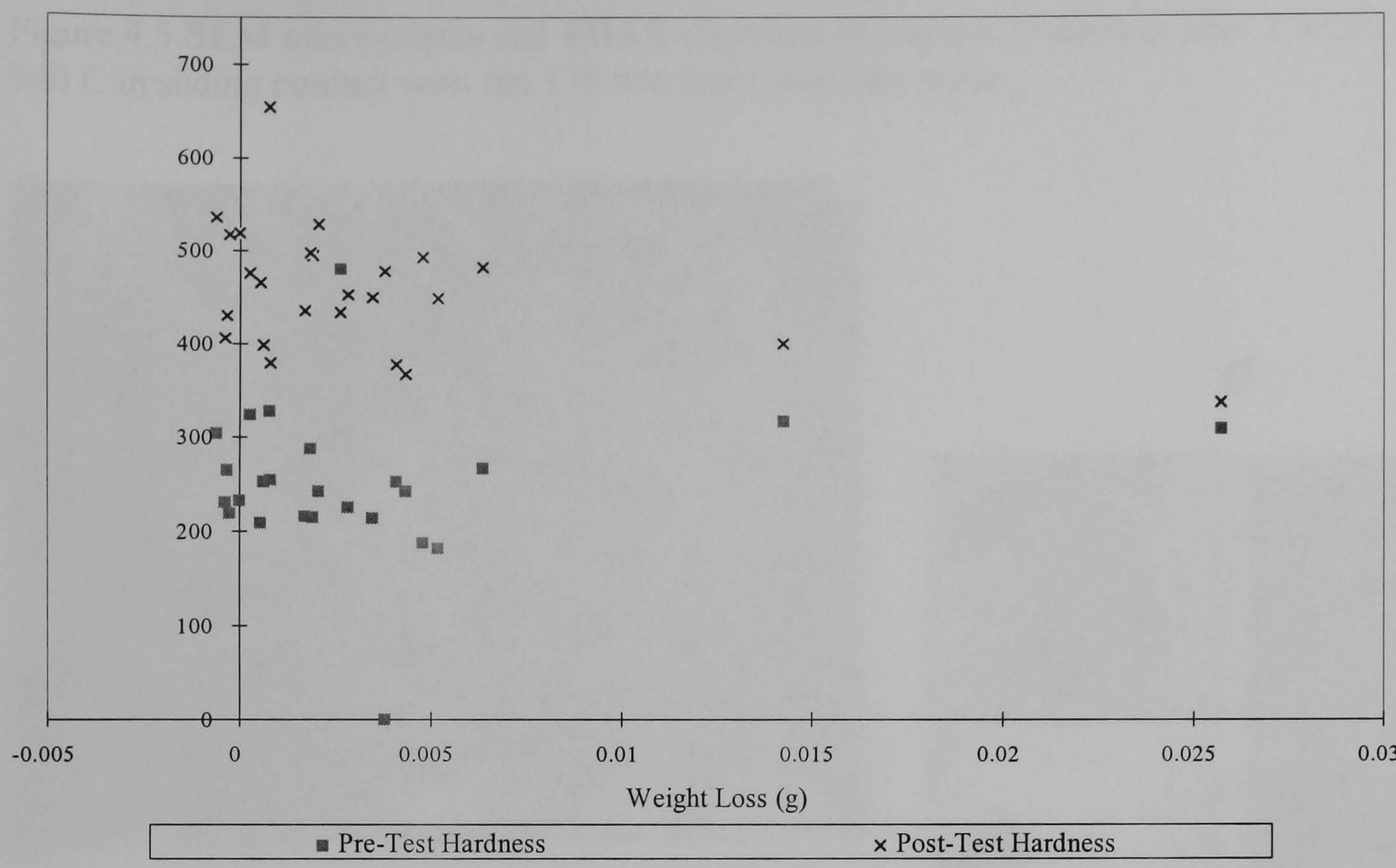

Figure 4.3 Weight change of 25 candidate bristle materials plotted against pre-test and post-test hardness after 7 hours 10N and 5m/s in sliding contact with the 150 mm rotor steel test wheel.

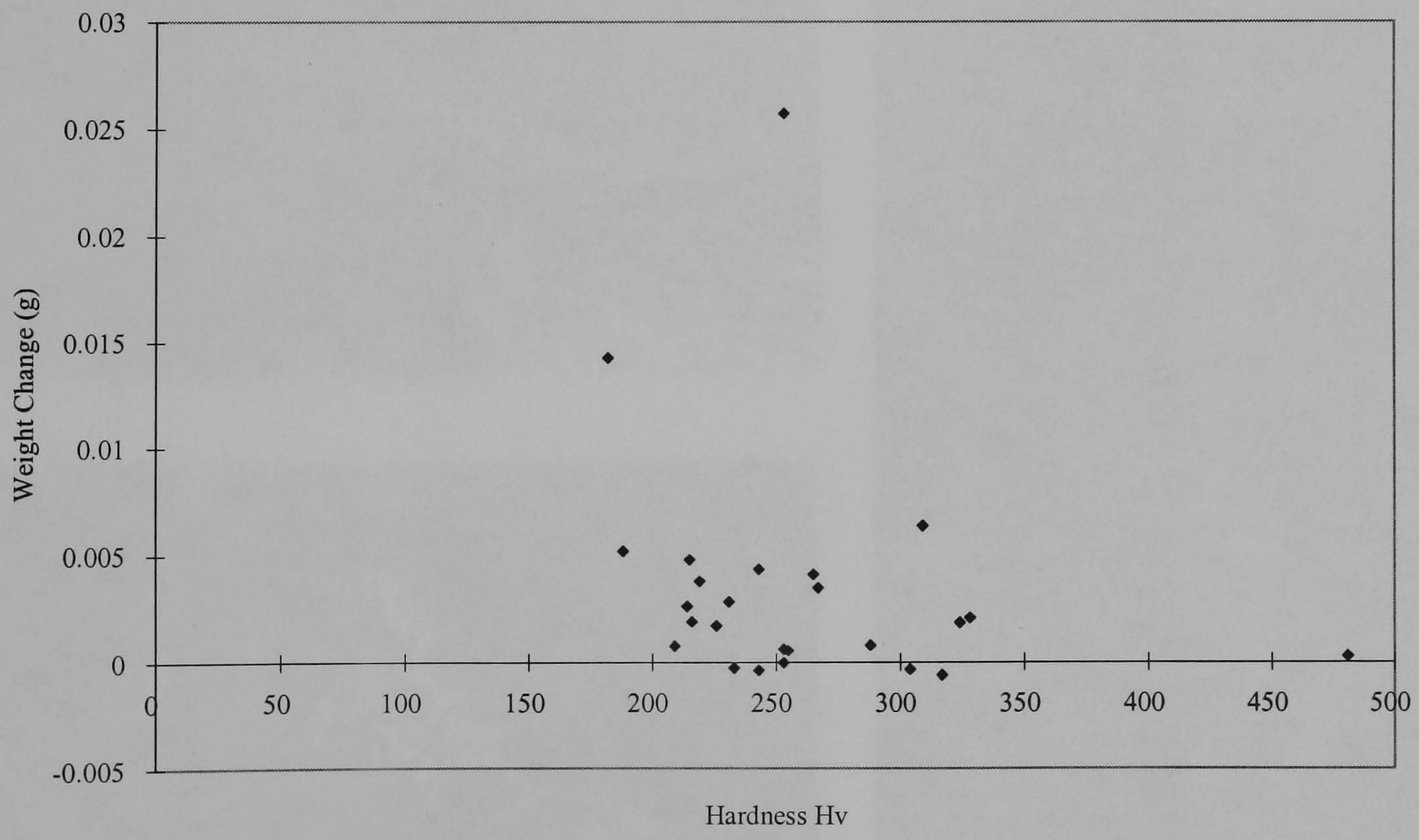

Figure 4.4 Pre-test hardness plotted against weight change of 25 candidate bristle materials after 7 hours 10N and 5m/s in sliding contact with the 150 mm rotor steel test wheel.

Figure 4.5 **SEM** micrographs and **EDAX** digimaps of Haynes 25 surface after 7 hours at 540 C in sliding contact with the 150 mm rotor steel test wheel.

a

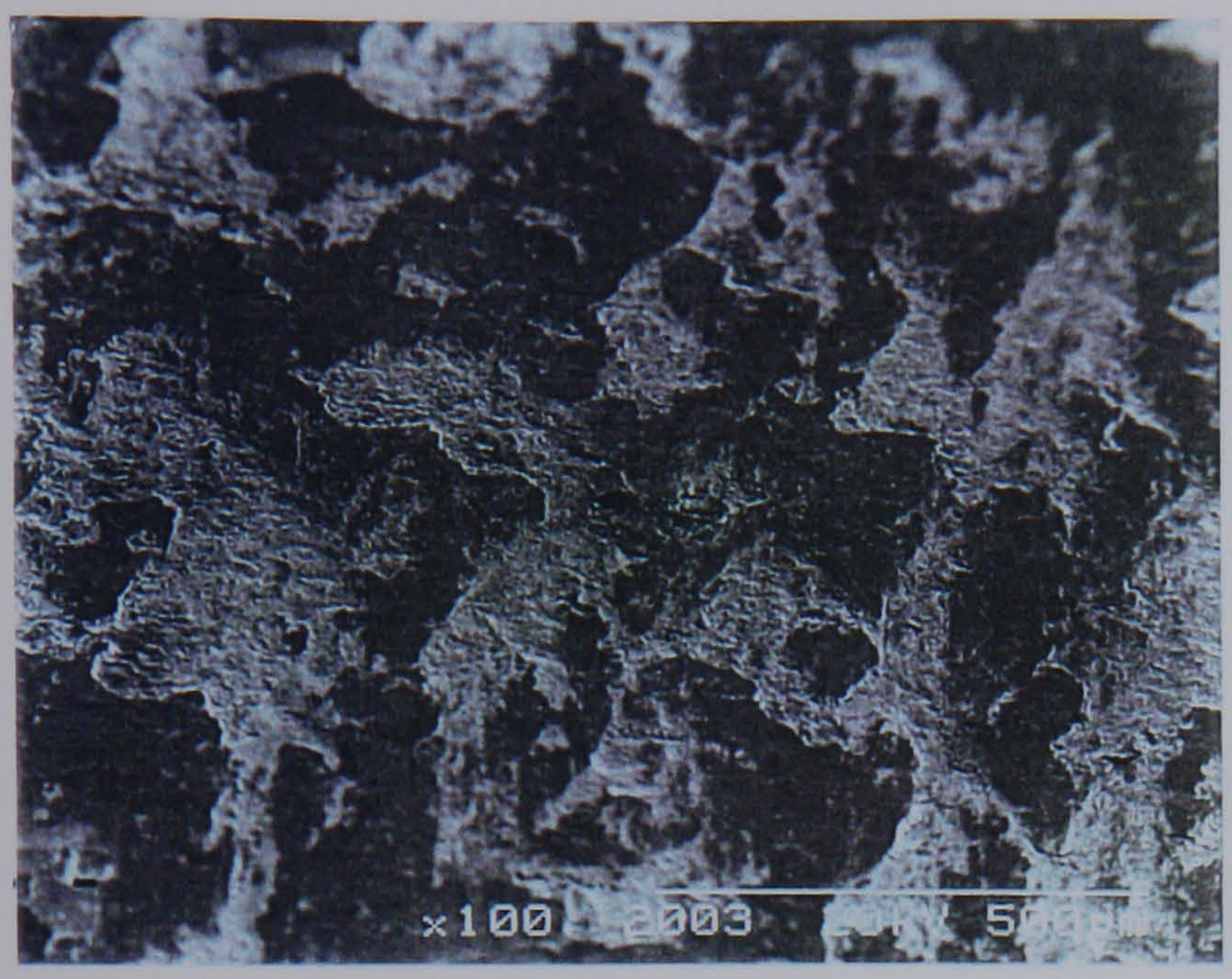

b

c

d

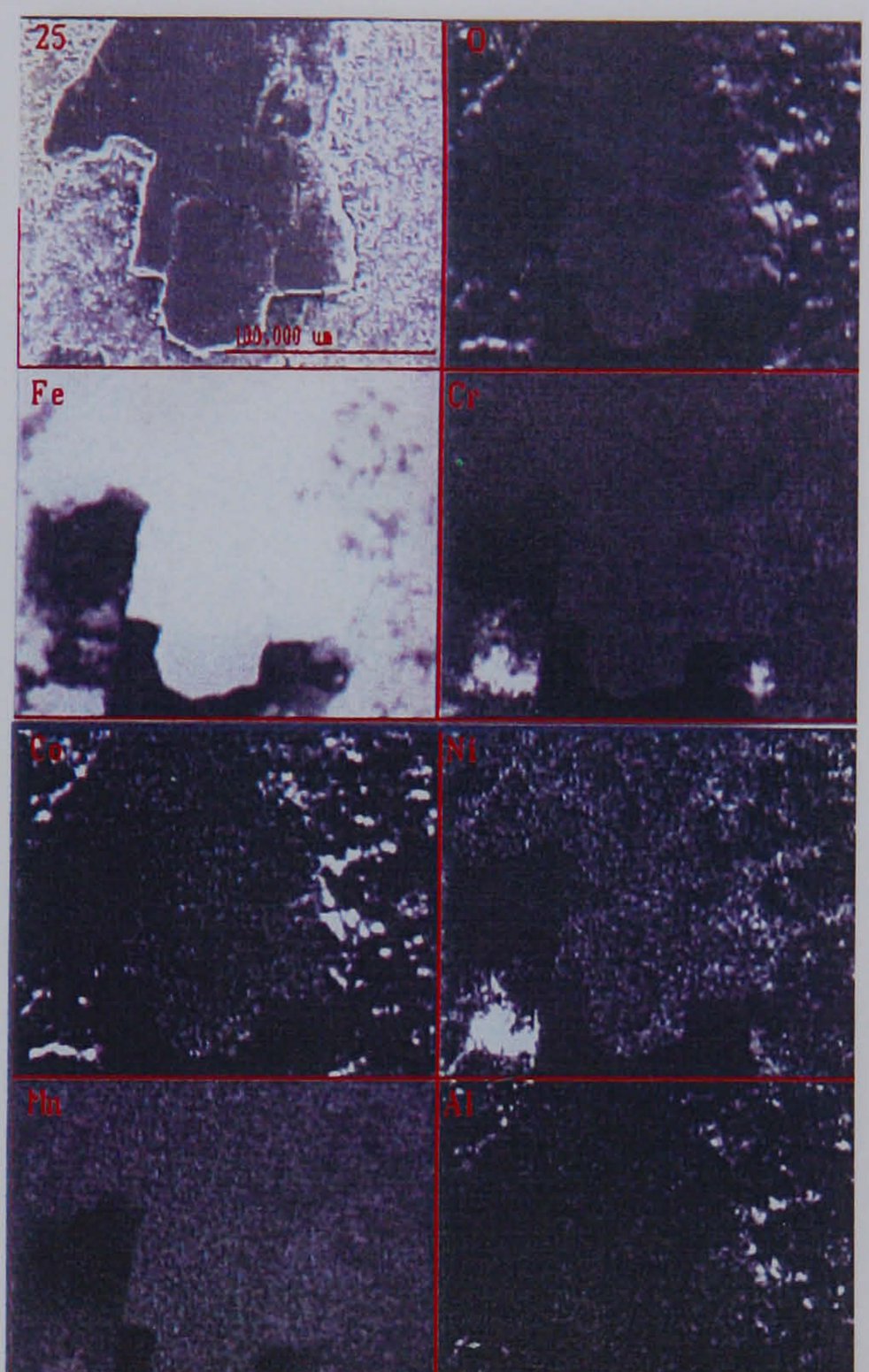

Figure 4.6 **SEM** micrographs and **EDAX** digimaps of X-750 surface after 7 hours at 540 C in sliding contact with the 150 mm rotor steel test wheel.

a

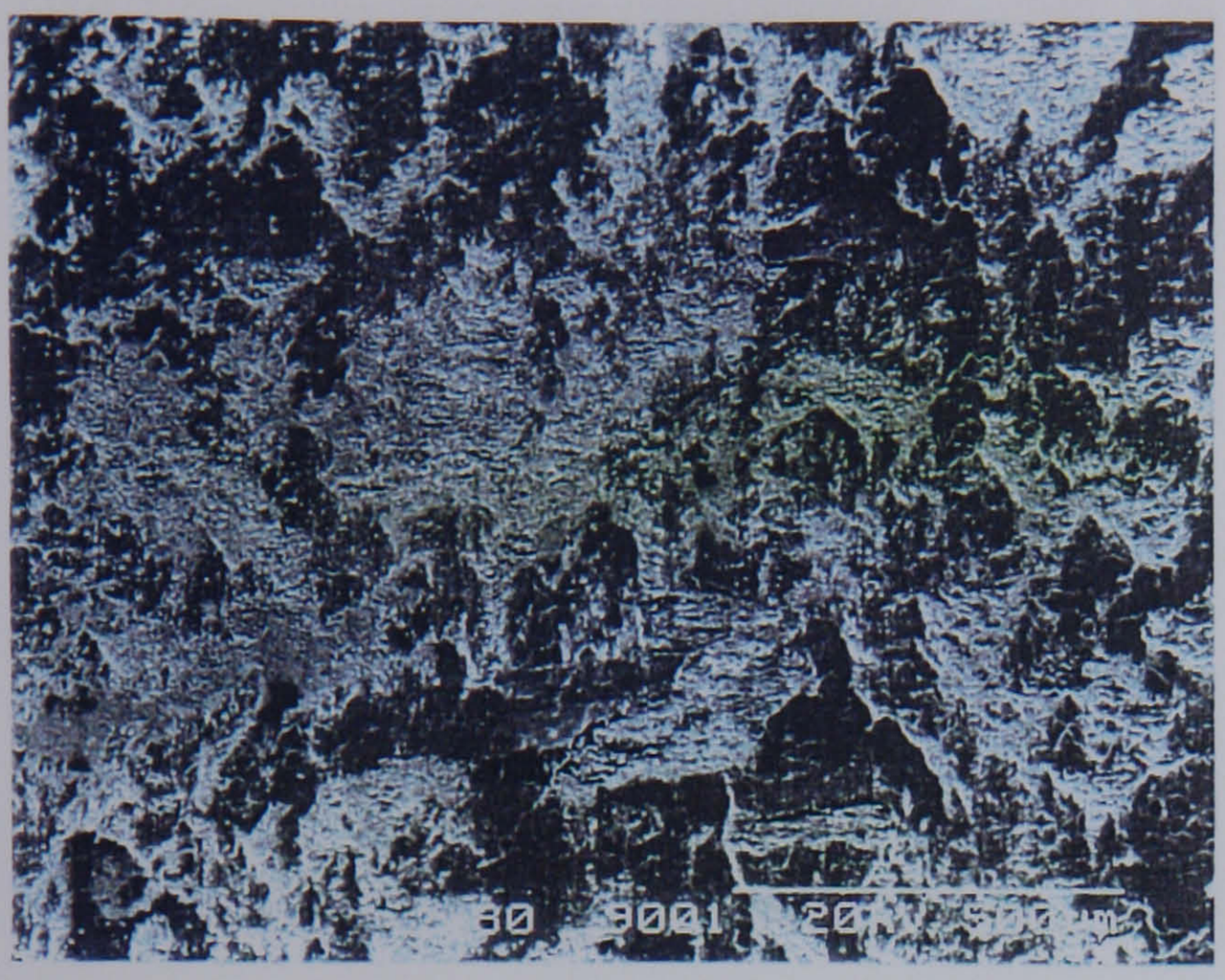

b

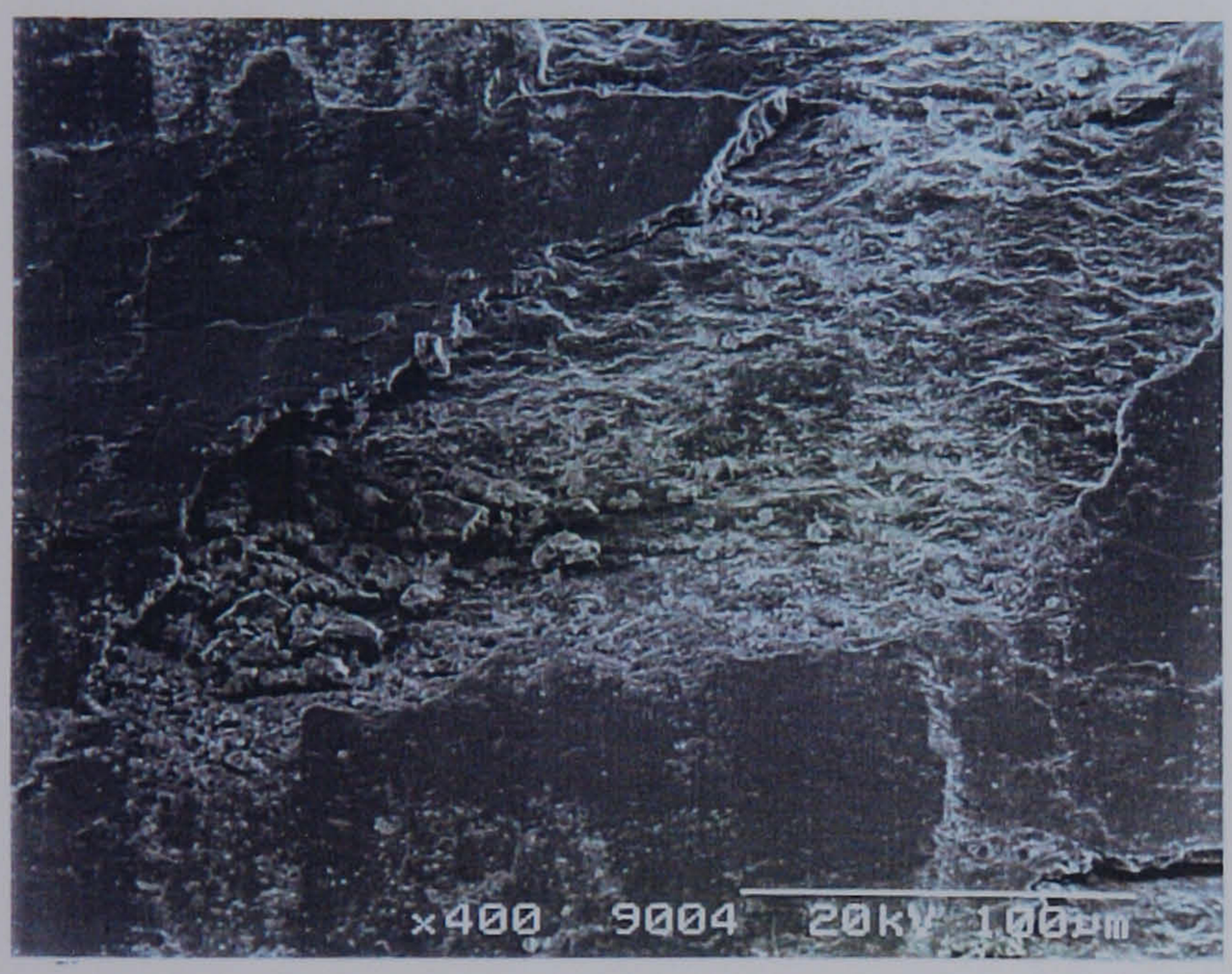

C

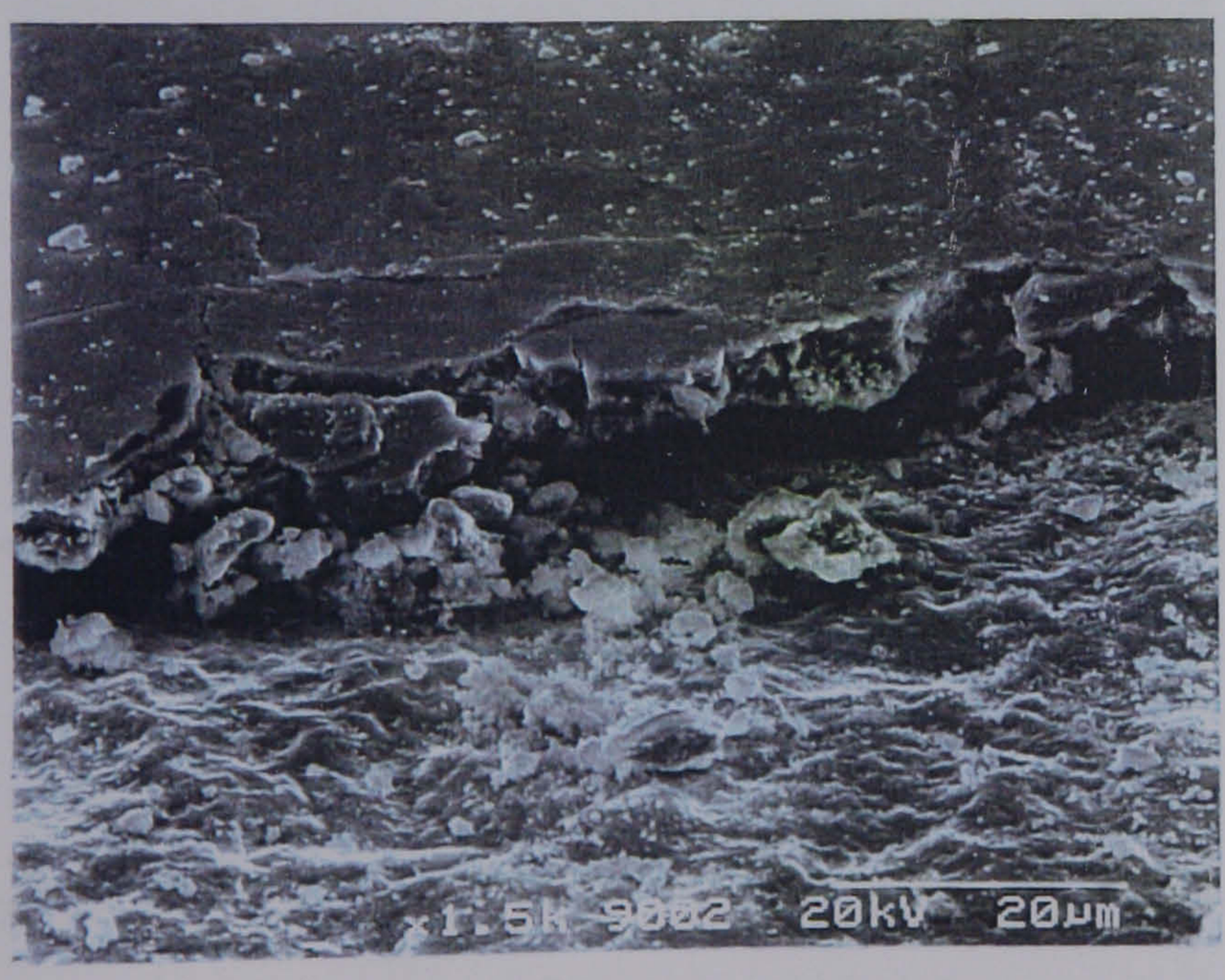

d

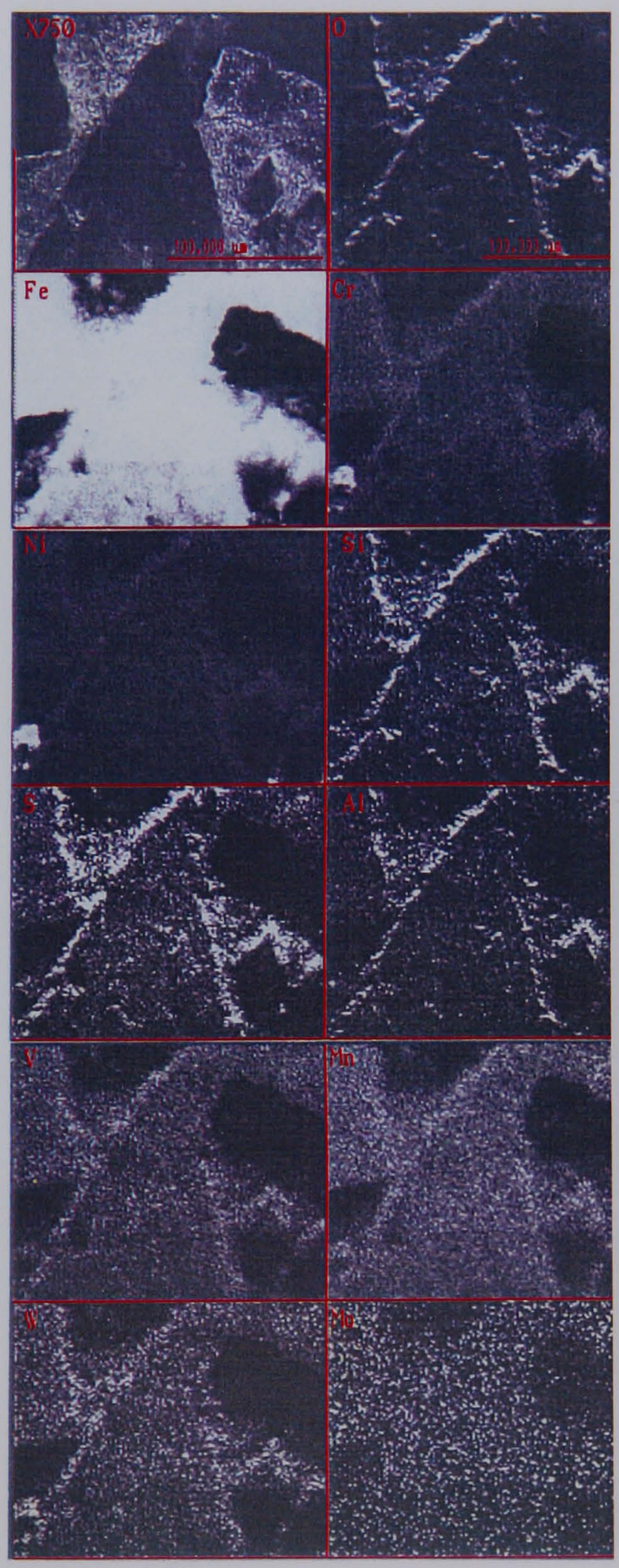

Figure 4.7 **SEM** micrographs and **EDAX** digimaps of Waspalloy surface after 7 hours at 540 C in sliding contact with the 150 mm rotor steel test wheel.

a

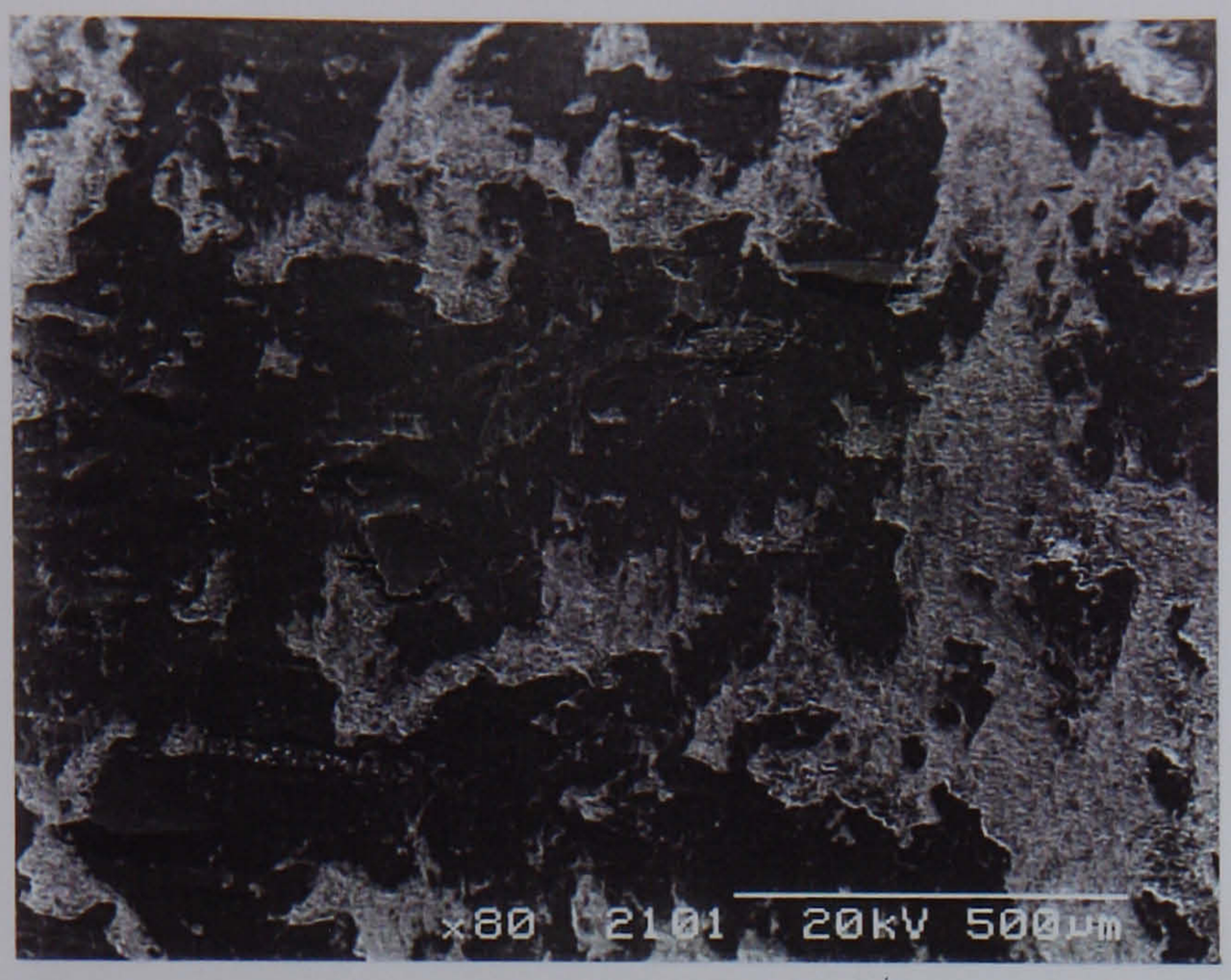

b

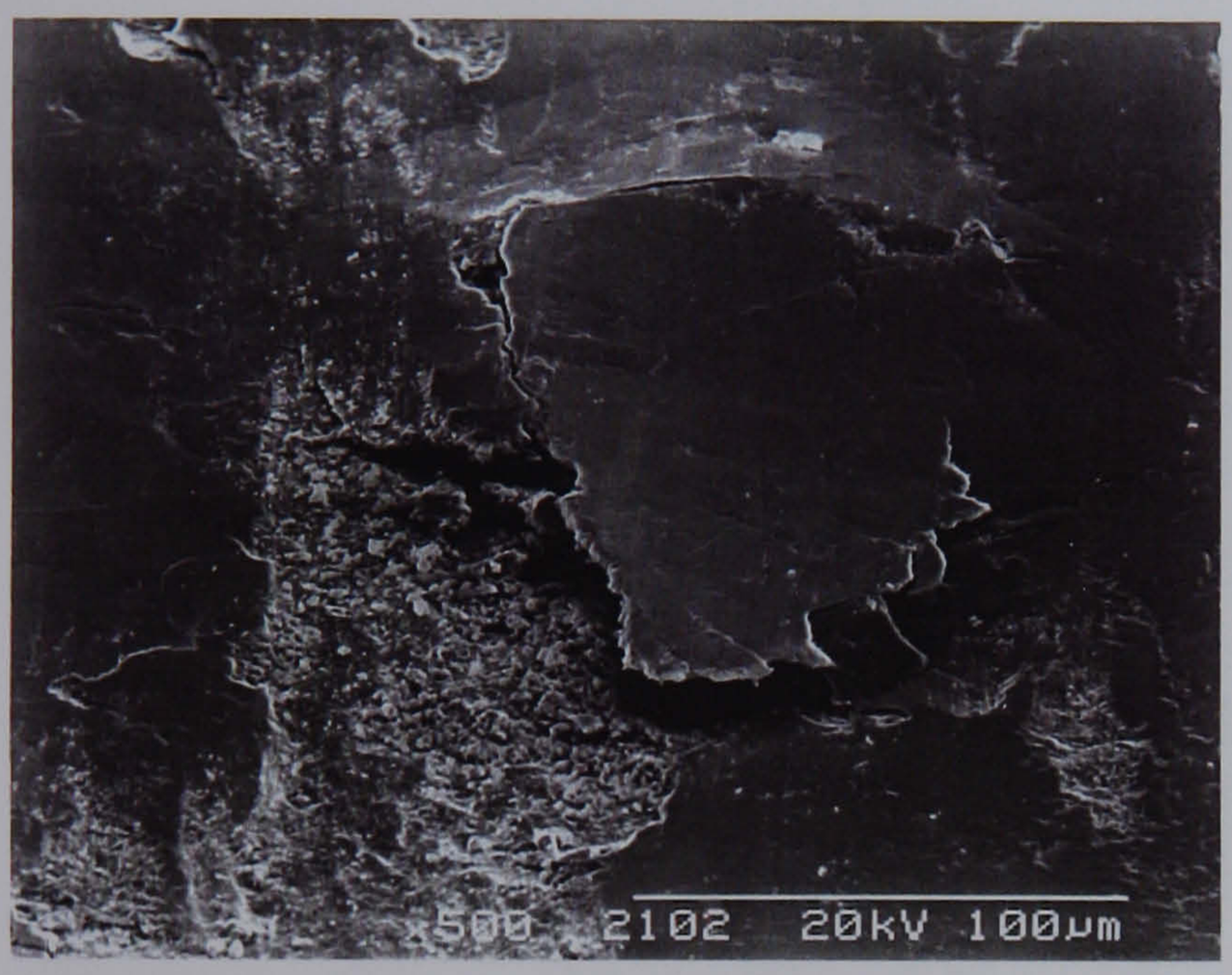

c

d

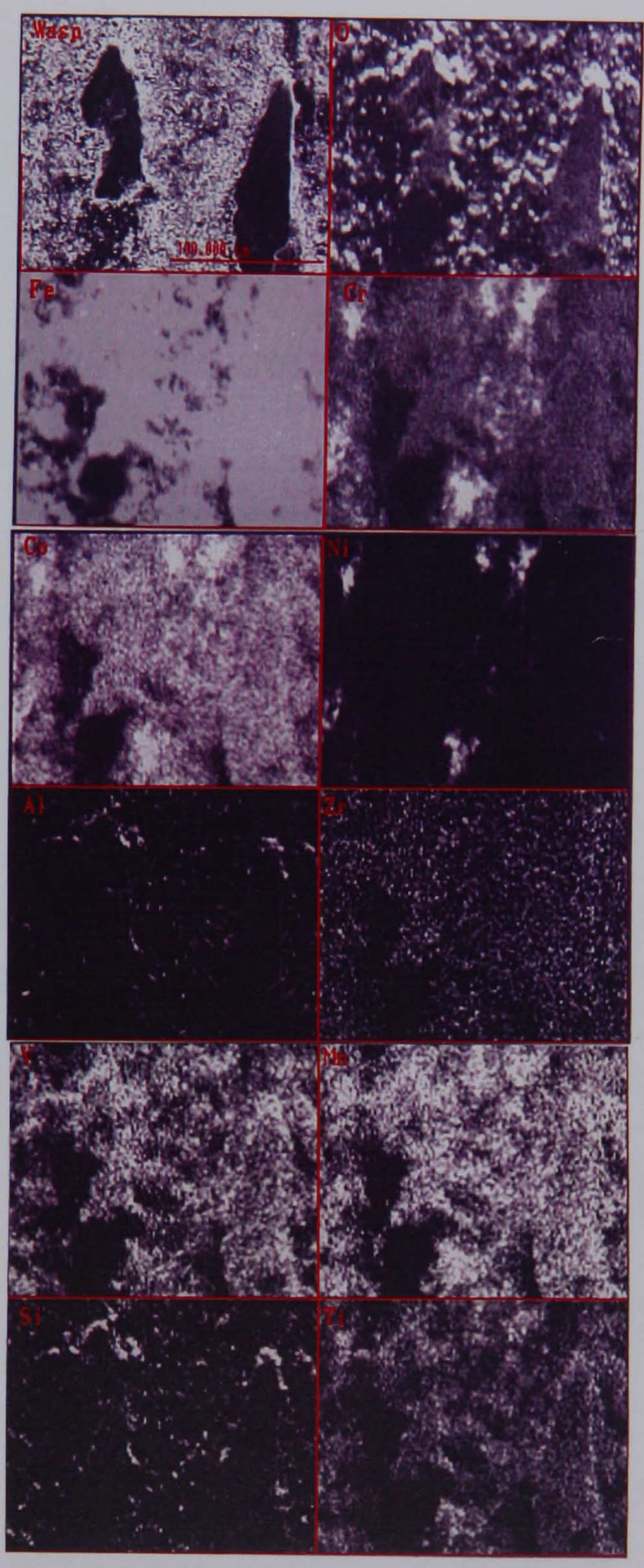

Figure 4.8 **SEM** micrographs and **EDAX** digimaps of Ultimet surface after 7 hours at 540 C in sliding contact with the 150 mm rotor steel test wheel.

a

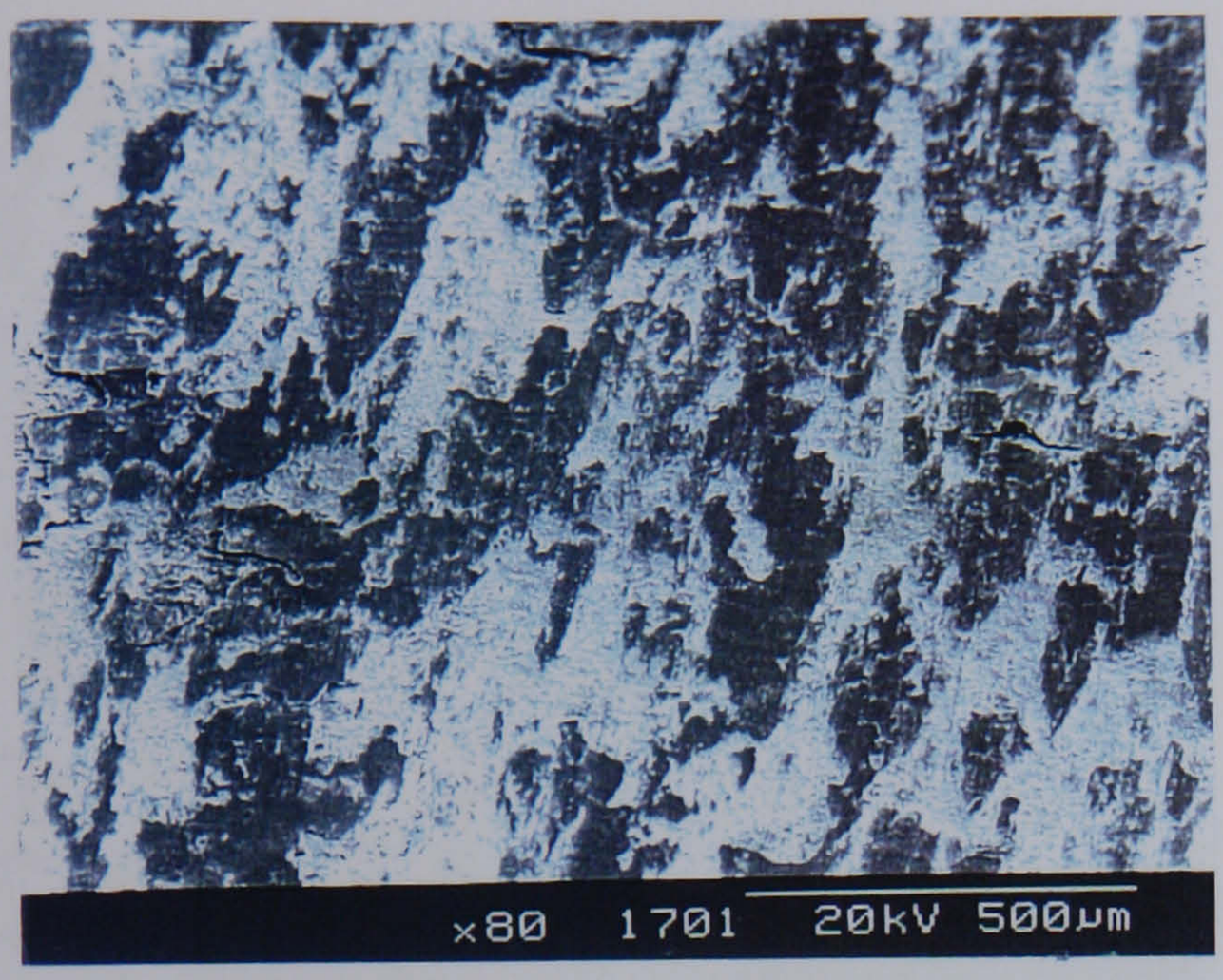

b

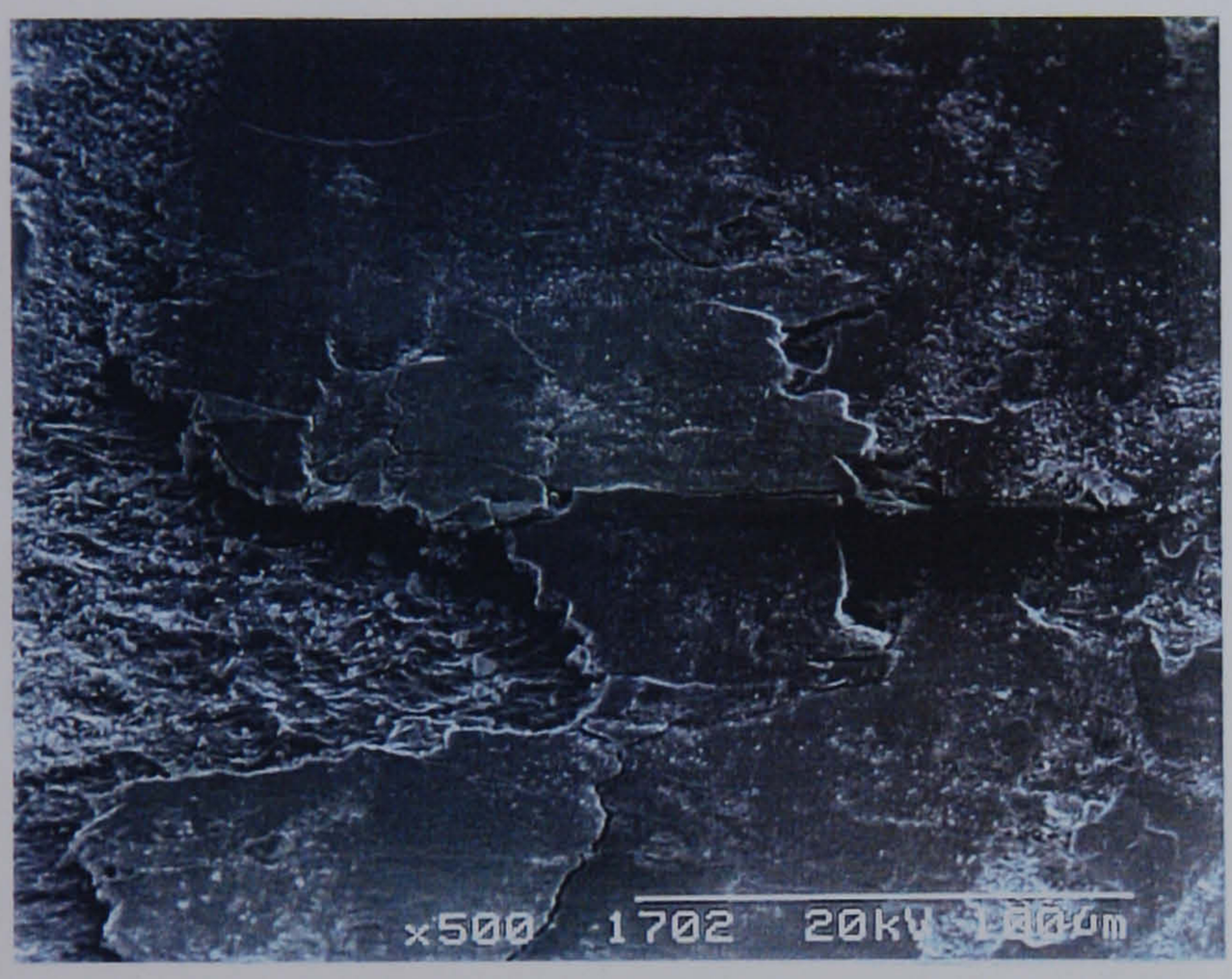

C

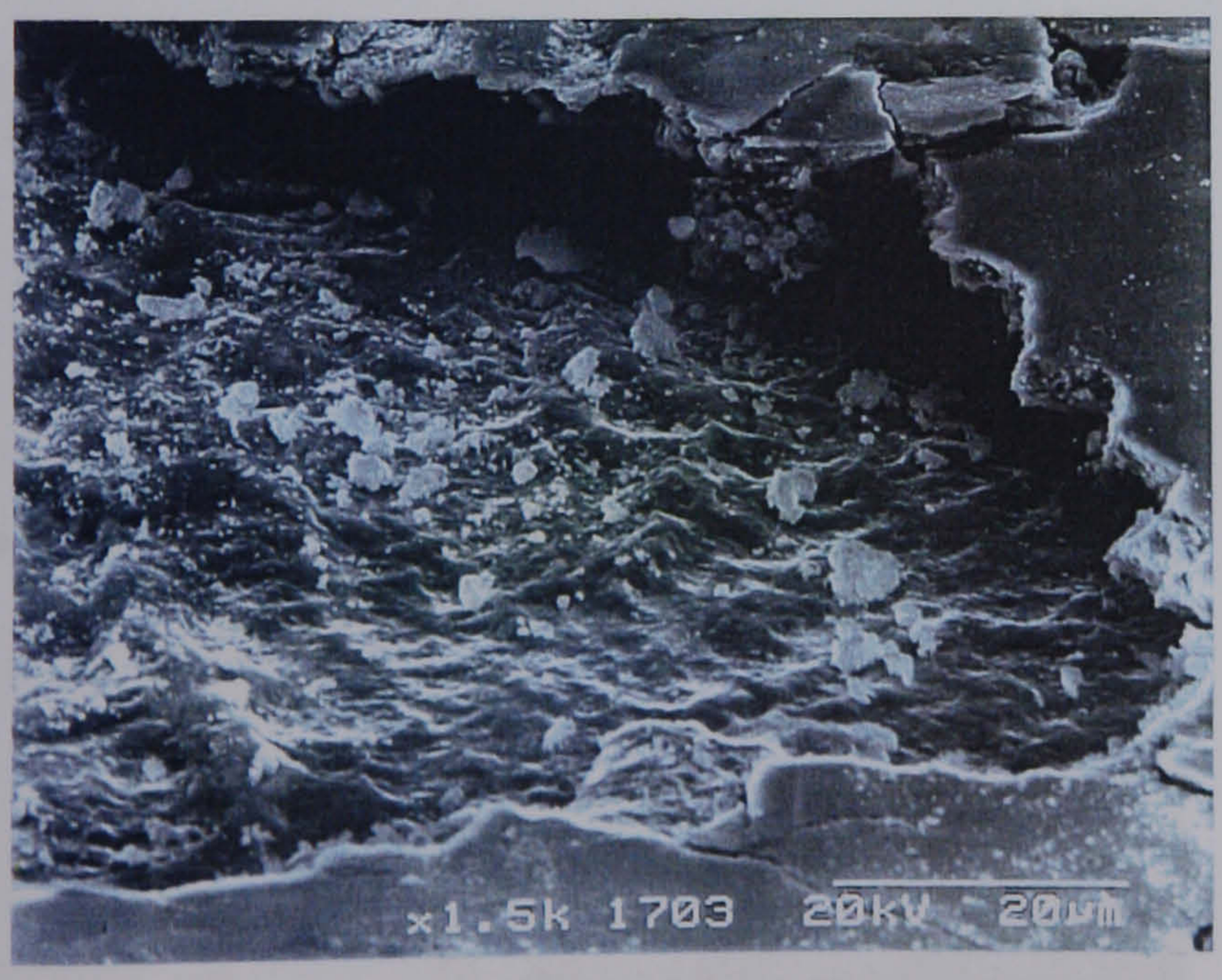

d

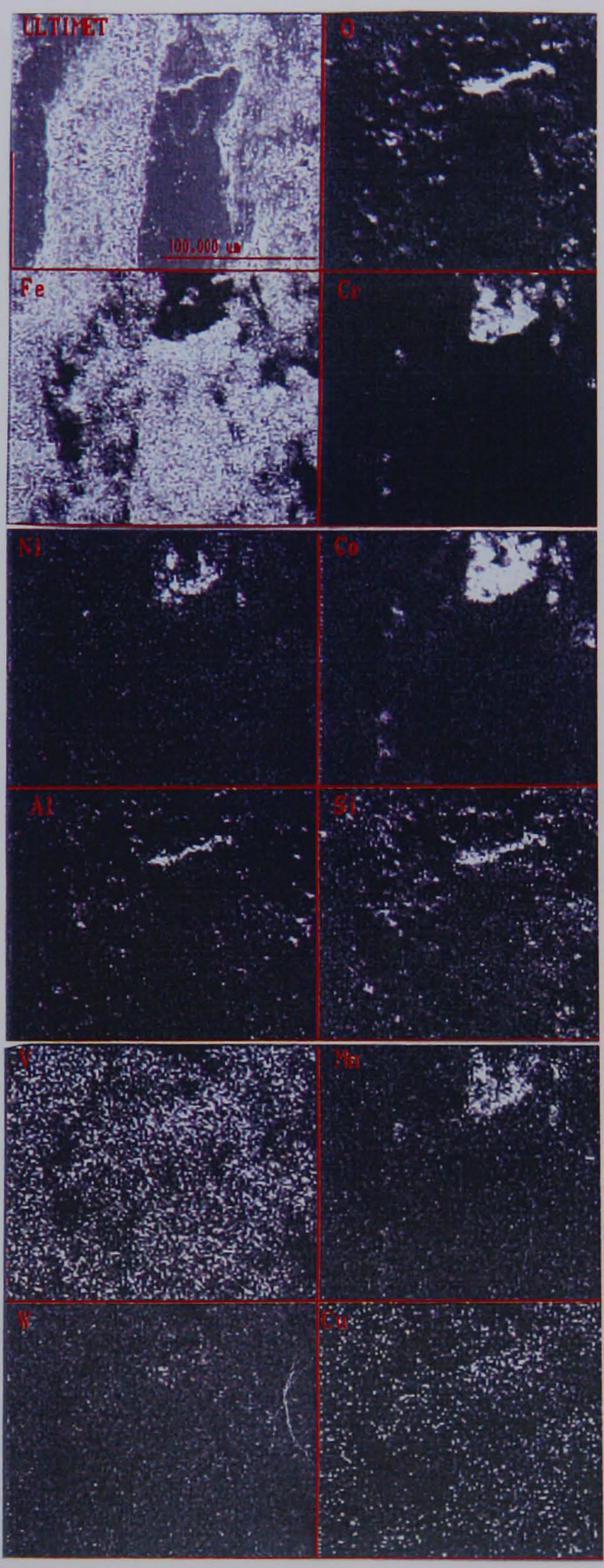

Figure 4.9 **SEM** micrographs and **EDAX** digimaps of Rotor Spec 297 surface after 7 hours at 540 C in sliding contact with the 150 mm rotor steel test wheel.

a

b

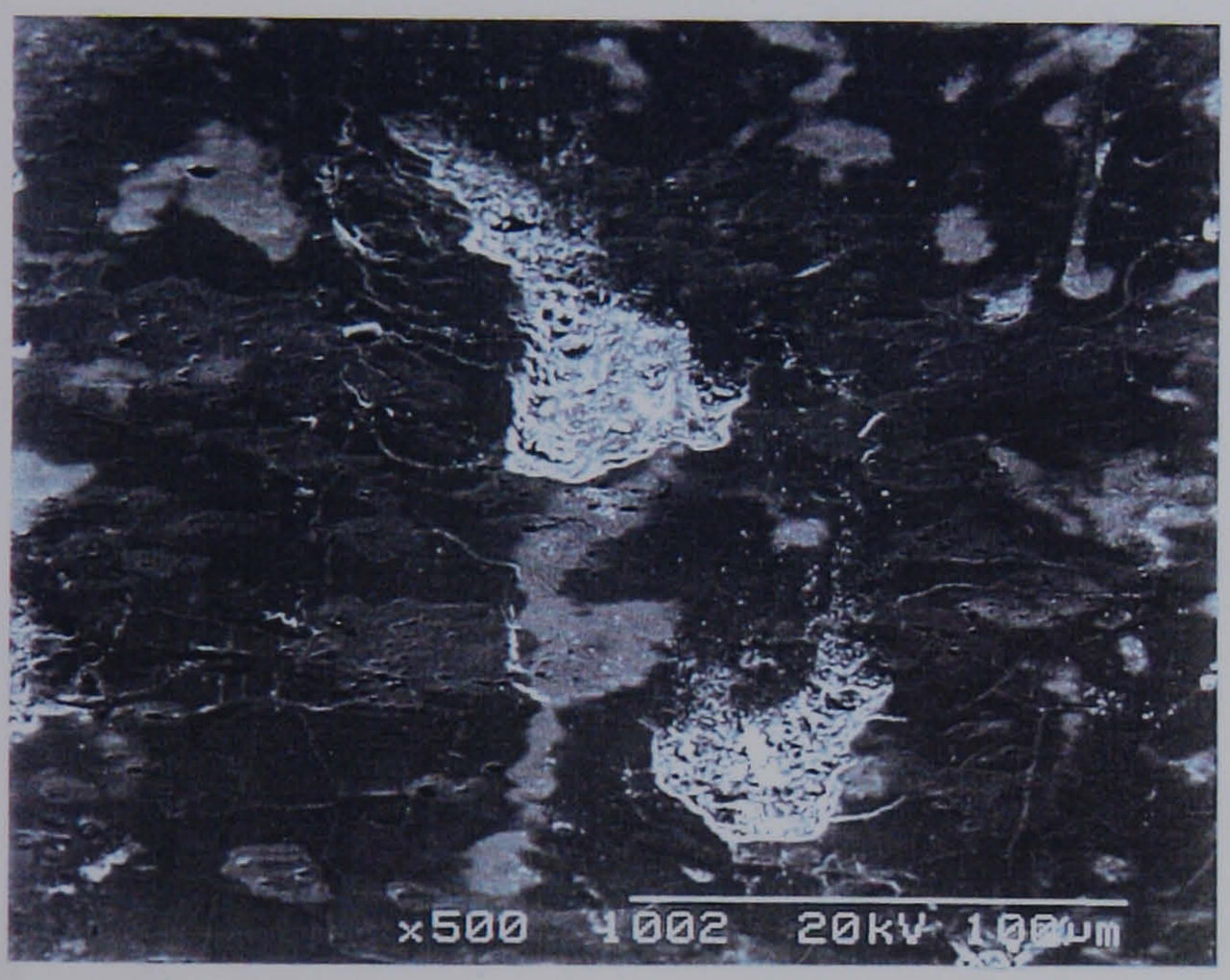

C

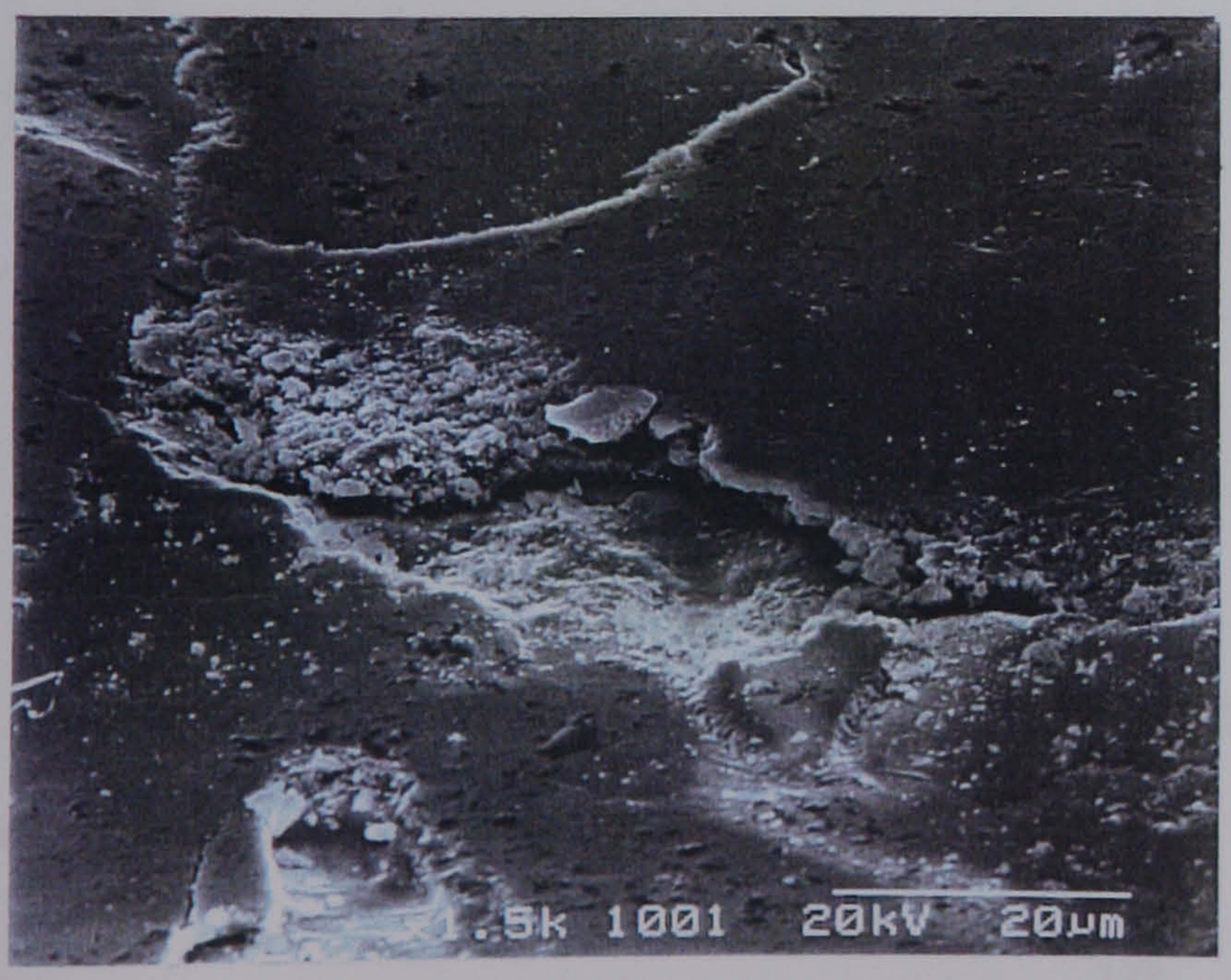

d

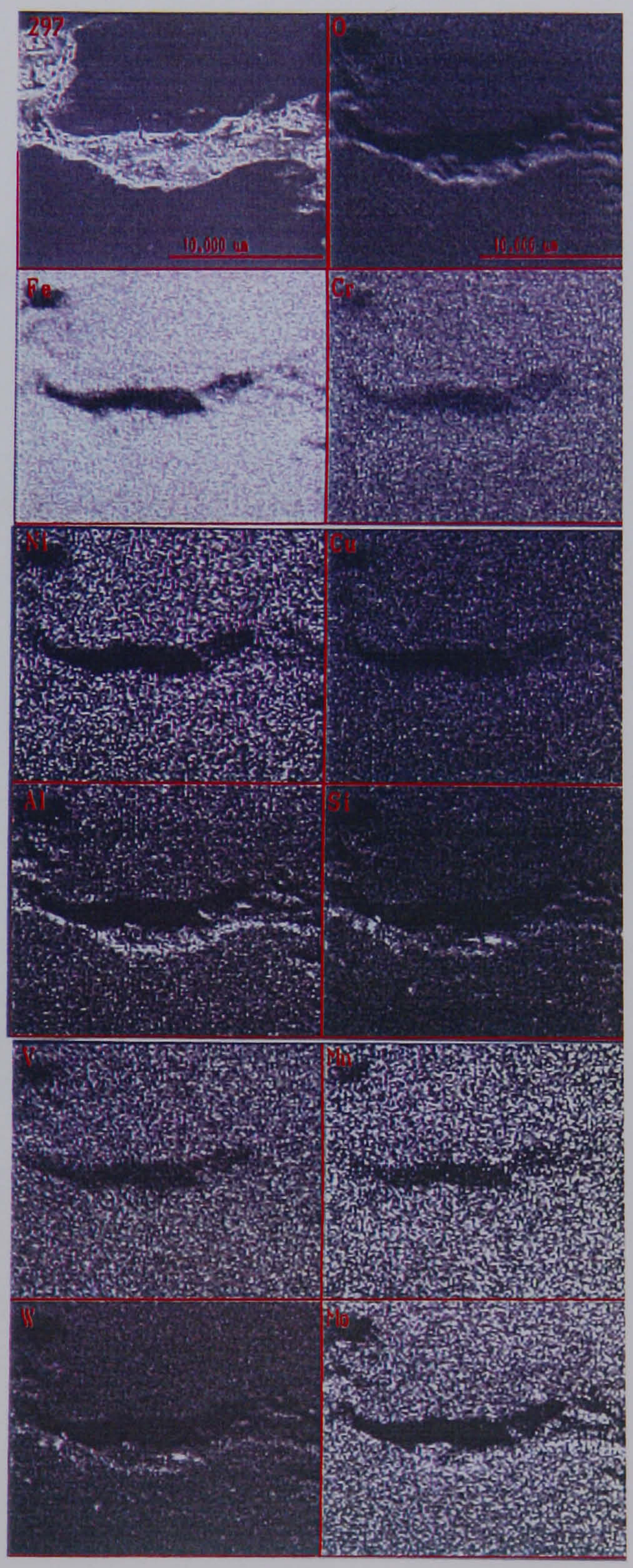

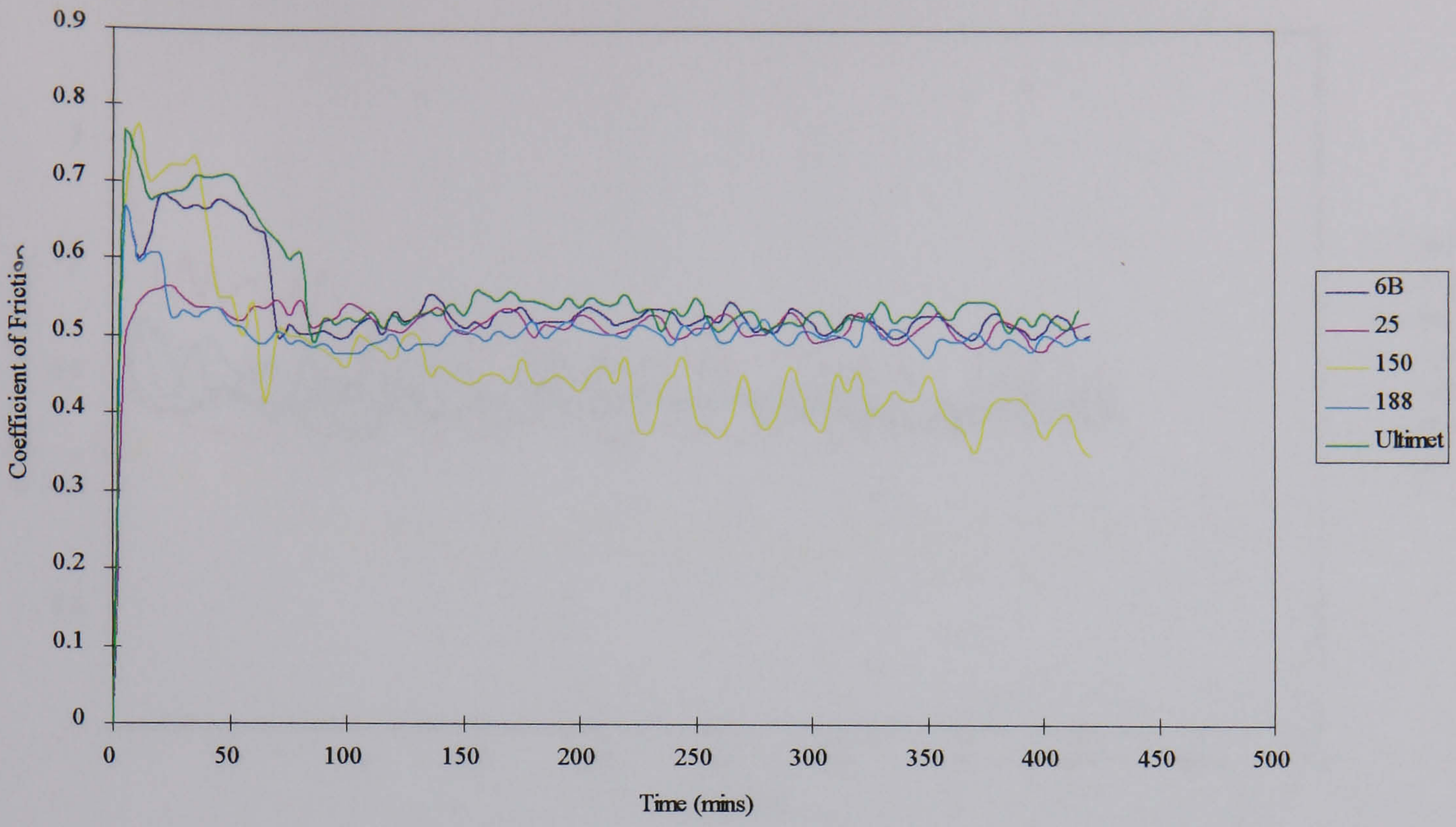

Figure 4.10 Coefficient of Friction against Time for Cobalt Base Candidate Bristle materials.

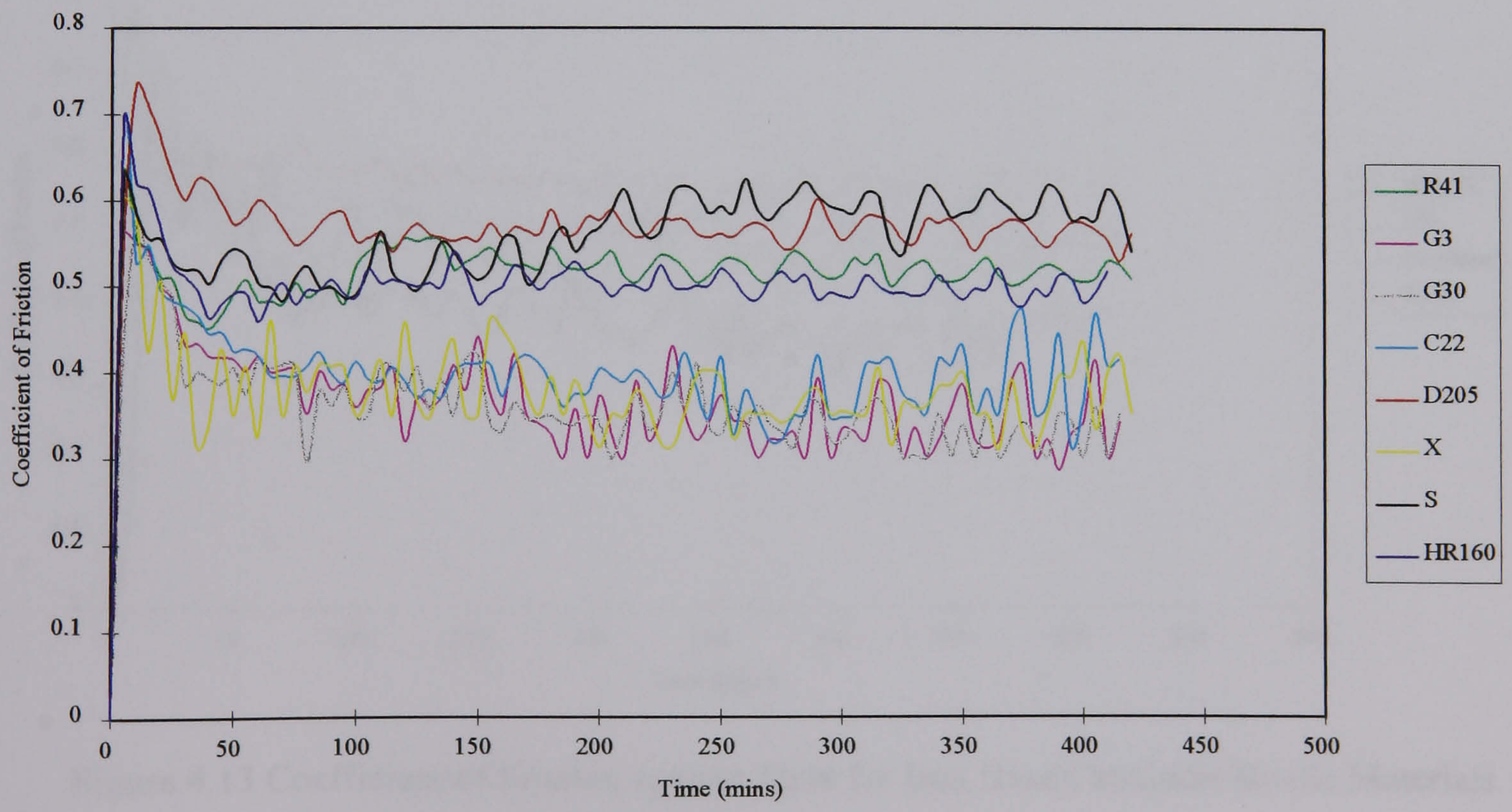

Figure 4.11 Coefficient of Friction against Time for Nickel Base Solution Hardened Candidate Bristle Materials.

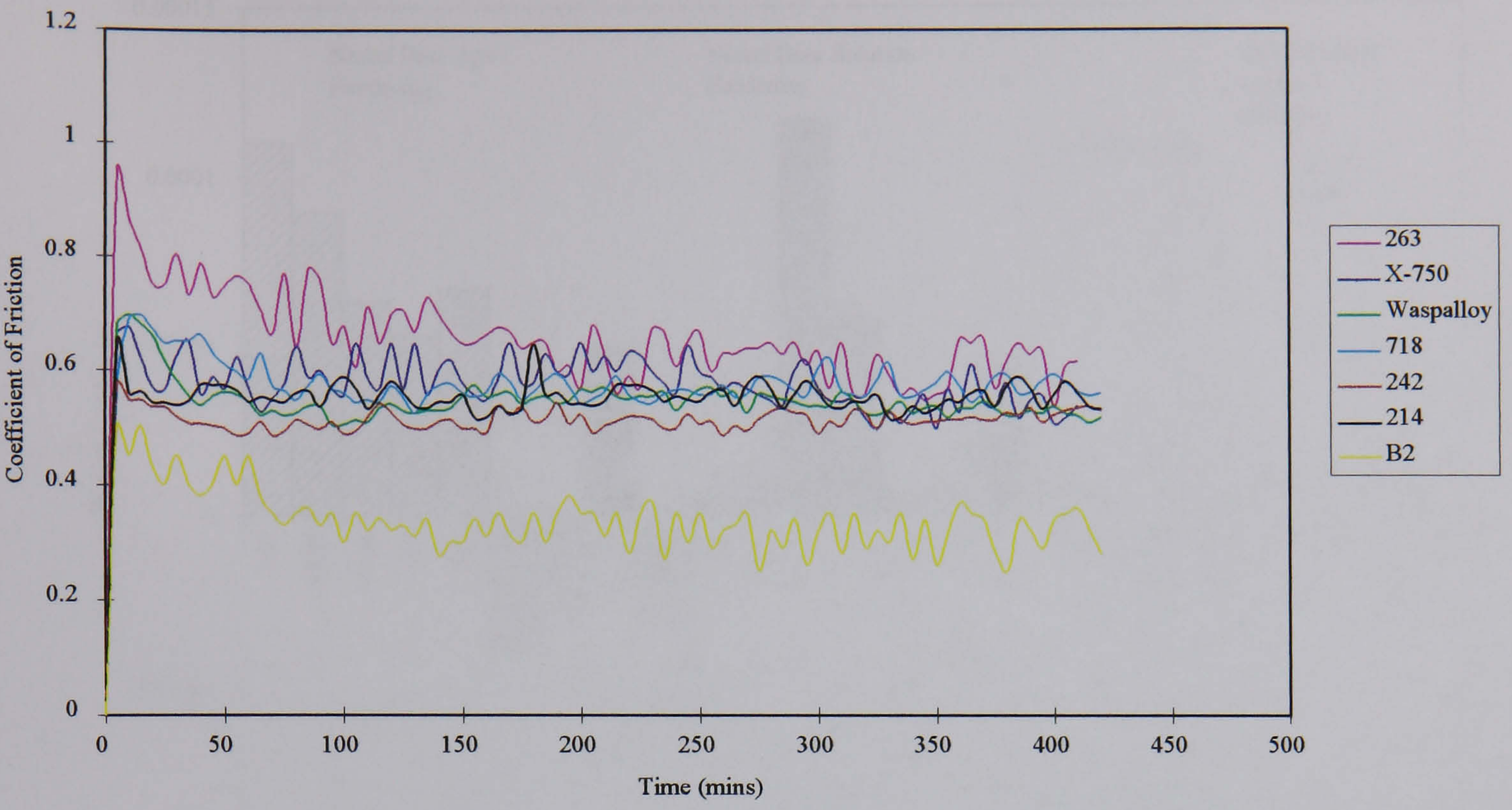

Figure 4.12 Coefficient of Friction against Time for Nickel Base Age Hardening Candidate Bristle Materials.

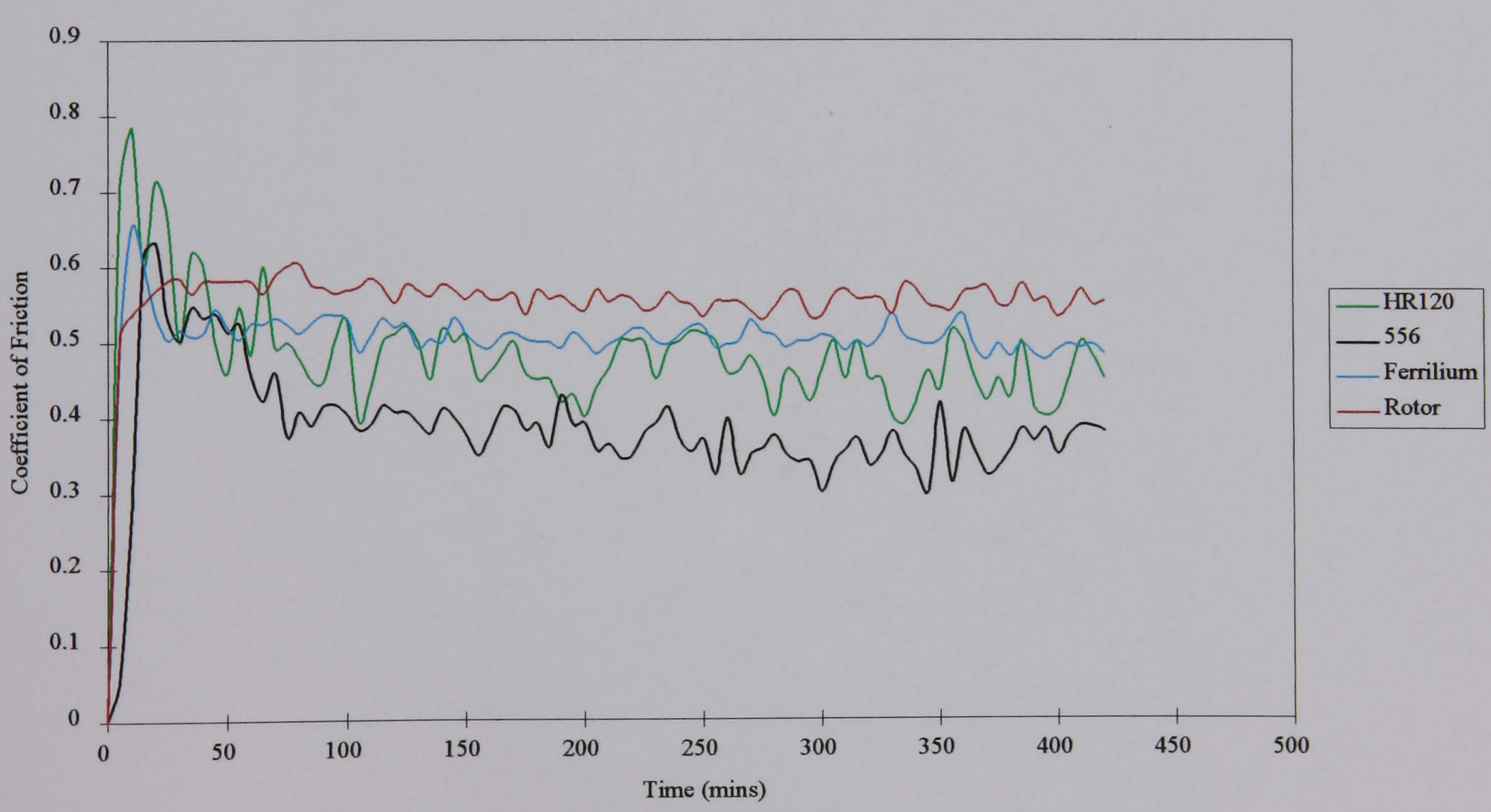

Figure 4.13 Coefficient of Friction against Time for Iron Base Candidate Bristle Materials.

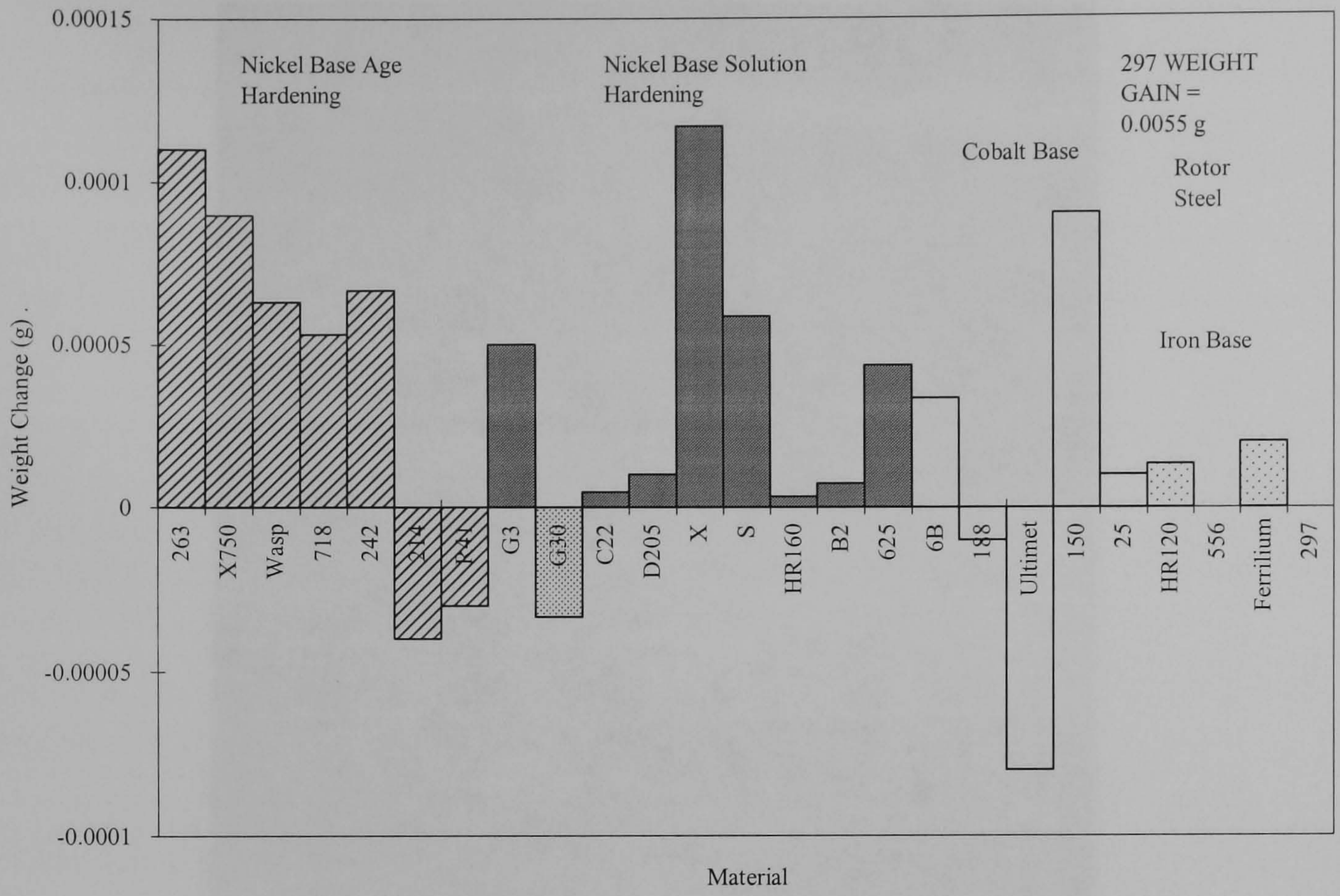

Figure 4.14 Weight change due to exposure to air at 540 °C for 7 hours.

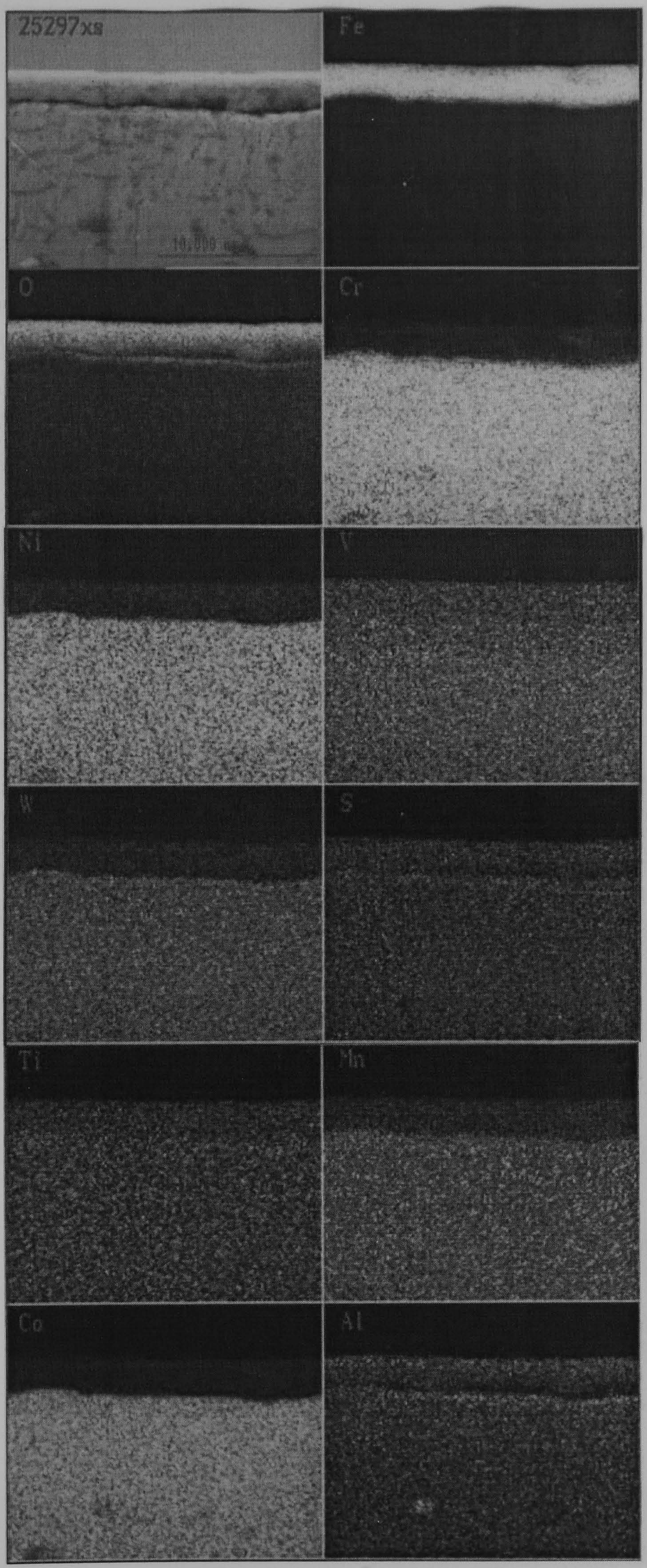

Figure 4.15 **EDAX** cross-sectional digimaps of Haynes 25 sample wear track showing possible trace elements. After 3 hours at 540 °C in sliding contact with the 50 mm rotor steel test wheel.

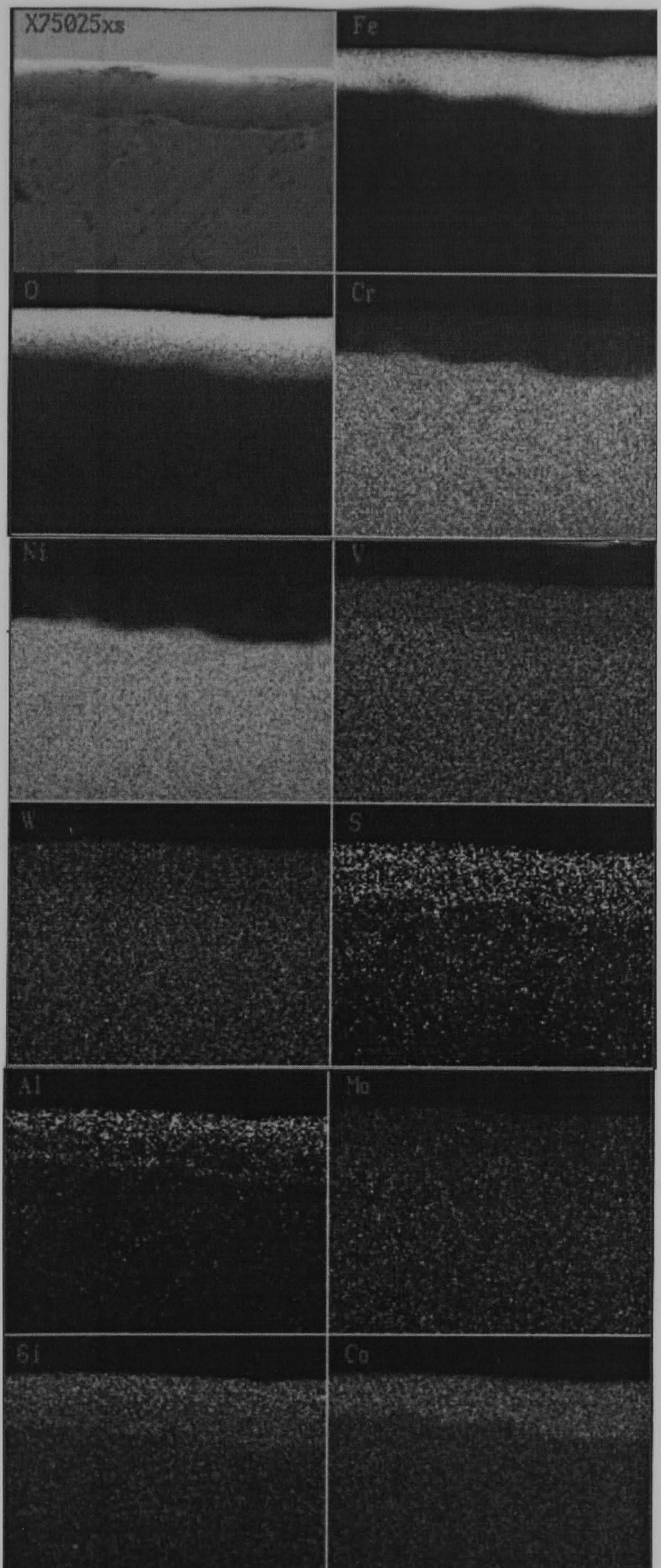

Figure 4.16 **EDAX** cross-sectional digimaps of Haynes X-750 sample wear track showing possible trace elements. After 3 hours at 540 °C in sliding contact with the 50 mm rotor steel test wheel.

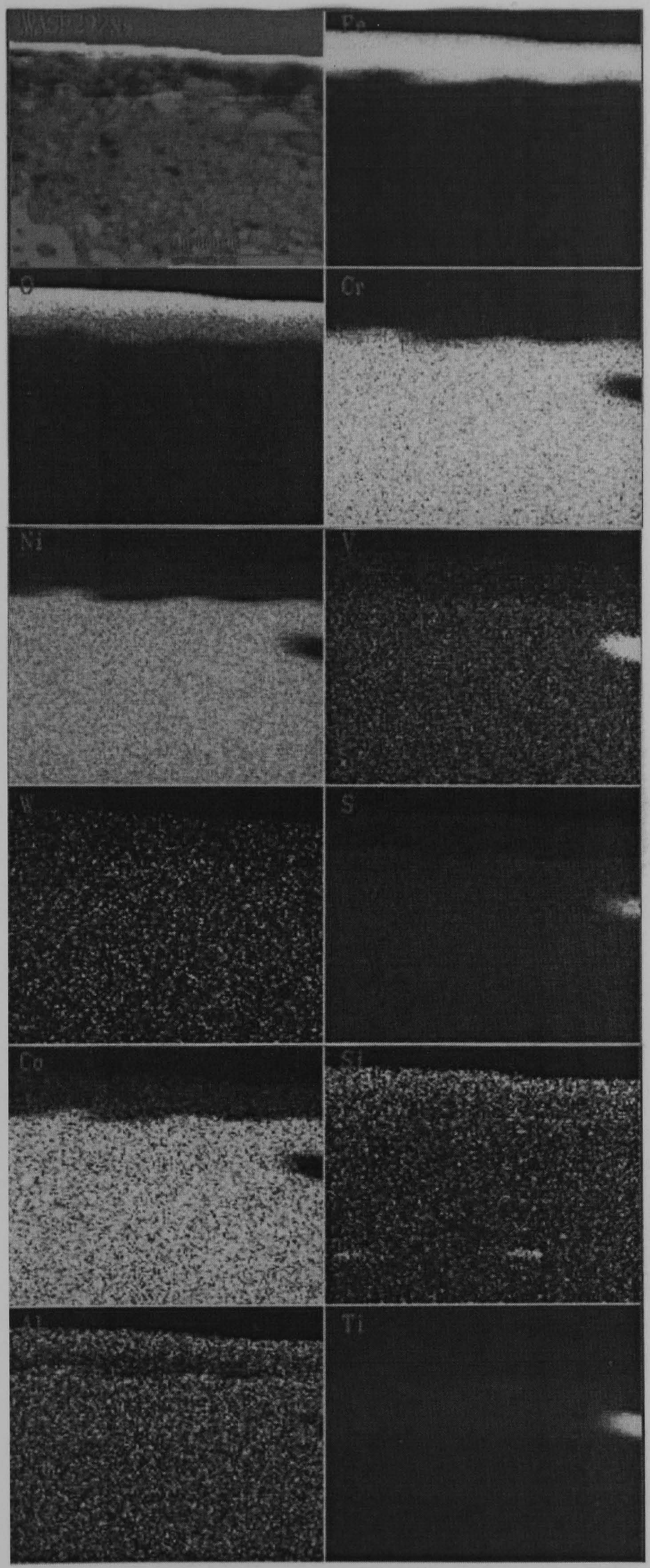

Figure 4.17 **EDAX** cross-sectional digimaps of Waspaloy sample wear track showing possible trace elements. After 3 hours at 540 °C in sliding contact with the 50 mm rotor steel test wheel.

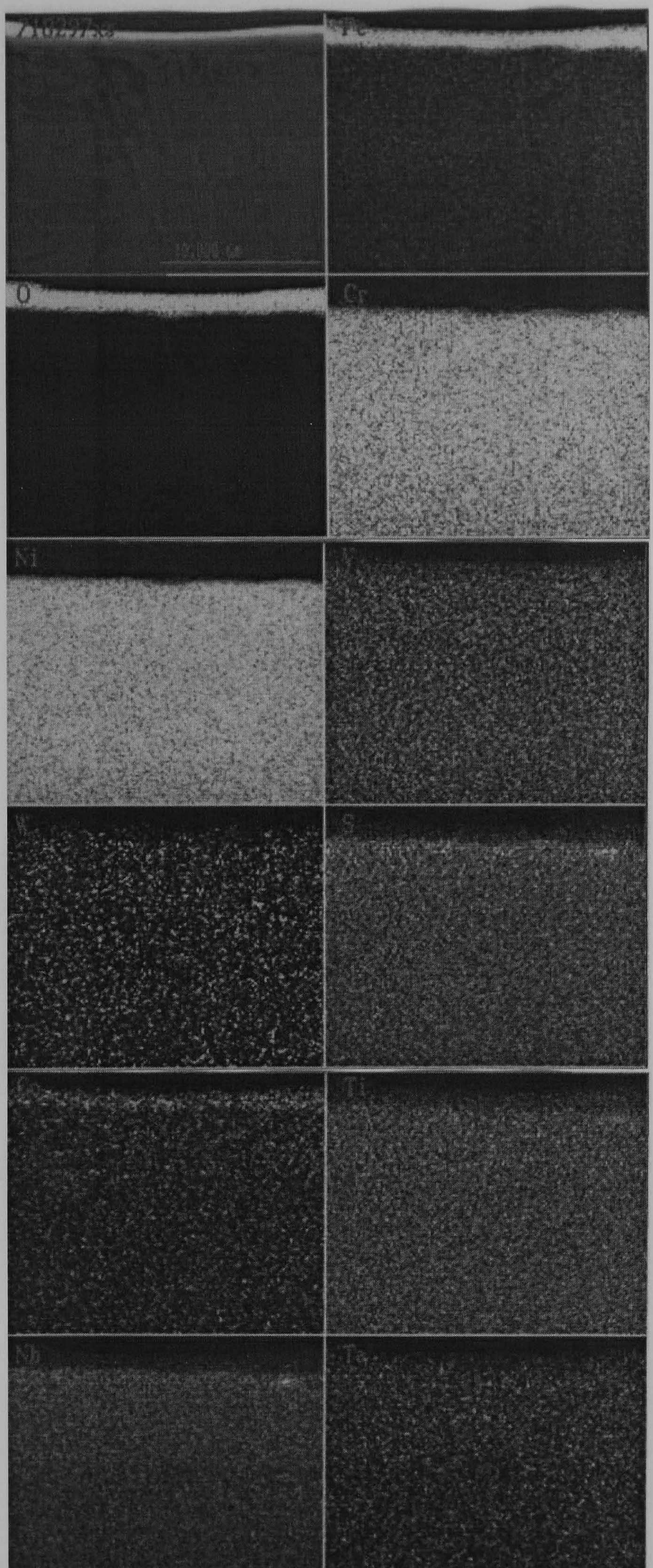

Figure 4.18 **EDAX** cross-sectional digimaps of Haynes 718 sample wear track showing possible trace elements. After 3 hours at 540 °C in sliding contact with the 50 mm rotor steel test wheel.

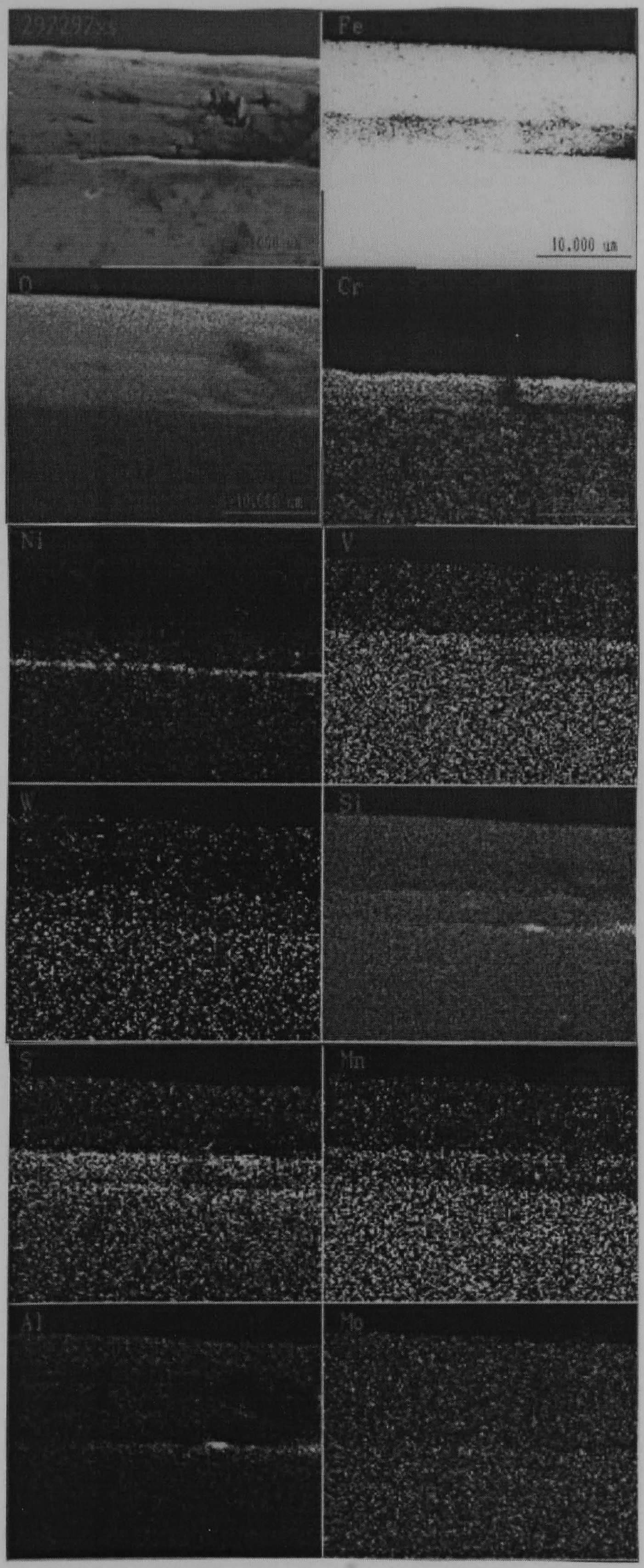

Figure 4.19 **EDAX** cross-sectional digimaps of rotor steel Spec. 297 sample wear track showing possible trace elements. After 3 hours at 540 °C in sliding contact with the 50 mm rotor steel test wheel.

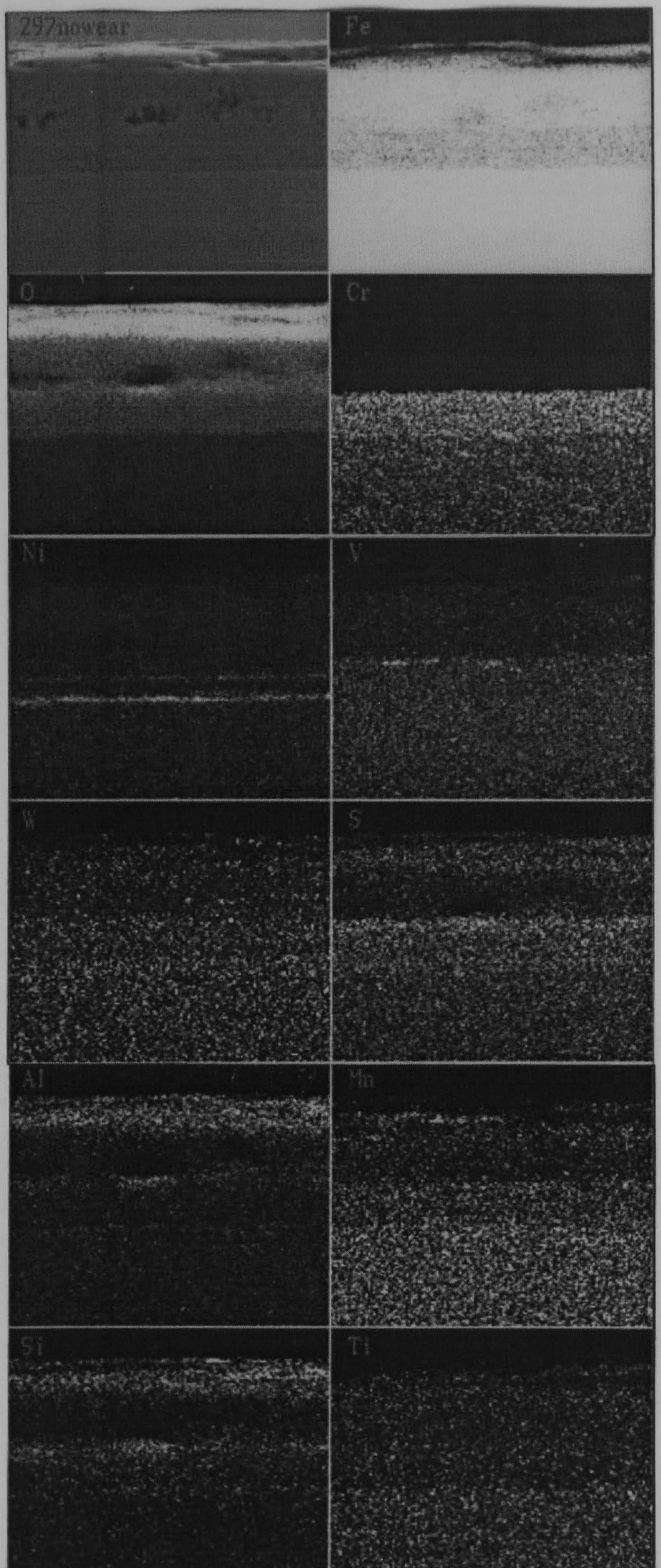

Figure 4.20 **EDAX** cross-sectional digimaps of possible trace elements on a sample of rotor steel Spec. 297 exposed to 540 °C for 3 hours (no wear).

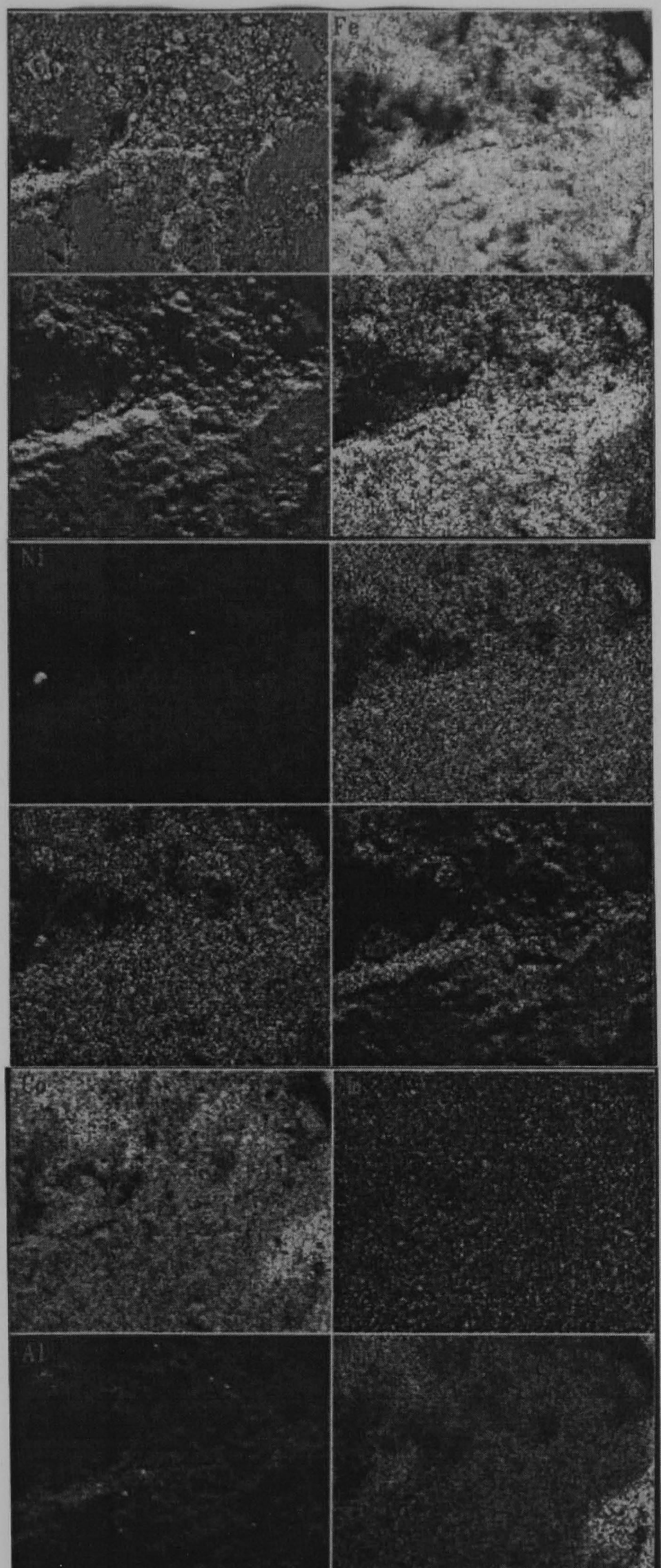

Figure 4.21 **EDAX** surface digimaps of rotor steel Spec. 297 showing possible trace elements from test wheel and Haynes 25 sample. After 3 hours at 540 °C in sliding contact with the 50 mm rotor steel test wheel.

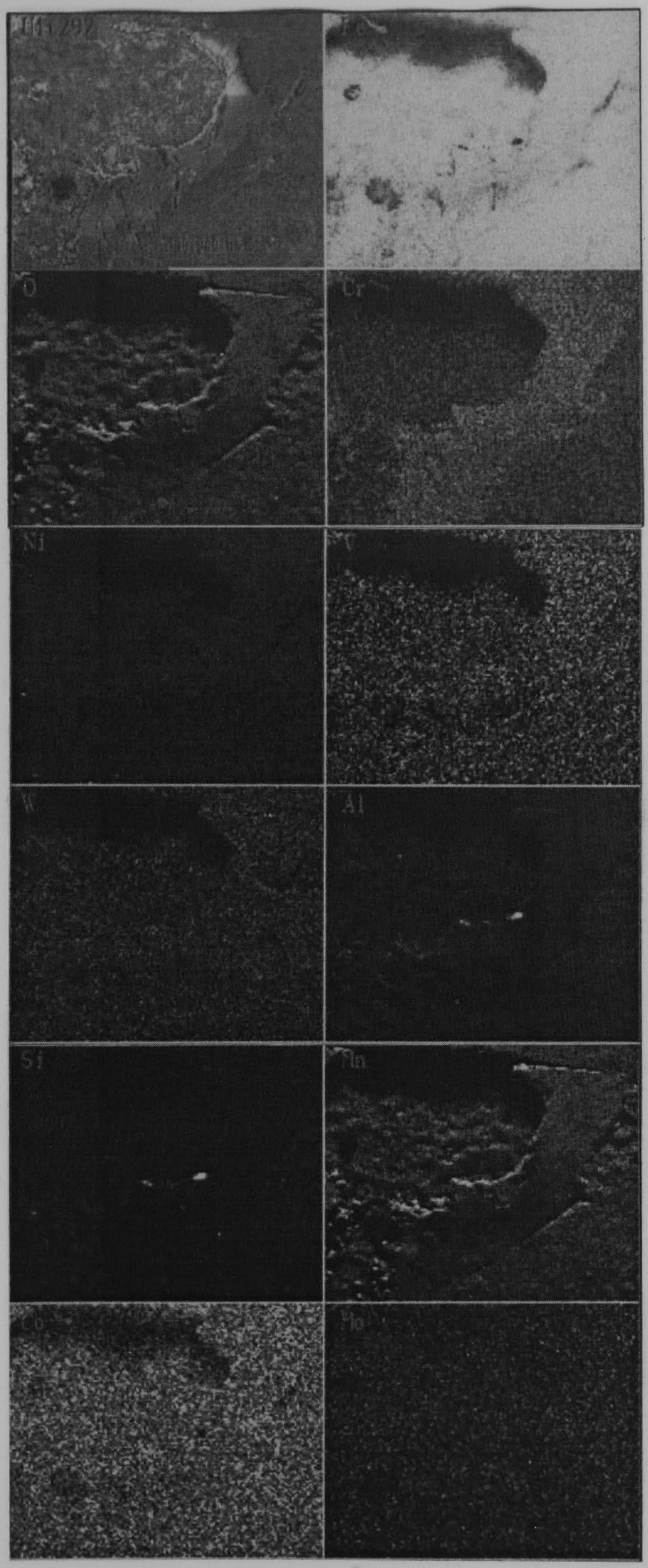

Figure 4.22 **EDAX** surface digimaps of rotor steel Spec. 297 showing possible trace elements from test wheel and Ultimet sample. After 3 hours at 540 °C in sliding contact with the 50 mm rotor steel test wheel.

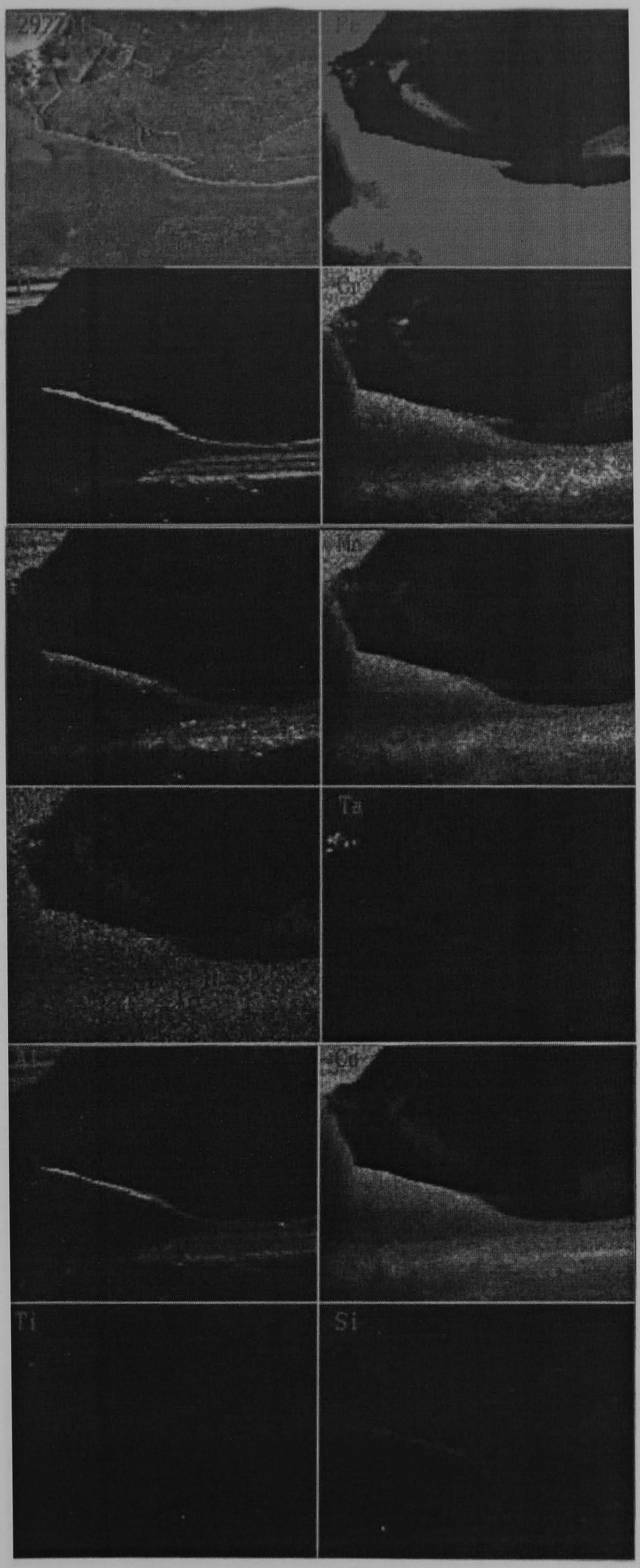

Figure 4.23 **EDAX** surface digimaps of rotor steel Spec. 297 showing possible trace elements from test wheel and Haynes X-750 sample. After 3 hours at 540 °C in sliding contact with the 50 mm rotor steel test wheel.

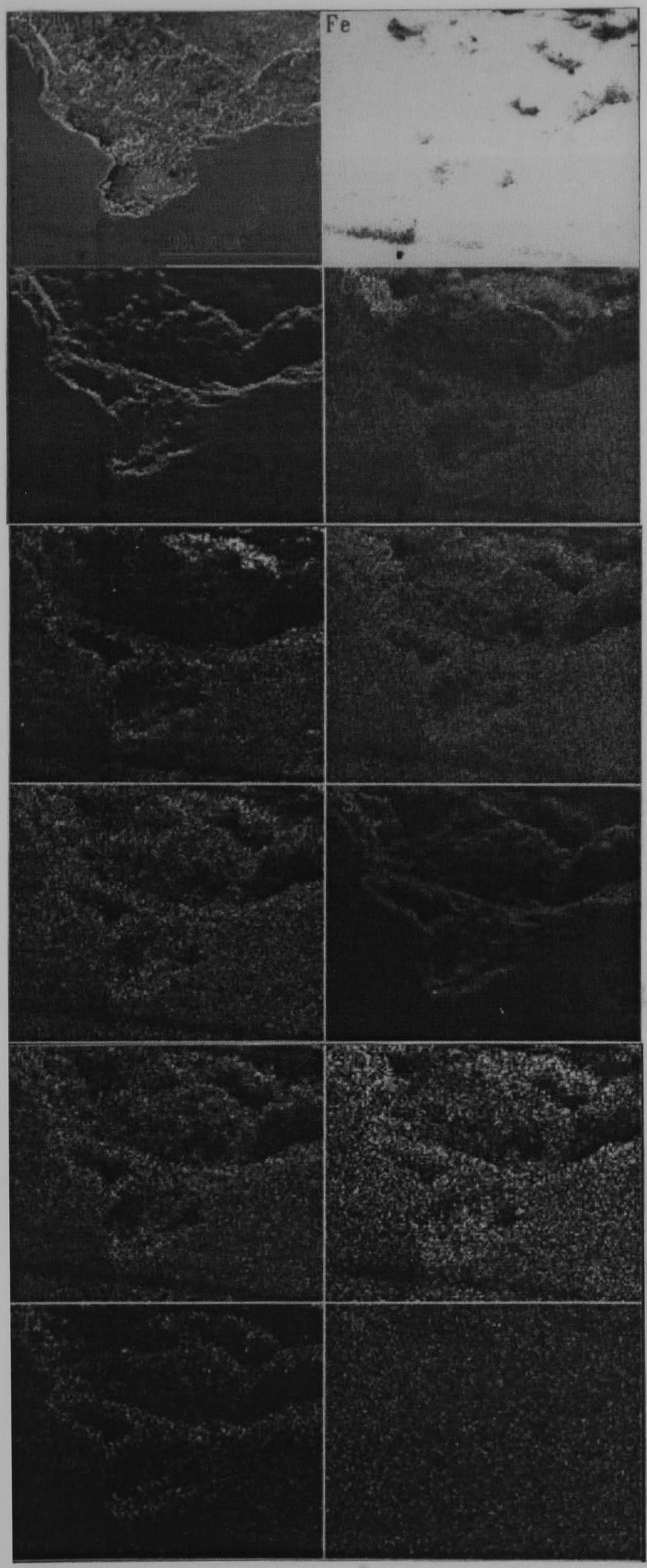

Figure 4.24 **EDAX** surface digimaps of rotor steel Spec. 297 showing possible trace elements from test wheel and Waspaloy sample. After 3 hours at 540 °C in sliding contact with the 50 mm rotor steel test wheel.

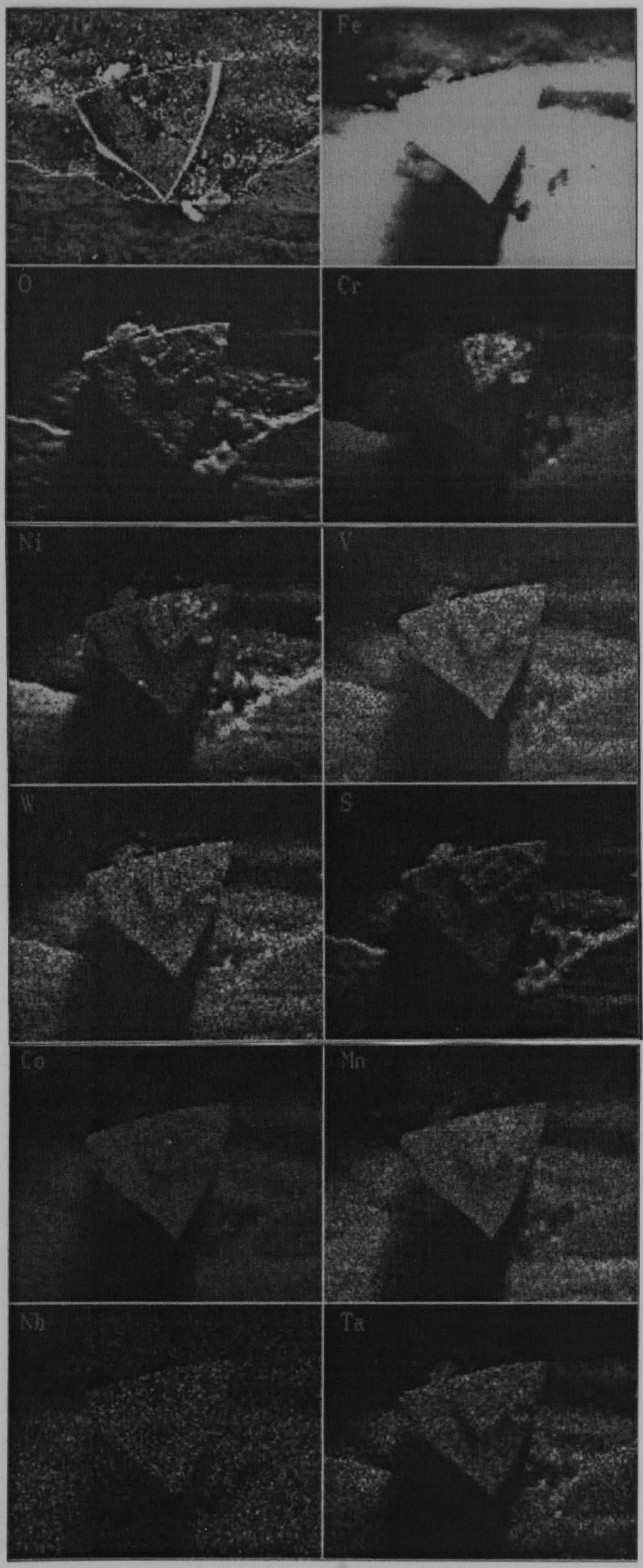

Figure 4.25 **EDAX** surface digimaps of rotor steel Spec. 297 showing possible trace elements from test wheel and Haynes 718 sample. After 3 hours at 540 °C in sliding contact with the 50 mm rotor steel test wheel.

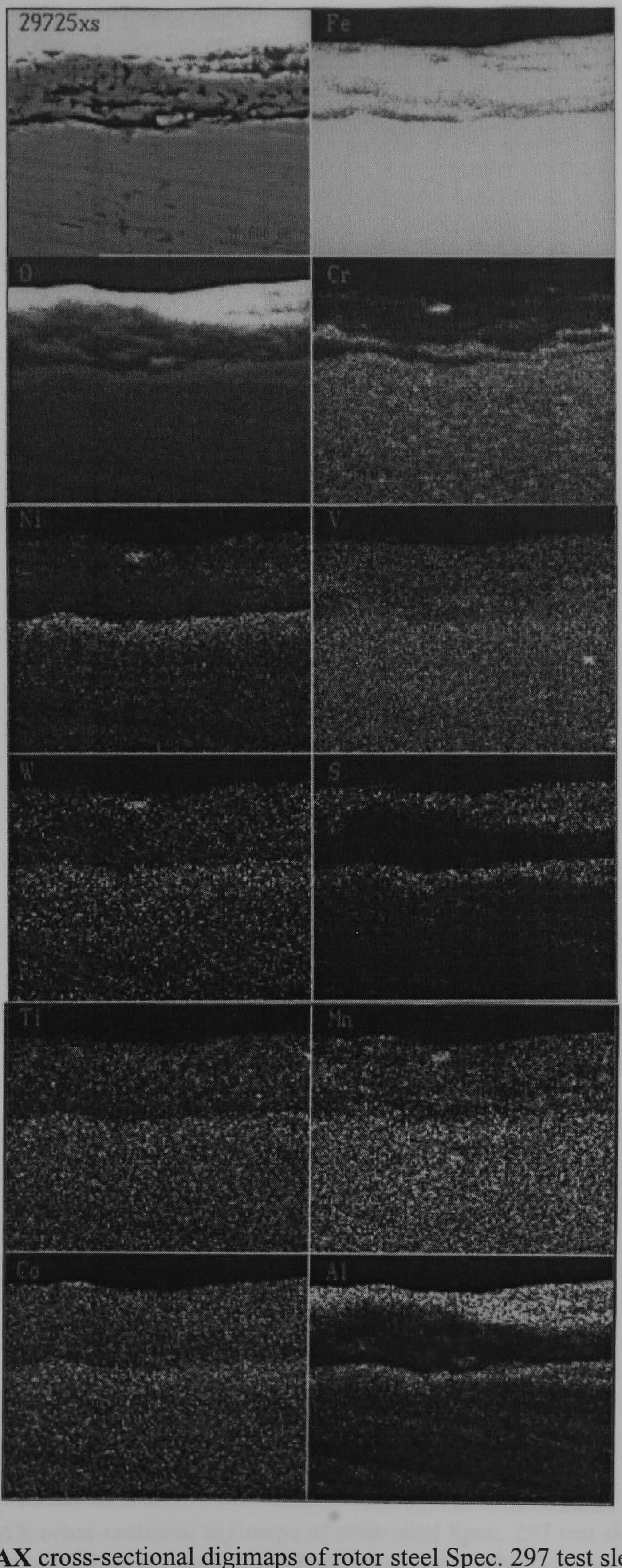

Figure 4.26 **EDAX** cross-sectional digimaps of rotor steel Spec. 297 test sleeve showing possible trace elements from test wheel and Haynes 25 sample. After 3 hours at 540 °C in sliding contact with the 50 mm rotor steel test wheel.

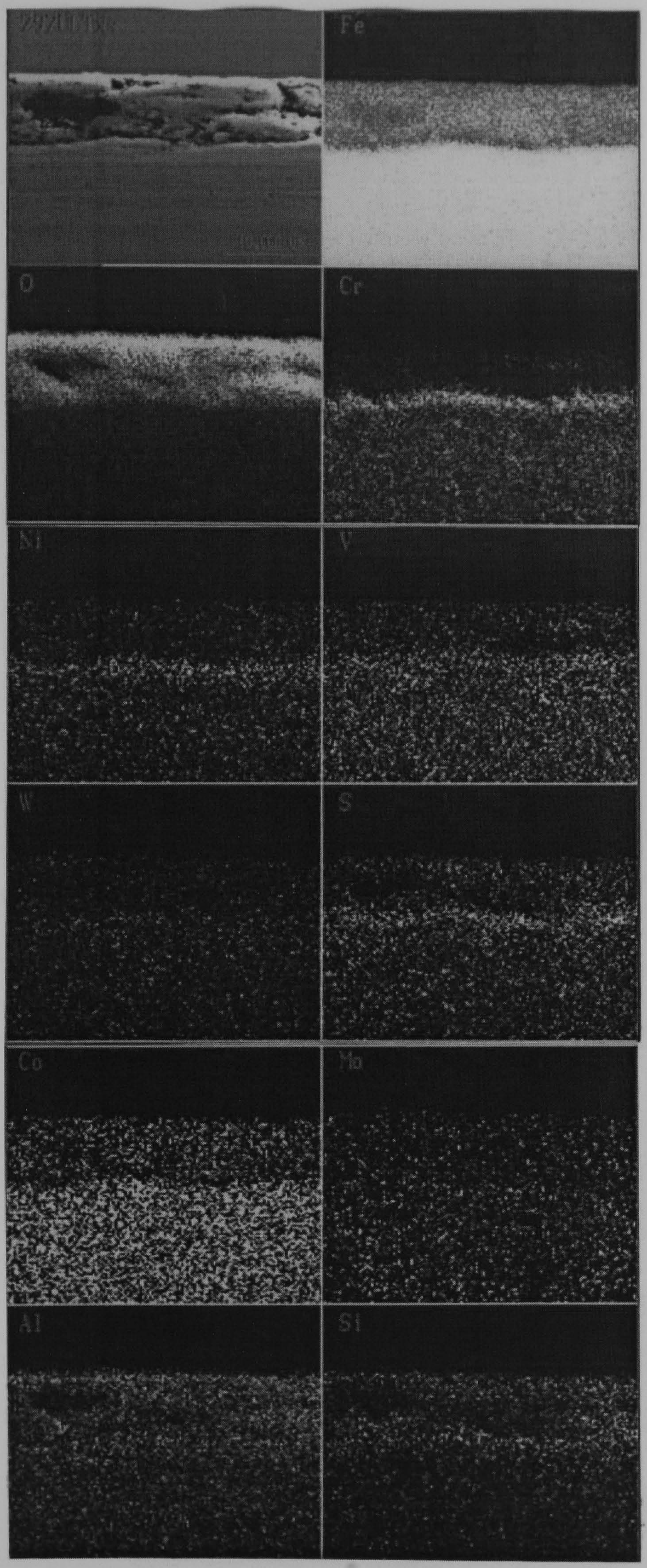

Figure 4.27 **EDAX** cross-sectional digimaps of rotor steel Spec. 297 test sleeve showing possible trace elements from test wheel and Ultimet sample. After 3 hours at 540 °C in sliding contact with the 50 mm rotor steel test wheel.

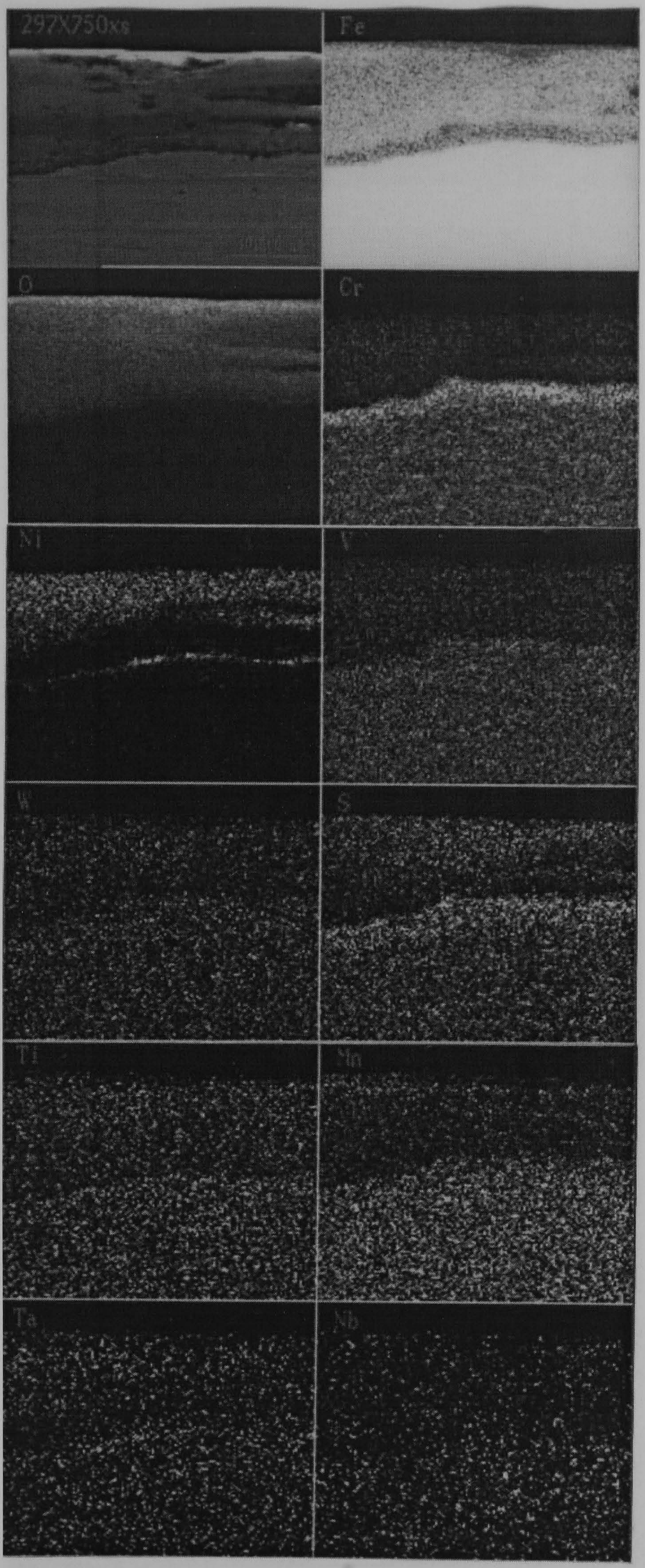

Figure 4.28 **EDAX** cross-sectional digimaps of rotor steel Spec. 297 test sleeve showing possible trace elements from test wheel and Haynes X-750 sample. After 3 hours at 540 °C in sliding contact with the 50 mm rotor steel test wheel.

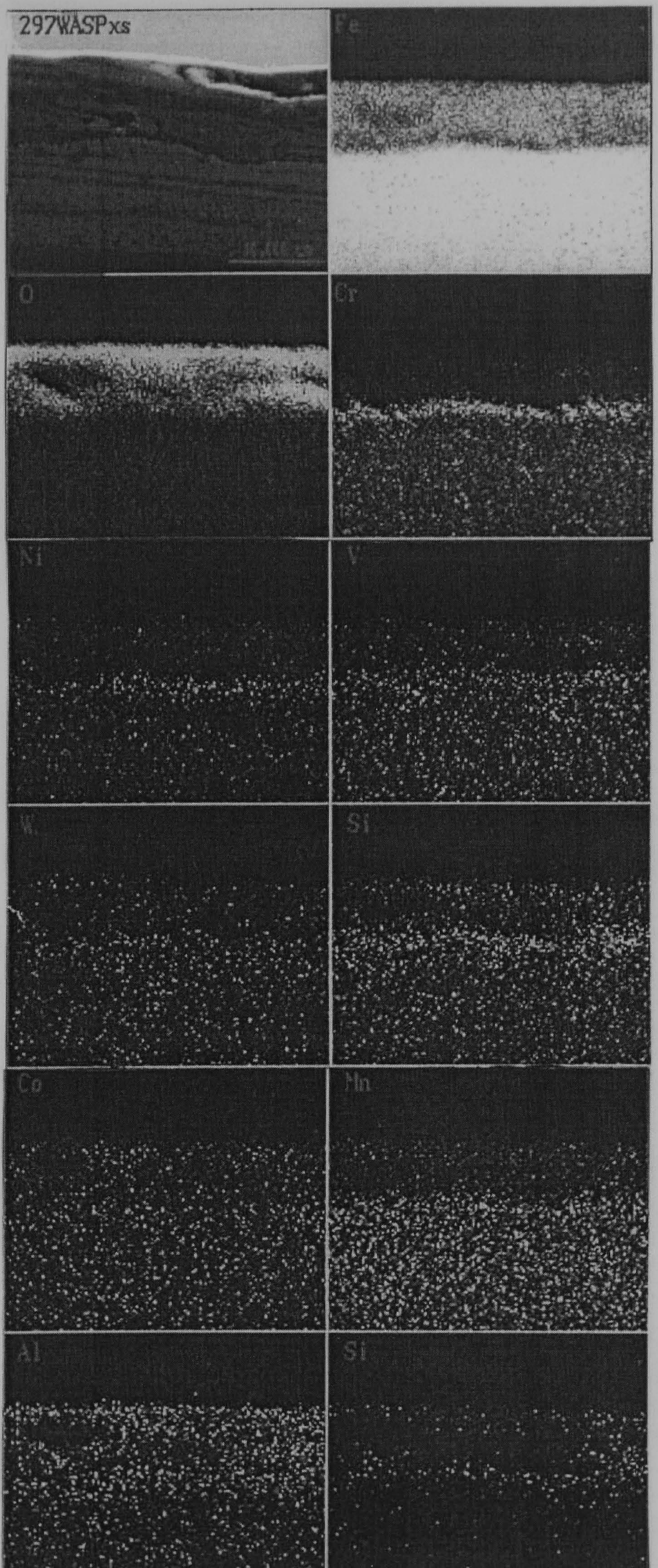

Figure 4.29 **EDAX** cross-sectional digimaps of rotor steel test Spec. 297 sleeve showing possible trace elements from test wheel and Waspaloy sample. After 3 hours at 540 °C in sliding contact with the 50 mm rotor steel test wheel.

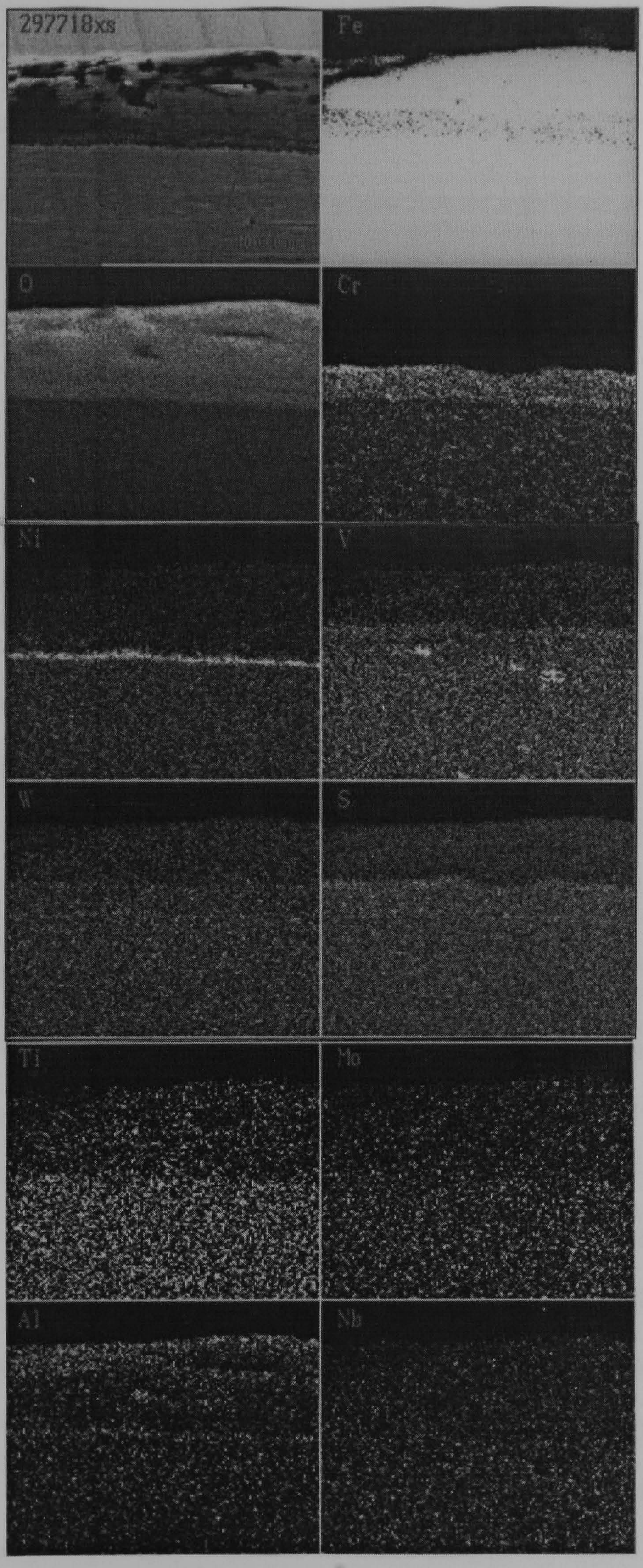

Figure 4.30 **EDAX** cross-sectional digimaps of rotor steel test Spec. 297 sleeve showing possible trace elements from test wheel and Haynes 718 sample. After 3 hours at 540 °C in sliding contact with the 50 mm rotor steel test wheel.

5.0 Literature Review: - Experimental Leakage Testing and Flow Through Brush Seals.

This chapter provides a critical review of the flow through brush seals. The chapter is divided into three sections, the introduction **(Section 5.1)**, experimental work **(Section 5.2)** and theoretical modelling **(Section 5.3)**. The experimental work is subdivided into flow visualisation **(Section 5.2.1)**, experimental leakage testing **(Section 5.2.2)** and experimental gas turbine engine testing **(Section 5.2.2)**. The theoretical section is divided into reviews of the two foremost leakage flow theoretical models, the **"Effective Thickness Model" (Section 5.3.1)** and the **"Bulk Flow Model" (Section 5.3.2).**

The literature review describes the limited published research, the test rigs, experimental conditions, historic developments and general findings. The literature review provides a framework for comparison, and improvement on testing methods and the current knowledge of leakage through brush seals. It provides a valuable insight into the state of the art of brush seal development and a basis for future work.

5.1 Introduction.

Historically the parasitic leakage flow through reciprocating and low speed rotating machines was controlled by primary packings and stuffing boxes **(Mark (1951), Buchter (1979), Leefe (1989))**. As rotating machinery speeds increased, cylindrical seals emerged but the non-contacting labyrinth seal with better leakage control and lower power consumption became a standard **(Egli (1935), Sneck (1980), Stoff (1980), Leefe (1989), Stocker (1977)).** Labyrinth seals have been continuously used to control the leakage of the working fluid through static and rotating sections of turbine generators. Continuing impetus to improve the efficiency of machines has driven the designers to improve the design from its original geometry to more complicated designs.

Improvements have concentrated on maintaining a difficult leakage path for the fluid by means of tight constrictions, expansion cavities and altering the direction of flow through large angles therefore dissipating kinetic energy. This process has given rise to several configurations of labyrinth seal including, gramophone, interleaved, castleated, staggered, stepped, and chevron. The two most common design types (straight through for gas turbines and interleaved for steam turbines) are shown in **Figure 1.5**. Almost every aspect of labyrinth seal design has been investigated with the aim of optimisation. The papers are too numerous to list here. However, a design clearance must exist between the fin tips and the land adjacent to it to prevent "hard rubs" during thermal and mechanical expansions throughout the operating cycle.

More recently in turbine generators, attention has concentrated on reducing the clearance between the fin tips and the sealing land adjacent to it. This has been achieved in several ways, without jeopardising the integrity of the seal. The use of spring backed and steam assisted moving seals has allowed the fin clearance to change, maintaining the minimum clearance possible for the running conditions. Honeycomb and feltmetal/metal fibre inserts have also been used to provide an abradable surface adjacent to the fin tip. If a rub occurs a small amount of abradable material will be removed with little thermal or mechanical damage to the fin tips or the rotor.

Advances in material processing and manufacturing techniques have allowed the development of contacting, compliant seals. The brush seal is the most prominent of these and has primarily been developed for use in military gas turbine, limited life aeroengines.

Research into the leakage through brush seals has been carried out both experimentally (flow visualisation and leakage testing) and theoretically (mathematical modelling and leakage prediction). Both of these areas of research assist the understanding and future development of brush seals.

5.2 Introduction to Experimental Work.

The primary function of the brush seal is to reduce leakage flow rate between stationary and rotating components. Experimental work on the flow through seals has been carried out in three main areas.

i.) Flow visualisation was concerned with identifying the flow patterns and types of flow associated with the flow through and around brush seals under changing conditions.

ii.) Leakage testing was performed to quantify the leakage flow rate through and around the brush seal with changing geometric constraints and operating conditions.

iii.) Engine testing was the ultimate test for specific brush seal applications combining leakage and wear testing. Several examples of engine testing have been successfully carried out in experimental military and commercial gas turbine engines.

5.2.1 Flow Visualisation.

Several flow visualisation studies have been carried out to determine the flow characteristics through porous media and around banks of cylinders. The findings improve the understanding of the microscopic and macroscopic flow, and can be used to improve designs and reduce bulk flow.

Chellaiah and Viskanta (1985) first attempted to detail the flow inside a porous media. They used a technique based on electrolysis where the colour of the fluid changed in the porous areas.

Poulikakos et al (1987, 1988), considered the forced flow through a duct partially filled with a porous material. The porous media was however only partially filling the duct and was isentropic and homogeneous. Only gross flow properties were considered such as total mass flow through the matrix and total pressure drop.

Braun, Hendricks and Canacci (1990) carried out experiments to characterise qualitatively and quantitatively the flow through brush seals and develop a bulk flow model. The authors have taken the approach that the brush seal configuration was very

analogous to the flow through a fluid saturated porous medium. A flow visualisation technique, **Full Flow Field Tracking (FFFT)** was developed and used by **Braun et al** for flow studies in the narrow gaps of hydrostatic and hydrodynamic journal bearings. This technique allowed qualitative and quantitative flow description throughout the entire brush seal system (before, through and after the brush). The equipment consisted of a perspex tunnel in which a brush seal was mounted together with a laser to provide a high quality light source. A video camera and computer with an image grabbing board were also used to record the flow. Water was pumped from one side of the tunnel through the brush seal and the fluid was seeded with light reflecting particles.

The **FFFT** technique allowed the images of the flow through the brush seals to be stored and examined closely. They show that the flows through the seal are highly variable and erratic. The flow effects at inlet, outlet, endwall and in-between rows were characterised. Major flow patterns were observed including lateral flow (normal and along the fibres), vortical rivering, and jetting **(Figure 5.1)**.

Braun et al started with a single brush seal and then continued to test double brush seals (and later four sequential brush seals) and also included the use of oil rather than water as the working fluid.

The allowable axial pressure drop through the brush appeared to be limited by both the physical properties of the single fibre and by those of the "groups of fibres" which formed the full brush. Material fatigue, wear, fibre motion reversal (rotational or rectilinear), fibre stiffness and seal dynamics were all identified as important factors in the behaviour of the brush seal.

Braun et al went on to modify their existing test facility to examine the flow patterns, velocities and pressure effects in banks of cylindrical tubes in a rectangular tunnel. Whilst their experimental facility showed the flow patterns over closely packed cylinders the effects of changing these patterns was not examined. The geometries and

exact pressure differential needed to be simulated to provide information relating to real seals in real applications that are subjected to many temporal, external conditions. **Braun et al** hoped that future work using flow visualisation techniques would identify the packing arrangements, bristle diameters, lengths, flexural modulus etc. to improve future development and optimisation of the brush seal.

Braun et al presented plots of the pressure drop through a single brush seal that showed the pressure drop is almost linear with distance through the seal.

5.2.2 Introduction to Leakage testing.

Few experimental tests covering the leakage through brush seals have been published. The results that are available are from several sources (that are referenced throughout this section) and have been achieved on several designs of test rig with a range of very different operating conditions. A large number of operating and geometric variables can substantially change the performance of brush seals. This makes close comparisons of results from different experimental test rigs difficult and sometimes misleading. The limited numbers of experimental tests have been fairly general and have briefly covered many aspects of brush seal function and design. The work and the findings have been summarised within the context of the specific test rig and operating conditions to avoid confusion.

Ferguson (1988) showed the revived interest in brush seals. A 90 % improvement in brush seal leakage over the equivalent five finned labyrinth seal was quoted. No experimental details were given, however several interesting graphs were published **(Figures. 5.2-5.5)**. The graphs clearly showed the advantages of the brush seal over labyrinth seals and helped to indicate several general design criteria for future brush seal arrangements. These were the effect of surface finish on bristle wear **(Figure 5.2)**, whereby a 0.88 μm finish was shown to quickly wear the bristle pack to size for size and a 0.35 μm rotor finish had a very low wear rate and allowed the bristle pack to remain at an almost

constant interference fit for 70 hours. **Figure 5.4** clearly shows the reduction in radial clearance with increase in pressure differential. This is known as blow down. **Figure 5.5** demonstrates the effect increasing rotational speed reducing seal leakage.

Flower (1990) described two test rigs built and used by Cross Manufacturing Limited (brush seal manufacturers). One rig ran at 20000 r.p.m. and the other at 45000 r.p.m. They also had the facility to simulate radial offsets. Little experimental detail was given but three general performance graphs were presented. The increase in leakage rate with increase in pressure differential is shown in **Figure 5.6.** The slightly reduced increase in leakage rate with increase in pressure differential after and offset test is shown in **Figure 5.7**. **Figure 5.8** demonstrates the hysteresis curve produced, giving rise to a lower leakage rate, when the pressure differential was increased and then decreased. This was due to blow down.

Hendricks, Proctor, Schlumberger, Braun and **Mullen (1991)** carried out experimental work using a 38 mm (1.5 inch) nominal bore diameter brush seal. These tests were carried out on a rig that consisted of a tapered plug rotor installed in a drill press. The brush seal was housed in the rig body (pressure vessel) and the inlet was below it.

Four nominal brush rotor radial clearances of -0.09, -0.048, -0.008, and 0.035 mm were tested. The brush seal had 200 bristles per mm of circumference. The bristles were made of Hastelloy X and were 0.05 mm in diameter. The backing plate fence height was 6.1 mm. The maximum peak to peak run-out on the drill press was 0.13 mm. Speeds were either 0 or 400 r.p.m. over a range of pressure drops from 0 to 0.83 MPa (120 p.s.i.). A video camera was also used to record any bristle interface motion. The results were compared to those predicted by a model previously developed by **Hendricks et al** (and discussed in **Section 5.3).**

The results of experimental tests carried out at four clearances by Cross Manufacturing using a 130 mm (5.1 in.) brush seal were plotted and compared to analytical

results from the "**Bulk Flow Model**" in **Figure 5.9.** The results were quite promising. The experimental results from the tests carried out by **Hendricks et al** on the 38 mm (1.5 in.) brush seal were plotted in a similar manner in **Figure 5.10** and again showed a reasonable agreement with the theoretical results produced by the **Bulk Flow Model**.

The leakage decreased with decrease in clearance but the decrease was larger than that predicted by the model. This indicated that further work was required on the model. Some improvement over the 0 r.p.m. results was seen at 400 r.p.m., indicating that rotation tended to average out the perturbations. For each clearance a hysteresis curve was noted which changed when the speed was altered from 0 to 400 r.p.m.

A flow straightener was added to reduce possible problems associated with the angle and proximity to the brush seal of the single fluid inlet. The flow straightener reduced seal performance for increasing pressure differential but improved the performance for decreasing pressure differentials. This was in contradiction to the findings of **Conner and Childs (1990)** as they found that changing inlet swirl conditions lead to no significant changes in brush seal characteristics.

Schlumberger, Proctor and Hendricks (1991) continued the experimental and theoretical study to examine the leakage effects due to eccentricity on a 136.47 mm (5.3730 inch) nominal bore diameter brush seals at low speeds (0 and 400 rpm). The tests were carried out with ambient air and nearly saturated steam at different eccentricities. The seal had a radial concentric interference of 0.071 mm and a fence height of 9.27 mm. There were 1060 bristles per centimetre of circumference and the rotor eccentricies were 0.03, 0.10, 0.38, and 0.43 mm. The results were compared with an annular seal model **(Flowcal),** a standard labyrinth seal model for steam and the "**Bulk Flow Model**".

As expected the flow rate through the seal increased with increasing pressure differential and eccentricity. This was especially noticeable for both air and steam when the eccentricity exceeded the installed interference. Shaft rotation of 400 r.p.m., appeared to

have little effect compared to stationary results with air but gave a leakage increase of a factor of two with steam. The steam results also showed a greater amount of hysteresis. The bulk flow model results and the standard labyrinth seal equation both performed reasonably well with concentric operation but no account was taken of eccentric operation. It was found that the brush seal was not damaged by large (0.03 - 0.43 mm) eccentricities but the 304 stainless steel rotor did show signs of wear.

No explanation was given for the differences in performance between steam and air and whilst a final value of surface roughness was given together with photographs to show an increase in the surface roughness of the rotor, no estimate of the material removed/ transferred was given.

Hendricks, Carlile, and Laing (1992) carried out studies to examine bristle flexure and hard rub characteristics. A tapered, 40 tooth rotor operating at 2600 r.p.m. was used to provide sharp leading edge impact in the bristles of a 38 mm (1.5 inch) diameter brush seal and hard rubbing on the rotor lands. It was generally thought that bristle loss and debris had a potential for destructive impact on power plant. The issues of bristle pullout, surface rubbing, bristle wear and debris were addressed.

Three tests were conducted on 3 different diameters on the rotor including an eccentric test accumulating over 1.3×10^9 flexure cycles. It was found that the bristles withstood the tests without pullout, fracture or massive debris generation, but were reduced in length by up to 0.2 mm. The rotor was radially grooved by up to 0.076 mm with erratic "whipped" leading edge surfaces. Radial bristle length losses of up to 0.2 mm occurred together with a reported leakage performance degradation of 30 %. The tests proved the durability (in terms of bristle pullout) of the seal under extremely undesirable conditions, however wear was relatively large.

Most of the debris generated was a fine black material that appeared amorphous, but the rust-coloured materials were iron rich and magnetic, implying Fe_3O_4. The debris

was "cauliflower" in form and highly porous with low adhesion, except for that which was fine enough to adhere to the bristles. Those fines were not readily dislodged. Non-uniform fines (or oxidation particles) adhering to the bristles tended to separate the bristles, increasing porosity, and may have enhanced leakage paths.

Carlile, Hendricks and Yoder (1993) carried out further tests using the drill press rig and tapered rotor arrangement previously mentioned. The leakage performance of a 1.5 inch diameter brush seal and an annular seal of similar axial length were tested with air, helium and carbon dioxide at various bristle/rotor interferences at static and low rotor speeds. The brush seal specification and the test conditions were given in **Table 5.1** and **Table 5.2.** In addition the effects of packing a lubricant into the bristles and also of reversing the pressure drop across the seal were investigated.

The brush seal reduced the leakage in comparison to the annular seal, between 3.5 to 9.5 times. Reversing the pressure drop across the brush seal produced leakage rates approximately the same as that of the annular seal. Addition of lubricant reduced the leakage by 2.5 times compared to a non-lubricated seal. This indicates that the lubricant serves to hold the bristles in place and block the porosity through the seal making it more effective. It was however noted that the static case showed a greater reduction in leakage than the dynamic.

The air and carbon dioxide data were generalised and successfully correlated using the corresponding state theory. The premise of corresponding states is that all thermodynamic surfaces can be mapped to a single surface when expanded about the thermodynamic critical point. Thus, the properties of a fluid can be predicted using another fluid when the proper mapping is used **((Mollerup (1978), Hendricks and Simoneau (1973), Simoneau and Hendricks (1977), Hendricks and Sengers (1980))**. It was found that hysteresis was negligible and there was a slight improvement in sealing for rotating

over static conditions. The helium data followed a different curve from the air and carbon dioxide and required further investigation.

Holle and Krishnan (1990) carried out ambient air leakage tests that identified geometry variations that enhanced the brush seal leakage and endurance characteristics. Two test rigs were used. The first enabled the testing of 53 mm (2.1 inches) to 130 mm (5.1 inches) diameter bore seals at ambient temperature and was capable of delivering 0.45 kg/s (1 lbm/sec) of air at a supply pressure of 6.9 bar (100 p.s.i.). A high temperature seal test rig **(HTSTR)** was also designed to provide up to 540 °C (1000 °F) inlet air at high pressure but at lower leakage rates. This rig was used to endurance test several 211 mm (8.3 inch) bore diameter brush seals. A model of an engine was tested for 100 hours near its design point environment in the **HTSTR**. Accelerated 10 hour wear tests for a range of brush seal geometries and materials were run at high inlet air temperatures. The exaggerated wear rates were achieved by large initial brush/journal interference to provide qualitative wear evaluations in shorter endurance runs

The generalised flow characteristics at static and dynamic conditions were given for a single ring seal and were plotted. The resultant plot can be seen in **Figure 5.11**. The plots were measured averages at ambient temperature. The seal results showed distinct differences (hysteresis curves) between pressure increase and decrease. **Holle et al** stated that this was due to the brush compacting as the pressure differential across the seal increased and the seal became denser. They claimed that the hysteresis loop could be eliminated or minimised by a sufficiently small brush to journal interference and an adequately smooth journal surface. One interesting test shows the effect on the flow factor over 10 hours time. **Figure 5.12** shows the results. The changes were mainly thought to occur due to fluctuations in the environmental temperature, pressure and rotor mechanics. It was also noted that the journal speed increase from static to a surface speed of 23500 r.p.m. caused a slight reduction of the leakage rate.

Basu, Datta, Johnson, Loewenthal and Short (1993) examined the hysteresis and bristle stiffening effects of conventional brush seals. Extensive testing of brush seals identified the phenomena of bristle "hysteresis" and "stiffening" with pressure as their two major drawbacks. After any differential movement of the rotor into the bristle pack due to radial excursions or centrifugal/thermal growths, the displaced bristles did not recover against the frictional forces between them and the backing plate. As a result significant leakage increase was observed. When a pressure differential was applied the bristles also exhibited considerable stiffening. Stiffening reduced seal life due to the increased bristle tip contact pressures.

Basu et al described the testing of a "low hysteresis" design of seal and two conventional seals (the inner and outer diameters being 163 mm (6.414 inches) and 137 mm (5.375 inches) respectively. The brush seal bristle pack stiffness was measured for different radial excursions under a pressure differential with a load cell both statically and dynamically.

Leakage hysteresis testing was then carried out dynamically with a concentric rotor, with an eccentric rotor and with a radial excursion. Hysteresis was noted when the pressure differential was increased and then decreased (for an interference fit). This was attributed to the differential growth. As the speed was increased to 16000 r.p.m. the leakage also increased. When the speed was subsequently decreased, the leakage continued to increase indicating an appreciable amount of leakage hysteresis. The leakage at the end of the cycle was approximately three times that at the beginning and only returned to the original value when the chamber was depressurised. The above hysteresis was attributed to radial growth of the rotor due to centrifugal forces and thermal expansion starting in the rotor and eventually expanding the bristle pack and holder.

With an eccentric rotor, the initial sweep moved the bristles radially outwards, where they stayed. This created a large radial gap. The final test imposed a brief radial

excursion that was then withdrawn. Again the bristles were moved radially outwards and did not return even after a reasonable amount of time.

Bayley and Long (1993) carried out a combined experimental and theoretical study of the flow and pressure distributions in a brush seal. Measurements of the mass flow rate together with the radial and axial distributions of pressure were taken on a non-rotating experimental rig using a 122 mm bore brush seal with a 0.25 mm radial interference. The experimental data was used to estimate seal porosity.

A model was used to present the predicted variations of shaft pressure with pressure ratio, bristle interference and seal porosity. In their model the inertial terms in the boundary layer equations were neglected allowing the resulting equations to balance the pressure and viscous forces. A porosity value was used that related the axial and radial through-flow areas h_x and h_y respectively and was expressed as $\phi = (h_y / h_x)^3$. A constant value was assumed for all the operating conditions that would obviously not be the case in a "real" brush seal.

The measured and predicted variations of radial pressure distribution under a backing ring and a full brush seal, under different seal pressure ratios were given. The results were compared and it was found that a porosity coefficient of 30 used in the analytical model allowed the best agreement with the experimental results throughout the pressure ratios of interest. The leakage model was used to predict the mass flow rate and the predicted and experimentally measured mass flow rates were plotted. **Figure 5.13** shows the results. They agreed reasonably well for these tests.

The theoretical predictions of the contact pressure of the bristles on the shaft show that this increased linearly with pressure ratio and for a given radial interference the shaft pressure increased when the porosity ratio was decreased. Increasing the radial interference also increased the shaft contact pressure. The pressure distribution under the bristle tips did

not appear to change with pressure ratio and decreased almost linearly with distance under the bristles.

Long and Marras (1995) examined experimentally the contact forces under a brush seal both indirectly through torque measurements and directly using a force blade located under the bristle tips. The tests were conducted on a non-rotating shaft having a nominal diameter of 122 mm, static radial interferences of 0.4, 0.2, 0.1, and 0.05 mm and a pressure range of 1 to 4.5 bar. The brush seal dimensions were similar to the brush seal used by **Bayley and Long (1993)**.

The experimental results were compared to theoretical predictions obtained using the simple model presented by **Bayley and Long (1993)**. The model was used to predict the variation of shaft pressures, with static build clearance and pressure ratio for different porosity ratios.

The results were as expected. For an initial interference the shaft pressure increased linearly with pressure ratio and for any given radial interference the shaft pressure increased with decreasing porosity ratio. For a specific initial clearance the pressure on the shaft was considerably less than with an initial interference. When in contact with the shaft, the dimensionless shaft pressure became virtually independent of the pressure ratio and dependant only on the initial clearance or interference.

Chart recorder traces obtained using a calibration plate instead of a brush seal on the torque measurement rig were given and showed the load to be in the region of 1.7-3.4 N due to the bearing friction and radial air flow. Traces were also given from a brush seal with an equivalent flow area and were found to be between 2.5-5.3 N. When the frictional losses were removed the brush seal loads reduced to 2-3 N for the pressure ratios and interferences tested. The coefficient of friction was found to be between 0.09-0.11.

A force blade method was also used to measure the contact forces for different pressure ratios. This clearly showed the linear nature of the contact forces with increasing pressure ratio.

It was found that whilst there were some large differences between the experimental and theoretical, the results did show some agreement and helped to show the shortcomings of the theory used. The model assumed laminar flow and there was evidence **(Long (1991))** that suggested the flow was turbulent. One experiment is badly conditioned for small static radial interferences and assumed a constant coefficient of friction with pressure ratio and therefore bristle shape. In the other experiment the contribution of the mechanism was unknown.

5.2.3 Experimental Tests Using Experimental Gas Turbine Engines.

Holle and Krishnan (1990) reported details of an early brush seal application in a T800 (LHX) engine test that successfully ran 24 hours and subsequently ran a further 12 hours during development testing. Further tests were then carried out in a T406 Plus engine at temperatures up to 777 °C (1430 °F) and surface speeds up to 250 m/s (820 ft/sec). Leakage and specific fuel consumption **(SFC)** improvements of 1% to 1.5 % were quoted together with lower pumping, windage and flow injection (mixing) losses. Fabrication and installation costs and maintenance advantages were also envisaged.

The rig tests on the T406 Plus compressor pointed out the importance of minimum ventilation requirement and the significant contribution of cavity windage to some brush seal applications. The 13 compressor inter-stage brush seals performed mechanically well during 71 hours of rig testing. The brush seal had an initial interference of 0.33 mm (0.013 in) and a carrier clearance designed for 1.5 mm (0.060 in). The initial wear rate averaged less than 0.013 mm/hr (0.0005 in/hr). On examination it was noted that lower surface speeds and temperatures had adverse effects on the alumina journals in contact with the

Haynes 25 bristles. At the higher pressures chatter marks were noted and hairline cracks could be seen in the alumina due to the differences in thermal expansion.

Cobalt blue ingestion at the compressor inlet verified the high recirculation through the 13 inter-stage brush seals but none was found in the engine hot section after a triplex (3 element) and a duplex (2 element) seal.

Slight disruption of the surface layers of bristles on the high pressure side of the brush was noted after 5 hours of operation on the 6 hot section seals. Some wear debris and broken bristles were also recovered from adjacent cavities upon strip-down but the cause was undetermined.

In conclusion **Holle et al** stated there were improvements in leakage flow and anticipated maintenance and mechanical advantage. They pointed out however, that the wear and durability of brush journal material combinations remained the biggest question. Therefore design compromises on overall sealing effectiveness, maximum wear condition and wear rate should be considered when selecting the initial brush/ journal interference

Chupp and Nelson (1990) used a test rig capable of rotating at up to 40000 r.p.m. The disk diameter was 130 mm (5.1 inch) which gave surface speeds of up to 275 m/s (900 ft/sec). Heated air could be introduced in to the rig at temperatures of up to 816 °C (1500 °F) and at pressures of either 4.5 bar (65 p.s.i.)or 13.8 bar (200 p.s.i.). The rig was fully instrumented and capable of holding multiple seals. The test program addressed a number of issues including: -

i.) Seal construction variables i.e. initial seal /disk interference, backplate radial gap (fence height), radial bristle length, packing thickness, bristle angle, bristle diameter, bristle material and bristle surface finish operation.

ii.) Disk surface treatment

iii.) Seal offset.

iv.) Number of seals in series.

v.) Operating temperature.

Table 5.3 shows the experiments carried out and some seal parameters. The study located 2 prime locations in several state of the art, Teledyne CAE, limited life engines and identified a representative engine cycle to follow in part of the seal testing.

The results presented included a comparison of the measured labyrinth seal results to calculated data for labyrinth seals at 3 clearances. The graph confirms the validity of the measurement approach, as the theoretical values agree well with the actual values. The results are plotted using the seal flow factor ($(W\sqrt{T_u}/(P_u/A_u)$, $lbm\sqrt{R}/(lbf\ sec)$ against a pressure parameter ($\sqrt{(1-(P_d/P_u)^2)}$) that approximately linearised the data **(Figure 5.14).**

Figure 5.15 shows the results for an engine simulation cycle. This showed two stages, the first 10 minutes and the subsequent 35 minutes. It was noted that the flow factor decreased as centripetal expansion effected the rotor with increased speed and hysteresis effects due to internal bristle friction (mainly due to the pressure differential) prevented the brush seal from reacting instantaneously. Hysteresis effects caused the flow factor to increase with a decrease in speed. The reaction time was about 7 minutes for the bristles to overcome the internal friction.

Figure 5.16 showed a typical measured flow performance plot that clearly showed a hysteresis effect whereby increasing pressure differential gave a lower flow factor than decreasing pressure differential. Results were taken at 3-6 minute intervals to allow the brush to stabilise. The results showed that the brush seal flow factor level was a third of that of the reference labyrinth seal.

Chupp and Dowler (1993) reported the 4 additional configurations in the above test programme. These being #4, #5, #8, and #A1 **(Table 5.3)**. They reflected the effects of backplate gap **(Figure 5.17)**, repeatability **(Figure 5.15)**, two seals in series **(Figure 5.18)**, and seal vendor **(Figure 5.19)**, respectively. A further series of tests carried out at Cross

Manufacturing facilities were also reported, exploring the effect of further changes in backing plate clearance. The results are given in **Figure 5.20**.

The conclusions from the **Chupp and Dowler's** test programme were: -

i.) Brush seal were viable seals and the test rig results were good. Brush seals offered an improvement by a factor of 3 to 7 over labyrinth seals.

ii.) Brush seals had an initial wear in period but still offered an improvement over labyrinth seals over the life of limited life engines.

iii.) Hysteresis and leakage performance characteristics were partly due to engine speed and pressure differential changes.

iv.) Brush seals could survive shaft excursions of 0.635 mm (0.025 inches).

v.) Modest brush seal interference changes had little effect on the leakage.

vi.) Multiple seals reduced leakage, allowed higher pressure differentials and reduced the sensitivity to changes in operating conditions.

vii.) The maximum recommended backing plate gap was 1.4 mm (0.055 inches).

viii.) Cost reduction by not including the final grinding operation and the surface coating on the shaft did not reduce the brush seal leakage performance.

ix.) Seals from two vendors performed similarly.

x.) The test temperature of 204 °C (400 °F) and 316 °C (600 °F) had only a very small effect on the leakage flow rate.

5.3 Introduction to Theoretical Modelling of Leakage Flow through Brush Seals.

The packing pattern of brush seals could be compared to the packing pattern of cylindrical tubes in a tunnel or cavity, perpendicular to the direction of flow. This arrangement has been used for many years in heat exchangers/ boilers etc. and has been studied both theoretically and using flow visualisation techniques **(Knudsen and Katz (1958))**. In these studies however, the energy dissipation due to the obstructions was minimised whilst maintaining a maximum surface area. The size of the turbulent wake was

thought to be of major importance. However, the packing arrangement for brush seals is highly transient due to changes in the operating conditions and hence the analogy is only specific to idealised steady state conditions. Moreover the scale of the geometry of brush seal bristle packs (as opposed to heat exchangers) involves fluid dynamic effects of a different magnitude and regime (i.e. microscopic boundary layer effects as opposed to bulk flow macroscopic effects)

Chupp, Holle and Dowler (1991) developed a model based on a single parameter, the **"Effective Brush Thickness"**. This was a measure of the compactness of the seal.

Characterisations have also been in the form of a series of orifices, a foraminous material **(Green and Duwez (1951))** and a numerical, comprehensive **"Bulk Flow Model"** of cross flow around a matrix of circular cylinders **(Mullen, Braun and Hendricks (1990))**. The geometry and dynamics of the brush seal mitigates against a simple solution. **Braun et al (1990-1995)** demonstrated the unpredictable nature of brush seal behaviour and the flow complexity by flow visualisation techniques.

5.3.1 Effective Thickness Model.

This leakage model for brush seals **(Chupp, Holle, and Dowler (1991))** used the bristle and brush seal geometry to calculate possible leakage areas both normal to the bristle pack and radially across the pack and backing plate. The model initially assumed a "square" staggered packing pattern with a transverse **(S_t)** to longitudinal **(S_l)** spacing ratio, S_t/S_l of 4. The model geometry is shown in **Figure 5.21**. The effective thickness **(B)** was then calculated for the specific geometries via iteration until the computed flow factor values matched those given in experimental results. **B** is described as a synthetic parameter of the brush seal. In conjunction with the other physical geometry of the brush seal design **B** allows the direct prediction of sealing performance in any environment. **B** is a measure of the compactness of the bristle pack. For a given number of bristles, the larger the value of **B** the more loosely compacted the bristles are, and the greater the leakage.

The model results, plotted using experimental results from several sources, confirmed the use of a single parameter to obtain an insight into the nature of the brush seal as pressure drop changes and could account for fluid temperature changes.

The original assumption of a staggered "square" packing pattern was modified by **Holle, Chupp and Dowler (1992)** to a spacing ratio of $St/Sl = 2\sqrt{3}$. The pattern was changed improving the model results.

Dowler Chupp and Holle (1992) further modified the model to remove an earlier limitation where the bristle pack had been linearised (i.e. straight as opposed to circular seals) to simplify development of the model. The modification accounted for the curvature effects in the brush caused by the size of the journal relative to the size of the seal. The improvement allowed for smaller seals of the same quality as larger seals exhibiting larger relative leakage due to exaggerated blooming of the brush at the journal interface. The results of previous work were plotted as leakage flow factor versus pressure ratio from five sources including Allison, Cross, E.G. and G, NASA and TCAE. **Table 5.4** gives some of the brush seal geometric parameters.

The effective thickness parameter required modification, as the thickness at the bore **(Bmin)** due to the curvature of the seal was significantly different to that at the clamping plate. The effective thickness parameter was modified to **B/Bmin** that was an indicator of, and can be used as, a measure of a brush seals leakage.

Chupp et al (1994) made further developments to the effective thickness model. The model was adapted (with reference to **Modi (1992)**) to represent the bristle packing as randomly distributed cylinders in contact along axial elements of their surfaces. An additional zero flow reference thickness at the mean brush diameter, **B0** was required to account for the perturbations of the random distribution during translation to the mean brush seal diameter. The reduced effective thickness **B/B0** is a "sealing efficiency" that compares the effective compactness of a brush to the theoretical compactness necessary to

stop all leakage through the bristle distribution at the mean diameter. **B/B0** is therefore always greater than 1.0. A value of **B/B0** of 1 to 1.05 was thought to be ideal for good quality seals at high pressure ratios.

Several areas have been identified where the value of **B/B0** may change. **B/B0** tended to increase as the seal size decreased due to the difficulties associated with the manufacture of brush seal with small diameters. This was especially true when the bore was less than 4 inches diameter.

B/B0 increased as the brush/ journal interface increased (probably the effect of mechanical action), as the bristle density increased (probably due to the effect of fabrication difficulty) **B/B0** also increased as brush annulus height increased (probably the effect of a combination of mechanical and fabrication difficulty).

However it was noted that **B/B0** remained constant with changing brush compliance.

5.3.2 Bulk Flow Model Porous Media.

The **"Bulk Flow Model"** developed by **Hendricks et al (1990-1995)** was also used to predict the leakage across brush seal assemblies. The theory is based on the work of **Gunter and Shaw (1945)** which dealt with flows in porous media and filters. The model took account of a large number of parameters (**Hendricks et al (1990-1995)**). However, many assumptions were also made because of the large number of variables associated with the brush seal geometry during operation.

The flow through the brush seal was the sum of the flow through the bristles and the clearance at the interface between the surface and the bristle tips. The model took account of laminar and turbulent flow in the radial, axial and circumferential direction both at the interface and inside the bristle pack. Laminar and turbulent flow were also accounted for. The bristles were assumed to act as simple cantilevers enabling the calculation of bristle deflection due to mechanical, aerodynamic and pressure differential loads. The

assumptions allowed further calculations to be made including, the load per unit length on the bristles, bristle tip pressure, the Reynolds number, the interface wear and heating, and the fatigue life of the bristle.

Braun, Hendricks and Canacci (1990) carried out experiments to characterise qualitatively and quantitatively the flow through brush seals and continued the development of the Bulk Flow Model. The flow visualisation techniques were discussed in **Section 5.3.** They compared the results of experimental work carried out by Cross Manufacturing, with theoretical predictions using their "Bulk Flow Model". The model accounted for 3 flow regions. These regions were at the interface of the seal and rotor, through the bristle pack and parallel to the bristles along the back washer.

The results using the model were in reasonable agreement with published results from Cross Manufacturing **(Figure 5.9)**. The experimental and theoretical results were all at low pressure differentials (0-2.5 bar) and were clearly worse at the lower flow rates and pressure differentials by up to 30%. However, the trends and orders of magnitude indicated by the calculations appeared to be correct. It should be noted that there did not appear to be a marked difference in the Cross data where the brush seal interference moved to a clearance fit. This was an extremely unusual result.

Hendricks, Proctor, Schlumberger, Braun and Mullen (1991) continued the experimental work on the drill press rig on brush seal/rotor interference effects on leakage rate at zero and low rpm using a tapered-plug rotor. The experimental results were compared to the results obtained using the "Bulk Flow Model". Again a reasonable comparison between experimental and analytical results was found for the configurations and conditions tested. It was noted however that the model required further modification and the flow physics through the brush seal required better understanding.

Table 5.1 Brush seal specification **(Carlile, Hendricks, and Yoder (1993))**.

Brush seal parameter	**Value**
Brush seal outside diameter	5.333 cm (2.0996 in.)
Brush seal inside diameter	3.792 cm (1.4930 in.)
Front washer inside diameter	4.699 cm (1.8500 in.)
Back washer inside diameter	3.923 cm (1.5444 in.)
Brush seal axial diameter	0.353 cm (0.139 in.)
Bristle Diameter	0.0051 cm (0.0020 in.)
Pack Density	1800/cm-circ (4500/in.-circ)
Angle of bristles from radial centreline	50^0
Bristle Material	Haynes 25
Rotor Material	304 Stainless Steel.

Table 5.2 Test conditions **(Carlile, Hendricks, and Yoder (1993))**.

Configuration	**Radial Clearance**	**Air**	**Helium**	**Carbon Dioxide**
Brush Seal	-0.0061 cm (-0.0024 in.)	×	×	×
Brush Seal	-0.0018 cm (-0.0007 in.)	×		
Brush Seal	-0.0033 cm (-0.0013 in)		×	
Brush Seal Reversed	-0.0053 cm (-0.0021 in.)	×		
Brush Seal Lubricated	-0.0061 cm (-0.0024 in.)	×		
Annular Seal	0.0053 cm (0.0021 in.)	×		
Annular Seal	0.0178 cm (0.0070 in.)	×		
Annular Seal	0.0302 cm (0.0119 in.)		×	

...Martin (Currie, Hendricks, and Poder (1993)).

Conf #	Initial Interf. (in)	Backplate height	Bristle height	Bristle angle	Bristle dia (in)	Bristle density (per in.circm)	Brushes in series	Plate/Bristle material.	Bristle surface finish	Shaft Treatment	Shaft initial roughness μin	Operating temp. F
1	0.005	0.030	0.286	45	0.0028	2450	1	N75/H25	Ground	AlO	30-40	600
2	0.005	0.030	0.286	45	0.0028	2450	1	N75/H25	Ground	AlO	30-40	400
3	0.001	0.030	0.286	45	0.0028	2450	1	N75/H25	Ground	AlO	30-40	600
4	0.005	0.020	0.286	45	0.0028	2450	1	N75/H25	Ground	AlO	30-40	600
5	0.005	0.030	0.286	45	0.0028	2450	1	N75/H25	Ground	AlO	30-40	600
6	0.005	0.030	0.286	40	0.0028	2450	1	N75/H25	Ground	AlO	30-40	600
7	0.005	0.030	0.286	45	0.0028	2450	1	N75/H25	Ground	Chr/Carb	20-30	600
8	0.005	0.030	0.286	45	0.0028	2450	2	N75/H25	Ground	AlO	30-40	600
9	0.005	0.030	0.286	45	0.0028	2450	1	N75/H25	None	None	10	600
10	0.005	0.030	0.286	45	0.0028	2450	1	N75/H25	Ground	AlO	30-40	1300+
11	0.005	0.030	0.286	45	0.0028	2450	1	N75/H25	None	AlO	30-40	600
12*	0.005	0.030	0.191	40	0.0020	4300	1	N75/H25	Ground	AlO	30-40	600
13	0.008	0.030	0.286	45	0.0028	2450	1	N75/H25	Ground	AlO	30-40	600
14	0.005	0.030	0.286	45	0.0028	2450	1	X-750	Ground	Chr/Carb	20-30	600
15*	0.005	0.030	0.286	45	0.0028	2450	1	N75/H25	Ground	AlO	30-40	600
A1	Similar to seal Conf.#1 except supplied by EG&G Sealol									AlO	30-40	600
A2	Textron 3-D braided compliant seal									AlO	30-40	600
REF	Reference 4 knife labyrinth seal with static CL = 0.008 in.									AlO	30-40	600

* = replaced by other vendors seal N75 = Nimonic 75 H25 = Haynes 25	AlO = Aluminium oxide coating, plasma sprayed METCO coating P105-13 per METCO instruction 105NS to a thickness of 0.006 to 0.010 inches after final grind, over a 0.003 inch thickness of METCO 450 bond coat.
Seal radial height = 0.45 in. Seal offset = 0.000 in. Bristle packing thickness = 0.027 in.	Chr/Carb = Chromium carbide coating, plasma sprayed METCO chromium carbide P81VF-10 coating per METCO bulletin 81VF-NS, to a thickness of 0.005 to 0.010 inches after final grind.

Table 5.4 Parameter values for brush seals evaluated **(Chupp and Holle (1991))**.

Seal Designation	**Data Source**	**T**	**Pr**	**db**	**λ**	**n**	**Dj**	**Du**	**Bo**
		(F)	max	(in)	(deg)	(bristles /in)	(in)	(in)	(in)
TCAE1000	Teledyne CAE	490	4.66	0.0028	45	2300	5.100	5.672	0.0198
TCAE600	Teledyne CAE	180	5.33	0.0028	45	2300	5.100	5.672	0.0197
NASAECC	NASA	70	3.91	0.0028	47.5	2471	5.379	5.954	0.0220
NASAINT	NASA	70	8.99	0.0020	53	4329	1.500	1.850	0.0184
CROSSTHK	CROSS MFG	70	6.44	0.0028	45	3500	5.100	5.832	0.0287
EGGSPWS	EG&G Sealol - 2x thick	90	2.94	0.0028	45	4337	5.395	6.165	0.0354
EGGLDS	EG&G Sealol - std thick	95	3.57	0.0028	45	2168	5.395	6.165	0.0181
ALSNDYN	Allison dynamic data	70	6.00	0.0028	45	2300	5.100	5.672	0.0199
ALSNSTAT	Allison static data	70	6.00	0.0028	45	2300	5.100	5.672	0.0198

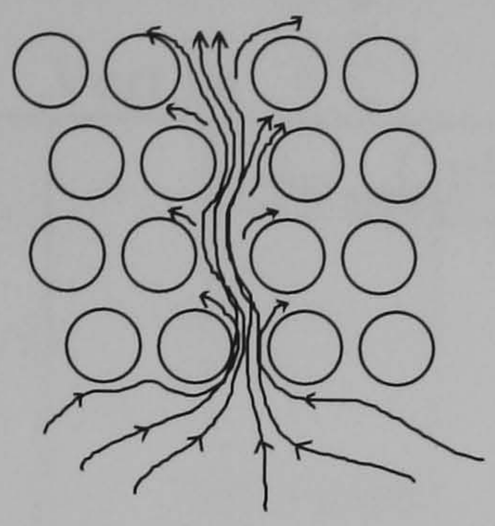

Rivering.

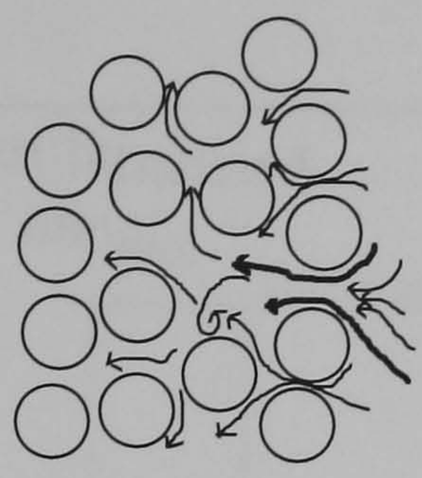

Jetting.

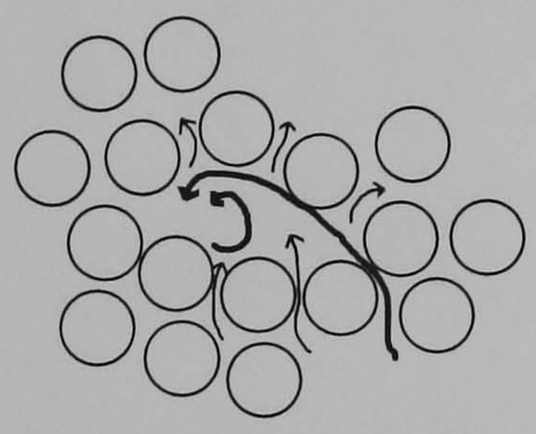

Vortical flow.

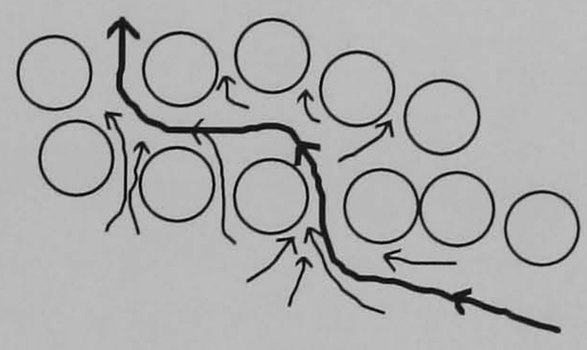

Lateral flow.

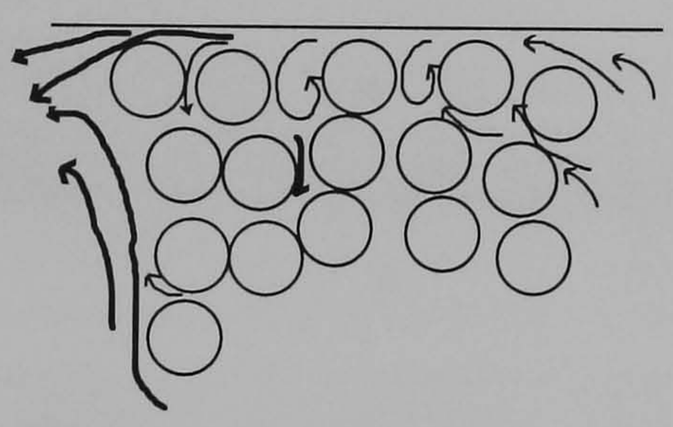

End-wall flow.

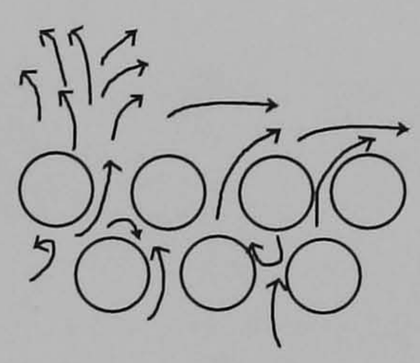

Flow at the bristle tips.

Figure 5.1 Sketches of typical flow formations in brush seals **(Braun et al (1991))**.

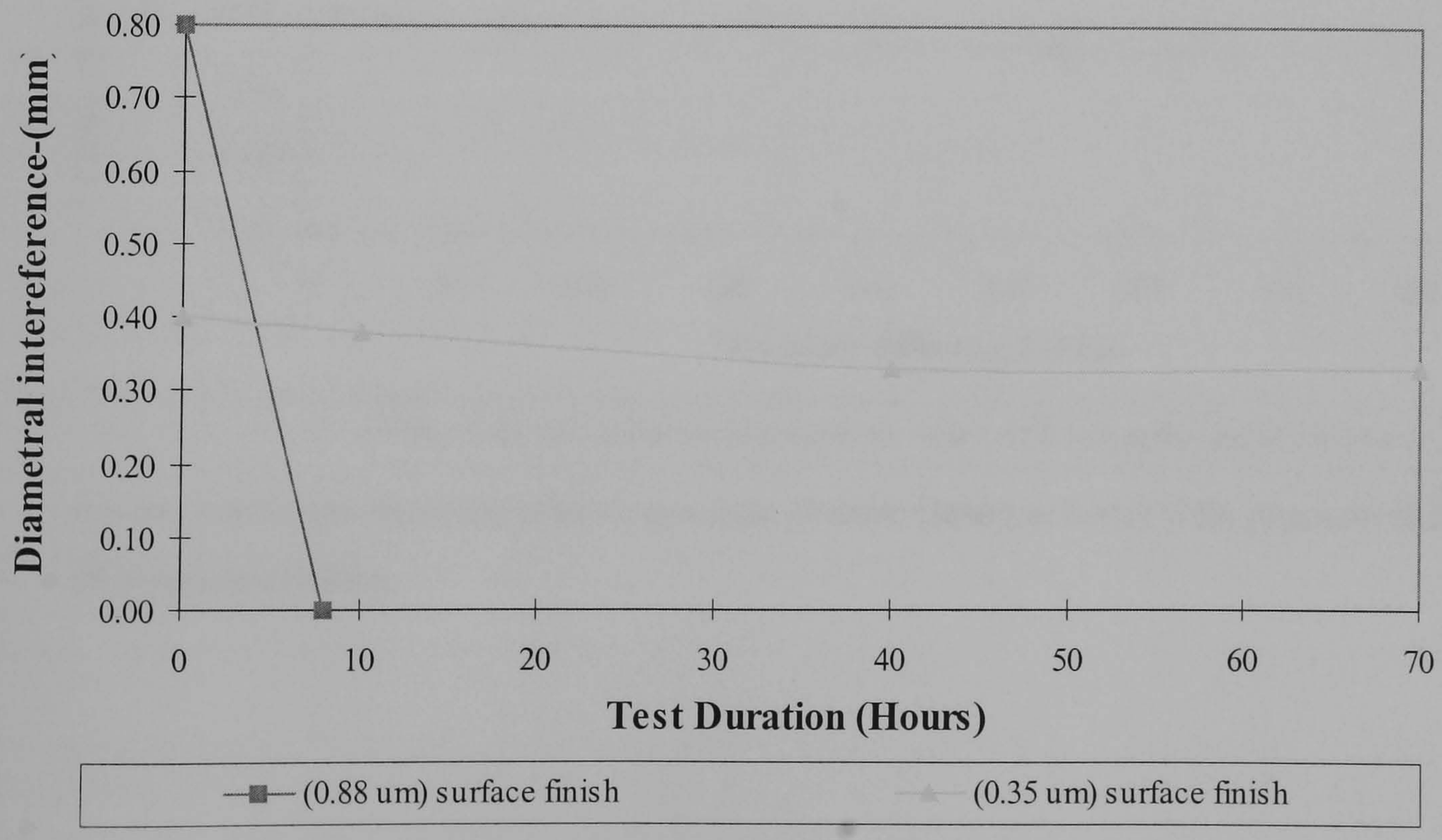

Figure 5.2 Effect of surface finish on bristle wear **(Ferguson (1988))**.

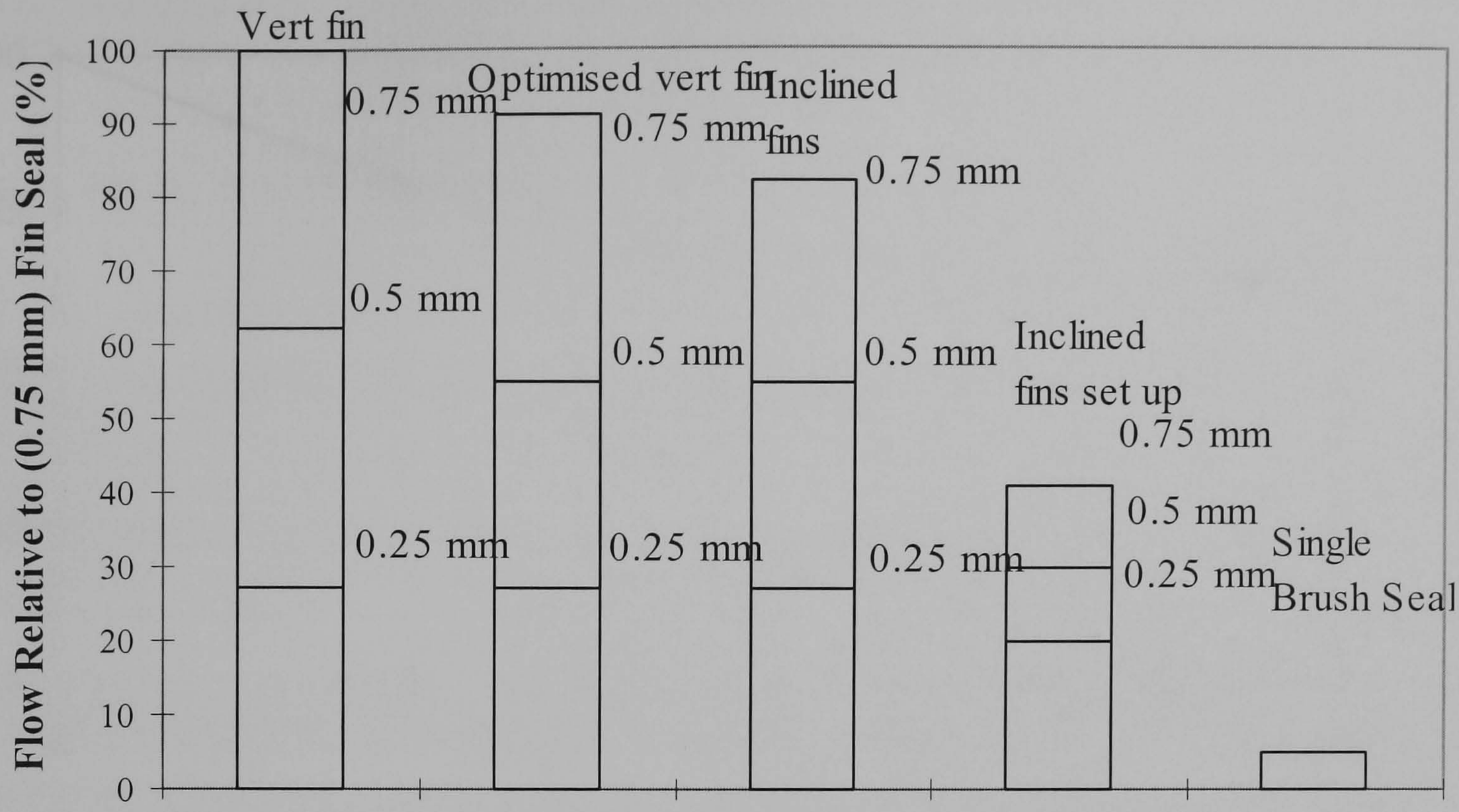

Figure 5.3 Sealing performance of brush seals compared with various five-finned labyrinth seals at a pressure ratio of 2.0 **(Ferguson (1988))**.

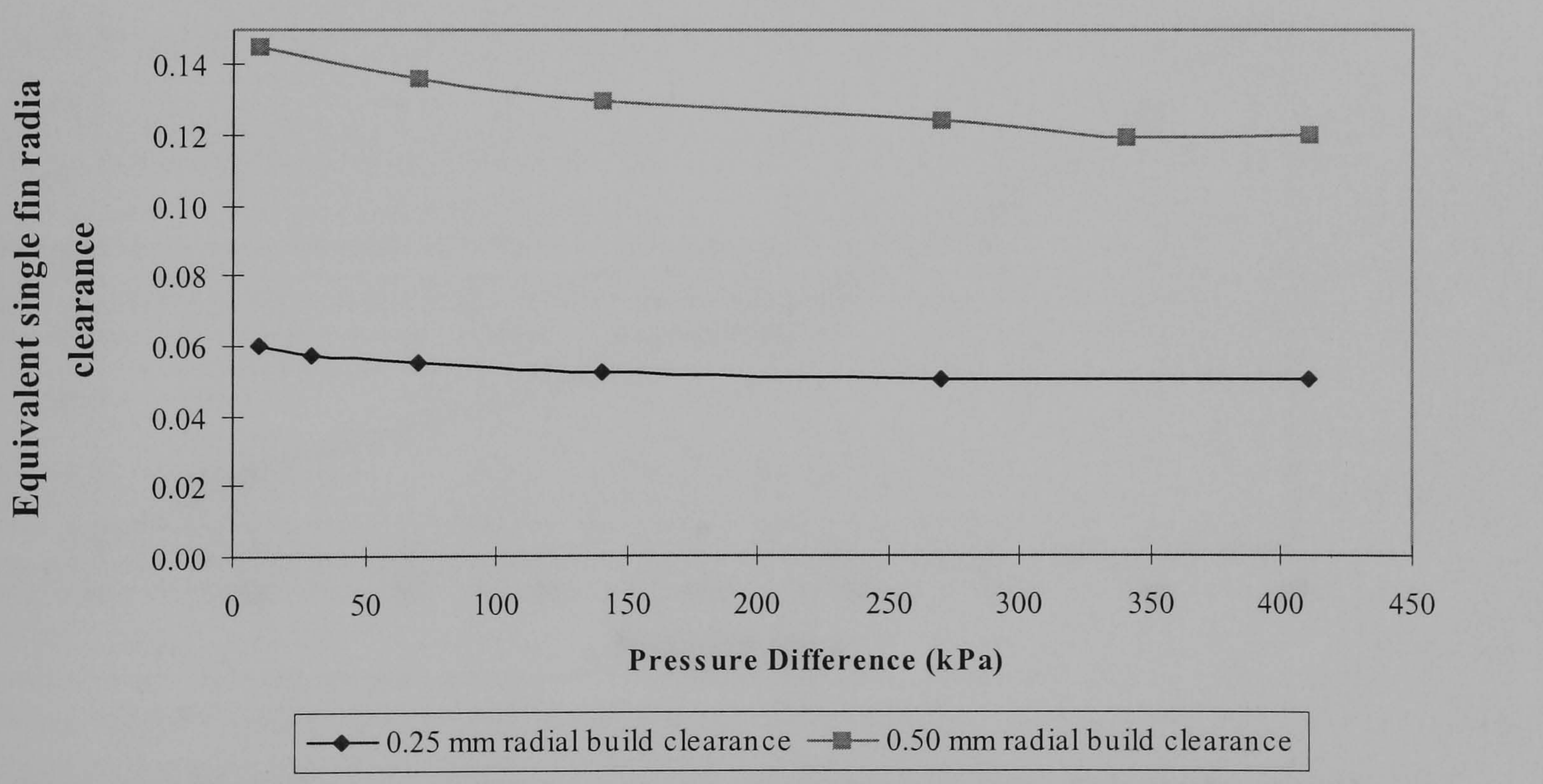

Figure 5.4 Graph showing effective bristle closure (internal bore) with pressure differential **(Ferguson (1988))**.

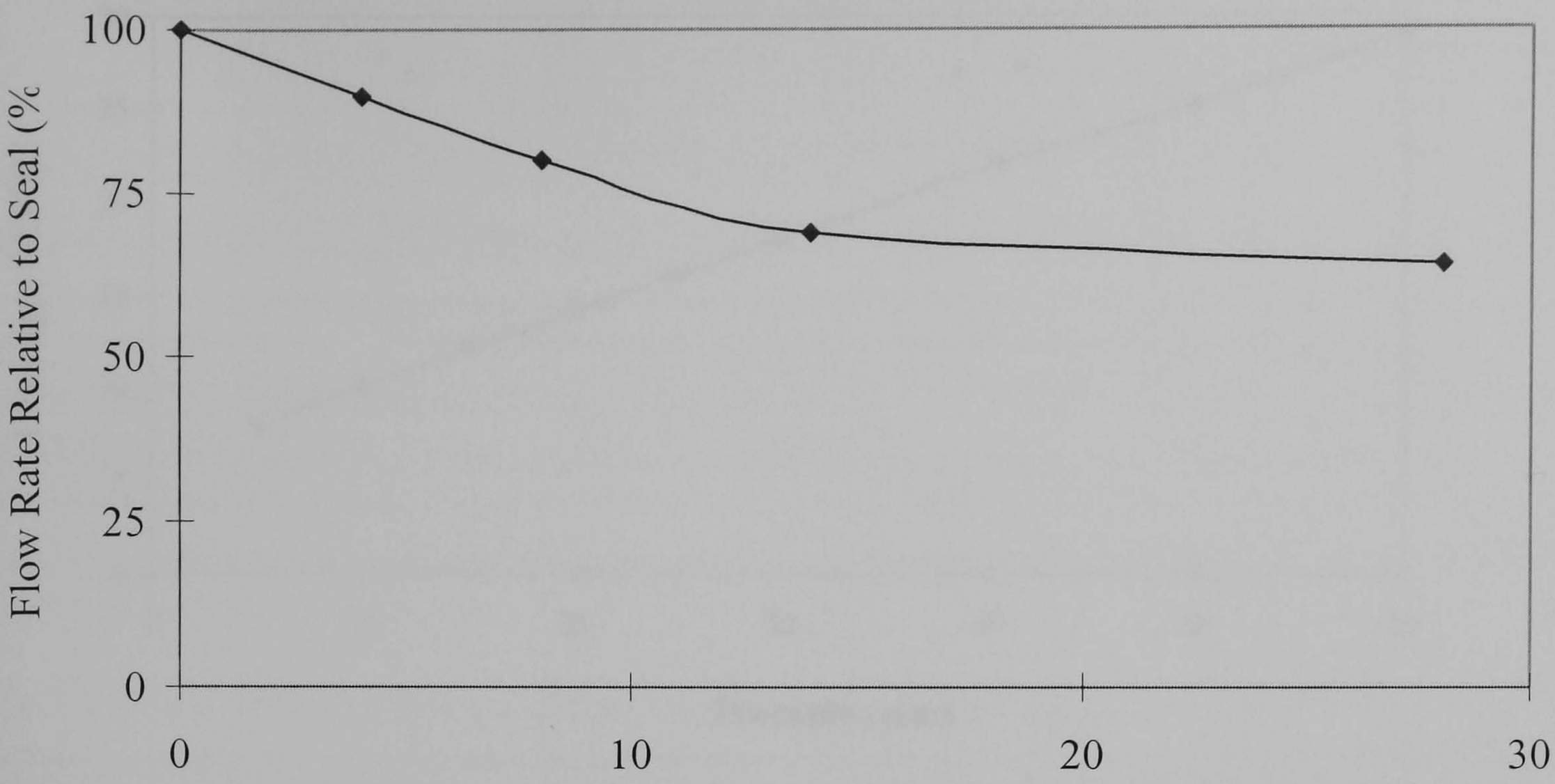

Figure 5.5 Effect of rotational speed on leakage flow test results **(Ferguson (1988))**.

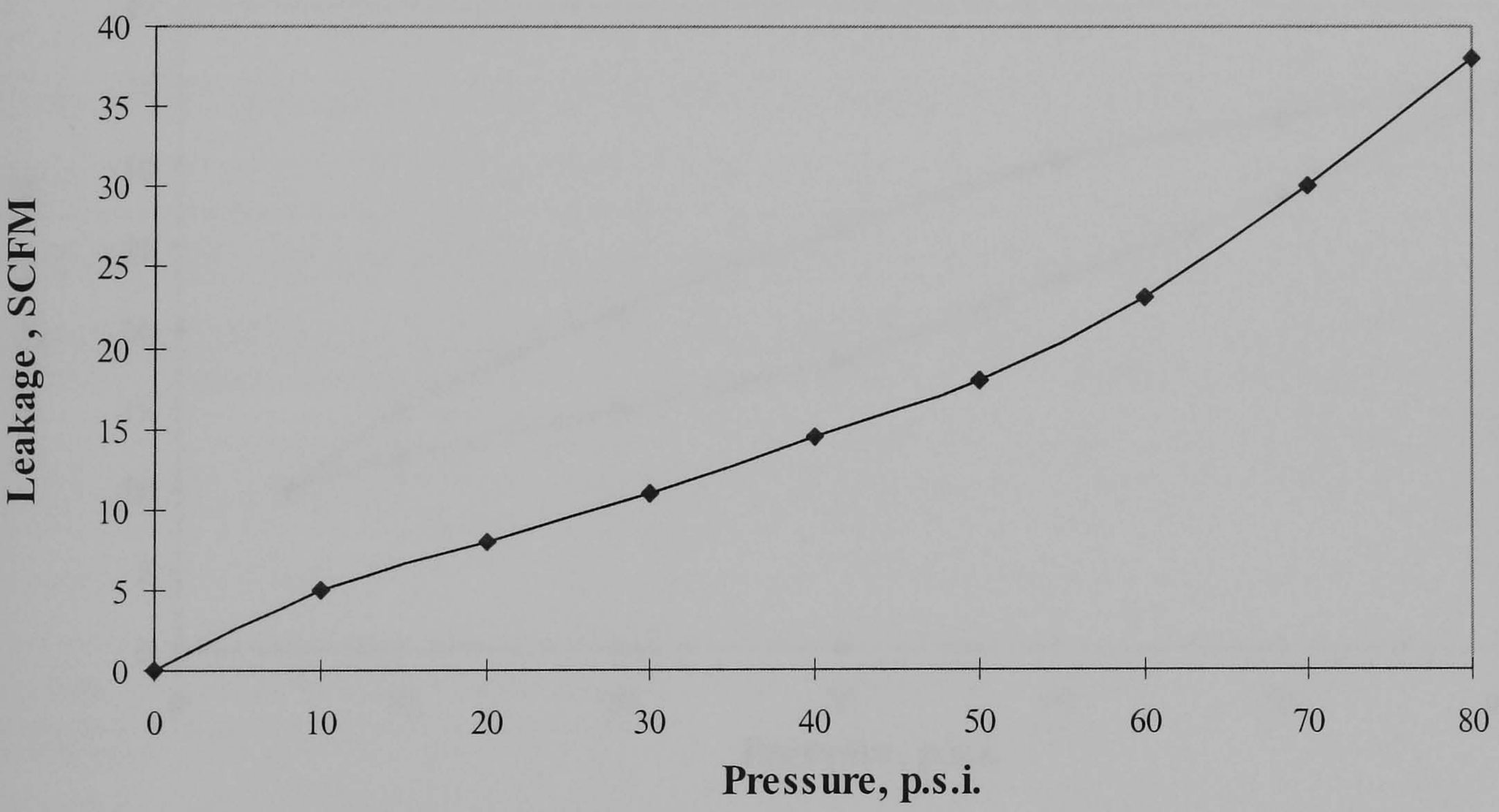

Figure 5.6 Typical pressure/leakage curve for a 130 mm (5.1 inch) diameter brush seal **(Flower (1990))**.

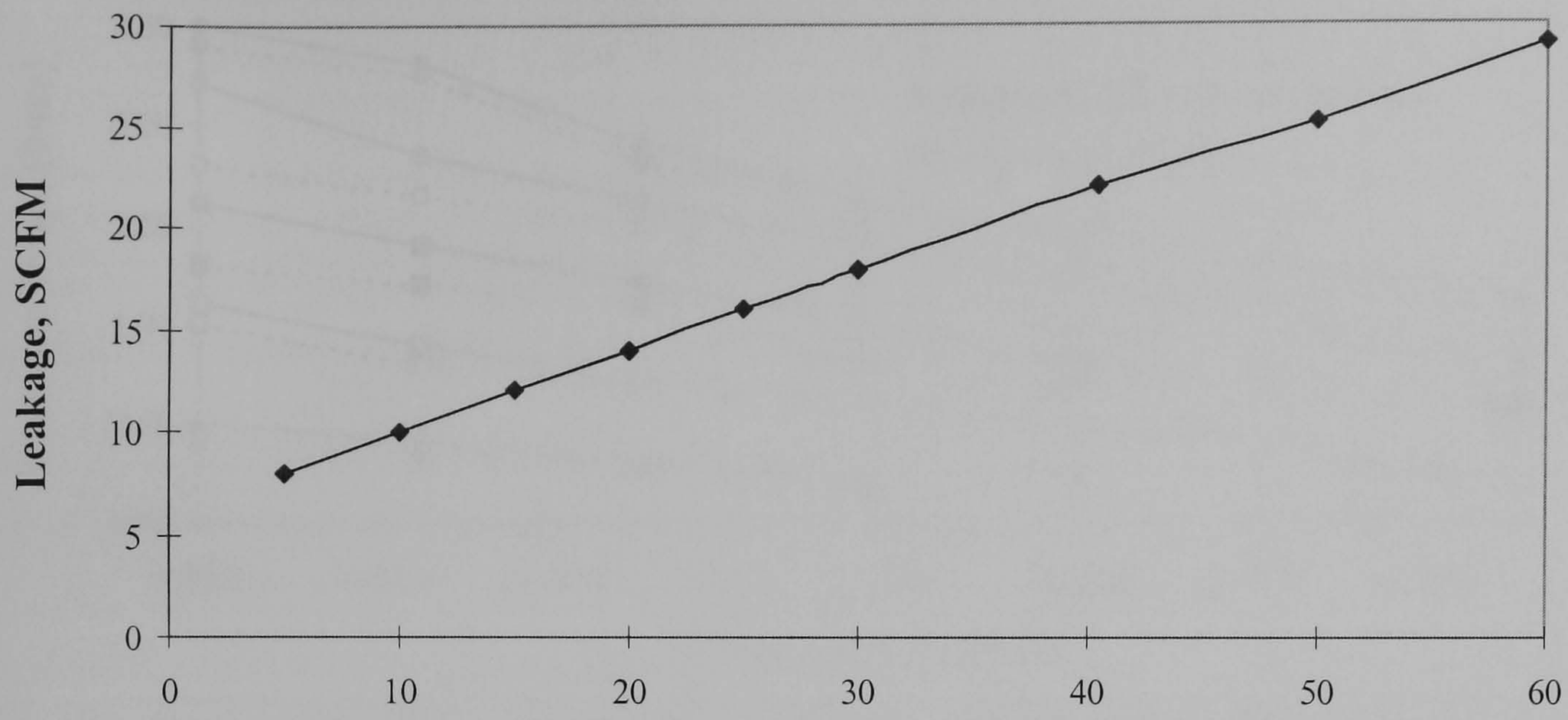

Figure 5.7 Typical pressure/leakage curve after offset test for a 130 mm (5.1 inch) diameter brush seal **(Flower (1990))**.

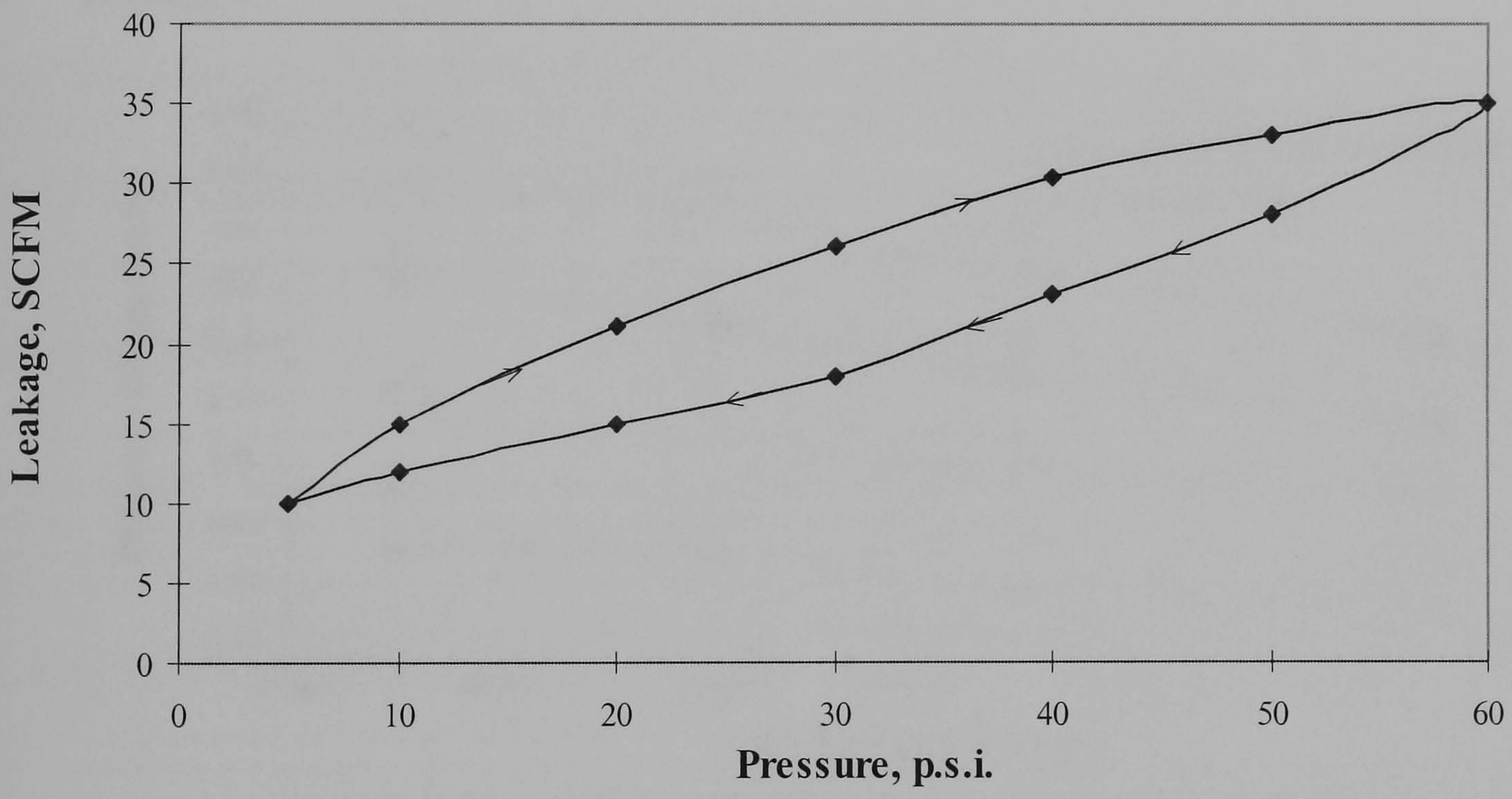

Figure 5.8. Typical hysteresis loop **(Flower (1990))**.

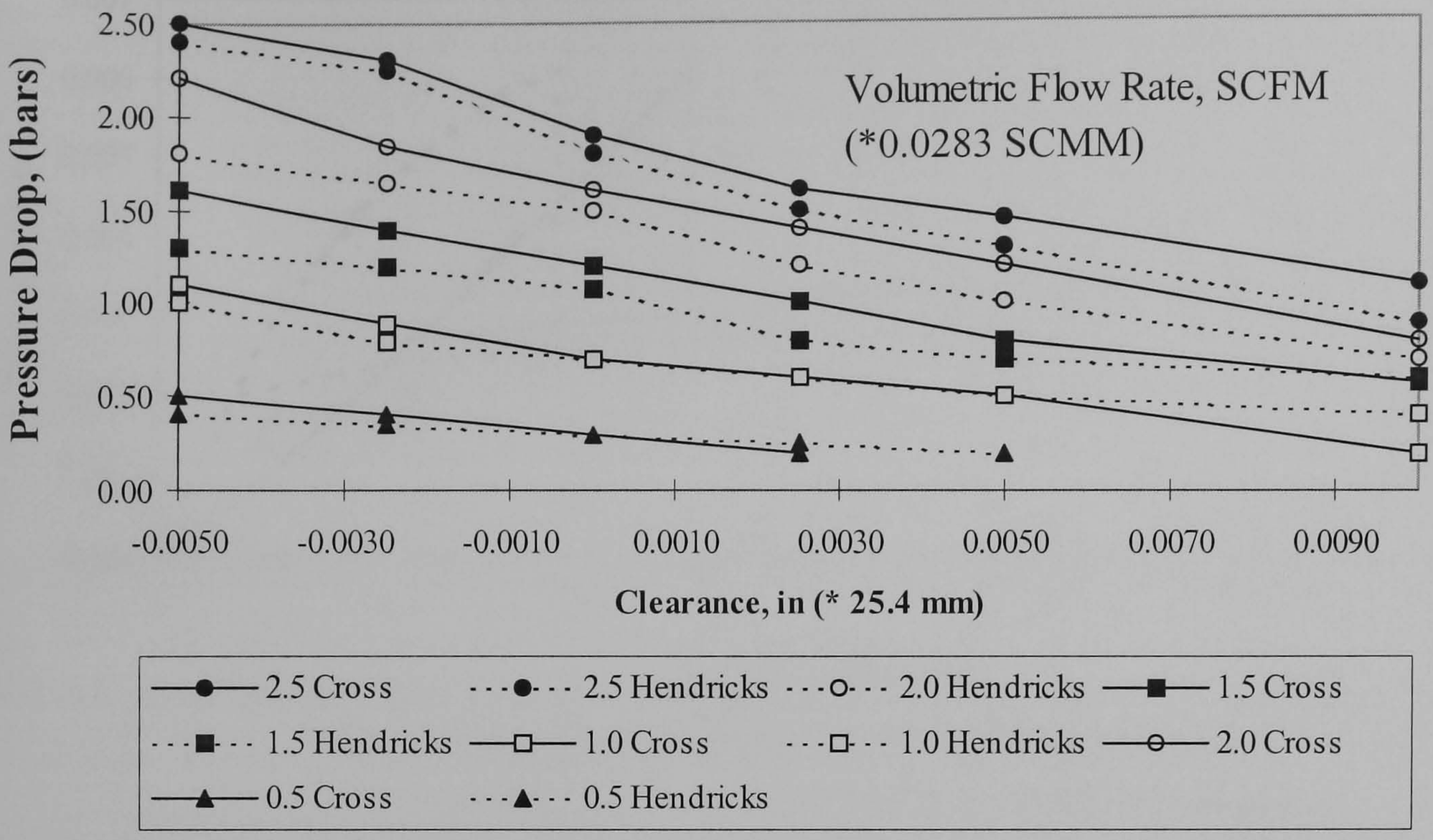

Figure 5.9 Analytical predictions of flow and pressure drop as functions of clearance for the experimental results from Cross Mfg. 130 mm (5.1 in.) brush seal **(Hendricks et al (1991))**.

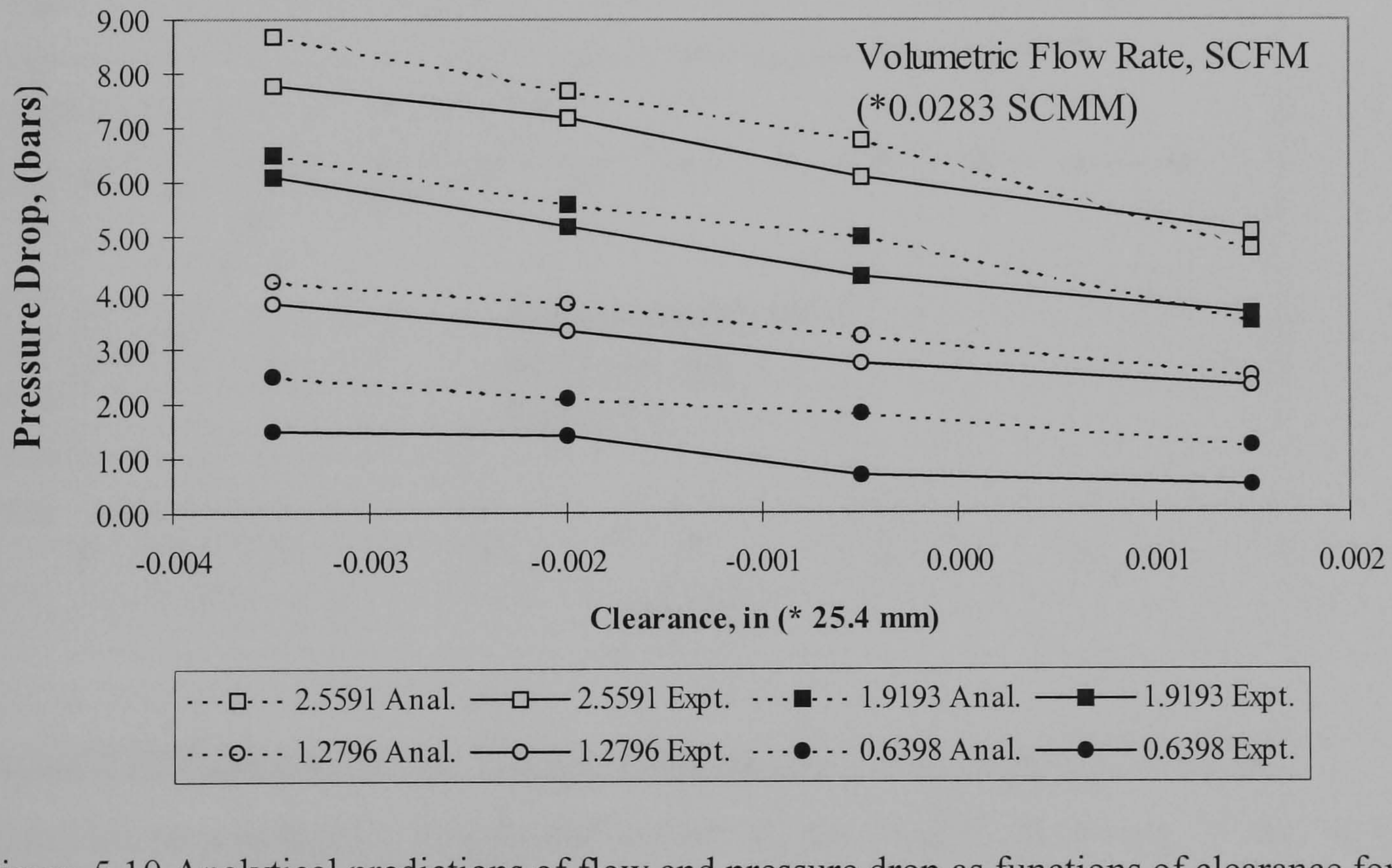

Figure 5.10 Analytical predictions of flow and pressure drop as functions of clearance for a 38 mm (1.5 in.) brush seal **(Hendricks et al (1991))**.

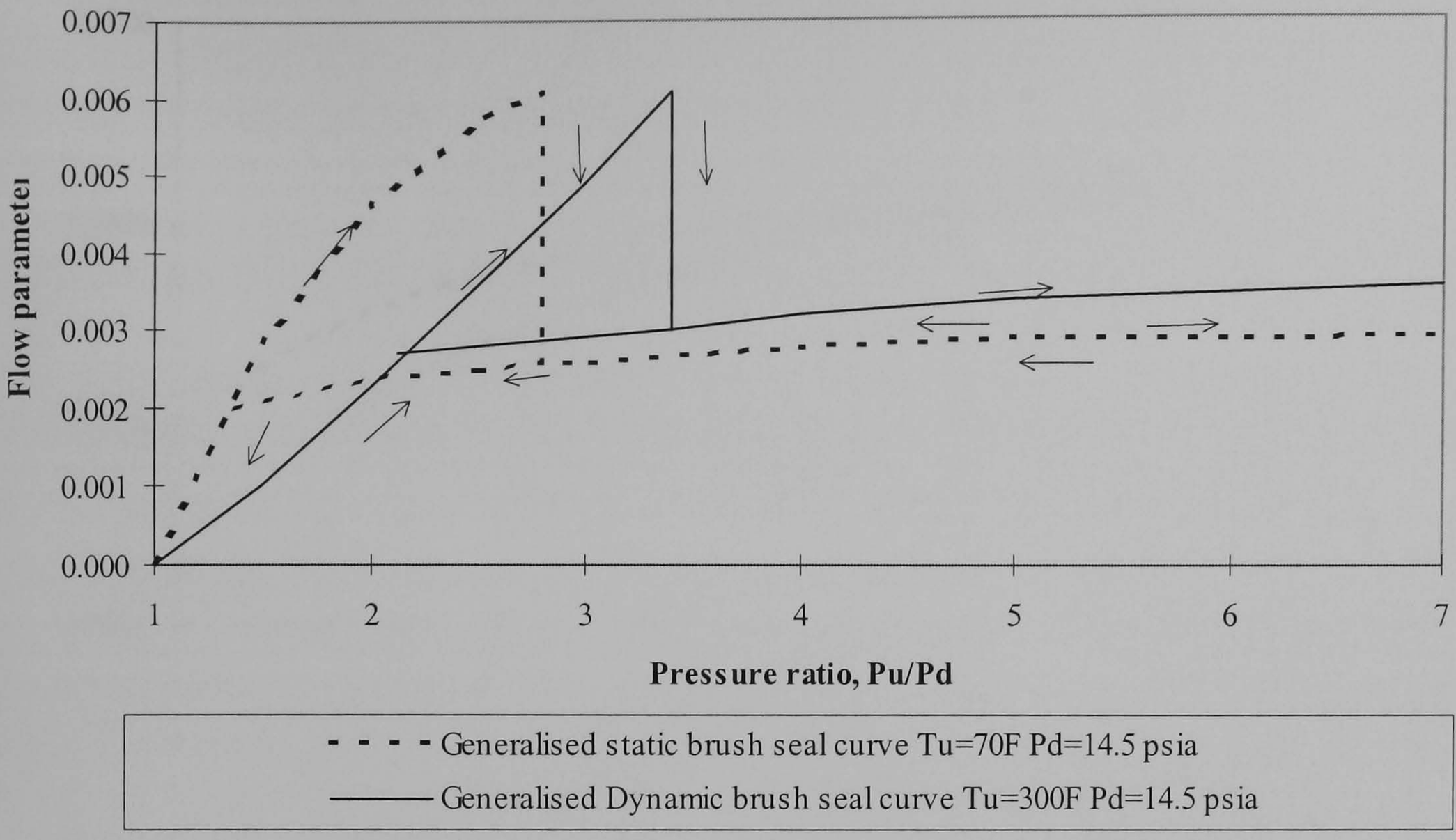

Figure 5.11 Generalised brush seal static and dynamic performance. Seal leakage parameter, f - lbm °R/lbf-sec (10^3) **(Holle and Krishnan (1991))**.

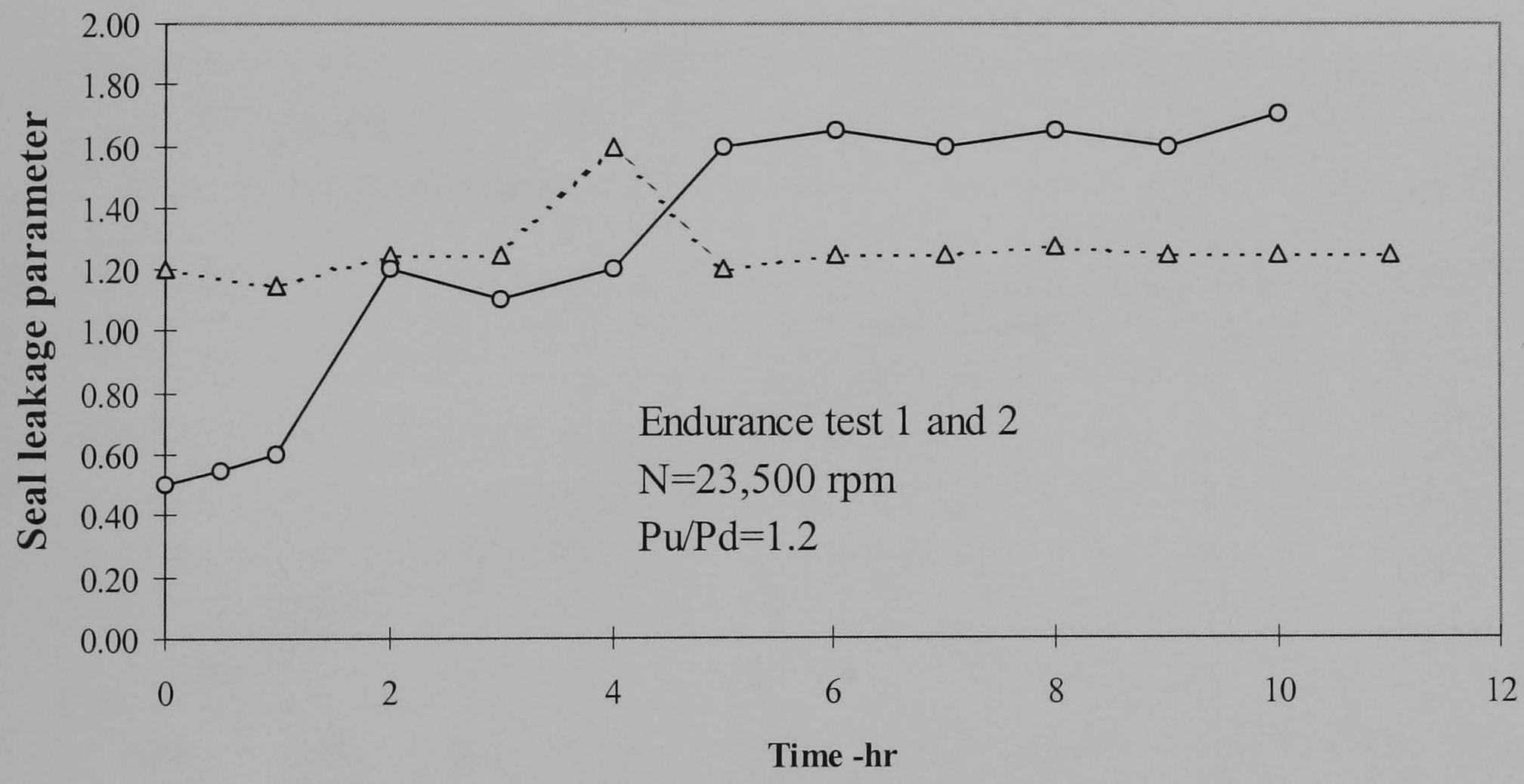

Figure 5.12 Typical brush seal leakage characteristics during accelerated wear rate endurance tests in the high temperature seal test rig. Seal leakage parameter, f - lbm °R/lbf-sec (10^3) **(Holle and Krishnan (1991))**.

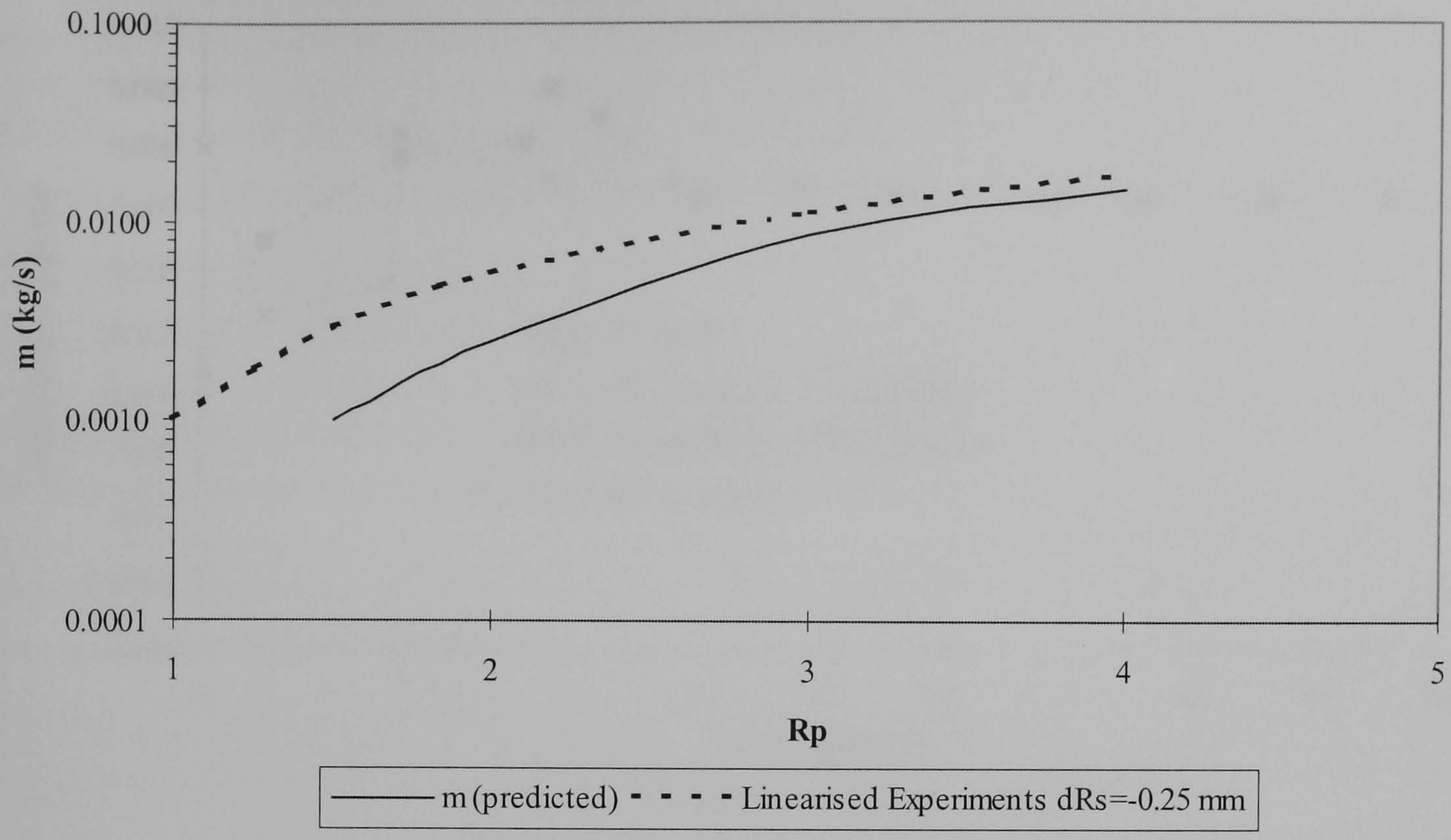

Figure 5.13 Variation of measured and predicted mass flows, m, with pressure ratio, Rp **(Bayley and Long (1992))**.

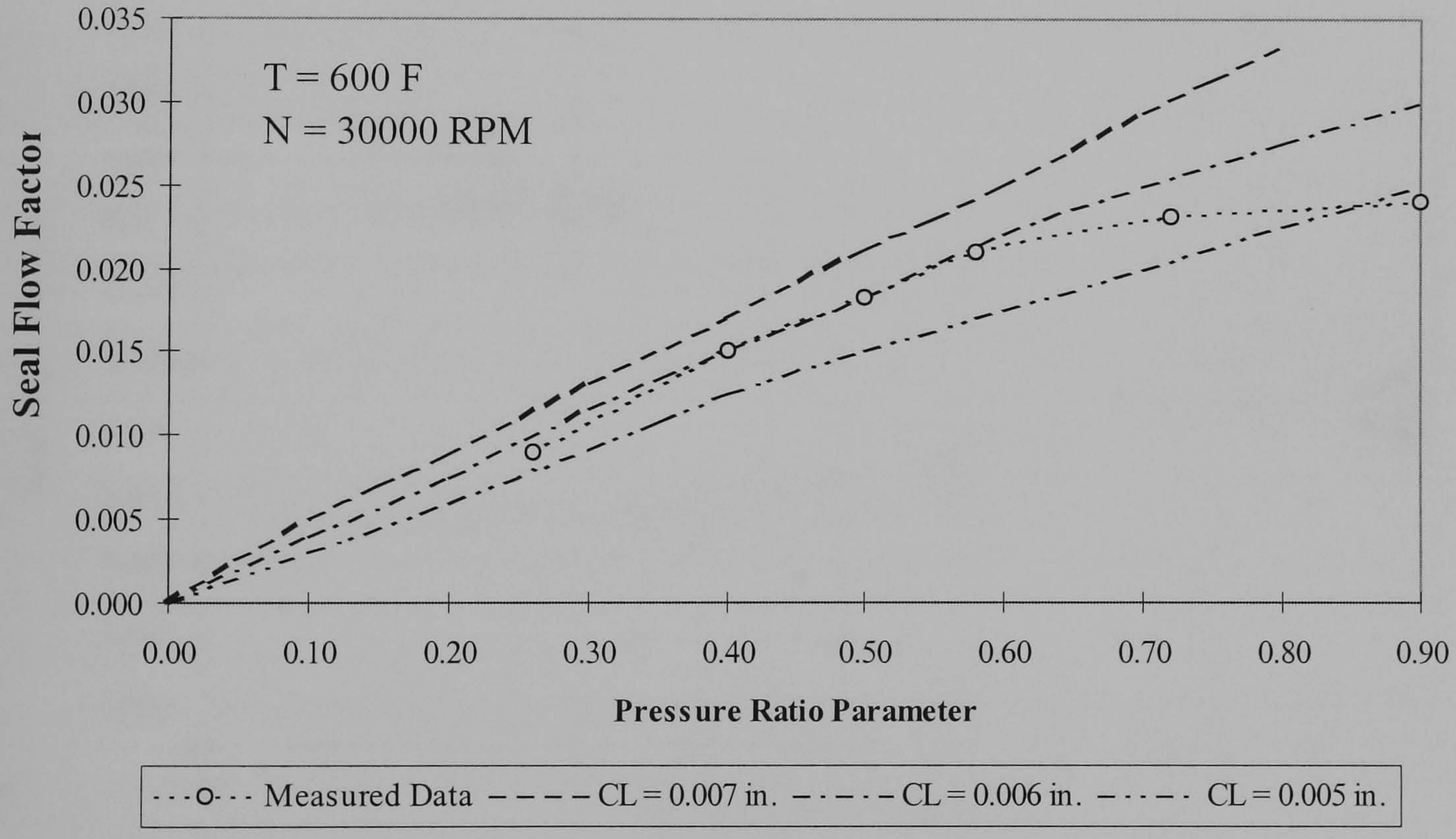

Figure 5.14 Comparison of measured and calculated flow performance for the labyrinth seal **(Chupp and Nelson (1992))**.

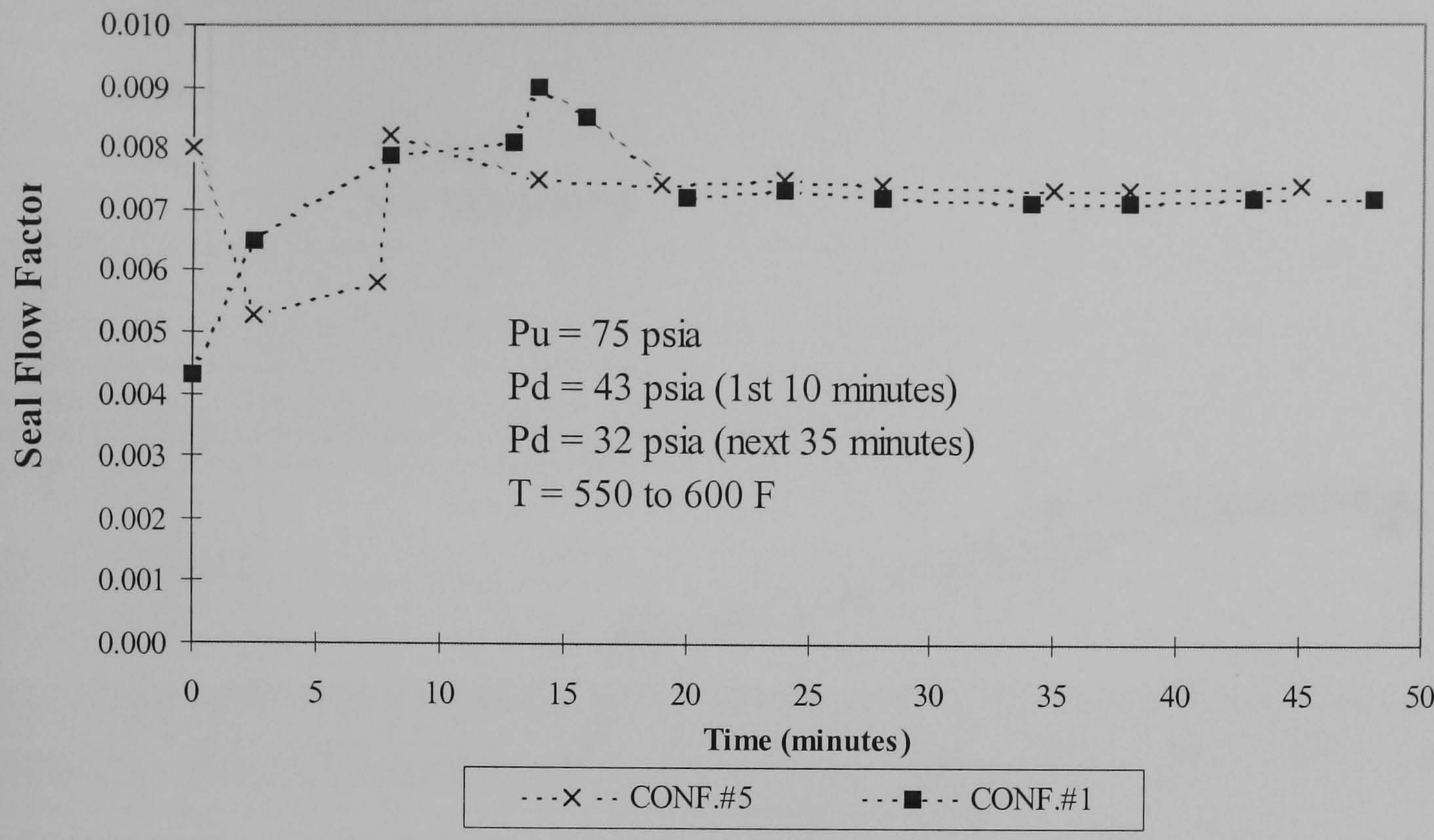

Figure 5.15 Engine simulation cycle results for brush seal configurations #1 and #5 **(Chupp and Nelson (1992))**.

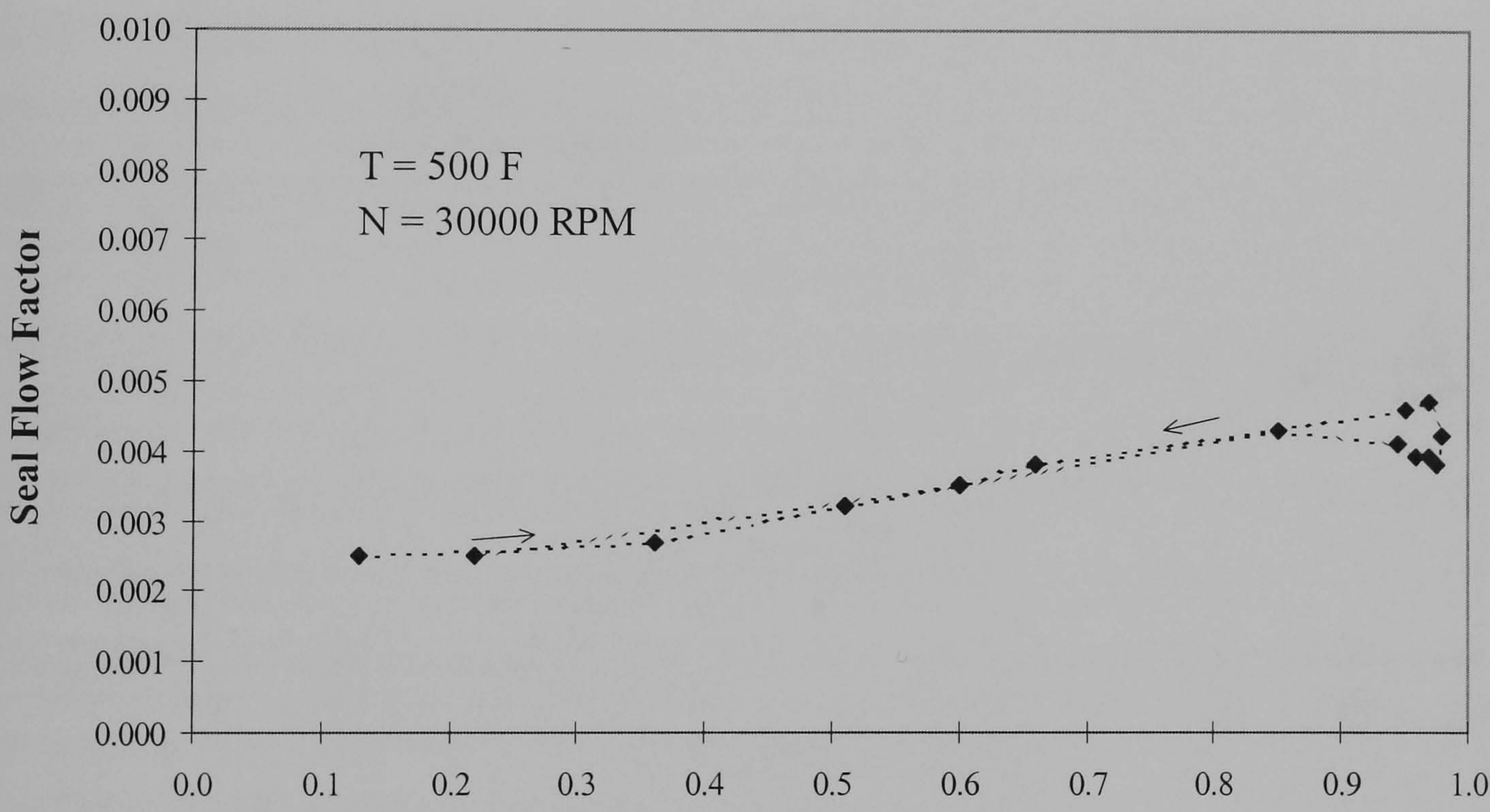

Figure 5.17 Measured flow performance for a brush seal configuration #4 with a smaller backplate gap **(Chupp and Nelson (1992))**.

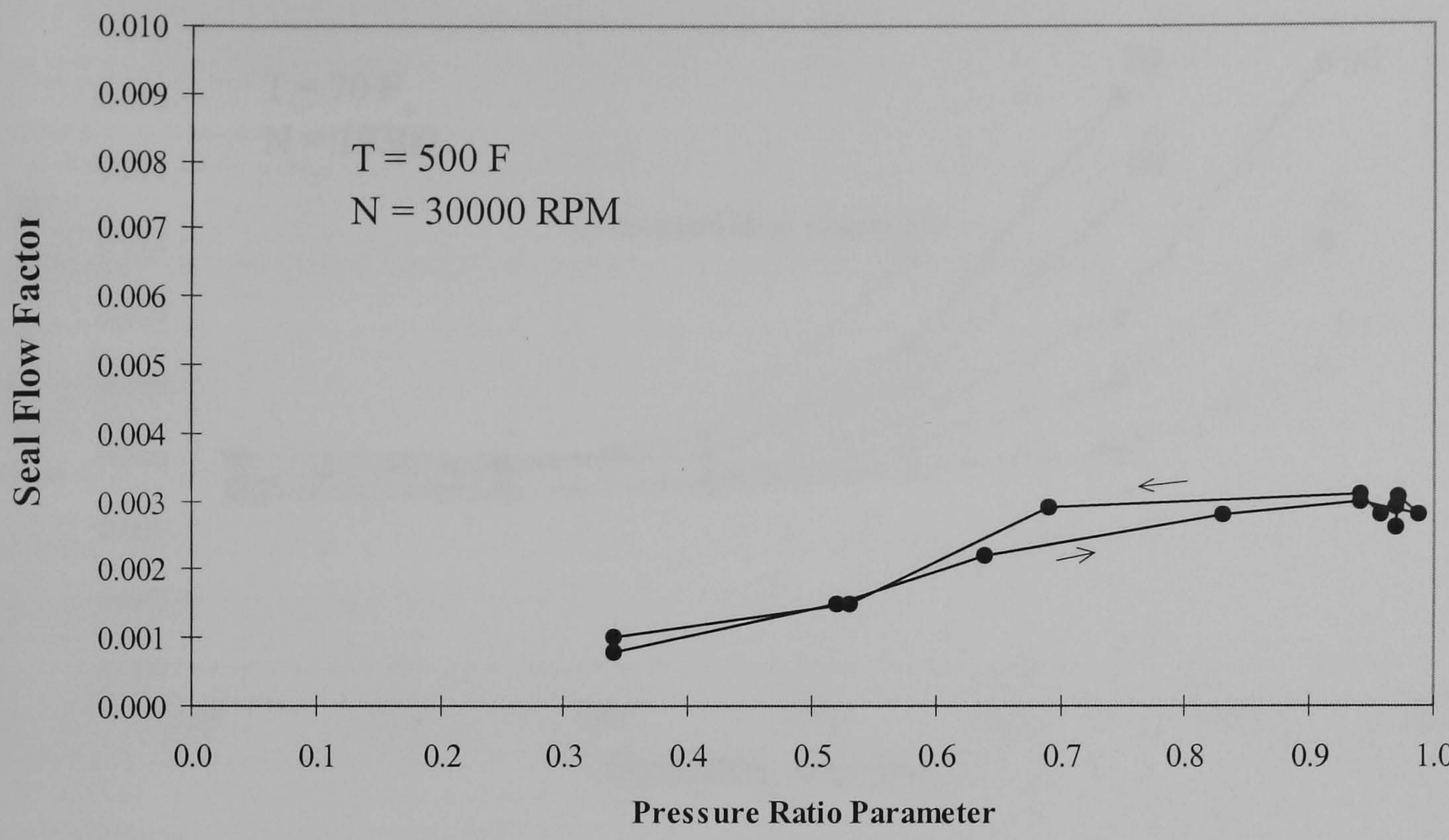

Figure 5.18 Measured flow performance for brush seal configuration #8 with two seals in series **(Chupp and Nelson (1992))**.

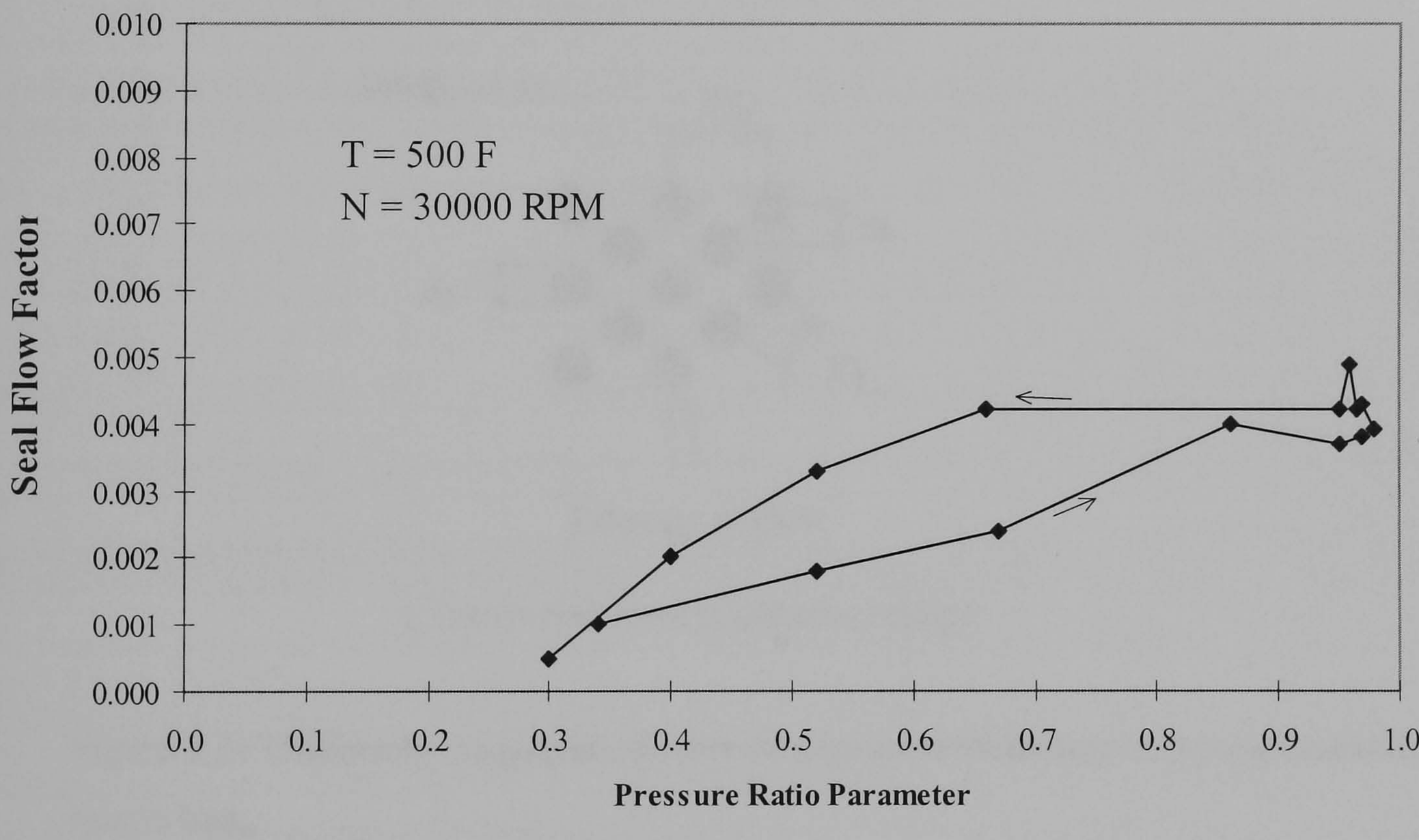

Figure 5.19 Measured flow performance for brush seal configuration #A1 manufactured by a second vendor **(Chupp and Nelson (1992))**.

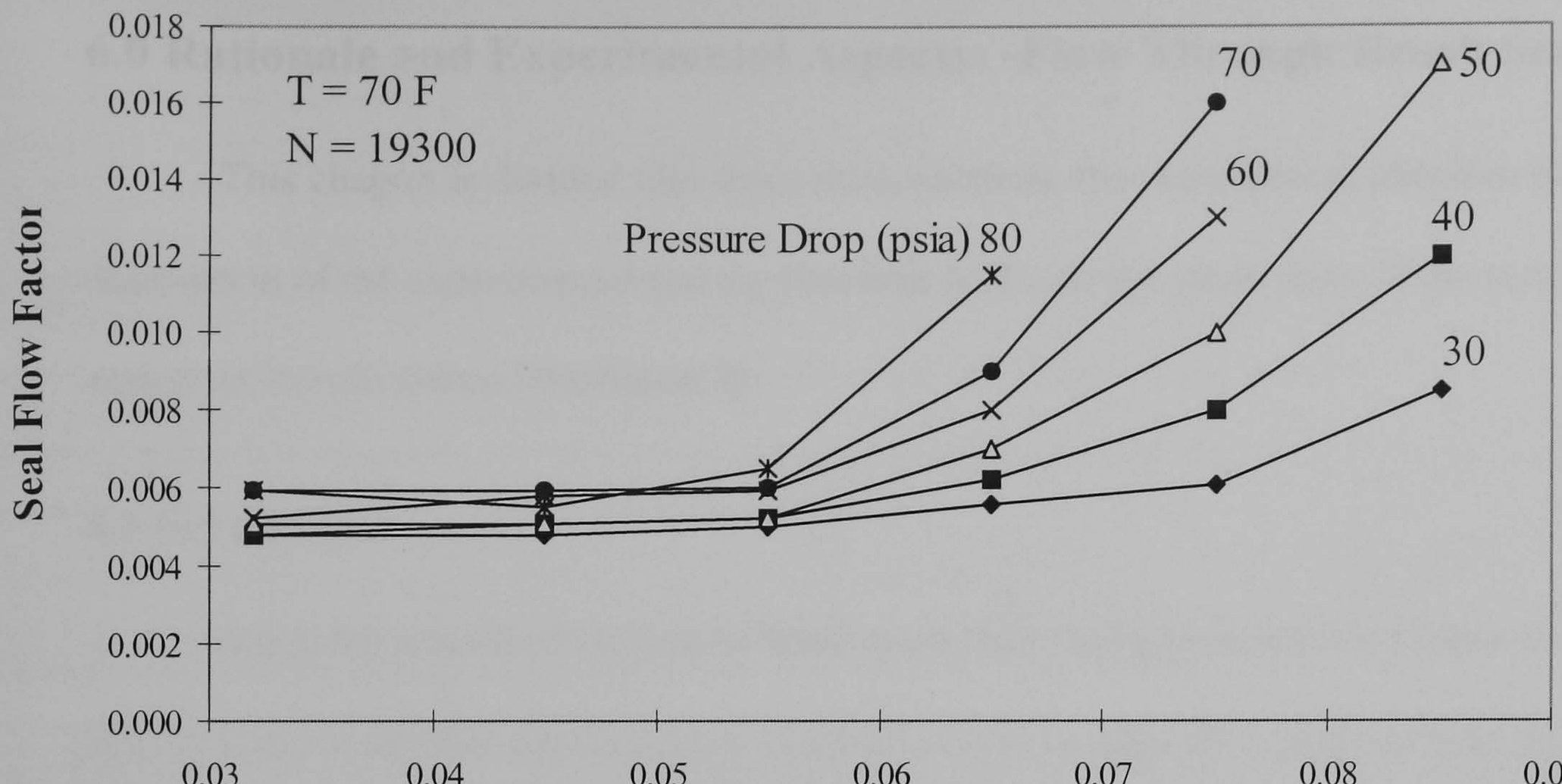

Figure 5.20 Cross plot of flow performance data from Cross Manufacturing showing effect of increasing backplate gap **(Chupp and Nelson (1992))**.

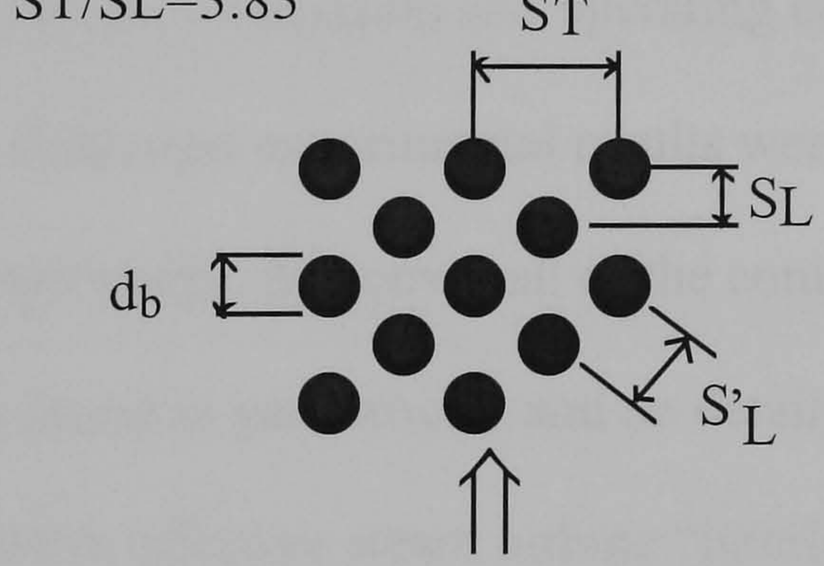

Figure 5.21 Uniformly staggered cylinder arrangement modelling an average random bristle bed.

6.0 Rationale and Experimental Aspects: -Flow Through Brush Seals

This chapter is divided into three main sections, the introduction **(Section 6.1)**, a description of the experimental test rig **(Section 6.2)**, and the main aims of the tests and the experimental procedure **(Section 6.3)**.

6.1 Introduction

Since the revival of interest in brush seals there have been several claims of being able to achieve substantial reductions in parasitic seal leakage flow compared to that of the "equivalent" five finned labyrinth seal. **Ferguson (1988)** and **Flower (1990)** claimed a reduction in leakage flow rate of 80 – 90%. Experiments performed at Teledyne CAE **(Chupp et al (1991))** also showed that leakage could be reduced by a factor of four to seven. The improvements quoted were all promising however the exact relationship between the seal design, installation and operating conditions with respect to leakage flow rate was unclear. Published experimental results were sometimes vague and the experimental details sparse. Moreover all of the comparisons were to "straight through" labyrinth seals as found in gas turbines and no details of the expected improvements compared to the more effective steam turbine "interleaved" labyrinth seal have so far been published. Many of the experimental tests that have been carried out have been on seals and test rigs that were far removed from the geometry and operating conditions of brush seals for possible application in a high pressure steam turbine.

A test programme was proposed to quantify the expected efficiency improvement that was expected by using brush seals rather than labyrinth seals and to investigate the leakage characteristics of the brush seal. This necessitated the design and manufacture of a purpose built test rig that would allow the comparison of brush and labyrinth seals. The test facility would be able to test "full size" seals under more realistic operating conditions and

would have the ability to determine the effect of several running variables. These are discussed in **Section 6.2**.

6.2 Main Aims of the Tests.

The brush seal leakage test rig **(BSLTR)** was designed to allow the following parameters to be altered, seal clearance/interference, shaft rotation speed, pressure differential, seal offset, and shaft eccentricity. The aim of the experimental testing was to investigate the following aspects: -

i.) Determine the leakage flow through a single fin labyrinth seal (or backing plate without a brush seal) for different clearances **(BPC)** and under different pressure differentials as a benchmark test and for comparison to theoretical labyrinth seal results experimental brush seal results.

ii.) Determine the leakage flow rate through 330 mm (13 inch), double and single thickness brush seals under pressure differentials from 0-5 bar for different brush seal bristle clearances/interferences **(BSC/I)**.

iii.) Compare the leakage flow through single and double thickness brush seals to each other and a standard single fin labyrinth seal.

iv.) Determine the effect on leakage flow of shaft rotation.

v.) Determine the effect of seal offset on leakage rate.

vi.) Determine the effect of shaft eccentricity on seals.

vii.) Determine seal leakage with manufacturing repeatability.

viii.) Determine the torque required to rotate a shaft with a brush seal installed with different clearances or installed interferences under different pressure differentials.

ix.) Identify the conditions where the brush seal bristle pack "blows down" and returns to normal.

x.) Investigate "blow down" effects.

xi.) Monitor the vibrational characteristics of the rotor with and without brush seals at a range of interferences and clearances.

6.3 Description of the Test Rig.

The design of the brush seal experimental leakage test rig was carried out with reference to other researchers test rigs and with two major design constraints. A pair of 330 mm, opposite handed, single and double thickness brush seals were available for testing. The purchase price of brush seals of a user-specified size (due to tooling costs prior to manufacture) meant that a rig was designed to accept the existing seals. Back to back seal testing was also thought to be necessary as it removed the problem of a large end thrust developed by a single seal rig. Two seals also had an averaging effect on the results and allowed small changes in the leakage rate to be more easily and reliably detectable.

The test rig **(Figure 6.1-6.2)** consisted of a central shaft supported horizontally between two self-aligning rolling element bearings. At one end a 50 hp motor with a thyristor control (variable speed 0-3000 r.p.m.) was connected to the shaft with a flexible drive coupling. Locked onto the shaft were two stepped rotors, machined from Parsons single cylinder rotor steel (Spec. 297) the stepped rotors had concentrically machined journal steps **(Table 6.1, Figure 6.3)**. The two stepped rotors were positioned so the steps increased in diameter from left to right in both cases. They were located onto the shaft by large locking nuts that were doweled in place. Between the two stepped rotors a space existed that acted as an expansion annulus.

The shaft and stepped rotors passed through a large diameter, cylindrical, open ended tube. The tube was machined on either end to accept either a single knife edge labyrinth fin or a 330 mm diameter brush seal of single or double thickness. These were mounted directly onto the tube end by 16 equi-spaced bolts and a retaining plate. Two seals could therefore be tested, back to back, without the large axial thrusts that would be produced by a single seal. Air was introduced to the tube (that effectively acted as a

pressure vessel) at 0-6 bar, by an inlet flange and flexible pipe. This was located on the top of the cylinder, directly in-between the two stepped rotors.

Moving the pressure vessel axially on slide rails until the two seals aligned with the appropriate land on the stepped rotors could change the seal interference/clearance. The required seal misalignment could be introduced by moving the slide rails in a direction perpendicular to the cylinder. Two eccentrically machined (0.50 mm peak-peak) could replace the stepped rotors stepped rotors to simulate shaft eccentricity.

The stepped rotor journal diameters were carefully chosen to provide the most relevant results for a selection of **BPC** and **BSI/C**. The five lands consisted of two bristle interference fits of 0.5 and 0.2 mm. It was felt that this degree of interference was comparable to that experienced in service conditions. The central land was a size for size (zero clearance/interference) fit, that was thought to be close to a "run in" seal fit. The final two bristle clearance fits of 0.5 and 0.9 mm represented the absolute minimum and a typical labyrinth fin clearance in a steam turbine. The single knife edge fin was designed to match the 0.5 and 0.9 mm clearance fit. Due to a manufacturing error the fin was machined to produce three fits of 0.18, 0.68 and 1.08 mm. Instrumentation was included to record atmospheric pressure and temperature, rig pressure and temperature, and up stream and down stream orifice plate pressure **(Figure 6.1** and **Table 6.3).**

A portable personal computer with built in data logger was used to monitor and record the test results via pressure transducers and thermocouples. These included ambient air pressure and temperature, air downstream inlet pipe pressure and temperature, rig internal air pressure and temperature, thyristor drive rotor speed. Results were recorded every two seconds and a selection of these were used to calculate the air flow rate through the orifice plate at user specified rig pressure differentials.

Manual recordings of pressures, pressure differentials and temperatures were also taken using pressure gauges, manometers (either water or mercury dependant on pressure differential) and thermometers. **Table 6.3** describes the instrumentation, the accuracies and

their positions. **Figure 6.1** shows the brush seal leakage test rig and the instrumentation included.

Leakage flows were calculated using the pressure differential across an orifice plate (in accordance with BS1042) located in the rig's inlet line. Depending on the type of seal being tested, the rig pressure and the seal/rotor fit the seal leakage varied enormously, consequently no single orifice plate could be used to cover the complete range of tests.

6.4 Experimental procedure.

The relevant seals were bolted onto end faces of the brush seal leakage rig body after applying a thin line of sealant to the mating faces to ensure an airtight joint. The seal was set to the required position with respect to the stepped rotor by moving the rig body axially. The specific seal was then set to the required concentricity (with respect to the shaft). Feeler gauges were slipped between the fin tip or brush seal backing plate and the stepped rotor and the rig body was carefully moved to equalise the gap at four 90 degree intervals. Once the concentricity was set and the air supply was opened to allow the supply to reach a steady state temperature, the individual experiments were ready to commence. In most test cases (with the shaft stationary and rotating) it was desirable to apply a 6.0 bar pressure differential across the test seals, however it was not always possible due to the limited capacity of the rig's air supply. The rig pressure was slowly increased, allowing the pressure to settle at appropriate intervals whilst the data logger recorded the transducer, thermocouple and shaft speed readings. When the pressure would increase no further, it was slowly reduced. Again readings were recorded. The recorded test parameters were discussed in **Section 6.3.1**. **Table 6.4** is a summary of the tests carried out.

Measurements of the torque required to turn the shaft (from rest) were made with two single thickness brush seals (of opposite hand) installed with a clearance and with interferences of up to 0.5 mm and seal differentials of up to 6.0 bar. The measurements were carried out using a calibrated spring balance. The balance was securely attached to a

position on the outer edge of the stepped rotor, a know distance away from the rotor axial centreline. The spring balance was then pulled vertically with a firm and constant load until the shaft began to rotate. The brush seal clearance fit readings were estimates of the forces required to overcome the shaft inertia and bearing friction. This value could be taken away from the values for interference fits to leave an estimate of the force required to overcome the frictional effect of interference fit brush seals. The additional force due to "blow down" could also be detected when the tests were carried out with a pressure differential applied.

An attempt was also made to monitor the shaft's dynamic vibrational characteristics with the brush seals rubbing on it (with and without a pressure differential applied) and with no seals installed at all. Accelerometers were mounted on the bearing pedestals and the response was recorded during operation.

Video recordings were made of the bristle pack movement during several tests, using a zoom lens. These recordings were made in an attempt to determine several visible features including, at what pressure differential "blow down" occurs, at what pressure differential the bristle backing plate/internal friction reduces to the extent that the bristles can to return to their unloaded position and the magnitude of the bristle radial movement expected for different test conditions.

Table 6.1 Brush seal leakage test rig rotor and seal fit details.

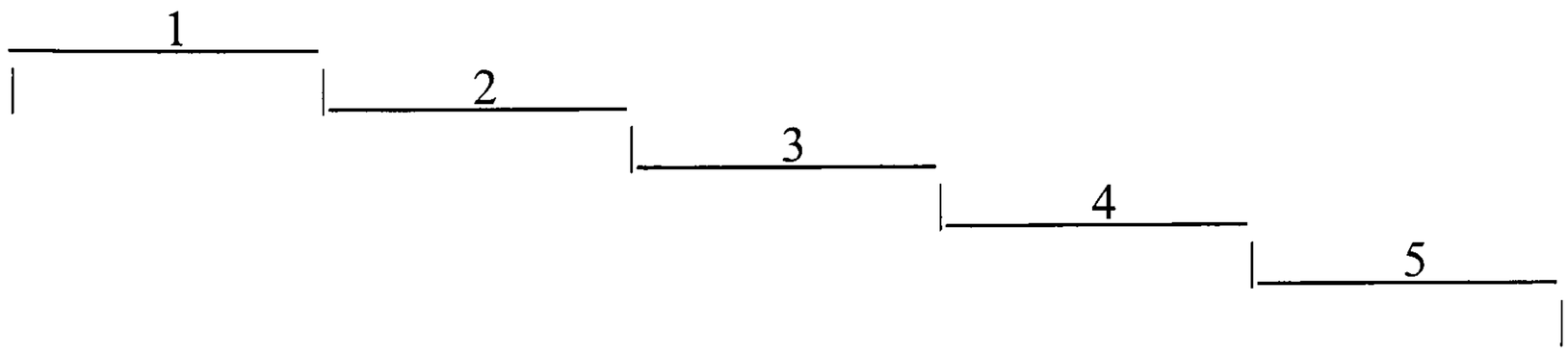

	Land 1	Land 2	Land 3	Land 4	Land 5
Rotor Diameter	328.0	327.4	327.0	326.0	325.2
Bristle Fit BSI/C*	-0.5	-0.2	0.0	+0.5	+0.9
Backing Plate Clearance BPC	0.4	0.7	0.9	1.4	1.8
Fin Clearance	N/A	N/A	0.18	0.68	1.08

All dimensions in mm.
BSI/C = Brush Seal Interference/Clearance.
BPC = Backing Plate Clearance.
* Note -ve = interference, +ve = clearance

Table 6.2 Brush seal leakage test rig 330 mm (13 inch) brush seal specifications.

Brush seals parameter	**Value**
Bristle Bore.	327 mm
Backing Ring Bore.	328.832 mm
Backing Ring Height.	14.4 mm
Backing Ring Outside Diameter.	357.632 mm
Bristle Overhang.	0.918 mm
Bristle Pack Thickness (single) (double).	≈ 1 mm ≈ 2 mm
Bristle Free Length.	16 mm
Backing Arrangement Thickness (single) (double).	3.9 mm 4.5 mm
Number of Bristles Wide (single). (double)	11 bristles wide 22 bristles wide
Number of Bristles per inch of circumference.	89 (2250) - 104 (2650) bristles per mm (inch) of circumference
Bristle Thickness.	$1.1e^{-4}$ mm
Bristle Angle.	45 degrees

Labyrinth Seal	**Value**
Fin Bore (design).	327.2 mm
Fin Bore (actual)	327.36 mm
Tip Width.	0.5 mm
Rake Angle.	15 degrees
Chamfer Height (vertical)	13.65 mm
Seal Outside Diameter	363.6 mm
Seal Thickness	5 mm

Table 6.3 Brush seal leakage test rig instrumentation.

Parameter	**Method**	**Position**
Atmospheric pressure	Wall barometer, pressure transducer	Wall next to rig
Atmospheric air temperature	Thermometer	Wall next to rig
Rig air temperature	Thermocouple	Rig body (internal)
Shaft speed	Thyristor drive digital control	Motor control panel
Orifice plate downstream pressure	Pressure transducer, pressure gauge, mercury manometer	In air pipe before rig.
Orifice plate up stream pressure	Pressure transducer, pressure gauge, water manometer	In air pipe before rig.
Rig pressure	Pressure transducer, pressure gauge	Rig body (internal)

Table 6.4 Estimation of experimental uncertainties.

Instrumentation/reading	Accuracy
Pressure transducers	+/- 0.005 bar 0.1 % (full scale deflection)
Pressure gauges	+/- 1 psi or +/- 0.07 bar
Barometer	+/- $0.5*10^{-5}$ mm, $6.8*10^{-4}$ bar
Orifice plates	In accordance with BS1042
Thermocouple	+/- 0.1 °C
Thermometer	+/- 0.5 °C
Manometer readings (Hg)	+/- $1*10^{-3}$ m, +/- $1.3*10^{-3}$ bar
Manometer readings (water)	+/- $1*10^{-3}$ m, +/- $1.0*10^{-4}$ bar
Orifice plate/brush seal/labyrinth fin dimensions	+/- $1*10^{-5}$m

Additional information
Orifice plate flow rate calculation (from dP) max. uncertainty 20% under low flow rate and low dP conditions.
Orifice plate flow rate calculation (from dP) average uncertainty 2% for all but low flow rate and dP conditions
Process data acquisition and control software - RTM 3500 Micro Speciality Systems v3.1
Results logged every 2 seconds
Standard acceleration: $g_n = 9.80665$ m/s
Standard atmospheric pressure: 1 atm = 1.01325 bar
Specific gas constant: R = 0.2871 kJ/kg K
Exponent of adiabatic expansion for air = 1.4
Calibrated spring balance +/- 1N

Table 6.4 Test Programme.

Seal Type	Speed	Land	Rotor Type	Offset
Labyrinth	0	3	Concentric	0
Labyrinth	0	4	Concentric	0
Labyrinth	0	5	Concentric	0
Labyrinth	1000	5	Concentric	0
Labyrinth	2000	5	Concentric	0
Labyrinth	3000	5	Concentric	0
Single BS	0	1	Concentric	0
Single BS	0	2	Concentric	0
Single BS	0	3	Concentric	0
Single BS	0	4	Concentric	0
Single BS	0	5	Concentric	0
Single BS	1000	1	Concentric	0
Single BS	2000	1	Concentric	0
Single BS	3000	1	Concentric	0
Single BS	1000	3	Concentric	0
Single BS	2000	3	Concentric	0
Single BS	3000	3	Concentric	0
Single BS	1000	5	Concentric	0
Single BS	2000	5	Concentric	0
Single BS	3000	5	Concentric	0
Single BS	0	2	Concentric	0.25
Single BS	0	3	Concentric	0.25
Single BS	0	3	Concentric	0.65
Single BS	0	3	Concentric	0.9
Single BS	0	4	Concentric	0.65
Double BS	0	1	Concentric	0
Double BS	0	2	Concentric	0
Double BS	0	3	Concentric	0
Double BS	0	4	Concentric	0
Double BS	0	5	Concentric	0
Single BS	0	2	Eccentric	0
Single BS	250	2	Eccentric	0
Single BS	500	2	Eccentric	0
Single BS	1000	2	Eccentric	0
Single BS	3000	2	Eccentric	0
Single BS	0	3	Eccentric	0
Single BS	1000	3	Eccentric	0
Single BS	2000	3	Eccentric	0
Single BS	3000	3	Eccentric	0
Single BS	0	4	Eccentric	0
Single BS	3000	4	Eccentric	0

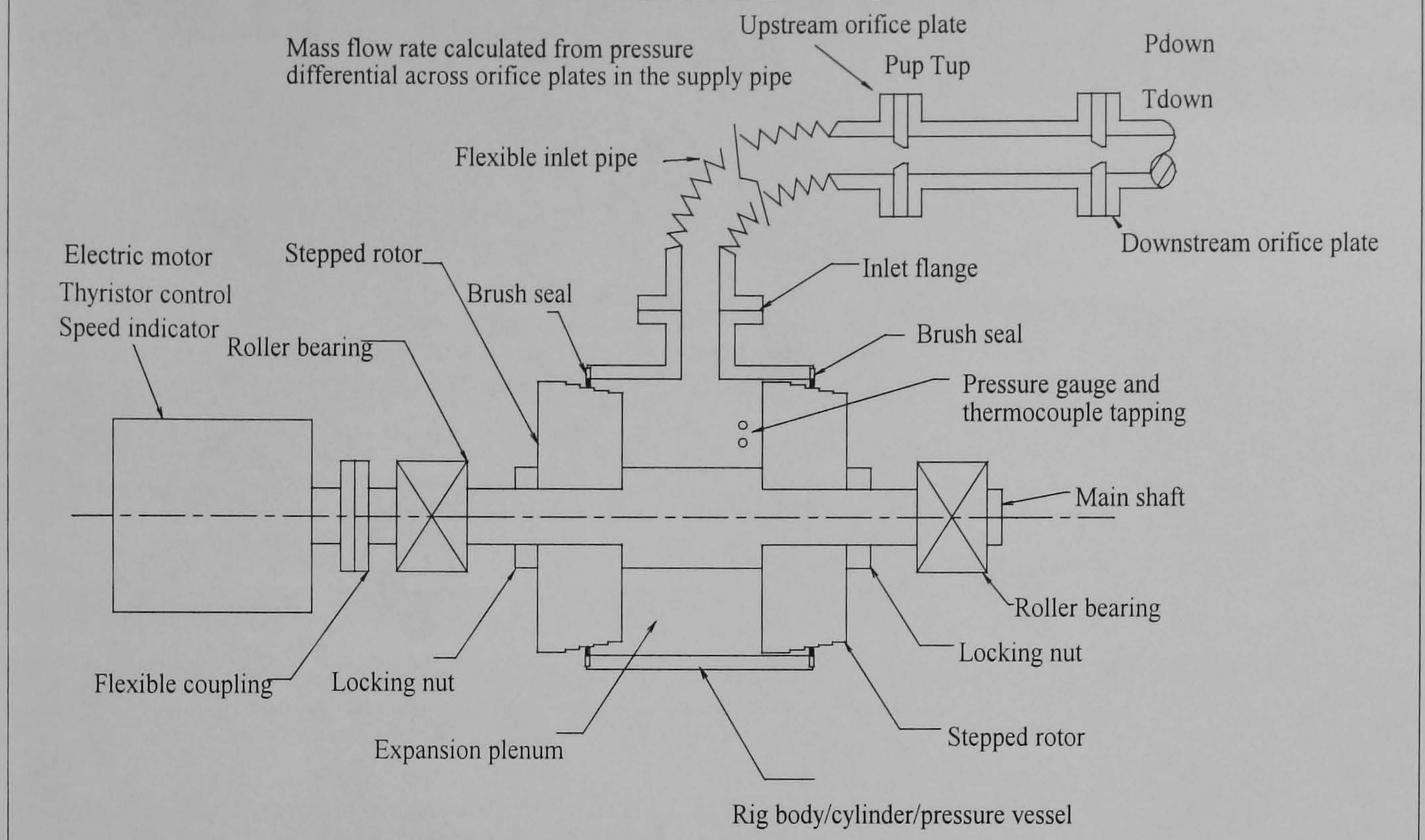

Atmospheric pressure and room temperature measured by a wall mounted transducer and thermocouple (and manually via a wall mounted barometer and thermometer).

Figure 6.1 Schematic of the brush seal leakage test rig.

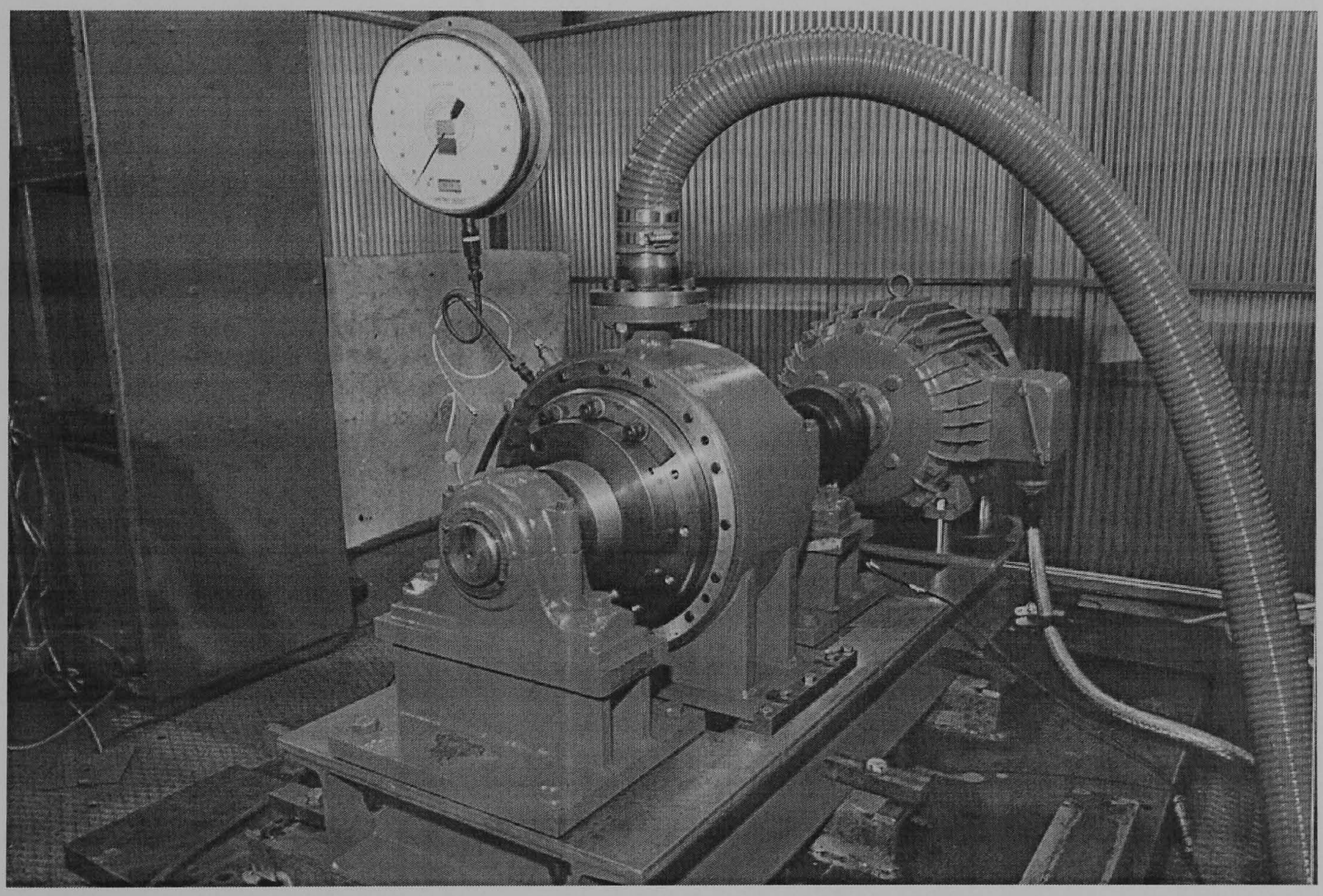

Figure 6.2 Photograph of the brush seal leakage test rig.

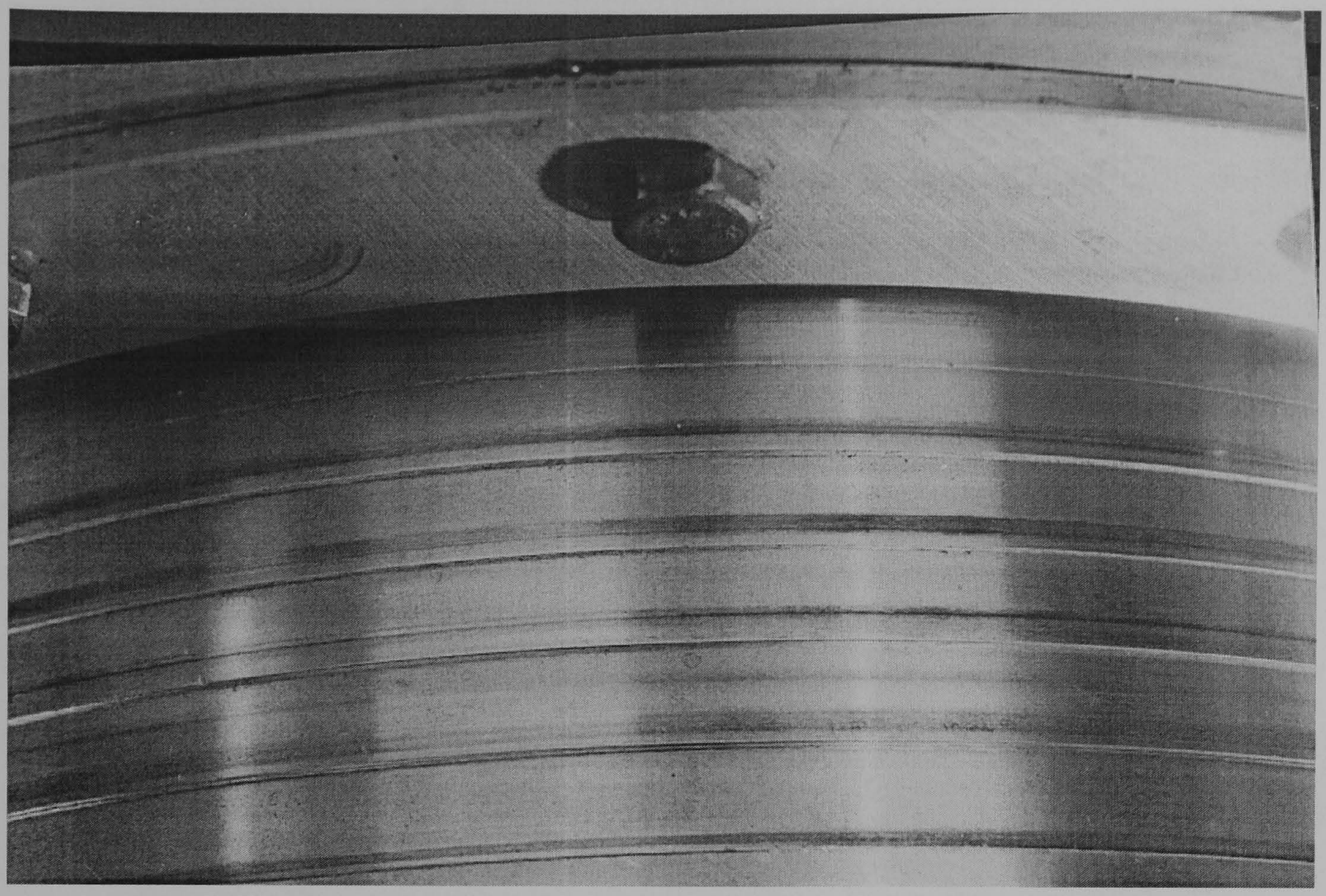

Figure 6.3 Photograph of the stepped rotor lands after testing showing wear tracks on all five lands.

7.0 Results, Discussion, Conclusions and Further Work: - Flow through Brush Seals.

The results of the experimental leakage testing are described, compared and discussed in this chapter. The results of groups of tests were compared with respect to different aspects of seal operating conditions or installation criteria. This chapter is split into five sections, the introduction **(Section 7.1)**, a description, discussion and comparison of experimental leakage test results **(Section 7.2)**, and a general discussion **(Section 7.3).** Conclusions are given in section **(Section 7.4)** and further work in section **(Section 7.5)**.

7.1 Introduction.

Visually inspected instrumentation (pressure gauges and thermometers) were recorded on log sheets and instrumentation that produced an electronic output signal (thermocouples, pressure transducers, and shaft speed) were recorded on a portable personal computer with a data acquisition card and data logging software **(Table 6.4)**. The results were incorporated in a spreadsheet. Leakage flow was then calculated from the BS1042 orifice plate equation, given the details of the orifice plate used, the pressure differential across the orifice plate and the temperature. The results were plotted as graphs showing leakage rate (kg/s) against pressure differential (bar). Three seals types were tested, a single fin knife edge labyrinth seal, a single thickness brush seal and a double thickness brush seal. The three seal types are described and discussed separately with subdivisions including results from rotating tests, off set rotor tests and eccentric rotor tests. The graph produced from the results are organised and presented in groups (on a single page) that are relevant to a single parameter of interest.

The base line set of labyrinth seal results (for the sake of comparison) are shown in **Figure 7.1.** These were from static tests at a range of clearances. The equivalent base line results for single and double thickness brush seals are given in **Figure 7.3** and **Figure 7.13**

respectively. The single fin labyrinth seal was included in these tests as a benchmark. The flow though single fin labyrinth seals is reasonably well understood and can be reliably predicted by theory. This enabled the test rig and instrumentation operation to be validated and the results re-calibrated if necessary. The single fin labyrinth test results also provided a means of directly comparing the brush seal leakage results to a standard seal of known performance on the same test rig.

The single thickness brush seal was of foremost importance in these tests. The double thickness seals were a more recent development and were of interest because of their improved sealing effectiveness compared to single thickness seals.

Every permutation of seal and operating condition tested is not given in the results section. Sufficient results are given to identify the general trends and these can be assumed to apply (where applicable) to the omitted results.

7.2 Description, Comparison and Discussion of Experimental Leakage Test Results.

7.2.1 The Single Fin Labyrinth Seal (Measured vs Calculated Leakage).

Figure 7.1 presents a comparison of measured and calculated flows for a single fin labyrinth seal. Three sets of results for stationary tests were produced for lands 3 (0.18 mm clearance), 4 (0.68 mm clearance) and 5 (1.08 mm clearance). The graphs were plotted with leakage rate (kg/s) against pressure differential (bar). The lines of results generated in each graph included the measured leakage rate, and two sets of calculated leakage rates. These were calculated using a single fin labyrinth seal leakage rate calculation given by **Kearton (1952), the St.Venent Equation (Equation 7.1).**

Assuming the flow through the constriction is isentropic.

$$\frac{W}{A} = \sqrt{\frac{2g\gamma}{\gamma - 1}\frac{p_o^2}{RT_o}\left\{\left(\frac{p_1}{p_0}\right)^{\frac{2}{\gamma}} - \left(\frac{p_1}{p_o}\right)^{\frac{\gamma-1}{\gamma}}\right\}} \qquad \textbf{Equation 7.1}$$

Where

W = Leakage mass flow rate (kg/s)

A = Effective leakage area (m^2) and includes the discharge coefficient C_d.

g = Acceleration due to gravity (m/s^2).

P_0 = Absolute upstream pressure (bar).

P_1 = Absolute downstream pressure (bar).

T_0 = Absolute upstream temperature (K).

R = Specific gas constant 0.2871 kJ/kmol.

γ = Exponent of adiabatic expansion (1.4 for air).

Kearton suggested the use of an empirically determined discharge coefficient with a maximum of Cd = 0.84. This coefficient was used to provide one set of calculated results and a further set was calculated using Cd = 1 as results using this coefficient more closely fitted experimental results.

An uncertainty analysis was carried out on the instrumentation required to provide the results to be used in leakage calculations. As a result of this analysis part of the discrepancy between the measured and calculated values could be explained by considering the experimental uncertainty in the measurement of the leakage flow rate. The uncertainty principally arose from the accuracy and operating range of the pressure transducers that were used to measure the pressure drop across the orifice plate. In the case of the smallest labyrinth flows the maximum uncertainty for leakage flows was in the order of 20 %. This rapidly reduced to approximately 2 % as the flow rate increased and the pressure differential across the orifice plate became larger. **Table 7.4** lists some of the experimental uncertainties.

Other sources of error included rig residual leakage, and non-circularity of the labyrinth fin. Both of these effects were minimal but were difficult to quantify. Oil contamination of the rig air supply was found to have a cumulative effect and could

contribute significantly to the sealing performance of brush seals. The effect is discussed in more detail in **Section 7.2.6**.

The top graph in **Figure 7.1** shows the results on land 3. Three separate lines were produced to compare the relationship between the measured and calculated results for leakage rate over a pressure differential range from 0.5 bar to 5.5. The three lines were linear and demonstrated that the calculated results using both discharge coefficients were lower than the measured results throughout the pressure range. At maximum pressure differential (5.5 bar), the measured leakage rate was 0.4 kg/s compared to 0.34 kg/s (Cd = 1) and 0.27 kg/s (Cd = 0.84). As the clearance increased on lands 4 and 5 the maximum obtainable pressure differential reduced to 3 bar and 2 bar respectively. The results for land 4 revealed an excellent agreement between the measured and calculated leakage rate using Cd = 1. The line using Cd = 0.84 was less comparable. At the maximum pressure (3 bar), the measured leakage mass flow rate was 0.65 kg/s, the calculated (Cd = 1) leakage rate was 0.64 kg/s and with Cd = 0.84 the leakage rate was 0.48 kg/s.

The plots on land 5 again indicate an excellent agreement for measured and calculated using Cd = 1, with a reduced agreement using Cd = 0.84. At 2 bar, the measured result and the calculated result using Cd = 1 was 0.8 kg/s, whilst the calculated result using Cd = 0.84 was 0.65 kg/s.

7.2.2 Brush Seal Behaviour with a Stationary Rotor and a Concentric Seal.

Figure 7.3 is a graph of the results comparing the static leakage rate through a single thickness brush seal for 5 seal fits. The fits are given in **Table 7.1.** The graphs for land 1, 2 and 3 indicated very similar results. The lines were reasonably linear, and during the tests there was a maximum leakage rate of between 0.07 kg/s and 0.09 kg/s at 5.5 bar. The plots for lands 1, 2 and 3 have little hysteresis but land 3 showed slightly more than land 1 and 2. The results from land 4 (the 0.5 mm clearance fit) revealed a dramatic change. The plot was not linear and the leakage rate increased to a maximum of 0.23 kg/s,

at a maximum pressure differential of 5 bar. A large hysteresis was also noticeable. Land 5 results displayed a similar pattern to land 4 but there was a maximum leakage rate of 0.37 kg/s at 4.5 bar during the tests.

Figure 7.13 highlights the leakage performance for stationary, double thickness brush seal for 5 seal fits. The trends were similar (but not the leakage rates) to those described for the single thickness seals in **Figure 7.3**. Lands 1, 2 and 3 results were linear with little hysteresis. There was a maximum leakage rate of 0.05 to 0.065 kg/s at 0.55 bar in those cases. Land 4 was still relatively linear but had a noticeable hysteresis. The leakage rate increased to 0.14 kg/s at a maximum pressure differential of 5 bar. Land 5 was again relatively linear with a hysteresis curve but the leakage rate increased to 0.23 kg/s at a maximum pressure differential of 3 bar.

A phenomenon known as bristle "blow down" effectively changed the size for size fit (on land 3) to an interference fit. At the start of the test (at zero pressure differential) the bristle fibres were in their normal position. The fibres adopted their production ground, internal diameter and lay angle, and were unloaded. As the pressure differential was applied (between 0 to 0.35 bar pressure differential), radial forces acted on the bristles. The bristles acted like cantilevers and the fibres were bent down towards the shaft outside diameter. The lay angle changed and the brush seal effective internal diameter was reduced. The bristle pack was sufficiently thick and resistant to fluid cross-flow to provide a degree of self-sealing due to the blow down. Radial and lateral forces were at a maximum at maximum pressure differential. These forces pushed the brush seal bristle pack against the backing plate. Bristle to backing plate, and internal bristle pack friction allowed the bristle pack to maintain its position when the pressure was reduced. The extra reduction in brush seal internal diameter allowed it a greater degree of sealing and hence the reduced leakage rate on depressurisation. The bristle pack only returned to normal when the seal pressure differential approached zero.

Blow down was observed in video recordings carried out on several clearance fit tests. Blow down started on pressure increase at approximately 0.35 bar (5 p.s.i.) and remained until approximately 0.35 bar (5 p.s.i.) on pressure decrease. No blow down appeared to occur in interference fit tests although realistically it was difficult to assess. Hysteresis due to blow down could therefore only be seen in set ups where the brush seal was positioned with an initial clearance. The video recordings show that the bristle pack blew down radially in clumps of bristles and adopted a saw tooth shape bore. This gradually became more concentric as pressure differential increased.

The results for lands 1, 2 and 3 in shown in **Figure 7.13** were similar in each test. The three bristle tip fits were a 0.5 mm interference, a 0.2 mm interference and a zero clearance. The backing plate clearances also changed with bristle fits and were 0.4, 0.7 and 0.9 mm respectively. The results therefore showed that for this seal geometry the leakage rate was reasonably independent of the backing plate clearance providing there was a bristle interference. If the brush seal geometry or interference range were to be altered this may no longer be the case. For example, if the backing plate length is reduced, increasing backing plate clearance, it may no longer provide the axial support required by the bristle pack under high pressure differential and the leakage rate may increase. If the backing plate length increases, to provide a low clearance, the backing plate alone would provide a very effective seal by choking the flow before it reaches the brush seal.

7.2.3 Brush Seal Behaviour with a Stationary Rotor and a Seal Off Set.

The effect of rotor off set on brush seal leakage is shown in **Figures 7.5, 7.6** and **7.7**. **Figure 7.5** demonstrates the effect of a 0.25 mm off set with the brush seal installed on land 2. For this set up the off set was approximately equal to the installed interference. The base line plot and the off set plot show that during these tests the maximum leakage rates were reasonably similar at between 0.065 kg/s to 0.07 kg/s at 5.5 bar. This was expected as the brush seal was in contact with the rotor throughout the test.

Figure 7.6 shows a more comprehensive range of off sets including 0, 0.25, 0.625 and 0.9 mm for a single thickness seal fitted on land 3. Land 3 was nominally a size for size fit at zero pressure differential, however blow down changed the fit to interference when the seal had a pressure differential imposed upon it.

The 0 and 0.25 mm off set plots were similar. They were linear with relatively little hysteresis. They have a maximum leakage rate of 0.09 kg/s at 5.5 bar. These results demonstrated that blow down was equal to or greater than 0.25 mm and it occurred at the beginning of the test and remained until the end.

The 0.625 mm off set test results showed a slightly increased hysteresis and that there was a maximum leakage rate of 0.11 kg/s and a reduced maximum pressure of 5 bar. This plot indicated that blow down was occurring (hence the hysteresis). The bristles were not able to achieve full seal contact or the porosity of the blown down area was reduced, compared to the normal bristle orientation. The most effective range of blow down appeared to be between 0.25 mm and 0.625 mm.

The final plot of the group shows the maximum off set achievable under static conditions. The rotor had an off set of 0.9 mm which caused the brush seal backing plate to touch the rotor opposite the off set. Hysteresis was evident and there was an increase in maximum leakage rate to 0.16 kg/s at 5 bar. The leakage rate was roughly twice that of the concentric seal. Blow down could not maintain a bristle contact and a clearance was visible.

Figure 7.7 reveals the effect of a 0.625 mm static rotor off set on a single thickness brush seal on land 4. Land 4 had a concentric clearance of 0.5 mm. Therefore the off set was approximately equal to the installed clearance. The concentric plot had the characteristic hysteresis due to bristle blow down and showed a slight deviation from linear. A maximum leakage rate of 0.23 kg/s at 5 bar was recorded. The 0.625 mm off set plot was a linear result, again with a hysteresis. The leakage rate increased to 0.27 kg/s at 4.5 bar. The increase in leakage rate could be explained by the slightly greater off set than

clearance. However, even if the off set equalled the clearance, the off set would still prevent blow down in that portion of the seal and effectively reduce the maximum blow down area achievable.

7.2.4 Comparisons of the Leakage through the Brush and Labyrinth Seals with a Stationary Rotor.

Comparisons between the single fin labyrinth and the single and double thickness brush seals (with a stationary shaft) are shown in **Figure 7.14**. Seal fits for relatively similar fin and backing ring clearances were chosen for comparison.

The first column in **Figure 7.14** are results graphs that compare the three seals at clearances of approximately 0.7 mm. A backing ring clearance of 0.7 mm gave a bristle tip interference of 0.2 mm. The plot of the measured fin leakage rate showed that the leakage rate was at a maximum of 0.7 kg/s at 3 bar. The single thickness seal had a significantly lower leakage rate of 0.04 kg/s at 3 bar and reached a maximum of 0.07 kg/s at 5.5 bar. The double thickness brush seal had an even greater reduction to 0.03 kg/s at 3 bar and a maximum of 0.06 kg/s at 5.5 bar. Both brush seals had linear plots with very little hysteresis. That was expected for an interference fit.

The second column of graphs in **Figure 7.14** allows a comparison of the results from three seals with a clearance of approximately 1 mm. The brush seal bristle pack had a nominal, size for size fit with a backing plate clearance of 0.9 mm. The labyrinth fin reached a maximum leakage rate of 0.8 kg/s at 2 bar. The single thickness brush seal demonstrated a leakage rate of 0.04 kg/s at 2 bar and reached a maximum of 0.09 kg/s at 5.5 bar. The double thickness brush seal had a leakage rate of 0.025 at 2 bar and a maximum of 0.065 at 5.5 bar. Again the brush seal plots were linear and had very little hysteresis.

The results demonstrated that brush seals offered a substantial improvement over single fin labyrinth seals when the fin clearances and backing plate clearances were similar.

For a clearance of 0.7 mm the single thickness brush seal provided a leakage reduction of 94 % and the double thickness seal provided a reduction of 96 %. At the clearance of approximately 1 mm the reductions were slightly greater at 95 % for the single thickness seal and 97 % for the double thickness seal.

The slight improvement at the greater clearance for these sets of results was expected because the labyrinth seal fin clearance enlarged allowing a higher leakage rate but the bristle pack was still in contact with the rotor, albeit at a slightly reduced sealing capacity. **Ferguson (1988)** made claims of a 90 % reduction in the leakage rate of brush seals over a five fin labyrinth seal for a range of interferences and clearances. The leakage rate through labyrinth seals is proportional to the square root of the number of fins. The results for the single thickness brush seal are therefore in line with **Ferguson's** claims.

Double thickness seals offered a slight improvement in sealing over single thickness seals for the tests shown in **Figure 7.13**. The improvement was approximately 2 %.

Further comparisons between the three seal performances could be drawn from **Figure 7.1**, **Figure 7.3** and **Figure 7.13**. The initial comparison between the labyrinth seal and brush seals compared fin tip clearance and backing plate clearance. Fin tip clearance and approximately the same bristle tip clearances were also compared. Results from land 3 at 5.5 bar showed the labyrinth seal had a leakage rate of 0.4 kg/s, the single thickness brush seal had a leakage rate of 0.09 kg/s and the double thickness brush seal had a leakage rate of 0.065 kg/s. Those were improvements of 78 % and 84 % respectively. On land 4 the leakage rates at 3 bar were 0.7 kg/s for the labyrinth seal, 0.175 kg/s for the single thickness brush seal and 0.11 kg/s for the double thickness brush seal. Those were improvements of 75 % and 84 % respectively. Finally on land 5 the labyrinth seal leakage rate was 0.85 kg/s at 2 bar whilst the single fin leakage rate was 0.275 kg/s and the double thickness brush seal was 0.2 kg/s. Those improvements were 68 % and 76 % respectively.

These results showed that even with an unfavourable comparison of labyrinth fin tip to brush seal bristle bore the brush seal offered a substantial improvement over a single fin labyrinth seal. For these tests the improvement was in the region of 70 % for the single thickness brush seal and 80 % for the double thickness brush seal.

The seal installation requirements meant that the labyrinth seal in some cases had a slightly larger clearance that the brush seal. This would obviously account for part of the improvement. However it was clear from the results that the bristle pack was an effective seal up to and past nominally size for size fits. Slight reductions in sealing for the brush seals were noted when moving from land 1 to land 2 and then land 3 **(Figure 7.13)**. In the interference fit range the leakage rate was low and was slightly effected by backing plate clearance. For clearance fits, blow down was shown to be in the order of 0.9 mm at 3 bar **(Figure 7.4)** but the extra area provided by blow down was reduced in sealing capacity compared to the design seal bore. The greater the blow down the less effective the extra sealing capacity. **Figure 7.3** and **Figure 7.13** show that the leakage rate went up substantially (doubled) when the fit moved from size for size to 0.5 mm clearance.

With installed clearances the leakage rate was thought to be related to the bristle tip clearance (including the extra, but reduced, beneficial effect of bristle blow down). Fluid could effectively flow under the seal rather than travel through the bristle pack.

7.2.5 Brush Seal Starting Torque.

Figure 7.4 shows the torque required to turn the rotor from rest for three different seal fits (0.5 mm interference, **Land 1**, size for size, **Land 3**, 0.9 mm clearance, **Land 5**) with two single thickness brush seals installed on the rig. These tests showed that both the degree of interference and the applied pressure differential substantially affected the friction of the seals and therefore the starting torque and possibly operating contact pressure and wear rate.

The top graph presents the results from land 1. The initial torque with zero pressure differential applied was 2.3 Nm. This was due to the installed interference, shaft inertia and bearing friction. The torque rose linearly up to 5 Nm at a pressure differential of 2 bar. A slight drop then followed to 4.5 Nm at 3 bar after which the torque increased linearly to a maximum of 6.5 Nm at 5 bar.

The plot generated from the results on land 3, the size for size seal fit showed that at zero pressure differential a torque of 1.1 Nm was required to rotate the shaft. The torque then rose linearly to a maximum of 3 Nm at 5.5 bar.

The final plot generated was of results from land 5. The readings started at zero pressure differential with a torque of 0.58 Nm. The torque then remained at approximately 0.6 Nm until a pressure differential of approximately 2 bar. At this point the torque rose dramatically to 0.8 Nm at 3 bar.

The final graph was revealing and will be discussed first. The brush seal was installed with a bristle pack clearance of 0.9 mm. Initially there was a visible seal clearance and the starting torque at zero pressure differential was approximately 0.6 Nm. This torque was not due to brush seal contact, but was due to rotor shaft inertia and bearing friction. When the pressure differential reached 2 bar, bristle blow down was sufficient to cause the bristle tips to touch the rotor surface. The torque dramatically rose to 0.8 Nm. Once the bristles were touching the shaft the torque would be expected to rise in a reasonably linear manner until the bristles were blown down as far as possible (given the stiffness of the bristle material).

The middle graph showed that the combined effect of brush seal interference, bearing friction and shaft inertia required a torque of 1.1 Nm to turn the shaft from stationary with zero pressure differential. Bristle to shaft friction must have contributed approximately 0.5 Nm as the bottom graph showed that 0.6 Nm was required to turn the shaft when there was no contact. A size for size fit implies that contact forces and friction were zero. However the nominal internal diameter may have reduced slightly due to small

amounts of residual internal bristle pack friction and contamination. When a pressure differential was applied blow down occurred. The contact forces and torque required to turn the shaft then rose in a steady linear fashion with increased pressure differential.

The top graph was unusual and the irregularity may have been due to experimental or operator error. The 2 Nm starting torque at zero pressure differential had a component due to bristle pack contact of 1.4 Nm. The brush seal had a substantial 0.5 mm initial interference so the graph would have been expected to be linear with increasing pressure differential. The drop in torque at 3 bar may have been due to a seal installation problem. When the brush seal was installed the bristle pack may have been splayed axially, causing the bristles to jam under the backing plate. This would have caused an increase in torque, as the bristles were unable to flex in their designed direction. Three short turns may have been sufficient to flex the bristle pack and allow it to return to its designed orientation.

The results from the tests carried out on **Lands 1 and 3** indicated that the increase in deflection, contact pressure and friction due to the bristle movement was approximately linear with pressure increase from atmospheric. The results from **Land 5** appeared to indicate that the seal did not blow down sufficiently to contact the rotor until a pressure differential of 3 bar. Until then the torque required was only to overcome inertia and friction in the rotor bearings. The tests clearly showed that "blow down" could be in the order of 0.9 mm radially. However **Figure 7.3** showed that whilst blow down could occur in seals with an installed clearance the movement was not necessarily uniform. The additional movement due to "blow down" had a reduced sealing effect (in current seal designs) compared to the non-pressurised (not "blown down") bristle overhang.

7.2.6 Brush and Labyrinth Seal Behaviour with a Rotating Rotor.

The measured leakage flows through the single fin labyrinth on land 5 with a rotating shaft are given in **Figure 7.2**. Tests were carried out at 0, 1000, 2000, and 3000 r.p.m. The results were plotted and showed that in all cases the leakage rate started at 0.3

kg/s at 0.5 bar and reached a maximum of 0.8 kg/s at 2 bar. The plots were linear and relatively similar, within experimental error.

Figures 7.8-7.10 are graphs showing the effect of leakage rate on a single thickness brush seal due to shaft rotation at 0, 1000, 2000, and 3000 r.p.m. Leakage rates were plotted against differential pressure for three different seal fits (0.5 mm interference-land 1, size for size-land 3, 0.9 mm clearance-land 5). Only very small leakage variations could be seen with speed. **Figure 7.8** presents the results from land 1. A maximum leakage rate of 0.015 kg/s at 6 bar was experienced for the four speeds tested. **Figure 7.9** displays the results from land 3 at 0, 1000, 2000, and 3000 r.p.m. The three plots with rotation had very similar results and showed that there was a maximum leakage rate of 0.07 kg/s at 6 bar. The plot with a stationary rotor however showed that there was a slightly increased leakage rate of 0.08 kg/s at 6 bar. **Figure 7.10** presents the four plots for rotating tests on land 5. Again the three sets of rotating results recorded were relatively similar to each other. They reached a maximum leakage rate of between 0.35 kg/s and 0.4 kg/s at 0.35 bar. The stationary plot reached a maximum at just over 0.45 kg/s at 3.5 bar.

The four graphs given in **Figure 7.10** revealed that the brush seal developed a substantial hysteresis when it was tested with a 0.9 mm clearance. The leakage rate as the test pressure was slowly increased, was greater than the leakage rate at the same pressure when the pressure was slowly decreased. At 2 bar the leakage rate was approximately 0.4 kg/s on pressure increase. On pressure decrease the leakage rate was 0.25 kg/s at 2 bar. The hysteresis observed in **Figure 7.10** could be explained by bristle blow down.

The slight reduction in leakage rate due to shaft rotation that was seen in the brush seal clearance fits during testing **(Figure 7.9** and **Figure 7.10)** may have been due to windage. The motion of the shaft caused turbulence, eddying and flow of boundary layers in the direction of the shaft rotation under and after the bristle pack. The fluid flow through the seal encountered the turbulence and flow normal to its direction of travel and was slowed down very slightly. The reduction in velocity effectively reduced the leakage rate

through the seal. Reduction in leakage due to rotation was not apparent for the labyrinth seal **(Figure 7.2)** or the brush seal fit with an interference fit **(Figure 7.8)**. This may have been due to two factors. The leakage rate for the brush seal was extremely low and therefore subject to a degree of experimental error that may mask the rotation effect. The clearance in the labyrinth seal test was relatively large and rotor rotation may only effect a relatively small clearance (i.e. windage is confined to thin boundary layers).

It was noted that the measured leakage for the static, concentric, single thickness interference fit brush seal in **Figure 7.8** was substantially reduced to that seen during the static tests in **Figure 7.3**. This was due to the seal becoming clogged with oil from the test air line. This was confirmed by washing the seals and repeating the test and observing that they returned to their original condition for a short period of time. After which visual inspection confirmed that they were once again clogged with oil. It was not possible to assess how successful or complete the washing procedure had been. Ultra-sonic cleaning was recommended between future tests.

7.2.7 Vibrational Characteristics.

An attempt was made to investigate the dynamic implications of a contacting brush seal rubbing on the rotor. Accelerometers were attached with magnets to the rig's pedestals (or as close as possible to the pedestals) and run-downs were monitored with;

i.) no seals installed, no air in the rig

ii.) single thickness brush seals, 0.5 mm interference, 4 bar (60 p.s.i.) pressure differential.

The two run-downs were plotted as waterfall plots and are given in **Figures 7.11-7.12**. There was little difference between the two run-down reponses. At 3000 r.p.m. vibration readings were also taken with the brush seals operating on land 1 (0.5 mm interference) with and without a 4 bar (60 p.s.i.) pressure differential applied across the single thickness brush seals. The results are given in **Table 7.1**. For this particular rotor system the presence of a contacting brush seal did not affect it's dynamic characteristics

however it should be noted that the rig's rotor was supported on rolling element bearings, which were infinitely stiff compared to the plain bearings used on large steam turbines. It was not known how applicable these observations (made on the rig) were to HP steam turbine rotors.

7.2.8 Brush Seal Behaviour with an Eccentric Rotor.

Figure 7.15 shows the effect of a 0.50 mm (peak to peak) rotor eccentricity on the leakage rate for a 0.2 mm bristle interference fit (land 2) for a single thickness brush seal. The four graphs with shaft rotation at 250, 500, 1000 and 3000 r.p.m. demonstrated similar trends. They are reasonably linear with a small amount of hysteresis and with a showed that there was a maximum leakage rate of 0.09 kg/s at 5.5 bar. The static result was again linear with a small amount of hysteresis but the leakage rate at 5.5 bar was smaller at 0.055 kg/s.

Figure 7.16, the eccentric tests with a size for size fit (land 3) shows a similar trend to **Figure 7.15**. All the rotating tests had a leakage rate of 0.12 to 0.14 kg/s at 5 bar compared to the static leakage rate of 0.09 kg/s at 5 bar.

When the installed clearance was increased to 0.5 mm (land 4), a slight difference in the results trend was apparent **(Figure 7.17)**. The leakage rate was similar in magnitude at 0.3 kg/s at 4.5 bar (maximum pressure differential) with static and rotating eccentric tests. The static test plots however had a large hysteresis curve compared to the rotating one and therefore a lower leakage rate on depressurisation.

When the results of the eccentric brush seal rotor tests were examined several general trends were observed. As the installed interference **(Figure 7.15)** was increased to size for size **(Figure 7.16)** and then clearance **(Figure 7.17)** the leakage rate increased. In the case of the interference and size for size fits, the seal clearly leaked more during rotating tests. This was because the rotor eccentricity had a sweeping effect on the brush seal that could be clearly seen in the video recordings carried out (at low speed). The

eccentricity caused a constant flexure of the bristles (adjacent to the positive eccentricity), that were radially displaced. The bristles should have returned to their original position after the rotor sweep however there may have been a time lag due to inter-bristle and bristle to backplate internal friction. The bristle deflection and lag time for return may have allowed a larger leakage area to occur and an increase in the leakage rate.

It was found however, that once rotating, the specific speed did not effect the leakage rate significantly. The tests carried out with a clearance **(Figure 7.17)** showed little change in leakage rate from stationary to rotating tests but there was a marked reduction in the hysteresis in the rotating tests. The eccentricity and clearance were nominally equal at 0.5 mm, however bristle blow down would generate a slight interference. The rotation would tend to brush an area of bristle pack and flex the bristles. This motion may have allowed the bristles to overcome internal bristle pack and bristle pack to backing plate friction and return to the leakage rate achieved on the pressure increase.

Comparison with previous tests with a concentric rotor were not possible because of the changes in leakage characteristics due to the effect of oil contamination. This could be seen when the results of the eccentric tests were compared to the single thickness results from the identically handed concentric tests. The static **Land 2** eccentric results **(Figure 7.15)** showed a reduced leakage rate compared to the concentric results **(Figure 7.3)**. This could only be explained by reduced leakage due to oil contamination. The **Land 3** static concentric **(Figure 7.3)** and eccentric **(Figure 7.16)** leakage tests were similar in magnitude. This was irregular given that the seal was contaminated. This was explained by oil contamination reducing the leakage rate and an increase in leakage area (due to the eccentricity) increasing the leakage rate. The **Land 4** static eccentric leakage rate **(Figure 7.17)** was greater than the **Land 4** concentric leakage rate **(Figure 7.3)**. Three effects again explained this. There was a reduced leakage rate through the bristle pack due to oil contamination, but a reduced dependency on the leakage through the brush seal bristle pack (as opposed to under it) due to the installed clearance. There was also a slight increase in

the actual clearance (under pressure due to blow down) because of the eccentricity compared to the concentric tests. This was because the eccentricity prevented "blow down" at the point of contact.

7.3 General Discussion.

It was demonstrated that brush seals offered considerable reductions in leakage flows, compared to a single fin labyrinth seals. They operated quite satisfactorily at differential pressures of up to 6.0 bar and with backing ring clearances of up to 0.9 mm. These were appropriate pressure differential and clearance conditions for simulating the first few blade rows in a HP steam turbine. This was where their application was thought to be the most cost effective **(Waite (1994))**. The test programme was of a short duration (approximately 10 hours of rotating tests) and whilst it can be reported that during this period bristle damage/wear and rotor wear were minimal it could not be claimed that the question of seal life was addressed in these tests. The rotor developed a polished track on all lands **(Figure 7.3)** but no measurable wear or change in surface finish could be detected. The appearance of the bristle ends (which form the seal bore) did not change significantly during the tests.

7.4 Conclusions.

i.) The leakage through a single thickness brush seal, which had a backing ring bore which was 1.8 mm larger than the bristle bore, when installed with a bristle interference (of less than 0.5 mm), was approximately 5 % of that through a single fin labyrinth seal which had a similar fin bore to that of the brush seal's backing ring.

ii.) The leakage through a double thickness brush seal, which had a backing ring bore which was 1.8 mm larger than the bristle bore, when installed with a bristle interference (of less than 0.5 mm), was approximately 3 % of that through a single fin labyrinth seal which had a similar fin bore to that of the brush seal's backing ring.

iii.) Both single and double thickness brush seals operated quite satisfactorily over the period of the test programme at pressure differentials of up to 6.0 bar, with backing ring clearances of up to 0.9 mm.

iv.) The leakage through the brush (and the labyrinth) seals were not significantly affected by the test rig's journal rotation (apart from the eccentric rotor tests).

v.) The effect of an off set rotor on the leakage through the brush seals only became significant when an installed bristle clearance or interference was exceeded.

vi.) The effect of an eccentric rotating (between 0 to 3000 r.p.m.) rotor on leakage was to increase the leakage rate for installed interferences and size for size fits. The effect became less significant when there was an installed seal clearance and the percentage flow through the bristle pack was reduced. Eccentricity did tend to reduce hysteresis in the case of an installed stationary clearance compared to the similar rotating case.

vii.) Hysteresis in the leakage rate versus pressure differential curve was noted due to bristle "blow down", and inter-bristle friction locking the pack in that position. The bristles remained locked until the pressure differential was removed. The leakage rate was lower on initial pressure increase compared to the pressure decrease.

viii.) Leakage through (as opposed to under) the brush seal bristle pack only appeared to be significant when there was an installed interference or small clearance that would be removed by bristle "blow down", and the pack effectively acted as a labyrinth fin with the "blown down" clearance.

ix.) Brush seals, when installed with an interference were sensitive to contamination; in the test programme their leakage characteristics were enhanced by a factor of six when they became choked with oil. When installed with a clearance the total seal leakage (through and under the seal) was unaffected by the oil. This implied that when there was a seal clearance the bristle pack acted as an effective labyrinth fin even without oil contamination.

x.) In the case of the test rig's rotor, which was supported on rolling element bearings the presence of a contacting brush seal (with an applied pressure differential of 4.0 bar (60 p.s.i.)) did not affect it's dynamic characteristics.

7.5 Further Work

i.) The effectiveness of a split or segmental seal, which would be suitable for installation into a HP steam turbine, still needs to be demonstrated. Such seals could be manufactured by Cross Manufacturing and have been tested by CAE Teledyne with promising results.

ii.) The feasibility of running a brush seal against a discontinuous surface needed to be considered. If it is feasible then the seals could be applied as "cylinder to rotating blade tip seals" in steam turbines.

Table 7.1 Comparison of Pedestal Vibration Data with and without 60 psi Pressure Differential Applied Across the Single Thickness Brush Seals at 3000 rpm.

Speed (rpm)	Gas Press (psi	Pedestal Vibration.											
		Drive end ,vertical			Drive end, horizontal			Free end, vertical			Free end, horizontal		
		Tot. µm.	Fund. (Pk-Pk)	Ang.	Tot. µm.	Fund. (Pk-Pk)	Ang.	Tot. µm.	Fund. (Pk-Pk)	Ang.	Tot. µm.	Fund. (Pk-Pk)	Ang.
2986	60	14	9	70	14	8	54	19	15	86	29	27	51
2994	60	15	8	80	19	9	43	20	14	87	31	28	52
2996	60	14	8	72	16	7	54	21	13	83	31	28	53
2996	60	14	8	76	16	7	56	20	14	84	31	28	51
2996	60	14	8	71	17	8	58	21	14	84	31	28	51
2996	60	15	8	75	14	8	54	20	14	82	30	27	49
2996	60	14	9	74	13	7	58	19	14	85	30	27	50
2995	60	14	8	73	14	7	52	20	14	86	31	27	48
2994	0	15	8	79	16	8	48	19	13	86	29	26	51
2994	0	14	8	76	15	8	52	19	13	84	30	27	50
2994	0	15	8	80	15	8	54	20	14	84	30	27	49
2994	0	14	8	74	15	8	49	19	14	83	30	28	50
2994	0	14	8	78	15	8	40	19	13	82	31	27	50
2994	0	14	8	74	16	8	52	0	14	87	30	27	50
2994	0	14	8	76	16	7	47	20	14	83	30	27	50
2994	0	14	8	78	16	8	51	18	13	87	30	27	51

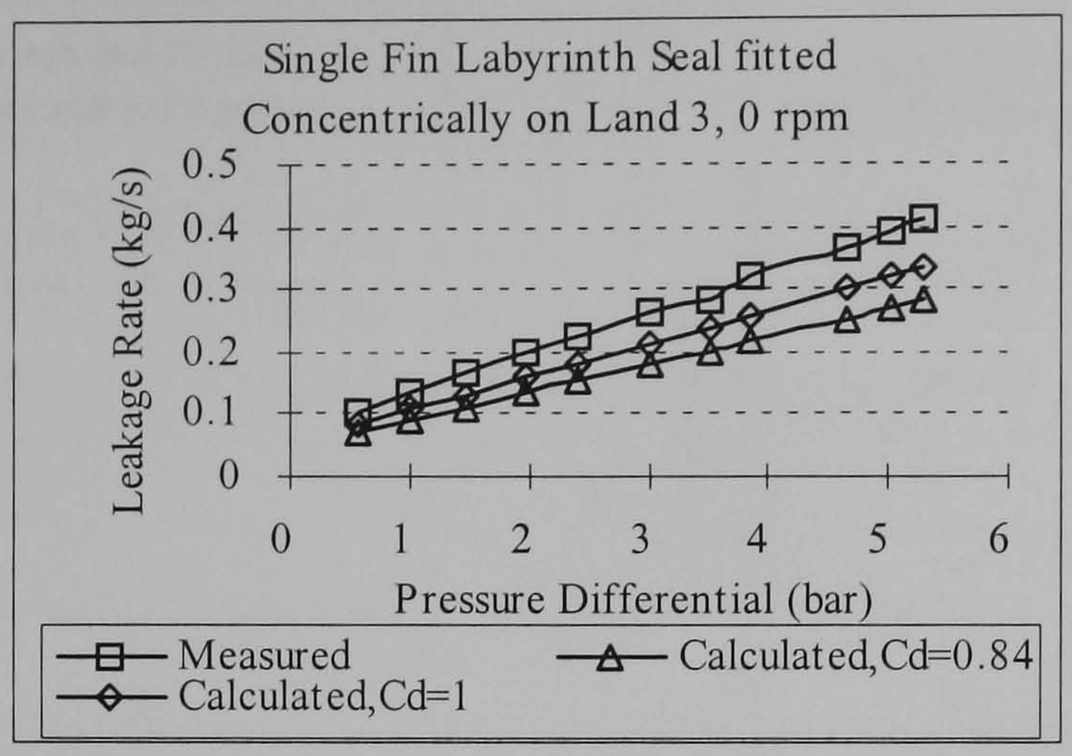

Figure 7.1 A Comparison of measured and calculated leakage flows for a single fin labyrinth seal.

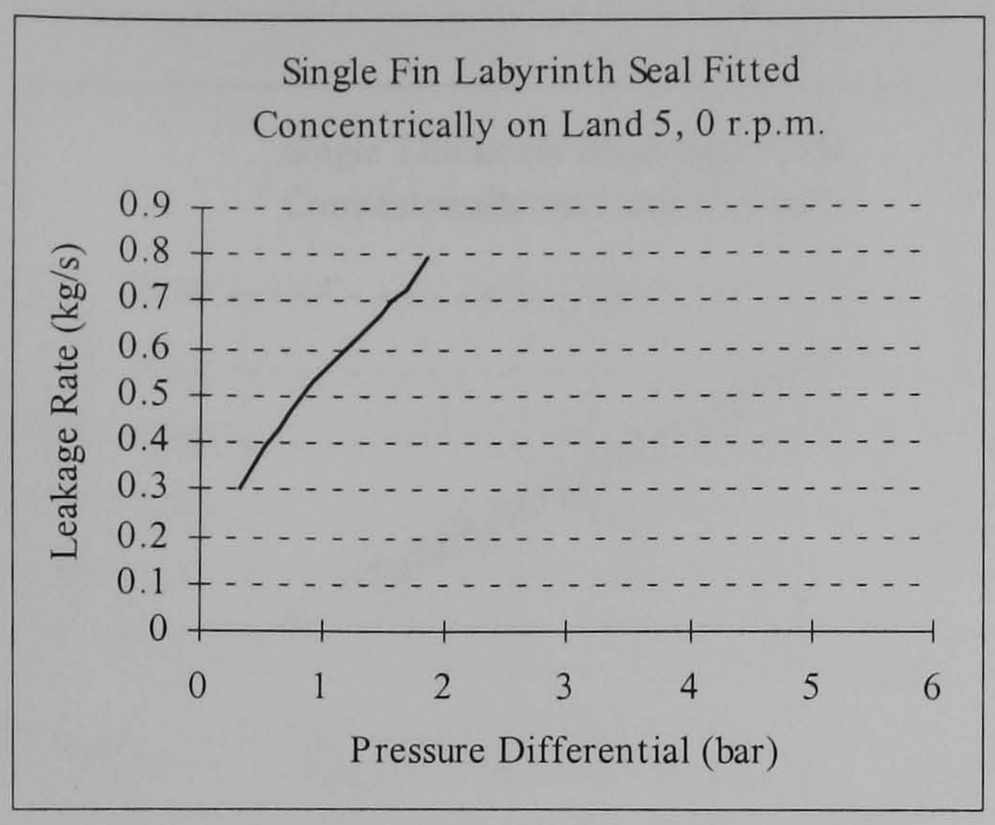

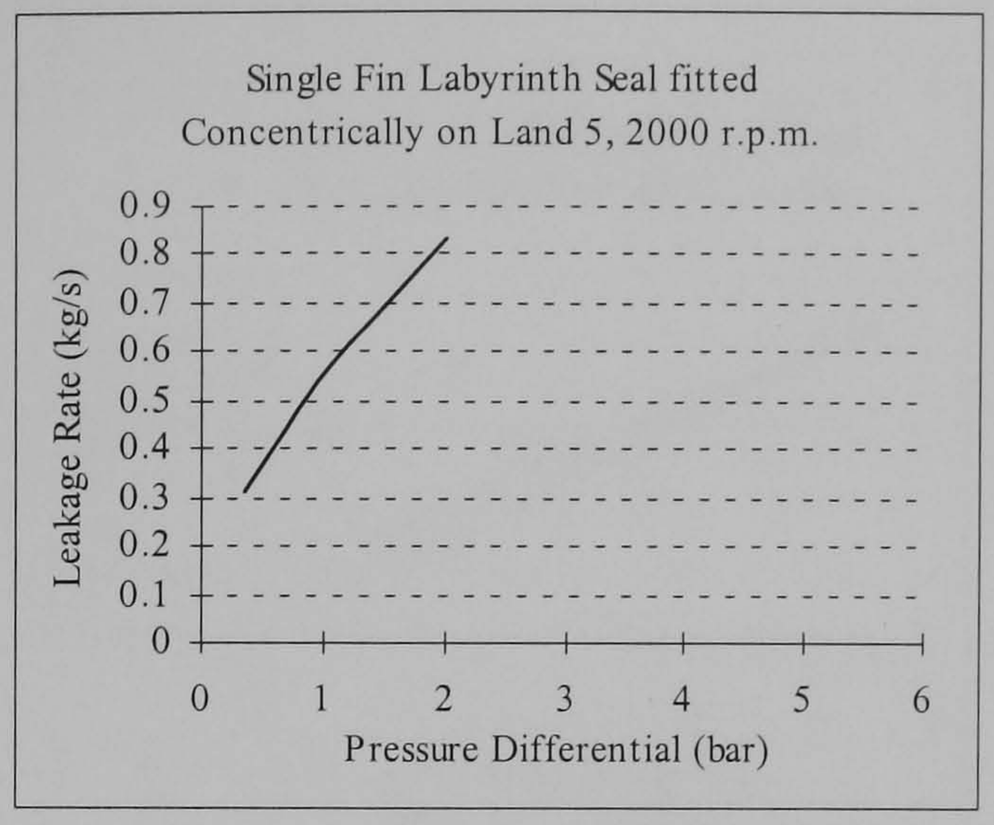

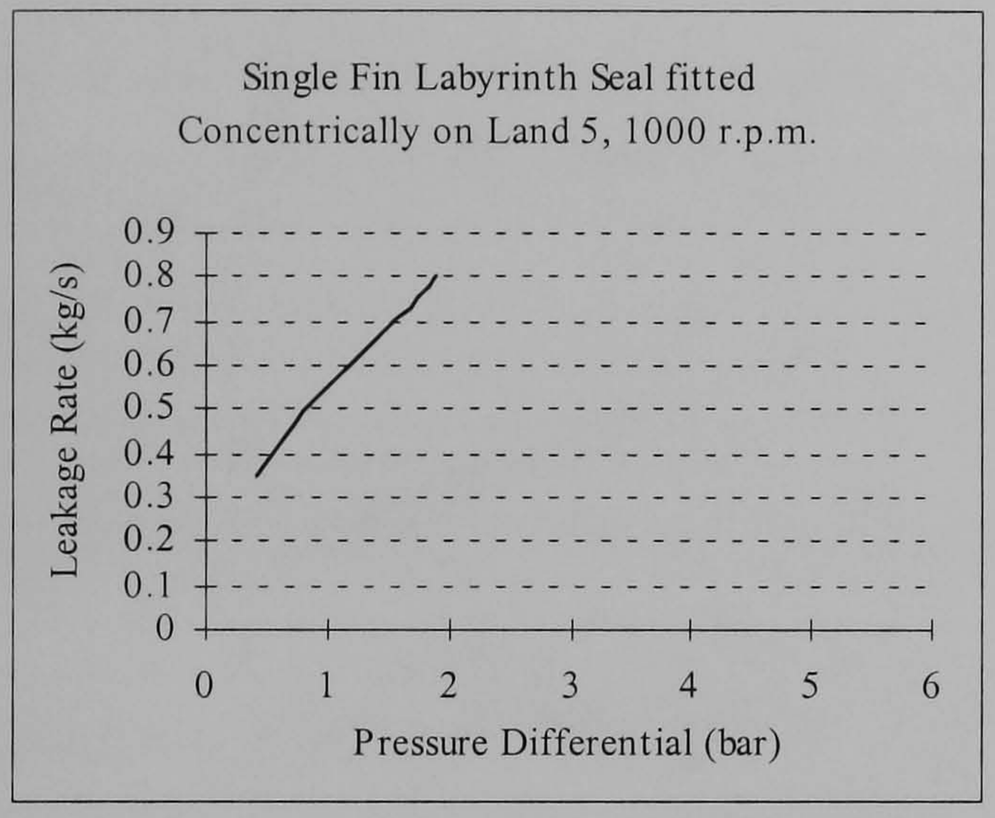

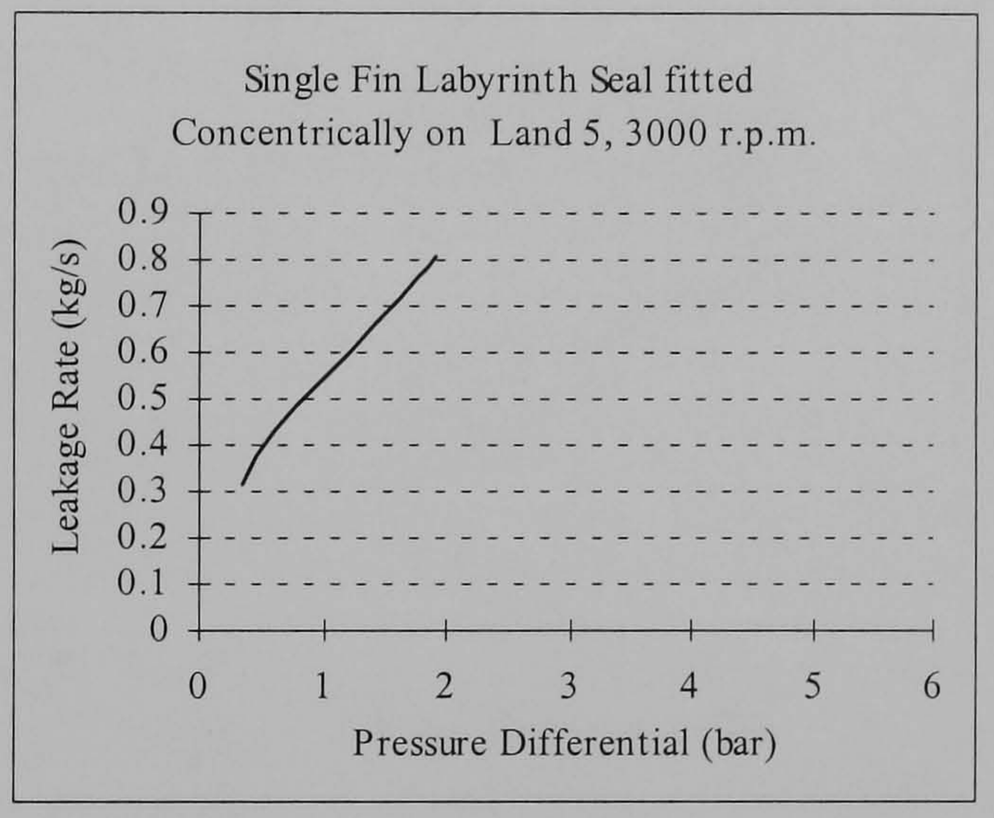

Figure 7.2 Measured flows for a single fin labyrinth seal with a rotating shaft.

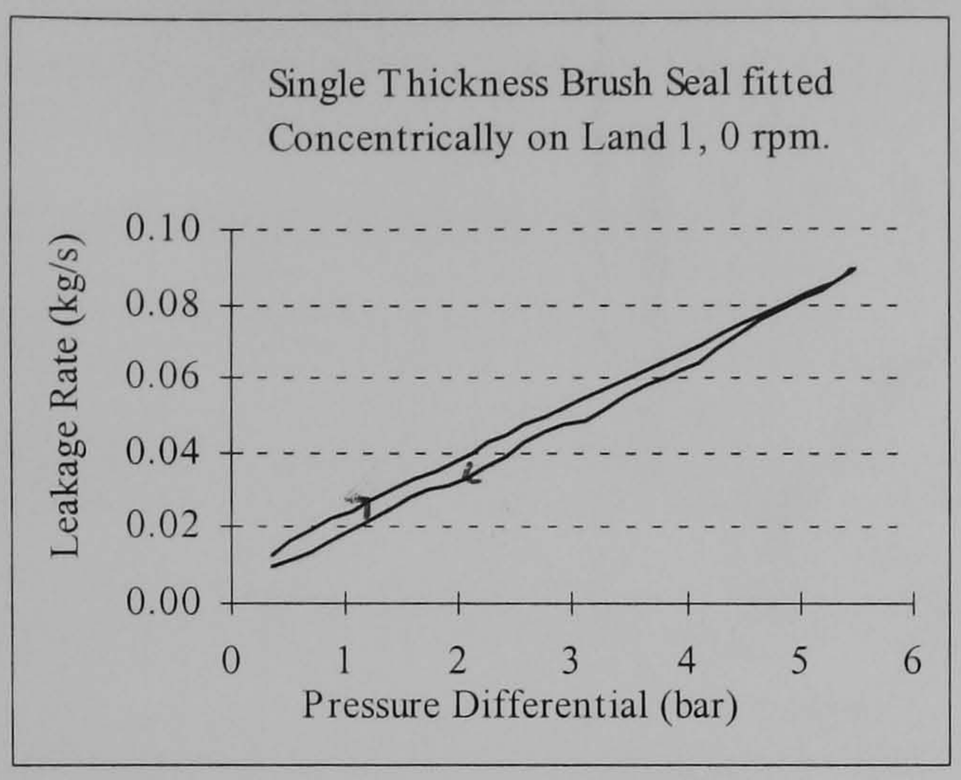

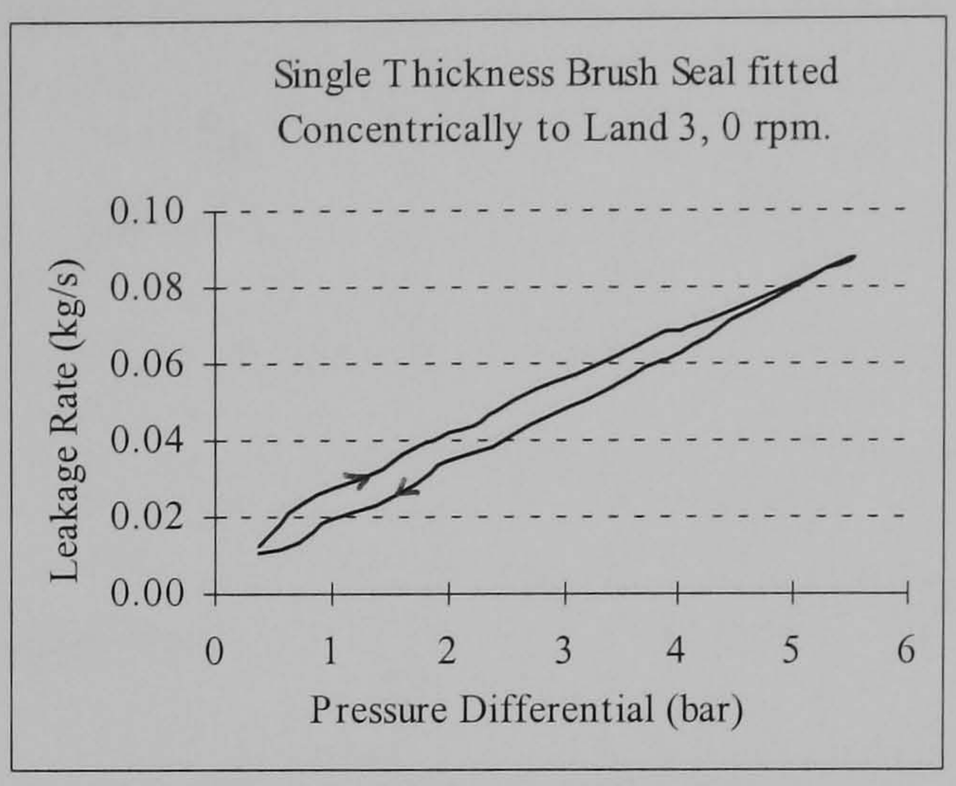

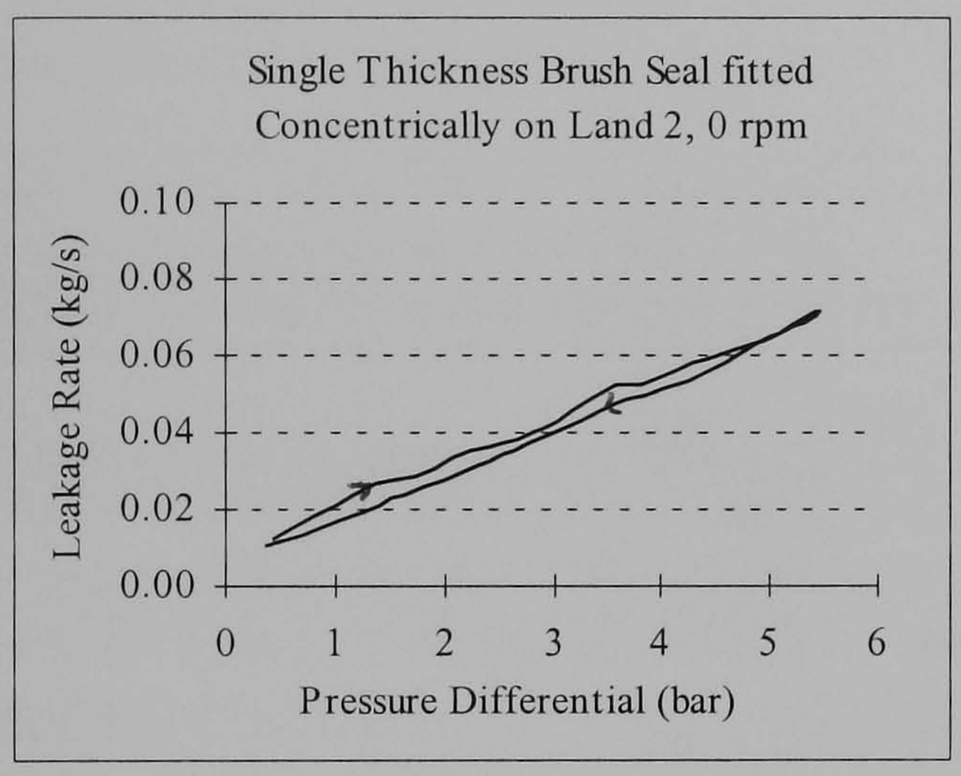

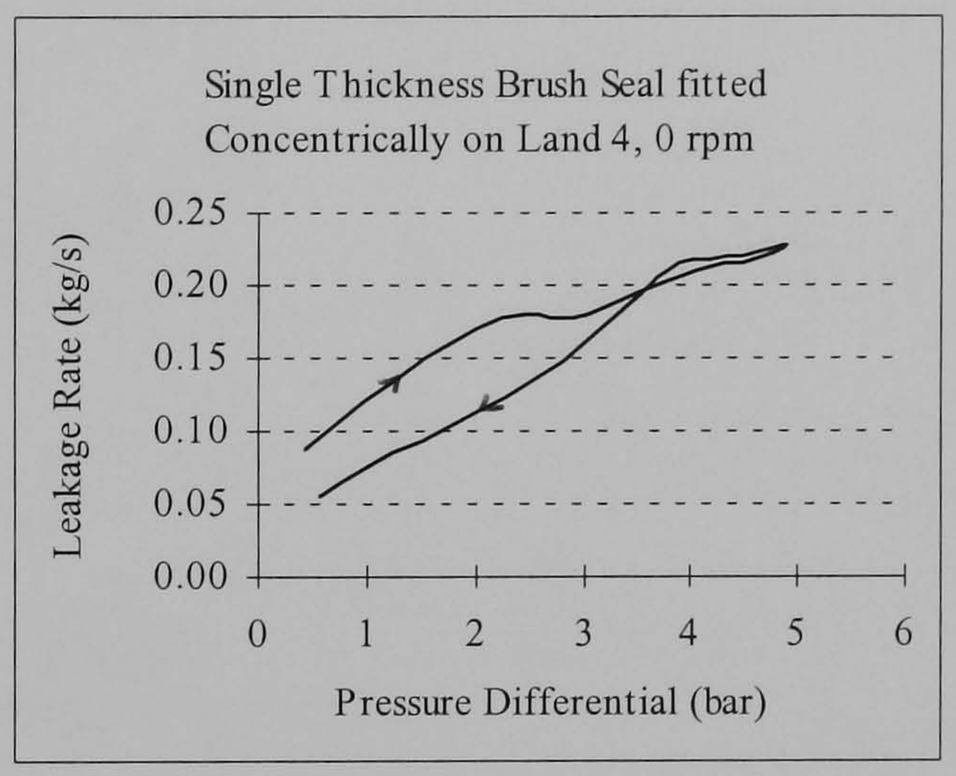

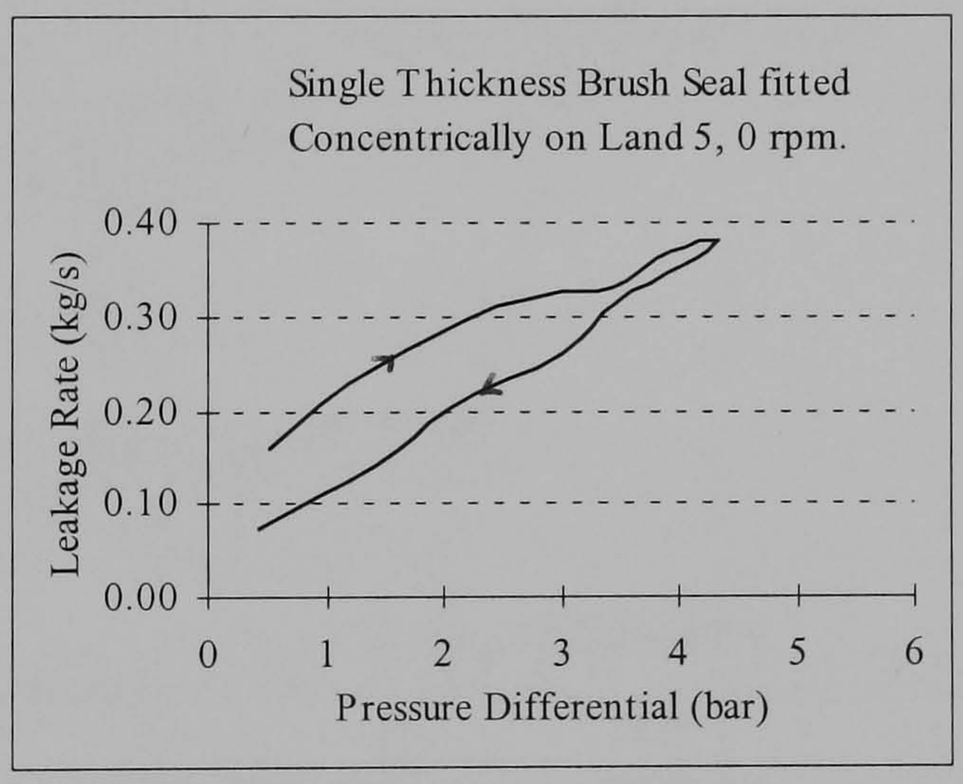

Figure 7.3 Leakage rate through one single thickness seal with two identically handed seals installed.

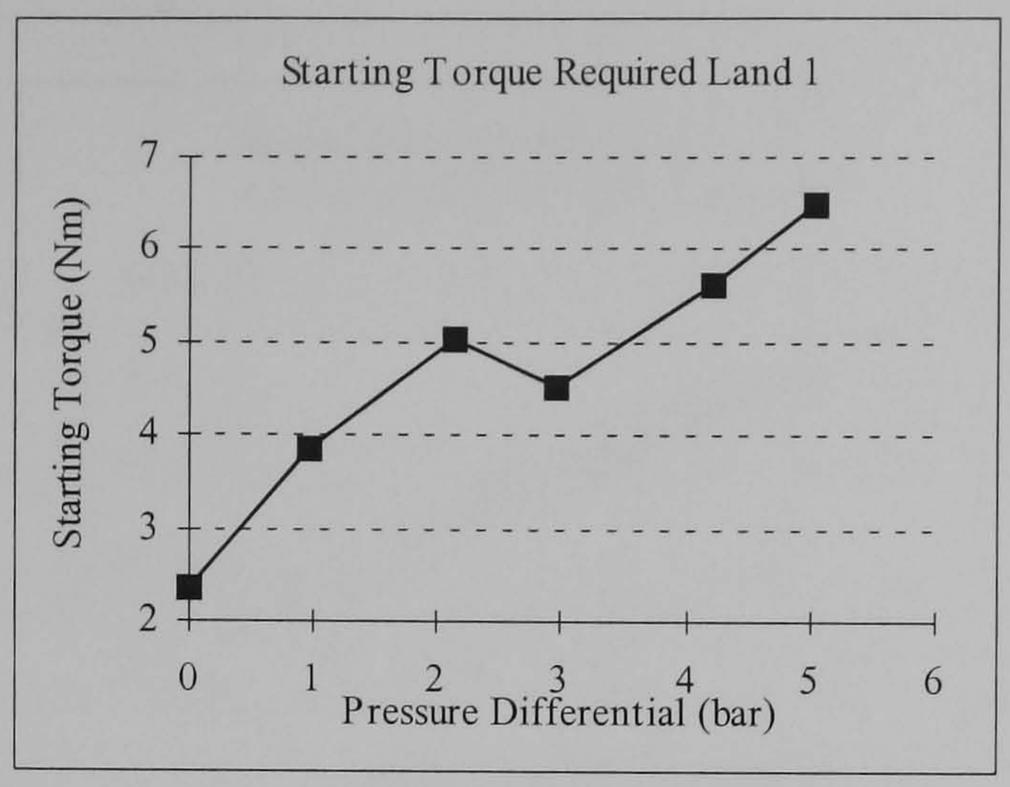

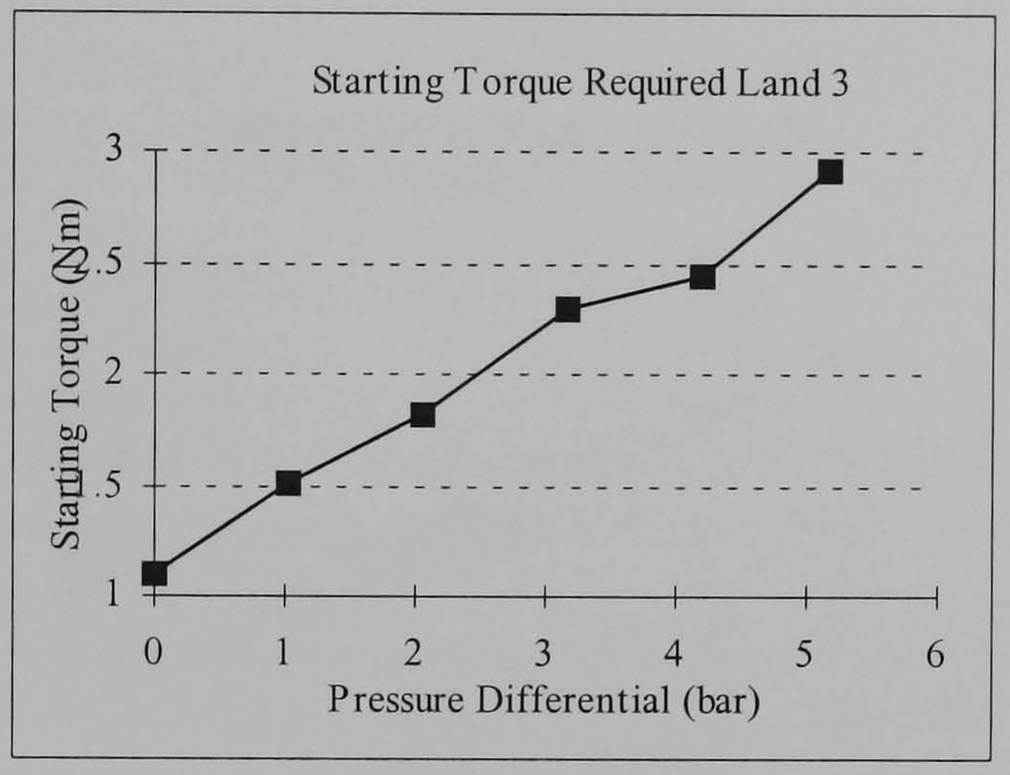

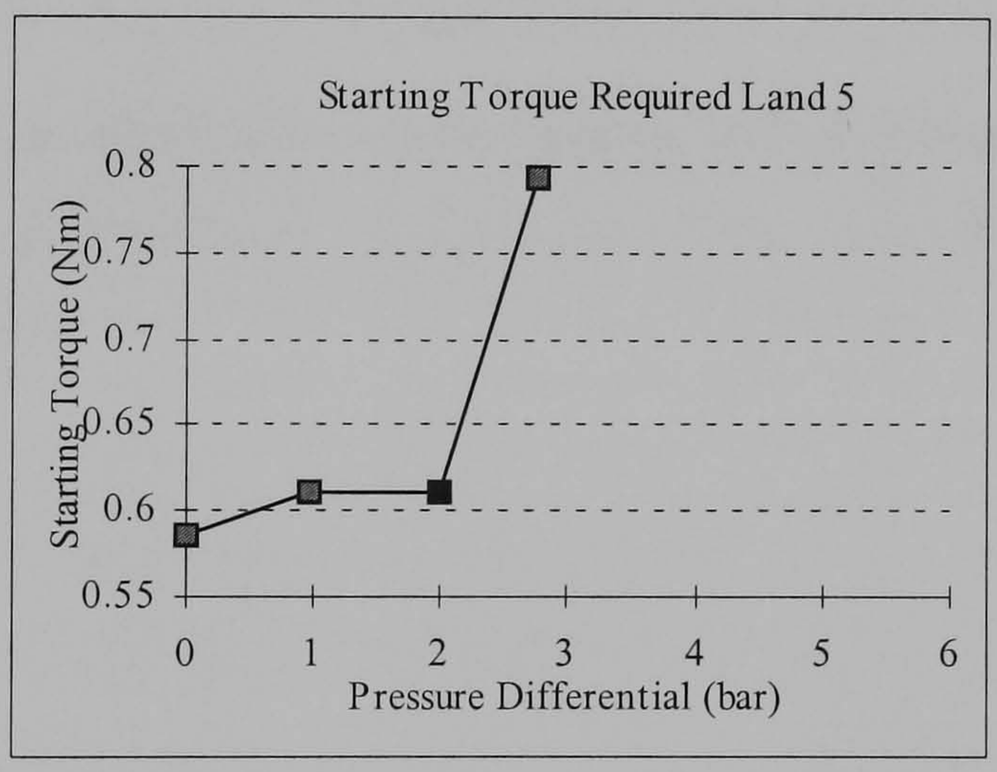

Figure 7.4 A comparison of the starting torque required to turn the shaft from rest with two single thickness, oppositely handed seals installed.

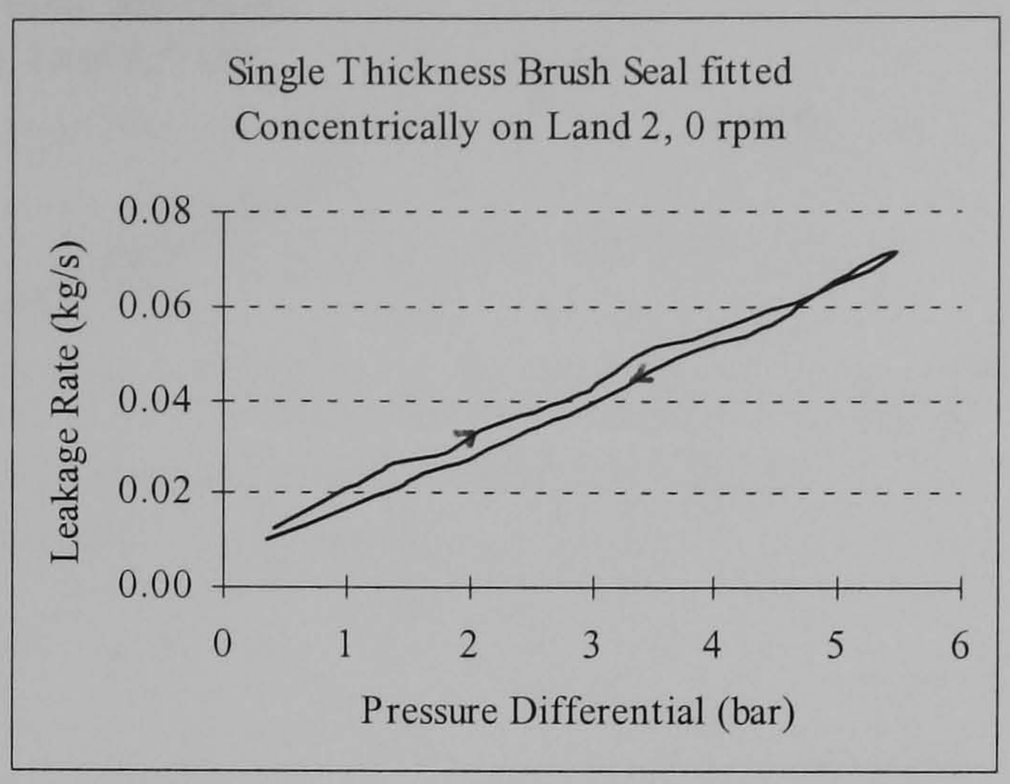

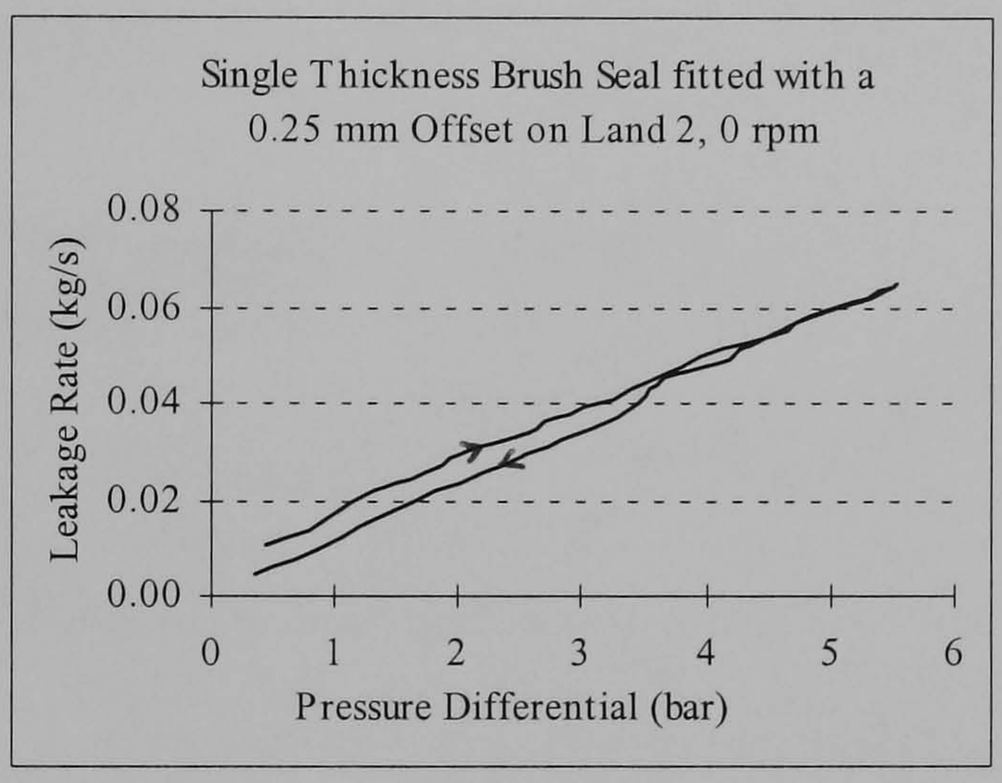

Figure 7.5 The effect of an offset rotor on the leakage rate of one single thickness brush seal with two identically handed seals installed (where the offset is approximately equal to the installed interference.)

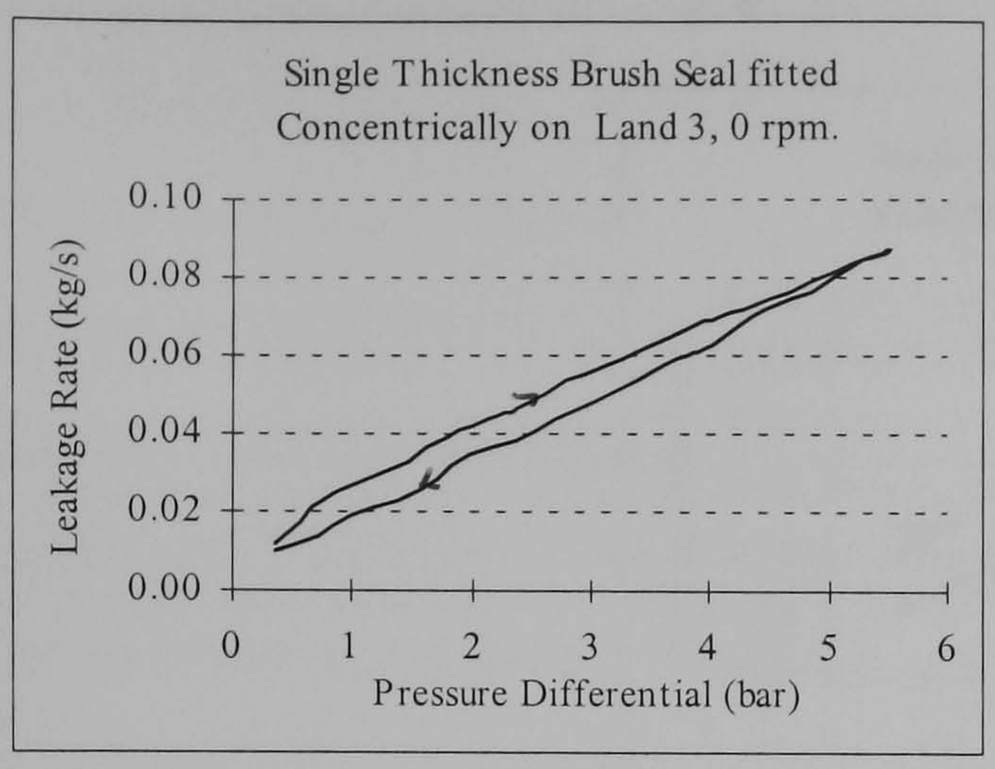

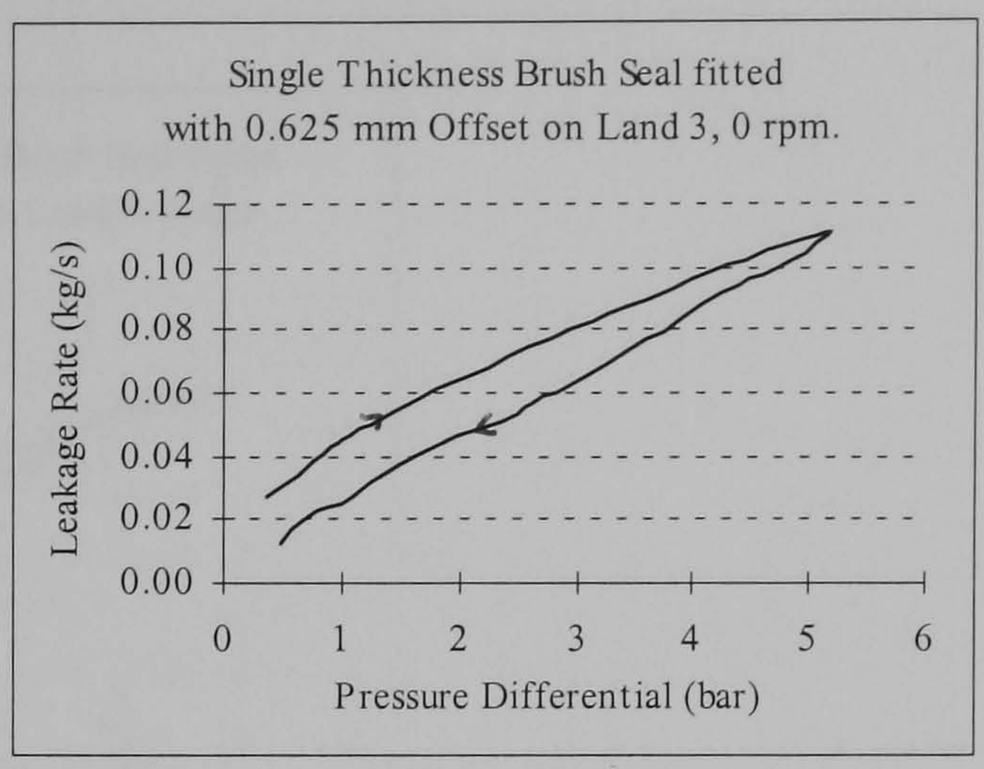

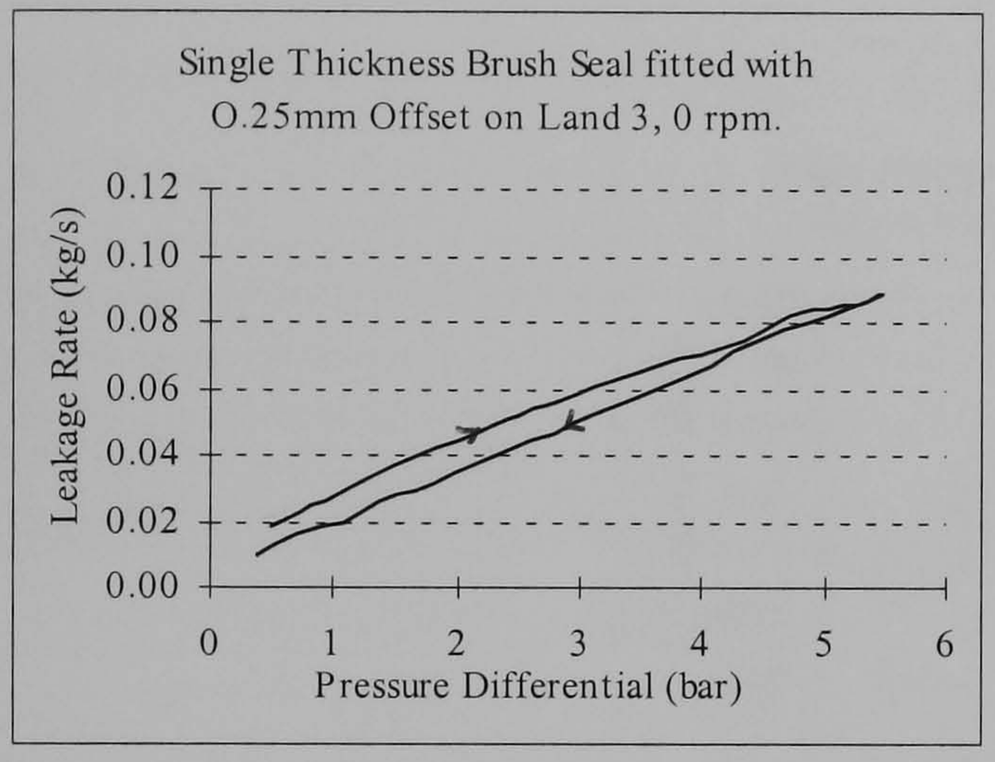

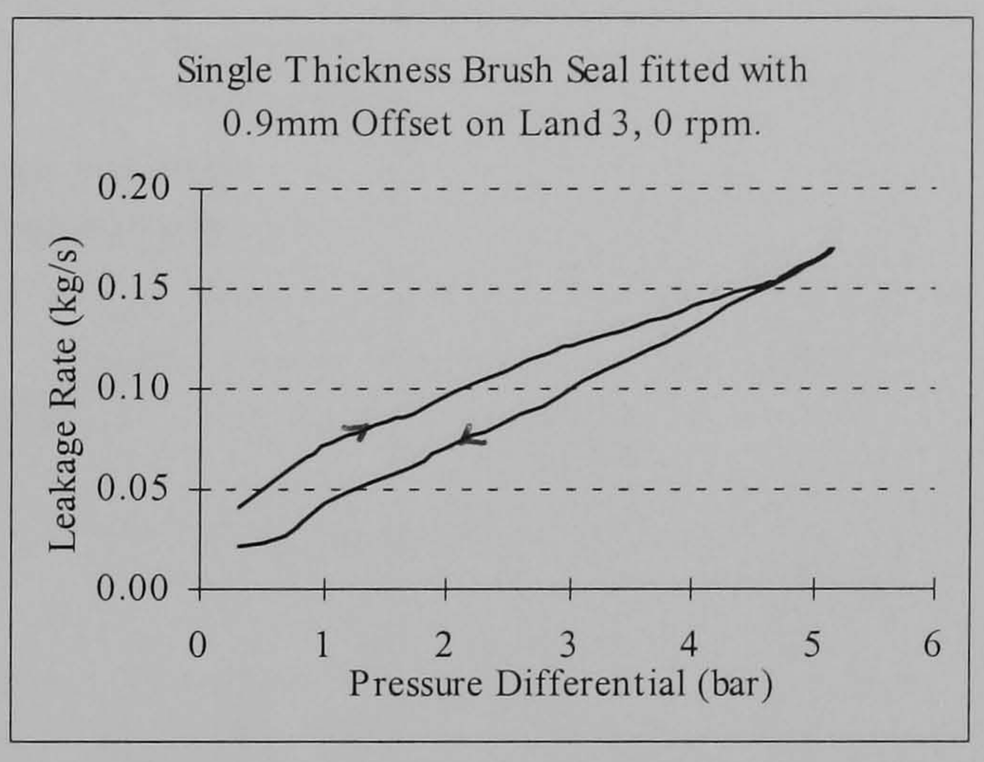

Figure 7.6 The effect of an offset rotor on the leakage rate of one single thickness brush seal with two identically handed seals installed.

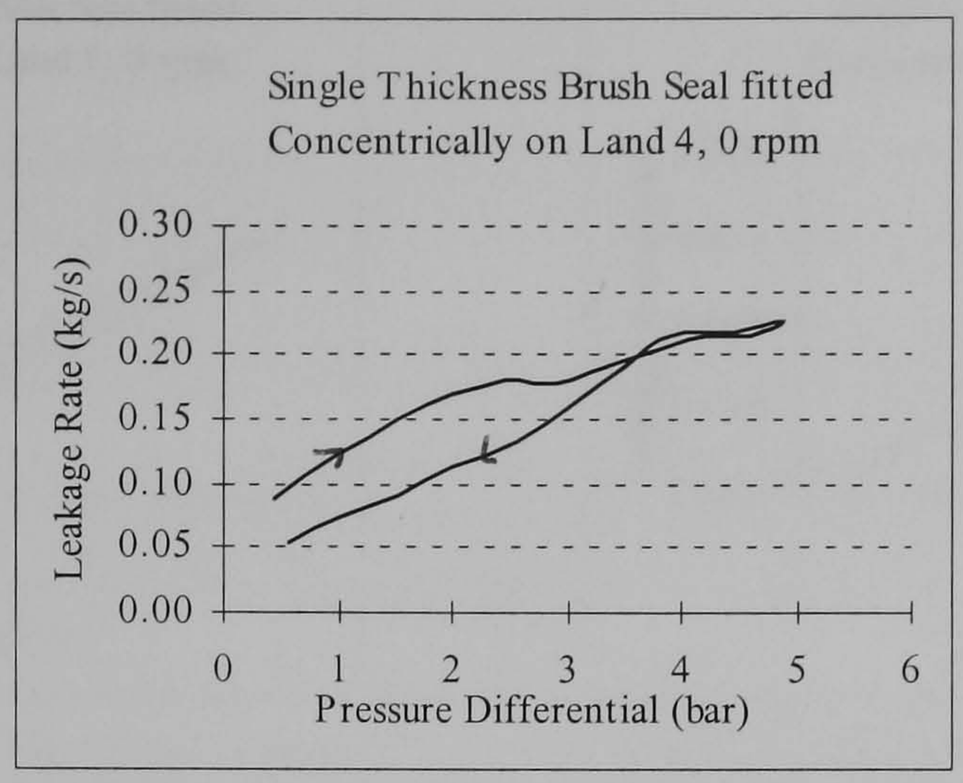

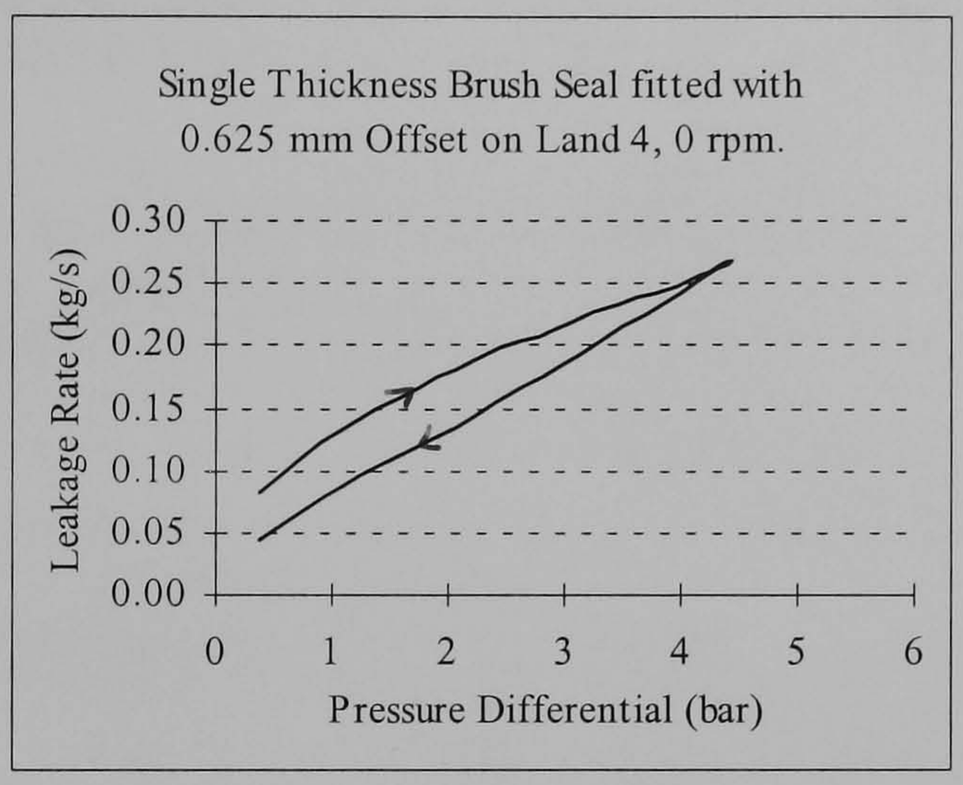

Figure 7.7 The effect of an offset rotor on the leakage rate of one single thickness seal with two identically handed seals installed (where offset is approximately equal to the installed clearance.)

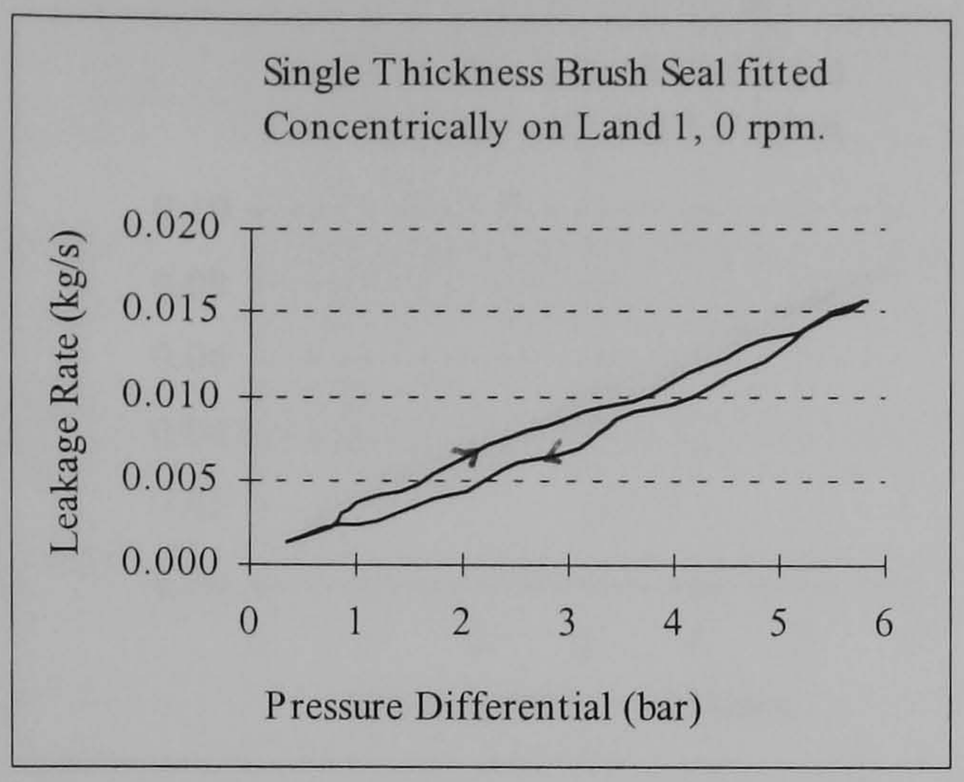

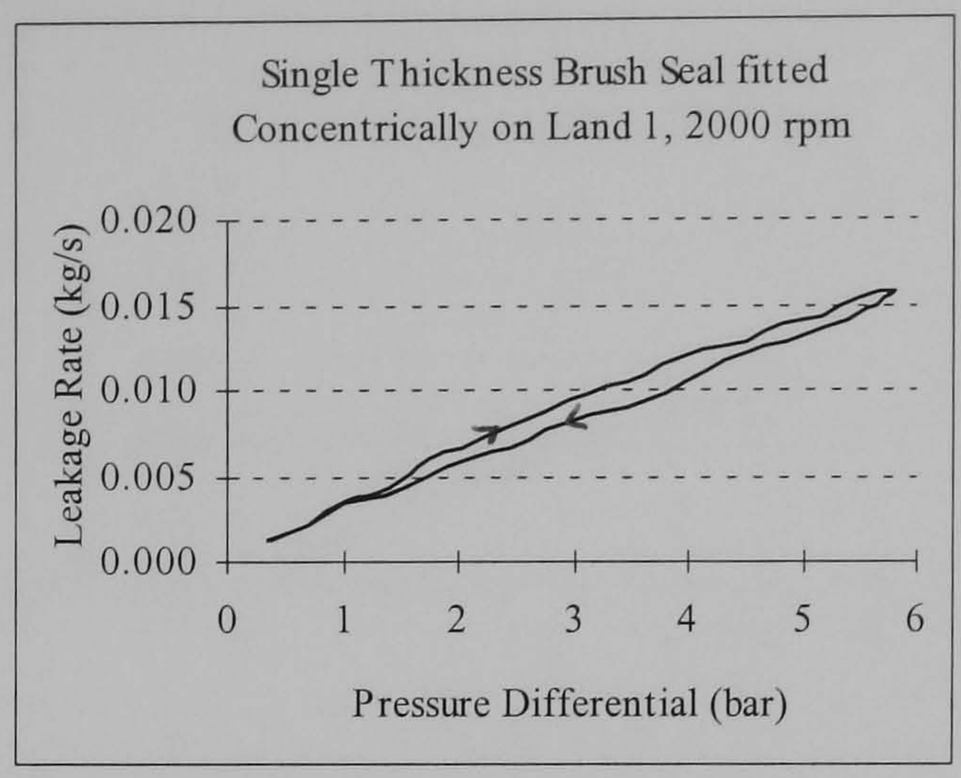

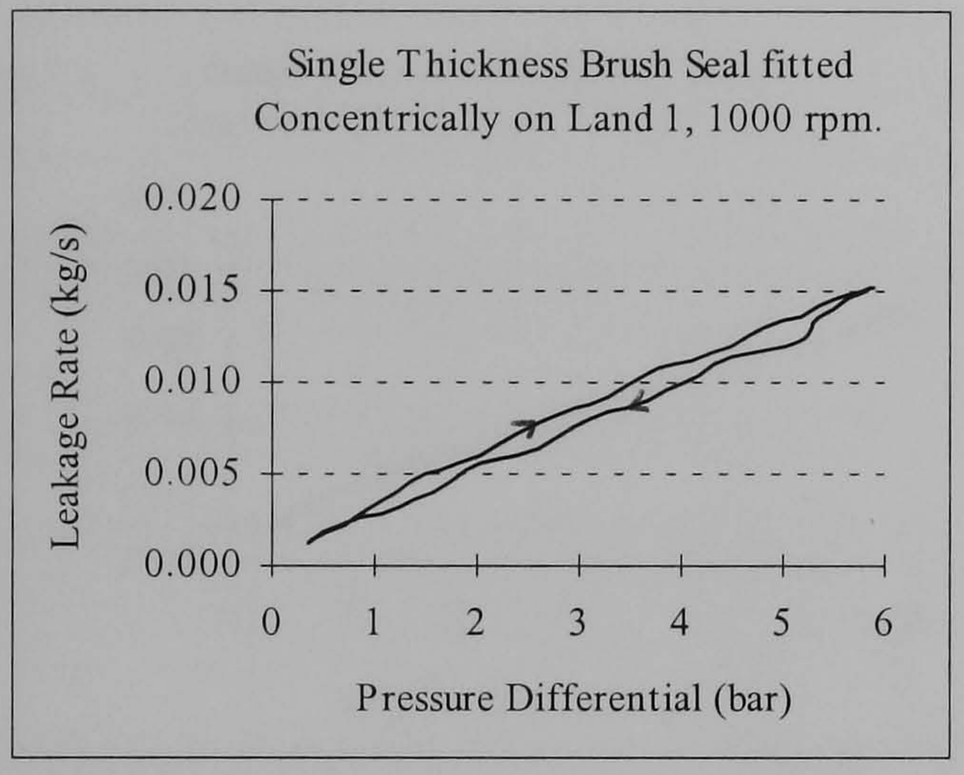

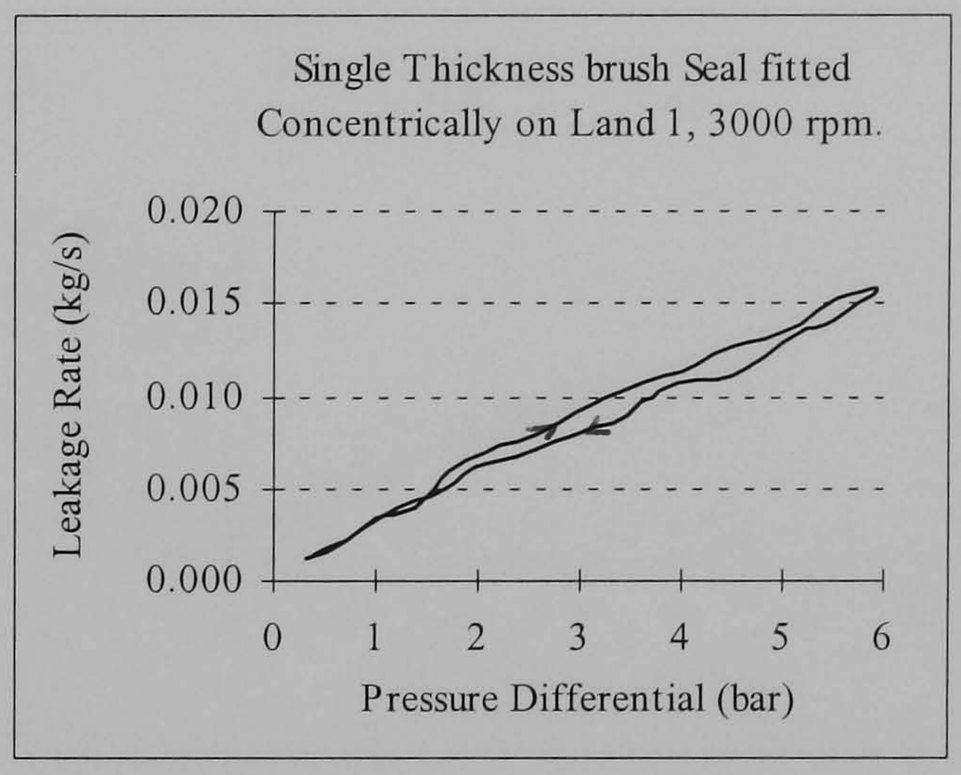

Figure 7.8 Measured leakage flows for one single thickness brush seal with two single thickness oppositely handed seals installed.

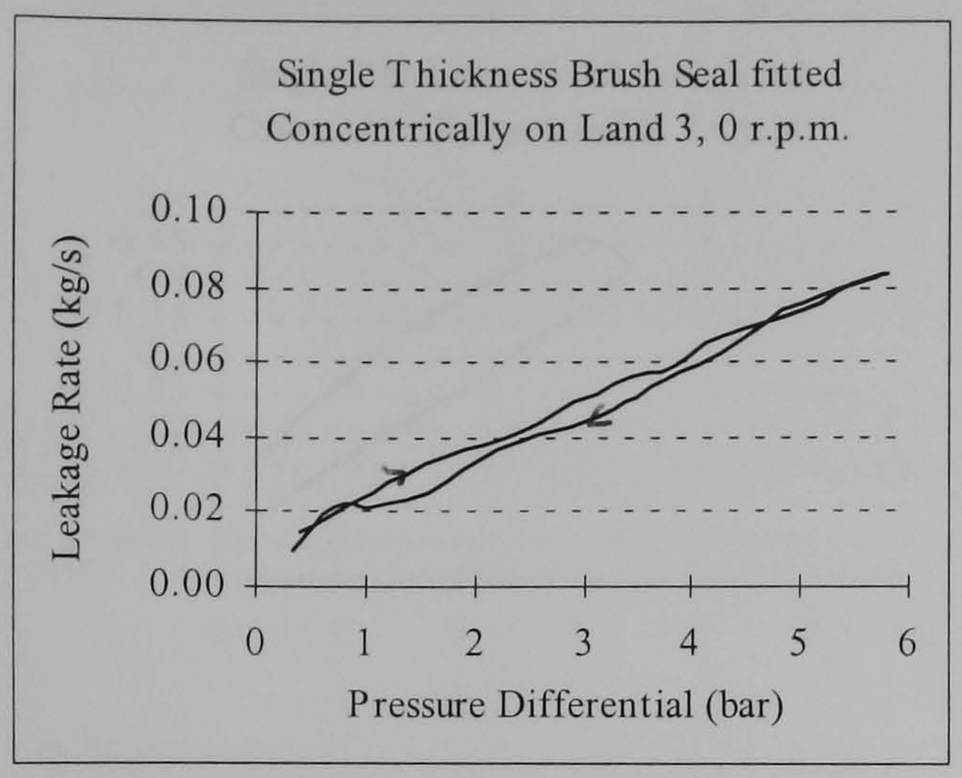

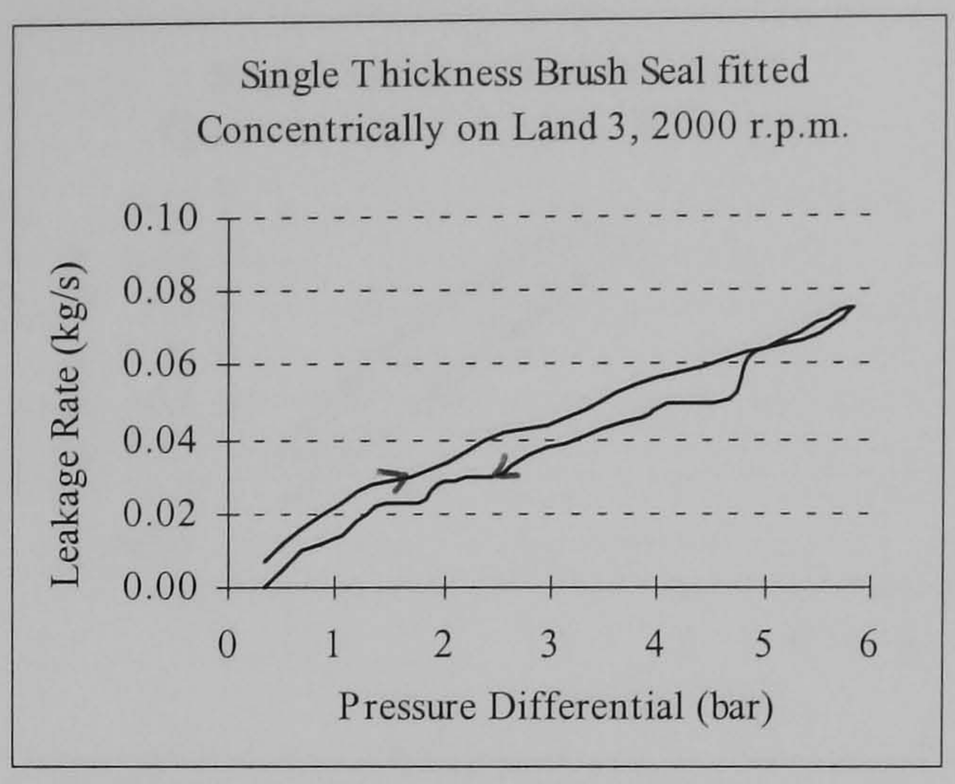

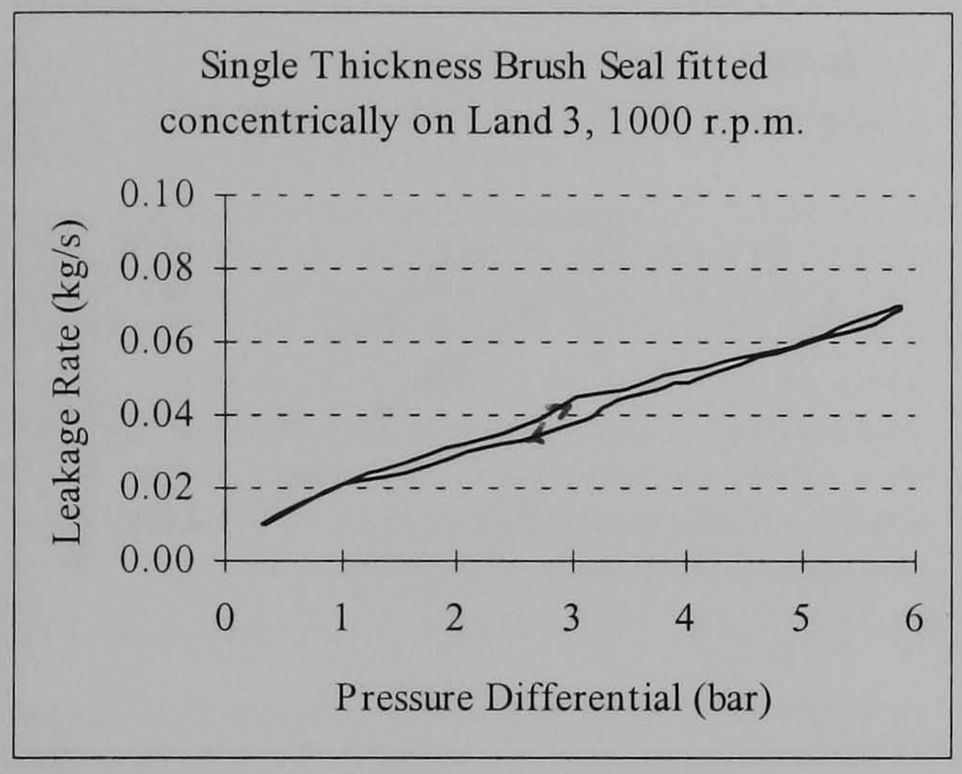

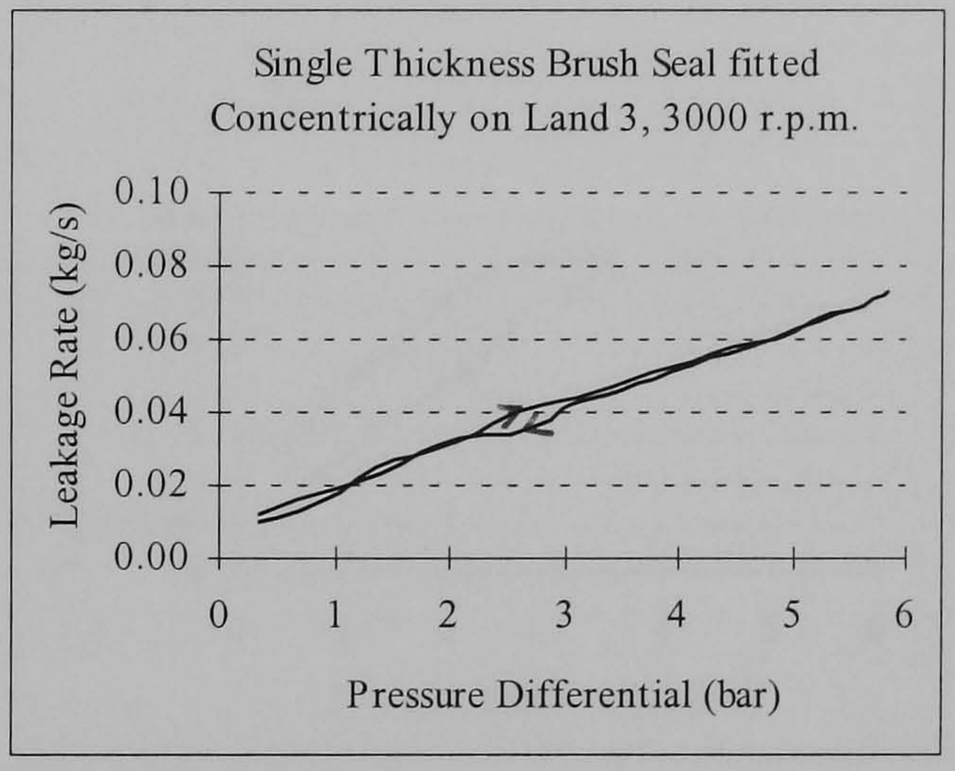

Figure 7.9 Measured leakage flows for one single thickness brush seal with two single thickness oppositely handed seals installed.

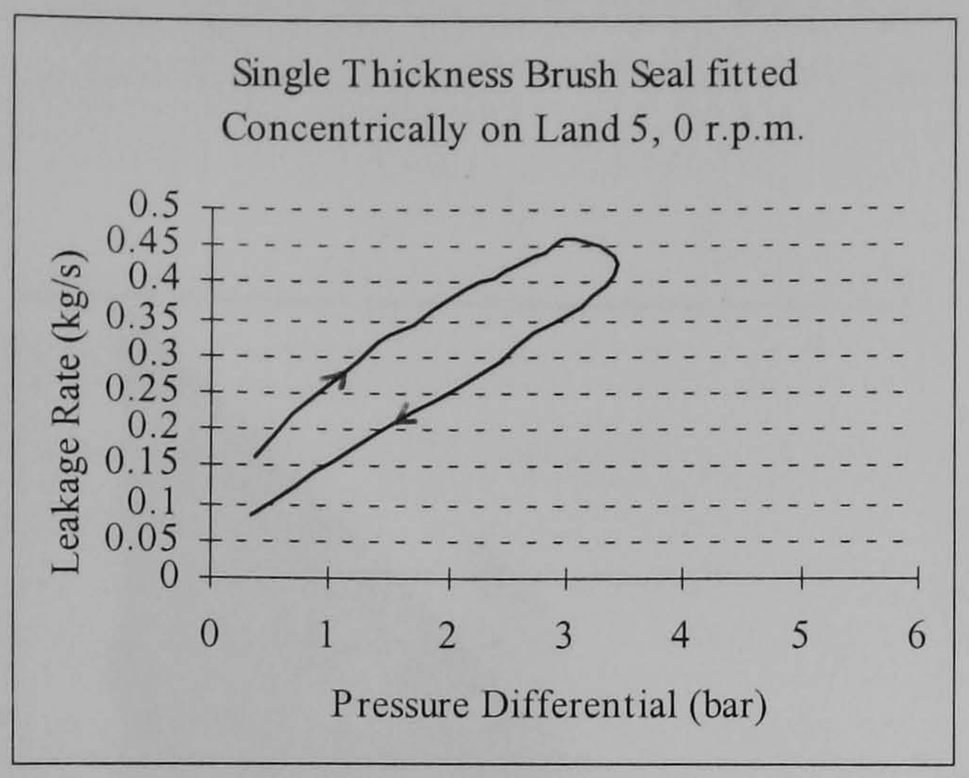

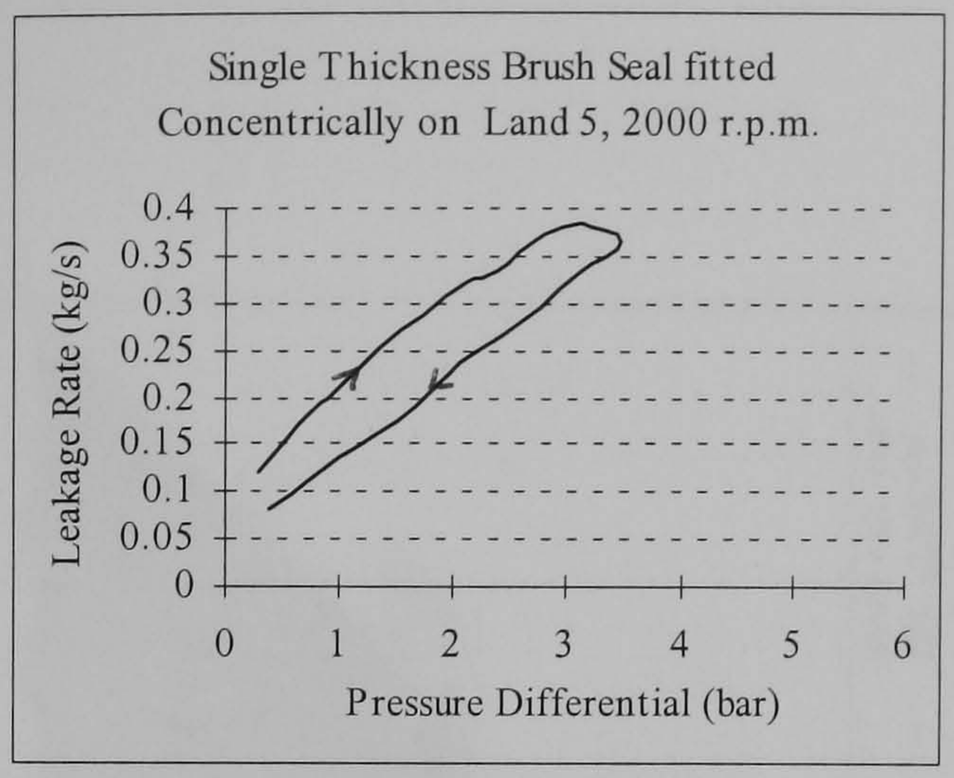

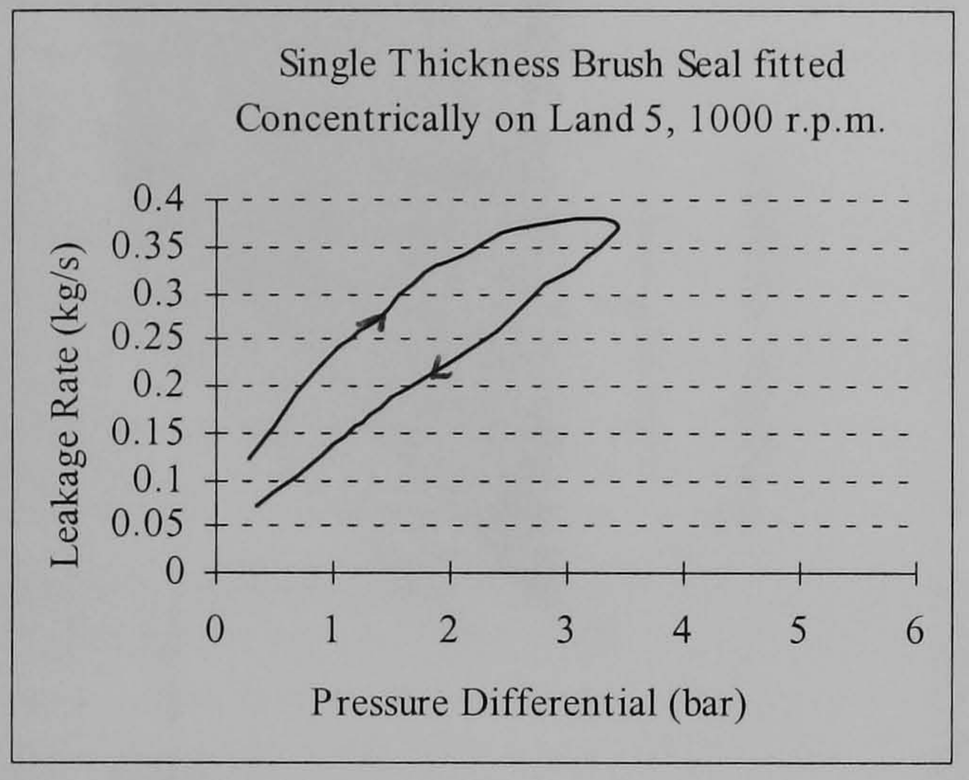

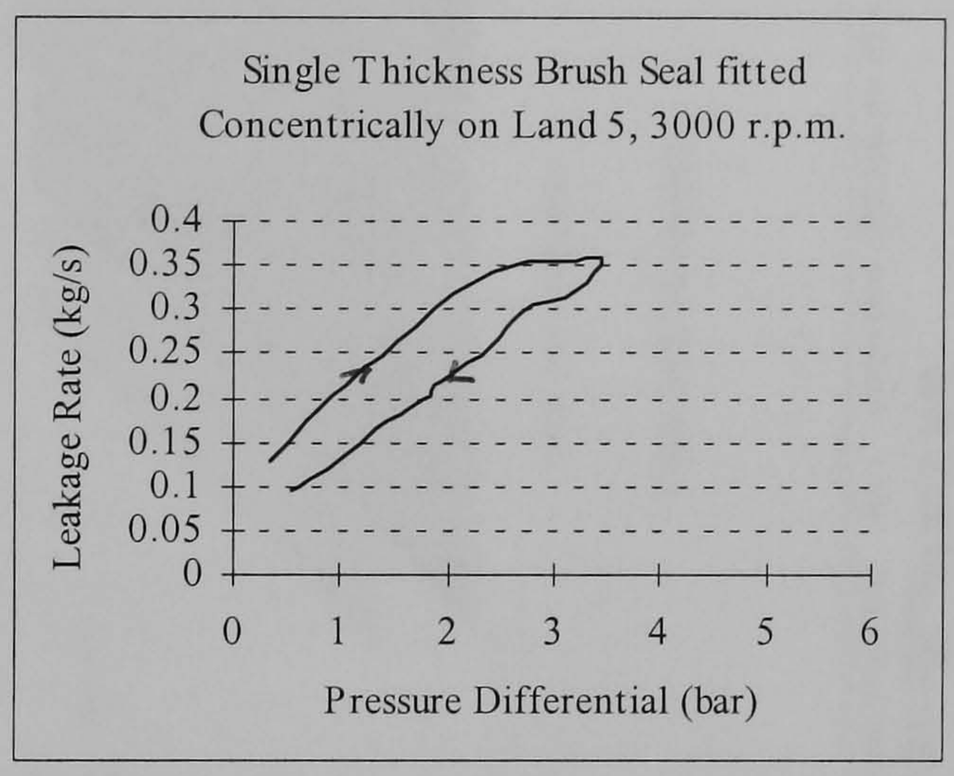

Figure 7.10 Measured leakage flows for one single thickness brush seal with two single thickness, oppositely handed seals installed.

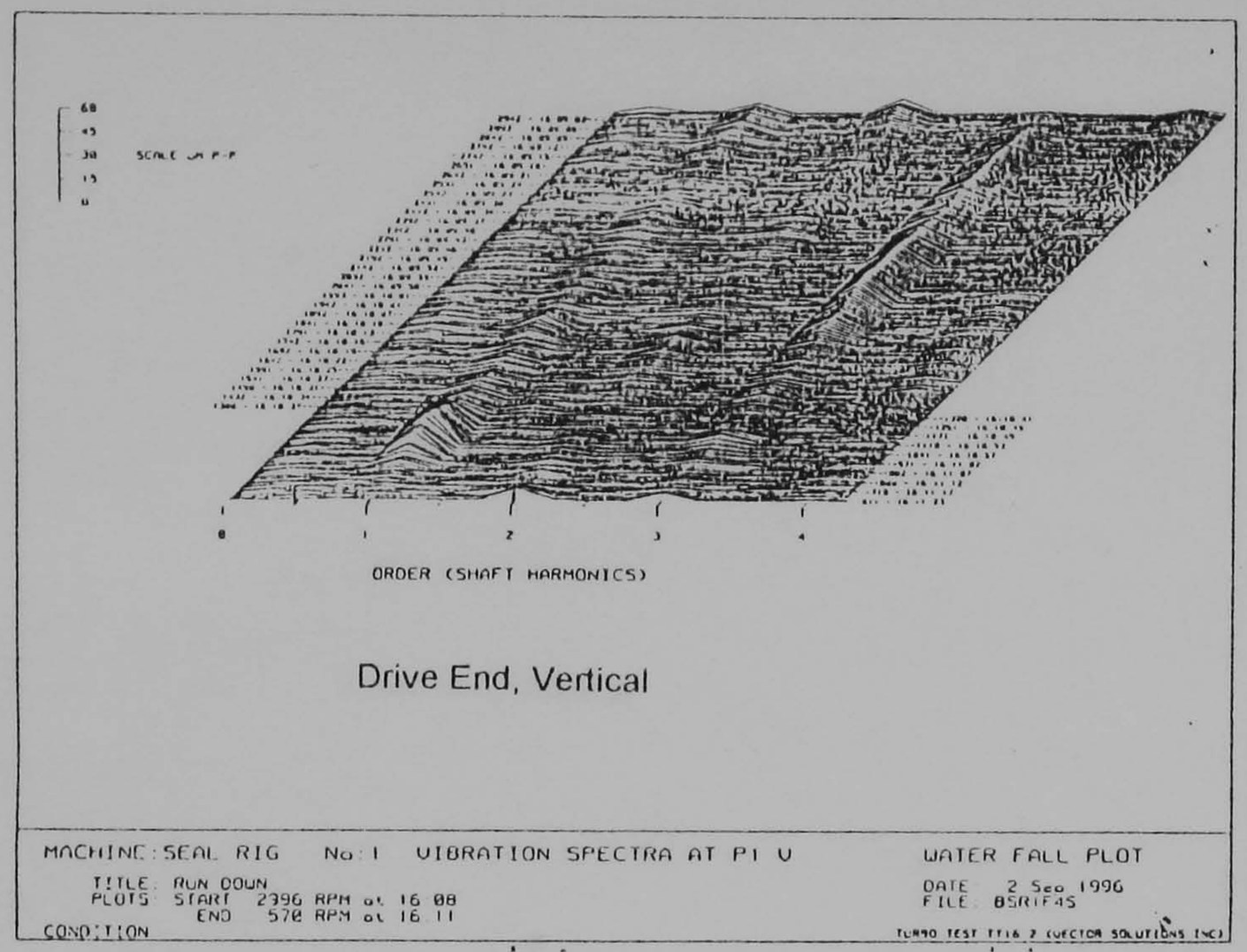

Drive End, Vertical

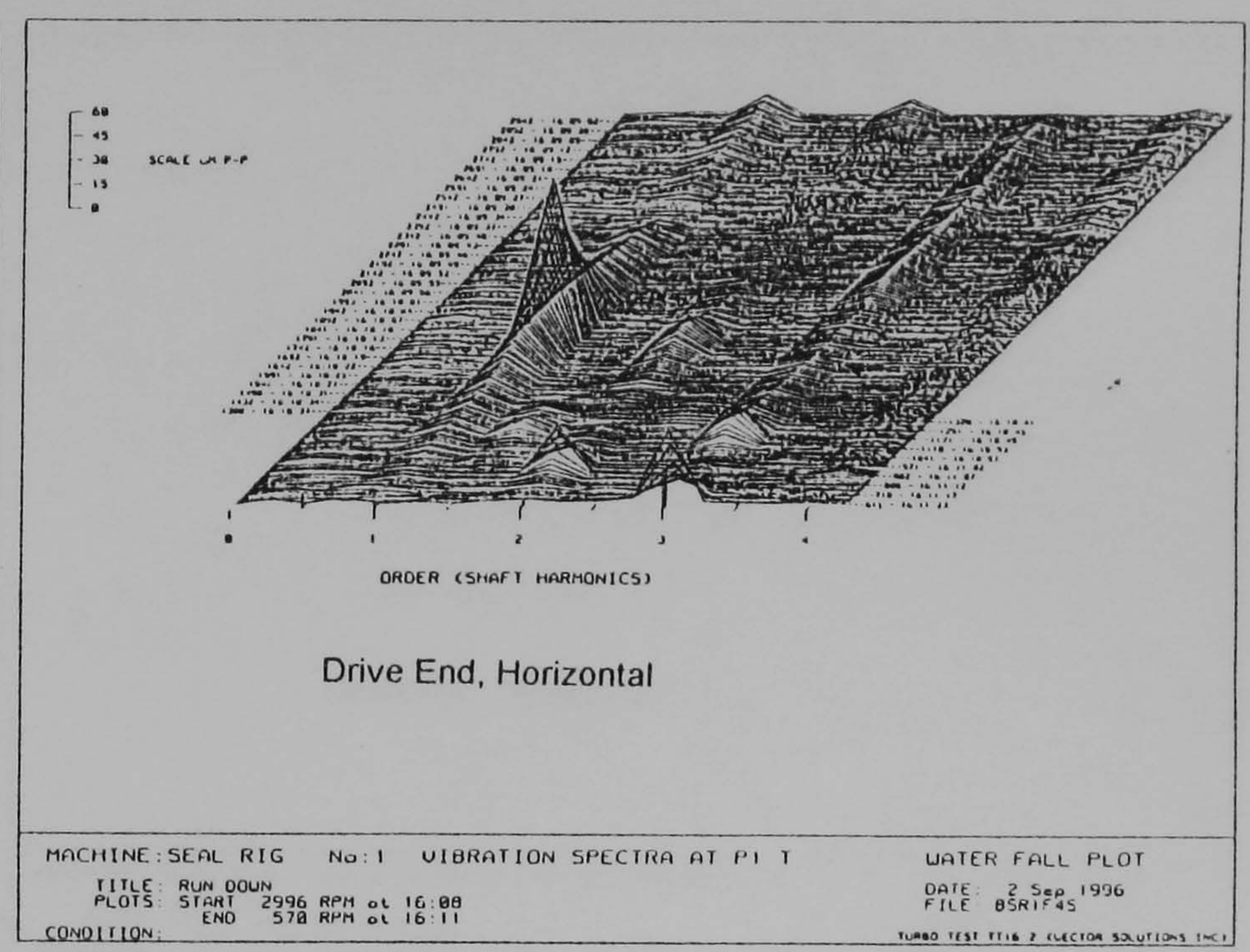

Drive End, Horizontal

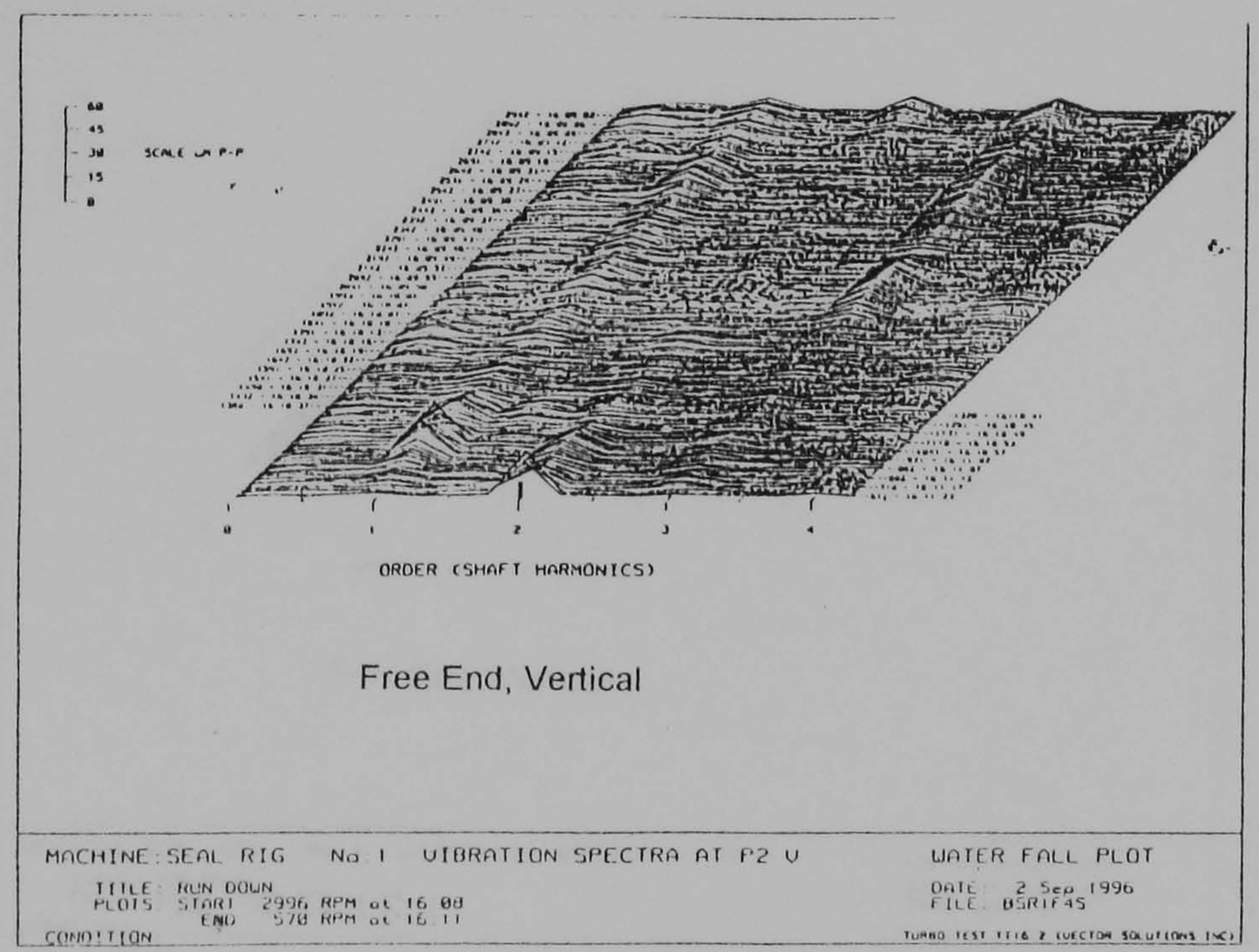

Free End, Vertical

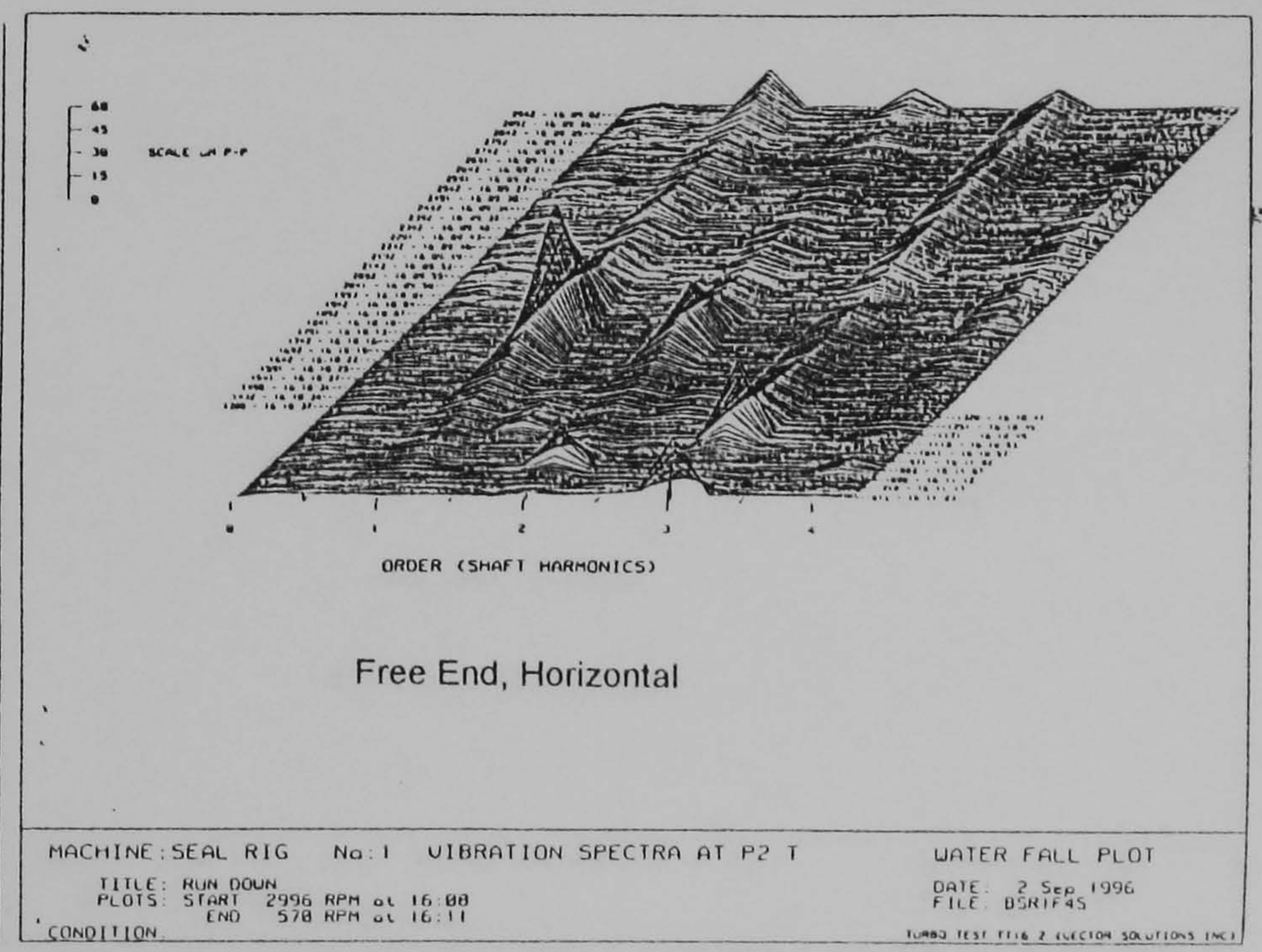

Free End, Vertical

-no seals installed, no air in rig

Figure 7.11 Waterfall plot of the vibrational characteristics of the **BSLTR** bearing pedestals during run-down with no seals installed and no pressure differential.

Bearing Pedestal Response During Run-Down.

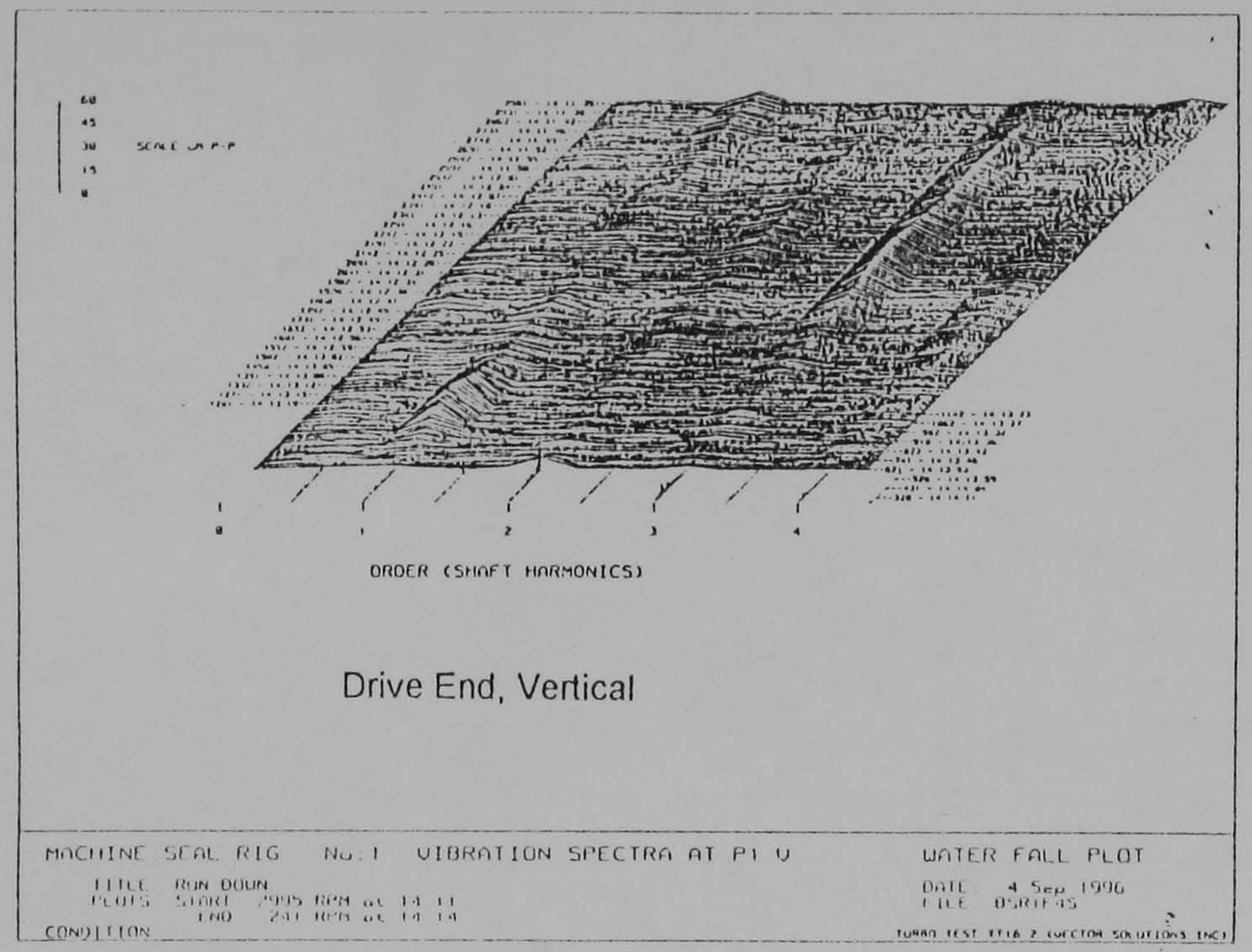

Drive End, Vertical

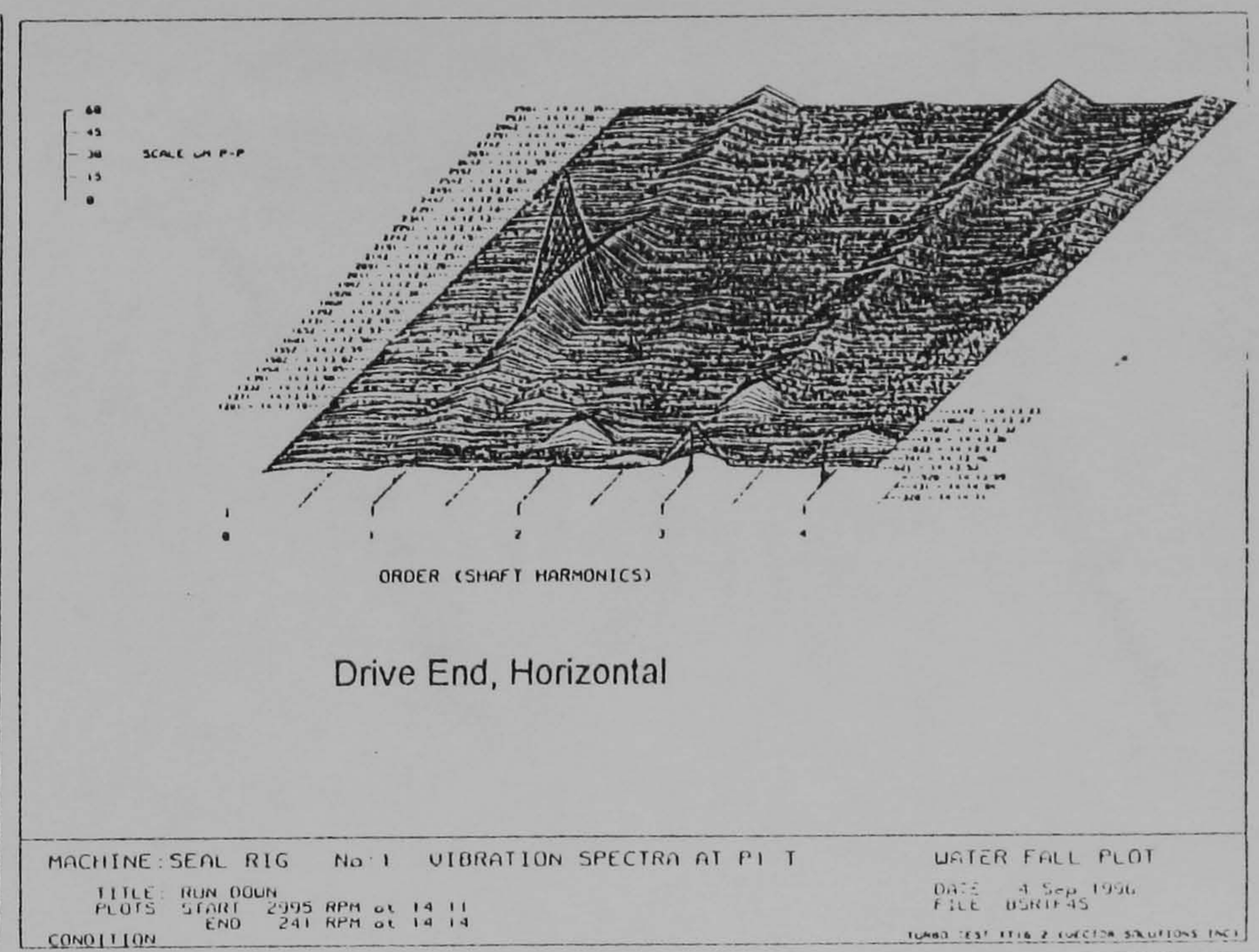

Drive End, Horizontal

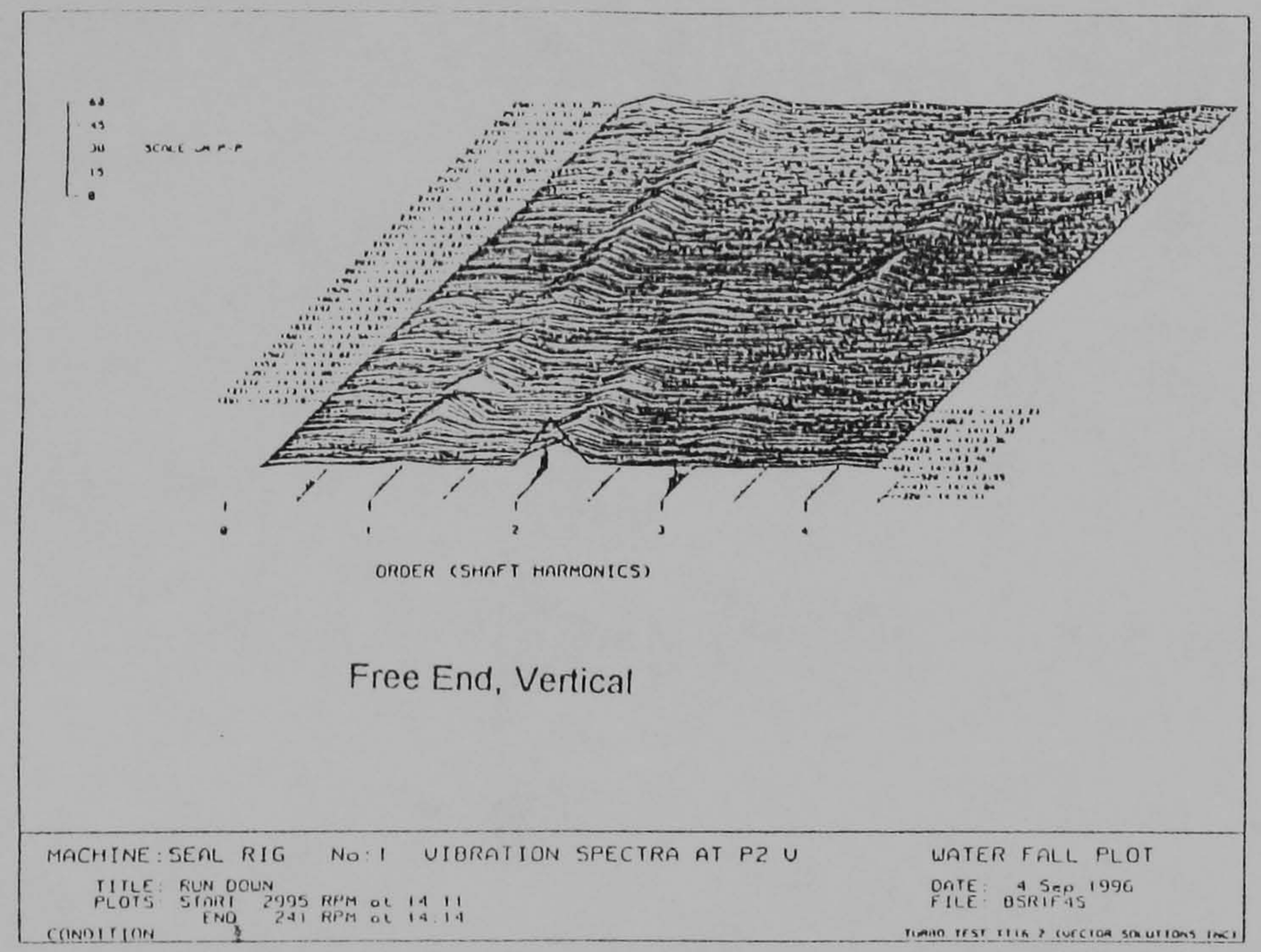

Free End, Vertical

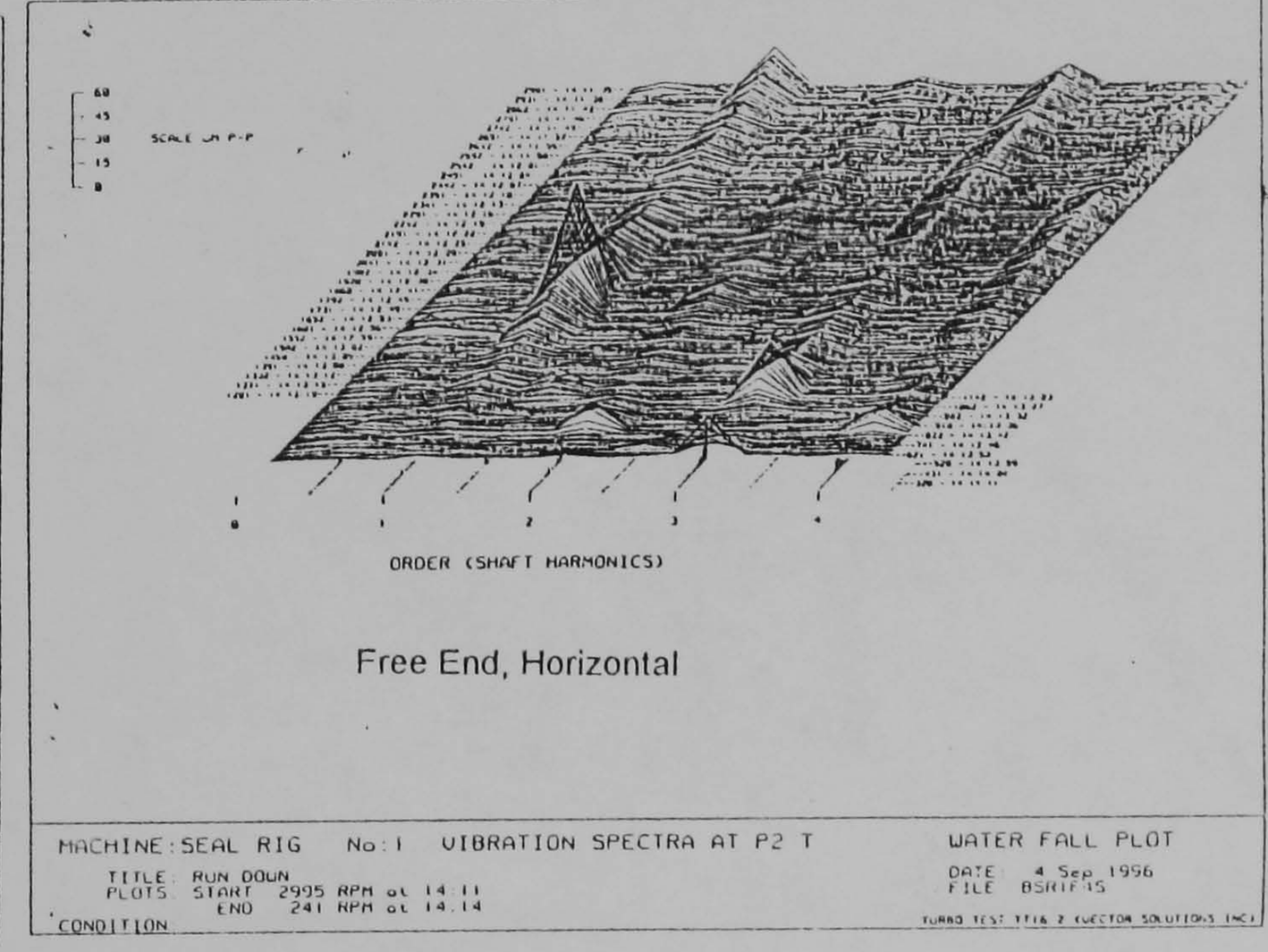

Free End, Horizontal

-with brush seals installed, 60 psi pressure differential

Figure 7.12 Waterfall plot of the vibrational characteristics of the **BSLTR** bearing pedestals during run-down with two single thickness brush seals installed and a 4 bar pressure differential.

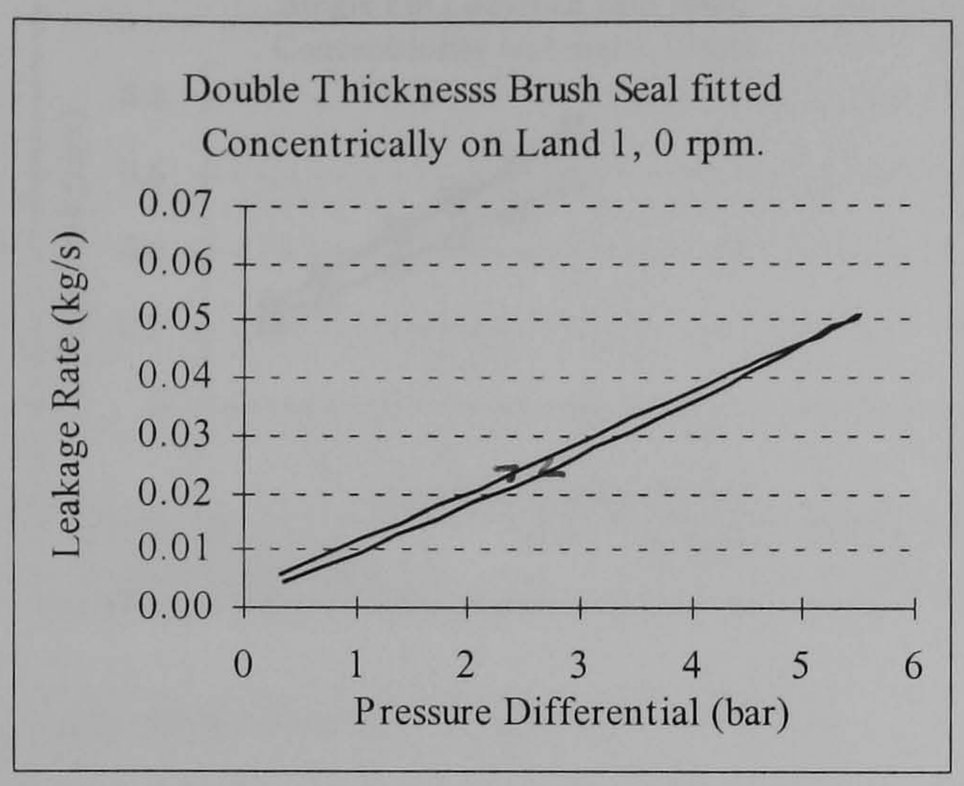

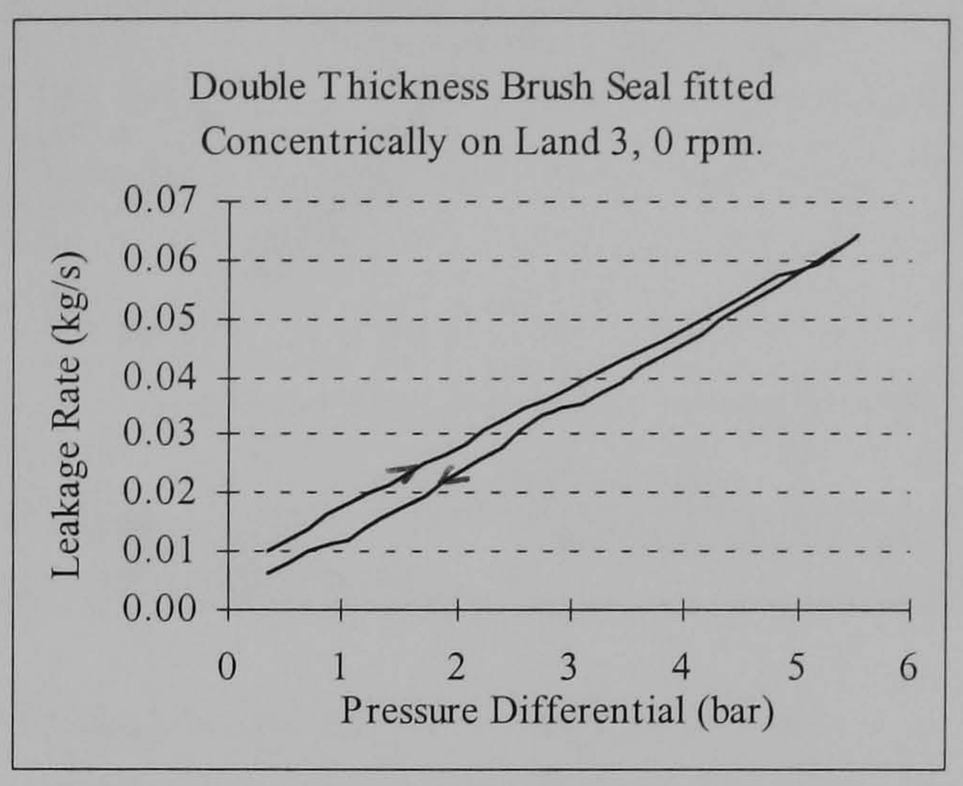

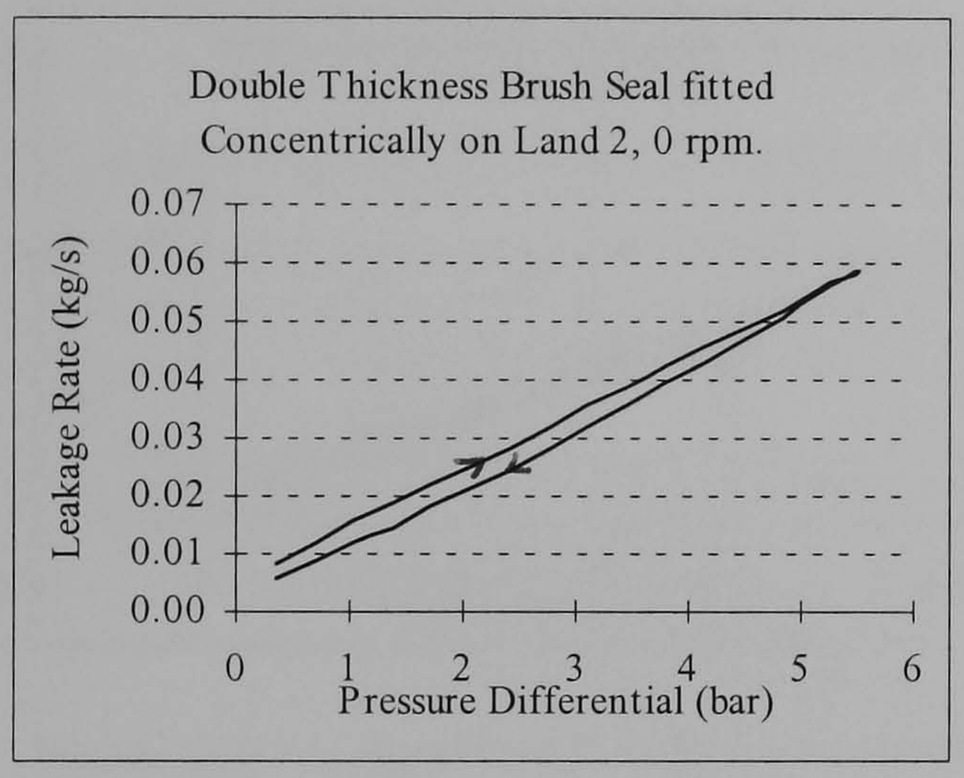

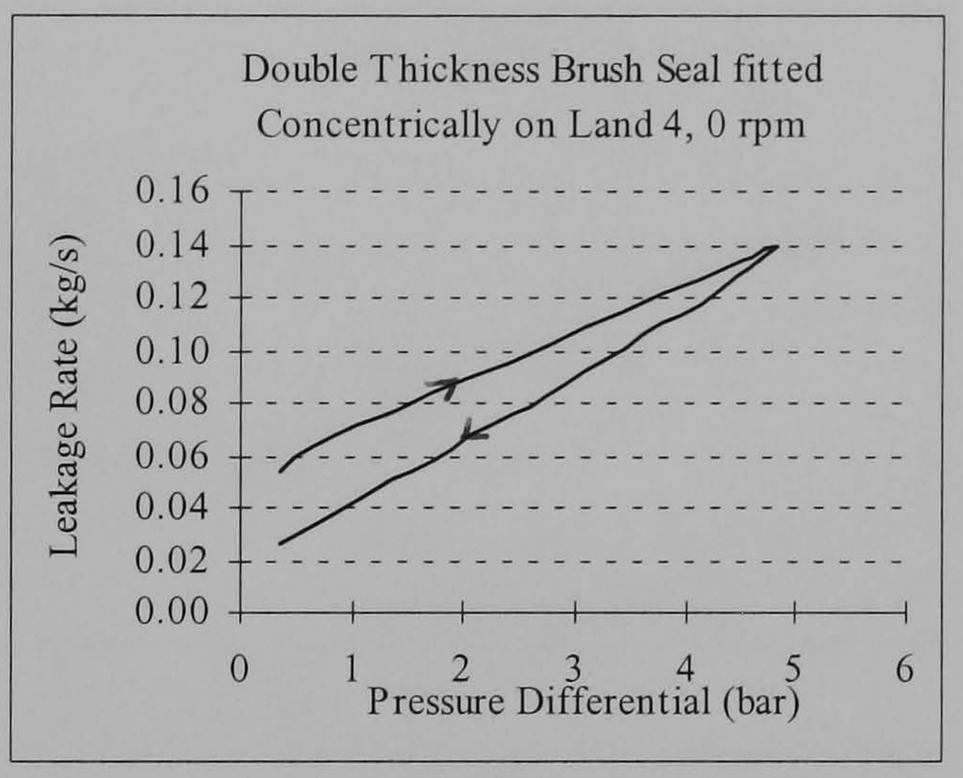

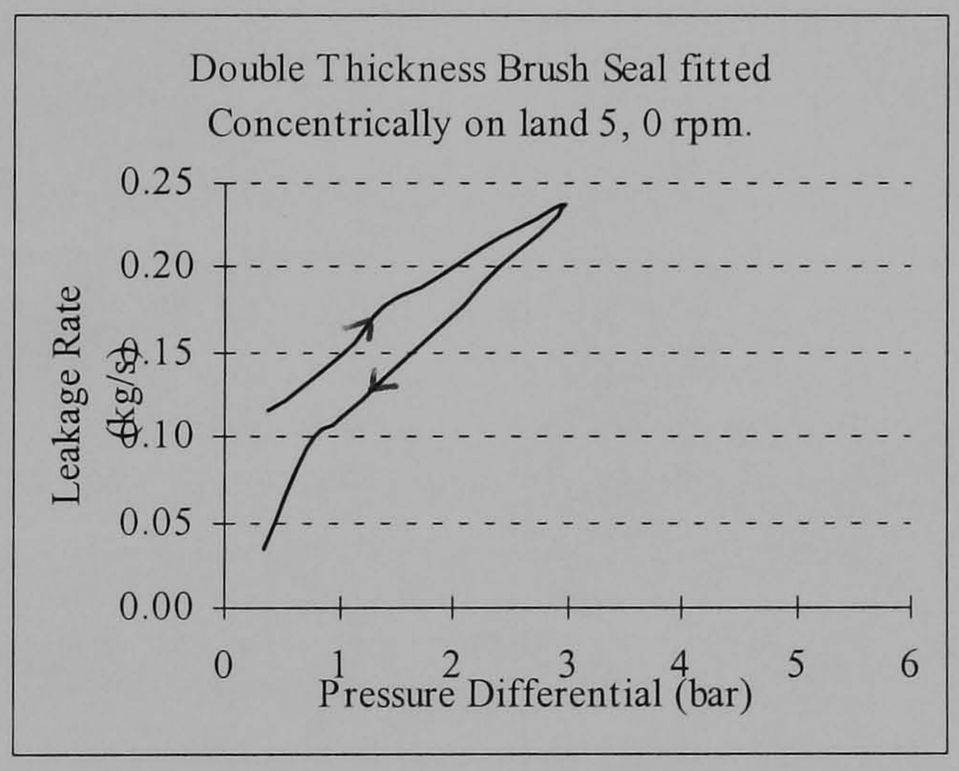

Figure 7.13 Leakage rate through one double thickness seal with two identically handed seals installed.

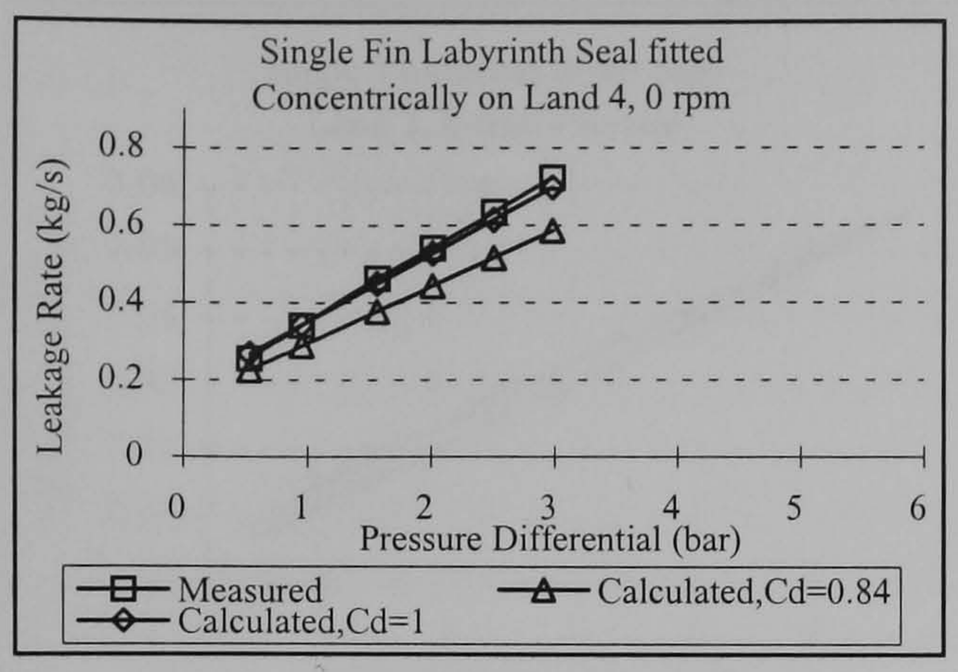

Labyrinth Radial Clearance 0.68 mm

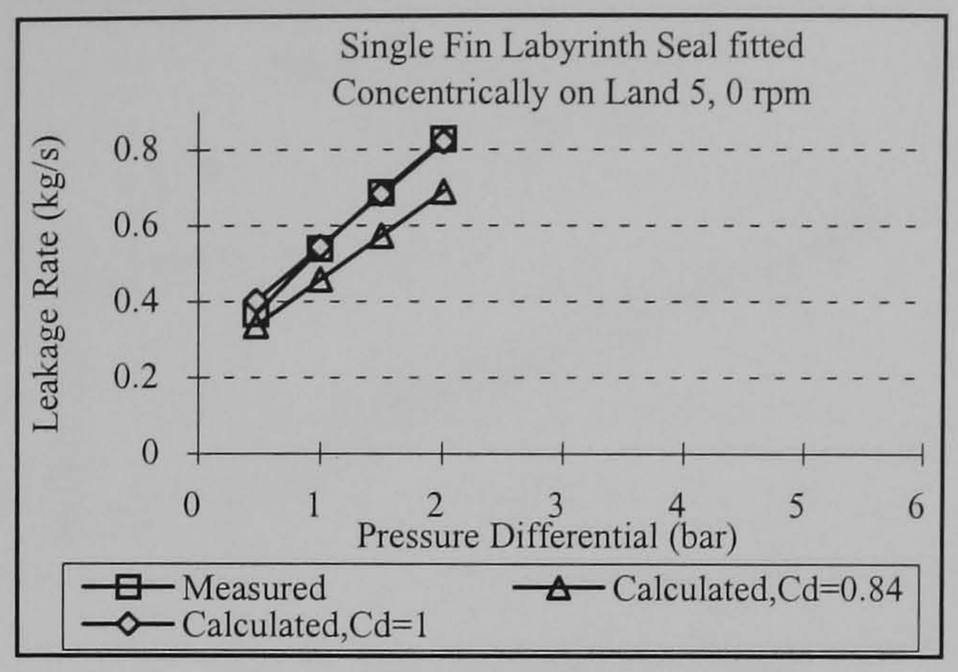

Labyrinth Radial Clearance 1.08 mm

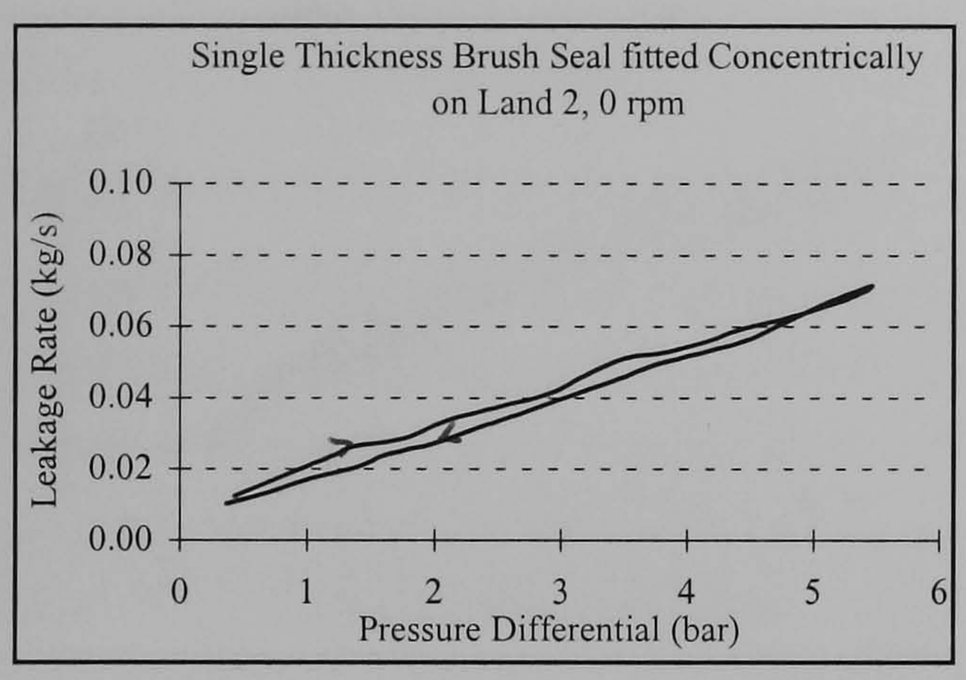

Brush Seal backing Ring Clearance 0.7 mm

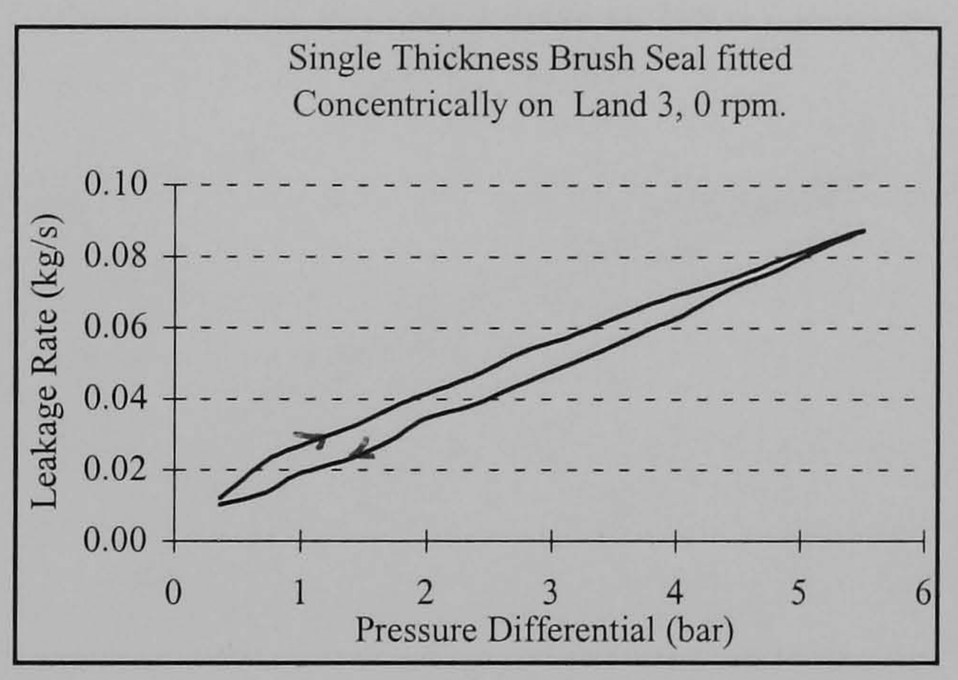

Brush Seal backing Ring Clearance 0.9 mm

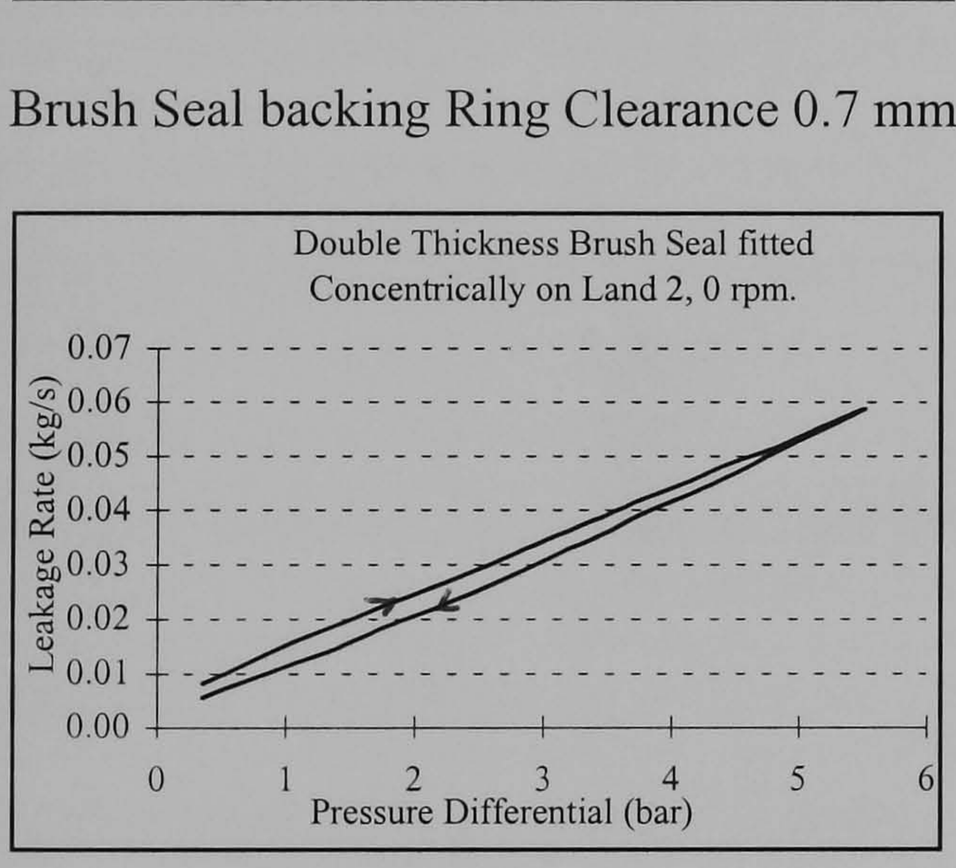

Brush Seal backing Ring Clearance 0.7 mm

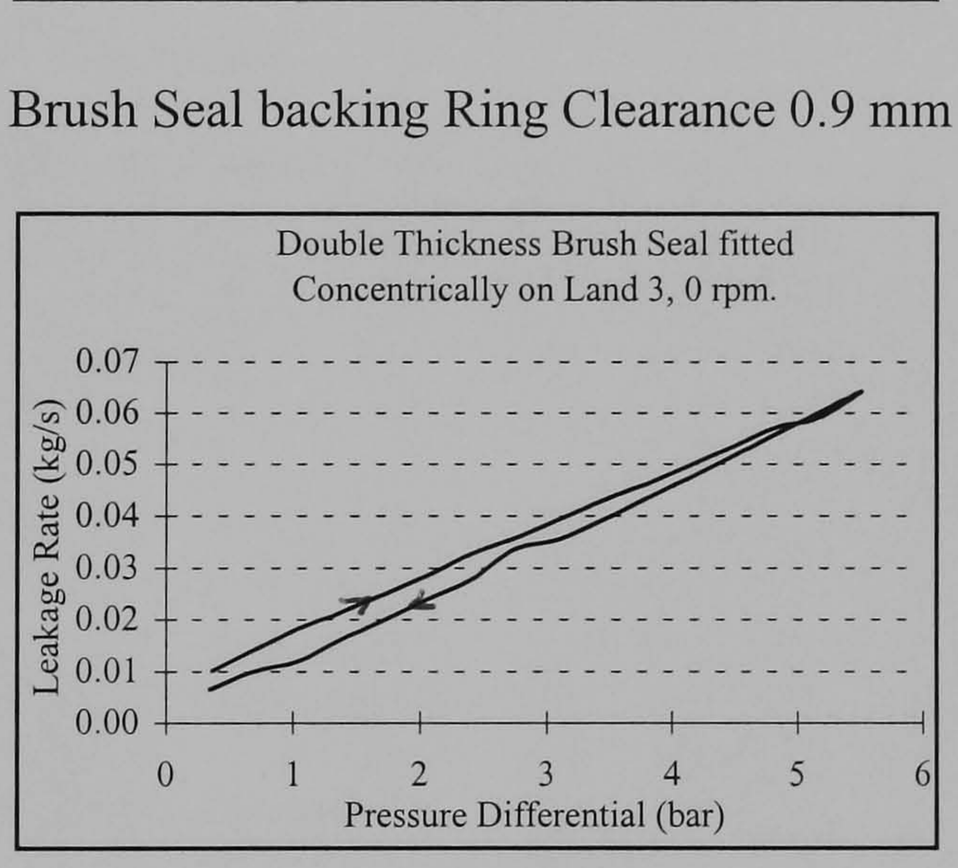

Brush Seal backing Ring Clearance 0.9 mm

Figure 7.14 Comparison of leakage for a single fin labyrinth seal to single and double thickness brush seals with comparable fin and backing ring clearances.

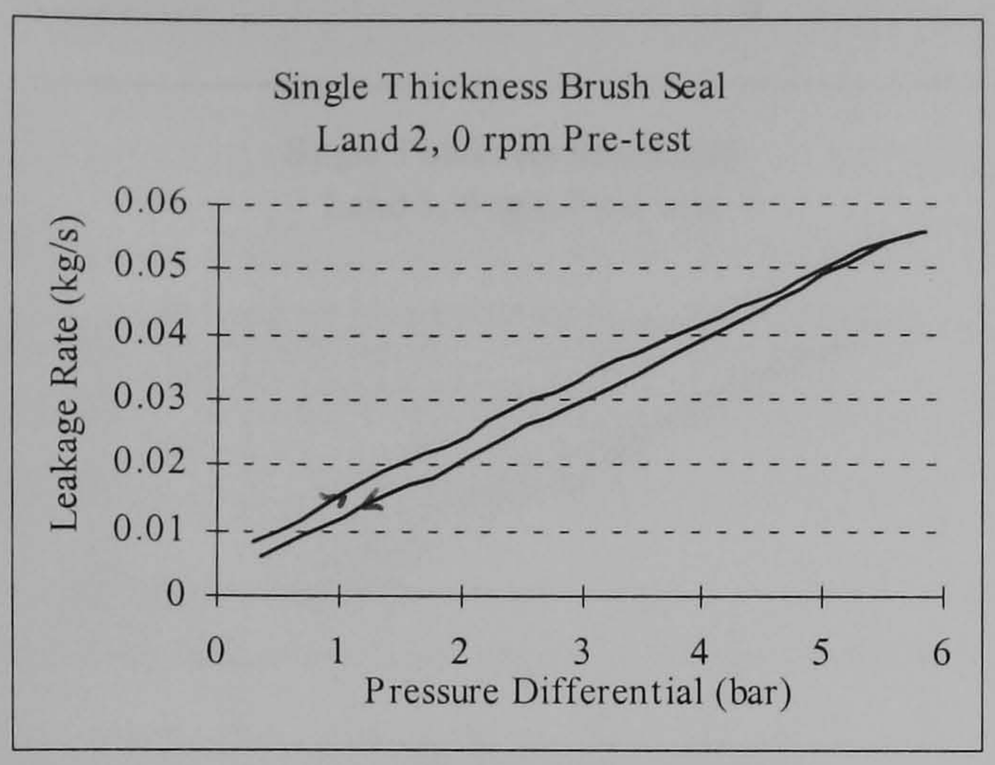

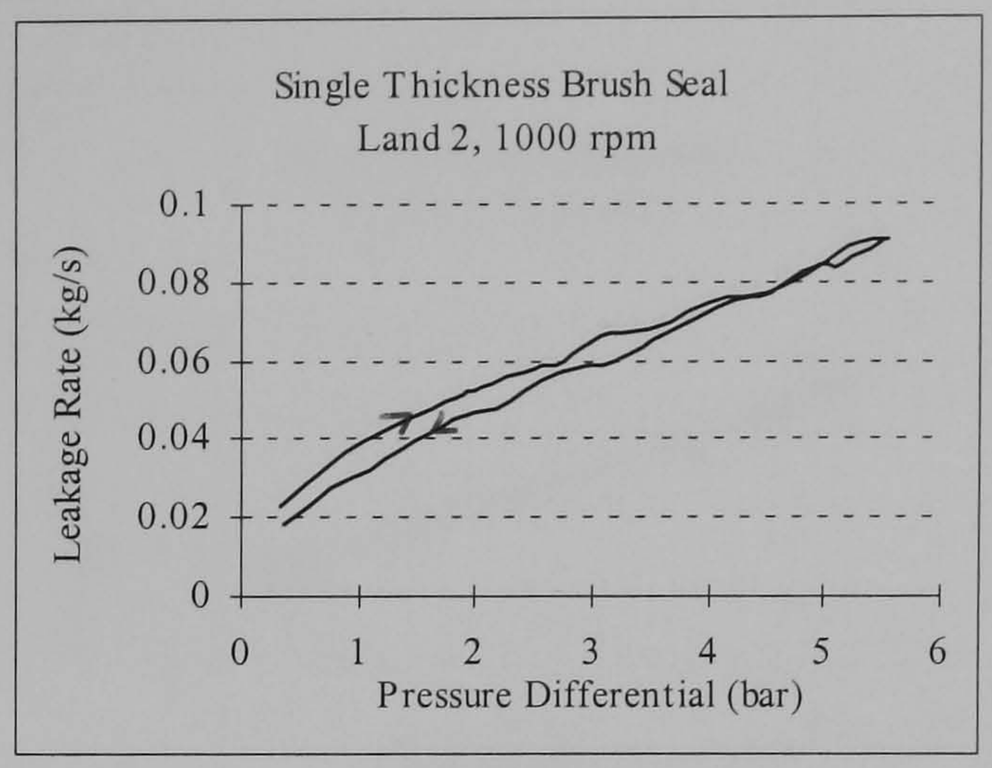

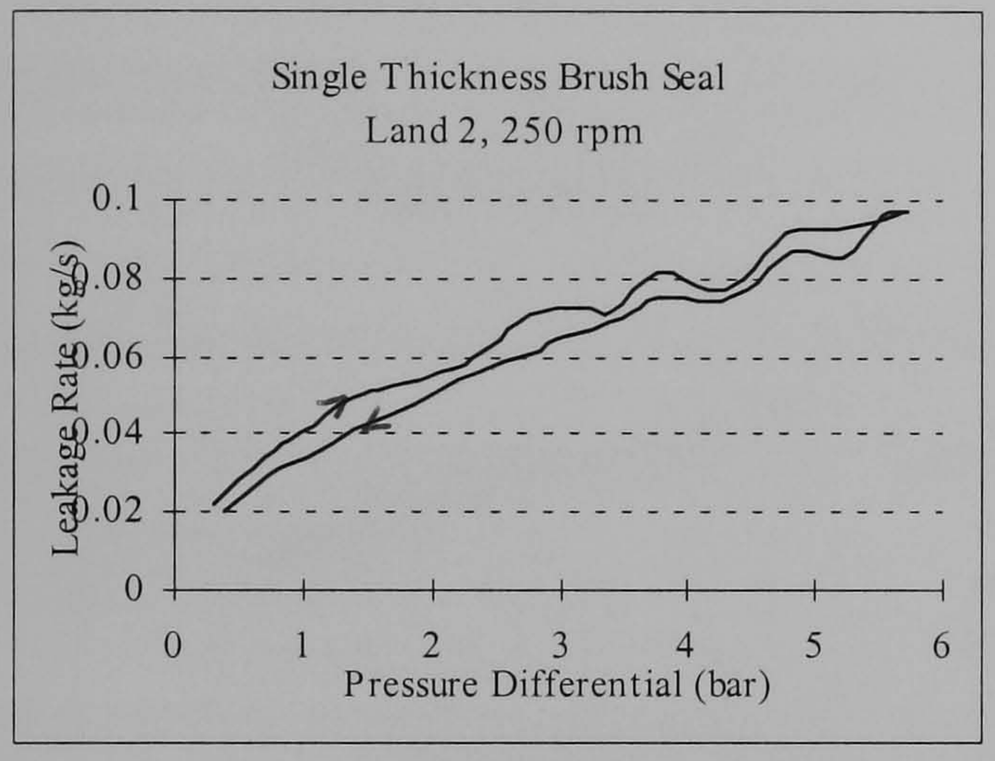

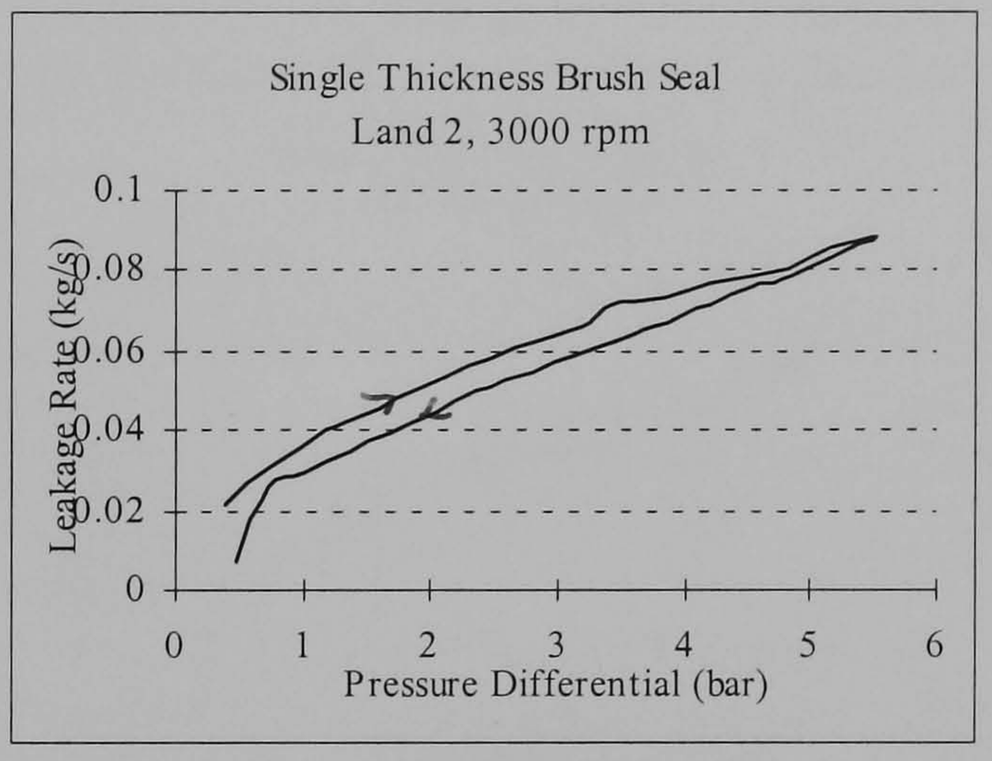

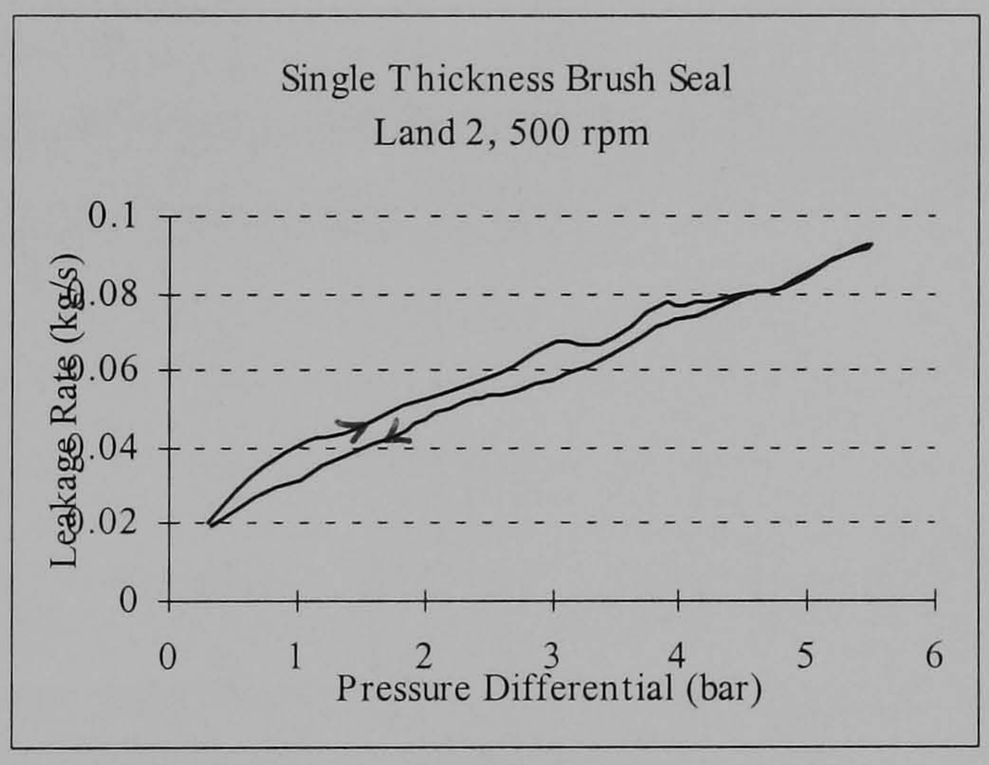

Figure 7.15 The effect of a 0.50 mm (peak -peak) rotor eccentricity on the leakage for a 0.2 mm bristle interference fit for a single thickness brush seal.

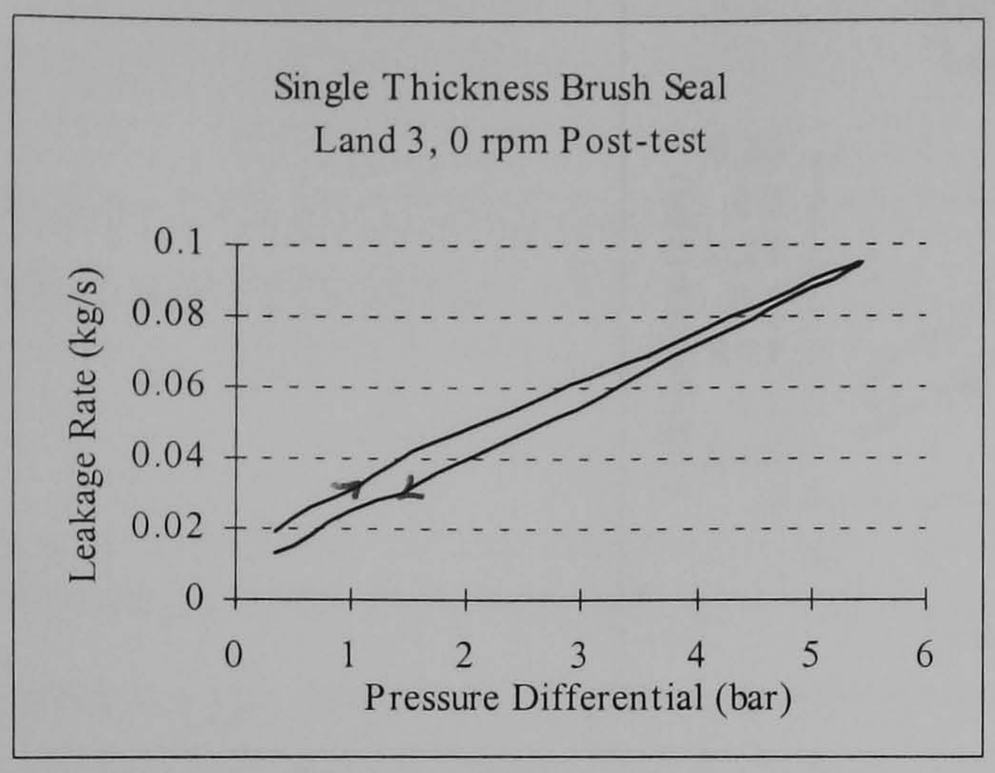

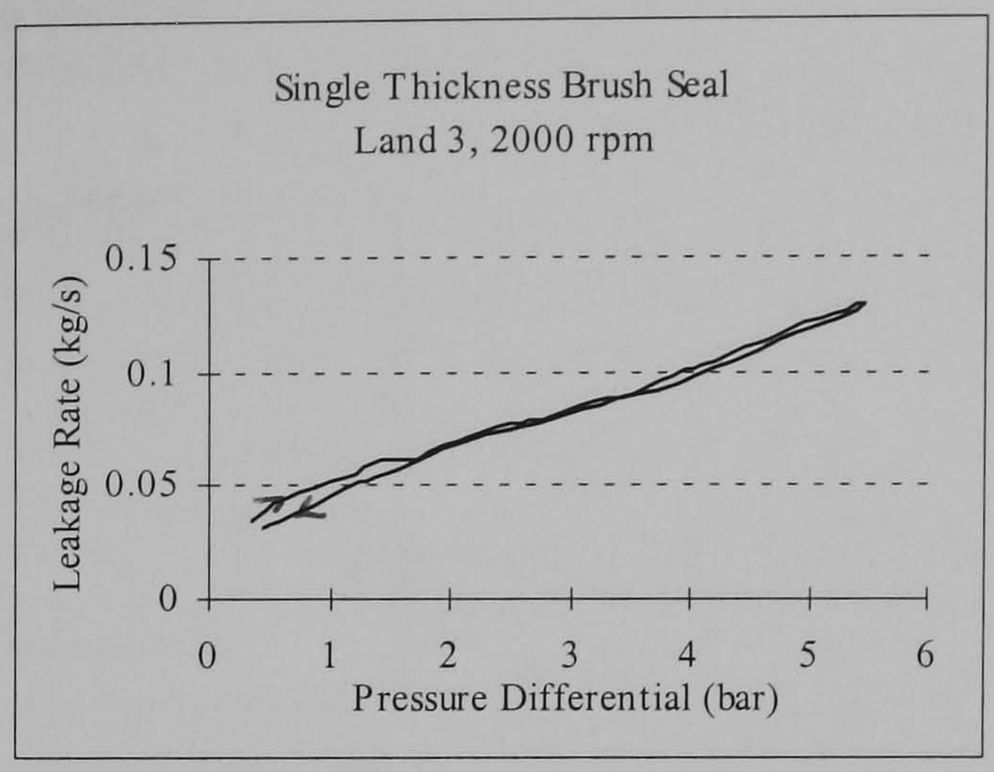

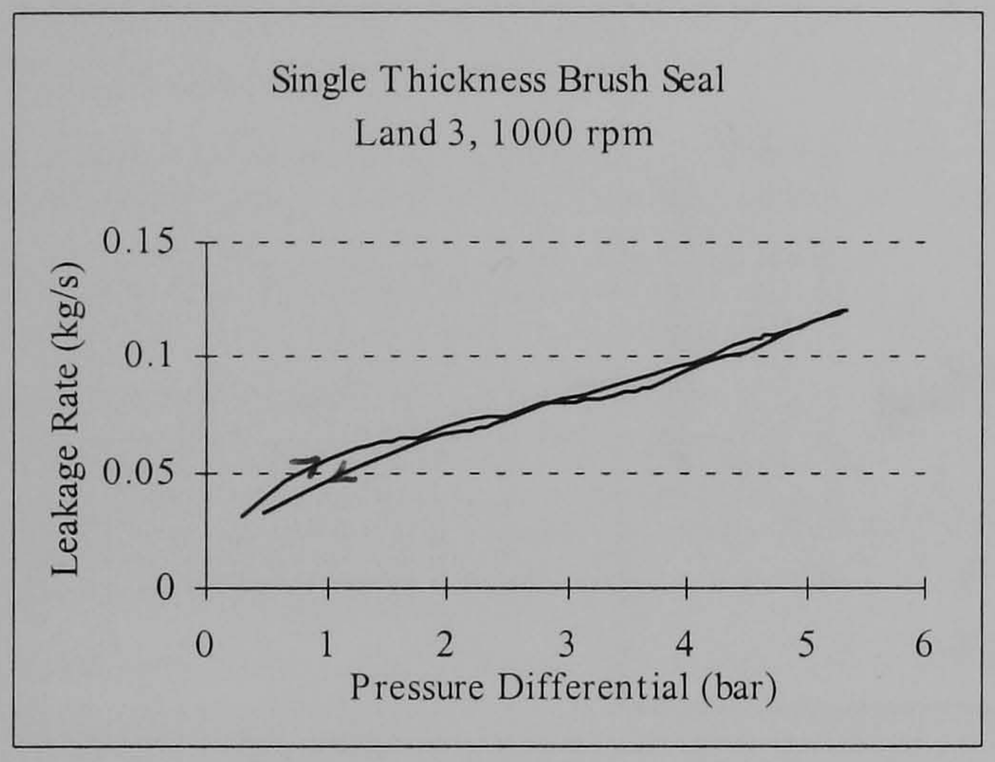

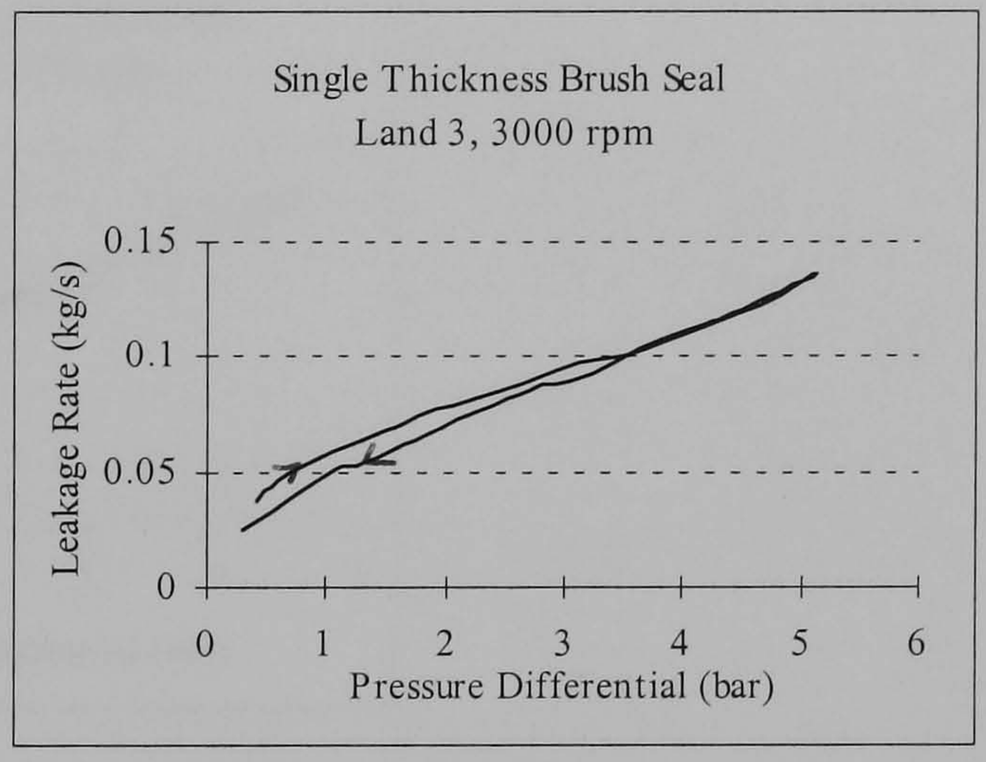

Figure 7.16 The effect of a 0.50 mm (peak-peak) rotor eccentricity on the leakage for a size for size bristle fit for a single thickness brush seal.

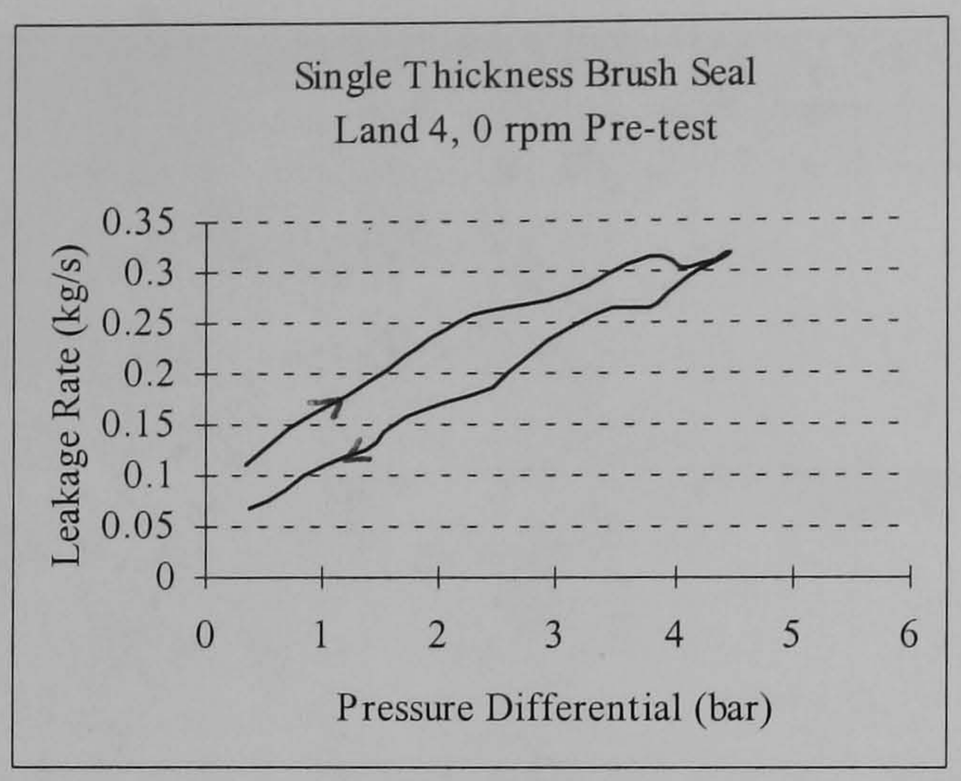

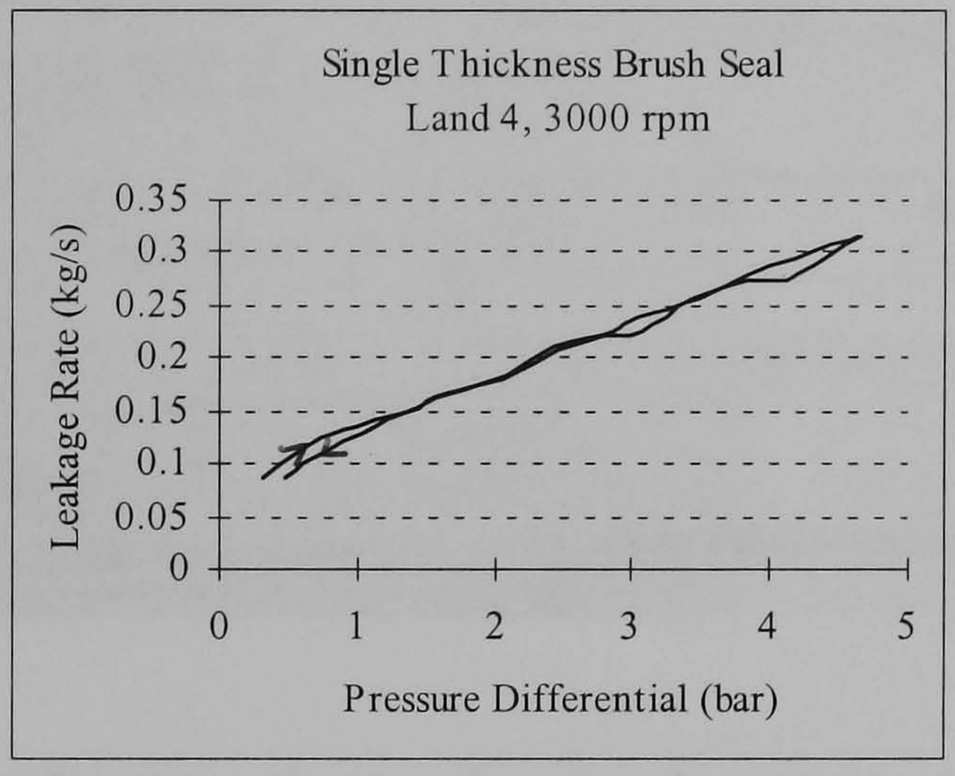

Figure 7.17 The effect of a 0.50 mm (peak-peak) rotor eccentricity on the seal.

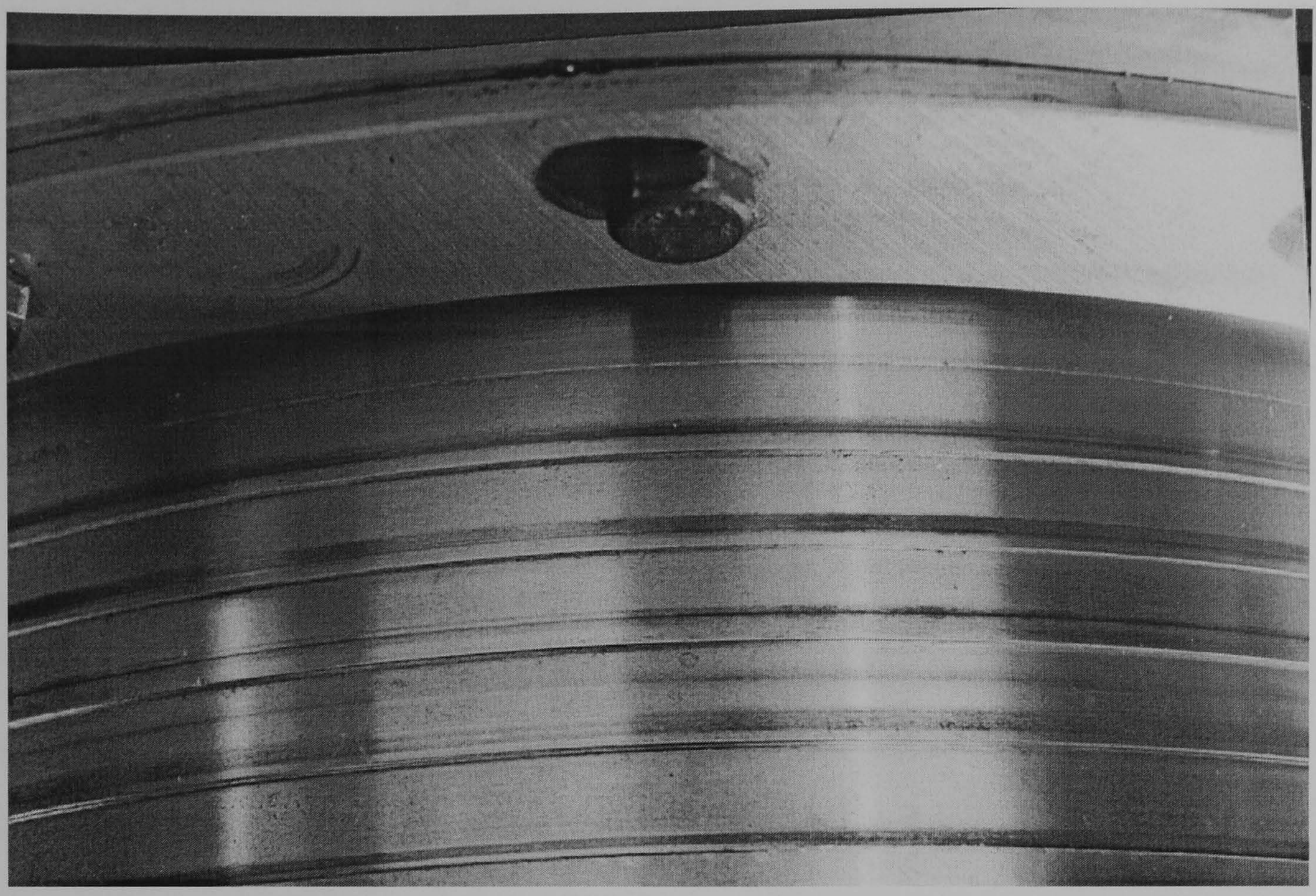

Figure 7.18 Photograph of the stepped rotor showing the wear tracks on all five lands.

8.0 Literature Review: - Computational Fluid Dynamics Modelling of Brush Seals.

This chapter is split into three sections. These are the introduction **(Section** 8.**1)**, followed by the background to the flow through porous media **(Section** 8.**2)** and then the literature review on the **CFD** approach to modelling brush seals **(Section 8.3)**.

8.1 Introduction

Ferguson (1988) showed brush seals to offer a significant 90 % improved sealing performance over conventional five-finned labyrinth seals installed in gas turbines. However, whilst bulk flow measurements have been made the understanding of the macroscopic and microscopic flow processes was not fully developed. An understanding of these processes is essential to optimise the design and application of brush seals and to predict their leakage flow rate under different conditions. Experimental design and leakage testing is very time consuming and expensive for the large number of applications possible, therefore Computational Fluid Dynamics **(CFD)** and numerical modelling offer a more cost effective and relatively quick route for product development before (and after it has been proven to be reliable, instead of) prototype manufacture and testing.

Publications by several authors who carried out experimental and theoretical analysis gave an insight into possible flow characteristics. **Chupp and Dowler (1993)** showed the leakage rate hysteresis curve and its relationship to the rotor speed and several other design parameters during experimental tests. **Braun, Mullen et al (1990)** carried out substantial experimental flow visualisation tests through cylinder arrays characterising the complex flows such as river jetting, vortical flow and cross-flow.

Several attempts at numerical modelling were also carried out. **Dowler et al (1992)** used a porous media model to estimate the flow resistance through a brush seal based on work carried out on cylinders in cross-flow. **Hendricks et al (1991)** developed a bulk flow

model based on results for porous media and filters. **Bayley and Long (1993)** presented an axisymmetric two-dimensional model that treated the brush as a Darcian porous medium. The porosity value was the ratio of resistance coefficients in orthogonal directions. These papers, models and experiments are discussed more fully in **Chapter 6.**

So far much of the theoretical numerical modelling that has been carried out has used in house algorithms and codes and not commercially available **CFD** packages. The fundamental flow equations and many of the assumptions are equally applicable to both theoretical numerical and **CFD** modelling however this section only reviews the **CFD** models and some of the background to them.

The brush seal pack has been modelled in two ways, either as an area of porous media or as a regular bank of tubes (analogous to a heat exchanger). Both methods rely heavily on assumptions and idealised bristle pack conditions. The background to some of the porous media equations is briefly described in **Section 8.2**.

8.2 Background to flow through porous media.

In 1856 the French engineer **Henri Darcy (1803-58)** published experimental results from which he deduced what is now know as **Darcy's Law**. This could be expressed as

$$V = - k \phi' \qquad \textbf{Equation 8.1}$$

where V = average seepage velocity

ϕ' = hydraulic gradient and

k = coefficient of permeability in the direction of flow.

As an approximation k was often assumed to be a constant. Darcy's law could be considered to be valid for creeping flows with very low values (nearly equal to zero) of Reynolds number Re and for flows with Re<1. The extent of the flow regime covered by the Darcy Law involved the pre-laminar regime and a part of the laminar regime with small magnitudes of fluid velocity. The effects of inertia terms in the Navier Stokes equations could be ignored in comparison to those of the viscosity terms.

The flow behaviour was essentially non-linear in the laminar regime and beyond a value of Re<1 it may be necessary to use non-linear, non- Darcy laws. Two non-linear laws commonly used in finite element **(FE)** formulations were

$$\phi' = aV + bV^2 \qquad \textbf{Equation 8.2}$$

and

$$\phi' = cV^m \qquad \textbf{Equation 8.3}$$

where a, b, c and m were non-dimensional materials constants that could be determined from permeameter tests, and V is average seepage velocity **Scheidegger (1957)).**

Equation 8.2 is called the **Forcheimer Law** with a and b (the resistance coefficients) assumed to be invariant. The second equation was known as the **Missbach** or **Exponential Law**. The **Forcheimer** relation could be assumed to be valid for various ranges of Re = 0.5,5-25,25-100 within the laminar regime and it was thought that it was applicable for it to be extended into the turbulent flow regime **(Desai (1975)).**

Forcheimer's Law can be written as

$$-\frac{dp}{dx} = a\mu V + b\rho V^2 \qquad \textbf{Equation 8.4}$$

$$V = \frac{m}{\rho A} \qquad \textbf{Equation 8.5}$$

where

p = static pressure (N/m^2)

x = axial co-ordinate direction (m)

V = average velocity (m/s)

m = mass flow rate (kg/s)

A = flow area (m^2)

ρ = density (kg/m^3)

μ = viscosity (kg/m/s)

and

a = viscous resistance coefficient

b = inertial resistance coefficient

(permeability was sometimes introduced which was the inverse of coefficient a)

In its original form **Forcheimer's Law** assumed isotropic flow and isothermal conditions and constant μ, a and b. This was obviously not the case for brush seals as the flow in the x, y, and z directions were significantly different, and the temperature, viscosity and a and b coefficients may change during operation.

8.3 Literature Review on the CFD Approach to Brush Seals.

Mullen, Braun and Hendricks (1990) used a finite element program **(FIDAP) to** model a 6x6 matrix of uniformly spaced circular bristles with a uniform flow field upstream. Two, two-dimensional models were generated, having different packing spacing and mesh coarseness **(Figure 8.1).**

The flow area for the first model was 25.4 mm (1 inch) high by 0.457 mm (0.018 inch) in width by 0.76 mm (0.030 inch) thickness including upstream and downstream elements. The bristle diameters were 0.071 mm (0.0028 inch) and spaced 0.0051 mm (0.0002 inch) apart providing a cell size of 0.076 mm (0.003 inch) square.

The inlet and exit boundaries were held at prescribed pressures and calculations were carried out at steady state for a 0.345 bar (5 p.s.i.) pressure drop with a working fluid of air. Periodic boundary conditions were prescribed along the side regions and no slip conditions are applied around each bristle.

In the second model the bristles were spaced at 0.0127 mm (0.0005 inch) apart for a cell size of 0.0838 mm (0.0033 inch). Two different mesh refinements were used to estimate the error introduced by the Finite Element **(FE)** discretisation. These were models with 624 elements, 761 nodes and with 3105 elements and 2784 nodes. The model with the slightly larger cell spacing and higher Reynolds number (300 compared to 150) provided results that were the closest to the experimental results. **Mullen et al** attributed the differences in the results to imperfections in the bristle matrix, variations in bristle geometry, materials and fluid driven interactions.

The flow rates of the two models were compared with experimental results supplied by Cross Manufacturing. These are shown in **Table 8.1** and show that the two models produced results that were reasonably similar to the experimental results.

A velocity vector plot was also given which possessed symmetry and spatial uniformity. This was in contrast to the results of flow visualisation techniques that show complex flow irregularities such as "packing", "jetting", "vortices", and "rivering".

While the volume flows were within 50 % of the measured values of published results the observed flow field appeared to be turbulent. It should be noted that when calculating friction factors for flow through filters, **Hersh and Walker (1980)** and **Gunter and Shaw (1945)** indicated a transition from laminar to turbulent flow for a Reynolds number around 200. The numerical analysis was laminar and the viscous effects were less than those for turbulent flows. Moreover, the inertial effects were also less so a trade off may have tended to mitigate the inaccuracies of the model.

Braun and Kudriavtsev (1993) produced a numerical simulation of a brush seal section. This was a model of a two-dimensional uniform flow with zero angle of incidence past an array of round cylinders (pins). They pointed out that whilst there has been a wide body of numerical work treating the flow around a cylinder in cross-flow **(Kawamura et al (1986) Fornberg (1980), Ohya et al (1992), Li et al (1992))** few researchers focused their attention on the nature of the flow changes when it interacts with a bank of tubes **(Reynell et al (1991))**. The effects of the cylinder arrangement and the array size on the flow structure were (and are) not fully understood especially when the pitch to diameter ratio **(PTDR)** was small (<<1).

The computational model was validated on grids of 31x31 and 61x61 points with a range of Reynolds numbers of $\mathbf{Re_h}$ (Reynolds number based on channel height) = 2500 to 25000 (or $\mathbf{Re_d}$ (Reynolds number based on pin diameter) = 500 to 5000). The model used for code verification was the flow and pressure field around a body with a cylindrical cross-section positioned in the centre of a square channel. The diameter of the body

occupied 20 % of the channel characteristic length. The results showed that with increasing Reynolds number the error in pressure differential increased if the grid sizes remained constant. A grid size of 139x139 was used in the full model, which provided reasonable resolution.

Seven full models were tested **(Figure 8.2)**. The first three models were a staggered array of 6x11 bristles with a $\mathbf{PTDR_L}$ (longitudinal pitch to diameter ratio) = $\mathbf{PTDR_T}$ (transversal pitch to diameter ratio)=1 at $\mathbf{Re_h}$ = 2000. The second and third models differed by having a space in between the first three columns and the last three columns, called "Zone C". These spaces were three and five bristle diameters respectively. The forth and fifth model had 7*11 bristles and had $\mathbf{Re_h}$ values of 100 and 2000. Two further models were also given to show the effect of a decrease in the $\mathbf{PTDR_L}$ on the structure of the flow patterns. These had Re_h = 2000 and $\mathbf{PTDR_L}$ = 0.66 and 0.33.

Full and close up velocity vector plots were given showing the flow patterns for the models. The characteristic jetting between pins and formations of recirculation zones in the wake of the pins was noted. However the pin spacing was such that it did not allow the growth of the recirculation zones and forced their closure within one pin diameter in the first model. In the wake of the last row of pins the shedding of eddies was noticeable as well as the formation of steady recirculation zones. The computed non-dimensional pressure drop was 28.8.

The first of the models with two formations of three rows of pins each showed that the recirculation zones longitudinally occupied the entire space whilst laterally they were limited by the rivering jets to one width diameter. The computed pressure drop was 29.08. The second model with a larger cavity between the rows showed that the wake terminated at approximately three diameters behind the last row of the first block. This allowed the jets to expand and merge all along the cross-section only to re-accelerate upon entering the first row of pins of the second block. That phenomenon was associated with an additional expenditure of mechanical work that caused an increase in the pressure drop to 31.53.

The next two models showed similar effects to the first three, however wall effects were more visible in the example that contained 11 pins rather than 10 in the final row. Recirculation in the wake of the pins was almost negligible for the example with $\mathbf{Re_h} = 100$ but for the example with $\mathbf{Re_h} = 2000$ two standing vortices could be seen.

Pressure plots were also given across the bristle pack ($\mathbf{Re_h} = 100$) which clearly showed the drop occurring at the leading edge of any given row, followed by a pressure recovery in the wake of the row. At $\mathbf{Re_h} = 2000$ a similar phenomenon occurred but the pressure recovery was minimal. These effects were linked to the mechanism of kinetic energy consumption believed to be instrumental in the sealing process.

Further velocity vector plots were given to show the effect of a reduction in the $\mathbf{PTDR_L}$ from 1 to 0.66, and 0.33 performed at 2000. This decrease caused a reduction (and even complete disappearance) of the recirculation zones behind the pins of the inner cylinders whilst exerting little influence on the size or shape of the wakes behind the last row of cylinders. The pressure differential values were given in **Table 8.1.**

Experimental flow visualisation tests were also carried out on a 3x11 array at $\mathbf{Re_h} =$ 197, 500 and 956. The results for the first test showed small recirculation zones behind the pins that closed within 1/2 a pin diameter and did not influence the jets or impede the remaining flow. At $\mathbf{Re_h} = 500$ the flow started to be less symmetrical (showing a s shaped jet) due partially to non-equal pitches between the flow near the upper wall and near the lower wall. At $\mathbf{Re_h} = 956$ two recirculation zones of butterfly like structure that were roughly symmetric appeared. These zones were due to the interaction of transversal low pressure zones and longitudinal pressure inversions and had the effect of sealing the exit of the array.

A comparison of experimental and numerical results showed a 7% difference for $\mathbf{Re_h} = 195$ but that grew worse for $\mathbf{Re_h} = 327$. This deterioration was attributed to the error introduced by a scaling factor.

The study showed that the distance between zones of densely packed pins influenced the total pressure differential across the brush seal due to the nature of the recirculation zones. The interaction of successive pressure drops and partial pressure recovery contributed to the overall pressure drop, as did the large recirculation zones in the wake of the array of pins.

Kudriavtsev and Braun (1995) went on to use a **CFD** simulation of the secondary flow system in a gas turbine engine. Three interconnected disk cavities separated by a brush seal were located along the secondary path **(Figure 8.3)**. The core flow was driven by a pressure differential.

A computational algorithm was developed in conjunction with **FLOCON** (a computer program) to predict the flow patterns and leakage based on the numerical solution of the transient laminar Navier -Stokes equations. The purpose of the study was to present an integrated brush seal disk cavity flow model to demonstrate the effectiveness of that approach and to emphasise the necessity for further work in that direction.

The brush body was modelled approximately as a saturated porous medium using **Darcy's Formula**.

$$-\frac{dP}{dx} = \frac{\mu}{k}\mathrm{U} \qquad \textbf{Equation 8.6}$$

and /or the **Brinkman** assumptions **(Burmeister (1993)**

$$-\frac{dP}{dx} = \frac{\mu}{k}U - \frac{\mu}{\varepsilon}\nabla^2 U \qquad \textbf{Equation 8.7}$$

where ε was the porosity of the porous media, k was the permeability, U was the speed and P was the pressure.

The Darcy number k was vitally important to characterising the sealing capability of the brush. Accuracy was established via three different methods. The numerical approach required the numerical modelling of the Navier-Stokes equations through the

brush (a cross-section of 11x7 bristles) to obtain average pressure drop values and finally to calculate permeability using Darcy's formula.

The theoretical approach allowed the calculation of brush seal permeability using

Ergun's Formula (1952)

$$k = \frac{d^2 \varepsilon^3}{A(1-\varepsilon)} \qquad \textbf{Equation 8.8}$$

where d = brush seal bristle diameter, ε was the porosity of the porous media, k was the permeability, U was the speed and P was the pressure.

and A=150

$$-\frac{dP}{dx} = \frac{A(1-\varepsilon)}{d^2 \varepsilon^3} \mu U_D + \frac{0.143 U^2{}_D}{\varepsilon^{\frac{3}{2}} k^{\frac{1}{2}}} \qquad \textbf{Equation 8.9}$$

The experimental approach was used to obtain the effective permeability value through and under the brush seal and backing plate at a given clearance. In this case results presented by **Carlile et al (1993)** provided enough information for the estimation of brush seal permeability coefficient $\mathbf{k_u}$. **Table 8.2** gave some of the physical characteristics and parameters used in the computation.

Several boundary conditions were applied to the computational domain. The main flow entered with zero radial and circumferential velocity, and an axial velocity of 100 m/s. The maximum velocity at the disk tip was also 100 m/s. The permeability value chosen was $k_u = 6.0 * 10^{-13}$. This value can be found from **Equation 8.9** with ε = 0.216 and d = 0.075 mm.

A non-uniform computational grid 207x145 (23 axial regions and 14 radial regions) was used and this was thought to be the minimum required for accurate resolution of the complex vortex separation processes.

The results of the **CFD** analysis were given for rotating and non-rotating cavities and showed the global flow patterns that occurred in the interstate cavities. The flow patterns were extremely complicated and showed a multitude of vortices in each section. It

appeared from the results that for the geometry and flow patterns considered in that study, the rotational effects were minimal.

Rotating and non-rotating close up contour plots of the brush flow showed that the radial component was comparable in size to the axial component. Further close ups of the cavity behind the brush seal showed that the flow stream remained attached to the shaft surface whether it rotated or not.

A series of plots taken at intervals of 10^4 iterations demonstrated different flow patterns that appeared in the seal cavity as time progressed. The rotating and non-rotating were slightly different with the stationary plots tending towards three vortices and the rotating plots tending towards two. This proved that a periodic quasi-steady state behaviour existed.

Under high shaft rotation and small flow leakage the strong axial flow along the shaft allowed the formation of Taylor vortices between the inner rotating shaft and the outer stationary cylinder (vane). This form of fluid instability created three almost equal length vortices that filled the entire cavity. The appearance of Taylor vortices indicated the domination of the rotational effects upon the axial flow shear layer that contained the leakage.

The study concluded that the integrated cavity seal approach allowed increased insight in the many complicated flow features that influenced the flow field and that brush seal modelling when the brush was only represented by its axial (horizontal) cross-section was not self supporting.

Sharatchandra and Rhode (1996) carried out a numerical study of the effects of rotor induced swirl velocity on the performance of a brush seal. The analysis involved the solution of the full Navier Stokes equations in a two-dimensional, idealised configuration using a strongly conservative finite volume method developed by the authors, in conjunction with the **QUICK** differencing scheme **(Leonard 1979).**

The study carried out microscopic flow analysis on a single module (5 bristles in a staggered square) that was thought to be representative of the interior of a bristle pack after the second or third rows **(Figure 8.4)**. The staggered square configuration was idealised in that the bristle lay angle was neglected. The model grid generated was 64x30 and contained two inlets and two outlets in orthogonal directions. **Sharatchandra and Rhode** used this approach to exploit the approximately streamwise periodic nature of the flow in the bristle packs. That allowed a much finer resolution of local velocity and pressure distributions with the use of the computational resources available.

The paper considered the cross-flow (normal to the leakage flow) induced by rotation of the shaft. These effects were confined to a very small region near the bristle tips. This was thought to be important because the high bristle temperatures due to frictional heating may effect bristle wear.

The validity of the computations were tested by comparisons with the flow measurements of **Bergalin et al (1949)** who measured pressure drops associated with cross-flow in tube banks corresponding to the staggered square configuration with a dimensionless diagonal pitch of 1.25.

The grid dependence tests showed that the **QUICK** scheme yielded grid independence on courser grids and the results were virtually insensitive to the number of points used providing they were greater than 15.

Reynolds Number (axial) was plotted against non-dimensional pressure drop for the Power Law **(Patankar (1980)**, **QUICK** scheme and measured (interpolated) experimental values from **Bergalin et al**. The three lines were in good agreement.

Further plots showed the effect of changes in bristle spacing from a pitch of 1.1 to 1.05. As expected, the tighter spacing between bristles resulted in lower leakage, indicating better sealing characteristics. It was also noted that near the rotor surface the leakage decreased with increasing tangential Reynolds number. This was consistent with the

experimental observations of **Ferguson (1988)** that demonstrated reduced leakage with increased shaft rotation.

Streamline plots were also given which for models having an axial Reynolds number of 50 and 150 and a tangential Reynolds number of 200 for pitches of 1.1 and 1.05. The differences were slight. Several interactions were noted however, including, bifurcations, recirclulation zones and regions of dramatic change of direction induced by nearby, intense acceleration such as that near hairpin shaped vortices.

The plots showed that smaller spacing not only decrease leakage, but also decreased the rate at which leakage increases with increased overall pressure drop.

The **QUICK** convective differencing scheme was shown to be somewhat more realistic than the Power-Law scheme and it was proven that a first order streamwise periodic boundary condition treatment enabled the numerical convergence of flows having two orthogonal directions.

Chew and Hogg (1997) developed a one-dimensional form of a porous medium model for the calculation of brush seal leakage flow. They demonstrated its use for a wide range of experimental data from **Carlile (1993), Bayley and Long (1993)** and **O'Neil (1993)** for brush seals with interference fits. **Table 8.4** gives some of the seal dimensions and a brief comparison of test details.

The basis of the model was **Forchiemer's Law (1901) (Equation 8.4)** which incorporated a viscous (a) and inertial (b) coefficient. The dimensions of a and b were $1/length^2$ and $1/length$ respectively (where length was the bristle pack thickness). Dimensional arguments suggested that seals with similar bristle packing would have coefficients that would scale with the bristle diameter d so that ad^2 and bd remain constant.

Bristle packing was difficult to measure during operating conditions. **Chew and Hogg** therefore suggested that the radially observable packing pattern (voids and bristles) be estimated and used in the calculation.

The unknown porosity coefficients were estimated by manipulation of several porosity calculations that had previously been applied to packed beds. These included ones reported by **Scheidegger (1957)** given by **Ergun and Orning (1949).**

$$-\frac{dp}{dz} = 5\alpha\frac{S^2}{\varepsilon^3}\mu V + \frac{\beta S}{8\varepsilon^3}\rho V^2 \qquad \textbf{Equation 8.10}$$

where p = static pressure

z = axial co-ordinate direction

μ = viscosity

ρ = density

V = average streamwise velocity

ε = the porosity equal to the volume of voids divided by total volume,

S = the wetted surface area per unit volume,

and α and β were constants.

For low Reynolds numbers, the flow reduced to the **Carmen-Kozeny** equation.

For a brush seal with a lay angle ϕ to the tangential direction s and ε were estimated as follows.

$$\varepsilon = 1 - \frac{\pi dN}{4l\sin\phi} \qquad \textbf{Equation 8.11}$$

$$S = \frac{\pi dN}{l\sin\phi} = \frac{4(1-\varepsilon)}{d}$$

N = number of bristles per unit circumferential length.

l = bristle pack streamwise thickness

d = bristle diameter

From the definition of the resistance coefficients a and b and the previous two equations, algebraic manipulation gave the following equations.

$$ad^2 = \alpha\frac{80(1-\varepsilon)^2}{\varepsilon^3}, \quad bd = \frac{\beta}{2}\frac{(1-\varepsilon)}{\varepsilon^3} \qquad \textbf{Equation 8.12}$$

According to **Kay and Nedderman (1974)** the empirically determined values $\alpha = 1$ and $\beta = 2.23$ fitted results over a wide range of Reynolds numbers.

It was suggested that the resistance coefficients would be expected to remain constant for seals with similar bristle packing. Plots using **Carliles** results for three gases, **Bayley and Longs** and **O'Neils** results (a wide range of operating conditions and seal dimensions) all showed that the flow resistance followed a quadratic variation with Re. This indicated that the Darcian porosity approach to flow modelling was inappropriate.

The model required the use of a bristle pack streamwise thickness value to calculate the non-dimensional bristle pack thickness which could have a minimum of L= 0.866. A value of L= 1.1 was found to give agreement with **Carlile's** data for a 0.8 mm axial thickness seal. L= 1.035 was used with **Bayley and Longs** seal which corresponded to a seal pack thickness of 0.7 mm as quoted in their paper. **O'Neil's** results were then plotted L=1.25 was used. This corresponded to a 0.76 mm pack thickness.

The one-dimensional model appeared to be very simple and reasonably accurate at predicting interference fit seal leakage flows providing the bristle pack non-dimensional thickness was known. However it was pointed out that if a clearance existed the resistance to flow through the seal would be highly anisotropic and two-dimensional. The one-dimensional model presented gave leakage flows as being directly proportional to the area available for flow between the backing plate and shaft. This conflicted with **Chupp and Dowler's (1993)** conclusion based on seal test data, that increasing backing plate clearance had little effect until a point was reached where the bristles began to deflect.

Chew, Lapworth and Millener (1995) developed a CFD based model of brush seals, which they tested against experimental data from other workers. **Figure 8.5** gave a schematic of their experimental brush seal. The model treated the brush as an axisymmetric, anisotropic porous region with non-linear resistance coefficients. The **CFD** code used was based on an algorithm described by **Moore (1985).** The governing equations were discretised by integration over a set of control volumes using linear interpolation

rules. The discretised equations were iterated towards convergence using the **SIMPLER** algorithm described by **Patankar (1980).**

Forchiemer's Law (Equation 8.4) was used to describe the porosity of the bristle pack in three directions. The six coefficients were defined (where a was the principal viscous resistance coefficient and b was the principal inertial resistance coefficient), a_s (parallel to the bristles), a_n (normal to the bristle in the r- plane), $\mathbf{a_z}$ (axial direction), $\mathbf{b_s}$, $\mathbf{b_n}$, and $\mathbf{b_z}$ with the assumption that $\mathbf{a_n} = \mathbf{a_z}$ and $\mathbf{b_n} = \mathbf{b_z}$, the coefficients were uniform throughout the bristle pack and did not vary with pressure differential across the seal.

The solution domain had no-slip, no-penetration assumptions for the boundary conditions on the solid walls. Total pressure and flow angles were specified at the inlet and at the outlet static pressure was specified. Relaxation and artificial viscosity was used to damp oscillations and prevent divergence.

Typical meshes used had 76 axial and 48 radial grid locations. Eight rows of bristles and a pack thickness of 0.61 mm were assumed. Fluid and materials properties were chosen to approximately match experimental conditions. A mesh dependency test with a pressure ratio of 3 and a grid with 85 axial and 79 radial locations was carried out. Some dependency was found. Mass flow, pressure exerted by the bristle pack on the shaft (according to the bulk flow model) and the maximum axial bristle deflection were found to differ by 4%, 12% and 4% respectively. The results were thought to be acceptable for an initial evaluation and demonstration of the model.

A plot was given showing the experimental backing plate pressures and the various calculated pressures using different values of a_z, b_z and a_s, a_z. The plot showed the degree of anisotropy and indicated that the best set of coefficients tested were as follows, $\mathbf{a_z} = \mathbf{a_n} = 60\mathbf{a_s} = 5.317*10^{11}\ m^{-2}$, and $\mathbf{b_z} = \mathbf{b_n} = 1.998*10^{6\ m-1}$, $\mathbf{b_s} = 0$.

A further plot showing mass flow rate against pressure ratio for the experimental results, the **Bayley and Long** model and the **Chew** model showed that the **Chew** model was in good agreement with the experimental results.

Examples of the predicted velocity field in the vicinity of the seal were given for a model where there was a 0.75 mm bristle to shaft clearance and zero clearance with a pressure ratio of 1.5. The plots showed that leakage occurred mainly through the clearance when one existed. Flow through the pack was weak and radially inward. When there was no clearance the flow occurred through all of the porous media and was significantly effected by the backing plate. The coefficients were modified to more closely resemble the experimental results.

Several examples of bristle bending calculation results were also given for a range of pressure differentials. The contact pressures were in the range of 200 to 2000 kPa and rose relatively linearly with increase in pressure differential.

Chew et al concluded that their mathematical model predictions were in agreement with experimental observations and that the non-linear porous resistance law gave better agreement than a Darcian (linear) treatment. A single set of resistance coefficients were used which gave good agreement with mass flow measurements for an interference seal at pressure ratios up to 4. However, these coefficients did not give agreement with measured mass flow rates for a build clearance seal when it was assumed to be fully blown down.

This clearly indicated there was scope for further investigations of both the resistance laws and the behaviour of the seals. The bristle bending calculations showed that deflections in the axial direction were quite small. Larger deflections were seen in the orthogonal plane with aerodynamic forces tending to press the bristles against the shaft.

Further work was also carried out in parallel with that mentioned above. **Turner Chew and Long (1997)** conducted experimental and **CFD** mathematical modelling using a brush seal at two bristle to rotor clearances (0.27 and 0.75 mm) **(Figure 8.6)**. The experimental programme examined the radial pressure distributions along the backing ring, the axial pressure distribution along the rotor and the mass flow rate through a range of pressure ratios. The experimental programme was also used to calibrate the **CFD** model described previously.

The **CFD** model included inertia and viscous resistance coefficients for three directions and for three seal configurations (**Table 8.3).** These corresponded to conditions where the bristle pack was not blown down (remaining in its built condition) or the pack was fully blown down so that the bristle tips touched the shaft. For the blown down pack it was assumed that $\mathbf{a}_z = 60\mathbf{a}_s = \mathbf{a}_n$ and $\mathbf{b}_s = 0$, but the resistance coefficients were adjusted to give a reasonable fit to the backing ring pressure distribution and mass flow measurements.

The experimental apparatus was designed to measure the pressure variations on the brush seal backing plate and under the brush seal pack. Multiple pressure tappings were laser drilled into the backing plate (20x0.25 mm) and the stationary rotor (24x0.25 mm). Tests were carried out for a range of upstream absolute pressures between 108 kPa and 400 kPa.

Radial pressure distributions for experimental and **CFD** models were plotted non-dimensionally with pressure against radial position. Reasonable agreement was achieved. Axial pressure distribution was also plotted in a similar manner. These results were more prone to experimental error or irregularity. They showed that the CFD model tended to give an even pressure drop through the bristle pack whilst the experimental results indicated a substantial initial drop at a pressure ratio of 1.3 after the initial row, followed by a few small oscillations. At the pressure ratio of 2.5 blow down occurred and the pressure drop appeared to be in the latter half of the bristle pack.

Two plots were also given for mass flow rates (showing **CFD** and experimental) results for 0.27 and 0.75 mm clearance. The **CFD** results (non blown down) were in reasonable agreement with the 0.27 mm clearance experimental results at low pressure ratios whilst the blown down results were closer at higher pressure ratios (up to 4). The maximum leakage rate predicted was 0.08 kg/s whilst the experimental value was 0.05 kg/s. The 0.75 mm clearance results showed a similar pattern to the 0.27 mm results but had the addition of an extra set of experimental results where the brush seal had been subjected to a shock load. This lowered the mass flow rate results in the low to

intermediate pressure ratios (1-3). The maximum mass flow rate predicted was 0.2 kg/s whilst the experimentally recorded result was 0.125 kg/s.

The results from the **CFD** analyses were used in the bending calculations. Axial deflections (0.75 mm clearance with blow down at a pressure ratio = 2) were shown to have a maximum of 0.1 mm at the rear of the bristles and indicated bulging of the pack in the front of the seal by 0.05 mm. Rotor loading due to aerodynamic forces were seen to be a maximum of $1.6*10^5$ N/m^2 and reducing the clearance forces was seen to reduce the effect of the blow down. Radial displacements were also plotted against coefficient of friction and showed that if the friction between the backing plate and the bristle pack was sufficiently high the blow down effect was suppressed. The point at which this occurred was dependent on both the pack-to-rotor clearance and the pressure ratio.

It was concluded that the non-Darcian approach could give a good agreement to experimental results even with a uniform resistance. However it was noted that experimental data was somewhat limited and there was scope for further calibration of the model when further data became available. Variable resistance coefficients were suggested, dependant on the movement of the bristle pack together with a link between the bending routine and **CFD** code to allow an iterative calculation to be carried out. Further areas of uncertainty included the effect of rotor circumferential flow on the pressure distribution.

Table 8.1 Comparison of flow rate (in^3/sec) results from **FIDAP** compared to Cross Manufacturing experimental results **(Mullen, Braun and Hendricks (1990))**.

	Mesh i)	**Mesh ii)**
Cell Size	0.0030	0.0033
Flow Rate FIDAP	2.3167	11.962
Flow Rate Cross	3.74	11.8
Reynolds' number	150	300

Table 8.2 Physical characteristics and parameters used in the numerical computations **(Kudriavtsev and Braun (1995))**.

Parameter	**Value**
Brush seal Darcy number.	$Da = k_u = 6*10^{-7}$
Rotational ratio.	$R = w_{max}/U_{in} = 1.$
Main flow Reynolds number.	$Re_m = 1.2*10^{-4}$
Vane flow Darcy number.	$Da = k_x = 10^{-4}$
Computational domain dimensions.	$L_0 = 1$ mm.
Normalising length.	$l_x = 28.1$
Non-dimensional axial size.	$l_r = 34.48$
Non-dimensional tip cavity radius.	$R_{shaft} = 160.0$
Brush seal characteristics.	$R_m = 183.48$
Brush permeabilities	$\varepsilon = k_u/k_v = 0.01$
Permeability (k_x)	$k_{Ergun} = 6.0*10\text{-}13$ $k_{exp} = 5.0*10\text{-}13$
(k_{exp} calculated from Carlile, Hendricks and Yoder (1993) data).	
Bristle diameter.	d = 0.075 mm
Brush seal porosity.	$\varepsilon = 0.216$
Brush seal clearance.	$l_{cl} = 0.08$ mm

Table 8.3 Resistance coefficients for "blown down" clearance seals **(Turner, Chew and Long (1997))**.

Interference/clearance	$\mathbf{a_n}$	$\mathbf{a_s}$	$\mathbf{a_z}$	$\mathbf{b_n}$	$\mathbf{b_s}$	$\mathbf{b_z}$
-0.27 mm	$5.317*20^{11}$	$8.8617*10^9$	$5.317*10^{11}$	$1.998*10^6$	0	$1.998*10^6$
0.27 mm	$1.8284*10^{10}$	$3.0473*10^8$	$1.8284*10^{10}$	$1.710*10^5$	0	$1.710*10^5$
0.75 mm	$1.4*10^9$	$2.3333*10^7$	$1.4*10^9$	$7.0*10^9$	0	$7.0*10^4$

Table 8.4 Brush seal dimensions and brief comparison of some test details **(Chew and Hogg (1997))**.

	Carlile et al. (1993)	**Bayley and Long (1993)**	**O'Neil (1993)**
Outer diameter	0.05333 m	0.15171 m	0.35772 m
Backing ring dia.	0.03923 m	0.12456 m	0.33048 m
Front plate inner dia.	0.04699 m	0.14240 m	0.34835 m
Bristle Bore dia.	0.03792 m	0.12176 m	0.32761 m
Seal axial width	$3.53*10^{-3}$ m	$3.85*10^{-3}$ m	$3.951*10^{-3}$ m
No. Of bristles per in. of circumference.	4500	2400	2400
Bristle dia. (d)	$5.1*10^{-5}$ m	$3.85*10^{-3}$ m	$3.9510*10^{-5}$ m
Bristle inclination to tangential direction (ϕ)	40°	45°	45°
Rotor interference.	$6.1*10^{-5}$ m	$2.5*10^{-4}$ m	3.15*10-4 m
Relative seal size	Single small diameter	3 x size of Carlile	7 x size of Carlile
Fit	Different fits	0.25 mm interference	Various fits and backing ring clearances.
Speed	Static and low rotor speeds		Stationary
Other tests	Viscous fluid to improve sealing		
Fluid	Air, CO_2 and He	Air	Air
Pressure	Downstream P=100 kPa	Downstream P=100 kPa	Downstream P=800 kPa. Upstream P= 1500 kPa
Temperature	Inlet Temperature 285-295 K	Inlet Temperature 293 K	Inlet Temperature 293 K
Pressure Ratio	Pressure ratio up to 7.9	Pressure ratio up to 4	Pressure ratio up to 2.5

Table 8.5 Resultant pressure differentials due to variations of the $\mathbf{PTDR_{L\,B}}$ **(Braun and Kudriavtsev (1993))**.

Part A	**Re = 2000**				
$PTDR_L$	1	0.83	0.66	0.33	0.16
ΔP	35.33	35.01	34.73	34.57	49.1
Part B	**Re=100**				
$PTDR_L$	1	0.83	0.66	0.50	-
ΔP	67.3	70.84	74.56	81.13	--

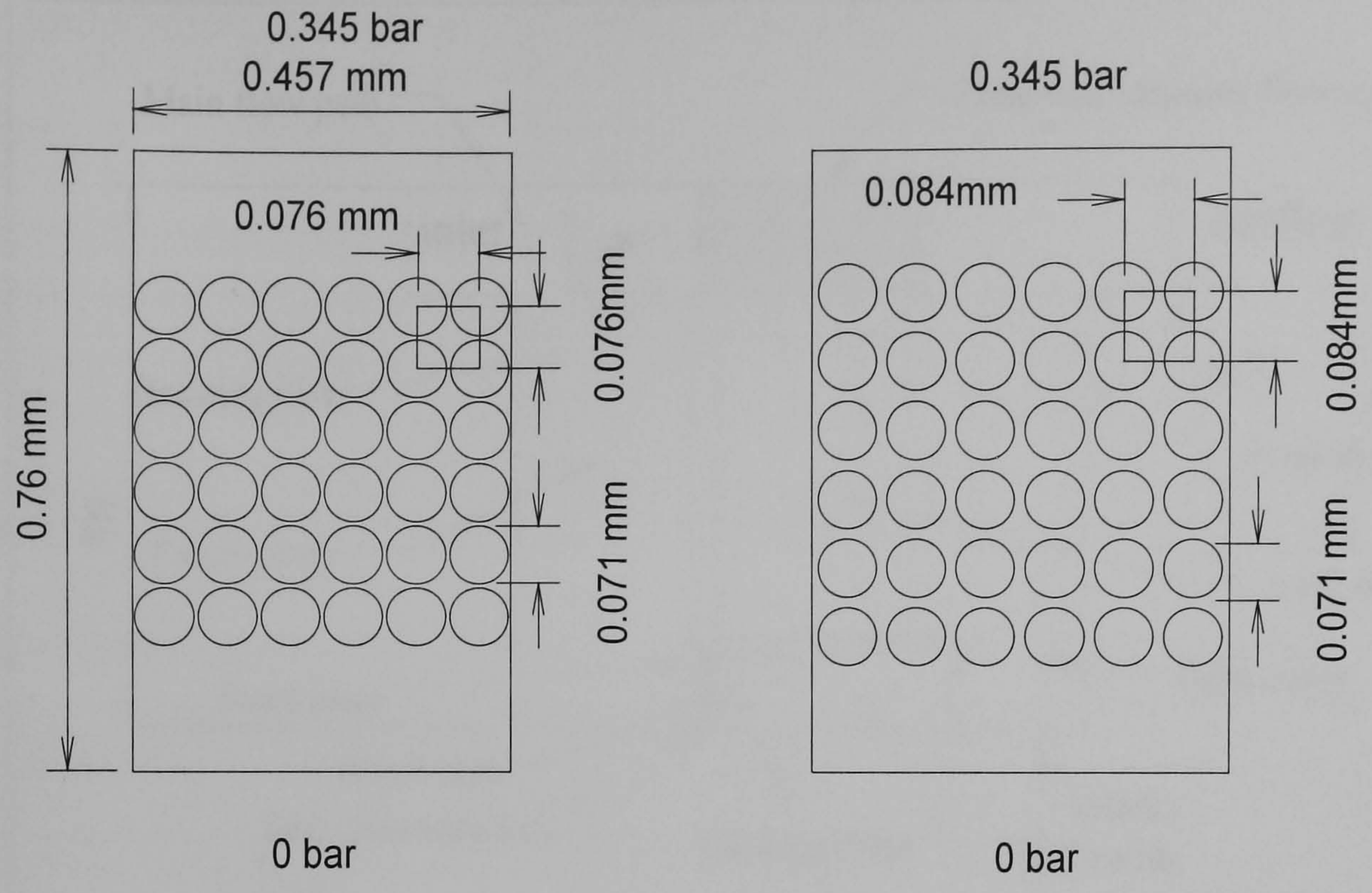

Figure 8.1 Schematic of the two model geometries generated for use with **FIDAP (Mullen, Braun and Hendricks (1990)).**

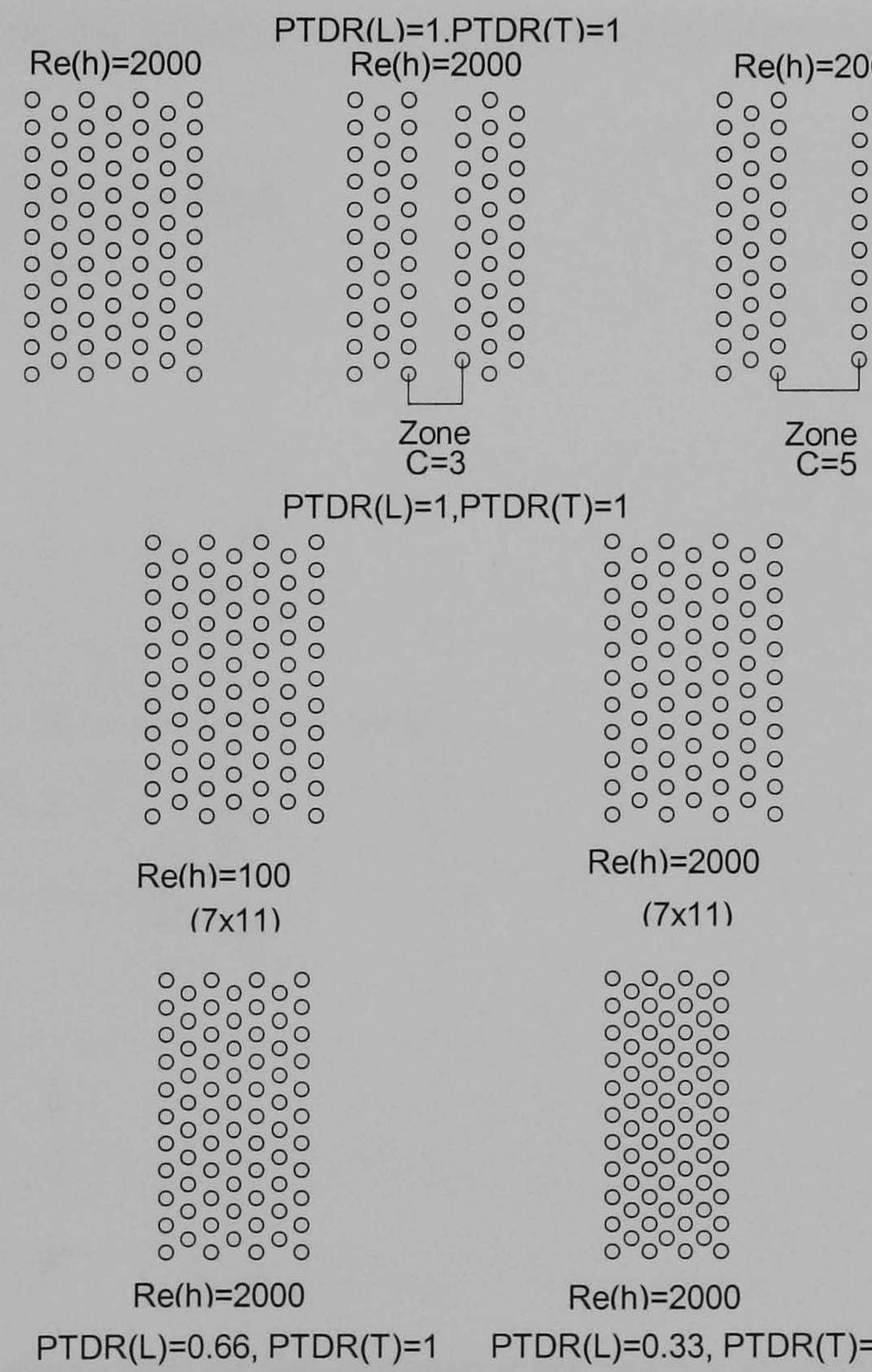

Figure 8.2 Seven of the basic brush seal models tested **(Braun and Kudriavstev (1993))**.

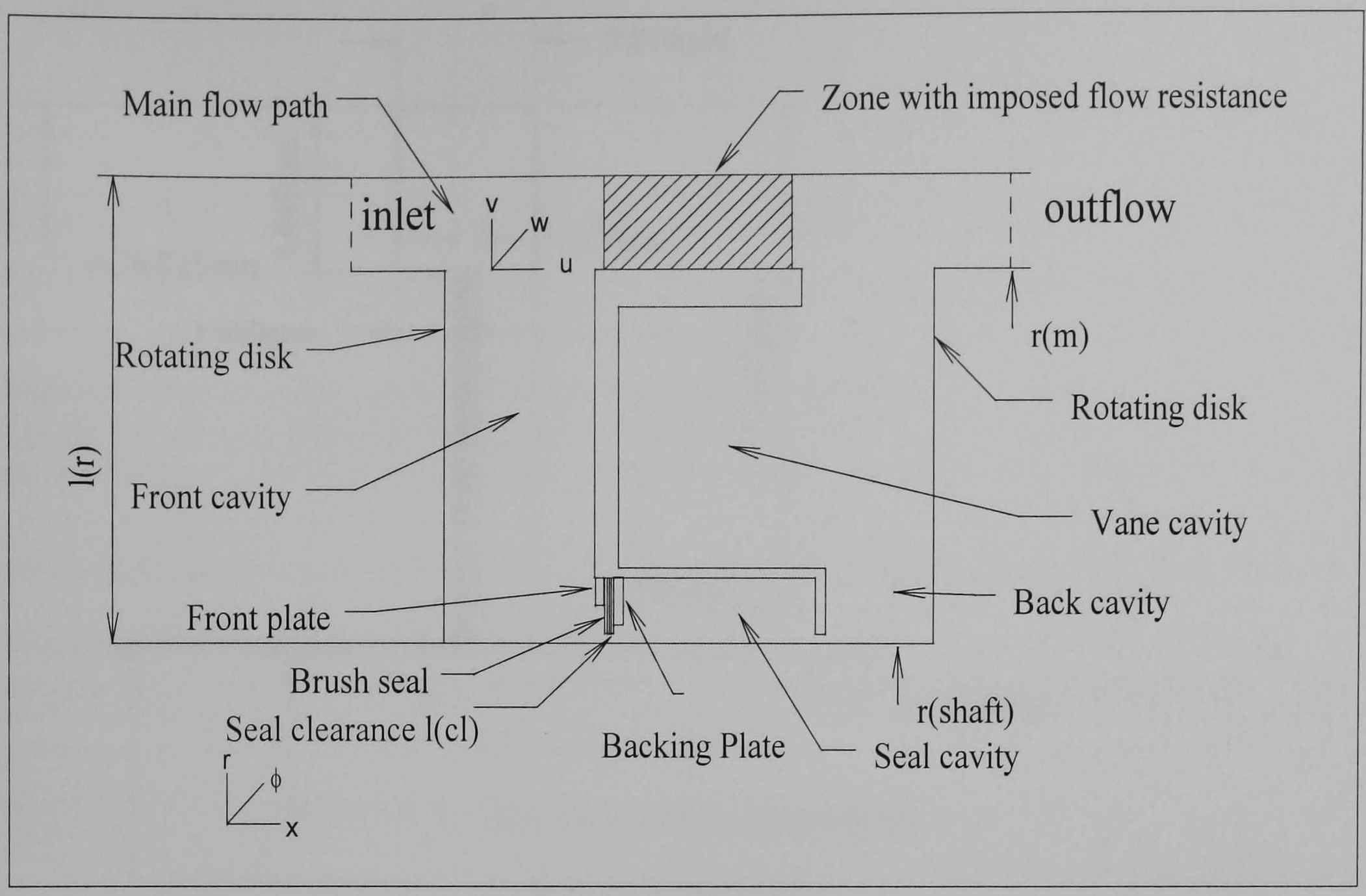

Figure 8.3 Schematic of the brush seal and cavity arrangement tested **(Kudriavtsev and Braun (1995).**

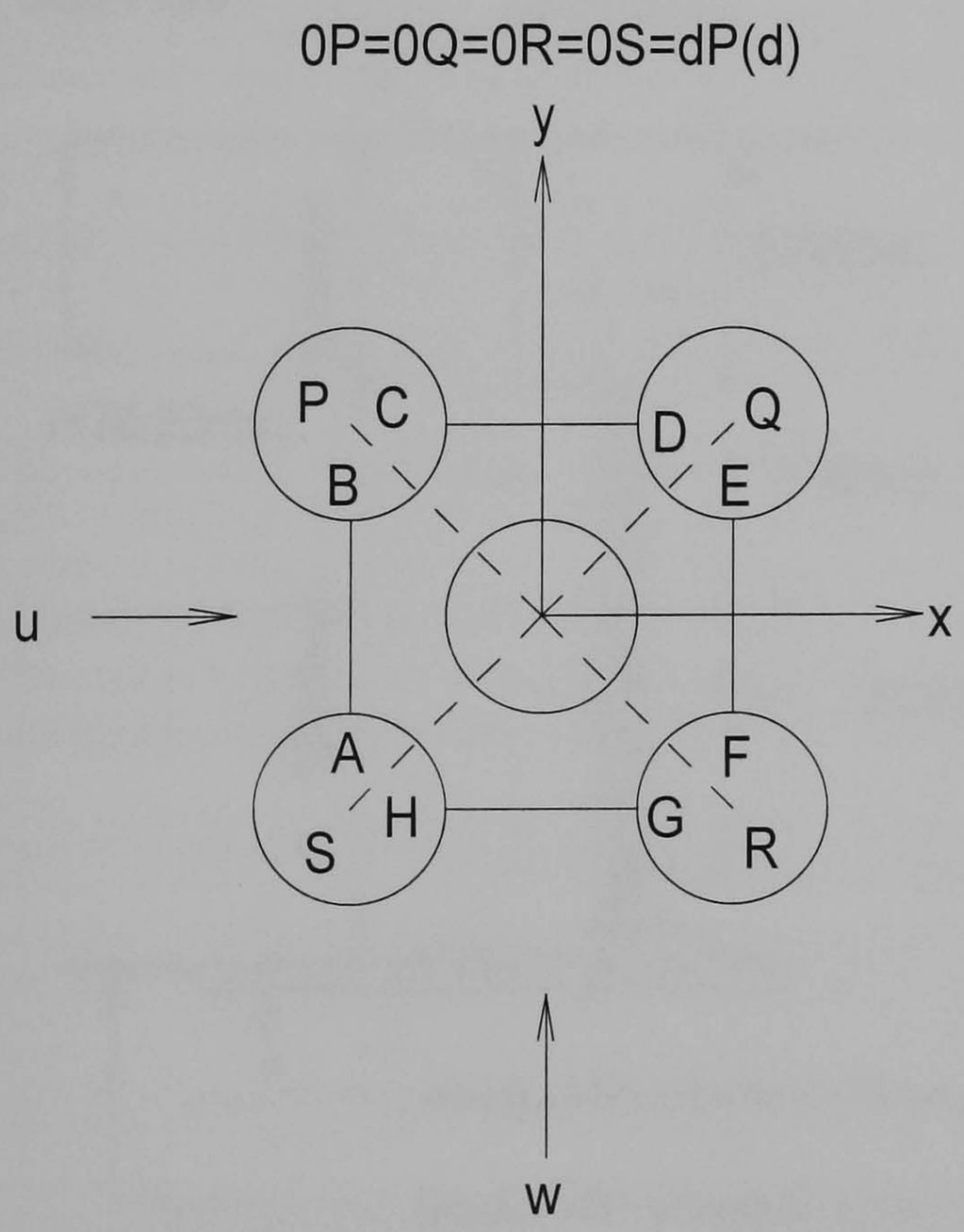

Figure 8.4 Schematic depiction of the domain enclosing a streamwise repeating module of bristles **(Sharatchandra and Rhode (1996))**.

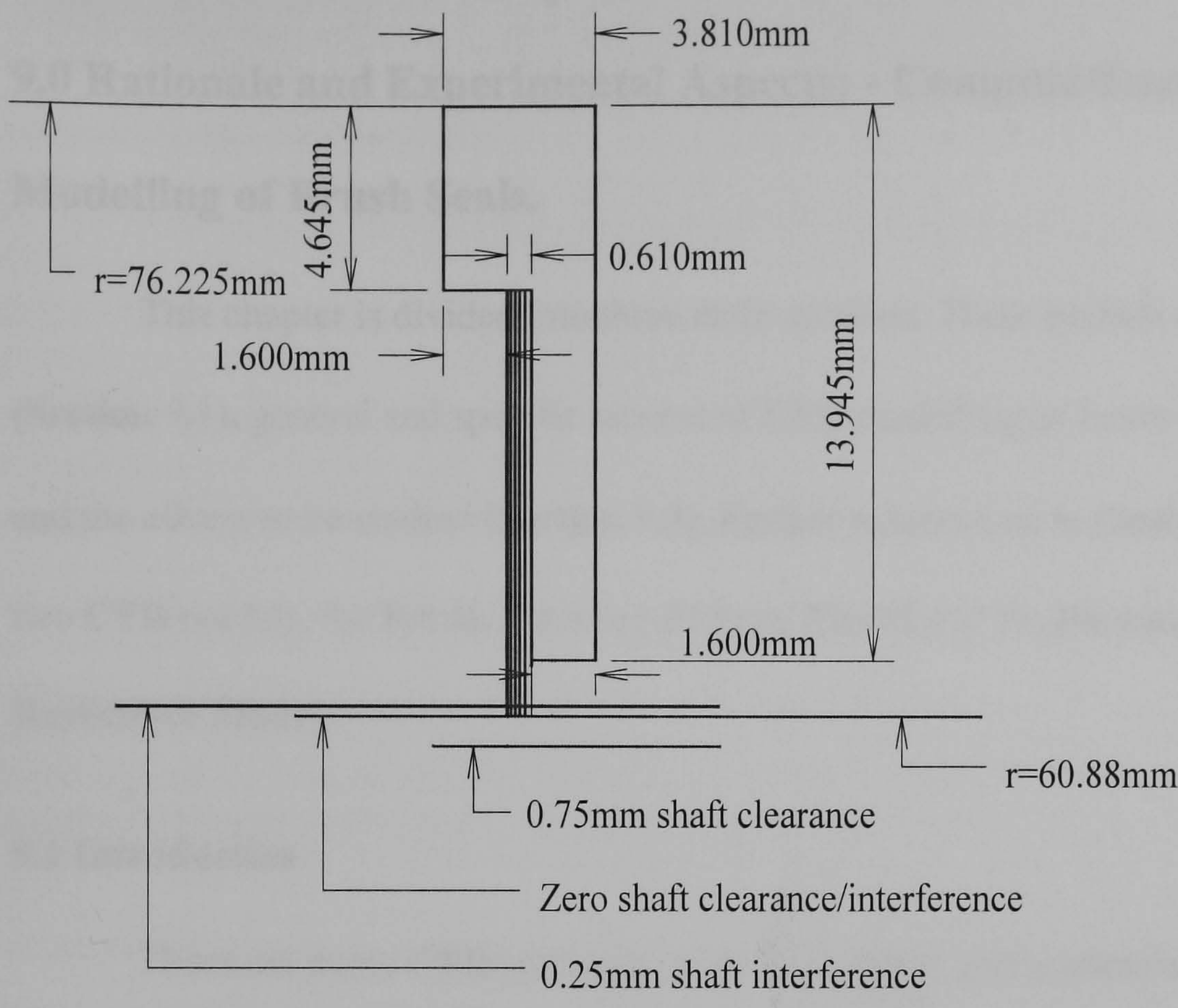

Figure 8.5 Schematic of brush seal **(Chew, Lapworth and Millener (1995)).**

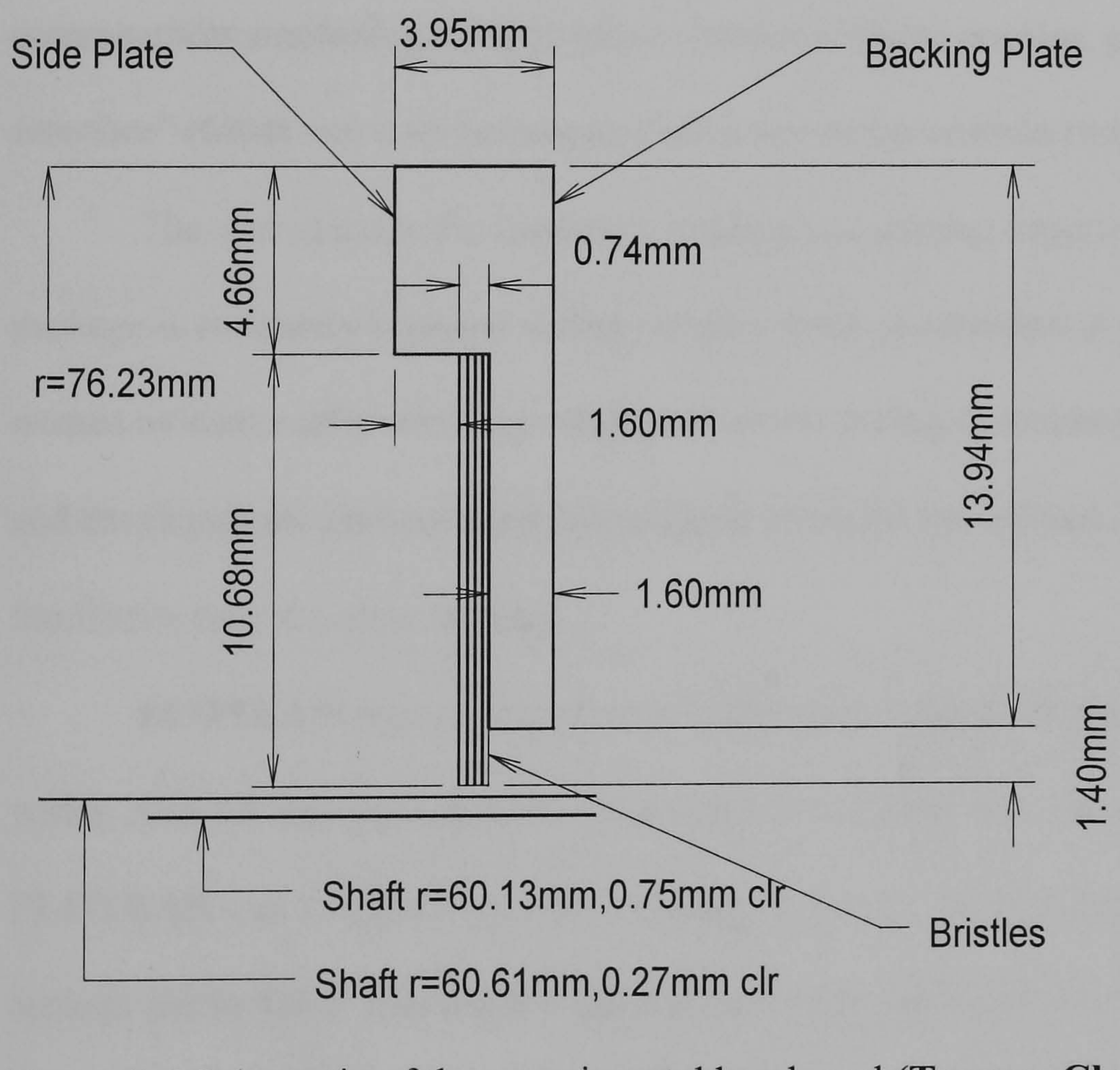

Figure 8.6 Schematic of the experimental brush seal **(Turner, Chew and Long (1997)).**

9.0 Rationale and Experimental Aspects: - Computational Fluid Dynamics Modelling of Brush Seals.

This chapter is divided into three main sections. These include the introduction **(Section 9.1),** general and specific aspects of **CFD** modelling of brush seals, **(Section 9.2)** and the effects to be studied **(Section 9.3).** Further subsections in **(Section 9.2)** discuss the two **CFD** models, the **Bristle Packing Pattern Model** and the **Porous Media/Distributed Resistance Model**.

9.1 Introduction

There are many **CFD** packages in use in industry and academia. The packages range from purely "in house" codes designed to solve very specific problems, to fully developed commercially available packages with a flexible problem domain, good "Graphical User Interface" **(GUI)** and well documented reference and procedure manuals.

The cost of software, hardware, training and gaining experience and confidence in a package is extremely high and within industry these investments in packages cannot be wasted by continually changing allegiance to new packages without justification. New codes and developments are becoming increasingly available but without historic confidence and familiarity they are often avoided.

FLOTRAN was a relatively new **CFD** code. It used a finite element based technique within **ANSYS** that was a proven stress and thermal finite element package. Until recently **FLOTRAN** was a separate program and was relatively crude in its mathematical solution options and its **GUI**. This made it unreliable for complex problems and unpopular. The latest version of **FLOTRAN** was fully incorporated into the **ANSYS** package and shared the same **GUI**. This offered a user-friendlier environment for **CFD** modelling.

FLOTRAN was selected to carry out **CFD** modelling because the software and hardware existed at the University of Northumbria and reasonable access was available. Very

little training was required to start using the package because of the fully developed **GUI** and accompanying documentation.

The purpose of this work was to further the understanding of the leakage characteristics of a brush seals under a variety of conditions and geometries. Microscopic flow patterns were to be examined to identify features that reduced (or increased) sealing. A reliable theoretical model was required, to enable the prediction of the leakage rates and characteristics of brush seals having different geometries and operating conditions. A reliable theoretical model would reduce the need for expensive and time consuming prototype seal manufacture and testing.

9.2 CFD Modelling of Brush Seals

The flow through brush seals is a highly complex three-dimensional problem, involving many variables. To overcome some of the difficulties the brush seal was modelled in two-dimensional form, from two perspectives perpendicular to each other. The first model treated the brush seal as a rigid bank of tubes (analogous to a heat exchanger). The seal was modelled looking at the bristle tips. The cross-flow through the seal in the axial direction could be modelled and the results examined. This model was referred to as the **Bristle Packing Pattern Model. Figure 9.1** gives a schematic of this model. Some of the dimensions are given in **Table 9.1.**

The second model was a cross-section of the brush seal in the axial direction. The full profile of the seal was modelled including the backing plate and the bristle pack, which was modelled as an area of porous media or distributed resistance. This model was called the **Porous Media/Distributed Resistance Model. Figure 9.2** gives a schematic of this model. Some of the dimensions are given in **Table 9.2.**

Several conditions were applied to simplify the flow through brush seals. Some of the conditions were specific to the type of model being used. These were as follows: -

i.) The packing pattern/resistance coefficients were regular/constant and did not change with operating conditions.

ii.) In the porous media model, the bristle area was modelled as a 3D anisotropic, direction dependent, uniform homogeneous distributed resistance, as specified by the user though viscous and inertial flow coefficients.

iii.) The fluid inlet to the bristle pack was assumed to be fully developed, uniform, laminar and only possessing velocity vectors in the axial direction.

iv.) The fluid outlet from the model (down-stream from the brush seal and after fluid effects due to the seal) was assumed to be fully developed, laminar, uniform and only possessing velocity vectors in the axial direction.

v.) The fluid specified was air at room temperature. This was comparable to the experimental testing but obviously not comparable to actual brush seal applications either in steam turbines or gas turbines.

vi.) The brush seal was modelled using the incompressible flow equations.

vii.) The brush seal was modelled using the turbulence equations.

However, the nature of **CFD** modelling is such that the results are probable answers, not absolute solutions. The better the mathematical modelling of the many aspects of fluid dynamics, the better the results become. Complex flow patterns, irregular geometries and a multitude of model variables and flow effects that change as the solution progresses can cause difficulties in achieving reliable results with the present state of the art in **CFD**.

The models were built up in a systematic way starting with keypoints. These were specified at exact co-ordinates to ensure the correct seal geometry. The keypoints were the basis for the production of lines and areas. When the outline of the model was complete, nodes were introduced to the lines. The nodes controlled the mesh pattern, density and regularity. Once the nodes were specified the model was meshed automatically.

The boundary conditions were set after the model was fully meshed. Zero VX, VY and VZ velocity were set on the nodes on the top and bottom tube boundaries and on the

outside of the bristles or backing plate to define them as solid. **FLOTRAN** required at least one inlet or outlet velocity and at least one inlet or outlet pressure specified. This prevented the exact replication of the experimental work where the flow was driven by introducing a known pressure differential. Instead an inlet velocity was specified at the inlet to the tube (in m/s) and a pressure (atmospheric (1 bar)) on outlet from the tube. Changes in inlet velocity produced changes in the pressure differential across the bristle pack. Values of inlet velocity were chosen to produce a pressure differential in the 0-5 bar range where possible.

In both models there was a compromise between grid or mesh size and density and computational time and resources. The areas of interest were meshed finely whilst the areas of little interest were more coarsely meshed to reduce the number of elements and computational time. The changes in mesh coarseness were gradual and the element shape was carefully controlled. Mesh dependency was checked by gradually reducing the mesh density until little further change in concurrent results occurred for the same model.

The default convergence criteria were not always reached within a reasonable time-scale. The models were therefore allowed to run for a specific number of global iterations, again until little further change in the results occurred for the same model. In all cases the residuals file, the energy balance and the mass balance monitor were also checked to ensure the solutions were of a suitable standard.

9.2.1 Bristle Packing Pattern Model.

The models were 11 bristles wide (axial direction) by 3 bristles tall (radial direction) and were enclosed in a tube to allow crossflow to occur. The tube was sufficiently long to allow full flow development before and after the bristle pack.

Brush seals were manufactured using carefully controlled production techniques to ensure good dimensional accuracy, regular packing density and good seal repeatability. The exact manufacture was described previously in **Chapter 1**. The density per mm of circumference was controlled by the manufacturing process and was therefore known for a

given seal. As was the individual bristle diameter and the measured bristle pack thickness. Rolls-Royce brush seals were generally 11 bristles thick in the axial direction. Given this information and the bristle pack axial thickness, the number of bristles in a given area was calculated. Once the number of bristles is known for an area, a theoretical idealised packing pattern was calculated. Possible packing patterns include "square", "rectangular", "regular hexagonal" and "irregular hexagonal". The bristle centre to centre spacing ratios were sometimes known as a ratio of transverse rows (S_T) to longitudinal columns (S_L). **Chupp et al (1991)** used a ratio of S_T/S_L=4. The models were all 11 bristles wide by 3 bristles tall.

9.2.2 Porous Media/Distributed Resistance Model

The Porous Media Model was built up using the same systematic method described previously for the **Bristle Packing Pattern Model**. The porous media area had the dimensions of a real brush seal bristle pack, as did the backing plate and the associated clearances for them both. Again the brush seal was modelled in a tube sufficiently long to achieve full flow development before and after the seal.

The area of bristle pack was designated an area of distributed resistance and given a "real constants" set number. The resistance coefficients could then be set individually and were automatically applied to the area. The distributed resistance equations built into **FLOTRAN** were non-linear (similar to **Forchiemer's Law**) and three-dimensional. This allowed the setting of the viscous and inertial term in three directions. If no porosity coefficients were set the brush seal distributed resistance was ignored in calculations and the model was effectively of a single fin labyrinth seal. This type of model was used to compare with the experimental labyrinth seal results and determine the effect of the backing plate alone on sealing performance.

The coefficients used were either empirical values calculated from experimental leakage results, values calculated using the **Bristle Packing Pattern Models**, values taken

from other published results or were tailored to more closely fit the experimental results by an iterative process.

Initially the flow through the porous media was assumed to be isotropic. However, experimental testing showed that the flow through brush seals was far from isotropic. The flow in the three directions, radial (s), axial (z) and tangential direction (n) was found to be significantly different. Experimental evidence showed that flow in the radial direction, along the length of the bristles was significantly greater than in the axial and tangential directions. **Bayley and Long (1990, 1993)** gave the ratio to be 30. **Chew and Hogg (1995, 1997)** further developed this idea and concluded that for the Roll-Royce brush seals they were testing the ratio of axial to radial flow was 60:1. The flow in the z direction (tangential flow) was thought to be similar to that in the axial direction. The porous media was modelled using the non-linear, **Forcheimer Law**, that had both a viscous and inertial term. In the case of flow along the bristles, the radial direction, the relatively straight flow path allowed the approximation of no inertial resistance. The basis of the relationship between the resistance coefficients used in this study was similar to that described by **Chew et al (1995,1997).**

9.3 Effects to be Studied.

Generally the results of the **CFD** analysis were of interest at two levels for both models. These were the bulk flow numerical results and the flow patterns produced. The bulk flow results enabled direct (interpolated) comparison to the experimental bulk flow results. The detailed flow patterns from the velocity and pressure vector and distribution plots showed recirculation areas, vortices, areas of high turbulence and kinetic energy dissipation. These were compared and contrasted to previously published flow visualisation and **CFD** studies. The microscopic flow patterns were also instrumental in the understanding of some of the irregularities of the results from the **CFD** analysis and the experimental leakage testing.

The **Bristle Packing Pattern Model** had several objectives: -

i.) To determine compare and contrast the flow patterns and bulk flow characteristics through both square and hexagonal packing patterns.

ii.) To determine porosity coefficients for the square and hexagonal packing pattern, use them in the **Porous Media Model** and compare and contrast the results with published coefficients.

The **Porous Media Model** had the objective of determining the flow patterns and bulk flow for the following model variations using several different sets of porosity coefficients.

i.) A backing plate with a clearance of 1 mm.

ii.) A backing plate with a clearance of 1.8 mm.

iii.) A brush seal with zero bristle pack clearance and backing plate clearance of 1 mm.

iv.) A brush seal with 1 mm bristle pack clearance and backing plate clearance of 1.8 mm.

The results were to be further compared and contrasted to published results and results from the experimental leakage testing.

Bulk flow leakage characteristics were best presented and compared to the experimental leakage work by the relationship between inlet velocity and pressure differential. The majority of the result graphs given were therefore in that format. Microscopic flow patterns were examined using flow distribution plots available in the post-processor section of the **CFD** package. These included pressure distribution plots, velocity vector plots, and velocity distribution plots. Areas of high and low pressure and velocity, recirculation zones, flow patterns and areas of high turbulence were easily identified.

Several other options were available within **FLOTRAN** to modify the standard **CFD** solution equations. Some of the options of interest included the turbulence equations, rotating walls (swirl), and compressible/incompressible flow. These features were also investigated.

Table 9.1 Packing Pattern Model Dimensions

	"Square"	**"Hexagonal"**
Bristle Diameter	0.071	0.071
Bristle Density	2400	2400
Bristle Pack width	1	1
Number of bristles wide	11	11
Column spacing (centre-centre)	0.09	0.16
Row spacing (centre-centre)	0.09	0.1

Table 9.2 Porous Media/Distributed Resistance Model Dimensions

	Model i)	**Model ii)**
Backing Plate Clearance	1 mm	1.8 mm
Backing Plate Height	9 mm	8.2 mm
Backing Plate Width	0 mm	1 mm
Porous Media Clearance	0	1
Porous Media Height	10 mm	9 mm
Porous Media Width	1 mm	1 mm

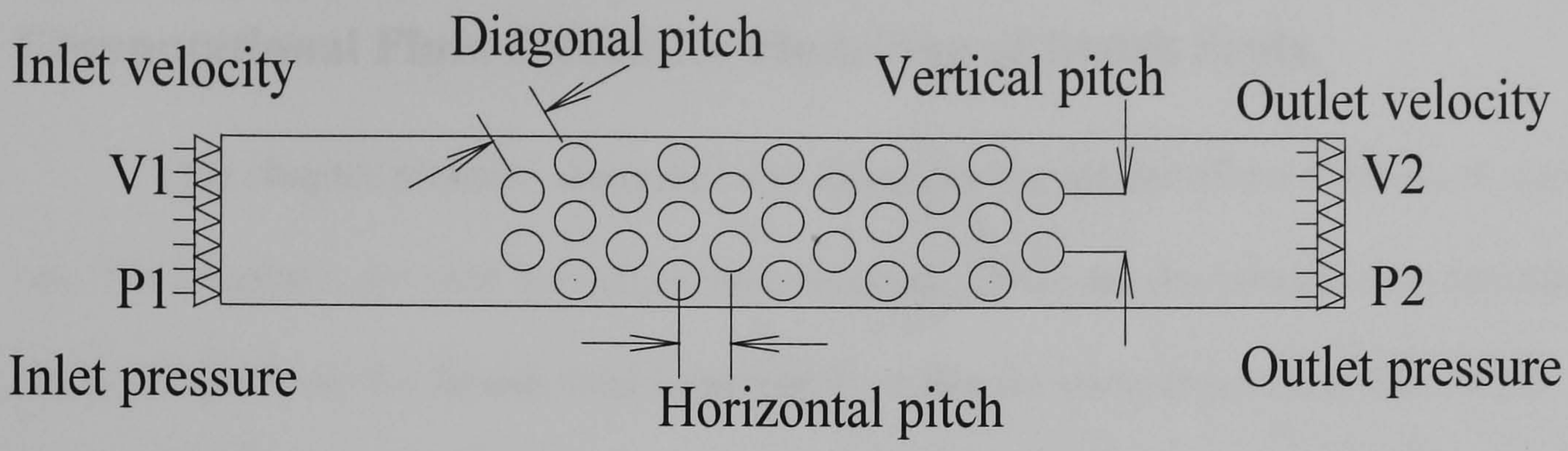

Figure 9.1 Schematic of the Bristle Packing Pattern Model.

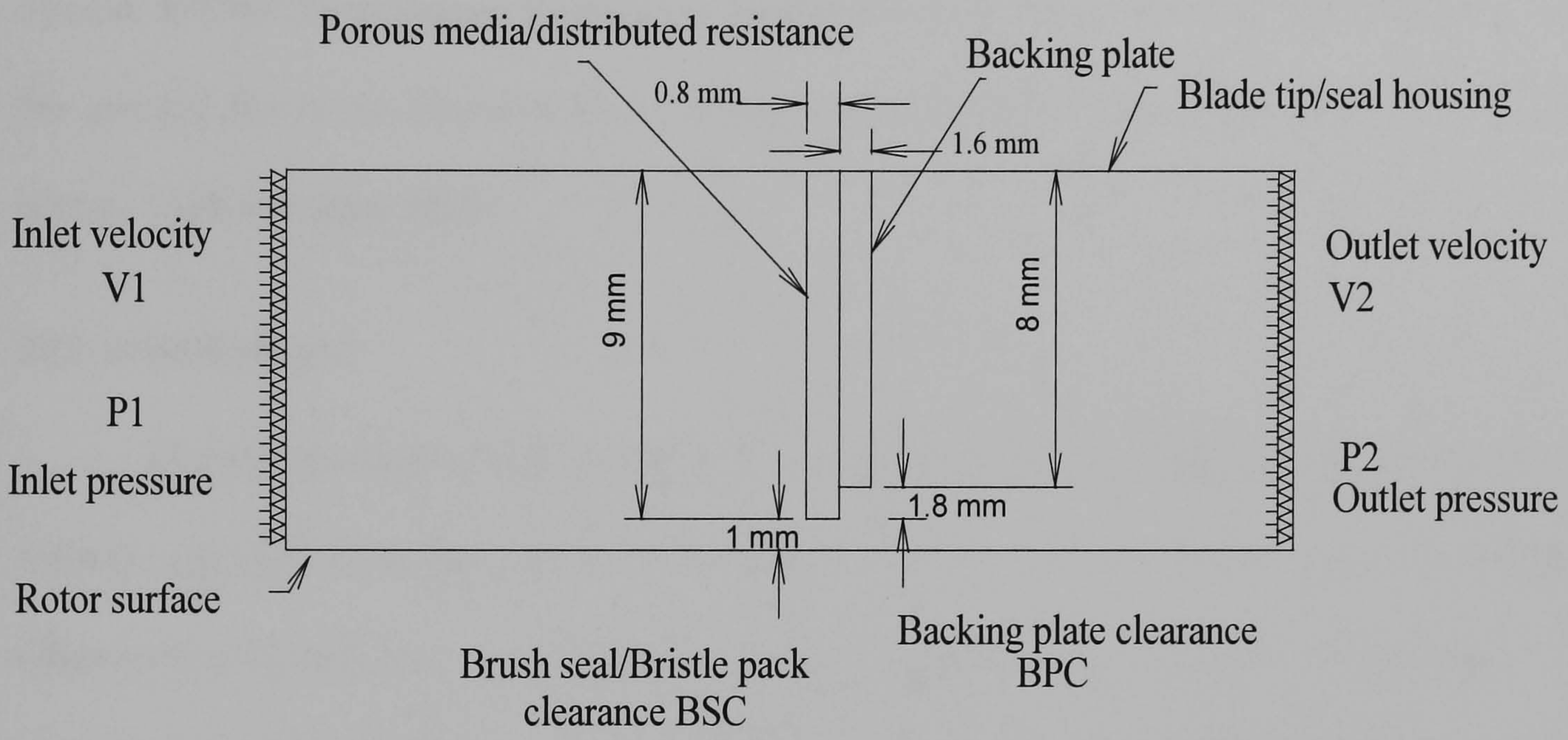

Figure 9.2 Schematic of the Porous Media/Distributed Resistance Model.

10.0 Results, Discussion, Conclusions, and Further Work: - Computational Fluid Dynamics Modelling of Brush Seals.

This chapter presents, describes and discusses the results of the **CFD** work carried out. The chapter is divided into eight main sections. These are the introduction **(Section 10.1)**, results from the **Brush Seal Leakage Test Rig** for comparison to **CFD** results **(Section 10.2)**, results from the **Bristle Packing Pattern Models (Section 10.3)**, results from the **Backing Plate (labyrinth fin) Models (Section 10.4)** and results from the **Porous Media /Distributed Resistance Model (Section 10.5)**. The final three sections are the general discussion **(Section 10.6)**, conclusions **(Section 10.7)** and recommendations for further work **(Section 10.8)**.

10.1 Introduction.

The results for the **CFD** models were generated in several formats. These were as follows: - graphs showing pressure differential (Pa) against inlet velocity (m/s), plots of the **CFD** models showing the model outline, computational meshes, pressure distribution, velocity vectors/distribution and a table showing numerical data (including porosity coefficients and the calculated and experimental porosity coefficients).

A large number of **CFD** models were required to simulate the **BSLTR** results. The pressure differential against inlet velocity plots summarised the many **CFD** results for different model conditions. Each point on the line was the result of an individual **CFD** analysis. The only change to the model input conditions for a given set of points on a line was the inlet velocity (this effectively altered the pressure differential across the seal). Experimental results from the **BSLTR** were also produced (and are presented at the beginning and where appropriate) in a form suitable for comparison to **CFD** work.

Theoretical results were plotted using **Chew et al** porosity coefficients, porosity coefficients calculated from results from the **Bristle Packing Pattern Model** and porosity coefficients calculated from the experimental results.

10.2 Results from the Brush Seal Leakage Test Rig for comparison to CFD results.

The experimental results from the **BSLTR** are given extensively in **Chapter 7**. However these results were not in a format directly comparable to the **CFD** results. The **CFD** models were under computer package constraints that would not allow the direct replication of experimental test rig conditions (i.e. pressure driven leakage). These constraints were discussed previously in **Chapter 10**. The experimental **BSLTR** results in **Figure 10.1** were reformatted (from **Figure 7.1** and **Figure 7.2**) to show pressure differential (Pa) against inlet velocity (m/s).

The plots in **Figure 10.1** show the pressure differential across a single knife edge labyrinth fin with **BPC** = 1.08 mm, and 0.68 mm and a brush seal with **BPC** = 0.9 mm and **BSC** = 0.

As the inlet velocity increased the pressure differential across the seal also increased. When the **BPC** was reduced, the sealing capacity of the seal for an equal inlet velocity increased. The effect of the change in **BPC** is demonstrated by an increase in pressure differential. The results for brush seals with changes in **BPC** and **BSI** indicated that the **BPC** (within the range 0.4 to 0.9 mm) had little effect on the brush seal leakage rate providing the brush seal bristles remained in contact with the rotor surface. The sealing capacity of the seal appeared to be almost entirely dependent on the bristle pack and not the **BPC**. The pressure differential maintained by the brush seal was significantly better that those maintained by the two single labyrinth fins.

The results were taken from experimental work carried out on the **BSLTR** and were converted to pressure differential against inlet velocity from mass flow rate against pressure differential assuming incompressible flow and knowing the density and leakage

area. The experimental results taken from the **BSLTR (Figure 7.1** and **Figure 7.3)** were relatively linear and as a result the plots given in **Figure 10.1** were also linear.

Forcheimer's Law (Equation 8.4) that describes the flow through porous media indicts a quadratic relationship between pressure differential and inlet velocity. Examples of the theoretical relationships are given in **Figure 10.8** and **Figure 10.9.** However, the assumption that a brush seal performs purely as an area of porous media is an over simplification of its operation. In reality, the flow through a brush seal was thought to perform as a combination of the flow through a square edged, parallel sided labyrinth seal and a poorly controlled constantly changing area of porous media. When a clearance exists under the brush seal bristle tips and the rotor surface, the bulk flow appeared to travel through the clearance (with little going through the bristle pack). Under these circumstances the brush seal could be modelled almost entirely as a labyrinth seal with a leakage area defined by the effective blown-down bristle bore and the rotor surface.

St Venent's Equation (Equation 7.1) describes the flow through a labyrinth seal and would also suggest a non-linear relationship between pressure differential and mass flow rate/inlet velocity. However, within the range of inlet velocities, mass flow rates, and pressure differentials (and experimental uncertainties) tested in the **BSLTR** the response would be approximately linear.

10.3 Brush Seal Bristle Packing Pattern Models.

Figure 10.2 Finite element grid plot of the "Square" packing pattern.

Figure 10.2 shows a portion of finite element grid developed to examine the flow through a regular "square" packing pattern. The mesh consisted of quadrilateral and triangular elements of an acceptable size and shape (i.e. as close to a square or equilateral triangle as possible). The element spacing was subtly increased at cylinder boundaries and between cylinders where the fluid dynamic effects may be more pronounced. This aided model convergence and accuracy. A large number of elements were required in flow

constrictive areas. However, a fine balance was maintained between mesh spacing and computational restrictions so as not to exceed either the maximum number of allowable elements or the memory/hard disk requirements.

Figure 10.3 Pressure plot of the "Square" packing pattern.

The full plot of the bristle area (not including the flow development before and after the bristle pack) is presented in **Figure 10.3**. In the first examples of bristle packing pattern models the **CFD** geometries were generated in mm and the fluid properties amended to reflect mm as the unit of length (as opposed to m). The pressure gradients were shown in N/mm^2 (and should be divided by $1*10^6$ to convert to N/m^2 or divided by $1*10^{11}$ to convert to bar). The pressure differential across the bristle pack was approximately 3 bar. The pressure distribution was reasonably uniform but there were small areas of localised low pressure between bristles (in the flow direction) where the flow was constricted. The pressure distribution plot near the top and bottom model boundary revealed even lower pressure distributions due to the further constrictions imposed by the proximity of the boundary to the nearest cylinder. The pressure range appeared to extend into the negative range. The areas of negative pressure were very small. They were caused by the **CFD** code not being able to cope with the complexity of the flow regime and failing to calculate real values. The areas of negative pressure were insignificant compared to the bulk pressure differential and were ignored.

Setting of periodic boundary conditions may have proven to be a better option to reduce the cumulative effect of boundary wall conditions when calculating the bulk flow.

Figure 10.4 Velocity vector plot of the "Square" packing pattern.

Figure 10.4, the velocity vector plot shows the magnitude and direction of the fluid velocity within the bristle pack. The values of the velocity vector ranges were generated in

mm/s. They should be divided by $1x10^3$ to convert to m/s. The very highest values were however ignored as they corresponded to extremely small components of the flow in areas where the code was susceptible to error. Only the bulk flow conditions were thought to be modelled accurately and were considered.

The velocity was generally at its highest in the model in areas identified as having low pressure **(Figure 10.3).** These were typically between bristles in the direction of flow. However these extremely high velocities were probably erroneous. More significant were the bulk velocity values of 0-235 m/s. The flow between bristles was reasonably uniform. However, on exit from the area of constriction, the flow appeared to adhere to the boundary layer of the cylinder and enter the area between cylinders in adjacent columns. Flow entered this area from both sides of the cylinder it had just flowed around. This created turbulence and small eddies. The portion of flow with the larger velocity vectors travelled round the cylinders in the general direction of fluid motion in an "s" shape. It continually adhered to the boundary layers and was then forced to change direction by the flows entering the same area from the adjacent row above or below.

Figure 10.5 Finite element grid plot of the "Hexagonal" packing pattern.

The "hexagonal" packing pattern is shown in **Figure 10.5**. The **FE** mesh consisted of quadrilateral elements. The bristle pack area was meshed in such a way that all of the interior (except the model edges) was reasonably uniform.

Figure 10.6 Pressure plot of the "Hexagonal" packing pattern.

The pressure plot in **Figure 10.6** shows that the pressure distribution through the bristle pack was generally less uniform than the "square" packing pattern. As with the "square pattern" the pressure gradient values were generated in N/mm^2 and should be divided by $1x10^{11}$ to convert to bar. The pressure distribution was not in clearly defined

incremental bands from inlet to outlet. The irregularity of the flow path caused changed in pressure distribution between the rows and columns. However, the mean pressure drop per column was relatively similar from inlet to outlet.

Figure 10.7 Velocity vector plot of the "Hexagonal" packing pattern.

The "hexagonal" pattern velocity vector plot is given in **Figure 10.7.** It demonstrated a quite marked difference to the "square" pattern. Again a conversion factor of dividing by $1x10^3$ should be applied to convert from mm/s to m/s. The flow appeared to mainly remain in the area between adjacent rows and only a small amount entered the area between columns. The flow that did enter the area between columns was small in magnitude and turbulent in nature.

Figure 10.8 Inlet velocity against pressure differential for "Square" and "Hexagonal" bristle packing patterns.

Figure 10.8 is a summary graph of the results from the **CFD** analyses of flow through "straight" and "hexagonal" bristle packing patterns. The graph was generated to examine the relationship between inlet velocity and pressure differential for the two patterns. Two sets of results are trend lines and the equations that describe the lines were added to the graph. Two trend lines given for each pattern were both quadratic polynomials. They were a "best fit" line that described the results exactly as they were given from start to finish, and a trend line that was forced to go through the origin (zero fit). The trend lines were used to calculate the porosity coefficients for the two packing patterns using **Forcheimer's Law**. As expected, the plots for the "square" and "hexagonal" packing patterns showed that for a given inlet velocity the "hexagonal" pattern was able to maintain a higher pressure differential than the "square" pattern. The "hexagonal" pattern was approximately twice as efficient at sealing as the "square" pattern.

Table 10.1 Comparison of Chew et al and CFD calculated C and k coefficients.

The quadratic equations describing the relationship between pressure differential and inlet velocity were calculated from the **CFD** plots of the flow through "square" and "hexagonal" packing patterns described previously. The inertial and viscous porosity coefficients were calculated using **Forchiemer's Equation**. These coefficients are given in **Table 10.1** for the "best fit" and "zero fit" trend lines for the "hexagonal" and "square" packing patterns. The **Chew et al** coefficients for three different brush seal **BPC** and **BSI/C** and the calculated coefficients from the **BSLTR** are also given for comparison in **Table 10.1**. The calculated coefficients were promising, as they were reasonably similar to those produced by **Chew et al** and took no account of the sealing potential of a backing plate behind the bristle pack (as the **Chew et al** coefficients did).

Figure 10.9 Theoretical inlet velocity against pressure differential comparing Chew et al and CFD calculated C and k coefficients.

The graph in **Figure 10.9** shows the theoretical relationship between pressure differential and inlet velocity (as described by **Forchiemer's Equation**) for the **Chew et al** coefficients, the "square" and "hexagonal" packing patterns, and the experimental **(BSLTR)** calculated porosity coefficients given in **Table 10.1**. Direct comparison of the **Chew et al** coefficients, the experimental result coefficients and the packing pattern coefficients was used as a guide to the validity of the work. It was clear that theoretically the results were of the correct order of magnitude.

The **Chew et al** inertial and viscous coefficients were calculated using experimental data. They were porosity values for the brush seal as a whole (i.e. the bristle pack and the backing plate) and were independent of operating conditions (inlet velocity, pressure

differential and brush seal leakage phenomena such as blow down.) In reality the bristle pack porosity would be highly variable and dependent on many factors.

The coefficients calculated from the bristle packing pattern models did not take into account the vertical/radial flow down the bristle length and down the backing plate. Vertical flow was thought to interfere with the axial flow, under the brush seal, and increase the sealing capacity.

The coefficients from the "best" and "zero" fit were plotted and it could be seen that the "best" fit in all cases showed a greater capacity for sealing at a given inlet velocity. The two trend lines for the "straight" pattern were quite separate however there was little difference between the two trend lines for the hexagonal pattern.

The plot using **Chew et al** coefficients for **BPC**=2.15, **BSC**=0.75 gave a very similar result to that of the plot using the hexagonal "zero" fit coefficients. As expected the two further **Chew et al** coefficient plots at smaller **BPC** and **BSC** showed an increase in pressure differential for a given inlet velocity.

The final plot of porosity values calculated from the **BSLTR** was extremely promising as the plot line was reasonably similar to the plot using **Chew et al** for a **BPC**=1.15 mm and a **BSI**=0.25 mm. The experimental results were for a **BPC** of 0.9 mm and a **BSC** of 0 mm.

10.4 Backing Plate (Labyrinth Fin) Model.

Figure 10.10 Line plot of the Backing Plate Model.

The line plot shown in **Figure 10.10** gives the outline of different sections of the porous media model. The dimensions are given in **Table 10.2** and **Figure 10.2.** They corresponded to actual brush seal dimensions as tested in the **BSLTR** and given in **Table 6.2.** The model was generated and fluid dynamic properties were installed with metres as the unit of length. The model results were therefore in N/m and m/s for the pressure and velocity distribution plots respectively.

The model was designed to be easily modified to allow for changes in the **BPC** and **BSC**. The plot produced showed a backing plate (centre right) that could be easily modified to have four possible clearances and an area of distributed resistance (centre left). The distributed resistance could have four different clearances or could have no clearance or no porous media coefficients assigned to it.

Figure 10.11 Finite element mesh of the Backing Plate Model finite. BPC=1 mm.

The finite element mesh for the porous media model with a **BPC**=1 mm is given in **Figure 10.11**. The mesh was generated with regular quadrilateral elements that became progressively finer towards the rotor surface.

Figure 10.12 Pressure plot of the Backing Plate Model. BPC=1 mm.

The pressure distribution plot **Figure 10.12** shows the pressure differential for a backing plate (fin) with no porous media and with a 50 m/s inlet velocity. The pressure gradients produced were given in N/m^2 (Pa) and the model indicated a pressure differential of 1.8 bar. The backing plate geometry was not that of a typical single fin knife edged labyrinth seal but the clearance was comparable to that used in the **BSLTR**. An area of reduced pressure was visible at the leading edge of the backing plate tip. This point corresponded to an area of high velocity and boundary layer separation as the flow from the area in front of the backing plate flowed past the constriction. Another area of low pressure was found behind the backing plate. As the fluid flowed through the **BPC** it was unable to change direction rapidly enough to fully occupy the area behind the fin. This created a recirculation area of low pressure.

Figure 10.13 Velocity vector plot of the Backing Plate Model. BPC=1 mm.

The velocity vector plot shown in **Figure 10.13** helped to explain the area of pressure variation in the pressure plot. It could be seen that the area of highest velocity was at the leading edge of the fin. This was expected as the entire volume of flow in the cavity (before the fin) had to change flow direction and squeeze past the **BPC**. The increase in velocity corresponded to the pressure reduction at the leading edge of the fin. As the fluid passed under the fin it continued to have a high velocity but as the fluid flowed through the constriction the velocity was reduced and the flow expanded to occupy the full depth of the flow chamber. The dramatic flow past the backing plate caused a recirculation zone in the area behind the fin.

Figure 10.14 Finite element mesh of the Backing Plate Model. BPC=1.8 mm.

The finite element mesh generated can be seen in **Figure 10.14.** It was similar to the one given in **Figure 10.11.** The only difference was the backing plate clearance of 1.8 mm instead of 1 mm.

Figure 10.15 Pressure distribution plot of the Backing Plate Model. BPC=1.8 mm.

Two main areas of low pressure can be seen in **Figure 10.15**. These areas were similar to those found in **Figure 10.12.** They were at the leading edge of the backing plate tip and in the area behind the backing plate. In this example a VZ velocity was applied on the rotor surface to simulate the rotor surface running speed of 100 m/s. This appeared to make very little difference to the pressure distribution.

Figure 10.16 Velocity vector plot of the Backing Plate Model. BPC=1.8 mm.

Figure 10.16 shows a velocity vector plot of the flow constriction under the fin tip. The flow vectors were uniform and all heading in the same direction. As the vectors converged the velocity rose on the upstream side of the backing plate, to a maximum at the

leading edge of the fin tip. The viscous forces here were overcome and the fin tip fluid boundary layer separated. The flow split into two parts, one following the rotor wall and the other flowing upwards towards the cylinder surface. The flow expanded after the fin tip clearance to occupy the full depth of the passage and was drawn towards the area of low pressure at the rear of the backing plate. As the flow approached the cylinder wall it again split to form two recirculation zones. The first was in the low pressure area behind the backing plate and the second was to the right of the high velocity upward flow. The flow after the second recirculation zone quickly became relatively uniform and laminar.

Figure 10.17 Comparison of CFD and experimental leakage results for fins with different BPC with and without swirl.

Figure 10.17 is a graph summarising the **CFD** work on a brush seal backing plate (or square edged, parallel sided, single labyrinth fin) and shows pressure differential across the seal against inlet velocity for **BPC**=1 and **BSC**=1.8. Two lines additional lines representing the two fins with the rotor surface set as a rotating wall with a VZ velocity of 100m/s were also generated.

Generally, in some cases of flow through or next to rotating components, swirl effects the bulk flow. It was thought that the rotating wall might induce swirl that could affect the fluid flow through the brush seal or labyrinth seal. Several studies (discussed in **Chapter 5 and Chapter 8**) indicated that a rotating shaft influences the flow through brush seals. The results from the **BSRTR** showed that a rotating shaft had a negligible effect in cases where there was a clearance fit and a small effect in cases where there was an interference fit. Performance changes due to rotation affected the seal hysteresis on pressurisation/depressurisation more than bulk flow.

However, from the results presented in **Figure 10.17**, swirl appeared to have little effect on the fin with **BPC**=1. However, it had a small effect on the fin with **BPC**=1.8. The

rotating wall slightly increased the sealing capacity of the seal. This may have been due to the swirling flow reducing the axial flow by producing negative axial velocity vectors. This was a reasonable explanation of the phenomenon, however, there was little evidence of swirl in any of the **CFD** plots apart from a very small boundary layer that was only visible on examination of a high magnification plot.

Experimental results from the **BSLTR** are also given in **Figure 10.17** for **BPC**=0.68 and **BPC**=1.08. Swirl or shaft rotation had little effect on the experimental results compared to stationary rotor results therefore only one plot for each **BPC** was produced. The **CFD** results predicted that the seals had a greater sealing potential than the experimentally determined results indicated.

10.5 Porous Media/Distributed Resistance Models.

Figure 10.18 Pressure plot of the Porous Media Model. BPC=1 mm, BSC=0 mm.

The pressure plot **Figure 10.18** shows the effect of introducing a distributed resistance to the model. The distributed resistance was modelled in the area before the backing plate, representing the brush seal bristle pack. Setting viscous and inertia resistance coefficients in the three orthogonal directions achieved this. The majority of pressure drop was across the porous media, the boundary of which was clearly defined. In this example the pressure drop was 0.74 bar. The pressure gradients were not equally spaced across the porous media and the pressure reduction appeared to start relatively high up in the porous media. The porous media also had a guiding effect on the flow and quite effectively changed the flow direction within a small axial distance and channelled it downwards towards the fin clearance. This was partially due to the non-isotropic settings used to more realistically model the porosity of a real brush seal bristle pack.

Figure 10.19 Velocity vector plot of the Porous Media Model. BPC=1 mm, BSC=0 mm.

Figure 10.19 is a velocity vector plot and shows the dramatic flow guiding effect of the porous media. The vectors approached the porous media in a uniform, almost horizontal direction and were diverted almost vertically downwards. This was accompanied by an increase in velocity that continued past the bottom of the fin. The flow was directed past the fin leading edge and therefore reduced the boundary layer separation at that point. The flow velocity magnitude increased through the fin clearance and the flow expanded into the cavity in a reasonably uniform manor. In this case the swirl (VZ) velocity of 100 m/s was far in excess of the **VX** velocities. This reduced the resolution or increased the scale of the colour bands of the plot to equal sizes with 100 m/s as a maximum. The **VX** velocity was very low throughout this model.

Figure 10.20 Pressure plot of the Porous Media Model. BPC=1.8 mm, BSC=1 mm.

A full brush seal with a **BPC** of 1.8 mm and a **BSC** of 1 mm was modelled and is presented in **Figure 10.20**. The bristle pack clearance had a marked effect on the pressure plot. The results of changes in the **BPC** can be seen in **Figure 10.14** (where the brush seal bristle pack had zero clearance and the backing plate had a clearance of 1 mm) and **Plot 10.19** (where the backing plate (fin) had a clearance of 1 mm). Again the porous media guided the flow vertically downwards, past the end of the leading edge of the fin tip. The bottom of the porous media was modelled with a square edge similar to that of the fin, and produced a localised area of fluid boundary layer separation at the leading edge of the porous media end. The area on the upstream surface of the fin, and part of the fin clearance cavity was occupied by an area of low pressure that was lower than that on the downstream side of the fin. This must have been due to the relatively high flow resistance of the porous media compared to the fin tip clearance. The fluid travelled down the boundary layer of the porous media and partially into it, rather than fully entering it. The flow down the upstream side of the porous layer produced the low pressure area at the rear of the area.

Figure 10.21 Velocity vector plot of the Porous Media Model. BPC=1.8 mm, BSC=1 mm.

The velocity vector plot **Figure 10.21** shows that this seal geometry arrangement produced a very different flow pattern to previously modelled geometries. As in previous models the porous media guided the flow down almost vertically past the end of the backing plate bottom. However the percentage of flow was reduced in this area. The majority of fluid flowed under the porous media through the clearance and then expanded through the backing plate clearance. The flow split into two. Some of the fluid travelled along the bottom rotor boundary layer, whilst the other fluid flowed at 45 degrees upwards, past the downstream edge of the backing plate. The velocity vectors gradually reduced, before the fluid reached the cylinder wall and two recirculation zones were formed at either side of this area of high velocity. A further recirculation zone was also present, behind the porous media and under the backing plate tip. The velocity vectors appeared to be large in this zone and helped to reduce the flow through the adjacent area of porous media.

Figure 10.22 A comparison of CFD and experimental leakage results for a brush seal with and without swirl BPC=1 mm, BSC=0 mm.

The effect of a VZ velocity of 100 m/s, simulating the rotor surface speed is shown in **Figure 10.22**. Clearly for these geometries and porosity coefficients the VZ velocity had little effect. The experimental results from the **BSLTR** for a brush seal with a **BPC**=0.9 and **BSC**=0 were also generated and can be seen in **Figure 10.22**. VZ rotor velocity had a negligible effect on the **BSLTR** results. Again the **CFD** results appeared to over estimate the sealing capacity of a brush seal and in this case the discrepancy increased with increasing inlet velocity.

Figure 10.23 A comparison of CFD leakage results for a brush seal with and without swirl BPC=1.8 mm, BSC=1 mm.

In the case of a larger **BPC**=1.8, **BSC**=1 shown in **Figure 10.23**, the setting of a VZ velocity of 100 m/s had a small effect on the pressure differential for a given inlet velocity. Rotor velocity increased the sealing capacity of the brush seal (compared to the stationary **CFD** results) for the range of 30 to 65 m/s and then reduced the capacity after this. The precise effect of swirl required further investigation to determine its exact nature, as experimental error could well have produced these anomalies.

Figure 10.24 A comparison of CFD and experimental leakage results for different porosity coefficients BPC=1 mm, BSC=0 mm.

The sealing capacity of a seal arrangement incorporating a distributed resistance is highly dependent on the porosity coefficients used. **Figure 10.24** is a graph showing the three proposed **Chew et al** sets of coefficients applied to a single model geometry arrangement (instead of their specific design geometries) with a **BPC**=1 and **BSC**=0. The equations describing the best-fit lines are also given. The **Chew et al** porosity values were calculated from experimental leakage rig results and were specific to the seal geometry, **BPC** and **BSC** and operating conditions **Chew et al** stipulated. An experimental result from the **BSLTR** was also included in the graph for comparison. It was apparent that for **CFD** modelling using **FLOTRAN** and the model geometries and conditions tested, different porosity coefficients were required for experimental and theoretical agreement. This was expected and was partially due to slight differences between the **BSLTR**, **Chew et al** and **CFD** geometries and operating conditions. **FLOTRAN** may also have tended to over estimate the sealing capacity, as proven by the labyrinth fin **CFD** and experimental results. The **Chew et al** experimental data and operating conditions were not available for comparison but the coefficients were calculated for a wide range of different inlet

velocities, fluid temperatures and types. Proposed **CFD** porosity coefficients for the models with **BPC**=1 **BSC**=0 would lie somewhere between the **Chew et al BPC**=1.15 **BSC**=0.25 and the **Chew et al BPC**=1.67 **BSC**=0.27 if the theoretical results were to agree more fully with the experimental results.

Figure 10.25 Comparison of calculated leakage results directly from Chew et al and recalculated results from CFD using Chew et al coefficients.

The theoretical relationship between inlet velocity and pressure differential through areas of porous media having different coefficient values is plotted in **Figure 10.25**. The coefficients used to plot the theoretical relationship between pressure differential and inlet velocity were from **Chew et al** (for three different **BPC** and **BSI**/C). Recalculated plot lines were also included. The "recalculated" porosity coefficient values were determined by recalculating the inertial and viscous coefficients using the **CFD** bulk leakage result plots created from the **Chew et al** original porosity coefficient values. Plotted in this way the **Chew et al** coefficients were not tied to their specific brush seal geometry and the changes in results were for changes in resistance coefficients and not backing plate clearance. The recalculated coefficients were coefficients for a full seal including an area of porous media with the three **Chew et al** coefficients and a **BPC**=1. The experimental result plot line was from the **BSLTR** and represented the porosity of a full brush seal with a **BPC**=0.9 and **BSC**=0. The experimental coefficients produced a theoretical plot line that lied between the **Chew et al BPC**=1.15 **BSI**=0.25 and the **Chew et al BPC**=1.67 **BSC**=0.27. If these coefficients had been used as **CFD** porosity coefficients the experimental and theoretical results would have been closer.

10.6 General Discussion

FLOTRAN was successfully used to model both bristle packing pattern arrangements, labyrinth fins (backing plates) and brush seals consisting of an area of

porous media and a backing plate. Options within **FLOTRAN** were set to model air at a specific ambient inlet temperature and the model was tailored to include turbulence equations, incompressible flow, and rotating boundary walls.

Models were relatively easily constructed, meshed and boundary conditions applied. Some difficulty in convergence and model stability was encountered but was usually overcome by modifying the mesh or solution criteria parameters. The major drawback with **CFD** modelling of brush seals using **FLOTRAN** was the computational time required both to produce models, change models, run solutions, and examine the results, (given the computational resources available).

Bristle Packing Pattern Models allowed a good insight to the pressure, velocity distribution and the velocity vectors through both the idealised "square" and "hexagonal" patterns. The **CFD** model bristle packing patterns were designed to have a similar bristle density to the **BSLTR** experimental brush seals. The calculated porosity values from the bristle packing pattern models were thought to be reasonable estimates for 2D isotropic axial flow through an idealised brush seal pack with no backing plate. The "hexagonal" pattern had the higher flow resistance of the two patterns modelled. This was expected and was thought to be a better approximation of the actual packing pattern in a real brush seal.

Backing plates (labyrinth fins) with different fin tip clearances were modelled with changes in inlet velocity. The results were of the same magnitude as experimental results. However, the **CFD** models tended to over-estimate the sealing potential of the backing plate. This may have been due to experimental fin geometries and clearances that were slightly different to those of the **CFD** model, **BSLTR** experimental error and **CFD** model convergence problems. The leading edge of the backing plate tip played a major role in the flow through the clearance and was responsible for boundary layer separation at this point. The flow travelling at relatively high velocity through the **BPC** caused areas of turbulence and recirculation. The recirculation areas after the backing plate were thought to improve

sealing in a multi-fin seal and the fin tip shape influenced the size and position of the recirculation area.

A direction dependent porous media/distributed resistance area was successfully modelled with **FLOTRAN** and provided a reasonable approximation of a brush seal bristle pack under ideal conditions. An insight into the flow through porous media was given with respect to the coefficients used, and the **BPC** and **BSC**. The porous media tended to guide the fluid flow downwards. This had the effect of reducing the fluid boundary layer separation at the leading edge of a backing plate tip. If a clearance at the base of the porous media was introduced, the porous media effectively acted as a labyrinth fin and the majority of fluid flow travelled though the clearance.

Given the correct porosity values the **CFD** model could replicate experimental results for specific brush seal geometry and operating conditions. However, the porosity values may not be universally applicable to other model geometries (**BPC**, **BSC**) or for use in other **CFD** packages. Further modifications to the porosity coefficients would be required to ensure that the **CFD** results reproduced the experimental results for all inlet velocities, **BPC** and **BSI/C**.

Swirl/VZ velocity of 100 m/s appeared to make a small difference to the flow resistance of the seal, but this changed with **BPC**, **BSC**, porosity coefficients and inlet velocity. The effect on velocity and pressure distribution was visually very small and confined to a small boundary layer. **CFD** experimental error was sufficiently large by comparison to ignore the effect of 100 m/s VZ velocity on total model pressure differential for the **CFD** models defined.

10.7 Conclusions.

i.) FLOTRAN was successfully used to model bristle packing patterns, backing plates and brush seals using a porous media/distributed resistance and gave a useful insight into the flow patterns within both models under different conditions.

ii.) Porosity coefficients calculated from the **Bristle Packing Pattern Model** are not directly applicable to the **Porous Media Model** as the results obtained are very low compared to the experimental results.

iii.) FLOTRAN tended to overestimate the sealing capacity of labyrinth seals compared to experimental data by as much as 50 %.

iv.) The geometry of the backing plate tip had a significant effect on the flow patterns produced from the **Backing Plate Model** and the **Porous Media Model** when the bristles were modelled to touch the rotor.

v.) When Porous Media Models were generated where there was a clearance between the area of porous media and the rotor almost all of the flow went through the clearance below the porous media. The area of porous media effectively acted as a square edged labyrinth seal and the flow patterns were controlled by the tip geometry. In real brush seals the bulk of the flow may also travel through the clearance but the controlling fin tip geometry would not be square edged and would not have a constant geometry or clearance.

vi.) Porosity coefficients used in the brush seal **CFD** modelling were only valid for specific seal geometries, **BPC** and **BSC** (and possibly the specific **CFD** package) due to the changing operation of the seal under different conditions.

viii.) Plots of theoretical pressure differential against inlet velocity using **Forchiemer's Law** indicated that the **Chew et al** coefficients would underestimate the results by 70 to 80 % compared to the experimental porosity coefficients (calculated from results using the nearest geometry available).

ix.) Porosity coefficients "recalculated" using a single iterative process produced results that were closer to the experimental results but were as much as 40 % too high.

10.8 Recommendations for Further Work.

i.) Repeat the process of modelling using **FLOTRAN** and the Porous Media/Distributed Resistance Model with geometries that corresponded to other configurations tested in the

BSLTR and determine the **FLOTRAN** porosity coefficients accurately (using an iterative process).

ii.) Use the calculated porosity values to model geometries similar to other published experimental brush seal leakage results to validate the universal applicability of the calculated porosity coefficients.

iii.) Repeat modelling with and without rotating walls to further investigate the effect of swirl on sealing.

Table 10.1 Comparison of **Chew et al** and CFD calculated C and k Coefficients.

	Chew	**Chew**	**Chew**	**Expt. Result**	**Straight pattern (i)**	**Straight pattern (ii)**	**Hex pattern (i)**	**Hex pattern (ii)**
k	2.00e6	1.71e5	7.00e4	7.36e4	4.39e4	3.22e4	7.09e4	6.86e4
C	5.32e11	1.83e10	1.40e9	2.00e10	8.22e10	1.21e10	1.69e10	1.48e9
BPC	1.15	1.67	2.15	0.9	n/a	n/a	n/a	n/a
BSC /I	I=0.25	C=0.27	C=0.75	0	n/a	n/a	n/a	n/a

BPC= Backing plate clearance

BSI/C Brush seal interference/clearance

(i) "Best "curve fit

(ii) "Zero" curve fit- forced to go through the origin

k = Viscous coefficient

C = Inertial coefficient

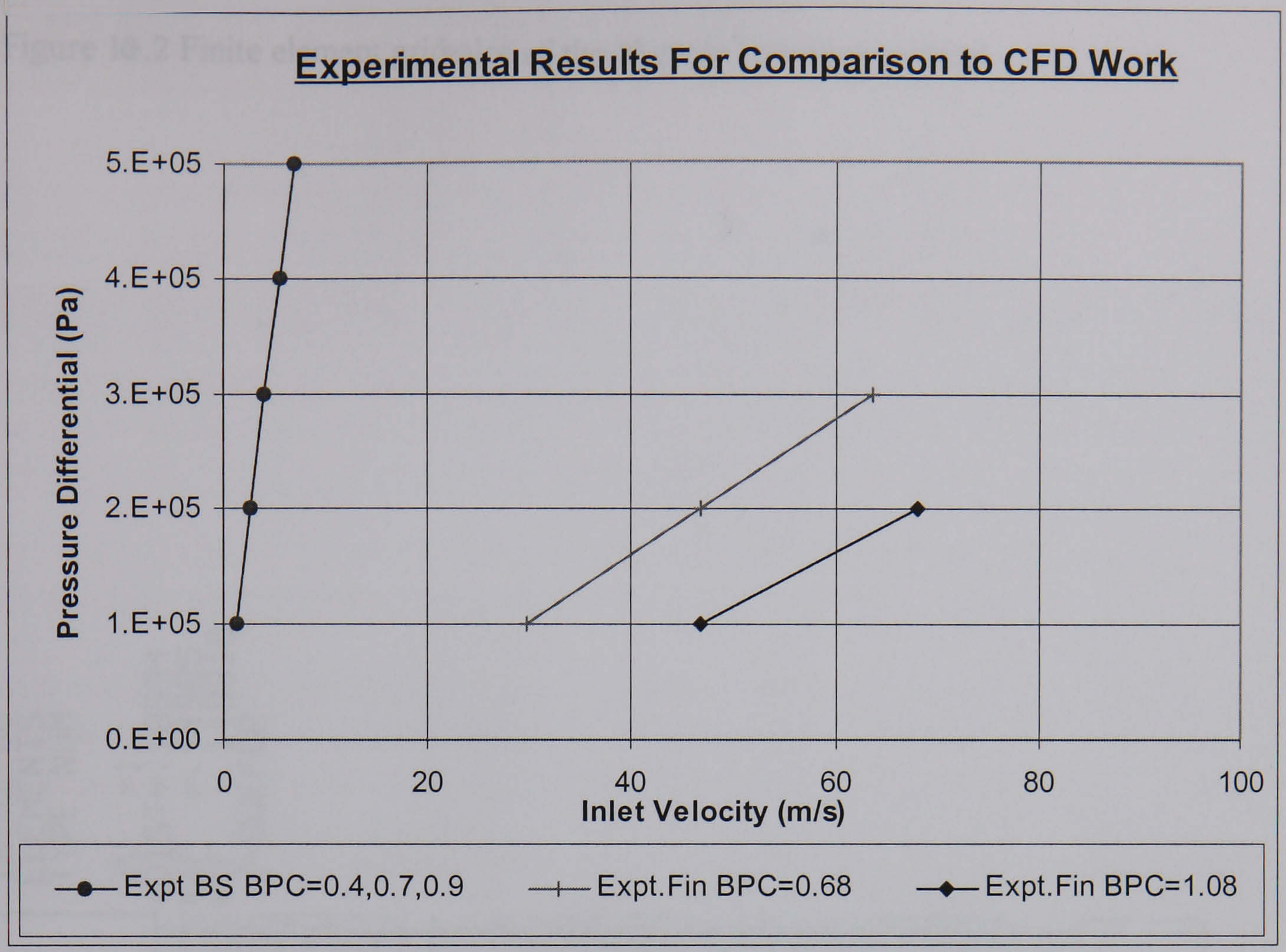

Figure 10.1 A graph of experimental results from the Brush Seal Leakage Test Rig for comparison to CFD results.

Figure 10.2 Finite element grid plot of the "Square" packing pattern.

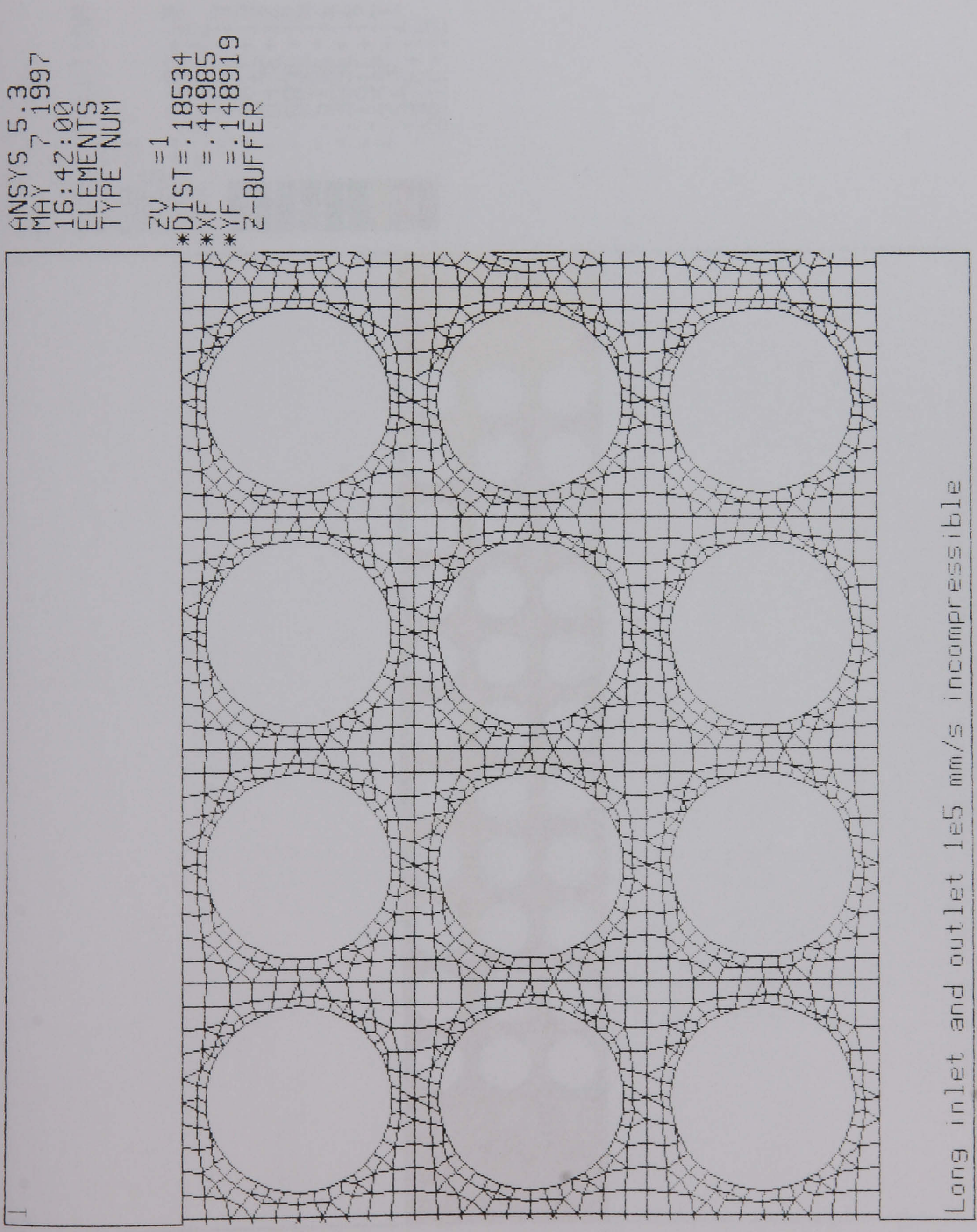

Figure 10.3 Pressure distribution plot of the "Square" packing pattern.

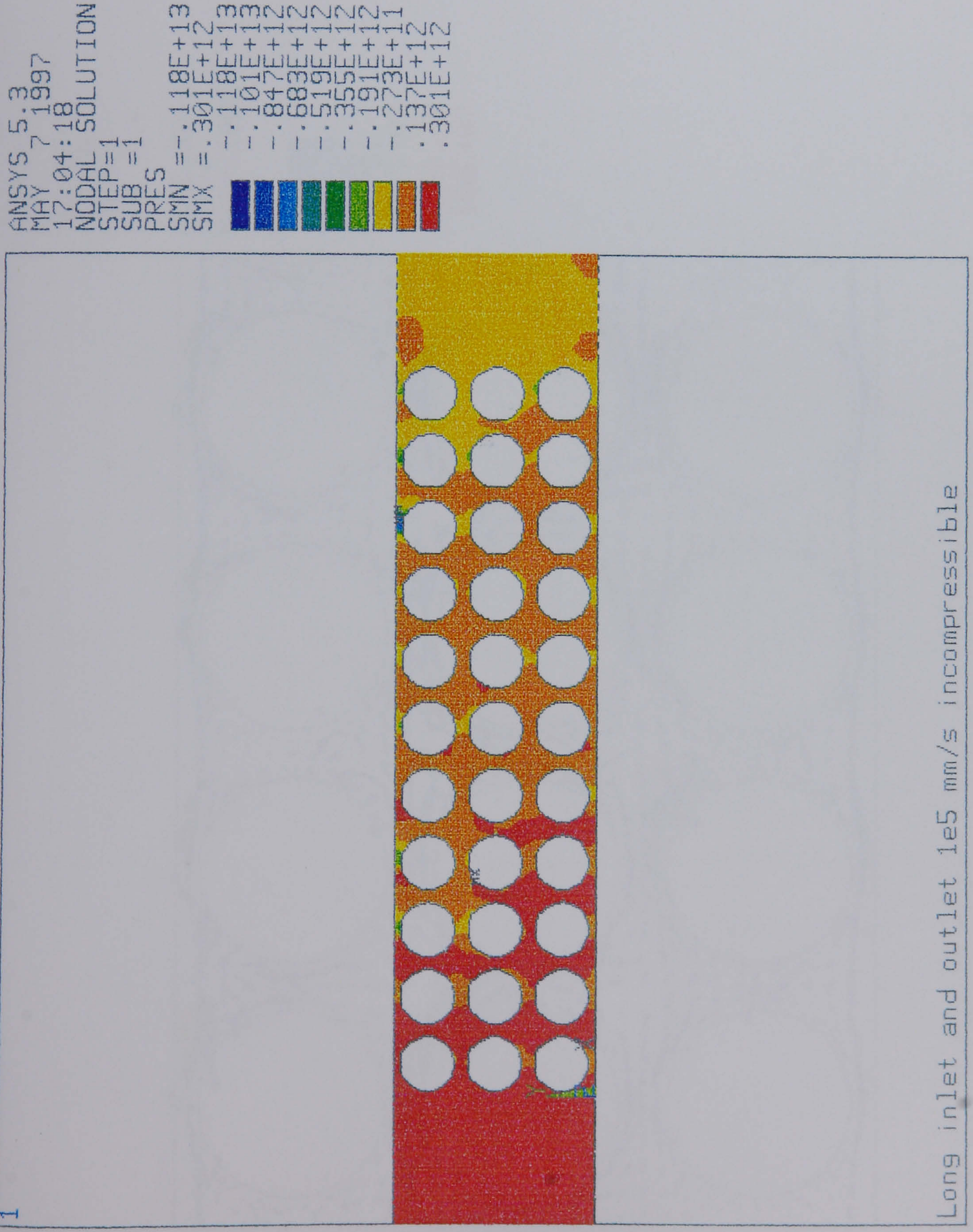

Figure 10.4 Velocity vector plot of the "Square" packing pattern.

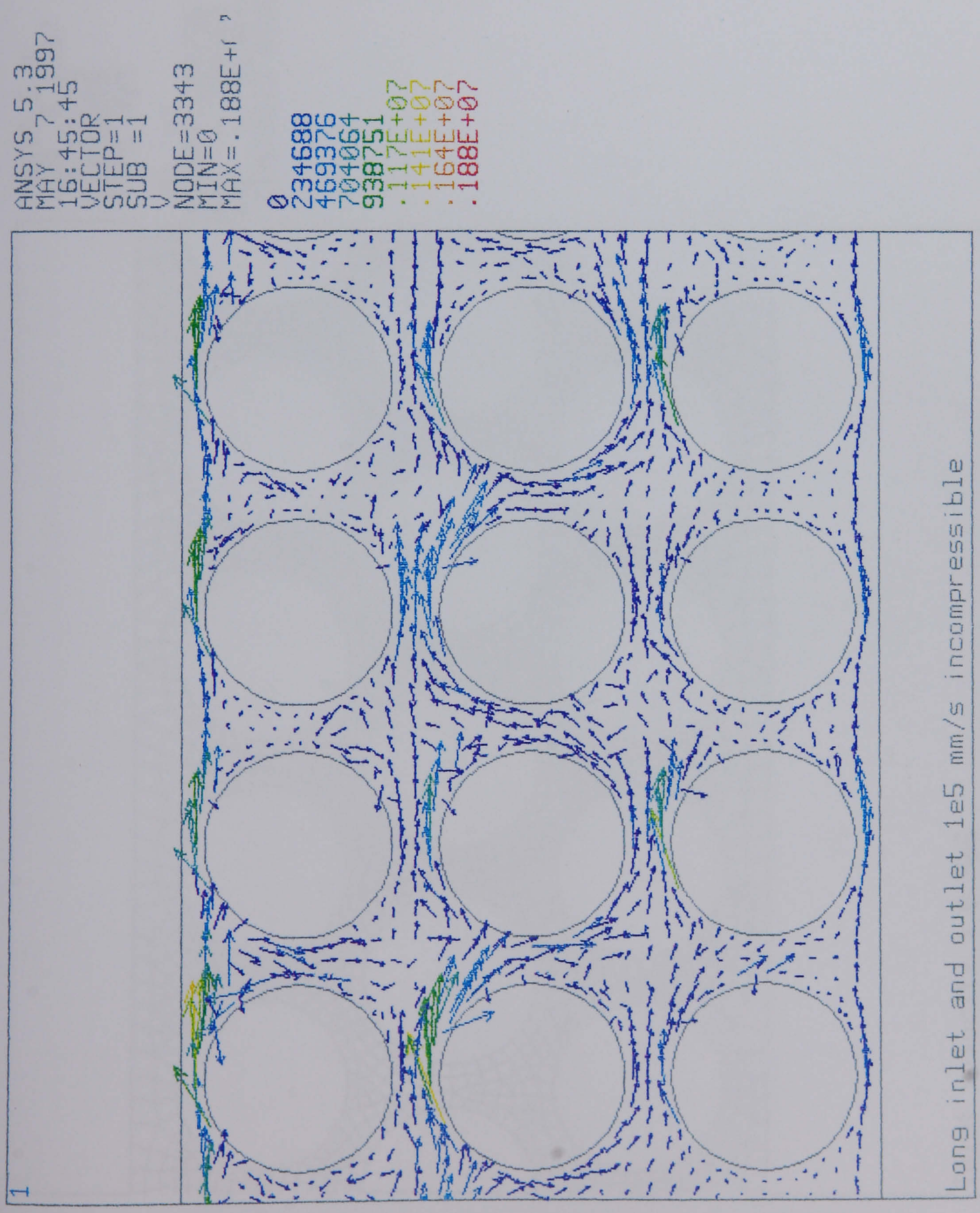

Figure 10.5 Finite element grid plot of the "Hexagonal" packing pattern.

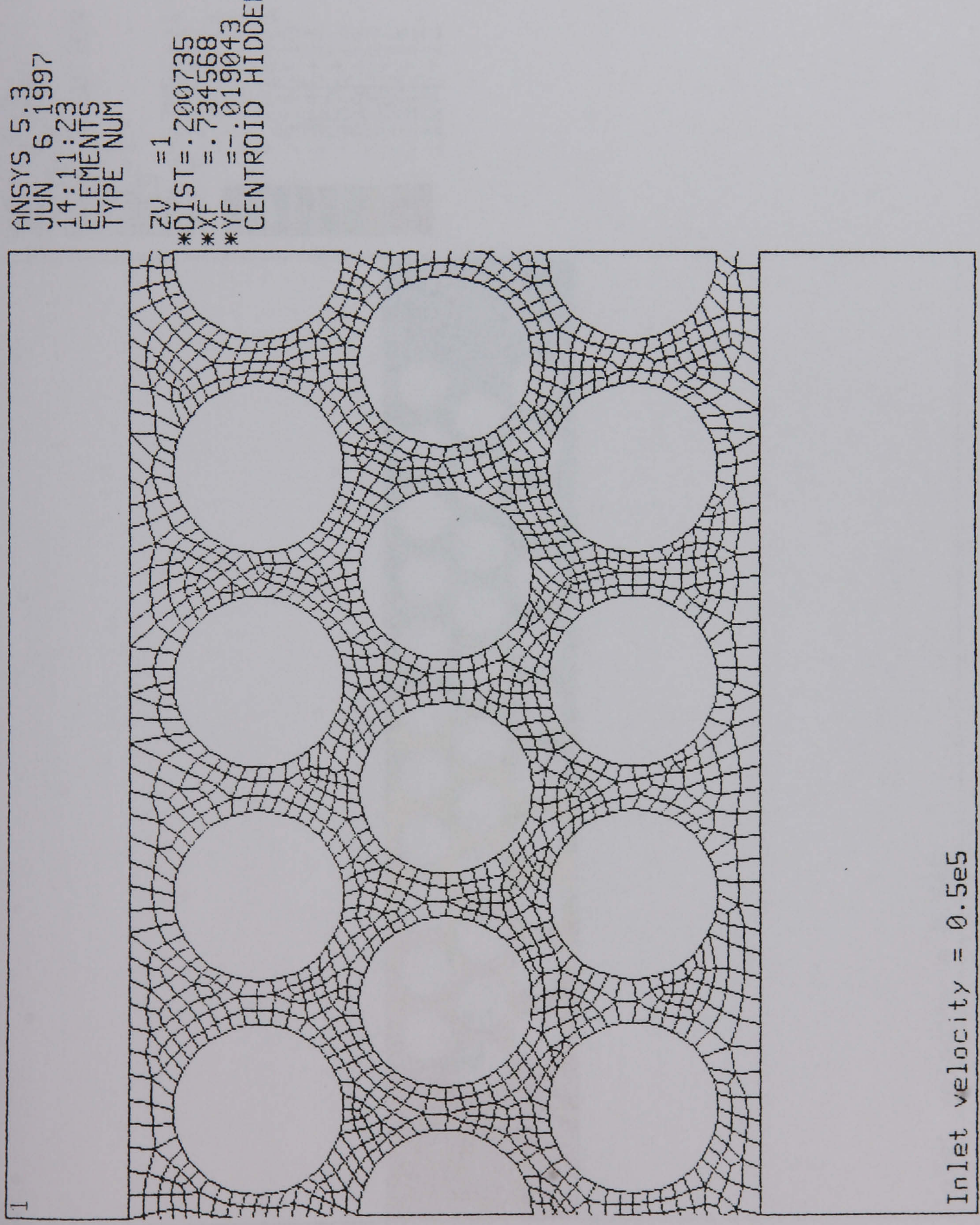

Figure 10.6 Pressure distribution plot of the "Hexagonal" packing pattern.

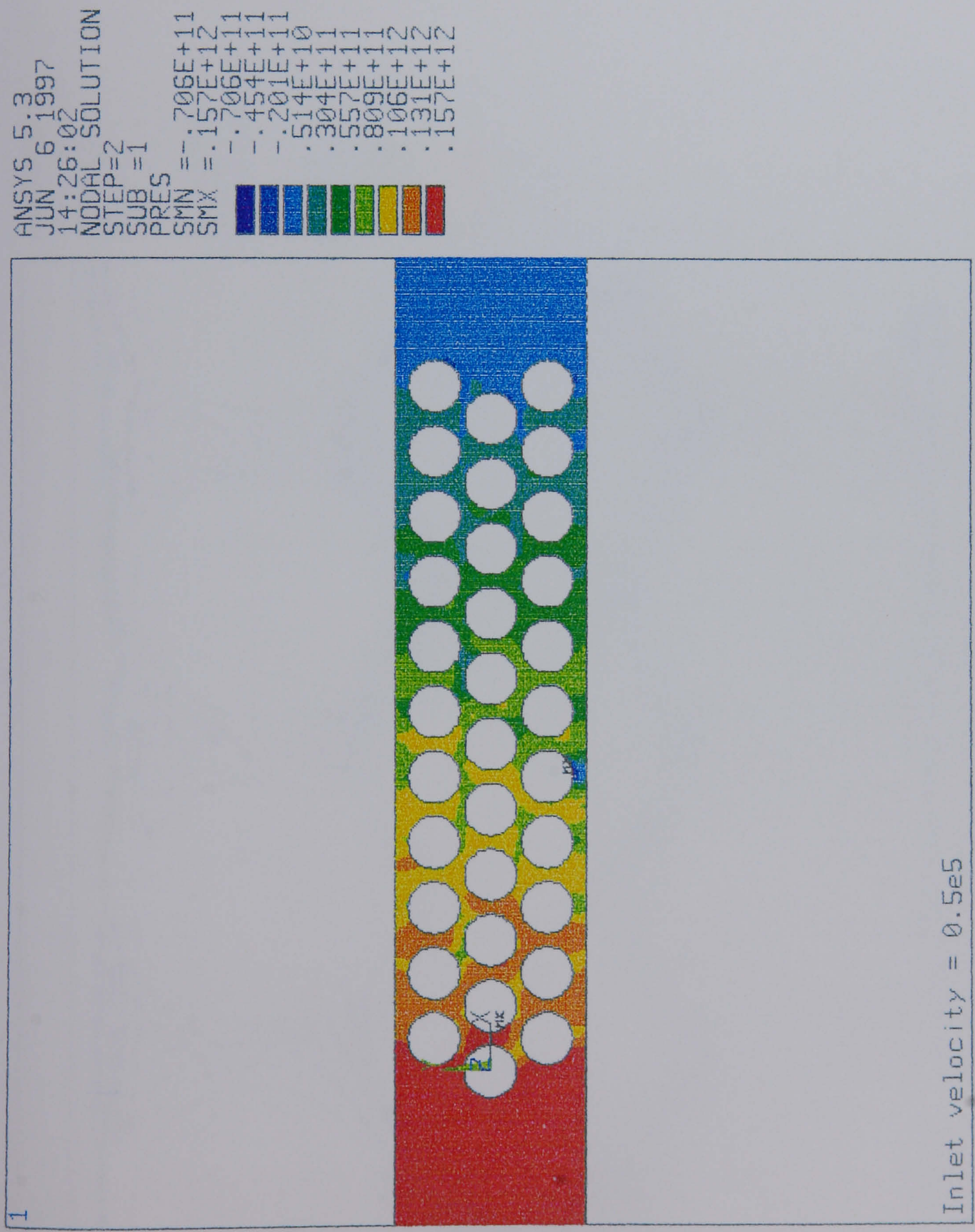

Figure 10.7 Velocity vector plot of the "Hexagonal" packing pattern.

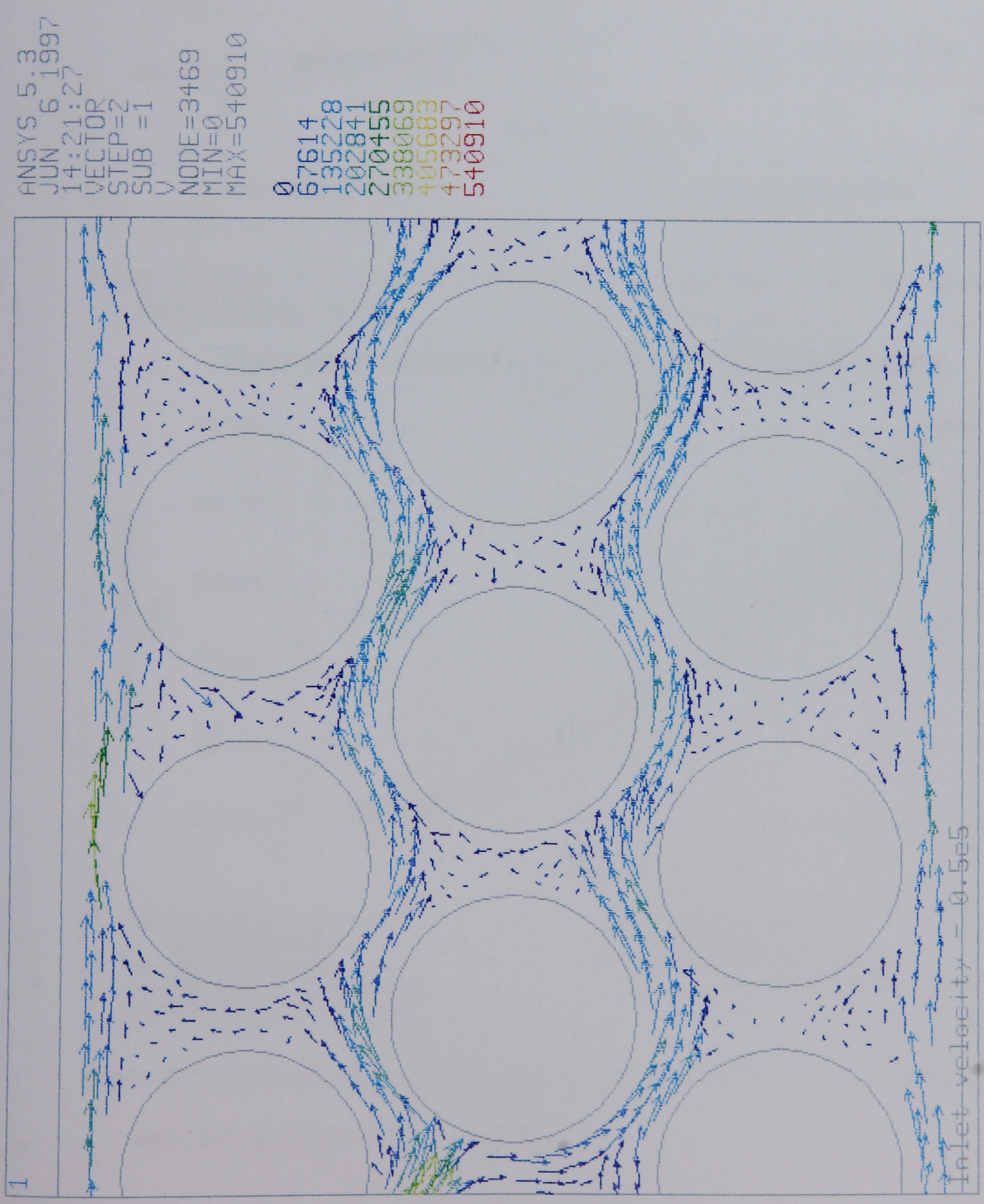

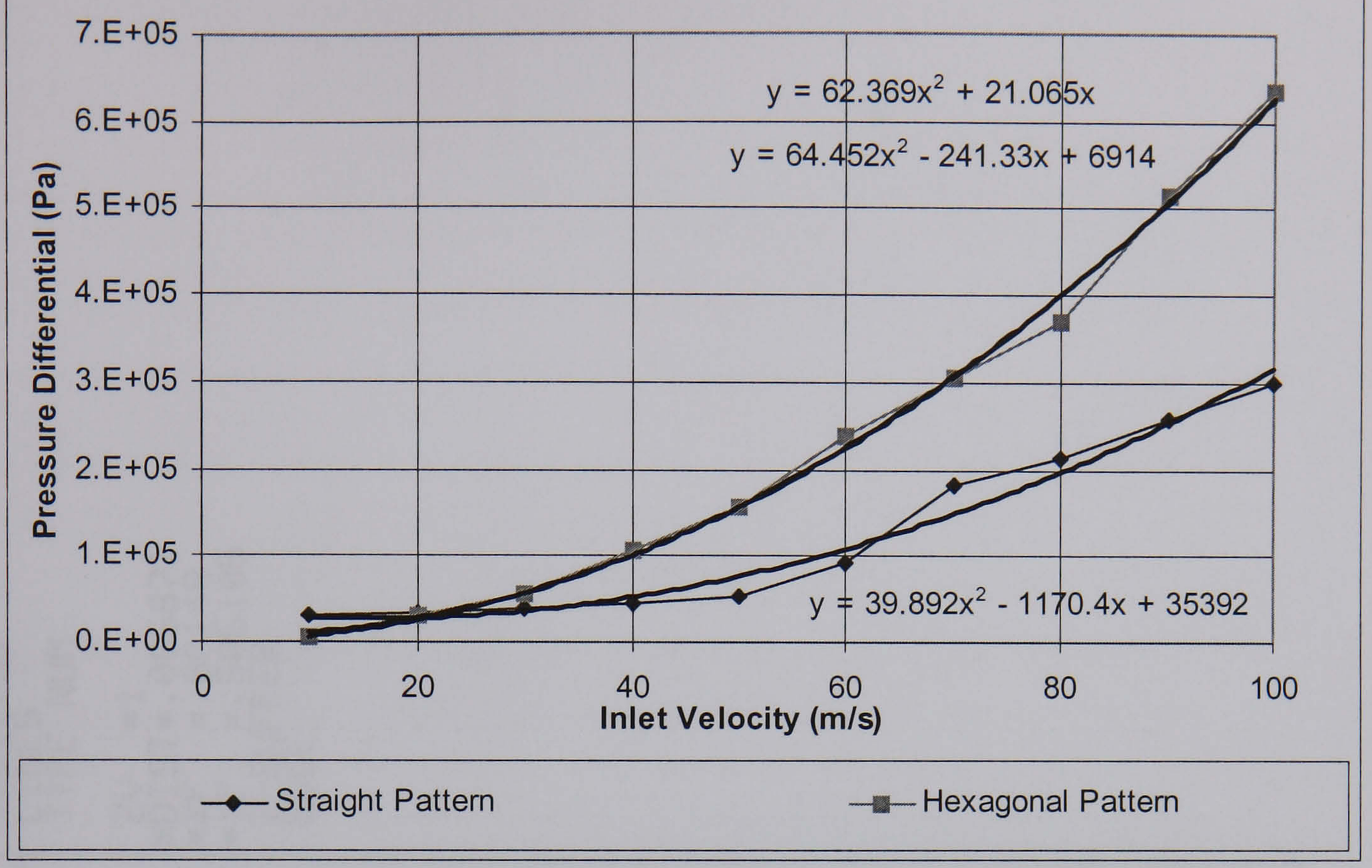

Figure 10.8 Inlet velocity against pressure differential for "Square" and "Hexagonal" bristle packing patterns.

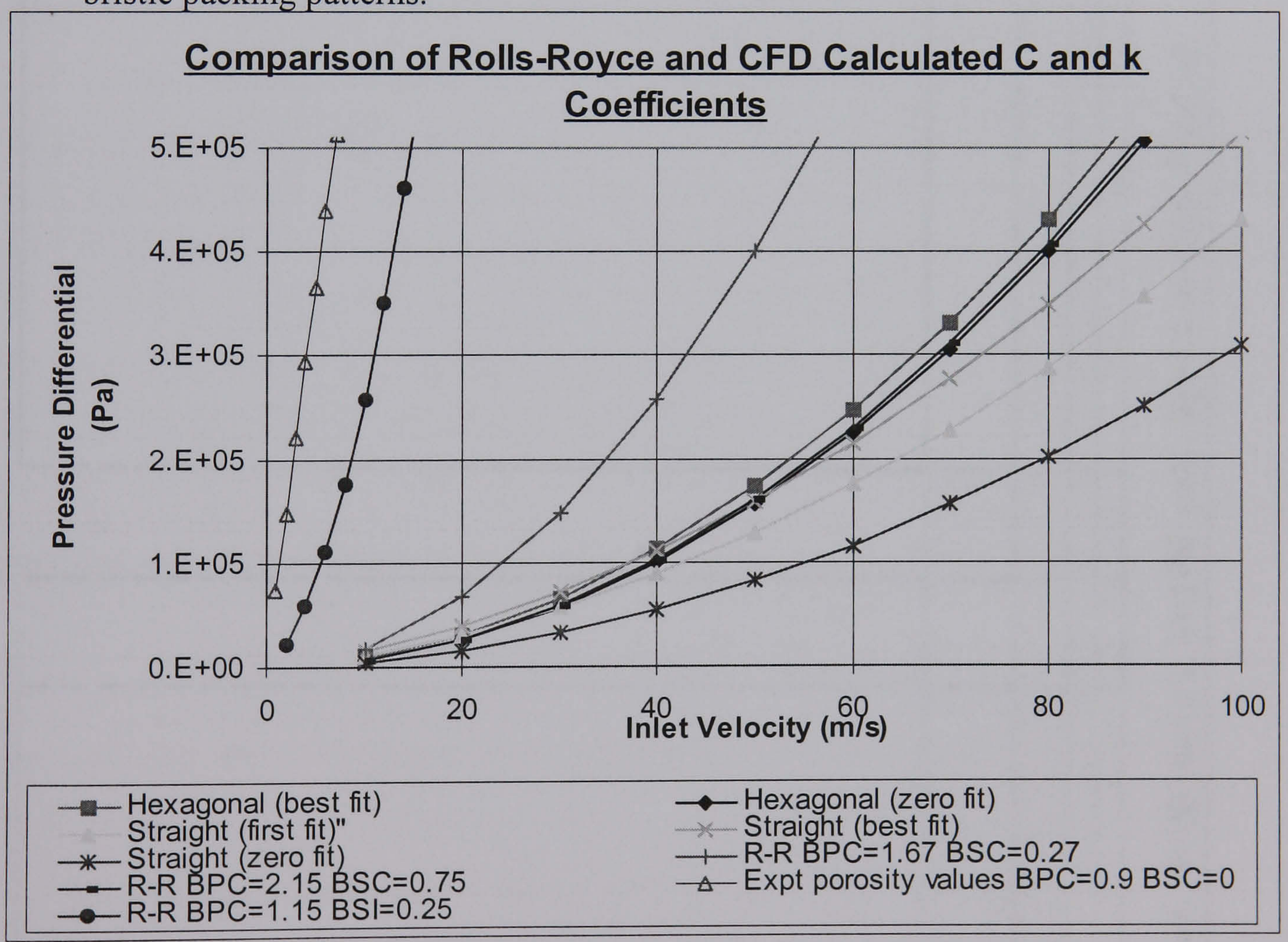

Figure 10.9 Theoretical inlet velocity against pressure differential comparing Chew et al and CFD calculated C and k coefficients.

Figure 10.10 Line plot of the Backing Plate Model.

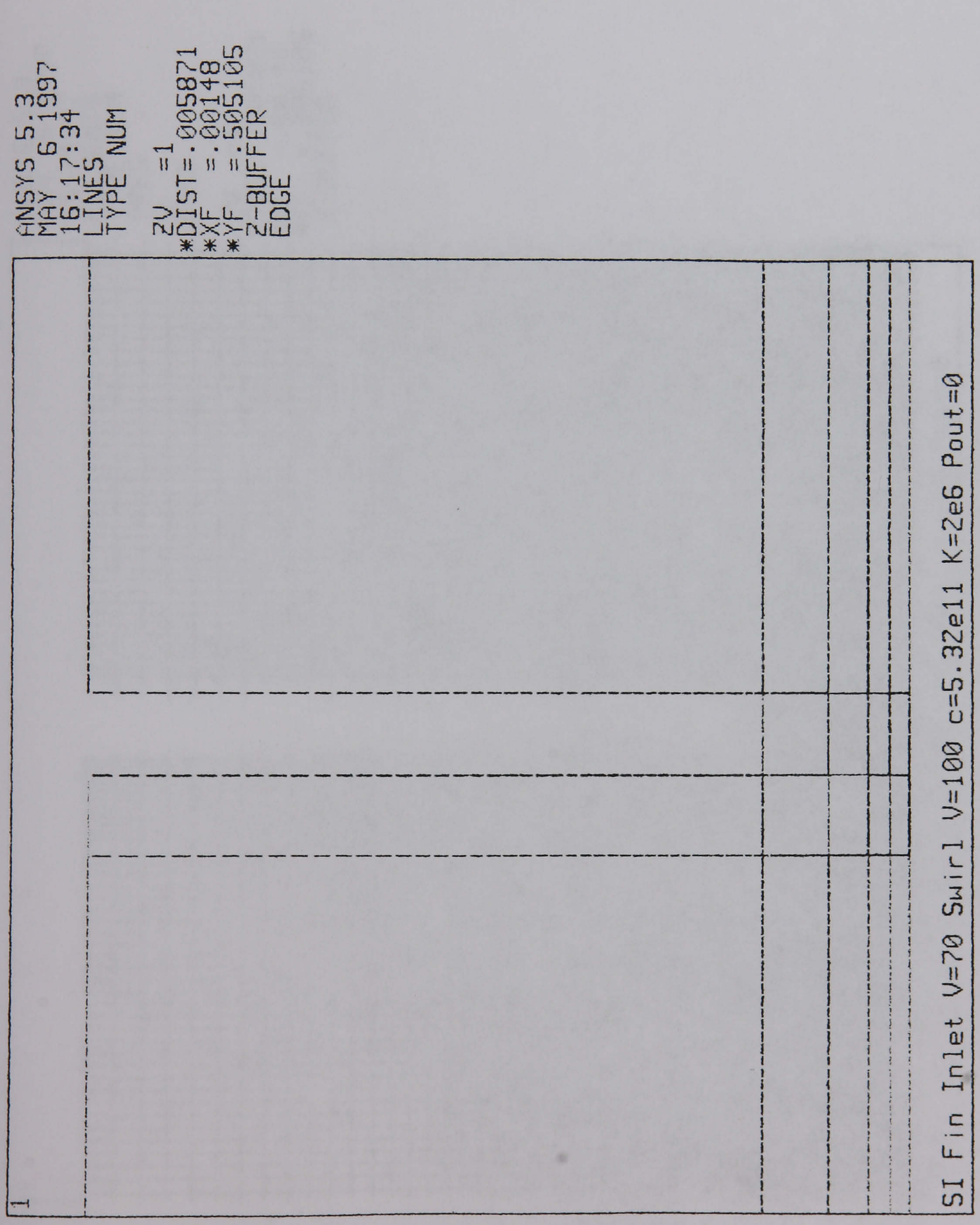

Figure 10.11 Finite element mesh of the Backing Plate Model finite. BPC=1 mm.

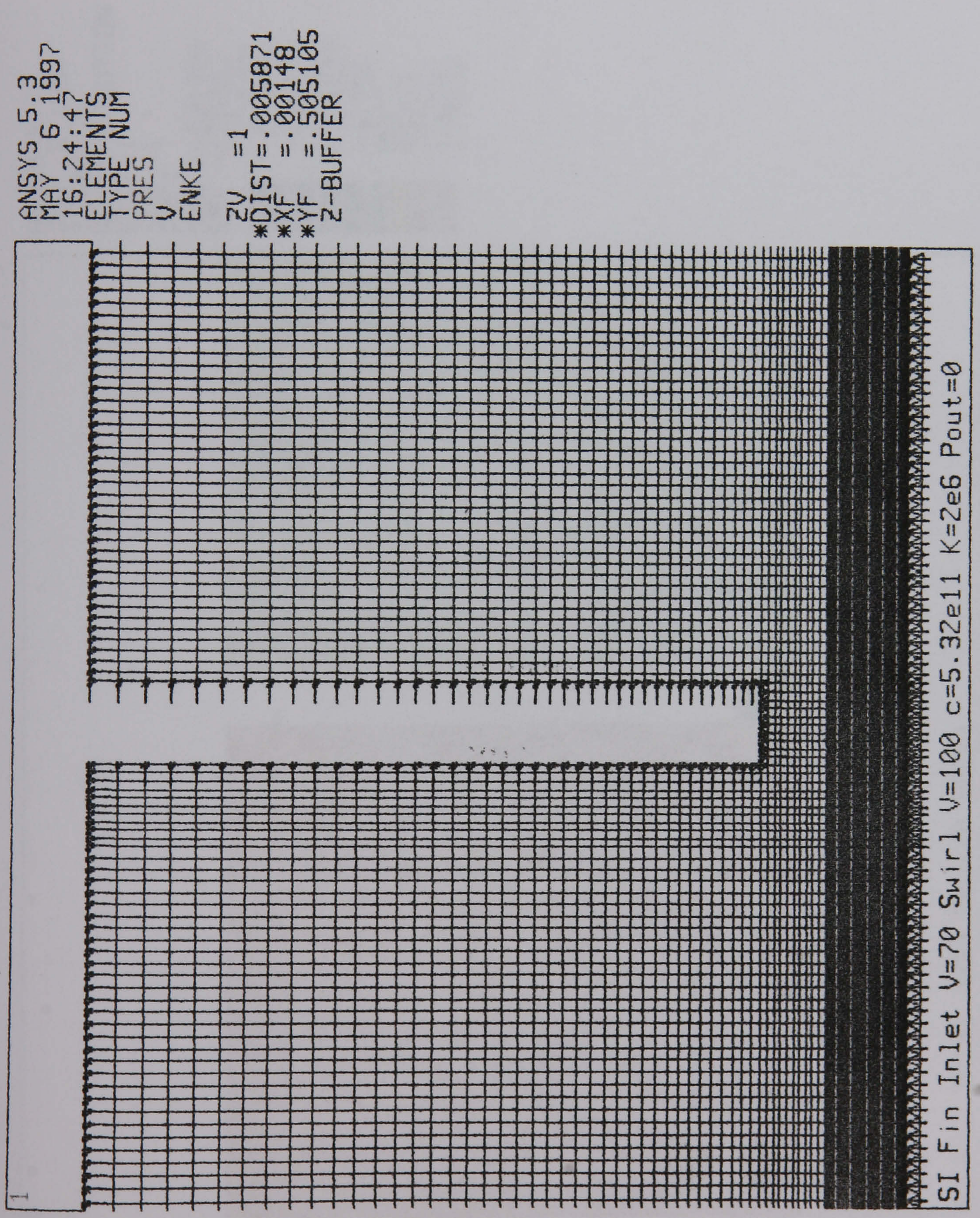

Figure 10.12 Pressure distibution plot of the Backing Plate Model. BPC=1 mm.

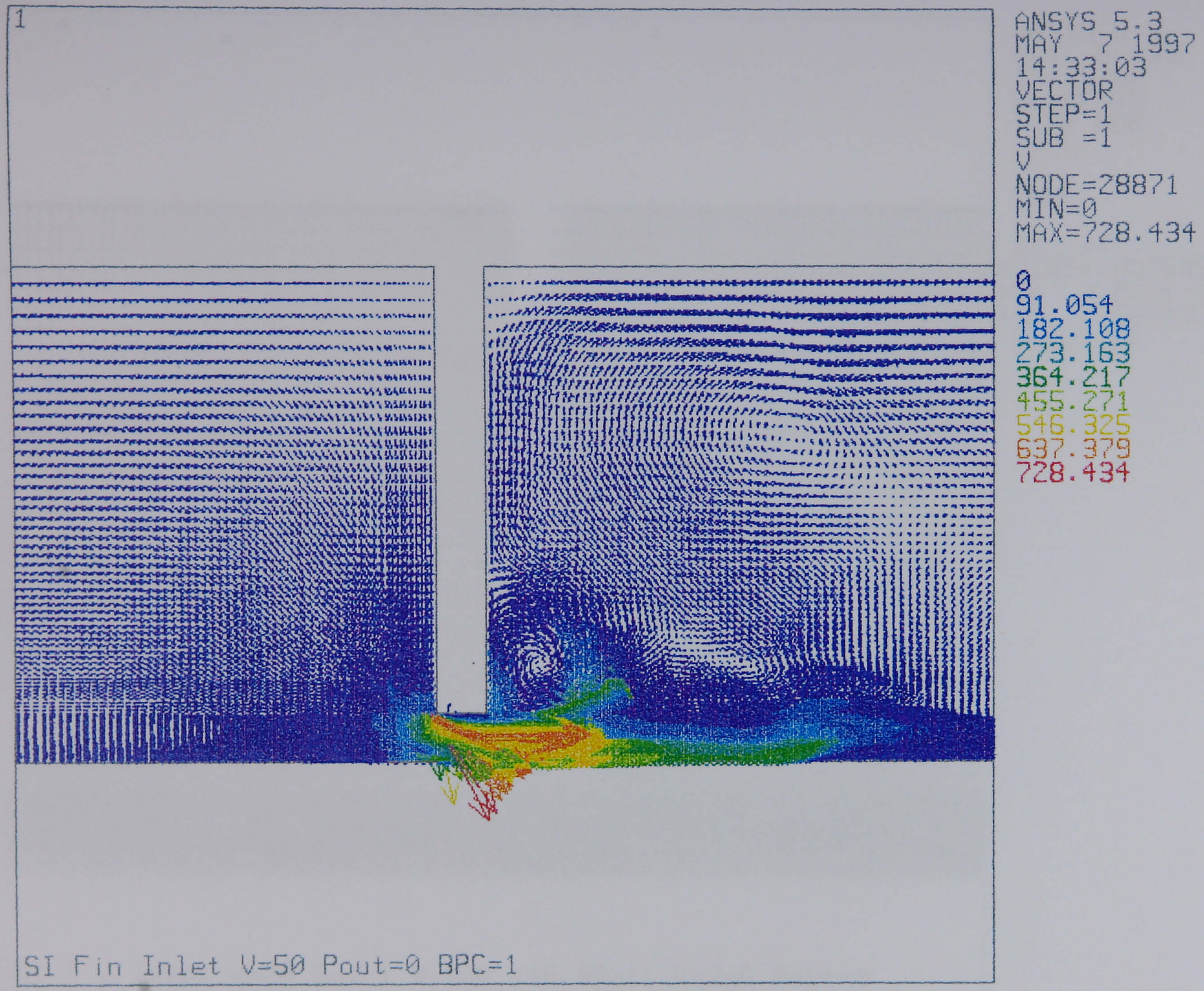

Figure 10.13 Velocity vector plot of the Backing Plate Model. BPC=1 mm.

Figure 10.14 Finite element mesh of the Backing Plate Model. BPC=1.8 mm.

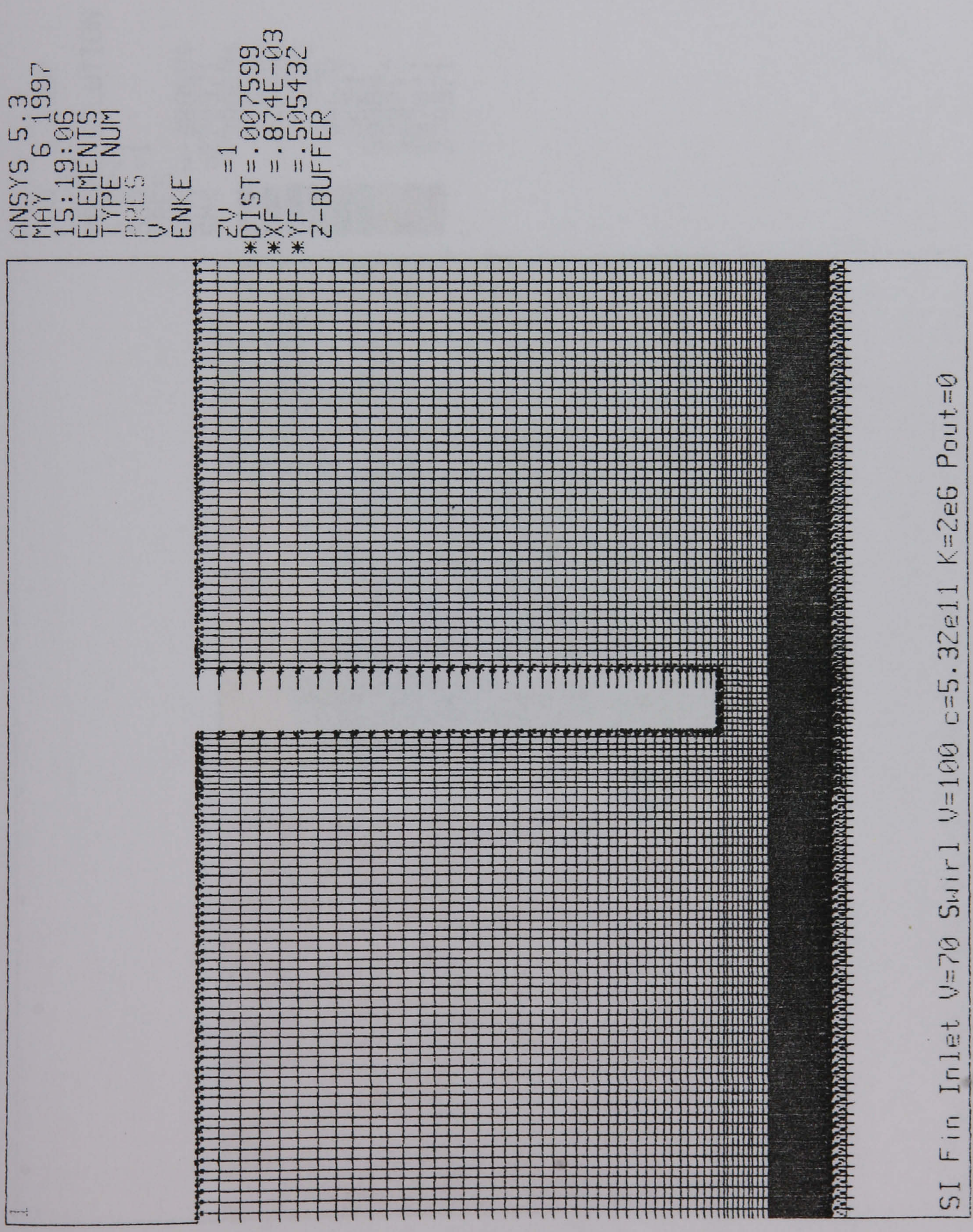

Figure 10.15 Pressure distribution plot of the Backing Plate Model. BPC=1.8 mm.

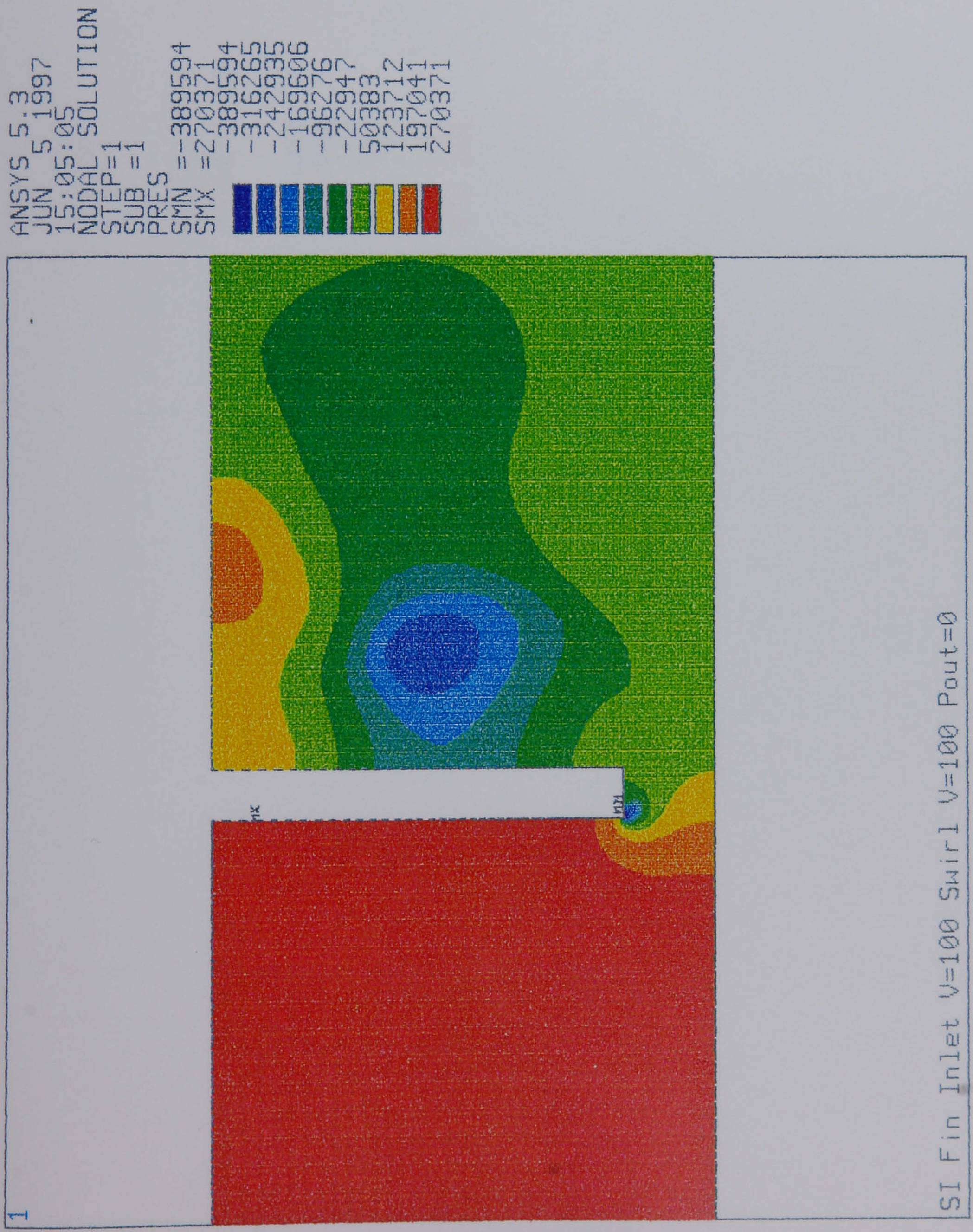

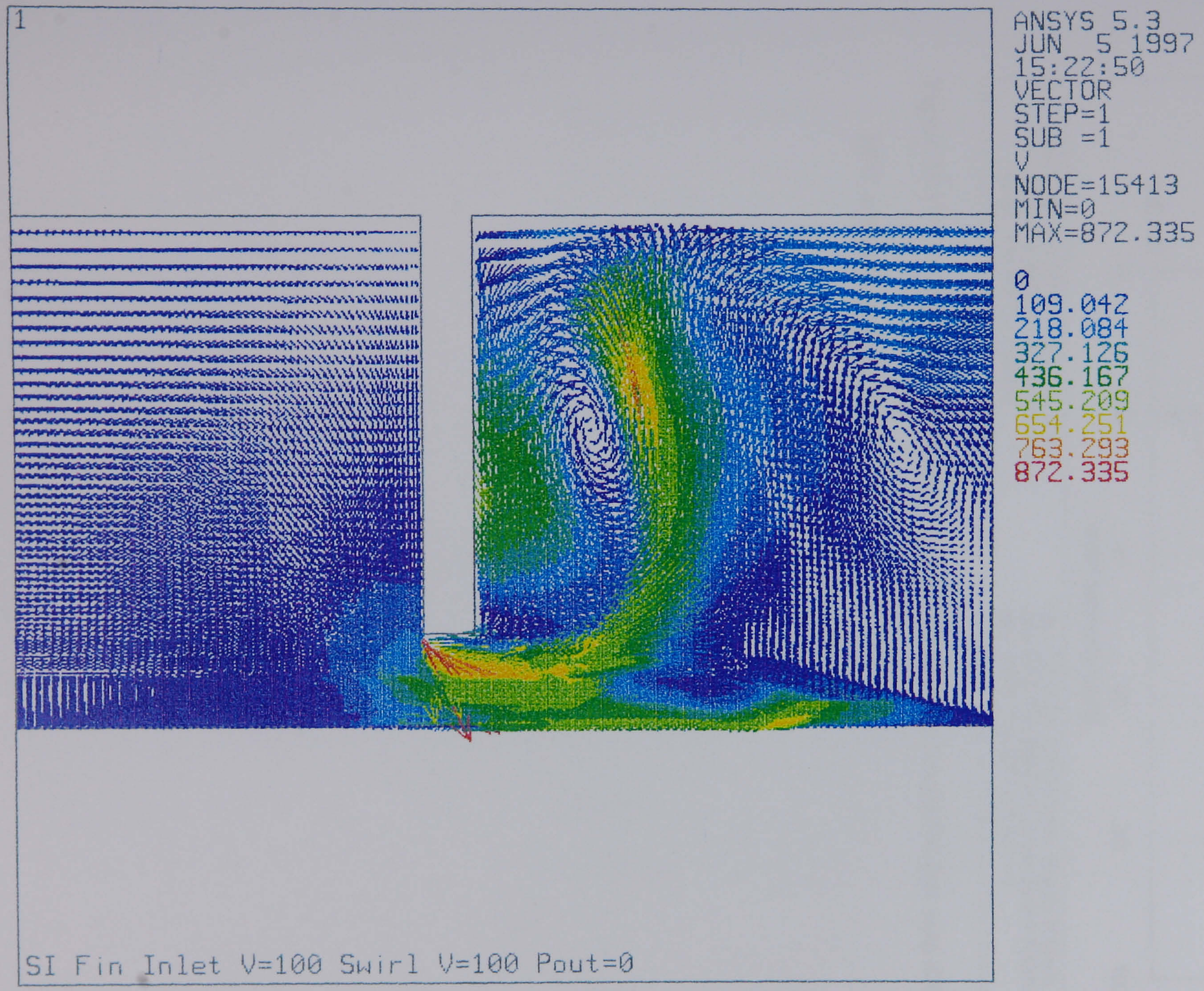

Figure 10.16 Velocity vector plot of the Backing Plate Model. BPC=1.8 mm.

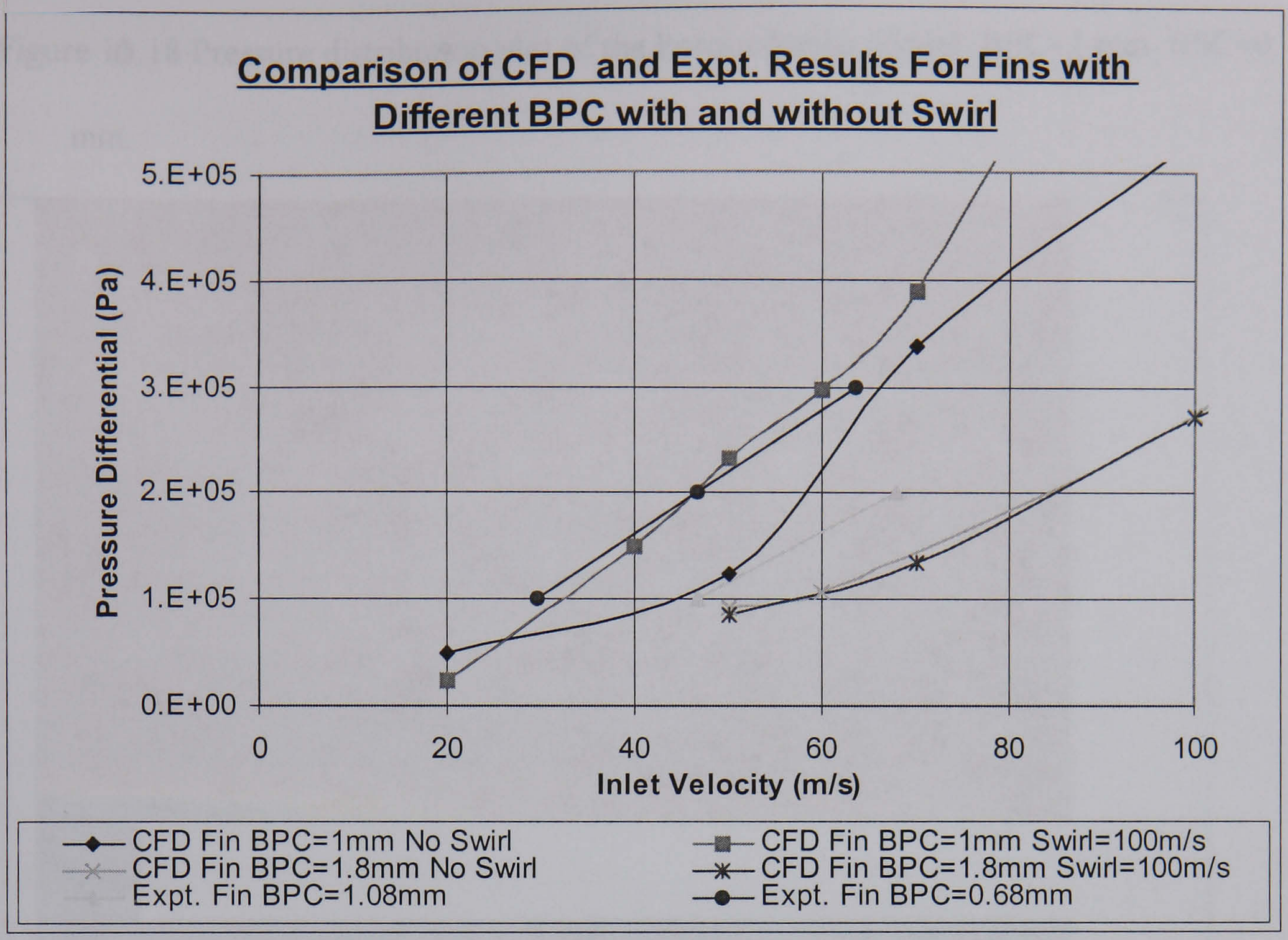

Figure 10.17 Comparison of CFD and experimental leakage results for fins with different BPC with and without swirl.

Figure 10.18 Pressure distribution plot of the Porous Media Model. BPC=1 mm, BSC=0 mm.

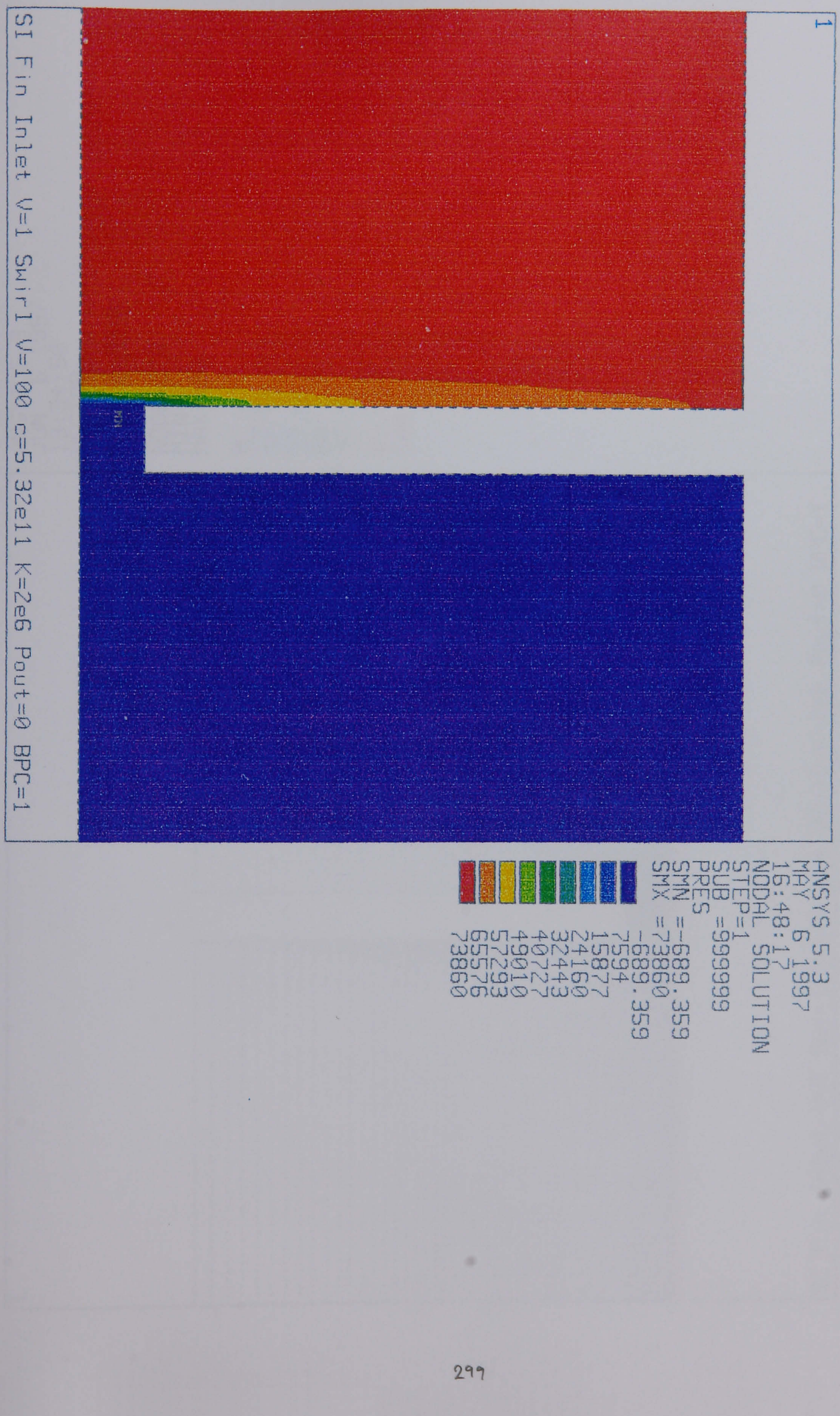

Figure 10.19 Velocity vector plot of the Porous Media Model. BPC=1 mm, BSC=0 mm.

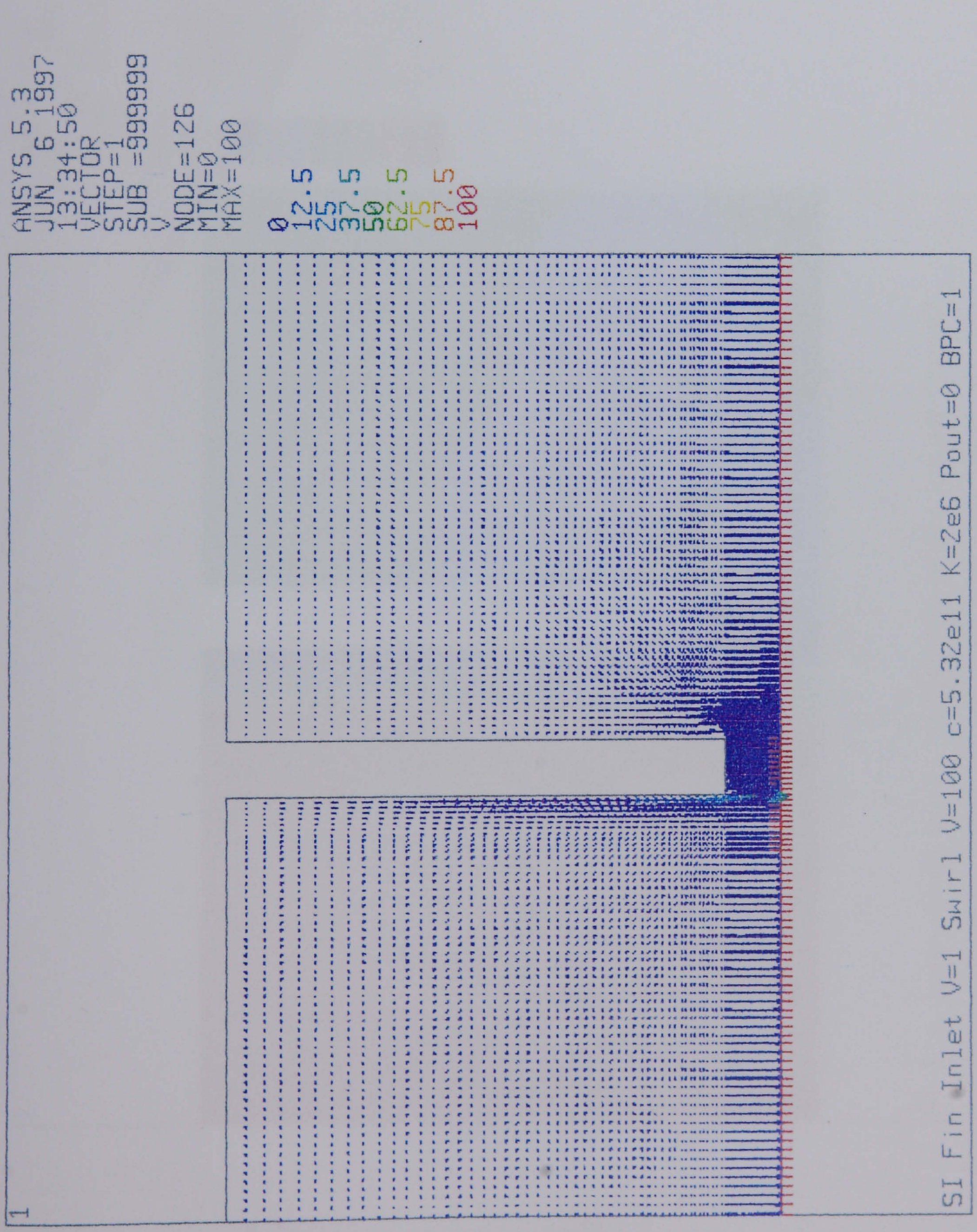

Figure 10.20 Pressure distribution plot of the Porous Media Model. BPC=1.8 mm, BSC=1 mm.

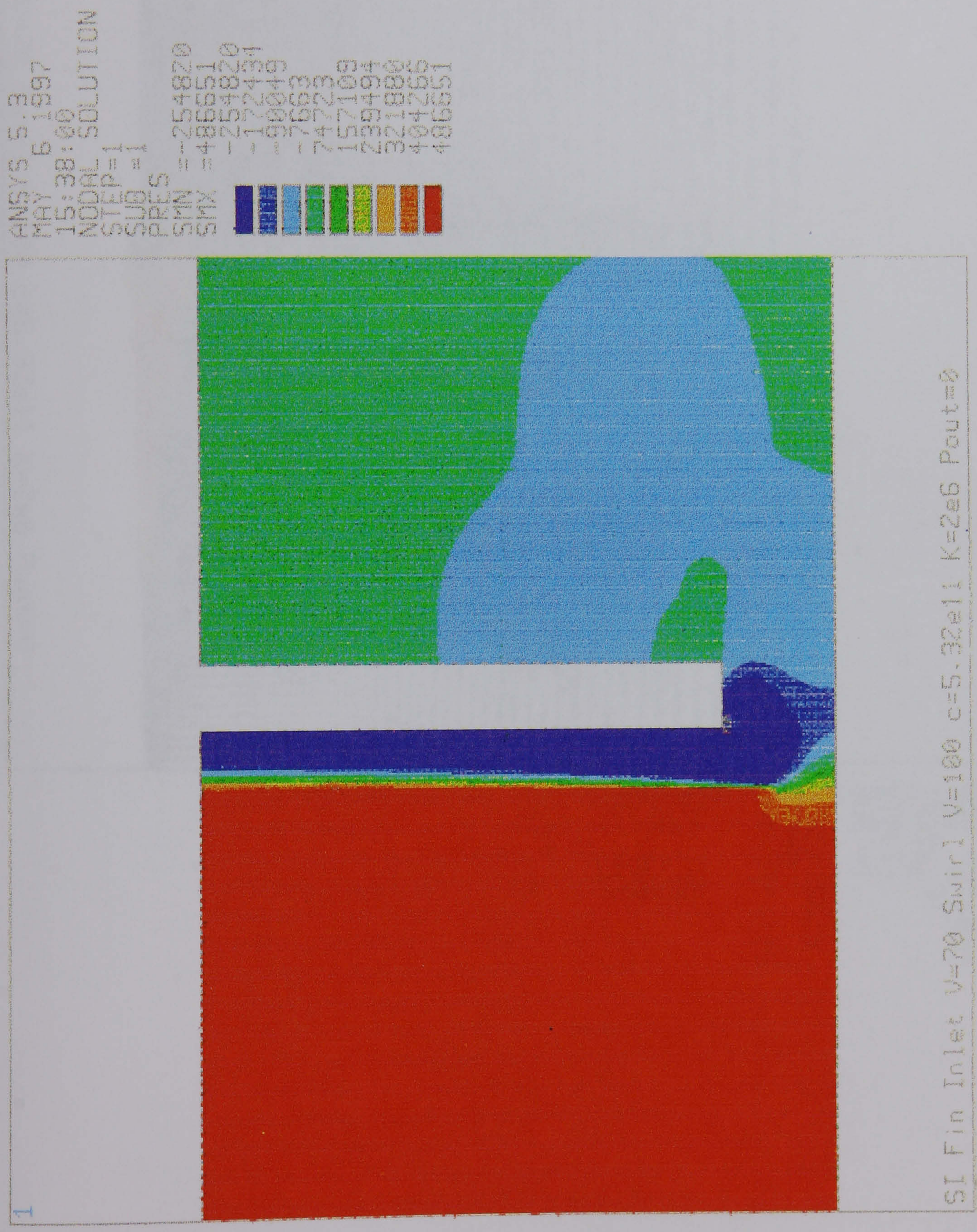

Figure 10.21 Velocity vector plot of the Porous Media Model. BPC=1.8 mm, BSC=1 mm.

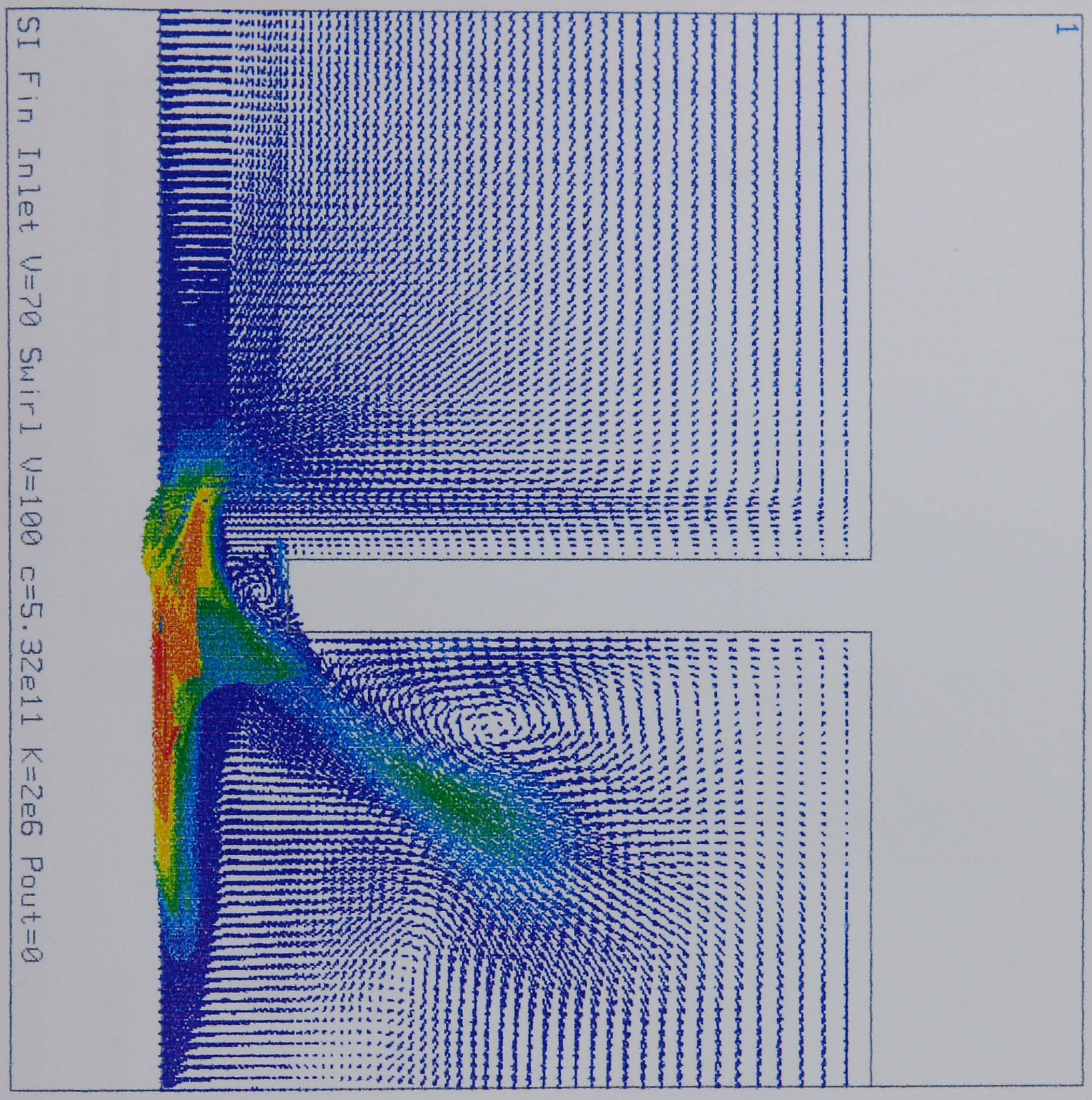

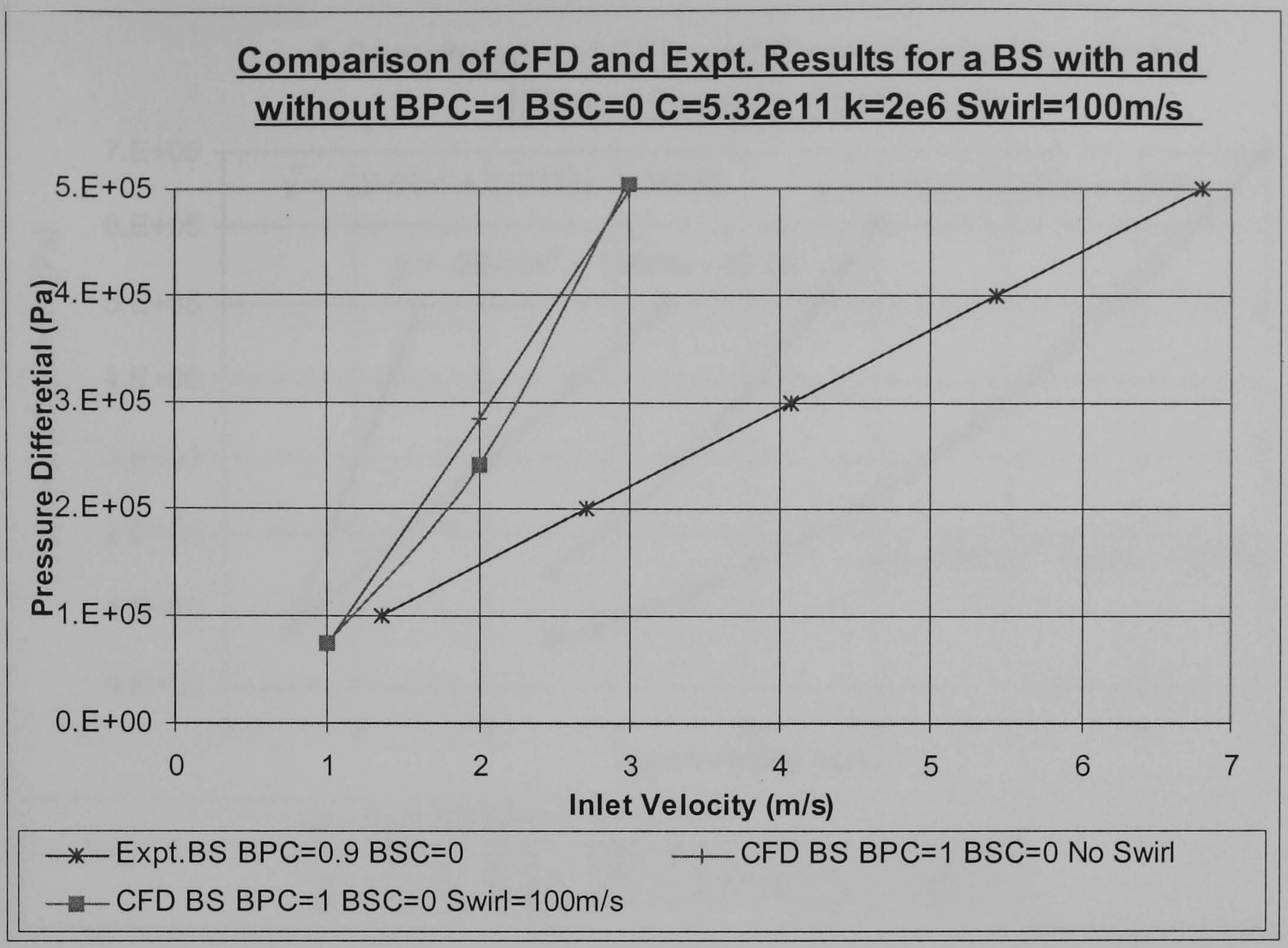

Figure 10.22 A comparison of CFD and experimental leakage results for a brush seal with and without swirl BPC=1 mm, BSC=0 mm.

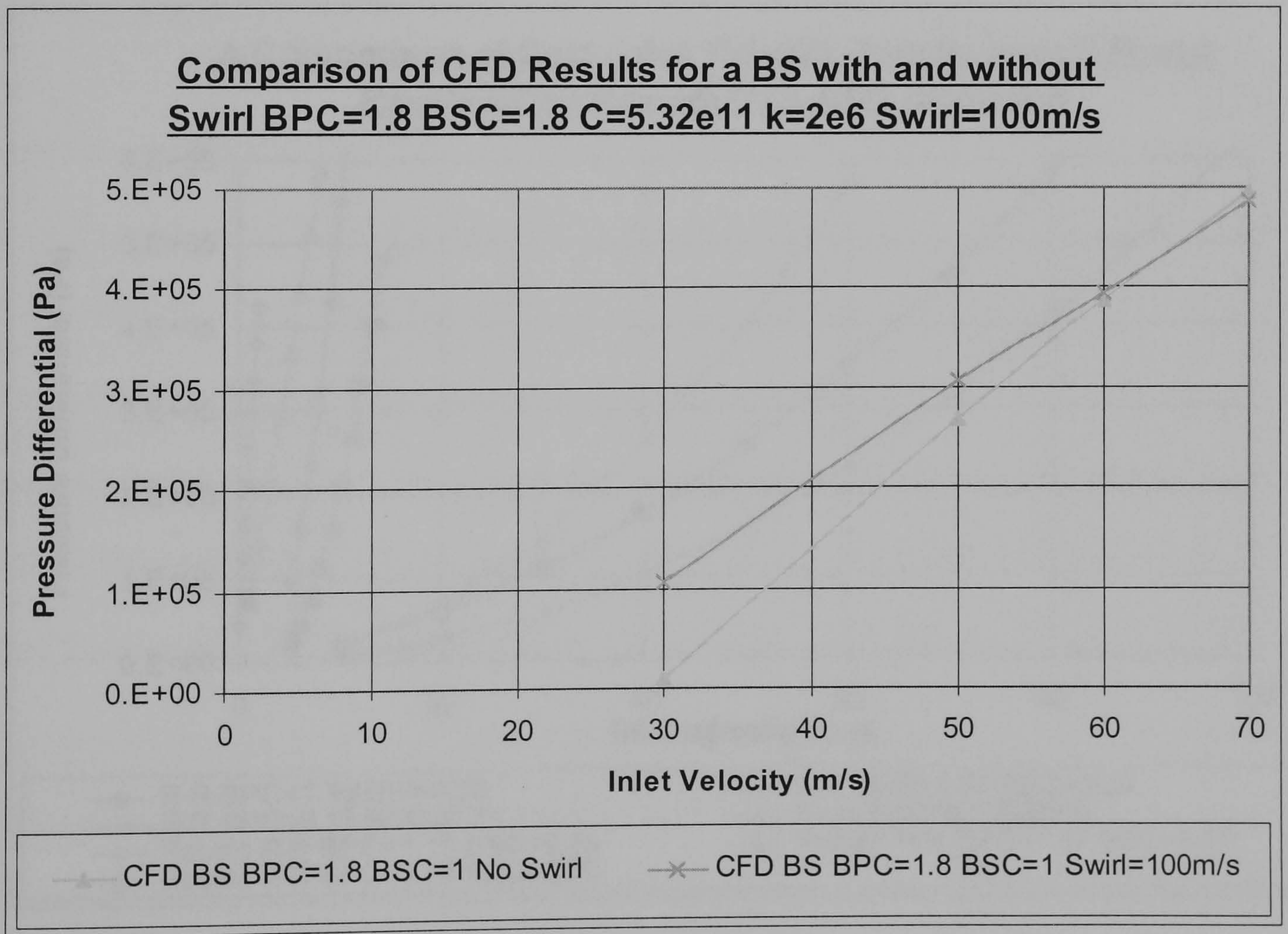

Figure 10.23 A comparison of CFD leakage results for a brush seal with and without swirl BPC=1.8 mm, BSC=1 mm.

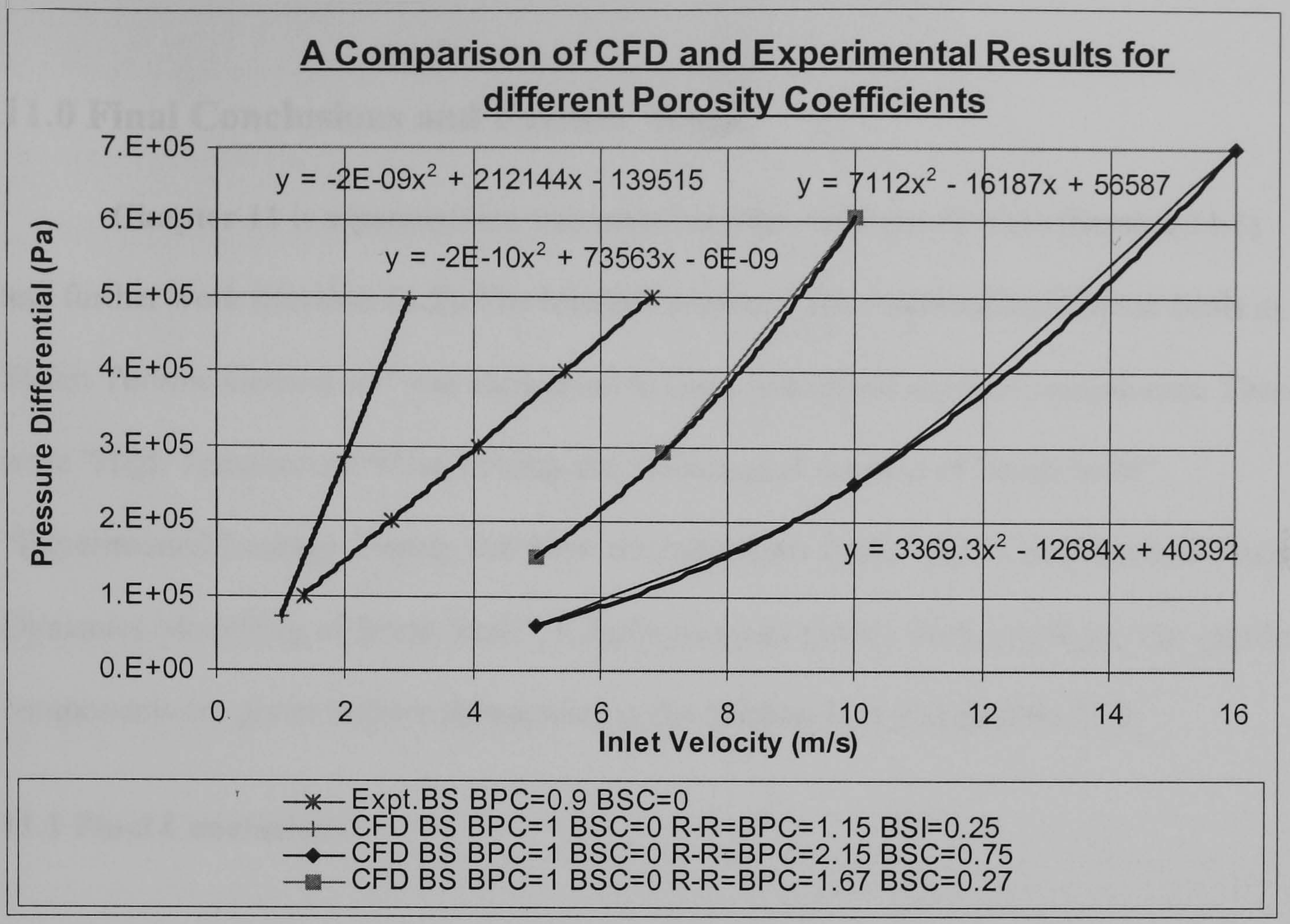

Figure 10.24 A comparison of CFD and experimental leakage results for different porosity coefficients BPC=1 mm, BSC=0 mm.

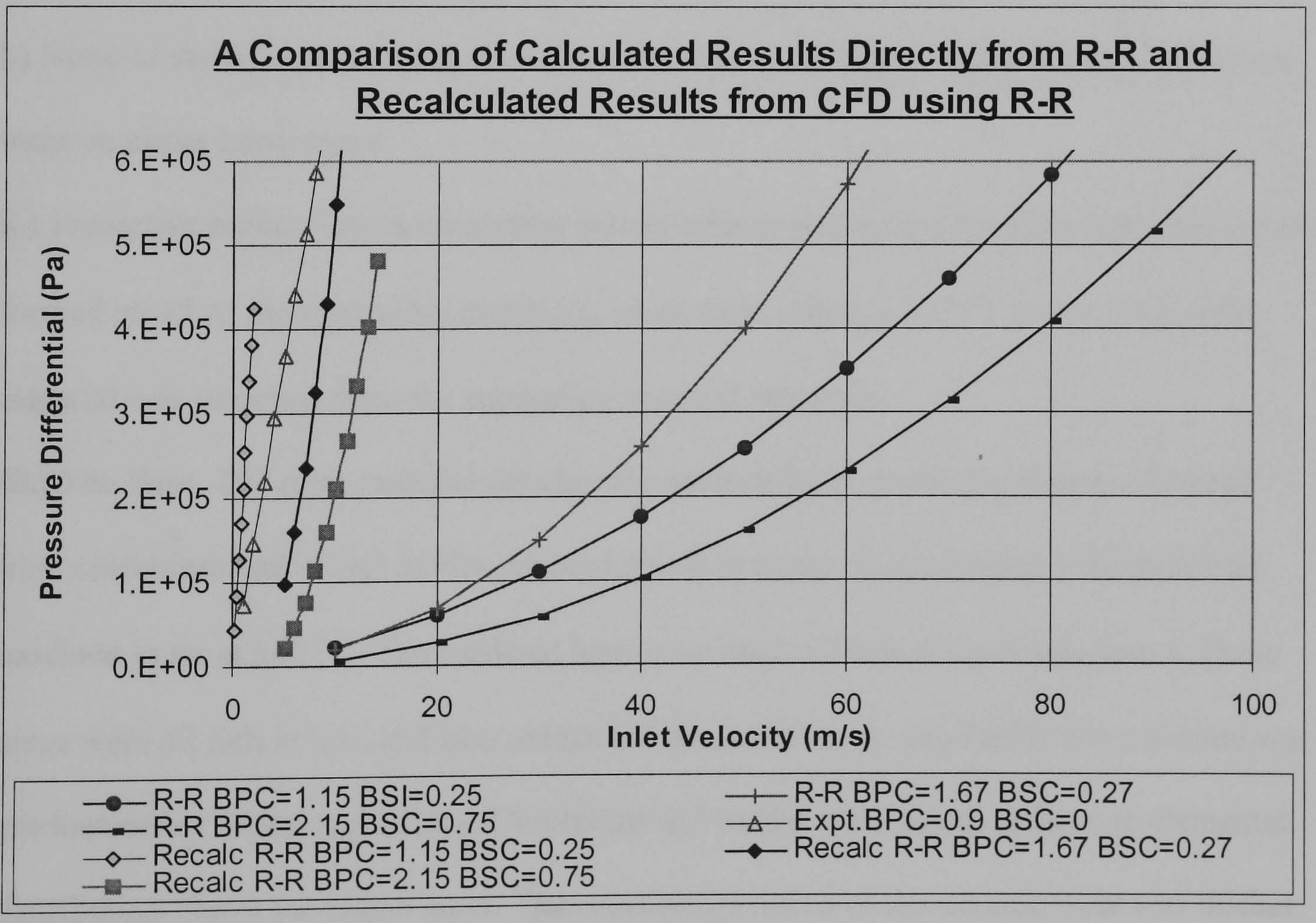

Figure 10.25 Comparison of calculated leakage results directly from Chew et al and recalculated results from CFD using Chew et al coefficients.

11.0 Final Conclusions and Further Work.

Chapter 11 is separated into two main sections, final conclusions **(Section 11.1)** and further work **(Section 11.2).** The research project, "The Application of Brush Seals in Steam Turbine Generators" was carried out in three related but separate components. These were "High Temperature Wear Testing and Tribological Aspects of Brush Seals", "Experimental Leakage Testing and Flow through Brush Seals" and "Computational Fluid Dynamics Modelling of Brush Seals". Conclusions and further work relating to the specific components are given in three subsections under **Section 11.1** and **Section 11.2.**

11.1 Final Conclusions.

11.1.1 High Temperature Wear Testing and Tribological Aspects of Brush Seals: - Conclusions.

i.) None of the tribopairs tested were found to initiate substrate cracks or exhibited severe wear on either component.

ii.) Protective surface layers consisting mainly of iron and oxides from the test wheels were formed on all of the superalloy materials, when wear tested at 540 °C in air. Very little material was removed from the superalloy material substrate.

iii.) The Spec. 297 rotor material developed a surface layer consisting mainly of mixed iron, chromium and nickel oxides when exposed to wear test conditions or when it was oxidised in air at 540 °C. The oxidised layer consisted of three distinct sub-layers. These areas were all rich in iron and iron oxides but the lower layer, attached to the substrate was predominately nickel and oxides. Chromium and oxides were found to have an elemental distribution above the nickel layer. The remaining portion of the surface layer was thicker and consisted of iron and iron oxides (with very little other elemental density). Very little bristle candidate material was found in any of the surface layers.

iv.) The weight change for all of the superalloy candidate materials was very small due to the wear resistance of the glaze layer.

v.) Weight change of the sample materials as a whole appeared to be largely independent of pre-test surface hardness. However, within superalloy base material groups there was a general trend towards decreased weight loss with increase in pre-test hardness.

vi.) Weight change in these high temperature wear tests was thought to offer a reasonable indication of pre-glaze wear resistance.

vii.) Nickel base age hardening and cobalt base materials generally lost less weight (or gained weight due to material transfer from the test wheel) than either nickel base solution hardened or iron base materials.

viii.) Combining the wear test results with gas turbine service experience it would appear that none of the superalloy materials performed significantly better in terms of their overall tribological properties (material transfer/wear resistance) compared to Haynes 25. It is therefore recommended that Haynes 25 be selected as a bristle material for initial applications of brush seals for high pressure steam turbines. However, rotor wear must be monitored carefully.

iv.) Rotor wear was very small and was not quantified.

11.1.2 Experimental Leakage Testing and Flow through Brush Seals: - Conclusions.

i.) The leakage through a single thickness brush seal, which had a backing ring bore which was 1.8 mm larger than the bristle bore, when installed with a bristle interference (of less than 0.5 mm), was approximately 5 % of the leakage through a single fin labyrinth seal which had a similar fin bore to that of the brush seal's backing ring.

ii.) The leakage through a double thickness brush seal, which had a backing ring bore which was 1.8 mm larger than the bristle bore, when installed with a bristle interference (of less than 0.5 mm), was approximately 3 % of the leakage through a single fin labyrinth seal which had a similar fin bore to that of the brush seal's backing ring.

iii.) Both single and double thickness brush seals operated quite satisfactorily over the period of the test programme at pressure differentials of up to 6.0 bar, with backing ring clearances of up to 0.9 mm.

iv.) The leakage through brush and labyrinth seals was not significantly affected by the test rig's journal rotation (apart from the eccentric rotor brush seal tests).

v.) The effect of an offset rotor on leakage through the brush seals only became significant when an installed bristle clearance or interference was exceeded.

vi.) The effect of an eccentric rotor rotating at 0 to 3000 r.p.m., was to increase the leakage rate for installed interferences and size for size fits. The effect became less significant when there was an installed seal clearance and the percentage flow through the bristle pack was reduced. Eccentricity did tend to reduce hysteresis in the case of an installed stationary clearance compared to the similar rotating case.

vii.) Brush seals, when installed with an interference, were sensitive to contamination; in the test programme their leakage characteristics were enhanced by a factor of six when they became choked with oil i.e. they became better seals. When installed with a clearance, the total seal leakage through and under the seal, was unaffected by the oil. This implied that when there was a seal clearance, the bristle pack acted as an effective labyrinth fin even without oil contamination.

viii.) Vibrational dynamic characteristics of the rig were not affected by a contacting brush seal with an applied pressure differential of up to 4.0 bar (60 p.s.i.). However the main shaft was supported on ball bearings as opposed to the white-metal bearings a HP steam turbine shaft would be mounted on.

ix.) Hysteresis in the leakage rate versus pressure differential curve was noted due to bristle "blow down", and inter-bristle friction locking the pack in that position. The bristles remained locked until the pressure differential was removed. The leakage rate was lower on initial pressure increase compared to the pressure decrease.

x.) Leakage through (as opposed to under) the brush seal bristle pack only appeared to be significant when there was an installed interference or small clearance that would be removed by bristle "blow down", and the pack effectively acted as a labyrinth fin with the "blown down" clearance.

11.1.3 Computational Fluid Dynamics Modelling of Brush Seals: - Conclusions.

i.) FLOTRAN was successfully used to model bristle packing patterns, backing plates and brush seals, using a porous media/distributed resistance and gave a useful insight into the flow patterns within all the models under different conditions.

ii.) Porosity coefficients, calculated from the results of the Bristle Packing Pattern Model, produced poor results when they were used in the Porous Media Model. The results obtained were very low compared to the experimental results.

iii.) Porosity coefficients used in the brush seal **CFD** modelling were only valid for each specific seal geometry, **BPC** and **BSC** (and possibly the specific **CFD** package) due to the changing operation of the seal under different conditions and the relatively simple theory that described the porous media.

iv.) FLOTRAN tended to overestimate the sealing capacity of labyrinth seals compared to experimental data by as much as 50 %.

v.) The geometry of the backing plate tip had a significant effect on the flow patterns produced from the **Backing Plate Model** and the **Porous Media Model** when the bristles were modelled to touch the rotor.

vi.) When **Porous Media Models** were generated where there was a clearance between the area of porous media and the rotor almost all of the flow went through the clearance below the porous media. The area of porous media effectively acted as a square edged labyrinth seal and the flow patterns were controlled by the tip geometry. In real brush seals the bulk of the flow may also travel through the clearance but the controlling fin tip geometry would not be square edged and would not have a constant geometry or clearance.

vii.) Plots of theoretical pressure differential against inlet velocity using **Forchiemer's Law** indicated that the **Chew et al** coefficients would underestimate the results by 70 to 80 % compared to the experimental porosity coefficients when using the nearest geometry available.

viii.) Porosity coefficients (re)calculated using a single iterative process produced results that were closer to the experimental results, but were as much as 40 % too high.

11.2 Further Work.

11.2.1 High Temperature Wear Testing and Tribological Aspects of Brush Seals: - Further Work.

i.) High temperature wear tests with bristle tufts or full brush seals under increased sliding velocities and longer durations, should ideally be carried out with new rotor sleeves that can be sectioned. This will help to determine the effect on the wear rate of sample surface geometry and sliding velocity.

ii.) Long term wear assessment should be carried out with real brush seals under real steam turbine conditions. This is most feasible by installing a brush seal in tandem with a labyrinth seal and including instrumentation to allow monitoring of the seal performance at regular intervals. A quantitative seal and rotor wear rate should be determined. The wear rate can only be determined accurately by the installation of brush seals into a steam turbine or a very expensive test rig replicating the conditions in a steam turbine more closely.

11.2.2 Experimental Leakage Testing and Flow through Brush Seals: - Further Work.

i.) Further experimental leakage tests could be carried out to explore the characteristics of split segmental seals that would be suitable for installation in a steam turbine.

ii.) Experimental leakage tests could also be carried out with a brush seal adjacent to a discontinuous rotor surface (similar to blade shrouds) to determine the suitability of installation as a cylinder-to-rotating blade tip seal in steam turbines.

11.2.3 Computational Fluid Dynamics Modelling of Brush Seals: - Further Work.

i.) FLOTRAN should again be used to repeat the process of modelling using the Porous Media/Distributed Resistance Model, with geometries that correspond to other configurations tested in the **BSLTR. FLOTRAN** porosity coefficients should then be calculated.

ii.) The calculated porosity coefficients could then be used to model geometries similar to other published experimental brush seal leakage results. This process could be used to assess the validity or universal applicability of the calculated porosity coefficients to experimentally tested designs. Once a number of porosity coefficients are calculated for a range of installed interferences and clearances, design curves could be plotted to enable the selection of porosity values for previously untested brush seal designs.

iii.) Repeat modelling with and without rotating walls could be used to further investigate the effect of swirl on sealing.

References.

Akagaki, T., Rigney, D.A. (1991) Sliding Friction and Wear of Metals in Vaccum. Wear 149, p 353-374

Annual Report of the University of Oxford Technology Centre in Heat Transfer and Aerodynamics (1993)

Antonopoulos, K.A., Gosman, A.D. (1986) The Prediction of Laminar Inclined Flow Through Tube Banks. Computers and Fluids VOL 14, NO 2. 0045-7930/86

Archard, J.F. (1953) Contact and Rubbing of Flat Surfaces. Journal of Applied Physics. VOL 24, Number 8, pp 981-988

Archard, J.F. (1961) Single Contacts of Mutiple Encounters. Journal of Applied Physics. Vol 32, Part 8, pp 1420-1425

Archard, J.F. (1985) Friction Between Metal Surfaces. Wear

Archard, J.F., Rowntree, R.A. (1988) The Temperature of Rubbing Bodies: Part 2, The Distribution of Temperatures Wear, 126

Atkinson, E. (1991) Effects of Material Choices on Brush Seal Performance. Lubrication Engineering, 46th Annual Meeting , Montreal, Quebec, Canada, April 29-May 2, 1991

Barnes, D.J., Stott, F.H., Wood, G.C. (1977) The Frictional Behaviour of Iron and Iron - Chromium Alloys at Elevated Temperatures. Wear, Jan 12

Barnes, D.J., Wilson, J.E., Stott, F.H., Wood, G.C. (1977) The Influence of Specimen Geometry and Sliding Mode on the Friction and Wear of Iron - Chromium Alloys in Controlled Environments. Wear 45, p. 97-111

Barnes, D.J., Wilson, J.E., Stott, F.H., Wood, G.C. (1977) The Influence of Oxide Films on the Friction and Wear of Fe-5% Cr Alloy in Controlled Environments. Wear 45, p. 161-176

Basu, P., Datta, A., Johnson, R., Loewenthal, R., and Short, J. (1993) Hysteresis and Bristle Stiffening Effects of Conventional Brush Seals. AIAA Paper NO. 93-1996, Fluid Components Technology Group R&D, Cranston, Rhode Island.

Batchelor, A.W., Stachowiak, G.W., Cameron, A. (1996) The Relationship Between Oxide Films and the Wear of Steels. Wear, 113 p 203-223

Rigney, D.A. (1994) The Roles of Hardness in the Sliding Behaviour of Materials. Wear, 175 p 63-69

Batchelor, G.K. (1967/1990) An Introduction to Fluid Dynamics. Cambridge University Press, ISBN 0 521 09817 3

Mark's Standard Handbook for Mechanical Engineers. Baumeister, T. (1978) p 9/46

Bayley, F.J., and Long, C.A. (1992) A Combined Experimental and Theoretical Study of Flow and Pressure Distributions in a Brush Seal. Thermo-Fluid Mechanics Research Centre, Sussex.

Beevers, G.S., Sparrow, E.M., (1969) Non-Darcy Flow Through Fibrous Media. ASME Journal of Applied Mechanics, p 711-714

Bergelin, O.P., Brown, G.A., Hull, H.L.,Sullivan, F.W. (1950) Heat Transfer and Fluid Friction During Viscous Flow Across Banks of Tubes.-III A Study of Tube Spacing and Tube Size. Transactions of the ASME, p 181- 188 August

Bhansali, K.J. (1979) Adhesive Wear of Nickel and Cobalt Base Alloys. Stellite Division, Cabot Corporation, Kokomo, Indiana, (U.S.A.), Wear, 60 p 95-110, April

Bhansali, K.J., Miller, A.E. (1982) The Role of Fault Energy on Galling and Wear Behaviour. Wear 75, p 241-252

Bian, S., Maj, S., Borland, D.W (1993) The Unlubricated Sliding Wear of Steels: The role of the Hardness of the Friction Pair. Wear, 166 p 1-5

Bill, R.C. (1979) Wear of Seal Materials in Aircraft Propulsion Systems. Propulsion Laboratory, Avradcom Research and Technology Laboratories, Lewis, Wear, June

Bisson, E.E. (1969) Various Modes of Wear and Their Controlling Factors. ASTM STP 446, p 1-22

Boucher, D.F., Lapple, C.E. (1948) Pressure Drop Across Tube Banks. Chemical Engineering Progress, Vol 44, Part 2, p 117-134.

Superalloys - A Technical Guide. Bradley, E.F., p 163-183

Braun, M.J. (1988) Digital Image Processing for Quantification through Full Flow Field tracing (FFFT) in Narrow Geometries at Low Reynolds Numbers. Proc. 1ST Fluid Dynamics Congress AIAA / ASME / SIAM , Cincinnati

Braun, M.J., and Hendricks, R.C. (1990) Flow Visualisation and Motion Analysis for a Series of Four Sequential Brush Seals. , AIAA-90-2482, NASA, Cleveland, OHIO.

Braun, M.J., Canacci, V.A., Hendricks, R.C., (1990) Flow Visualisation and Quantitative Velocity and Pressure Measurements in a Simulated Single and Double Brush Seals. 90-AM-7F-2, 45TH Annaual Meeting in Denver , Colerado., University of Akron, NASA Lewis Research Center, Cleavland, OHIO, May 7-10

Braun, M.J., Canacci, V.A., Russell, L.M. (1992) Full Field Flow Visualisation and Computer - Aided Velocity Measurements in a Bank of Cylinders in a Wind Tunnel. Experiments in Fluids 13, 117-127

Braun, M.J., Kudriavtsev, V.V. (1993) A Numerical Simulation of a Brush Seal Section and Some Experimental Results. 93-GT-398, Presented at the International Gas Turbine and Aeroengine Congress and Exposition. Cincinnati, Ohio. May 24-27

Braun, M.J.,Dzodzo, M.,Canacci, V.A.,Lattime, S.B. (1993) Qualitative and Quantitative Non-Intrusive Study of Flow Patterns, Velocities and Pressure Effects in Banks of Cylindrical Tubes in a Rectangular Tunnel. SPIE VOL.2052 Laser Anemometry Advances and Applications. University of Akron, Department of Mech Eng, OHIO 44325, USA

Braun,M.J., Hendricks,R.C., Canacci,V.A. (1990) Flow Visualisation in a Simulated Brush Seal. ASME 90-GT-217, NASA, Cleveland, OHIO, Proceedings of the Gas Turbine and Aeroengine Congress and Exposition, Brussels Belgium, June 11-14

Braun,M.J., Hendricks,R.C., Canacci,V.A. (1990) Non-Intrusive Qualitative and Quantitative Flow Characterisation and Bulk Flow Model for Brush Seals. NASA, Cleveland, OHIO, Proceedings of the Japan International Tribology Conference, Nagoya

Broniarek, C.A. (1981) Damping Characteristics of Solid Brush Current Collection Systems. Wear, Mech. Eng. Dept., Tuskegee Institute, Sept

Brush Seals of Ceramic Material for Thermal Turbomachines., United States Patent, No. 4,809,990

Buckley, D.H. (1968) Adhesion, Friction and Wear of Cobalt and Cobalt-Base Alloys. Cobalt, Part 38 p 20-28

Buckley, D.H., Johnson, R.L. (1960) The Influence of Silicon Additions on Friction and Wear of Nickel Alloys at Temperatures to 1000 F. A.S.L.E. Trans, Vol 3 Part 93 p 93-100

Carlile, J.A., Hendricks, R.C., and Yoder, D.A.(1993) Brush Seal Leakage Performance with Gaseous Working Fluids at Static and Low Rotor Speed Conditions. Journal of Engineering for Gas Turbines and Power. April, Vol. 115, p.397-403.

Challen, J.M., Oxley, P.L.B. (1986) Prediction of Archard's Wear Coefficient for Metallic Sliding Friction Assuming a Low Cycle. Fatigue Wear Mechanism. Wear,111 p 275-288

Chen, L.H., Rigney, D.A. (1990) Adhesion Theories of Transfer and Wear During Sliding of Metals. Wear, 136 p 223-235

Chew, J.W., Lapworth ,. B.L., Millener, P.J., (1995) Mathematical Modelling of Brush Seals. Int.J.Heat and Fuid Flow, Vol 16, p 493-500

Chew, J.W., Hogg, S.I. (1997) Porosity Modelling of Brush Seals. Journal of Tribology, Vol 119, July

Chilton, T.H., Genereaux, R.P. (1933) Pressure Drop Across Tube Banks. Trans. Am. Inst. Chem. Engrs., Vol 29, p 161-173

Chupp, R.E., and Dowler, C.A. (1991) Performance Characteristics of Brush Seals for Limited Life Engines. ASME Paper 91-GT-281., Teledyne CAE, Toledo, OHIO.
Chupp, R.E., Holle, G.F. (1994) Generalizing Circular Brush Seal Leakage Through a Randomly Distributed Bed. A.S.M.E. 94-GT-71, Presented at the International Gas Turbine and Aeroengine Congress and Exposition, The Hague, Netherlands, June 13-16
Chupp, R.E., Holle,G.F., Dowler, C.A. (1991) Simple Leakage Model for Brush Seals. AIAA Paper 91-1913., Teledyne CAE, Toledo, Oh.
Chupp, R.E., Johnson, R.P., Loewenthal, R.G. (1995), Brush Seal Development for Large Industrial Gas Turbines. AIAA 95-3146, 30th AIAA/ASME/SAE/ASEE Joint Propulsion Conference.and Exhibit., San Diego, CA., July 10-12
Chupp, R.E., Nelson, P. (1990) Evaluation of Brush Seals for Limited-Life Engines. AIAA Paper 90-2140, Teledyne CAE, Toledo, Ohio.
Collins, R.E. (1961) Flow of Fluids Through Porous Materials. Reinhold Chemical Engineering Series, Reinhold Publishing Corporation, New York, Chapman and Hall, Ltd., London
Conner, K.J. (1990) Rotordynamic and Leakage Characteristics of a 4 - Stage Brush Seal. Texas A and M Univ College Station Turbomachinery Labs, Dec.
Conner, K.J., Childs, D. (1990) Rotordynamic Coefficient Test Results for a 4 - Stage Brush Seal. AIAA 26TH Joint Propulsion Conference, Orlando, Florida, July
Connor, J.J., Brebbia, C.A. (1976) Finite Element Techniques for Fluid Flow. Newnes-Butterworths
Derby, J., England, R. (1992) Tribopair Evaluation of Brush Seal Applications. AIAA 92-3715, EG&G, FCTG, Cranston, Rhode Island, July
Desai (1975) Finite Elements in Fluids
Dollin, F., Brown, W.S. (1937) Flow of Fluids Through Openings in Series. The Engineer, Aug.
Dowler, C.A., Chupp, R.E., and Holle, G.F. (1992) Simple Effective Thickness Model for Circular Brush Seals. AIAA Paper 92-3192, Aero-Propulsion & Power Directorate, Wright - Patterson Air Force Base, OH.
Earles, S.W.E. and Tenwick, N. (1972) Friction and Wear Properties of Nimonic 75 at Ambient Temperatures up to 810 C. Wear Vol 19, p287-299
Braun,M., Hendricks,R., Yang,Y. (1991) Effects of Brush Seal Morphology on Leakage and Pressure Drops. AIAA-91-2106, University of Akron & NASA Lewis Research Centre, 27TH Joint Propulsion Conference, Sacramento, CA, June 24-26
Egli, A.The Leakage of Steam Through Labyrinth Seals. FSP-57.5, Philadelphia, P.A
Ergun,S.(1952) Fluid Flow through Packed Columns. Chemical Engineering Progress VOL.48, NO2., Carnegie Institute of Technology, Pittsburgh, Pennsylvania
Ferguson, J.G. (1988) Brushes as High Performance Gas Turbine Seals. ASME Paper 88-GT-182, Rolls-Royce PLC, Bristol
Flower, R. (1992) United States Patent "Brush Seals" Patent No. 5,090,710, Feb 25th
Flower., R. (1990) Brush Seal Development System. AIAA-90-2143, Cross Manufacturing Co. Ltd., Wiltshire, England.
Foley, R.T., Peterson, M.B. and Zapf, C. (1963) Frictional Characteristics of Cobalt, Nickel and Iron as Influenced by their Surface Oxide Films. Trans ASLE, Vol 6, p 29
Fornberg, F., (1980) A Numerical Study of Steady Viscous Flow past a Circular Cylinder. Jounal of Fluid Mechanics, Vol 98 Part 4, p 819-855
Gaft, V.A.Z., Krivonogov, V.G., Petushkov, V.A. (1989) Investigation into the Mechanism of Sealing in Shaft Stuffing Boxes. Wear, 132 p 39-48
Gallagher, R.H., Oden, J.T.,m Taylor, C., Zienkiewicz, O.C. (1975) Finite Elements in Fluids. Volume 1 Viscous Flow and Hydrodynamics, John Wiley and Sons, ISBN 0 471 29045 9
Ganesan, P., Smith, G.D. (1988) Oxide Scale Formation on Selected Candidate Combustor Alloys in Simulated Gas Turbine Environments. J.Material. Eng. Vol 9, No.4, 9:337-343
Gardner, J., Basu,P., Datta, A. (1992) A New Compliant Seal Concept for Aerospace Applications. Rotating Machinery 1992, Proceedings of the 4th International Symposium on Transport Phenomena and Dynamics of Rotating Machinery, EG&G FCTG R&D
Gee, M.G. (1993) NPL Report DMM(A)96. Guidelines for Unlubricated Sliding Wear Tests: Part 1. General Approach. April
Grimison, E.D. Correlation and Utilization of New Data on Flow Resistance and Heat Transfer for Cross Flow of Gases Over Tube Banks. Transactions of the ASME. PRO-59-8, p 583-594.
Gross, D. Estimated Air Leakage through Doors for Smoke Control. Journal of Fire Technology Vol 26, ISSN/ISBN 0015-2684
Gunter, A.Y., Shaw, W.A. (1945) A General Correlation of Friction Factors for Various Types of Surfaces in Crossflow. Transactions of the ASME. p. 634-670, November
Haworth, R.D., Jr (1949) The Abrasion Resistance of Metals. Trans ASM, Vol 41 p. 819-869
Hawthorne, H.M. (1993) Brush-on-Disk Simulation Tribotesting of Materials for Gas Turbine Compliant Seal Components. Tribology International, 9th Sept
Hendricks, R.C., Carlile, J.A., Yoder, D., Braun, M.J. (1992) Investigation of Flows in Bristle and Fibreglass Brush Seal Configurations. NASA, Lewis Research Centre, Cleveland OH 44135, U.S.A., Rotating Machinery 1992, Proceeding of the 4th International Symposium on Transport Phenomena and Dynamics of Rotating Machinery.
Hendricks, R.C., Griffin, T.A., Bobula, G.A., Bill, R.C. (1993) Integrity Testing of Brush Seal in Shroud Ring of T-700 Engine. ASME 93-GT-373, International Gas Turbine and Aeroengine Congress and E. Cincinnati, Ohio. May 24-27
Hendricks, R.C., Liang, A.D., Proctor, M.P (1992) Development of Advanced Seals for Space Propulsion Turbomachinery. 921028, NASA Lewis Research Centre
Hendricks, R.C., Proctor, M.P., Schlumberger, J.A., Braun, M.J., and Mullen R.L. (1991) Some Preliminary Results of Brush Seal/Rotor Interference Effects on Zero Leakage at Zero and Low RPM using a Tapered Plug Rotor. AIAA-91-3390-CP, NASA, Cleveland, OHIO, University of Akron, OHIO, Case Western Reserve University, Presented at the International Gas Turbine Aeroengine Congress and Exposition, Orlando, June3-6
Hendricks, R.C., Schlumberger,S., Braun, M.J., Choy, F., Mullen, R.L. (1991) Bulk Flow Model of a Brush Seal System. ASME 91-GT-325, NASA Cleveland, Ohio.
Hersh, A.S, Walker, B., (1980) Acoustical Behaviour of Homogeneous Bulk Materials. AIAA-80-0986, AIAA 6th Aeroacoutics Conference, Hartford, Connecticut, June 4-6
Hicks, B. (1987) High Temperature Sheet Materials for Gas Turbine Applications. Materials Science and Technology Vol.3, Sept
Hinsley, C.F., Male, A.T. and Rose, W.G. (1968) Frictional Properties of Metal Oxides at High Temperatures. Wear Vol 11, p.173
Hodkinson, B. (1940) Discussion (Labyrinth Seals). Proc. IMechE, Vol. 142, p 459-467
Holle, G.F., Chupp, R.E., Dowler, C.A. (1992) Brush Seal Leakage Correlations Based on Effective Thickness. Rotating Machinery 1992, Proc. of the 4th Int. Symp. on Transport Phenomena and Dynamics of Rotating Machinery.
Holle, G.F., Krishnan, M.R. (1990) Gas Turbine Engine Brush Sea Applications. AIAA 90-2142, GMC, Indiana.

Holle, G.F., Krishnan, M.R. (1990) Gas Turbine Engine Brush Sea Applications. AIAA 90-2142, GMC, Indiana.
Huge, E.C. Experimental Investigation of Effects of Equipment Size on Convection Heat Transfer and Flow. Resistance in Cross Flow of Gases Over Tube Banks. Transactions of the ASME, PRO-59-7, p.573-582
Hwang, M.F., Pope, A.(1995) Advanced Seals for Engine Secondary FlowPath. AIAA-95-2618, 30th AIAA/ASME/SAE/ASEE Joint Propulsion Conference.and Exhibit, San Diego, CA., July 10-12
INCO ALLOYS INTERNATIONAL (1993) Product Handbook
Jiaren Jiang, Stott, F.H., Stack, M.M. (1994) Some Frictonal Features Associated With the Sliding Wear of the Nickel Base Alloy N80A at Temperatures to 250 C. Wear 176, p 185-194
Joeseph, D.D., Nield, D.A., Papanicolaou, G. (1982) Non-Linear Equation Governing Flow in a Porous Medium. Water Resources Research, Vol 18, Part 4, p. 1049-1052
Johnson, M.P., Moorhouse, P., Nicholls, J.R. (1990) Hot Wear Tests on Candidate Materials. Diesel Engine Combustion Chamber Materials for Heavy Fuel Operation., DTI Industry Valve Project
Jones,D.P., Krier, H. (1983) Gas Flow Resistance Measurements Though Packed Beds at High Reynolds Numbers. Transactions of the ASME, Vol 105, p. 168-173, June
Karamis, M.B., Odabas, D. (1991) A Simple Approach to Calculation of the Sliding Wear Coefficient for Medium Carbon Steels. Wear, 151, p. 23-34
Kawamura, .T., Takami, H., Kuwahara, K., (1986) Computation of High reynold Number Flow around Circular Cylinder, Fluid Dynamics Research. Vol 1, p. 145-162
Kearton, W.J. (1926) Turbo-Blowers and Compressors. Sir Isaac Pitman and Sons Ltd.
Kearton, W.J. (1955) The Flow of Air Through Radial Labyrinth Glands. Proc. Inst. Mech. Eng., Vol.169, Part 30, p.539 - 550
Kearton, W.J., Keh, T.H. (1952) Leakage of Air Through Labyrinth Glands of Staggered Type. Proc. Inst. Mech. Eng., Vol. 166, p.180-195
Kingsbury, E.P., Rabinowicz, E. (1959) Friction and Wear of Metals to 1000 C. Trans Am Soc Mech Eng., Vol 81, No2, p. 118
Knudson, J.G., Katz, D.L. (1958) Fluid Dynamics and Heat Transfer. McGraw-Hill Series in Chemical Engineering
Krause, H., Senuma, T. (1981) A Contribution Towards Improving the Applicability of Laboratory Wear Tests to Practice. Wear 74, p. 67-83
Li, J., Sun, J., Roux, B., (1992) Numerical Study of Oscilllating Cylinder in Uniform Flow and in the Wake of an Instream Cylinder. Journal of Fluid Mechanics. Vol 273, p. 457-478
Lin, D.S. (1969) The Effect of the Degree of Work Hardening on the Friction and Wear of Metals During Abrasion. Wear 13, p. 91-97
Lin, D.S., Stott, F.H., Wood, G.C., Wright, K.W., Allen, J.H. (1973) The Friction and Wear Behaviour of Nickel Base Alloys in Air at Room Temperature. Wear, 24 p. 261-278
Lipets, A.U., Lafa, Yu I. (1965) Aerodynamic Resistance of Close Packed Staggered Tube Bundles. Thermal Engineering, Vol. 12, Part 6, p. 38-41.
Lokshin, V.A., Fomina, V.N. (1971) Investigation of the Aerodynamic Drag of Staggered Cross-Flow Tube Bundles. Thermal Engineering, Vol. 18, Part 7, p. 77-80
Ludwig, L.P. (1978) Gas Path Sealing in Turbine Engines. NASA TM-73890, Lewis Research Centre, Cleaveland OHIO
Lupton, W.H., Reichner, P. (1981) Ultra High Fiber Brush Design and Tests. Wear, U.S. Navel Research Laboratory, Washington, D.C., Sept
Mahler, F., Boyes, E. (1995) The Application of Brush Seals in Large Commercial Jet Engines. United Technologies Corporation. Pratt and Whitney., AIAA-95-2617, 30th AIAA/ASME/SAE/ASEE Joint Propulsion Conference.and Exhibit., San Diego, CA., July 10-12
Martin, H.M. (1913) The Design and Construction Of Steam Turbines. Chapter XVIII
Massey, B.S. (1968) Mechanics of Fluids. Sixth Edition, Von Nostrand Reinhold (International), ISBN 0-278-00047-9
Meyer, C.A., Lowrie, J.A. (1974) The Leakage Through Straight and Slant Labyrinths and Honeycomb Seals. ASME 74 -WA / PTC - 2, Dec
Mohandes, M.A., Jones, T.V., Russell,C.M.B. (1984) Pressure Loss Mechanism in Resistances Inclined to an Air Flow With Application to Fintubes. 1st National Heat Transfer Conference Leeds.
Mokhtar, M.O.A. (1982) The Effect of Hardness on the Frictional Behaviour of Metals. Wear 78, p. 297-304
Morrow, J. (1910) On the Theory of Labyrinth Packing. Proc.University of Durham Phil Soc., Vol 3, p. 281-285
Moult, DR. E. S (1975) Seals for Rotating Shafts. Engineering.
Mullen, R.L., Braun, M.J., and Hendricks, R.C. (1990) Numerical Modelling of Flows in Simulated Brush Seal Configurations. AIAA-90-2141, NASA, Cleveland, OHIO.
Munson, J., Steinetz, B. (1994) Specific Fuel Consumption and Increased Thrust Performance Benefits Possible with Advanced Seal Technology. AIAA 94-2700, 30th AIAA/ASME/SAE/ASEE Joint Propulsion Conference, Indianapolis, IN. June 27-29
Nighingale, A.F (1975) Teaching Tribology to Undergraduate Engineers, Basic Tribology Module. Jan
Ninham, A. (1980) The Effect of Mechanical Properties on Erosion. Wear
Ohnuki, A. (1985) Friction and Wear of Metals at High Temperature. Trans JSLE, Vol 30, Part 5, p. 329-334
Ohya, Y., Nakamura, Y., Ozono, S., Tsuruta, H., Nakayama, A Numerical Study of Vortex Shedding from Flat Plates with Square Leading Edges. J. Fluid Mech.,Vol 263, p. 445-460
Omohundro, G.A., Bergelin, O.P., Colburn,. A.P. (1949) Heat Transfer and Fluid Friction During Viscous Flow Across Banks of Tubes. Transactions of the ASME, p. 27-34., January.
Patankar, S.V., Lui,C.H., Sparrow, E.M. (1977) Fully Developed Flow and Heat Transfer in Ducts Having Streamwise-Periodic variations of Cross-Sectional Area. Journal of Heat Transfer, Vol 99, p.180-186
Perry, J.A.Jr (1949) Critical Flow Through Sharp Edged Orifices. Trans. ASME, Vol 71, p. 757-764
Peterson, M.B., Florek, J.J. and Lee, R.E. (1960) Sliding Characteristics of Metals at High Temperatures. Trans ASLE, Vol 3, No1, p. 101-109

Pierson, O, L. Experimental Investigation of the Influence of Tube Arrangement on Convection Heat Transfer and Flow Resistance in Cross Flow of Gases Over Tube Banks. Transactions of the ASME., PRO-59-6, p. 563-572.
Quinn, T.F.J. (1984) The Role of Wear in the Failure of Common Tribosystems. Wear 100, p. 399-436
Quinn, T.F.J. (1994) Oxidational Wear Modelling : Part II. The General Theory of Oxidational Wear. Wear 175, p. 199-208
Quinn, T.F.J., Winer, W.O. (1985) The Thermal Aspects of Oxidational Wear. Wear, 102 p. 67-80
Rabinowicz, E. (1958) New Coefficients Predict Wear of Component Parts. Product Engineering, June 23
Rabinowicz, E. (1977) The Dependanceof Adhesive Wear Coefficient on the Surface Energy of Adhesion. Proc..Int.Conf. on Wear of Materials., p. 36-40
Reichner, P. (1981) Wear Induced Profiles of Brushes on Eccentric Rotors. Wear, Westinghouse Research and Development Centre, Pittsburgh, PA, Sept.
Reid, J.V., Schey, J.A. (1987) The Effect of Surface Hardness on Friction. Wear, 118, (1987) p. 113-125, March 31
Reynell, M.J.W., Clark, I.W., Rosten, H.I., (1991) A Two-Level Micro/Macro Approach to the Simulation of Air Flow And

Heat Transfer in Typical Convection-Cooled Electrical Systems. ASME Paper 91-WA-EEP-33
Rigney, D.A. (1994) The Roles of Hardness in the Sliding Behaviour of Materials. Wear, 175 p. 63-69
Rigney, D.A., Hirth, J.P. (1979) Plastic Deformation and Sliding Friction of Metals. Wear 53, p. 345-370
Rodkiewicz, C. M., Wang, Y. (1993) A Dry Wear Model Based on Energy Conciderations. 031-679X/94/03/0145-07, Tribology International, Dept. Mech. Eng. University of Alberta, Canada, 3rd Nov.
Rosenfield, A.R. (1987) A Shear Instability Model of Sliding Wear. Wear, 116 p. 319-328
Rozeanu, L. and Pnueli, D. (1982) The Wear of the Harder Member in a Friction Couple. Wear, 87, (1983) p.317-330, Dec 11
RuthenBerg, M.L (1973) Mating Materials ans Environment Combinations for Specific Contact and Clearance-Type Seals. Lubrication Engineering, Vol. 29 p. 58-64, Feb
Scheidegger, A.E (1957) The Physics of Flow Through Porous Media. University of Toronto Press.
Scheidegger, A.E. (1974) The Physics of Flow Through Porous Media. Third Edition, University of Toronto Press, ISBN 0-8020-1849-1, LC 74-185869
Schlumberger, J.A., Proctor, M.P., Hendricks, R.C. (1991) Eccentricity Effects on Leakage of a Brush Seal at Low Speeds. NASA TM 105141, Lewis Research Centre, Cleaveland Ohio.
Shafia, M.A., Eyre, T.S. (1979) The Effect of Surface Topography on the Wear of Steel. Wear, Dept of Metallurgy, Brunel University, Middlesex.
Silence, W.L. (1978) Effect of Structure on Wear Resistance of Co-, Fe-, and Ni- Base Alloys. Journal of Lubrication Technology., Vol 100, p. 428-435, July
Singhal, A.K. (1992) Validation of CFD Codes and Assessment of CFD Simulations. Rotating Machinery 1992, Proc. of the 4th Int. Symp. on Transport Phenomena and Dynamics of Rotating Machinery., CFD Research Corporation, Huntsville, AL 35805
Smart, R.F., Moore, J.C. (1979) Materials Selection for Wear Resistance. Wear 56, p. 55-67
Sneck, H.J. (1973) Labyrinth Seal Literature Survey. ASME
Soda, N., Sasada, T. (1977) Mechanism of Lubrication by Surrounding Gas Molecules in Adhesive Wear. Proc.Int.Conf. on Wear of Materials, p. 47-54
Spink, G.M. (1990) Fretting Fatigue of a 2.5%NiCrMoV Low Pressure Turbine Shaft Steel - The Effect of Different Contact Pad Materials and of Variable Slip Amplitude. Wear, 136, p. 281-297
Stango, R.J., Heinrich, S.M., Shia, C.Y. (1989) Analysis of Constrained Filament Deformation and Stiffness Properties of Brushes. Journal of Engineering for Industry, August 1989,Vol. 111, p. 238-243.
Stodola et al. (1927) Steam and Gas Turbines. McGraw-Hill Book Company
Stott, F.H., Glascott, J., Wood, G.C. (1984) Factors Affecting the Progressive Development of Wear- Protective Oxides on Iron-Base Alloys During Sliding at Elevated Temperatures. Wear 97, p. 93-106
Stott, F.H., Glascott, J., Wood, G.C. (1985) The Sliding and Wear of Commercial Fe-12%Cr Alloys at High Temperature. Wear
Stott, F.H., Lin, D.S., Wood, G.C. and Stevenson, C.W. (1975) The Tribological Behaviour of Nickel and Nickel-Chromium Alloys at Temperatures from 20 to 800 C. Wear, 36, p.147-174, May 1
Stott, F.H., Wood, G.C. (1978) The Influence of Oxides on the Friction and Wear of Alloys. Tribology International, Vol. 11, p. 211-218
Thomas, M.W. Contribution of Metallic and Oxide Contact to Static Adhesion. Wear 64, p. 133-150.
Tien, J.K., Purushothaman, S. (1976) The Metallurgy of High Temperature Alloys. Proc.Symp Properties Of High Temperature Alloys (with Emphasis on Environmental Effects)
Tribology Handbook (1994) 22- Labyrinths, Brush Seals and Throttling Bushes.
Tucker, R.C., Miller, A.E. (1976) Low Stress Abrasive and Adhesive Wear Testing. ASTM STP 615, p. 68-90
Turbine Efficiency Design Manual. Parsons Turbine Generators
Turner, M.T., Chew, J.W., Long, C.A. (1997) Experimental Investigation and Mathematical Modelling of Clearance Brush Seals. Presented at the International Gas Turbine and Aeroengine Congress and Exhibition. Orlando, Florida, June 2-5, ASME 97-GT-282
Vafai, K., Tien, C., L. (1981) Boundary and Inertia Effects on Flow and Heat Transfer in Porous Media. Int.J.of Heat and Mass Transfer, Vol 24, p. 195-203
Waite, J. (1993) Preliminary Reading Report. MIF, Parsons Turbine Generators, 10th November
Waite, J. (1994) The Application of Brush Seals in Steam Turbines. GM00416, MIF, 17 May
Waite, J. (1994) Notes on meetings at Rolls-Royce, Derby (04.08.94.) to discuss CFD modelling of brush seals and the Rolls-Royce Material Databases. MIF, 4th August.
Waite, J. (1994) Brush Seal Applications. Notes on a Presentation (and subsequent discussion) given by Mr.J.Waite (University of Northumbria), at Parsons Turbine Generators 07.06.94. MIF, 7th June
Waite, J. (1994) A Frictional Model for Brush Seals. MIF, Parsons Turbine Generators, Oct.
Waite, J. (1996) Materials Review for Brush Seals in Steam Turbines. GS 96 - 4, MIF, Parsons Turbine Generators, 23rd. Jan.
Waite, J. (1996) High Temperature Wear Testing for Brush Seals in Steam Turbines. 65 96 - 5, MIF, Parsons Turbine Generators, 5th Jan
Waite, J. (1996) Brush Seals - Leakage Performance Tests at Parsons P.G.S.-An Interim PhD Report for the University of Northumbria. MEMS, University of Northumbria, Sept.
Waite,J. (1996) High Temperature Wear Testing and Oxidation Testing of Candidate Bristle Materials for Brush Seals in Steam Turbines. MIF, Parsons Turbine Generators, 1st.August
Ward, R. (1970) A Comparison of Recipricating and Continuous Sliding Wear. Wear 15, p. 435-448
Whitaker, S. (1969) Advances in Theory of Fluid Motion in Porous Media. Vol 51. p.14-28
Wittig, S., Jacobsen, K., Schelling, U., Kim, S. (1987) Numerical Predictions and Measurments of Discharge Coefficients in Labyrinth Seals. ASME 87-GT-188, May 31-June 4
Wittig, S., Jacobsen, K., Schelling, U., Kim, S. (1988) Heat Transfer in Stepped Labyrinth Seals. Journal of Engineering for Gas Turbines and Power, Vol. 110, Jan
Zabriskie, W., Sternlicht, B. (1959) Labyrith Seal Leakage Analysis. ASME, Sept
Zmitrowicz, A.(1987) A Thermodynamic Model of Contact, Friction and Wear: I Governing Equations. Wear 114, p. 135-168
Zmitrowicz, A. (1987) A Thermdynamical Model of Contact, Friction, and Wear: III Constitutive Equations for Friction, Wear and Frictional Heat. Wear 114-116
Zum Gahr, K.H. (1988) Modelling of Two-Body Abrasive Wear. Wear, 124 pp 87 -103